



**TECHNISCHE  
UNIVERSITÄT  
DRESDEN**

Fakultät Maschinenwesen

Institut für Werkzeugmaschinen und Steuerungstechnik

# Conference on Thermal Issues in Machine Tools

PROCEEDINGS

CIRP SPONSORED CONFERENCE  
DRESDEN 2018









# **Conference on Thermal Issues in Machine Tools**

**PROCEEDINGS**



**CIRP SPONSORED CONFERENCE  
DRESDEN 2018**

# ***Imprint***

## **Conference on Thermal Issues in Machine Tools**

Edited by

**Prof. Dr.-Ing. Steffen Ihlenfeldt**

**Prof. Dr.-Ing. Christian Brecher**

**Prof. Dr.-Ing. Matthias Putz**

**David Billington**

All rights reserved.

No part of this publication may be reproduced or transmitted by any means, electronic, mechanical, photocopying or otherwise without the prior permission of the publisher.

**TU Dresden**

**Institute of Machine Tools Development and Control Engineering**

**Chair of Machine Tool Development and Adaptive Controls**

Helmholtzstraße 7a, 01069 Dresden, Germany

e-mail: [mailbox@iwm.mw.tu-dresden.de](mailto:mailbox@iwm.mw.tu-dresden.de)

**Collaborative Research Centre CRC/TR 96**

e-mail: [sekretariat@transregio96.de](mailto:sekretariat@transregio96.de)

**©2018**

ISBN: 978-3-86780-586-5

## Editorial Committee

ARRAZOLA P.-J., Mondragon Unibertsitatea, Faculty of Engineering, Manufacturing Mechanical and Manufacturing Department

BIERMANN D., TU Dortmund, Institute of Machining Technology

BLEICHER F., TU Wien, Institute for Production Engineering and Laser Technology

BUDAK E., Sabanci University, Faculty of Engineering & Natural Sciences

DENKENA B., Leibniz Universitaet Hannover, Institute of Production Engineering and Machine Tools

DROSSEL W.-G., Fraunhofer Institute for Machine Tools and Forming Technology IWU

HOREJŠ O., Czech Technical University in Prague, Department of Production Machines and Equipment, RCMT

JEDRZEJEWSKI J., Wroclaw University of Technology, Faculty of Mechanical Engineering

KARAGUZEL U., Isik University, Mechanical Engineering Department

KNAPP W., ETH Zurich, Institute of Machine Tools and Manufacturing

LAW M., Indian Institute of Technology, Kanpur, Department of Mechanical Engineering,

MÖHRING H.-C., University of Stuttgart, Institute for Machine Tools

MORIWAKI T., Setsunan University, Faculty of Engineering

NEUGEBAUER R., Fraunhofer-Gesellschaft zur Förderung der angewandten Forschung e.V.

ÖZEL T., Rutgers State University of New Jersey, Manufacturing Automation Research Lab

URIARTE L., IK4 Tekniker, Parke Teknologikoa

VALASEK M., Czech Technical University in Prague, Faculty of Mechanical Engineering

WEGENER K., ETH Zurich, Institute of Machine Tools and Manufacturing

WERTHEIM R., Fraunhofer Institute for Machine Tools and Forming Technology IWU

ZÄH M., Technical University of Munich, Institute for Machine Tools and Industrial Management

# Table of Contents

## Holistic modelling strategies

<b>Efficient modelling and computation of structure-variable thermal behavior of machine tools</b>	13
--	----

S. Schroeder, A. Galant, B. Kauschinger, M. Beitelschmidt

<b>Parameter identification software for various thermal model types</b>	23
--	----

B. Hensel, S. Schroeder, K. Kabitzsch

<b>Minimising thermal error issues on turning centre</b>	35
--	----

M. Mareš, O. Horejš, J. Hornych

<b>The methods for controlled thermal deformations in machine tools</b>	47
---	----

A. P. Kuznetsov, H.-J. Koriath, A.O. Dorozhko

<b>Efficient FE-modelling of the thermo-elastic behaviour of a machine tool slide in lightweight design</b>	61
---	----

C. Peukert, J. Müller, M. Merx, A. Galant, A. Fickert, B. Zhou, S. Städtler, S. Ihlenfeldt, M. Beitelschmidt

## Design of thermal robust machine tools

<b>Development of a dynamic model for simulation of a thermoelectric self-cooling system for linear direct drives in machine tools</b>	75
--	----

E. Uhlmann, L. Prasol, S. Thom, S. Salein, R. Wiese

<b>System modelling and control concepts of different cooling system structures for machine tools</b>	<b>93</b>
---	-----------

J. Popken, L. Shabi, J. Weber, J. Weber

<b>The electric drive as a thermo-energetic black box</b>	<b>107</b>
---	------------

S. Winkler, R. Werner

<b>Thermal error compensation on linear direct drive based on latent heat storage</b>	<b>117</b>
---	------------

I. Voigt, S. Winkler, R. Werner, A. Bucht, W.-G. Drossel

<b>Industrial relevance and causes of thermal issues in machine tools</b>	<b>127</b>
---	------------

M. Putz, C. Richter, J. Regel, M. Bräunig

#### **Approaches considering environmental conditions**

<b>Clustering by optimal subsets to describe environment interdependencies</b>	<b>143</b>
--	------------

J. Glänzel, R. Unger, S. Ihlenfeldt

<b>Using meta models for enclosures in machine tools</b>	<b>159</b>
--	------------

F. Pavliček, D. P. Pamies, J. Mayr, S. Züst, P. Blaser, P. Hernández-Becerro, K. Wegener

<b>Model order reduction of thermal models of machine tools with varying boundary conditions</b>	<b>169</b>
--	------------

P. Hernández-Becerro, J. Mayr, P. Blaser, F. Pavliček, K. Wegener

<b>Effectiveness of modelling the thermal behaviour of the ball screw unit with moving heat sources taken into account</b>	<b>179</b>
--	------------

J. Jedrzejewski, Z. Kowal, W. Kwasny, Z. Winiarski

### **Thermal robust sub-assemblies**

<b>Analyzing and optimizing the fluidic tempering of machine tool frames</b>	<b>195</b>
--	------------

A. Hellmich, J. Glänzel, A. Pierer

<b>Thermo-mechanical interactions in hot stamping</b>	<b>211</b>
---	------------

L. Penter, N. Pierschel

### **Approaches considering cutting processes**

<b>Experimental analysis of the heat flux into the grinding tool in creep feed grinding with CBN abrasives</b>	<b>225</b>
--	------------

C. Wrobel, D. Trauth, P. Mattfeld, F. Klocke

<b>Development of multidimensional characteristic diagrams for the real-time correction of thermally caused TCP-displacements in precise machining</b>	<b>235</b>
--	------------

M. Putz, C. Oppermann, M. Bräunig

<b>Measurement of near cutting edge temperatures in the single point diamond turning process</b>	<b>245</b>
--	------------

E. Uhlmann, D. Oberschmidt, S. Frenzel, J. Polte

<b>Investigation of heat flows during the milling processes through infrared thermography and inverse modelling</b>	<b>257</b>
---	------------

T. Helmig, T. Augspurger, Y. Frekers, B. Döbbeler, F. Klocke, R. Kneer

<b>Thermally induced displacements of machine tool structure, tool and workpiece due to cutting processes</b>	<b>269</b>
---	------------

O. Horejš, M. Mareš, J. Hornych

### **Thermo-energetic analysis and modelling, shown by the example of spindles**

<b>A new calibration approach for a grey-box model for thermal error compensation of a C-Axis</b>	<b>281</b>
---	------------

C. Brecher, R. Spierling, M. Fey

<b>Investigation of passive torque of oil-air lubricated angular contact ball bearing and its modelling *</b>	<b>291</b>
---	------------

J. Kekula, M. Sulitka, P. Kolář, P. Kohút, J. Shim, C. H. Park, J. Hwang

<b>Cooling strategy for motorized spindle based on energy and power criterion to reduce thermal errors *</b>	<b>301</b>
--	------------

S. Grama, A. N. Badhe, A. Mathur

<b>Cooling potential of heat pipes and heat exchangers within a machine tool spindle</b>	<b>305</b>
--	------------

B. Denkena, B. Bergman, H. Klemme, D. Dahlmann

### **Control-integrated correction of thermal displacements**

<b>Structure model based correction of machine tools</b>	<b>319</b>
--	------------

X. Thiem, B. Kauschinger, S. Ihlenfeldt

<b>Optimal temperature probe location for the compensation of transient thermal errors</b>	329
--	-----

G. Aguirre, J. Cilla, J. Otaegi, H. Urreta

<b>Adaptive learning control for thermal error compensation on 5-axis machine tools with sudden boundary condition changes</b>	339
--	-----

P. Blaser, J. Mayr, F. Pavliček, P. Hernández-Becerro, K. Wegener

<b>Hybrid correction of thermal errors using temperature and deformation sensors</b>	349
--	-----

C. Naumann, C. Brecher, C. Baum, F. Tzanetos, S. Ihlenfeldt, M. Putz

#### **Technical and analytical measurement issues**

<b>Optimal sensor placement based on model order reduction</b>	365
--	-----

P. Benner, R. Herzog, N. Lang, I. Riedel, J. Saak

<b>Workpiece temperature measurement and stabilization prior to dimensional measurement</b>	377
---	-----

N. S. Mian, S. Fletcher, A. P. Longstaff

<b>Measurement of test pieces for thermal induced displacements on milling machines *</b>	389
---	-----

H. Höfer, H. Wiemer



<b>Model reduction for thermally induced deformation compensation of metrology frames *</b>	403
---	-----

J. v. d. Boom

<b>Local heat transfer measurement</b>	409
--	-----

A. Kuntze, S. Odenbach, W. Uffrecht

### **Holistic perspectives**

<b>Thermal error compensation of 5-axis machine tools using a staggered modelling approach</b>	421
--	-----

J. Mayr, T. Tiberini, P. Blaser, K. Wegener

<b>Design of a Photogrammetric Measurement System for Displacement and Deformation on Machine Tools</b>	431
---	-----

M. Riedel, J. Deutsch, J. Müller, S. Ihlenfeldt

<b>Thermography on Machine Tools</b>	443
--------------------------------------	-----

M. Riedel, J. Deutsch, J. Müller, S. Ihlenfeldt

<b>Test piece for thermal investigations of 5-axis machine tools by on-machine measurement</b>	453
--	-----

M. Wiesener, P. Blaser, S. Böhl, J. Mayr, K. Wegener

\* unreviewed articles

## **Holistic modelling strategies**

---



# Efficient modelling and computation of structure-variable thermal behaviour of machine tools

*S. Schroeder<sup>a</sup>, A. Galant<sup>a</sup>, B. Kauschinger<sup>a</sup>, M. Beitelschmidt<sup>b</sup>*

<sup>a</sup>Institute of Machine Tools and Control Engineering IWM, Technische Universität Dresden,  
01062 Dresden, Germany

<sup>b</sup>Institute of Solid Mechanics IFKM, Technische Universität Dresden, 01062 Dresden,  
Germany

**Abstract.** Thermal models are used to improve the thermal behaviour of machine tools. They are used for evaluation of design alternatives and for controller based correction. Therefore lumped parameter network models and finite element models with reduced model order are utilized. For both of these model variants methods for efficient modeling and computation are presented. Based on this, a new concept is presented that combines the two model variants appropriate for the given problem. This combination allows a continuous model development alongside the machine design process.

Peer-review under responsibility of the International Scientific Committee in the person of the Conference Chair Prof. Steffen Ihlenfeldt.

*Keywords:* Machine Tools; Thermal Behaviour; Modelling; Analysis; Correction

---

## 1 Simulation of the thermal behaviour of machine tools

A large part of machining errors of today's machine tools can be traced back to their thermo-elastic behaviour. Therefore, the control of this behaviour has a special relevance [1]. Models are used for evaluation and optimization of the behaviour as well as for the correction of thermal errors. In this article models are examined, that reproduce the behaviour of the machine tools along the entire thermo-elastic chain (Fig. 1).

The technological, energetic, thermo-elastic and kinematic system components of the thermo-elastic chain contain numerous specific details such as: hydroelastodynamic, hydrostatic, fluidic and electrical power losses; complex heat transfer mechanisms; fine-structured frames; cooling systems as well as structure variability through relative movement. In order to describe this multi-domain behaviour, a new simulation methodology was developed. It uses the

conventional methods of digital block simulation and finite element modelling (FEM) which are suitable for the machine tool behaviour and combines them with new methods to reduce the present deficits.

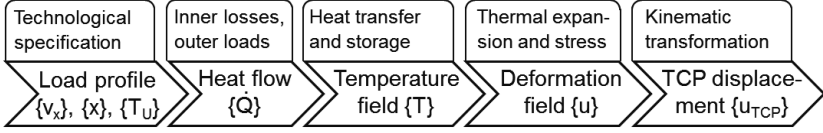


Fig. 1. Chain of cause and effect in the thermo-elastic behaviour of machine tools

The methodology is characterized by a geometrically oriented approach. Geometric bodies are derived from components of the machines. This generates models that describe the thermal storage, conducting and deformation behaviour of solids. The bodies are connected to a network via link elements. These body connections can represent many behavioural forms: from merging of two bodies to heat exchange depending on structural assignment. Furthermore, the solids can be applied with loads that describe the various forms of internal heat loss and heat exchange with the environment.

The modelling methodology has been developed in two forms, which differ particularly in geometric detailing. First lumped parameter modelling, which reproduce the machine tool structures with low geometric resolution. And second, FEM based modelling. This method allows for high geometric resolution and uses Model Order Reduction (MOR) methods to reduce the numerical effort. The two modelling types are suitable for different tasks during the life cycle of the machine tool. The lumped parameter modelling can be used for rough analysis tasks in the conceptual and early design stages. FEM based modelling, on the other hand, can be used for analyses in the design stage and for control-based correction. However, continuous support throughout the entire lifecycle of the machine is desirable. Ideally, the model should be developed alongside the design progress of the machine tool. The article introduces a concept that makes this approach possible.

## 2 Generalized lumped parameter network modelling

The basic building block of lumped parameter networks for representation of transient thermal processes is an elementary model of a thermal body. As shown in Fig. 2, the state of this body is described with the caloric mean temperature  $T$ . The system properties of the body are represented with the parameters of heat storage capacity  $C$  and heat conductance  $L$  to its environment. A source heat flow  $\dot{Q}$  can also be fed into the body.

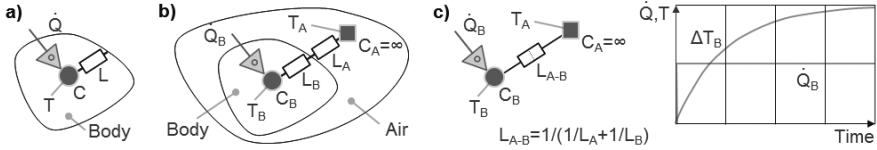


Fig. 2. Basic building block lumped network models (a) and linking of two basic building blocks to a minimal model of a body in air (b, c)

A net-like lumped parameter model for the simulation of real systems is obtained when several of these basic building blocks are linked together [2]. Fig. 2 b) shows this with a minimal example of a body in ambient air. The air can also be understood as a basic building block. The total conductance is determined from the connected partial conductance values of the building blocks. In this case, the temperature of the air is "clamped". Fig. 2 c) shows the typical exponential function like response of the body temperature if the body's heat source raises step wise.

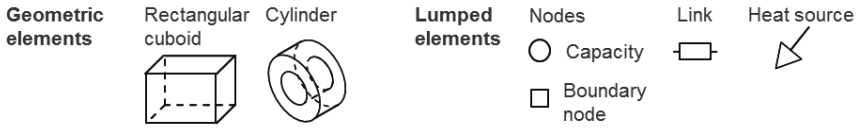


Fig. 3. Model elements for lumped parameter network modelling

For a generalized modelling approach, a kit of thermal elements has been developed (Fig. 3). Linking several instances of these elements creates the model description. From this, the basic building blocks of an executable network model with their parameters are automatically derived. The resulting model is then used for the simulation process of the thermal analysis.

The modelling of the entire system is based on the following scheme:

- The machine tool structure is divided into geometric basic bodies such as cuboids and cylinders. Simplified bounding bodies replace slender structures.
- A corresponding geometric element is created for each basic body.
  - Thermal material parameters are assigned to the element. If the body consists of several different materials, a homogenized material is used instead.
  - Thermal loads are applied to the elements either as surface or volume loads.
- The thermal environment of the geometric elements is represented by

node elements.

- The thermal connection between contacting body surfaces is automatically generated by link elements of infinite conductivity. Further thermal connections are created manually via link elements. The link elements are assigned with empirical approaches for heat transfer via convection, heat radiation, heat transfer by mass transport as well as for time-variable structural assignment.

### 3 MOR-FEM network modelling

The FEM based modelling with model order reduction (MOR-FEM) happens analogously to lumped parameter modelling. The geometry of the entire machine structure is first divided into individual assemblies. In contrast to the lumped parameter model, the reduction in the degree of freedom of the individual assembly models is not achieved by geometrical simplification. Instead mathematical MOR methods are applied on the FE assembly models.

MOR methods offer an efficient way to create computational timesaving, small-scale models with a good approximation capability directly from an FE model [3]. Investigations showed, the Krylov-MOR method is very well suited for the thermal domain. Applied to the closely meshed FE model of a machine frame, savings of three orders of magnitude in computing time and model degree of freedom could be achieved. The simulated temperatures of the reduced model showed mean deviations of 0.03 % in respect to the original [4].

Starting point of the reduction is a state space representation of the thermal sub problem (Eq. 1, left) after FEM discretization.

$$\begin{Bmatrix} u_1 \\ \vdots \\ u_k \end{Bmatrix} \rightarrow \begin{array}{c} \boxed{\begin{array}{l} \{T\} + [A]\{T\} = [B]\{u\} \\ \{y\} = [C]^T \{T\} \end{array}} \rightarrow \begin{Bmatrix} y_1 \\ \vdots \\ y_m \end{Bmatrix} \xRightarrow{\text{MOR}} \begin{Bmatrix} u_1 \\ \vdots \\ u_k \end{Bmatrix} \rightarrow \begin{array}{c} \boxed{\begin{array}{l} \{\hat{T}\} + [\hat{A}]\{\hat{T}\} = [\hat{B}]\{u\} \\ \{\hat{y}\} = [\hat{C}]^T \{\hat{T}\} \end{array}} \rightarrow \begin{Bmatrix} \hat{y}_1 \\ \vdots \\ \hat{y}_m \end{Bmatrix} \quad (\text{Eq. 1})$$

The MOR process transforms the original FE model (Eq. 1, left) into a reduced model (Eq. 1, right) that is structure and parameter equivalent and has less degree of freedom than the FE model. The input signals are time-dependent parameters that describe the loads applied to the FE model. The vectors  $\{T\}$  and  $\{\hat{T}\}$  are the corresponding state vectors in the original and reduced system. The output signals represent the observable state values as temperatures in FE nodes. The reduced output signal vector  $\{\hat{y}\}$  approximates  $\{y\}$ . The algorithms for transforming the system, control and measurement matrices  $[A]$ ,  $[B]$  and  $[C]$  into the corresponding reduced forms can be found in [4]. To sum it up:

- The generation of the reduced model is independent of concrete variables of the input signals and parameters.
- The structure of the original system is explicitly retained in the reduced system.
- The reduced model has a much smaller dimension compared to the non-reduced FE model and can therefore be calculated faster by several orders of magnitude.
- The second equation of Eq. 1 provides the rule for retransformation of reduced image "temperatures" to the full temperature vector of the original FE-model.

With the realized combination of FEM and MOR, a typical geometric complexity of machine tools can be efficiently modelled. This means that compact and computational timesaving models can now be generated from high-resolution FE models with non-linear boundary conditions (such as radiation).

The basic concept of MOR-FEM corresponds to the lumped parameter network modelling principle and is briefly outlined below. The model is implemented as a Simulink signal plan. The basic elements have been implemented as blocks of the proprietary Simulink library. A detailed description can be found in [5]. The modelling is based on the following scheme:

- First, the entire machine tool structure is broken down into assemblies without any relevant internal relative movements. The assembly geometry is not or only slightly refined.
- Afterwards, the following sub-steps are performed for each assembly:
  - The assembly geometry is imported into the FEM environment, cross-linked and provided with thermal material parameters. The assembly FE model is then generated.
  - The node areas for load applications (usually on surfaces) are marked.
  - The assembly FE model is transformed into the compact, timesaving MOR model using the MOR process described above.
- After all assemblies have been treated, they are connected to each other and to the environment nodes by means of special link elements, taking into account the structural variability and thermal boundary conditions.
- In the last step, the network model is parameterized, i.e. the input data (movement mode, external heat flows, ambient temperatures, etc.) are defined.



## 4 Incremental model development on the example of a hexapod

This chapter introduces the concept of incremental model development over the life cycle of a machine, considering the development steps concept phase, design phase and operating phase. The concept of incremental model development provides for a step-by-step development of the thermo-elastic machine model. The presented modelling methods are combined according to their respective advantages.

The procedure is explained using the example of the thermal behaviour of hexapod struts. The struts in this machine are of particular thermal relevance. Their electromechanical drive components heat the strut components by friction heat and electrical losses. The subsequent thermo-elastic longitudinal elongation of the strut has a negative influence on the machine's accuracy.

### 4.1 Concept phase

Initially, the concept phase involves making fundamental design and functional decisions. No absolute statements about specific constructive solutions are required. Rather, qualitative comparative statements on roughly outlined variants are of interest. The analysis models must represent the rough ideas in this phase. Simple geometric designs exist for the structural components of the machine components. These can be modelled very efficiently using the presented construction kit for lumped parameter network modelling.

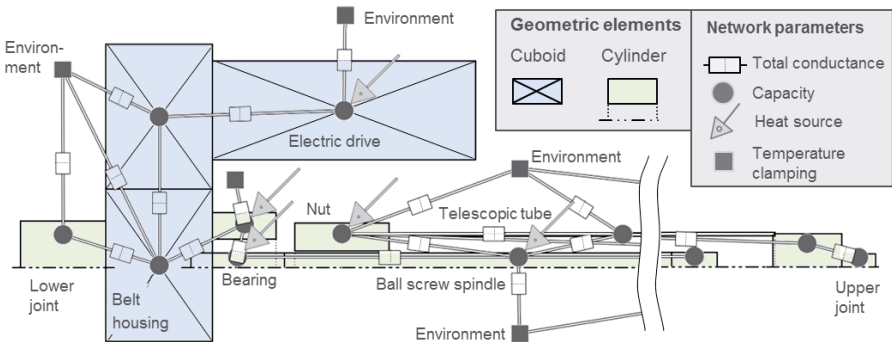


Fig. 4. Strut model consisting of model elements with the corresponding run-ready network model

Fig. 4 shows such a thermal concept model of the Hexapod strut. The joints, the belt housing and the motor are modelled with homogenized solid bodies. The rest of the components have largely realistic geometries. The heat transfer to the environment and the ambient air, some of which position-dependent heat

transitions between the ball screw spindle and surrounding components are modelled by means of link elements. The model is completed by heat sources representing the power dissipation of the motor, bearing and ball screw nut.

The model is used to evaluate design concepts. A chosen example of typical analyses is the thermal decoupling of the drive motor. The purpose of decoupling is to keep the motor's electrical losses away from the precision critical components. In the present case, the motor has been moved outwards from the axis centre and coupled to the ball screw spindle via a toothed belt. A representative snapshot of the calculated thermal behaviour is shown in Fig. 5. The snapshot has been created using a visualization methodology that makes the simulation results easily accessible to an interpretation. This is done by displaying the lumped model properties and the associated behavioural variables temperature and heat flow in the context of geometry. The properties and variables are represented by symbols. The area of the symbols scales with the quantitative value. This provides a qualitative overview of all relevant properties and conditions and allows to estimate the effect of individual machine components on the thermal behaviour.

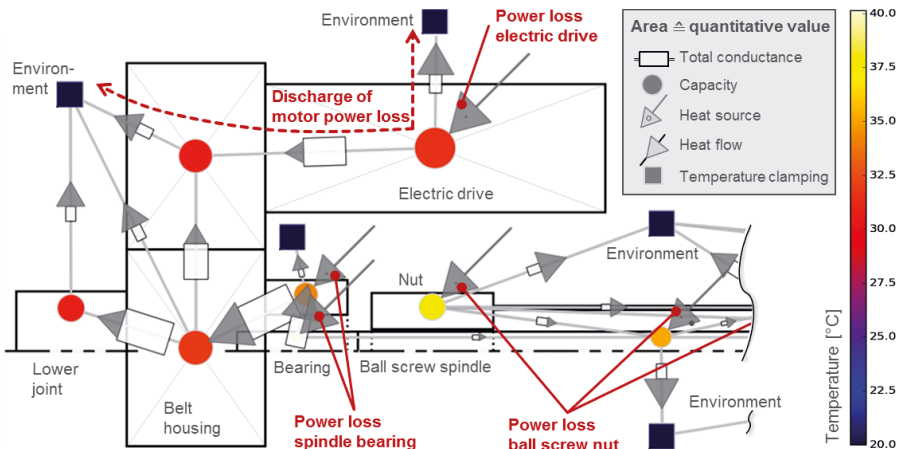


Fig. 5. Visualization of model and result variables of the simulative analysis

In the case of the drive, the arrow like heat source and the color-coded temperature rise indicates, that the motor is a significant heat source. However, the heat loss discharges to the environment – not to the accuracy-relevant parts like the lower belt housing, spindle and telescopic tube. This can be seen from the indicated direction of the triangular heat flow symbols. The heat flows over the outer drive surfaces and the upper belt housing to the environment. There-

fore, it can be concluded that the motor hardly influences accuracy because it doesn't affect the longitudinal strut expansion significantly.

## 4.2 Design phase

After the basic design decisions have been made in the concept phase, the machine components are now constructively designed. In the accompanying analyses, decisions on detailed design variants must be made. Quantitative model results are now of interest. The analysis models should be gradually adapted to the development progress. The model detail should be determined according to the thermal influence of the assembly. With increasing geometric complexity of the structural components, manual-modelling effort of lumped parameter network modelling increases. A transition to MOR-FEM is advisable here, as CAD data of individual assemblies are increasingly available.

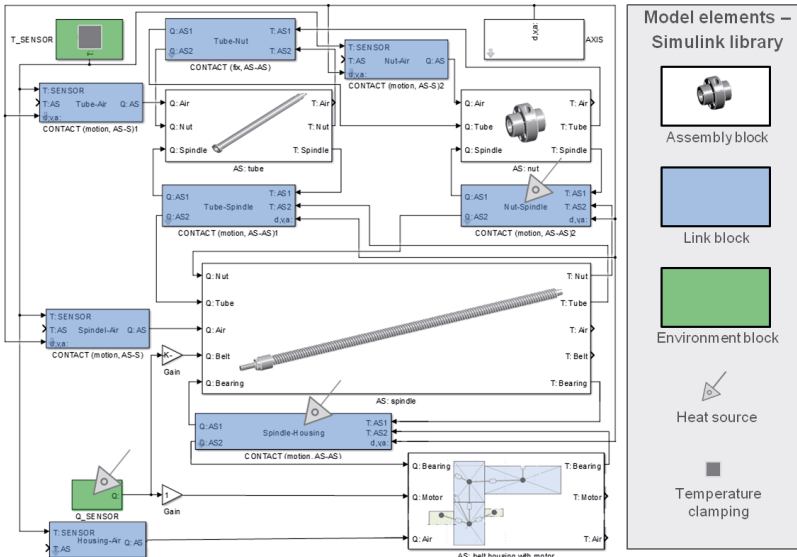


Fig. 6. Hybrid strut model with parts of MORFEM and lumped parameter network parts

The model doesn't need to be re-created, as the two types of modelling can be combined due to identical principles and mechanisms. In both cases the machine structure is divided into individual geometry-related network nodes. These nodes are connected by means of link elements that take thermal boundary conditions and structural variability into account. Finally, the network model derived from the model description has a compatible state space representation.

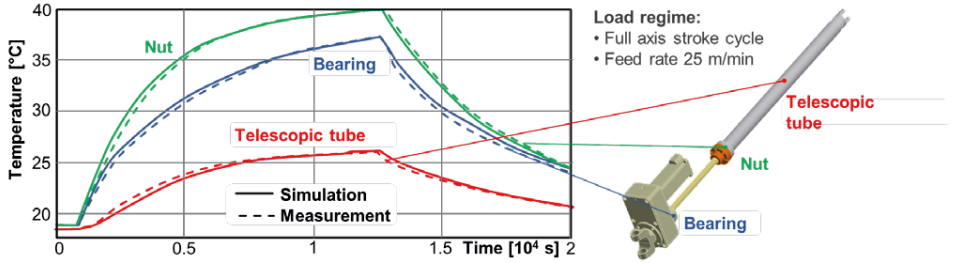


Fig. 7. Calculated and measured temperatures of the hexapod strut

Fig. 6 shows such a further developed model of the design phase. It is used to analyse the influence of thermal behaviour on accuracy. Therefore, the model must be able to quantitatively predict the precision-relevant thermo-elastic longitudinal expansion of the strut. Based on previous analyses, the precision relevant assemblies are selected and modelled in detail with MOR-FEM. After the adjustment of two main heat source parameters the comparison of measured and calculated temperatures (Fig. 7) shows a high level of correlation. Furthermore, it can be estimated from the increase of temperature that longitudinal expansions of 100  $\mu\text{m}$  will likely occur.

### 4.3 Operating phase

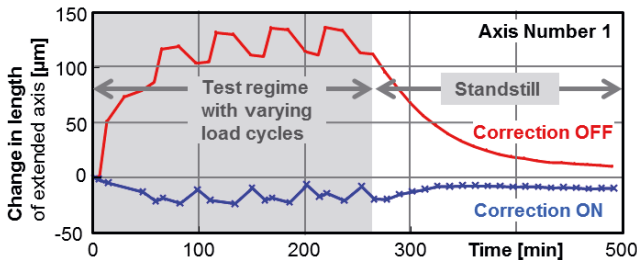


Fig. 8. Control assisted correction of the thermo-elastic hexapod strut elongation according to [6]

The control-integrated correction during operation is an effective measure to improve thermal behaviour. The model used for the analysis can be used to predict the correction values in the controller. The model is suitable for this real-time application because the ratio of simulation time to operation time is about 1:400. Such a correction application for the Hexapod has already been implemented, verified and successfully presented [7]. Figure 8 shows the effect of the correction. Due to the high accuracy of the model, the thermal error of the axis can be largely compensated.

## 5 Conclusion

A new methodology for the simulation of the thermo-elastic behaviour of machine tools in motion has been introduced. The methodology is characterised by the efficient application-oriented use of different network-based modelling techniques. This enables efficient model development as well as fast computation. The model does not have to be developed "from zero" at every stage of the life cycle of the real machine, but instead grows incrementally. The resulting models have a network character similar to networks used in digital block simulation tools and can describe many other physical domains besides thermo-elastic ones. This makes the proposed methodology also suitable for modelling of big machine tools with much broader thermal behaviour.

### *Acknowledgements*

*This research was funded by the German Science Foundation (DFG) within the CRC Transregio 96 "Thermo-energetic design of machine tools" projects A05 and B04.*

## 6 References

- [1] Mayr, J., Wegener, K., Uhlmann, E., Brecher, C., Knapp, W., et al. 2012. Thermal issues in machine tools. *CIRP Annals - Manufacturing Technology*;61(2):771–91.
- [2] Jungnickel, G., 2010. Simulation des thermischen Verhaltens von Werkzeugmaschinen. Modellierung und Parametrierung, Lehre Forschung Praxis. TU Dresden IWM.
- [3] Schilders, W., van der Vorst, H., Rommes, J., 2000. Model Order Reduction: Theory, Research Aspects and Applications. Springer Berlin Heidelberg.
- [4] Galant, A., Großmann, K., Mühl, A., 2015. Thermo-elastic simulation of entire machine tool, in: *Thermo-Energetic Design of Machine Tools, Lecture Notes in Production Engineering*. Berlin u.a., pp. 69–84.
- [5] Beitel Schmidt, M., Galant, A., Großmann, K., Kauschinger, B., 2015. Innovative Simulation Technology for Real-Time Calculation of the Thermo-Elastic Behaviour of Machine Tools in Motion. *Applied Mechanics and Materials*, 794, pp. 363-370.
- [6] Naumann, C., et al. 2017. Experimentelle Analyse modellbasierter Korrekturverfahren für Thermo-elastische Verformungen im Online-Einsatz an einer Demonstratormaschine. 5. Kolloquium SFB/TR 96, Chemnitz 23.03.2017
- [7] Großmann, K., Kauschinger, B., Merx, M., Riedel, M., Galant, A. 2014. Effiziente modell- und experimentgestützte Analyse des thermischen Verhaltens von Werkzeugmaschinen. *Industrie 4.0 – die intelligente Fabrik der Zukunft Tagungsband Wiener Produktionstechnik Kongress 2014*. Wien, Österreich: Klein Publishing GmbH; 2014. S. 271–80.

# Parameter Identification Software for Various Thermal Model Types

*B. Hensel<sup>a</sup>, S. Schroeder<sup>b</sup>, K. Kabitzsch<sup>a</sup>*

<sup>a</sup>Institute of Applied Computer Science, Technische Universität Dresden, 01062 Dresden, Germany

<sup>b</sup>Institute of Machine Tools and Control Engineering IWM, Technische Universität Dresden, 01062 Dresden, Germany

**Abstract.** For modeling the thermal behaviour of machine tools, a wide range of model types is used, reaching from finite element models over thermal network models to simple transfer functions. All model types have in common that the parameters of each model have to be optimized to fit to the real, modeled machine as closely as possible, i.e. the parameters have to be identified using real measurements. In this paper, a new software solution is presented which allows parameter identification in a unified way. Additionally, a comparison of the accuracy reached by different thermal models for the same modeled machine component is given.

Peer-review under responsibility of the International Scientific Committee in the person of the Conference Chair Prof. Steffen Ihlenfeldt.

*Keywords:* Parameter Optimization; Process Identification; Actuator Strut

---

## 1 Introduction

The quality of products that are produced with machine tools depends on a variety of factors. Besides exactness of manufacturing of the machine tool itself, the product quality is influenced by the deformation of the machine tool due to load and thermal expansion. The latter one is in the focus of this paper. Many models exist that describe the thermal behavior of machine tools or its components, reaching from complex finite element models over multibody dynamic systems, physical or geometric models, hybrid models, thermal resistance networks, state-space models, grey systems, and neural networks to simple transfer functions or linear regression models. Giving example references for each type of model would exceed the page limit of this paper; some broader overviews on thermal models are given in [1-6].

If a model is not used for predicting the behavior of a *not yet existing* machine (e.g. for design decisions), but for modeling an *already existing* object, the choice of parameter values of the model is not limited to theoretically computed values or empirical constants, but *measurements* at the real machine tool can be used for comparing simulation outputs with reality and subsequent adjustment of uncertain parameters.

The focus of this paper lies on the *thermal* simulation of *machine tools*. However, the proposed methods and the implemented prototype software are also suited for other physical domains where simulation models are used to model real objects with many different types of models.

Identification of model parameters is a quite common task in many engineering fields. Hence, there is a lot of literature regarding that topic [7-9]. However, most literature concentrates on some special cases, especially linear models like difference equations, differential equations, or transfer functions, because the ideal parameter values of such models can be computed *analytically*, i.e. without numerical optimization algorithms.

However, for thermal models of machine tools there exists a broader range of models. In particular, finite element models are often used for detailed simulation of geometrically complex deformation or heat flows. Such models are not supported by usual analytical process identification approaches. In practice, the parameters of such models are “optimized” by manual trial and error or using generic optimization algorithms, i.e. by repeated simulation with varied parameters and choice of the parameter set that minimized the mean difference between measurements and simulation outputs [10, 11].

Most literature on thermal models of machine tools does not mention parameter identification in detail. Several published works use regression or least-squares method (e.g. [2, 12-14]). Other system identification methods are used rarely [15,16]. Besides such generic approaches, many application-specific parameter identification concepts exist (e.g. [15, 17]).

In [18, 19] a new methodology and software prototype has been presented that has been designed to provide a *unique* parameter optimization software and user interface for *many* model types without the need for re-implementing existing models in a new software. However, in these papers only the basic features had been implemented. In the meantime, the concept has been extended and the implementation went on. In *this paper*, the focus lies on the new features of the software, i.e. a generic concept of coupling external simulation software like Matlab and ANSYS, that is often used for creating thermal models

of machine tools. The second contribution of this paper is a comparison of three models for the same modeled object. All models have been optimized with the new software. The comparison takes into account modeling effort, parameter count, accuracy etc.

## 2 Software overview

The basis of the software is a relatively small “core”, called the “identification coordinator”. The identification coordinator provides the basic functionalities for management of systems and transport of signals between files, simulation models, and optimization algorithms.

That software provides a plug-in interface that is used for providing different types of models [19]. This interface can also be used for coupling external software. The core (identification coordinator) provides different generic optimization methods, such that the software is flexible regarding model types.

There are currently four different strategies for coupling external modeling and simulation software to the core, shown in Fig. 1:

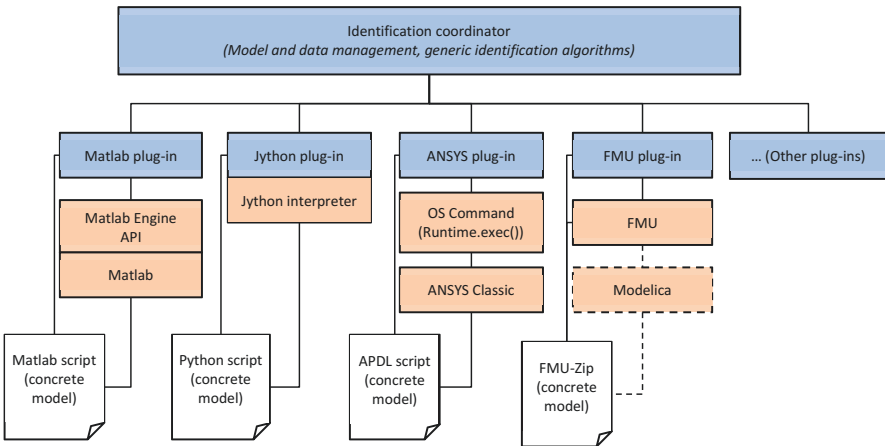


Fig. 1. Different kinds of interfaces to external simulation software, shown with one concrete example for each type of coupling.

1. If the external software provides an application programming interface (API), this can be called by the appropriate plug-in. This is the strategy for coupling software products like Matlab with the Matlab Engine API.
2. If the external software is small enough, it can be integrated in the plug-in itself. This is the way how script file interpreters like the Python inter-



preter Jython can be coupled, allowing simulating models described with Python scripts.

3. If the external software neither provides an API nor can be directly integrated into the software, it can usually be called by basic operation system functionalities with command line arguments. This is the typical strategy how e.g. script-based finite element model solvers like ANSYS can be integrated. The concrete machine tool model is described in a script (e.g. APDL script for ANSYS), the plug-in calls the external software with the path to that script.
4. Much simulation software supports the standardized interface FMI (Functional Mock-up Interface). Functional Mock-up Units are Zip-Files containing a describing XML-File, a shared library (e.g. DLL) including the model code, and perhaps additional files like data, images etc. A plug-in for the identification coordinator has been created that allows optimizing parameters of FMUs. In that way, all models that have been created with external software supporting an FMU export (e.g. Modelica) can be optimized using the identification coordinator.

The work flow of using the software is similar to that described in [18, 19].

### **3 Application example: Models of an actuator strut**

The new software has been used for optimizing the parameters of three different model types that have been modeled with three different software products. All three model types have been used to model the same object. The three models are briefly explained in the following and a comparison of the reached model accuracy, modeling effort, and identification effort is given.

#### **3.1 Application description**

The application example is an actuator strut. Actuator struts are used in machine tools for moving either the tool or the work piece. Fig. 2 shows the modeled actuator strut and the positions where temperature sensors have been installed.

The temperature has been measured at seven positions of the actuator strut and the air. At the beginning, the machine has been “cooled down” to have a common initial temperature field. After the start the tube (the right half of the object in Fig. 2) moved cyclically to the left and to the right what leads to nonuniform incremental heating of the machine and thermo-elastic deformation.

Fig. 3 shows one set of temperature measurements (for a feed-rate of 20m/min) that is taken as the “reference data” for parameter identification. It contains 74 samples that are roughly equidistant.

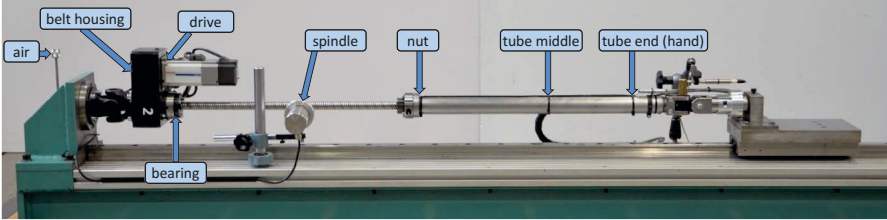


Fig. 2. Photo of the modeled actuator strut. Marked are the temperature sensor positions.

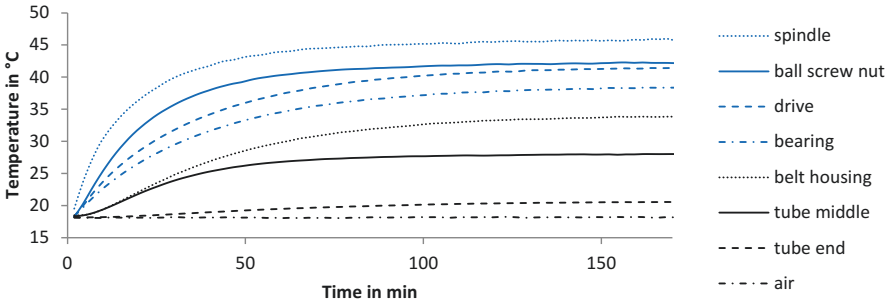


Fig. 3. Measurements used for parameter identification of all model types.

### 3.2 Model types

In this section, the three thermal model types are presented that are evaluated and compared.

#### Finite element model

Finite element models divide a geometric object into many small parts, called elements. The parts are described using partial differential equations, i.e., both the spatial and temporal characteristics are used for modeling.

Finite element models have, due to the many elements, potentially thousands of parameters, because each node can have own parameters. Additionally, boundary conditions (e.g., given temperatures or heat flows at boundaries) and initial conditions raise the number of parameters.

The actuator strut has only been modeled two-dimensionally. The model (mesh, i.e. the elements) is shown in Fig. 4. The mesh has 2480 nodes (4095 linear triangular elements) and has been created using Matlab PDE toolbox using the default mesh size.

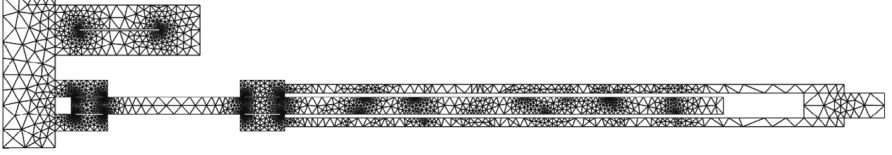


Fig. 4. Finite element model of the actuator strut (mesh/elements).

Each node is modeled using the differential equation for heat conduction

$$\rho \cdot c \cdot \frac{\partial T}{\partial t} - \text{div}(k \cdot \text{grad } T) = 0$$

or an adapted version that is discretized in space and time.  $\rho$  is the density,  $c$  the specific heat capacity,  $T$  the temperature offset compared to the initial temperature,  $k$  the coefficient of heat conduction,  $t$  the time.  $\text{div}$  is the divergence,  $\text{grad}$  the gradient. At the boundaries there are either Neumann boundary conditions (a given heat flow) or convective boundary conditions.

The strengths of finite element models are that the geometric relation of elements is directly taken into account and that a field of output variables (e.g., temperature field) is computed. The drawbacks are the large amount of parameters, the long simulation time, the long time for modeling and the problem of parameter reduction.

### Equivalent circuit model

The actuator strut can be modeled as a set of “nodes” (parts of the modeled object) between which heat flows. Each node has a heat capacity  $C_i$  and between each connected pair of nodes there is a heat conductance  $g_{ij}$ . Nodes where heat is produced (i.e. motor, bearing, and ball screw nut) have additionally a heat loss parameter  $\dot{Q}_i$ . The equation for each node with index  $i$  is

$$C_i \cdot \frac{d\vartheta_i(t)}{dt} = \dot{Q}_i + \sum_{j=1, j \neq i}^P g_{ij} \cdot (\vartheta_j(t) - \vartheta_i(t))$$

where  $P$  is the number of nodes and  $\vartheta_i(t)$  is the temperature of node  $i$  as a function of time  $t$ .

This type of model is analogous to an electrical circuit. Therefore, it is called an equivalent circuit model or a thermal network model. If the number of nodes is large, the difference to a finite element model decreases. The actuator strut has been modeled using 19 nodes (components), see Fig. 5. There are totally 209 parameters. That is too much for optimization. However, many parameters can be computed from theoretical investigations or are negligible. Additionally, several parameters are a result of the same physical constants, so the same value can be used for several parameters. More details about the model structure and the strategy of parameter reduction are given in [19]. After model reduction, only 5 parameters to be optimized are remaining. These parameters are the heat losses of the bearing, the motor, and the ball screw nut, as well as the heat conduction between the spindle and the air, and the heat conduction between the tube and the air.

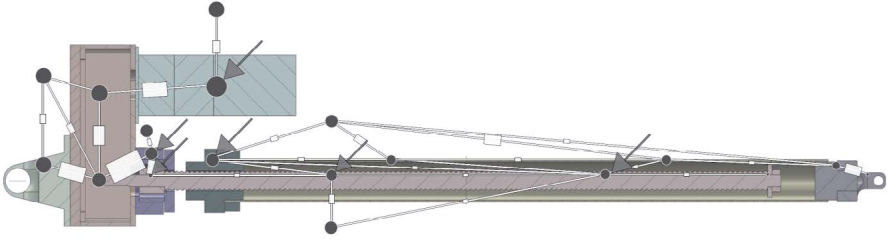


Fig. 5: Equivalent circuit model of the actuator strut.

### Set of transfer functions

Transfer functions are simple models, especially used in systems theory, signal processing, and controller design. For each measurement position  $i$  the transfer function

$$G(s) = \frac{Y_i(s)}{V(s)} = \frac{K_i}{1 + sT_i} e^{-L_i}$$

has been used that is equivalent to the differential equation

$$y_i(t) + T_i \frac{dy_i}{dt}(t) = K_i v(t - L_i)$$

where  $v(t)$  is the input (feed-rate),  $y_i(t)$  the output (temperature offset compared to initial temperature at the sensor position),  $T_i$  the time constant,  $L_i$  a time delay, and  $K_i$  the gain or proportional action coefficient.  $Y_i(s)$  and  $V(s)$  are the Laplace transforms of  $y_i(t)$  and  $v(t)$ , respectively;  $s$  is the Laplace variable [20]. This type of transfer function is called a FOPTD (first-order plus time delay)

model. For optimization, a discrete-time equivalent model is identified (discrete-time transfer function or difference equation) and subsequently converted to the continuous-time FOPTD model (see [19] for conversion equations).

Each FOPTD model has three parameters (gain or proportional action coefficient  $K_i$ , time constant  $T_i$ , and time delay  $L_i$ ). Thus, since there are seven sensor positions, seven independent FOPTD models are used and hence totally 21 parameters are optimized. As it is a linear model, the optimal values of  $K_i$  and  $T_i$  can be computed analytically and hence very fast. Only the time delay  $L_i$  has to be estimated in an iterative way.

More details about the used model structure can be found in [19].

### 3.3 Comparison of the model types

All three models have been optimized using the new identification coordinator, i.e. the optimal values of the unknown parameters have been computed based on the data of Fig. 3.

Regarding comparison of model types, first of all, the accuracy of each model after parameter optimization is compared. This is evaluated using the root-mean-square error (RMSE) for each sensor position  $i$ , i.e.

$$RMSE_i = \sqrt{\frac{\sum_{j=1}^N (T_{i,meas,j} - T_{i,sim,j})^2}{N}}$$

where  $N$  is the number of measurements (samples, here 74),  $T_{i,meas,j}$  is the measurement value (temperature) at measurement position  $i$  and sample  $j$ , and  $T_{i,sim,j}$  is the simulation output (temperature at sensor position) at measurement position  $i$  and sample  $j$ . The results are shown in Table 1. In the first seven rows, only one temperature sensor has been used as reference, i.e. all parameters are optimized for this position. In the last row, the mean of all seven  $RMSE_i$  has been optimized, what is in general *not* the mean of the cases before, if the parameters have influence on more than one measurement point. This is especially visible at the equivalent circuit model.

Table 1 shows that the set of transfer functions allows the closest model to the measurement data, although it has the simplest structure. That is because of the 21 parameters that have only little interaction. The other models have less independent parameters and each parameter has influence on all simulation outputs.

Table 1. Root-mean-square error in K for different model types at each sensor position (after model optimization), feed-rate 20m/min.

Optimized for Temperature Sensor (TS) position	Finite element model	Equivalent circuit model	Set of transfer functions
TS Spindle only	2.37	0.13	0.66
TS Nut only	0.83	0.16	0.74
TS Drive only	0.90	0.81	0.45
TS Bearing only	0.91	0.29	0.40
TS Belt housing only	1.24	0.30	0.51
TS Tube middle only	1.76	0.10	0.48
TS Tube end (hand) only	0.68	0.27	0.08
<b>Mean of all TS</b>	<b>1.24</b>	<b>1.73</b> ( <i>see explanation above</i> )	<b>0.47</b>

However, all models have in common that the underlying equations are linear. Because of that, since the real thermal behavior is nonlinear, for all model types the error (RMSE) is much larger if the optimized model is used for other feed-rates (comparable to [19]). Since two model parameters of the transfer function can be computed analytically, after reaching the result, it is clear that the theoretical optimum has been reached. The other models can never guarantee that the optimum has been reached.

Table 2 compares the model types regarding different criteria, especially the modeling effort and simulation time. The shorter the simulation time, the more simulations can be run in the same time and the faster the parameter optimization progresses. All optimization runs have been done on the same hardware; therefore the simulation times are comparable. Also Table 2 confirms the advantages of the set of transfer functions – the time for model creation is much smaller, and the optimization is the fastest.

## 4 Conclusions

New features of a recently designed software prototype have been presented that allows identification of model parameters in a unified form, but for different model types using different external modeling software. The software proved that it is especially suited for thermal models of machine tools (components) as there are many different model types that are used in that research field, all needing parameter identification. A comparison of three model types

made clear that both the accuracy of a model and the identification effort are not directly related to the model complexity.

Table 2. Comparison of model types regarding different criteria.

Criterion	Finite element model	Electrical circuit model	Set of transfer functions
Optimized independent parameters	7	5	21
Mean time for one simulation, in s	1.71	0.43	0.01
Approximated time for model creation, in h (assuming all necessary know-how regarding the modeling software)	3	40 (many parameters have to be computed manually)	<0.5
Used Software	Matlab 2016b script, PDE Toolbox	Python script	Java implementation
Analytical optimization	Not possible	Not possible	Partially ( $K_i$ and $T_i$ )
Mean RMSE, in K	1.24	1.73	0.47

### Acknowledgements

*This work has been funded by the German Research Foundation in the collaborative research centre/Transregio 96.*

## 5 References

- [1] Jedrzejewski, J., 2009. Thermal problems in Machine Tools Design and Operation, In: Mekid, S. (ed.): Introduction to Precision Machine Design and Error Assessment, CRC Press, Boca Raton.
- [2] Junyong, X., Youmin, H., Bo, W., and Tielin, S., 2008. Research on thermal dynamics characteristics and modeling approach of ball screw. International Journal of Advanced Manufacturing Technology (2009), 43, Springer, pp. 421-430.
- [3] Li, Y., Zhao, W., Lan, S., Ni, J., Wu, W., Lu, B., 2015. A review on spindle thermal error compensation in machine tools. International Journal of Machine Tools & manufacture 95 (2015), pp. 20-38.
- [4] Mayr, J., Jedrzejewski, J., Ulmann, E., et al., 2012. Thermal issues in machine tools. CIRP Annals – Manufacturing Technology, 61, pp. 771-791.

- [5] Großmann, K., ed., 2015. Thermo-energetic Design of Machine Tools: A Systemic Approach to Solve the Conflict Between Power Efficiency, Accuracy and Productivity Demonstrated at the Example of Machining Production. Cham: Springer.
- [6] Jungnickel, G., 2010. Simulation of thermal behaviour of machine tools – Modeling and Parameterization. (In German: Simulation des thermischen Verhaltens von Werkzeugmaschinen – Modellierung und Simulation). Technische Universität Dresden, Chair for Machine Tools and Control Engineering.
- [7] Söderström, T., Stoica, P., 1989. System Identification. Prentice Hall, Hemel Hempstead.
- [8] Isermann, R., Münchhof, M., 2011. Identification of Dynamic Systems – An Introduction with Applications. Springer, Heidelberg.
- [9] Ljung, L., 1999. System Identification – Theory for the User. 2<sup>nd</sup> ed., Prentice Hall, Upper Saddle River.
- [10] Sanayei, M., Rohela, P., 2014. Automated finite element model updating of full-scale structures with PARAmeter Identification Systems (PARIS). Advances in Engineering Software, vol. 67, 99-110.
- [11] Wernsing, H., Büskens, C., 2015. Parameter identification for finite element based models in dry machining applications. Procedia CIRP, vol. 31, 328-333.
- [12] Theuws, F.C.C.J.M., 1991. Enhancement of Machine Tool Accuracy: Theory and implementation. PhD thesis, Technische Universiteit Eindhoven.
- [13] Rahman, M., 2004. Modeling and measurement of multi-axis machine tools to improve positioning accuracy in a software way. PhD thesis, University of Oulu.
- [14] Chen, T.-C., Chang, C.-J., Hung, J.-P., Lee, R.-M., Wang, C.-C., 2016. Real-Time Compensation for Thermal Errors of the Milling Machine. Applied sciences 2016, volume 6, issue 4, article 101.
- [15] Abuaniza, A., Fletcher, S., Simon, M., Naeem, S., Longstaff, A. P., 2016. Thermal Error Modelling of a CNC Machine Tool Feed Drive System using FEA Method. International Journal of Engineering Research & Technology, 5 (3). pp. 118-126.
- [16] Kim, B.-S., Park, J.-K., 2014. Thermal error compensation for a high-precision lathe. Proceedings of the 9th international workshop on microfactories, Honolulu.
- [17] Spur, G., Lechler, G., Heisel, U., 1977. Methods for reducing thermal influences on the accuracy of machine tools. Proceedings of the 3rd International Conference on Production Engineering, 1977, pp. 10-22.
- [18] Hensel, B., Kabitzsch, K., 2016. Generator for modular virtual sensors. Proceedings of the 21<sup>st</sup> IEEE International Conference on Emerging Technologies and Factory Automation (ETFA 2016), Berlin, Germany, September 2016, 8 pages.
- [19] Hensel, B., Schroeder, S., Kabitzsch, K., 2017. New coordination software for parameter identification applied to thermal models of an actuator strut. Journal of Computational Engineering, vol. 2017, article ID 3169785.
- [20] Levine, W. S., 2000. Control systems fundamentals. Boca Raton: CRC Press.





# Minimising Thermal Error Issues on Turning Centre

*M. Mareš, O. Horejš, J. Horných*

Research Center of Manufacturing Technology RCMT, Czech Technical University in Prague,  
Horská 3, Prague, 128 00, Czech Republic

**Abstract.** Advanced compensation models of machine tool thermal errors were successfully applied on various kinds of milling machines and implemented directly into their control systems as described in the author's previous works. This paper is focused on applicability of the modelling approach to a completely different machine tool type from an operation principle and mechanical structure point of view: turning centre. The working space is smaller than in milling machine cases and mutual separation of participating heat sinks and sources on resultant thermal error is a real issue. Therefore, different potential inputs into several model structures is discussed in more details.

Peer-review under responsibility of the International Scientific Committee in the person of the Conference Chair Prof. Steffen Ihlenfeldt.

*Keywords:* Turning centre; Thermal error; Transfer function; Real-time compensation

---

## 1 Introduction

Thermally induced displacements at the tool centre point (TCP) of a machine tool (MT) structure cannot be sufficiently reduced by design concept and/or by temperature control without significant additional cost. On the contrary, indirect (software) compensation of thermally induced displacements at the TCP is one of the most widely employed techniques to reduce MT thermal errors due to its cost-effectiveness and ease of implementation.

Ordinarily, approximation models are based on measured auxiliary variables [1] (temperatures, spindle speed, etc.) used for calculation of the resulting thermally induced displacements at the TCP. Many strategies were investigated to establish the models, e.g. multiple linear regressions [2], artificial neural networks [3], transfer functions (TF) [4], etc. (for more details see [5]).

Although real-time software compensations of thermal errors exist, these compensations have a number of serious drawbacks. The majority of these

approaches only presume MT thermo-mechanical behaviour under conditions similar to the calibration measurements [6]. In this article it is shown that more than a reliable mathematical approach (demonstrated with a system of TFs in this case) is necessary to construct a robust approximation model. The modeling effort itself and correct exploitation of the input signals is essential as well.

## 2 Experimental setup

All experiments were performed on a turning centre with a sub spindle (used as a tailstock) as shown in Fig. 1. The MT was equipped with a number of thermal probes (Pt100, Class A, 3850 ppm/K) placed close to thermal sinks and sources (such as feed drives, spindle bearings, hydraulics, tool turret, surrounding etc.). A spindle speed signal value taken from the MT control system was also recorded.

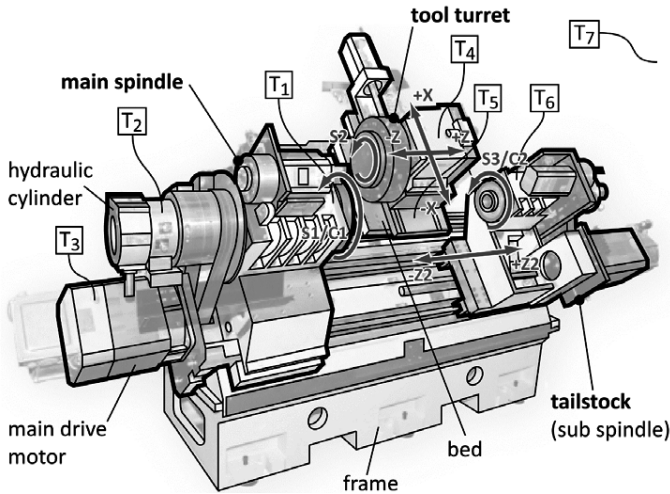


Fig. 1. Schema of turning centre and temperature probe placements.

MT thermal deformations measured between the workpiece surface and TCP ( $\delta_{TCP}$ ) generally consist of three elements (according to (Eq. 1)): MT frame deformation ( $\delta_{frame}$ ; influence of feed drive activity, spindle bearings, removed material, ambient temperature etc.), tool elongation ( $\delta_{tool}$ ; impact of cutting process) and workpiece deformation ( $\delta_{workpiece}$ )

$$\delta_{TCP} = \delta_{frame} + \delta_{tool} + \delta_{workpiece} \quad (\text{Eq. 1})$$

Analysis of tool and workpiece elongations is out of scope of this article. **The paper mainly focuses on issues concerning MT frame thermal deformations due to activity of the dominant thermal source – spindle rotation.**

Eddy current sensors firmly clutched in measuring fixtures were employed for noncontact sensing of displacement of a control bar in  $X$  and  $Y$  directions (namely  $\delta_{x1}$  and  $\delta_y$  according to Fig. 2). The measuring fixture was attached to the tool turret (the usual tool position) and the control bar was fixed into the main spindle representing a workpiece. Angular deformations of the control bar were also measured and neglected in comparison to the magnitude of linear deformations in both directions. One additional inductive sensor was used for sensing displacement between the tool turret and the tailstock (static sub spindle equipped with second control bar) in  $X$  direction (namely  $\delta_{x2}$ , see Fig. 2).

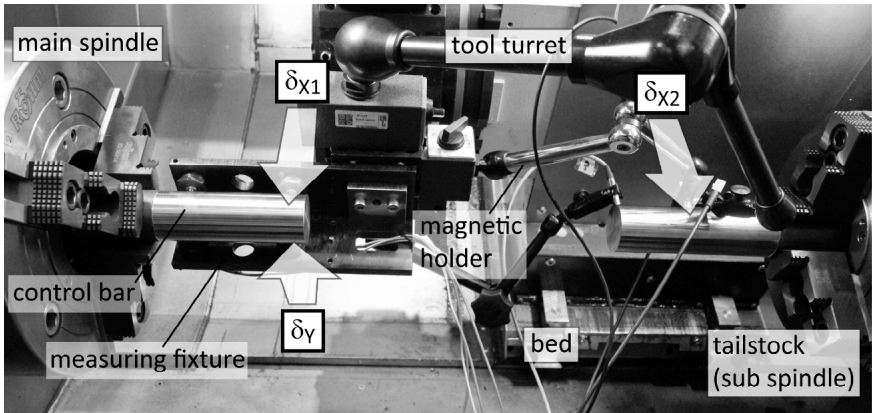


Fig. 2. Experimental setup of thermal deformation measurement according to ISO 230-3.

Progress and setup of a complete test (duration of 28 hours) is depicted in Fig. 3. The whole experiment is divisible into two parts:

- **Calibration** (constant spindle speed)
  - Heating phase (1000 rpm)
  - Cooling phase
- **Verification** (change in spindle speed)
  - Spectrum no. 1 (2000, 500, 1500, 2500, 1000 rpm)
  - Cooling phase
  - Spectrum no. 2 (2000, 1750 rpm)

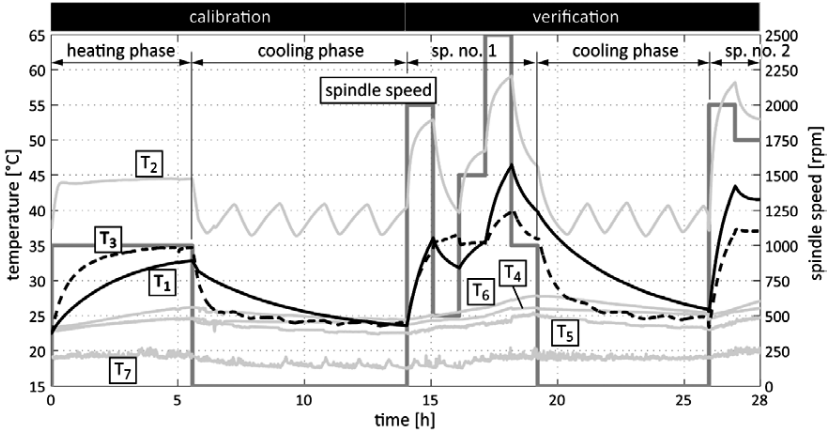


Fig. 3. Measurement development; inputs into compensation model.

### 3 Calibration, identification and modelling

A discrete TF was used to describe the link between the excitation (temperature) and its response (displacement). The differential form of the TF in the time domain is introduced in (Eq.2)

$$y(k) = \frac{u(k-n) \cdot a_n + \dots + u(k-1) \cdot a_1 + u(k) \cdot a_0}{b_0} - \left( \frac{y(k-m) \cdot b_m + \dots + y(k-1) \cdot b_1}{b_0} \right), \quad (\text{Eq. 2})$$

where  $y(k)$  is the TF output vector,  $u(k)$  is the input vector,  $a_n$  are weight factors of TF input,  $b_m$  are weight factors of TF output and  $k-n$  ( $k-m$ ) means the  $n$ -multiple ( $m$ -multiple) delay in sampling frequency. Linear parametric models of ARX or OE identifying structures were used. The quality of each TF was examined through linear time invariant (LTI) step response [7].

An approximation quality is shown in (Eq. 3). This value expresses the percentage of the output variation that is reproduced by the model [7].

$$fit = \left( 1 - \frac{\|Y - \hat{Y}\|}{\|Y - \bar{Y}\|} \right) \cdot 100. \quad (\text{Eq. 3})$$

The  $Y$  value in (Eq. 3) means the measured output (thermal deformation),  $\hat{Y}$  is the simulated (predicted) model output and  $\bar{Y}$  expresses the arithmetic mean over time of the measured output. The vector norm used in (Eq. 3) is generally expressed as  $\|y\| = \sqrt{y_1^2 + y_2^2 + \dots + y_n^2}$  where  $y$  is general vector.

Correlation analysis expressing interrelation between measured deformations and temperatures is represented by (Eq. 4).

$$r_{x,y} = \left| \frac{E(X \cdot Y) - E(X) \cdot E(Y)}{\sqrt{E(X^2) - E^2(X)} \cdot \sqrt{E(Y^2) - E^2(Y)}} \right| \cdot 100, \quad (\text{Eq. 4})$$

where  $r_{x,y}$  is correlation coefficient,  $E$  is expected value operator and  $X$  and  $Y$  are vectors of measured thermal deformations and temperatures.

Generally, calibration should describe a transient characteristic between two thermodynamic equilibria; one with the MT surroundings and one with all active thermal sinks and sources meant to be approximated (spindle speed in this case). Heating and cooling of the MT may cause thermal behavior to differ. Therefore, the calibration measurement usually consists of both phases.

### 3.1 X axis

Measured deformations between the tool turret and the main spindle ( $\delta_{x1}$ ) represent errors observed on the workpiece. However, those deformations have no apparent correlation with measured temperatures (see Table 1). In other words there is no desired linear dependency between measured deformations and temperatures. The reason is indispensable influence of thermal

load not only on the main spindle but also on the tool turret behavior as depicted in Fig. 4.

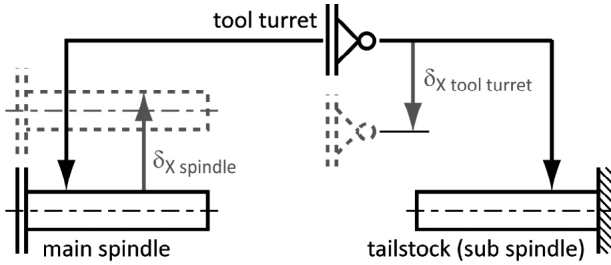


Fig. 4. Description of thermal behaviour in X axis.

A possible solution inheres in presumption that the tailstock is thermally insulated from influence by active thermal sources. The tailstock is regarded as a fixed point in the thermo-deformation chain spindle - tool turret - tailstock. Measured deformations in X direction are then reconstructed by a sum of tool turret

( $\delta_{X \text{ tool turret}}$ ) and spindle ( $\delta_{X \text{ spindle}}$ ) deflections towards the fixed point (see Fig. 4).

Separated thermal deformation of the tool turret expressed by measured values is shown in (Eq. 5) and the thermal deformation of the spindle in (Eq. 6)

$$\delta_{X \text{ tool turret}} = \delta_{X2}. \quad (\text{Eq. 5})$$

$$\delta_{X \text{ spindle}} = \delta_{X2} - \delta_{X1}. \quad (\text{Eq. 6})$$

Deformational elements  $\delta_{X \text{ tool turret}}$  (Eq. 5) and  $\delta_{X \text{ spindle}}$  (Eq. 6) already have good correlations with some of the measured temperatures. The correlation analysis between measured temperatures and deformations is presented in Table 1. Temperatures used in the approximation model are highlighted in the table.

Table 1. Correlation coefficients of measured temperatures and deformations during the whole test.

Deformations	Temperatures						
	$T_1$	$T_2$	$T_3$	$T_4$	$T_5$	$T_6$	$T_7$
	Correlation coefficient ( $r_{x,y}$ ) [%]						
Measured ( $\delta_{X1}$ )	36.5	36.7	67.8	28.9	10.9	6.03	27.4
Tool turret ( $\delta_{X \text{ tool turret}}$ )	96	56.4	<b>81.9</b>	41.6	77.5	64.3	21.7
Main spindle ( $\delta_{X \text{ spindle}}$ )	<b>93.9</b>	48.1	<b>63.2</b>	61	84.3	76.9	37.6

Approximation of desired thermal deformations between tool turret (tool position) and spindle (workpiece fixturing) is expressed by (Eq. 7). The influence of ambient temperature was neglectable during the whole experiment.

$$\delta_{x1 model} = \underbrace{\Delta T_3 \cdot \varepsilon_1}_{\delta_{X tool turret}} + \underbrace{(k_1 \cdot \Delta T_1 + k_2 \cdot \Delta T_3) \cdot \varepsilon_2}_{\delta_{X spindle}}, \quad (\text{Eq. 7})$$

Where  $\Delta T_1$  and  $\Delta T_3$  are temperatures in relative coordinates measured close to active heat sources (main spindle and its drive),  $\varepsilon_1$  is TF approximating deformations of the tool turret and  $\varepsilon_2$  is TF approximating deformations of the main spindle (calibration coefficients of identified TFs are summarized in Table 2.). Weight coefficients  $k_1 = -2.2$  and  $k_2 = 0.85$  in (Eq. 8) were obtained experimentally.

Measured and calculated displacements are shown in Fig. 5. The approximation quality of identified TFs are there expressed by the *fit* value (Eq. 3).

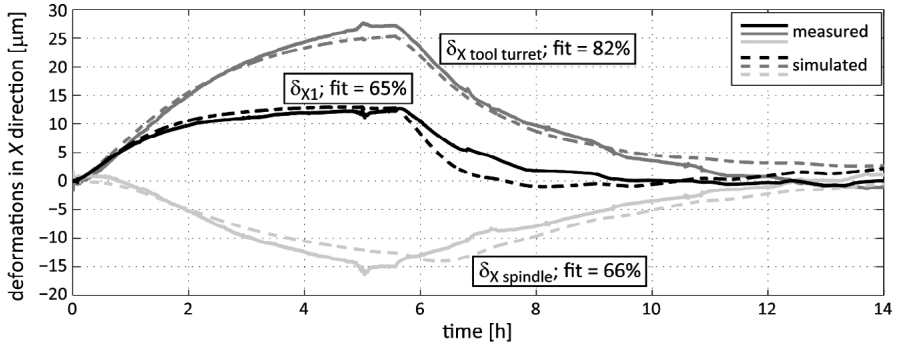


Fig. 5. Measured and simulated thermal displacement in X direction during calibration test.

### 3.2 Y axis

A strong correlation was observed between measured deformations in Y direction and temperature  $T_1$ . The influence of the tool turret deflection on thermal deformations in Y axis is linear. There is no need to take it into account. Contrary, it is necessary to describe heating and cooling phases separately. Approximation of thermal deformations between tool turret and spindle ( $\delta_y$ ) is expressed as:



$$\delta_{Y\ model} = (k_3 \cdot \Delta T_1) \cdot \varepsilon_3 + (k_4 \cdot \Delta T_1) \cdot \varepsilon_4. \quad (\text{Eq. 8})$$

Coefficient  $k_3$  in (Eq. 8) indicates heating and  $k_4$  the cooling phase. In practice, it means that  $k_3 = 1 \wedge k_3 = 0$  when the main spindle is active and otherwise,  $k_3 = 0 \wedge k_3 = 1$  when spindle speed is equal to 0.  $\varepsilon_3$  and  $\varepsilon_4$  are TFs approximating thermal deformations occurred during heating and cooling phases.

Measured and calculated displacements of examined direction Y along with the *fit* value (Eq. 3) are shown in Fig. 6.

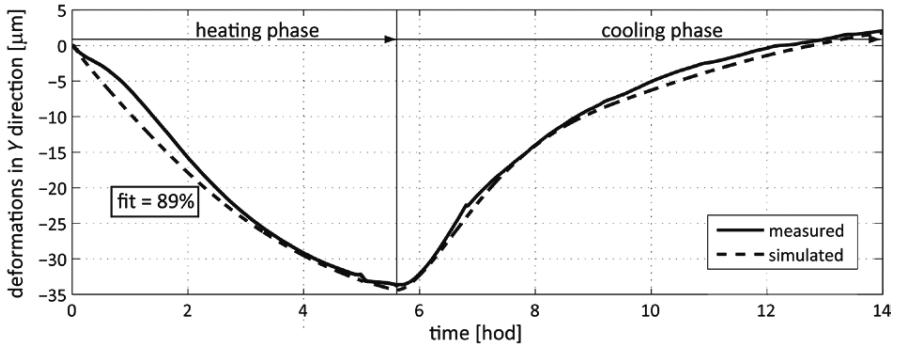


Fig. 6. Measured and simulated thermal displacement in Y direction during calibration test.

The next table summarizes the calibration coefficients of identified TFs used in (Eq. 7) and (Eq. 8).

Table 2. Calibration coefficients of identified TFs for approximation of MT thermal errors.

TF ( $\varepsilon$ )	Coefficients									
	$a_0$	$a_1$	$a_2$	$a_3$	$b_0$	$b_1$	$b_2$	$b_3$	$b_3$	
1	1.6	-3.19	1.59	-	1	-1.9567	0.9568	-	-	
2	0.257	-0.252	-0.262	0.258	1	-1.0534	-0.0578	-0.7212	0.83244	
3	-0.198	0.1982	-	-	1	-1.39	-0.1077	0.4978	-	
4	0.032	-0.035	-0.028	0.0309	1	-1.8147	0.5392	0.3662	0.0907	

## 4 Verification of modelling approach

The setup of experiments to verify the identified models from (Eq. 7) and (Eq. 8) was chosen from the following point of view: testing model's sensitivity to changes in heat source magnitude as compared with calibration measurement. Setup of the verification test containing processes of input values into compensation models is depicted in Fig. 3.

Measured and simulated thermal deformations during the verification test in  $X$  and  $Y$  directions are depicted in Fig. 7. The approximation quality expressed by the *fit* value (Eq. 3) is likewise presented in the graphs.

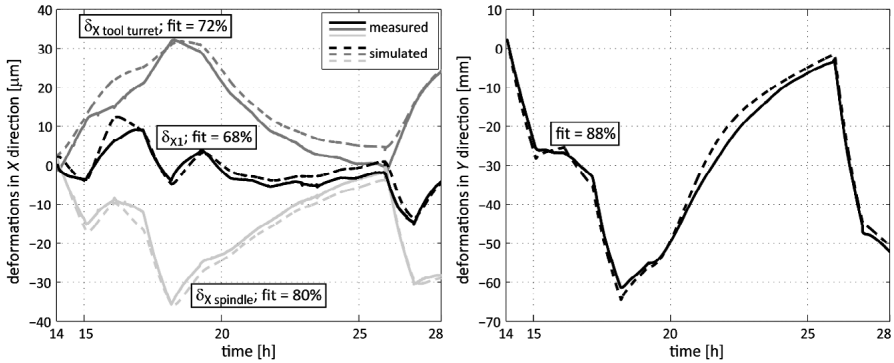


Fig. 7. Measured and simulated thermal displacement in  $X$  and  $Y$  directions during verification test.

The approximation quality attained during the verification test (Fig. 7) is equal or better in comparison with the calibration measurement (Fig. 5 and Fig. 6).

## 5 Conclusions

A reliable compensation model of MT thermal errors caused by activity of the main relevant heat sources (spindle and its drive) was introduced. The model is based on TFs. This dynamic approach suits well a general condition to minimize an amount of input signals. The condition has positive consequences in easy enlargement of the model to describe all influences participating in overall thermal error as one unit. The model was built up for compensations in two machine directions  $X$  and  $Y$  and was successfully verified under different conditions from calibration test (see Fig. 3 and Fig. 8).

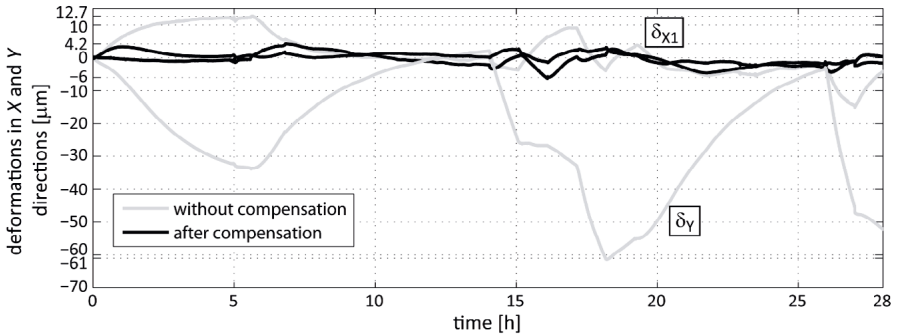


Fig. 8. Thermal behaviour of turning centre with and without compensation during complete test.

The following conclusions were discerned during the modelling:

- A correlation factor value, in general, may not have linear dependency with the approximation quality of the identified model. Models formed of temperature inputs with the highest percentage value  $r_{x,y}$  to measured deformations have not achieved the required stability.
- It is necessary to place great emphasis on the model's structure alongside the choice of a suitable mathematical approach (compare structures of  $X$  (Eq. 7) and  $Y$  (Eq. 8) models).
- The reduction from a former 74 to 10  $\mu\text{m}$  was achieved in all directions altogether by applying an introduced compensation models (see Fig. 8).

Further research should be conducted on cutting process impact on MT thermal errors, with full consideration of MT multi-functionality from the thermal behaviour and accuracy point of view.

#### Acknowledgements

*This paper (Thermal error minimization issue on turning centre) has received funding from the Technology Agency of the Czech Republic (Project TH02010849).*

## 6 References

- [1] Mayr J., Egeter M., Weikert S., Wegener K., 2015. Thermal error compensation of rotary axes and main spindles using cooling power as input parameter, *Journal of Manufacturing Systems*, 37/2, 542-549.
- [2] Postlethwaite, S., Allen, J., Ford, D., 1998. The use of thermal imaging, temperature and distortion models for machine tool thermal error reduction, *Proc. Inst. Mech. Eng. Pt. B: J. Eng. Manuf.*, 212/8, 671-679.
- [3] Mize, C., Ziegert, J., 2000. Neural network thermal error compensation of a machining center. *Precision Engineering*, 24/4, 338-346.

- [4] Mareš, M., Horejš, O., Hornych, J., 2014. Approach to thermal error modeling and compensation of a six-spindle automatic lathe. *Machines et Usinage à Grande Vitesse (MUGV)*, Clermont Ferrand, France.
- [5] Mayr, J., Jedrzejewski, J., Uhlmann, E., Donmez, M.A., Knapp, W., Härtig, F., Wendt, K., Moriwaki, T., Shore, P., Schmitt, R., Brecher, C., Würz, T., Wegener, K., 2012. Thermal issues in machine tools. *CIRP Annals - Manufacturing Technology*, 61/2, 771–791.
- [6] Prabhu Raja, V., Ramesh Babu, S., Devara Venkata Krishna, Kanchana, J., Thyla, P. R., 2014. A novel approach for thermal error modeling in CNC turning centre. *International Journal of Mechanical & Mechatronics Engineering IJMME-IJENS* 14/02, 77-84.
- [7] Ljung, L., 2009. *System identification toolbox 7 User's guide*.



# The Methods for Controlled Thermal Deformations in Machine Tools

*A.P. Kuznetsov<sup>a</sup>, H.-J. Koriath<sup>b</sup>, A.O. Dorozhko<sup>a,b</sup>*

<sup>a</sup>Moscow State University of Technology “STANKIN”, 127055, Moscow, Russia

<sup>b</sup>Fraunhofer Institute for Machine Tools and Forming Technology IWU, Reichenhainer Str. 88, 09126 Chemnitz, Germany

**Abstract.** Existing control methods for the thermal stability of machine tools are based on two fundamentally different principles: - changes in the position of objects of the impact; - change of the thermal state of the objects of the impact. It is substantiated and experimentally shown that the thermal spindle displacement for any machine design solution occur no more than three types of laws out of sixteen possible types of laws. A new concept and algorithm of an sensorless thermal controller for the spindle axis displacement is proposed.

Peer-review under responsibility of the International Scientific Committee in the person of the Conference Chair Prof. Steffen Ihlenfeldt.

*Keywords:* Machine tools; Accuracy; Temperature; Deformation; Control

---

## 1 Introduction

### Nomenclature

$\delta r$	deformation
T	temperature

Thermal deformations of a metal-cutting machine cause deviations in the relative movement of the tool and the workpiece from the ideal (nominal or specified). Tool and workpiece are the final links in the kinematic chain as for geometrical shaping as for the coordinate thermo-physical structure of the machine. Error caused by the thermal position / orientation shift of units and parts of machine are proportional to their functional thermal state [1,5-8,10].

Summarizing the state of research on thermal processes in machines and reflecting various methods for modifying the thermal robustness and thermal behavior of machine tools, their parts, components and units, figure 1a shows a general scheme for principles and methods to control the thermal precision of machine tools, as its main functional characteristics. Exceptional attention was

given to general principles and methods, but less to special solutions resulting in positive effects for one machine tool, their parts, components and units.

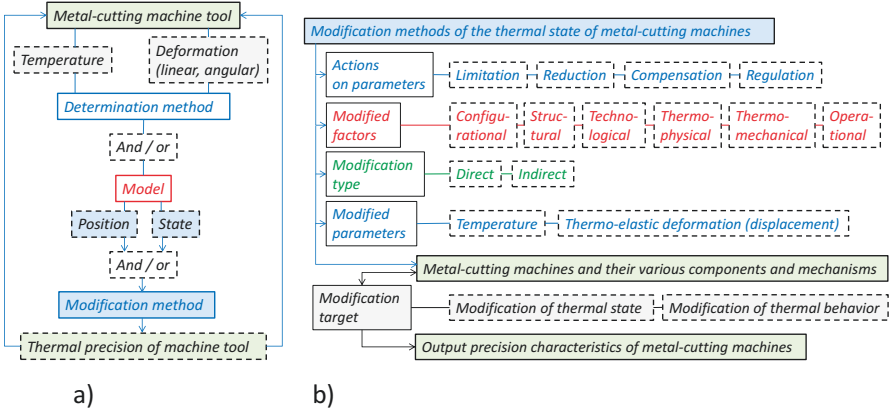


Fig. 1 a) General scheme for principles and methods to control the thermal precision of machine tools; b) Classification for modification methods of the thermal state of machine tools.

Analysing numerous research studies over the past 30 years, we have identified, synthesized and formulated the structure of interrelations and different levels for control methods of thermal phenomena in machines. Fig.1 b shows a classification for modification methods of the thermal state of machine tools, derived from generalizations and split in six classes of control structures, covering most of the areas of the performed studies.

Review, synthesis and analysis of the implementation of control methods aiming at effects on the thermal state of metal-cutting machine tools dedicated to generalizing work [1,2,3,9,10]. Following Fig. 1 b a classification of research results with relevant publications aiming at the following targets is proposed:

- Reduction in the number of heat sources [1,5-8];
- Thermal flow management [1,2,3,6,7,10];
- Design of thermo-robust machine structure [1,2,5,6,7,9];
- Compensation of thermal errors [1,2,3,9,10,17,18,19];
- Error compensation control (depending only on temperature, or else on the position/orientation and the temperature) [1,2,3,9,10,16,17,18,19].

It is also noted that the existing compensation methods are based on:

- Direct thermal position/orientation error measurement methods [2,9,17,19];

- g) Indirect temperature measurement methods at local points of the machine and the calculation based on the thermal model [1,2, 7,8,9,17,19];
- h) Indirect parameter measurement methods according (e.g. rotation frequency, motion velocity along the axes, etc.) and calculation based on the created or selected mathematical model [1,2,4,5,7,8,10];
- i) Combined methods from the above listed [1,4,5,7,21,22];
- j) Other methods, including combinations of previous ones [1,4,5,7,22-25].

Methods that link interacting parameters as mathematical methods to create control or influence models on the thermal behavior of machine tools and improve the manufacturing accuracy are (see fig. 1a,b):

- k) Linear and non-linear regression [1,2,3,17,18,19];
- l) Neural networks [20];
- m) Fuzzy logic [1,2];
- n) Transfer function [1,22];
- o) Grey system theories [1,2];
- p) B-spline [1,2];
- q) Uniform transformation matrices [1,2,3,17,18,19].

Here, action types on parameter modification include the classes: limitation, reduction, compensation, and regulation of parameter modifications. Modification type factors are: configuration, structural, technological, thermo-physical, thermo-mechanical, and operational. Limitation methods are linked to a limited effect of thermal sources on thermal active machine components. Thermal sources (e.g. electrical drives and hydraulic unit) are separated from the machine tool aiming at limited heat input, or isolated aiming at limited effect from external heat sources and the cutting process. Reduction methods oriented towards a reduced heating temperature and/or thermo-elastic deformation. Application solutions are internal heat source cooling, increased heat convection surface (grooves), increased thermal convection parameter (air exchange), use of low dimension expansion materials, and creation of thermo-elastic deformations in required and defined directions etc.

Compensation methods change the relative position or orientation between machine units and parts (usually the tool and work piece) based on information (indirect or direct) about the operational temperature and/or thermo-elastic machine deformations. Today compensation methods are wide used as easy and effective means for an increased precision of metal cutting machine tools. Practical systems based on: - the machine (part, unit) temperature measurement for resulting axis control, - the machine temperature or a different factor



(e.g. power loss, rpm) measurement for indirect deformation estimation, - the machine temperature measurement and comparison to a standard and/or mathematical model for thermal machine deformations, - a factor measurement for indirect deformation estimation, and last – the measurement of machine unit linear deformations.

## 2 General terms for thermal state control

A general scheme for thermal state control of machine part or unit temperatures and thermal deformations (else correction or compensation) is shown in figure 2.

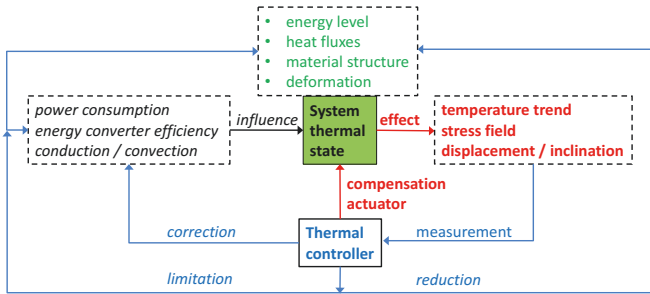


Fig. 2. General scheme for thermal state control

General methods for thermal state control (see fig. 2) base on closed-loop systems supporting a nominal thermal state of machine parts, units or a relative position / orientation of thermo-active machine units. Input information from the machine tool thermal state is transformed into output control signals for heating / cooling unit operation or drives (machine servo drive or additional actuator) for high precision part or unit position / orientation in order to keep or align a relative linear position or angle.

Above listed thermal robustness modification methods build two different types (see fig. 1a):

- r) Position / orientation shift of active objects [1,2,3,9,10,17,18,19,21-25];
- s) Thermal state change of modified objects [1,2,3,6,7,10,24].

In general, equation (1) defines the value, action type and modification method [9, 10, 11,12]:

$$\delta r = \sum_{i=1}^{n-1} \left( \prod_{j=1}^{n-(i+1)} M_i \right) \cdot K_{ji} \cdot \delta r_i^0 + \sum_{i=1}^{n-1} \left( \prod_{j=1}^{n-(i+1)} M_i \right) \cdot (B_i^\alpha) \cdot r_i + \sum_{i=1}^{n-1} \left( \prod_{j=1}^{n-(i+1)} M_i \right) \cdot (B_i^\alpha) \cdot K_i \cdot \delta r_i^0 \quad (\text{Eq. 1})$$

where  $n$  – amount of quasi thermo-stable links;  $j=n-1$  – amount of thermo-active elements;  $\delta r = |\delta x \delta y \delta z 1|^T$  – relative thermal deformation based on a position error of the tool and work piece;  $\delta r_i^0 = |\delta x_i^0 \delta y_i^0 \delta z_i^0 1|^T$  – linear position shift of thermo-active elements located at quasi thermo-stable links;

$K_{ji} = \frac{j_{\Sigma}}{j_2} - \frac{j_{fc}}{j_6} \frac{j_{\Sigma}}{j_2} + (1 - \frac{j_{\Sigma}}{j_2}) K_0 = \frac{j_{\Sigma}}{j_2} (1 - K_{fc} - K_0) + K_0$  – relative thermal shift coefficient of thermo-active elements at quasi thermo stable links;

$K_{0i} = \delta_{0i} / \int_0^1 \beta T_i(x, \tau) dx$ ;  $K_{fci} = j_{fci} / j_{bi}$ ;  $j_{fci} = P_{fci} / \int_0^1 \beta T_i(x, \tau) dx$ ;  $j_{bi} = E_i F_i / l_i$ ;

$j_{\Sigma i} = [j_{li}^{-1} + j_{2i}^{-1} + r_i / E_i F_i]^{-1}$ ;

$\delta_{0i}$  – gap inside quasi thermo-stable links;  $P_{fci}$  – force in a pre-stressed thermo-active element;  $j_{\Sigma i}$ ;  $j_{bi}$ ;  $j_{li}$ ;  $j_{2i}$  – integral stiffness of thermo-active element and quasi thermo-stable link;  $E_i$ ,  $F_i$  – Young's modulus and square area of a thermo-active element;  $T_i(x, \tau)$  – temperature distribution of a thermo-active element;  $M_i = M_{ip} = M_{ipx} M_{ipy} M_{ipz}$  – position matrix of thermo-active elements;  $(B_i^{\alpha})' = B_i^{\alpha} - I$ ,  $I$  – is a unit matrix;  $B_i^{\alpha} = B_{ix}^{\alpha} B_{iy}^{\alpha} B_{iz}^{\alpha}$  angle orientation  $\delta \alpha_{ix,y,z}$  matrix of thermo-active elements.

Parameters building equation (1) define the structural elements and build internal links. Therefore equation (1) defines a general thermo-elastic structure for metal-cutting machine tools. Equation (1) in general terms is explaining every one thermo-physical structure of a metal-cutting machine tool, consisting of  $n$  quasi thermo-stable links between  $n-1$  thermo-active elements, and defines the mathematical expression of a general thermo-physical structure, see also [10,13]. From this general equation are derived special solutions for the full structure variety as a function of quasi thermo-stable link type, of the thermal behavior, of the geometrical dimensions of thermo-active elements, of their temperature distribution and others. This general equation provides the application base for a complete analysis of thermal machine states and their thermal robustness. Therefore, the definition and fundamental expression of methods, means and parameters for the control of machine thermal states is performed by equation (1) aiming at the parameter and factor creation, analysis and research targeting a shift in the machine thermal robustness with defined resolution and precision. Based on equation (1), typical time-variable thermal spindle shifts (as linear position, as angle orientation) relative between the tool and work piece are caused by a time-variable operation mode. In order to illustrate

the principles and essence of selected methods, to determine the feasibility and to evaluate the required control systems for thermal state of the machine let's write equation (1) in the expanded form and substitute in equation (1) the values for the temperature  $T(x, \tau)$  and similarity criteria functions of the thermal behavior of parts and assemblies in a metal cutting machine (for easy calculations let's use in the example two heat exchanger elements for the thermal structure of the machine):

$$\delta r = \left[ \frac{j_2}{j_2} (1 - K_{np} - K_0) + K_0 \right]_1 M_1 \left\{ \beta \int_0^1 T(x, \tau) dx \right\} + \left[ \frac{j_2}{j_2} (1 - K_{np} - K_0) + K_0 \right]_2 \left\{ \beta \int_0^1 T(x, \tau) dx \right\} + M_1 (B_1^\alpha)' \cdot r_1 + (B_2^\alpha)' \cdot r_2 +$$

$$+ \left[ \frac{j_2}{j_2} (1 - K_{np} - K_0) + K_0 \right]_1 \cdot M_1 (B_1^\alpha)' \cdot \left\{ \beta \int_0^1 T(x, \tau) dx \right\} + \left[ \frac{j_2}{j_2} (1 - K_{np} - K_0) + K_0 \right]_2 (B_2^\alpha)' \left\{ \beta \int_0^1 T(x, \tau) dx \right\}$$

After converting, the first term results in:

$$\left[ \frac{j_2}{j_2} (1 - K_{np} - K_0) + K_0 \right]_1 M_1 \cdot \beta \cdot r_1 \cdot [Q / (F \lambda 2 \sqrt{1 / (r_1 d)} \sqrt{Bi})] [1 - \exp(-K_{gl}^{-1} K_{gl}^y Bi_1 Fo_1 \Psi_1 \tau)] =$$

$$= U_1 [1 - \exp(-K_{gl}^{-1} K_{gl}^y Bi_1 Fo_1 \Psi_1 \tau)] = U_1 [1 - \exp(-m_1 \tau)]$$

Therefore, performing similar transformation operations on remaining elements of equation (1), we get a summarized expression, determining the regularities of the thermal behavior and state of machine tools.

All measures for value changes target the value functions of thermal deformation, determined by the expression (1), to a minimum or to a zero value. For this, a large variety of options exist and may be implemented, some of them are listed in chapter 1.

Therefore, all 16 typical time-variable thermal spindle shifts caused by thermal deformations in metal-cutting machine tools and are clustered into following groups (see table 1):

1<sup>st</sup> group – steady increasing thermal deformation shift;

2<sup>nd</sup> group – one extremum in thermal deformation shift;

3<sup>rd</sup> group – two extremums in thermal deformation shift;

4<sup>th</sup> group – three extremums in thermal deformation shift;

5<sup>th</sup> group – one extremum with instable thermal deformation shift (sharp spikes or gaps) in start duration.

Table 1. Typical time-variable thermal spindle shifts caused by thermal deformations in metal-cutting machine tools

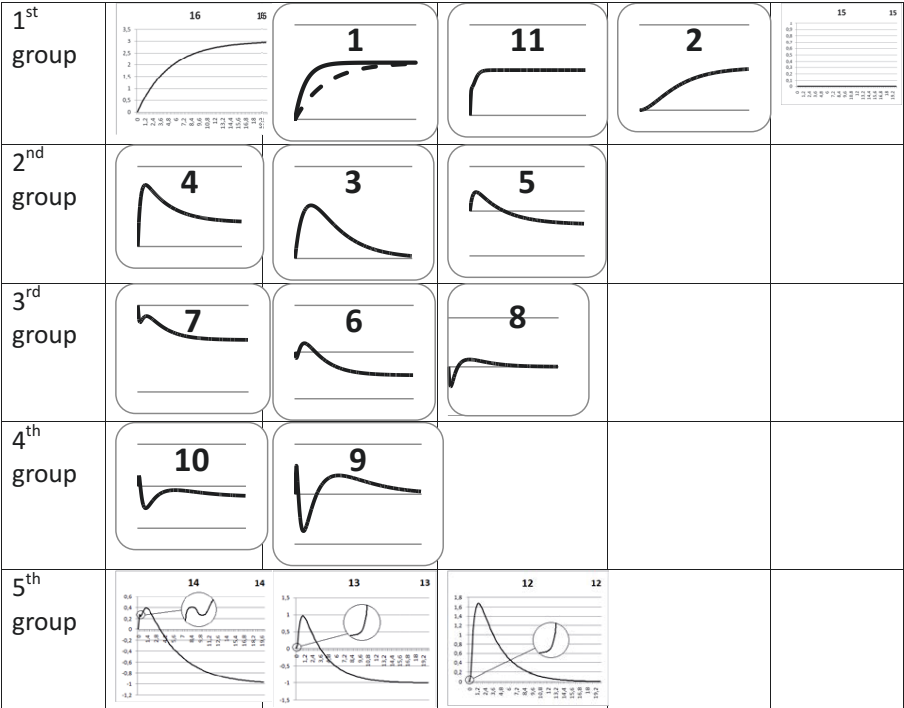
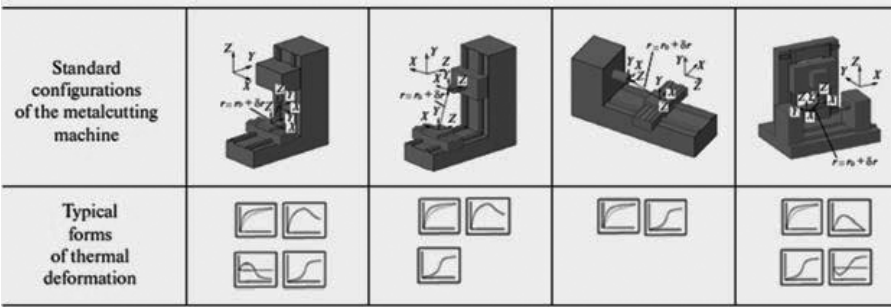


Table 2 shows most probable and time-variable thermal deformation shift types between the tool and work piece in metal-cutting machine tools for traditional kinematic structures.

Table 2. Time-variable thermal deformation shift types for traditional kinematic structures.



A functional link between measured machine unit temperature and changed position / orientation may be established by experimental tests. This functional link may be expressed by an equation in case of high measurement repeatability and stable thermal control, therefore builds the thermal controller for thermal deformation compensation. Therefore equation (1) in general may be expressed as a linear or nonlinear function of the temperature. A classification for the overall variety of thermo-elastic machine tool structures separates in three categories, defined and characterized by the involved element number and type. Relations type and furthermore resulting output precision depend correspondingly on the category:

1<sup>st</sup> model category – linear model  $\delta r = \sum_{i=1}^{n-1} \left( \prod_{j=1}^{n-(i+1)} M_{ji} \right) \cdot K_{ji} \cdot \delta r_i^0 = k_1 f(T_{\text{mdi}}^0)$  of

thermo-elastic machine tool structures, consisting of a linear relation between the output value  $\delta r$  and a thermal linear displacement of the thermo-active elements  $\delta r_i^0$ , caused only by their middle temperature  $T_{\text{mdi}}^0$ ;

2<sup>nd</sup> model category – nonlinear model

$$\delta r = k_1 f(T_{\text{mdi}}^0) + k_2 [\partial f(T) / \partial r] \cdot r = \sum_{i=1}^{n-1} \left( \prod_{j=1}^{n-(i+1)} M_{ji} \right) \cdot K_{ji} \cdot \delta r_i^0 + \sum_{i=1}^{n-1} \left( \prod_{j=1}^{n-(i+1)} M_{ji} \right) \cdot (B_i^\alpha) \cdot r_i$$

of thermo-elastic machine tool structures, considering a nonlinear relation between the output value  $\delta r$  and a thermal linear displacement of the thermo-active elements  $\delta r_i^0$ , caused by their middle temperature and thermal angle displacement of the thermo-active elements  $\delta r_i^0$  resulting from their middle temperature distribution  $T_{\text{mdi}}^0$ ;

3<sup>rd</sup> model category – nonlinear model

$$\begin{aligned} \delta r &= k_1 f(T_{\text{mdi}}^0) + k_2 [\partial f(T) / \partial r] \cdot r + k_3 [\partial^2 f(T) / \partial r^2] \cdot r = \\ &= k_1 f(T_{\text{mdi}}^0) + k_2 [\partial f(T) / \partial r] \cdot r + \sum_{i=1}^{n-1} \left( \prod_{j=1}^{n-(i+1)} M_{ji} \right) \cdot (B_i^\alpha) \cdot K_i \cdot \delta r_i^0 \end{aligned}$$

of thermo-elastic machine tool structures, considering a nonlinear relation between the output value  $\delta r$  and a thermal linear displacement of the thermo-active elements  $\delta r_i^0$ , caused by their middle temperature  $T_{\text{mdi}}^0$  and thermal angle displacement  $r_i$  of the thermo-active elements  $\delta r_i^0$  resulting from their middle temperature distribution  $\Delta T_i^0$ , and additional thermal angle displacement

of the thermal deformed thermo-active elements  $\delta r_i^0$  resulting from their middle temperature distribution  $\Delta T_i^0$ .

### 3 Thermal state control system application

Consequently, in general two different classes of thermal state control systems for metal-cutting machine tools are defined, targeting an increased precision and based on previous defined relations and thermal behaviour equivalence criteria:

1<sup>st</sup> class – structural thermal state control system, caused and defined by the action on one or more structural model parameters, resulting in the output value for relative displacement (linear or angle) of interacting elements (tool and work piece) in metal-cutting machine tools;

2<sup>nd</sup> class – computerized numerical state control system, caused and defined by the additional action – not on structural model parameters resulting in the output value for relative displacement (linear or angle) – but on the output value from a CNC control system (or more significant values for geometrical dimension creation) for elements and axes drives in machine tools, resulting and defining relative position or orientation:

- a) Computerized numerical thermal position control of thermo-active elements and quasi thermo-stable links;
- b) Computerized numerical thermal state control (temperature and/or thermos-elastic) of thermos-active elements and/or quasi thermo-stable links.

Defined standard functions for the thermal deformation and displacement control and specified machine tool structure (see table 1, 2) in three Cartesian coordinates are calculated with operational spindle speed and process time parameters. The resulting value for a defined thermal spindle displacement function is automatically converted into axis drive commands for same direction and same value. Thus, the relative position / orientation between machine axes units keep constant. A spindle stop leads to a machine cooling with defined thermal spindle displacement, depending on operational machine stand-still time. A reverse spindle displacement is calculated and converted into automatic compensation through reverse axes drive commands.

Figure 3a shows a scheme for the proposed compensation method of the thermal spindle displacement in a CNC machine tool.

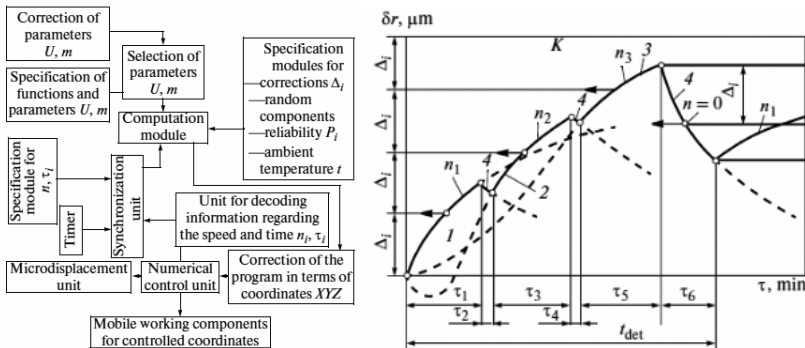


Fig.3. a) Automatic compensation of the thermal spindle displacement in a numerical controlled metal cutting machine; b) Scheme for the compensation of the thermal spindle displacement  $\delta r$  in time  $\tau$ ;

Standard functions for the thermal deformation and displacement control have been calculated for a variety of spindle speeds in heating and cooling operation. We now consider the automatic compensation of the spindle's thermal displacement in the machine tool (see fig. 3b curve  $K$ ): a) in the machining of a single part at spindle speeds  $n_1, n_2, n_3$ , with standard functions 1, 2, 3, and 4; b) in cooling of the machine tool, when the spindle speed is changed (time  $\tau_2$ ) and the tool is replaced (time  $\tau_4$ ) and when the final part is replaced and a new blank is installed (time  $\tau_6$ ). Automatic compensation of the spindle's thermal displacement (according to curve  $K$ ) is undertaken at intervals  $\Delta i$  for each controlled axis, in heating and cooling of the machine tool. (Determination of  $\Delta i$  is based on the required machining precision.) At startup of the machine tool and the onset of machining at spindle speed  $n_1$ , the spindle's thermal deformation corresponds to standard function 1 (see fig. 3b). When the thermal displacement is  $\Delta i$ , it is compensated by the corresponding displacement of the working component in the specified direction. After time  $\tau_1$ , the spindle speed is switched to  $n_2$ , and then the thermal displacement corresponds to standard function 2. During the speed change, the spindle does not turn, and machine tool cools according to standard function 4. During operation at spindle speed  $n_2$ , the thermal displacement corresponds to standard function 2. When the thermal displacement reaches  $\Delta i$ , it is compensated. Automatic compensation proceeds analogously in operation at spindle speed  $n_3$ , when the thermal displacement corresponds to standard function 3. When the finished part is removed and a new part is inserted, the spindle does not turn. The machine tool cools, and the thermal displacement of the spindle varies in accordance with standard function 4 over a time  $\tau_6$ . When the thermal displacement is equal to  $\Delta i$ , it is compensated by displacement of the machine tool working component

by an amount  $\Delta i$  in the opposite direction. In subsequent operation (cooling), the spindle's thermal displacement is compensated analogously.

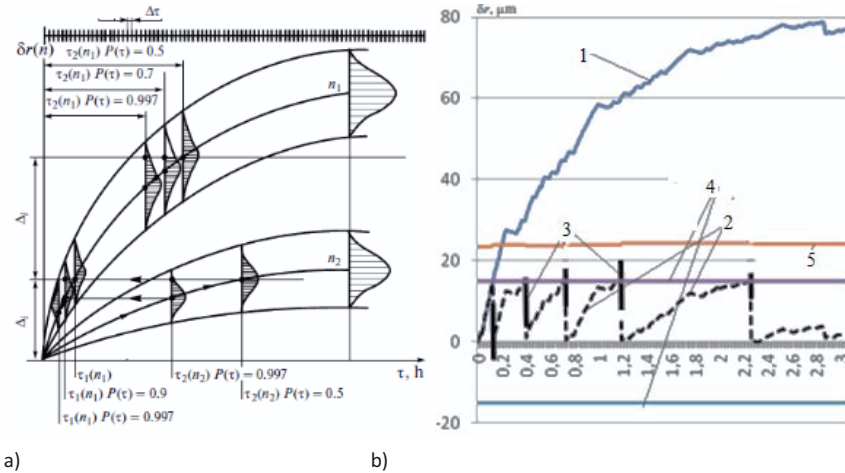


Fig. 4. a) Probabilistic scheme for automatic compensation of the thermal spindle displacement in a metal-cutting machine; b) Implementation on the machine tool TAJMAC-ZPS MCFV 1060 (curve 1- Simulation of thermal displacement of the spindle, 2- The model for compensation of thermal displacements during the machining, 3- The real displacement of the spindle, 4- the required range displacement of the spindle, 5- the air temperature.)

Implementation of the automatic compensation for the spindle's thermal displacement is undertaken periodically, during the heating and cooling of the machine tool, in terms of the quantity  $\Delta i$  determined for each controllable coordinate axis. Where necessary,  $\Delta i$  and the probability  $Pi(\tau)$  that it will be attained are established for each newly machined part, on the basis of the required precision and its maintenance over time, and are entered in the memory of the numerical control system for the metal-cutting machine (Fig. 4 a). At startup of the machine tool and the onset of machining, data regarding the operating time  $\tau$ , the spindle speed  $n$ , the current position of the working components (with respect to the controlled coordinates), and the ambient temperature are entered in the numerical control computer. The thermal displacement of the spindle with respect to each coordinate axis is calculated continuously at specified intervals  $\Delta \tau$  (Fig. 4 b). When the thermal displacement in any direction is equal to  $\Delta i$ , with specified probability  $Pi(\tau)$ , it is compensated by appropriate displacement of the machine tool working component in the specified direction. After time  $\tau_1$ , the spindle speed is changed to  $n_2$ . That will also change the thermal displacement of the spindle in accordance with the parameters for that spindle speed. During the change in speed, the spindle does not turn, and the



machine tool is cooled in accordance with the cooling function. In operation at speed  $n_2$ , there will be further thermal displacement of the spindle, which is again calculated continuously at specified intervals  $\Delta t_i$ . When the thermal displacement in any direction is equal to  $\Delta j$ , with specified probability  $P_i(\tau)$ , it is compensated by appropriate displacement of the machine tool working component in the specified direction. If the required probability  $P_i(\tau)$  is not met, the calculation of the spindle displacement continues. As soon as the probability reaches  $P_i(\tau)$ , the working components are moved accordingly.

## 4 Summary

This paper presents first results in creating systems that allow the control of spindle axis displacements without the direct application of a temperature sensor as information for control parameters. The system includes a probabilistic model of the thermal state of the machine. Practical test results show the actual feasibility and potential of this research direction.

Existing control methods of thermal deformations and temperature in machine tools require further development for their versatility in relation to different types of machines. In addition, all the prerequisites for the development of new control principles of the machine are energy - information systems. The complexity of the mathematical description of thermal processes and their dependence on number of thermal variables, determines the need to consider not only deterministic, but also probabilistic models of thermal machine control.

## 5 References

- [1] Yto, Y., Thermal Deformation in Machine Tools, New York: McGraw\_Hill, 2010.
- [2] Thermal issues in machine tools/ J.Mayr, J.Jedrzejewski, E.Uhlmann, M.A.Donmez, J.Knapp, F.Hartig, K.Wendt, T.Moriwaki, P.Shore, R.Schmitt, C.Brecher, T.Wurz, K.Wegener / CIRP Annals – Manufacturing Technology, 2012, v.61. – pp.771–791.
- [3] YangLi, WanhuaZhao, ShuhuaiLan, Jun Ni, Wenwu Wu, BinghengLu. A review on spindle thermal error compensation in machine tools. International Journal of Machine Tools & Manufacture 95(2015)20–3822.
- [4] Shuanqiang Yang, Jianxiong Chen and Shuwen Lin. A Software Method for Online Thermal Error Inspection and Compensation. International Journal of u- and e- Service, Science and Technology, Vol.9, No. 2 (2016), pp.195-206
- [5] G. Spur, G. Lechler, U. Heisel, Methods for Reducing Thermal influences on the Accuracy of Machine Tools Proceedings of the 3ed International Conference on Production Engineering., 1977, v 1. - p 10 -22.

- [6] Sokolov Yu. N. Temperature calculations in the machine tool. M: NTO Mashprom, 1965.-77c.
- [7] Weck M., McKeown P., Bonse R., Herbst U. Model reduction & compensation method of thermal deformations in machine tools,1995.
- [8] Attia M.H.Method for optimal real-time CNC control of thermal deformation compensation in machine tools, 1999
- [9] Kuznetsov, A.P., Teplovoe povedenie i tochnost' metallovezhuchchikh stankov (Thermal Behavior and Precision of MetalCutting Machines), Moscow: YanusK,2011.
- [10] Kuznetsov, A.P., Teplovoi rezhim metallovezhushchikh stankov (Thermal Conditions in Metal Cutting Machines), Moscow: MGTU Stankin, YanusK, 2013.
- [11] Kuznetsov A. P.Thermal Behavior of Components in Metal\_Cutting Machines. - Russian Engineering Research,2011,31,№4.-p.351-358.
- [12] Kuznetsov A. P. Patterns of Thermal Behavior of Metal-Cutting Machines. - Russian Engineering Research,2011,№10.-p.975-985.
- [13] Kuznetsov, A.P. and Kosov, M.G., Structural thermophysical analysis of metalcutting machines, Russ. Eng.Res., 2011, vol. 31, no. 6, pp. 599–606.
- [14] Kuznetsov, A.P., Similarity of the thermal behavior of components in metal cutting machines, Russ. Eng.Res., 2011, vol. 31, no. 4, pp. 351–358.
- [15] Kuznetsov, A.P. and Kosarev, M.V., Classification of standard types of thermal deformation in metalcutting machines, Stanki Instrum., 2013, no. 9, pp. 13–19.
- [16] Kuznetsov A. P.Temperature Control of Metal\_Cutting Machines. Russian Engineering Research. Vol. 35, No. 1, 2015. - pp. 46–50.
- [17] Vyroubal. J. Compensation of machine tool thermal deformation in spindle axis direction based on decomposition method. – Precision Engineering, 2012, №36. – pp.121–127.
- [18] Turek P., Jęgrzejewski J., Modrzycki W. Methods of machine tool error compensation. Journal of Machine Engineering, 2010, v.10, №4. – pp.5–25.
- [19] Ni J. CNC machine accuracy enhancement through real-time error compensation.Journal of Manufacturing Science and Engineering, 1997, v.119. – pp.717–725.
- [20] Yang H., Ni J.Thermal deformation simulation by use of neural networks, 2005
- [21] Patent US 6,651,019 B2, 17/38 G01C, G06F 19/00. Method and device for calculating the correction of thermal deformations of the machine, 2003.
- [22] Patent US 6,923,603. B23C 9/00; B23Q 11/12.Machine with the function of preventing thermal deformation, 2005.
- [23] RF Patent №2499658/A. P. Kuznetsov, M. G. Kosov, Krohin O. I. Method of automatic compensation of thermal displacement of the spindle machine tool with numerical control. B23Q 15/18,; Publ.27.11.2013, bul.№33.

- [24] RF Patent №2511075, B23B 25/06./ Kuznetsov A. P., Crachin O. I., Zenin, V. A. Method of automatic control of a thermal state of heat-loaded devices. Published: 10.04.2014, Bull. No. 10.
- [25] Russian Federation Patent No. 2 573 854. B23B 25/06. Method of compensation of thermal deformation of machine tools c NC./ Kuznetsov A. P. Published: 27.01.2016 Bull. No. 3

# Efficient FE-modelling of the Thermo-elastic Behaviour of a Machine Tool Slide in Lightweight Design

*Christoph Peukert<sup>a</sup>, Jens Müller<sup>a</sup>, Marcel Merx<sup>a</sup>, Alexander Galant<sup>a</sup>, Axel Fickert<sup>a</sup>, Bin Zhou<sup>a</sup>, Simon Städtler<sup>a</sup>, Steffen Ihlenfeldt<sup>a</sup>, Michael Beitelschmidt<sup>b</sup>*

<sup>a</sup>Institute of Machine Tools and Control Engineering, TU Dresden, 01062 Dresden, Germany

<sup>b</sup>Institute of Solid Mechanics, TU Dresden, 01062 Dresden, Germany

**Abstract.** In order to represent the thermo-elastic behaviour of a machine structure with braced aluminium plates, the contact characteristics between the plates have to be taken into account. For the purpose of an efficient analysis, the elastic and thermal partial model is tailored to the different requirements of these physical domains. The difficult identification of the system's stiffness matrix is carried out indirectly by means of comparison with an experimental modal analysis. Findings from simulations and measurements are compared to validate the thermal and elastic model. A combined thermo-elastic simulation is carried out by mapping the temperature field obtained from the coarse thermal model to the mechanical model.

**Keywords:** FE-modelling; thermo-elastic behaviour; machine tool

---

## 1 Introduction

Machine tools represent highly complex production systems. The quest for an increase in productivity, especially in high-speed machining, leads to the application of innovative concepts in the design and control of machine tools. The experimental lightweight machine MAX (Fig. 1), developed at the Institute of Machine Tools and Control Engineering of the TU Dresden, is used as a test rig for fundamental investigations of novel structural concepts [1] as well as efficient methods for reducing thermal induced errors [2]. One approach for reducing thermo-elastic errors of machine tools is to apply the structure model based correction technique [3]. In this paper, an efficient thermo-elastic modelling methodology is presented using the example of the Z-slide of the experimental machine. The Z-slide is composed of aluminium plates which are prestressed with tie rods as shown in Fig. 1. The pre- and post-processing is performed in the FE environment ANSYS Workbench.

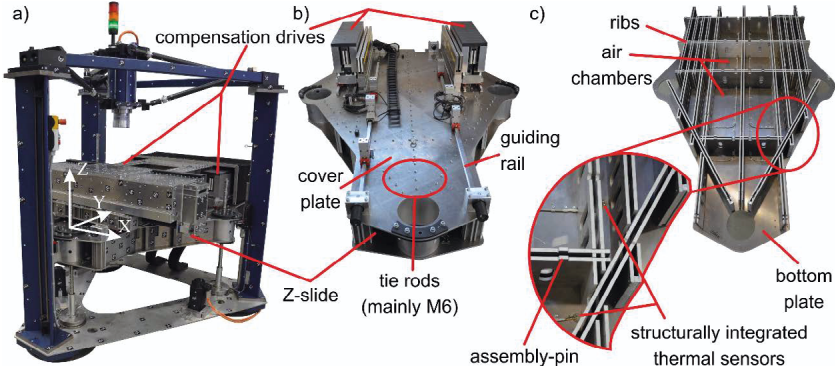


Fig. 1. (a) Experimental machine MAX; (b) assembled Z-slide and (c) internal structure of the Z-slide.

## 2 Mathematical Description of the Thermo-elastic Behaviour

In general, the FEM can be used to analyse the static, dynamic and thermal respective thermo-elastic machine behaviour. The dynamic problem can be expressed with the following system of differential equations (FEM discretisation):

$$\mathbf{M} \cdot \ddot{\mathbf{u}} + \mathbf{D} \cdot \dot{\mathbf{u}} + \mathbf{K} \cdot \mathbf{u} = \mathbf{f} \quad (\text{Eq. 1})$$

$\mathbf{M}$ ,  $\mathbf{D}$  and  $\mathbf{K}$  represent the mass, damping and stiffness matrix. The vector  $\mathbf{f}$  is the load vector and  $\mathbf{u}$  is the vector of the displacements. The structural-dynamic problem depicted in Eq. 1 also contains information on the static behaviour of the modelled structure.

If the thermal behaviour is also considered, the submatrices of the thermal capacities  $\mathbf{C}_T$  and the conductance values  $\mathbf{K}_T$  are added to the system of equations. The structure of the system of equations itself is not changed. The coupling between temperature  $\mathbf{T}$  and thermo-elastic equivalent loads is realised by means of the so-called thermal stiffness matrix  $\mathbf{K}_{uT}$ , wherein the stiffness  $\mathbf{K}$  and the material's expansion behaviour are considered. The load vector is extended by the heat flow  $\dot{\mathbf{q}}$ .

$$\begin{bmatrix} \mathbf{M} & \mathbf{0} \\ \mathbf{0} & \mathbf{0} \end{bmatrix} \cdot \begin{pmatrix} \ddot{\mathbf{u}} \\ \ddot{\mathbf{T}} \end{pmatrix} + \begin{bmatrix} \mathbf{D} & \mathbf{0} \\ \mathbf{0} & \mathbf{C}_T \end{bmatrix} \cdot \begin{pmatrix} \dot{\mathbf{u}} \\ \dot{\mathbf{T}} \end{pmatrix} + \begin{bmatrix} \mathbf{K} & \mathbf{K}_{uT} \\ \mathbf{0} & \mathbf{K}_T \end{bmatrix} \cdot \begin{pmatrix} \mathbf{u} \\ \mathbf{T} \end{pmatrix} = \begin{pmatrix} \mathbf{f} \\ \dot{\mathbf{q}} \end{pmatrix} \quad (\text{Eq. 2})$$

Eq. 2 clearly shows that the stiffness matrix  $\mathbf{K}$  is required for both the dynamic and the thermo-elastic modelling. In addition, the mass distribution according to the mass matrix  $\mathbf{M}$  is reflected in the distribution of the heat capacities according to the capacitance matrix  $\mathbf{C}_T$ . In purely thermo-elastic calculations

however, only the effects of static deformation need to be taken into account since the natural frequencies of the structural dynamics, are usually not excited by slow thermal processes. Therefore, the problem can be transformed into Eq. 3.

$$\mathbf{K} \cdot \mathbf{u} = \mathbf{f} - \mathbf{K}_{uT} \cdot \mathbf{T}; \mathbf{C}_T \cdot \dot{\mathbf{T}} + \mathbf{K}_T \cdot \mathbf{T} = \dot{\mathbf{q}} \quad (\text{Eq. 3})$$

It can be seen that in this form the system consists of the thermal transient part and the static linear system of equations. The system can therefore be solved in a two-step process. First, the thermal system (Eq. 3, right) is calculated and then the static equation system (Eq. 3, left) can be solved in a greater time interval.

Also, in terms of effective modelling, it is worthwhile to separate the thermal and mechanical behaviour. In this way, a transient thermal model with comparatively coarse tetrahedral mesh and small time step size can be combined with an elastic model with high-quality mechanical hexahedral mesh and coarse time step size. In addition, a model order reduction can be applied to the thermal problem in order to significantly reduce the required computing time [4].

Different approaches can also be used for geometric model refinement. In the thermal domain, for example, the tie rods represent negligible thermal conductance values compared to the rest of the geometry and can be removed from the model. In the dynamic model, on the other hand, the tie rods need to be considered, because of their noticeable influence on the mass distribution.

The model tuning of the thermal system behaviour according to Eq. 3, right is relatively simple, assuming that a sufficient rise in temperature can be achieved and non-linear, hardly describable heat flows due to convection and radiation are low. In order to match the thermo-elastic model in Eq. 3, it is necessary to identify the stiffness matrix  $\mathbf{K}$ , which is related to the thermal stiffness matrix  $\mathbf{K}_{uT}$  via the material's expansion coefficients. However, it is very difficult to measure the static stiffness of complex structures, especially for large sections, since the resulting deformations are usually small. In addition, defined boundary conditions and the adjustment of the exact orientation of the loads can only be achieved with great effort. An alternative approach is to obtain the mass and stiffness matrix by evaluating experimental modal analyses. Corresponding to Eq. 1 the stiffness matrix can be determined by solving the eigenvalue problem assuming low damping and known mass distribution. Therefore, the following section deals with the modelling and adjustment of the structural dynamic behaviour for the example of the Z-slide of the experimental machine.

### 3 FE-Modelling and Analysis of the Elastic Behaviour of the Z-slide

In order to achieve high reproduction accuracies, a high-quality mesh is required [5]. According to the literature, there is a strong preference for using linear hexagonal finite elements for mechanical problems [6], while tetrahedral elements are preferred for thermal problems. Many researchers addressed the problem of all-hexahedral-meshing (e.g. [7]), because of the absence of robust automatic hex-meshing algorithms. In aeronautic applications, for example, this is the standard meshing-strategy [8]. The elastic FE-model presented in this paper consists of hexahedral elements in order to achieve high calculation accuracy with low computing time. Hence, particular attention is paid to the pre-processing.

#### 3.1 Geometry Preparation and Mesh Generation

Since only those parts of the geometry are of interest, which have a significant influence on the model's behaviour, the geometry is simplified by removing filigree, geometrical elements such as small holes, chamfers, small radii, nuts and bolts etc. Furthermore, replacing parts of the model's geometry, such as tie rods, with idealised FE-elements, such as link elements (see Fig. 2, b), simplifies the model and helps to avoid unwanted mesh refinements. The density of some components has been adjusted to maintain the overall mass distribution. This is important since the mass distribution of the system, represented by the mass matrix  $\mathbf{M}$ , needs to be modelled accurately, to ensure that the obtained eigenfrequencies and eigenvectors determined by Eq. 1, reflect the stiffness behaviour of the system corresponding to its stiffness matrix  $\mathbf{K}$ . Therefore, the 327 tie rods (4 % of the overall mass) are considered (compare Fig. 2, b). Replacing the tie rods may result in some difficulties, though. Since the holes, through which the tie rods are mounted, were removed to avoid unwanted mesh refinements in those areas, the top and bottom plate of the model need to be segmented to create nodes at the former locations of the tie rods. This allows the creation and attachment of link elements to substitute the tie rods. Decomposition of the geometry into predominantly cuboid bodies, which the meshing algorithm can process more easily, finalises the geometry preparation (see Fig. 2, a).

Finite elements of various shape, size and polynomial order were investigated for meshing the model, including shell and solid elements. An assessment on the model's reproduction accuracy concluded that linear hexahedrons, with the size of the models aluminium plate's thickness (8 mm), yielded the most

accurate solution to eigenvalue problems with an acceptable time effort. The all-hexahedral mesh is shown in Fig. 2, a.

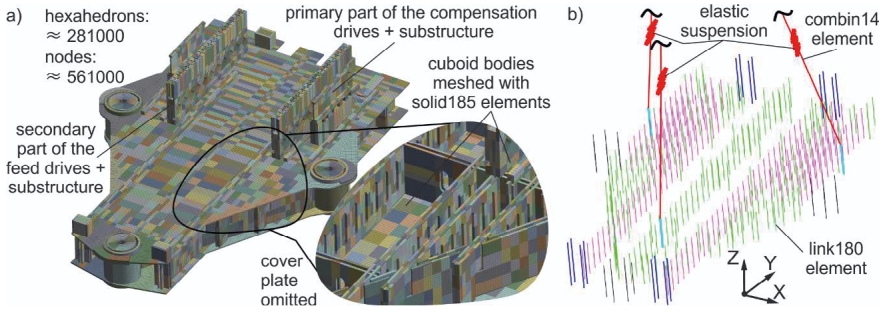


Fig. 2. Z-slide: (a) prepared model with an all-hexahedral mesh; (b) line elements to model the tie rods and the elastic suspension.

### 3.2 Contact Modelling

Due to the large number of contact areas between the aluminium sheets, homogenisation of the contact behaviour is necessary. In addition, linear contact models are used to perform simulative modal analysis. This is reasonable, since preservation of the pretension can be assumed for all operating conditions. Due to roughness, measured contact stiffness values are significantly lower than theoretical values predicted from smooth surfaces in contact [9]. Since the aluminium plates and ribs are water jet cut, significant squareness deviations of the edges are unavoidable, which also influence the contact stiffness. Preceding investigations showed that a contact model is needed to map the numerous contacts between the aluminium sheets of the structure. Thereby, the stiffness distribution can be adjusted properly. A variety of contact models were created and compared to represent the tangential and normal contact stiffness between the sheets. Contact models using linear springs, a layer of thin material in the contact-area (transversely isotropic material behaviour), in conjunction with multipoint constraint based contacts and other ANSYS contact elements, were used to connect the aluminium plates of the structure. Adjustable ANSYS contact elements using the Pure Penalty-algorithm were used in this paper. Since ANSYS Workbench provides only one parameter to adjust the contact stiffness, additional APDL commands are included to parameterise the normal and tangential contact stiffness independently. In order to obtain reliable parameters of the contact stiffnesses, pre-investigations on a simpler but comparable test rig were carried out. The identified normal and tangential contact stiffness are found to be  $765 \text{ N/mm}^3$



and  $400 \text{ N/mm}^3$  respectively. These parameters were used in the presented model of the Z-slide for dynamical, elastic as well as for thermo-elastic analyses.

### 3.3 Comparison of the Measured and Simulated Elastic Behaviour

The stiffness of the elastic suspension, used for mounting the Z-slide during the experimental modal analyses, was measured to parameterise the corresponding springs in ANSYS (compare Fig. 2, b). The averaged modal damping ratio of the Z-slide yielded approximately 0.005. This value was used for the simulative modal analysis. From Fig. 3 it is evident, that the (global) system behaviour can be represented by the model accurately. However, by performing deformation measurements, it has to be verified whether the model can predict the local stiffness behaviour. Furthermore, the model needs to be improved by adjusting the model parameters in order to predict vibrations, dominated by the substructure of the linear motor components, as can be seen in Fig. 3 at approx. 265 Hz. Therefore, in particular, the contact parameters between the top plate and the substructure of the linear motor components need to be optimised. According to [10], the simulation-based approach for identifying the contact stiffness on the basis of experimental modal analyses can be applied.

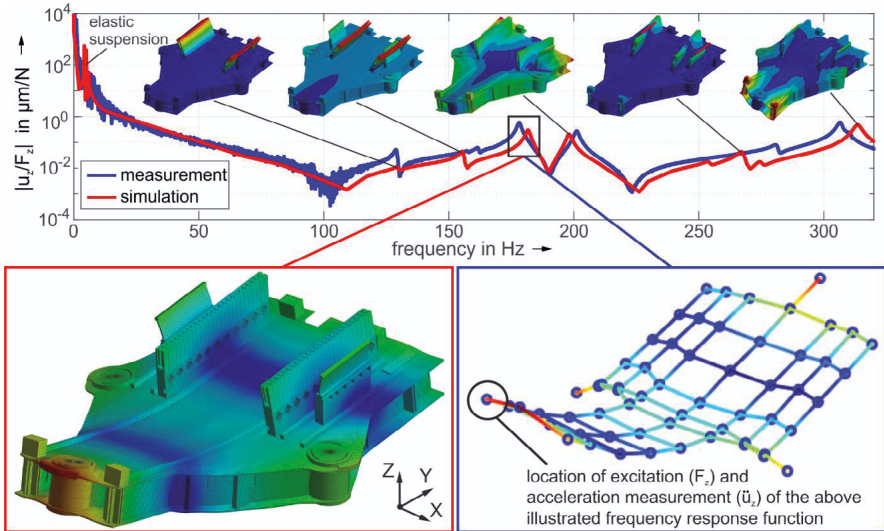


Fig. 3. (top) frequency response function; (bottom, left) characteristic mode-shape: simulation; (bottom, right) characteristic mode-shape: measurement (60 positions investigated).

## 4 Investigation on the Thermal Behaviour of the Z-slide

### 4.1 Modelling of the Thermal Behaviour

Similar to the above mentioned pre-processing, the Z-slide is prepared in such a way that the thermally non-relevant details are removed. Since no decomposition of the geometry into cuboid bodies is required for tetrahedral meshing, the pre-processing is rather simple. After assigning the correct material, and thus the thermal material parameters, to each body, the Z-slide is meshed with linear tetrahedron elements (see Fig. 4, a). The mesh is controlled by dividing the entire geometry into groups of bodies and defining the appropriate maximum tetrahedron edge length for each group. The mesh quality is measured by the ratio of the min. to max. edge length. This value exceeds  $\frac{1}{4}$  for 95 % of the tetrahedrons. A convergence study with loads, typical for machine tools, revealed that the relative errors were less than 1 %.

The Z-slide has numerous contact areas. From a thermal point of view, in machine tools, the connection of two bodies can be assumed to be an *ideal contact*. This means that the heat flows from one body to another without any thermal resistance. Due to the design of the Z-slide, the aluminium plate connections do not represent an ideal contact. The correct parameterisation of the heat transfer coefficient in the joint between the horizontal and vertical aluminium plates of the Z-slide is therefore a prerequisite for achieving a high model accuracy and thus have to be identified based on thermal load tests. The remaining contacts, e.g. the contacts between the guiding rails and the top plate, are assumed to be ideal.

Inside the Z-slide there are almost closed air chambers (see Fig. 1, c). For accurate prediction, the interaction of the structure with the trapped air must be taken into account. For this purpose, the interior is divided into four air chambers and each chamber is assigned to a point mass. The point mass represents the properties of the trapped air, such as specific heat capacity, volume, density and starting temperature. The inner surfaces of the respective air chamber are then connected with the corresponding point mass, in order to allow the heat flow from the surface nodes to the mass point and vice versa, with defined thermal resistance (heat transfer coefficient  $\alpha_{K_i}$ ). This coefficient represents the convective heat transfer value between the enclosed air and the walls of the inner chamber, and has to be identified based on experiments. The effect of heat conduction in the air is much smaller than that of convection (compare [11]) and can be neglected accordingly. In the same way, because of

the low emission coefficient of the surfaces of the aluminium plates, the radiation component can be neglected. The individual air mass points are not connected to each other or to the outside air, as the air chambers are almost completely separated by the ribs.

In order to model the external convection loads including environmental radiation, a convective boundary condition with the corresponding heat transfer factor  $\alpha_{K_e}$  is defined for the outer surfaces. Assuming stationary air or uniform laminar air flow (no forced convection), the heat transfer factor  $\alpha_{K_e}$  is also identified considering thermal load tests. The ambient temperature is determined from measurements.

## 4.2 Experimental Analysis of the Thermal-Behaviour

The Z-slide was fixed on the ball screws at approx. 600 mm above the ground. The X-Y-slides, which are mounted on the Z-slide, were removed. The heat is transferred into the immovable structure via heating foils glued onto the top plate and onto the motor substructure (see Fig. 4, a). These are modelled by appropriate heat flow boundary conditions. The thermal behaviour is measured with 36 structural temperature sensors, as well as 3 external and 4 internal air temperature sensors (see Fig. 4, b). In total, eight experiments were conducted and three different thermal load collectives were investigated.

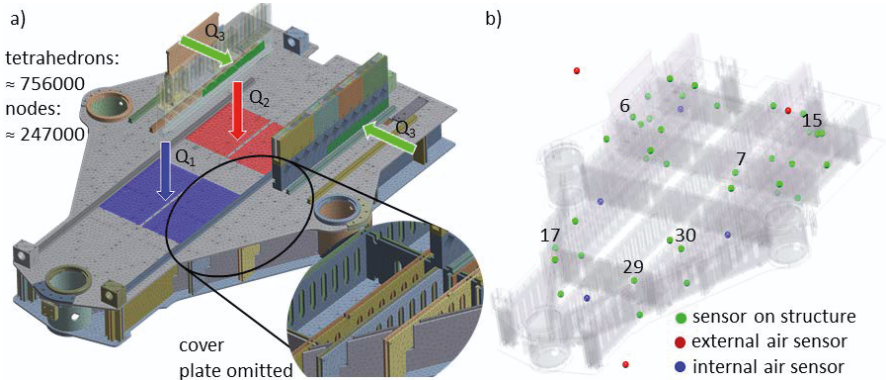


Fig. 4. Setup of the thermal experiments: (a) location heating foils; (b) sensor locations.

## 4.3 Identification of Thermal Parameters

The following heat transfer parameters were identified using the bisection method:  $\alpha_{K_e}$  for external convection,  $\alpha_{K_i}$  for internal convection and  $\alpha$  for the

plate contacts. The corresponding initial values were  $\alpha_{K_e,init} = \alpha_{K_i,init} = 10 \text{ W/m}^2\text{K}$  and  $\alpha_{init} = 1000 \text{ W/m}^2\text{K}$ . The loading regime can be seen in Fig. 5.

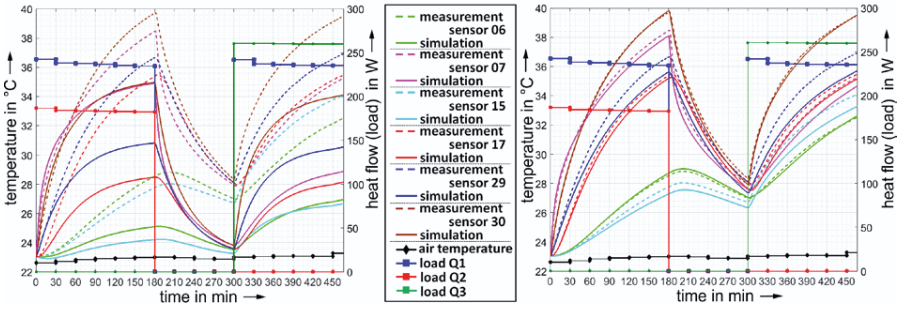


Fig. 5. Measured and simulated temperatures: (a) initial and (b) optimised parameterisation

Fig. 5 also compares the measured and simulated temperature curves for selected locations as shown in Fig. 4, b. It can be seen that the model-accuracy with optimised parameters,  $(\alpha_{K_e,opt}, \alpha_{K_i,opt}, \alpha_{opt}) = (3.3, 3.1, 2700) \text{ W/m}^2\text{K}$  illustrated in Fig. 5, b, is much better than with mismatched (initial) parameters depicted in Fig. 5, a. Fig. 5, b also demonstrates that the thermal behaviour can be predicted accurately. A conducted sensitivity analysis revealed that the heat transfer values of the contacts have the greatest influence on the accuracy of the simulation results. Fig. 6 shows the difference between the simulated and measured temperatures of the sensors applied to the structure (time averaged). With optimised parameters, the mean relative error can be reduced significantly.

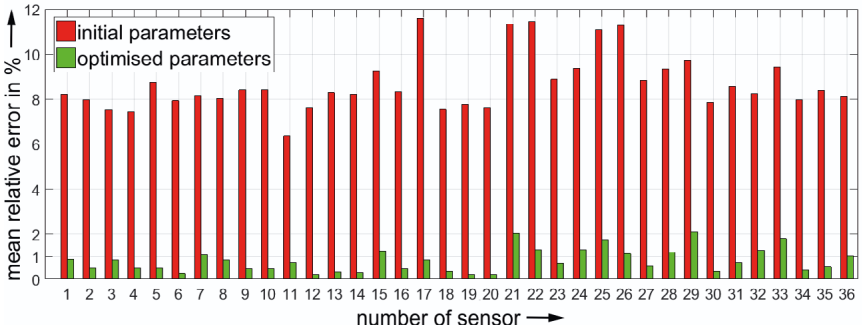


Fig. 6. Model inaccuracy for initial and optimised parameterisation (structurally integrated sensors)

## 5 Thermo-elastic Behaviour

In order to perform a thermo-elastic analysis, both models need to be combined. This is achieved by mapping the temperature field, obtained from simulations with the thermal-model using a tetrahedral mesh (Fig. 7, a), on the mechanical-model with hexahedrons (Fig. 7, b).

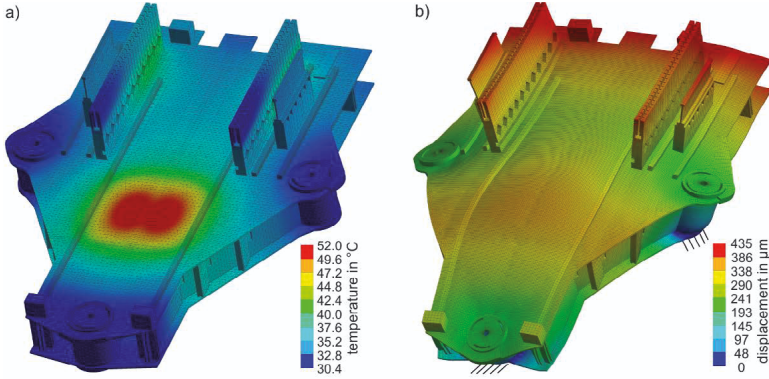


Fig. 7. (a) simulated temperature field and (b) corresponding deformation

For the simulation, the same setup as described in Section 4.2 and the loading regime shown in Fig. 5 were used. For this static mechanical analysis, the Z-slide is fixed in Z-direction at the supports of the ball screws. Fig. 7 illustrates the temperature field (a) and the corresponding displacement field (b) after 8 h. Also, from Fig. 7, b the influence of the tie rods can be seen. Because of the different coefficients of thermal expansion of the tie rods ( $12 \mu\text{m}/(\text{m}\cdot\text{K})$ ) and the aluminium plates ( $23 \mu\text{m}/(\text{m}\cdot\text{K})$ ), local bulges can be observed.

## 6 Summary

In this paper, an efficient methodology for thermo-elastic FE-analyses was introduced on the example of a lightweight machine structure with braced aluminium plates. A special feature of this approach is the adjustment of the stiffness matrix  $\mathbf{K}$  based on the model matching of the dynamic system behaviour. This enables an effective way of obtaining  $\mathbf{K}$ , which is essential for an accurate thermo-elastic modelling and analysis. The basis of the approach is given by a high-quality mechanical model with an all-hexahedral mesh, used to simulate the mechanical (dynamical and thermo-elastic) behaviour in high resolution with minimal computation effort. The stiffness parameters of the contact regions were identified by model matching of simulative and

experimental modal analyses. With a coarser meshed thermal model, the heat transfer coefficients in the contact areas were identified by means of thermal load tests. Finally, both models were combined to perform a simulative thermo-elastic analysis. The temperature field calculated with the thermal model was mapped on to the mechanical model.

### **Acknowledgements**

*This research was supported by a German Research Foundation (DFG) grant, received within the CRC/Transregio 96 “Thermo-energetic design of machine tools”, project A05 and C06, which is gratefully acknowledged.*

## **7 References**

- [1] Großmann, K., Möbius, V., Höfer, H., Müller, J., Kauschinger, B., 2009. DE102009057207
- [2] Großmann, K. (Ed.), 2015. Thermo-energetic Design of Machine Tools, 1<sup>st</sup> ed., Lecture Notes in Production Engineering. Springer International Publishing, Cham.
- [3] Thiem, X., Riedel, M., Kauschinger, B., Müller, J., 2016. Principle and Verification of a Structure Model Based Correction Approach. In: 7<sup>th</sup> CIRP International Conference on High Performance Cutting (HPC), 46, 107-110.
- [4] Beitelschmidt, M., Galant, A., Großmann, K., Kauschinger, B., 2015. Innovative Simulation Technology for Real-Time Calculation of the Thermo-Elastic Behaviour of Machine Tools in Motion. Applied Mechanics and Materials, 794, 363-370.
- [5] Bathe, K.-J., 2014. Finite element procedures, 2<sup>nd</sup> ed., Prentice Hall.
- [6] Benzley, S. E., Perry, E., Merkley, K., Clark, B., Sjaardema, G., 1995. A Comparison of All Hexagonal and All Tetrahedral Finite Element Meshes for Elastic and Elasto-plastic Analysis. In Proceedings, 4<sup>th</sup> International Meshing Roundtable, 179-191.
- [7] Staten, M. L., Owen, S. J., Blacker, T. D., 2005. Unconstrained Paving & Plastering: A New Idea for All Hexahedral Mesh Generation. Hanks, B. W. (ed.): Proceedings of the 14<sup>th</sup> International Meshing Roundtable, Springer Berlin Heidelberg, 399-416.
- [8] Keskin, A., Kober, M., Stelldinger, E., Kühhorn, A., Böhm, H., Hornig, A., Hufenbach, W., 2015. On the quantification of errors of a preprocessing effort reducing contact meshing approach. 53<sup>rd</sup> AIAA Aerospace Sciences Meeting. Kissimmee, Florida, USA, American Institute of Aeronautics and Astronautics.
- [9] Shi, X., Polycarpou, A. A., 2005. Measurement and Modeling of Normal Contact Stiffness and Contact Damping at the Meso Scale. ASME. J. Vib. Acoust., 127, 1, 52-60.
- [10] Rudolph, H., Ihlenfeldt, S., 2017. Modellierung von elastischen Fügeverbindungen. Zeitschrift für wirtschaftlichen Fabrikbetrieb, 112, 10, 675-679.
- [11] Großmann, K., Rehn, S., Mühl, A., 2012. Thermische Simulation von Werkzeugmaschinen: Ersatzmodelle zur Beschreibung konvektiver Wärmeübertragung in Gestellinnenräumen. Zeitschrift für wirtschaftlichen Fabrikbetrieb, 107, 5, 315-321.



## **Design of thermal robust machine tools**

---





# Development of a dynamic model for simulation of a thermoelectric self-cooling system for linear direct drives in machine tools

*E. Uhlmann<sup>a</sup>, L. Prasol<sup>a</sup>, S. Thom<sup>a</sup>, S. Salein<sup>a</sup>, R. Wiese<sup>b</sup>*

<sup>a</sup>Institute for Machine Tools and Factory Management IWF, Technische Universität Berlin,  
Pascalstr. 8-9, 10587 Berlin, Germany

<sup>b</sup>Beuth University of Applied Science, Luxemburger Straße 10, 13353 Berlin, Germany

**Abstract.** The growing awareness for sustainable production and increasing energy costs as well as the commitment to legal restrictions lead to a rising demand for energy efficient solutions for long-life production facilities. The applicability of energy harvesting concepts, in order to increase the energy efficiency of highly dynamic machine tools with linear direct drives, is one research objective at the Institute for Machine Tools and Factory Management (IWF). Therefore, thermoelectric generators are placed in the heat flow between the primary part of a linear direct drive and the cooling system to convert parts of the thermal losses into electric energy. It was investigated, if a so called thermoelectric self-cooling-system is applicable to operate a pump of a water cooling circuit, only supplied by thermoelectric generators. To determine the harvested energy and to simulate the steady and the transient state of the system a thermoelectric model was developed. The comparison of simulative and experimental determined data indicates high model prediction accuracy. Hence, the model turns out to be a powerful tool for the development and analysis of water flow thermoelectric self-cooling-systems. The results show that the thermoelectric generators can provide sufficient energy to operate a water pump in a decentralized cooling system with reasonable coolant flow rates.

Peer-review under responsibility of the International Scientific Committee in the person of the Conference Chair Prof. Steffen Ihlenfeldt.

*Keywords:* Machine tool; Linear direct drives; Thermoelectric self-cooling; Energy efficiency

---

## 1 Introduction

In 2015 the industrial sector accounts for about 42 % of the global energy consumption [1]. A substantial proportion of this demand is used for the operation of machine tools [2]. As a result of a growing awareness towards energy saving solutions, the European Commission has passed a series of directives [3,4,5].

List of symbols		Subscripts	
A	Area (m <sup>2</sup> )	ab	Absorbed
C	Thermal capacity (J/K)	c	Cold side, outer surface ceramic
I <sub>L</sub>	Electrical load current (A)	cd	Heat conduction
L	Length (m)	c,eff	Cold ends of the semiconductor legs
m	Mass (kg)	cer	Ceramic
Nu	Nusselt number	cont	Thermal contact
P <sub>c</sub>	Cooling capacity (W)	cp	Cold plate
P <sub>el</sub>	Electric power generated by TEG (W)	cs	Cooling system
Q̇	Heat flow rate (W)	cv	Heat convection
R	Thermal resistance (K/W)	dev	Device to be cooled
R <sub>i</sub>	Electrical internal resistance of TEG (Ω)	exp	Experimental value
R <sub>L</sub>	Electrical load resistance (Ω)	ge	Generated
T	Temperature at a particular time t (K)	h	Hot side, outer surface ceramic
t	Time (s)	h,eff	Hot ends of the semiconductor legs
U <sub>L</sub>	Load voltage (V)	hs	Heat source
U <sub>oc</sub>	Open-circuit voltage (V)	in	Inlet coolant
Ṡ	Volumetric flow rate Ṡ (m <sup>3</sup> /h)	ind	Induced
<b>Greek letters</b>		J	Joule effect
ᾱ	Seebeck coefficient (V/K)	out	Outlet coolant
Δt	Time step (s)	P	Peltier effect
λ	Thermal conductivity (W/mK)	res	Reservoir
		sim	Simulated value

Within the subject of sustainable manufacturing, machine tools are considered as energy relevant by the EU legislation and thus, there is a need to follow eco-design measures as defined by directive 2009/125/EC [3]. In machine tool life cycle the energy consumption in the operation phase was identified as the dominant contributor [6]. Besides optimizing the energy efficiency and to meet the legal restrictions, the influence of thermal losses on the thermal behavior of machine tools must be considered. Inefficient energy transformation in machine tools induces heat flows and leads to an increasing temperature of precision related machine tool components. This change in temperature causes a thermo-elastic deformation of the machine tool structure, which directly influences the position of the tool center point, and therefore the working accuracy of machine tools [7]. In order to reduce the influence of heat sources on the accuracy of machine tools, both the development of energy efficient components with limited heat input and active cooling of relevant components are possible solutions [7]. Cooling systems are capable of ensuring an nearly uniform temperature distribution along the precision related components and therefore reduce the overall thermo-elastic deformations of the machine tool structure [7]. Energy related research reveals that auxiliary units for the supply and conditioning of fluidic media account for a major share of total energy consumption [8]. This applies especially for machine tools which are subjected to high requirements regarding productivity and accuracy. In high dynamic machine tools for productive manufacturing of high-precision parts linear direct drives (LDD) are increasingly applied to allow higher acceleration, feed rate, and thus rapid positioning compared

to conventional ball screw drives [9]. In relation to the motion profile of a machine tool axis the primary part of the LDD is responsible for significant thermal losses. The arrangement of the LDD next to precision related machine tool components requires a tempering to dissipate these thermal losses and to avoid high temperature gradients in the adjacent machine tool components [10].

SHABI ET. AL. [7] reveal that the cooling system of a machine tool with LDD of type DMU80 eVo linear, DMG Mori AG, Bielefeld, Germany, requires 26 % of the total energy consumption. Additionally, 25 % of the total energy consumption is supplied to further consumers of the fluidic system. Based on these results, SHABI ET. AL. [7] states a major potential to reduce the energy demand and to increase the efficiency of machine tools by improving the function of the fluid systems [7]. Therefore, decreasing the base load by implementation of a demand based fluid supply is a promising approach [8]. This procedure is intended to avoid oversupply of cooling fluid regarding pressure, amount and duration [8]. To achieve the objective of reducing the energy consumption of machine tools, extensive research efforts have been spent to identify, monitor, and visualize the main consumers as well as to develop shutdown control strategies for components during waiting time [10].

Moreover, there are detailed investigations about fluidic systems in machine tools to derive new concepts for the structure of the cooling system [11]. Based on experimental investigations SHABI ET AL. [11] show that sufficient cooling capacity is available but the cooling is insufficiently adjusted to the process and to the individual demand of the machine tool components. Based on a developed model of a decentralized supply-unit a demand-oriented cooling system has been studied. Therefore, it is proposed to provide the required cooling capacity for each component by controlling the coolant flow rate instead of the coolant temperature. This leads to a decoupling of thermal load and outlet temperature, and thus to maintain a stable outlet temperature. Due to the demand-orientated supply of cooling capacity, the control of volume flow rate is a promising approach to reduce the required total pump power [11].

## **2 Concepts of self-sustaining cooling systems for linear direct drives**

With the intention of further increasing energy efficiency of high dynamic machine tools, concepts for self-sustaining cooling systems with adaptive characteristics have been developed [12, 13]. Based on a decentralized and demand-orientated approach of a cooling system, thermoelectric generators (TEG) are arranged in a gap between the primary part of a LDD and a cold plate of the motor

cooling system. A TEG is a solid-state heat engine composed of several thermoelectric pairs connected in series by shunts to form an electric circuit [14]. Each pair comprises a n-type and a p-type doped semiconductor material [14]. Applying a temperature difference at the outer surfaces, TEG are capable to convert parts of the heat flow rate  $\dot{Q}_{ind}$  into electric energy. In the developed concept, it is aimed at operating the water pump completely by the harvested energy of the TEG without external power supply. TEG requires no moving parts, thus being more robust, compact, and noiseless than common electric power generators [15].

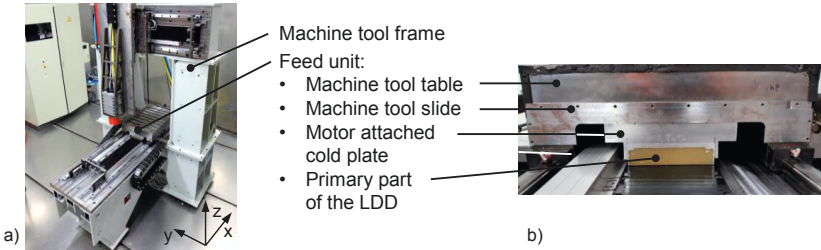


Fig. 1. (a) Three-axis portal milling machine as demonstrator [IWF];  
(b) Feed unit for integration of a thermoelectric self-cooling system [IWF]

The applicability of a so called thermoelectric self-cooling system has been demonstrated by MARTINEZ ET AL. [14] and KIFLEMARIAM ET AL. [16] for the temperature control of electronic components such as processors. This approach is intended to replace forced convection cooling systems in order to save electric energy [14]. Thermoelectric self-cooling systems show adaptive characteristics because the cooling capacity  $P_c$  is supplied as a function of the induced heat flow rate  $\dot{Q}_{ind}$ , thus load-dependent and self-regulated. As an example, the volumetric flow rate  $\dot{V}$  in a water cooling system is self-regulated by the electrical power  $P_{el}$  generated by TEG and induced heat flow rate  $\dot{Q}_{ind}$ . Temperature regulation by a control circuit is not intended. The output parameters volumetric flow rate  $\dot{V}$ , electrical power  $P_{el}$  and all temperature measurement points are completely subjected to the adaptive characteristics of the cooling system. The main goal of this work is to analyze the transferability of the approach concerning a cooling system for LDD in dynamic machine tool. Based on a developed model to simulate the steady and transient state of the system the output parameters are calculated. As a machine tool demonstrator for integrating and evaluating the self-cooling systems, a three-axis portal milling machine is available, Fig 1(a). Previous experimental investigations on a self-sustaining air cooling system with fans have revealed disadvantages by dissipating heat in the environment. The integration of

the described approach into the machine tool demonstrator takes place with a self-sustaining water cooling system, Fig. 2.

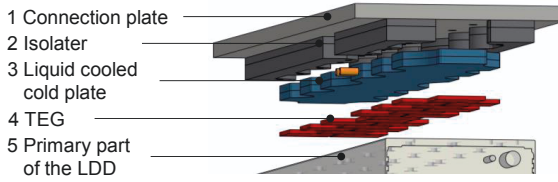


Fig. 2. Concept of integration thermoelectric generators in a feed unit of a machine tool [IWF]

The LDD of the machine tool demonstrator is equipped with a linear motor of type Al2830 without integrated cooling system, marketed by Beckhoff Automation GmbH & Co. KG, Verl, Germany. The motor-attached cold plate (Fig. 1(b)) is replaced by the components 1 - 5 in Fig. 2. Component 4 represents 19 TEG that are covering the primary part surface of an LDD. The TEG are sandwiched between the cold plate and the surface of the primary part. The isolator (2) between connection plate (1) and the primary part (5) is designed of a heat-insulating material. Hence, the induced heat flow rate  $\dot{Q}_{ind}$  is forced through the TEG arrangement. As a consequence, a temperature difference  $\Delta T_{TEG}$  arises at the TEG during operation of the LDD.

### 3 Dynamic model for simulation of a thermoelectric self-cooling system

For the design and analysis of a self-sustaining cooling systems, a model has been implemented in MATLAB/Simulink, Mathworks, Natick, USA. Supported by block libraries of the Simscape-Toolbox, the model is able to calculate the thermoelectric behavior of the conceptualized cooling-system. The developed model is composed of Simscape physical domains thermal, thermal-liquid, and electrical, which are in permanent interaction. The model architecture is derived from MARTINEZ ET AL. [15], while the following adaptations have been implemented. The model is based on preselected TEG of typ TEG1-40-40-10/100, marketed by EURECA MESSTECHNIK GMBH, Cologne, Germany. The temperature-dependent parameters of the TEG, thermal resistance  $R_{TEG}$ , electrical internal resistance  $R_i$  and Seebeck-coefficient  $\bar{\alpha}$  have been experimentally determined on a test bench. These parameters are displayed as a function of the mean temperature  $T_m$  between hot  $T_{h,eff}$  and cold side  $T_{c,eff}$  of the semiconductors legs. The semiconductors legs themselves are not considered in the model. Moreover, the thermoelectric Thomson-effect and the electrical resistances of the soldered joints are neglectable for the respective application and thus not considered.

Depending on the applied temperature difference  $\Delta T_{\text{TEG}}$  at the end of the semiconductor legs and based on thermoelectric Seebeck-effect the TEG generate an open-circuit voltage  $U_{\text{oc}}$ , which is given by Eq. (1).

$$U_{\text{oc}} = \bar{\alpha} \cdot (T_{\text{h,eff}} - T_{\text{c,eff}}) \quad (\text{Eq. 1})$$

If the module is connected to an electrical load resistance  $R_L$ , an electric power  $P_{\text{el}}$  is generated by TEG, which is given by Eq. (2).

$$P_{\text{el}} = \frac{U_{\text{oc}}^2 \cdot R_L}{(R_L + R_i)^2} \quad (\text{Eq. 2})$$

At the hot ends of the semiconductor legs, heat is absorbed by Peltier-effect, whereas heat is generated at the cold ends, which is given by Eq. (3) and Eq. (4).

$$\dot{Q}_{\text{p,h}} = -\bar{\alpha} \cdot T_{\text{h}} \cdot I_L \quad (\text{Eq. 3})$$

$$\dot{Q}_{\text{p,c}} = \bar{\alpha} \cdot T_{\text{c}} \cdot I_L \quad (\text{Eq. 4})$$

Along the semiconductor legs inside the TEG, heat is generated by Joule-effect, which is given by Eq. (5).

$$\dot{Q}_J = R_i \cdot I_L^2 \quad (\text{Eq. 5})$$

The determined temperature dependence of thermal resistance  $R_{\text{TEG}}$ , electrical internal resistance  $R_i$  and Seebeck-coefficient  $\bar{\alpha}$  are considered by Simulink lookup tables. As a consequence, the mentioned parameters are temperature-dependent between every time instant. In addition, the electrical power depended load resistance  $R_L$  of the water pump is also given in a Simulink lookup table. The four mentioned values are calculated for every time instant along the simulation time.

The model architecture based on thermal resistance networks is presented in [Fig 3](#). The thermal system behavior is derived by a mesh of representative nodes, each one connected to the surrounding nodes by a thermal resistances  $R$  and capacity  $C$ . The thermal resistances are distinguished into heat conduction resistors  $R_{\text{cd}}$ , contact resistors  $R_{\text{cont}}$ , and heat convective resistors  $R_{\text{cv}}$ .

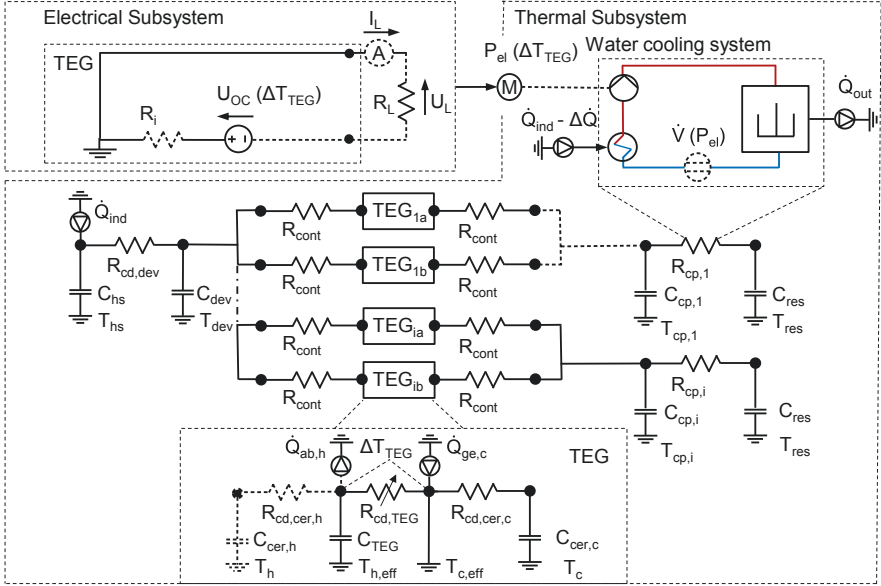


Fig. 3. Model structure for simulation of thermoelectric self-cooling systems [IWF]

The system is composed of the primary part of the LDD or a heating plate with internal heat generation, several TEG and a water cooling system with a cold plate and a pump. The first node on the left of the thermal resistance  $R_{cd,dev}$  represents the electric coil of the primary part or the cartridge heaters inside the test bench. The node on the right of the thermal resistance  $R_{cd,dev}$  represents the primary part of the LDD or the heating plate of the test bench. The heat flow rate  $\dot{Q}_{ind}$  is induced in the first node through an ideal heat source from the Simscape library. This heat flow is transferred to the external surface of the primary part of LDD through the conductive thermal resistance  $R_{cd,dev} = 0,065 \text{ K/W}$ , which is given by the technical data sheet. The thermal resistance  $R_{cd,dev}$  of the heating plate of the test bench is calculated with the geometry and the thermal conductivity  $\lambda$ . The thermal capacity  $C$  of the cartridge heaters and the heating plate of the test bench, respectively, are calculated considering masses  $m$  and specific heat capacity  $c$ . The heat flow rate  $\dot{Q}_{ind}$  is divided in a number of different heat flow paths. One heat path is composed of two adjacent TEG, four contact thermal resistors  $R_{cont}$  and a joint water cooled cold plate. Thus, the model is capable to simulate various temperature differences  $\Delta T_{TEG}$  caused by the heat up of the coolant over time. A geometric representation of this architecture is given by the test bench, [Fig. 4](#). In the presented model the TEG are connected thermally in parallel and electrically in series. In each thermal TEG-subsystem the electrical



isolation plates are represented by two nodes and two conductive thermal resistances  $R_{cd,cer}$ . The simulated temperatures  $T_h$  and  $T_c$  at these nodes correspond to the measured values on the hot and cold side of the TEG. The thermal resistance  $R_{cd,cer}$  and the thermal capacities  $C_{cer}$  were calculated by taking in account the geometry, thermal conductivity  $\lambda$ , masses  $m$  and specific heat capacity  $c$ .

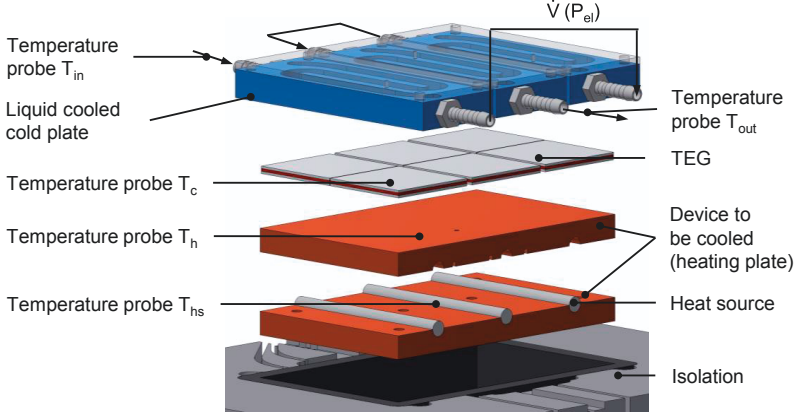


Fig. 4. Test bench to investigate the thermoelectric behavior of a self-cooling system [IWF]

In comparison to MARTINEZ ET AL. [15] the mentioned simplification was implemented by replacing the semiconductor legs by a homogeneous layer. However, the thermoelectric effects of Seebeck, Peltier, Joule, as well as temperature depended heat conductivity of this semiconductor layer are calculated for every time instant. The previously measured values are given as a function of the mean temperature  $T_m$  in Simulink lookup tables. The semiconductor layer is represented by two nodes connected by a temperature depended thermal resistance  $R_{TEG}$ . These nodes include the heat absorbed or generated by Peltier-effect and the heat generated by Joule-effect along the semiconductor legs. The absorbed heat flow rate  $\dot{Q}_{ab,h}$  on the hot side is given by Eq. (6).

$$\dot{Q}_{ab,h} = \dot{Q}_{Peltier,h} + \frac{\dot{Q}_{Joule}}{2} = -\bar{\alpha} \cdot T_{h,eff} \cdot I_L + \frac{R_i \cdot I_L^2}{2} \quad (\text{Eq. 6})$$

The generated heat flow rate  $\dot{Q}_{ge,c}$  on the cold side is given by Eq. (7).

$$\dot{Q}_{ge,c} = \dot{Q}_{Peltier,c} + \frac{\dot{Q}_{Joule}}{2} = \bar{\alpha} \cdot T_{c,eff} \cdot I_L + \frac{R_i \cdot I_L^2}{2} \quad (\text{Eq. 7})$$

Using ideal heat sources and sinks from the Simscape library, the calculated values are given to the mentioned nodes. The difference between them corresponds to the electrical power  $P_{el}$  generated by TEG and is given by Eq. (8).

$$\Delta\dot{Q} = |\dot{Q}_{ab,h}| - \dot{Q}_{ge,c} = P_{el} \quad (\text{Eq. 8})$$

Thus, the induced heat flow rate  $\dot{Q}_{ind}$  is decreased by this value  $\Delta\dot{Q}$ . The reduced heat flow  $\dot{Q}_{ind} - \Delta\dot{Q}$  is dissipated by the following arranged water cooling system. It is modeled by the thermal-liquid domain in Simscape. The last two nodes on the right side of the thermal subsystem between the thermal resistance  $R_{cp,i}$  represent the cooling system, Fig 3. The water cooled cold plates are modeled by a single node with their thermal capacity  $C_{cp}$  and connected to the following node by the heat resistor  $R_{cp}$ . The last node represents a water reservoir that provides coolant at a constant inlet temperature  $T_{in}$ . The heat convective resistors  $R_{cp,i}$  have an individual value for each heat path and is determined by the coolant temperature inside the cold plate. It is calculated on the basis of the tube surface  $A$  and the convective heat transfer coefficient  $h$ , which is given for a defined Nusselt number. The output parameter of the thermal-liquid subsystem is the coolant temperature  $T_{out}$  at the outlet.

Consequently, the model is able to calculate the temperature of each node for an instant of time  $t$ , updates the temperature-dependent parameters and determines the corresponding thermal resistance, thermal capacity, and heat flow rate, respectively. All these parameters are considered constant during a time step  $\Delta t$  [15]. The calculated temperature differences  $\Delta T_{TEG}$  between the hot  $T_{h,eff}$  and cold  $T_{c,eff}$  side of the semiconductor layer is transferred to the electrical subsystem, which is modeled in the electrical domain of Simscape, Fig 3. Firstly, the open-circuit voltage  $U_{oc}$  is determined using the temperature depended Seebeck-coefficient by Eq. 1. Secondly, the electrical load current  $I_L$  and the electrical power  $P_{el}$  are calculated with the model by closing the electrical series connection consisting of a number of TEG and an electrical load  $R_L$ , Eq. 2. The electrical load current  $I_L$  is an important parameter to determine the heat flows  $\dot{Q}$  based on Peltier- and Joule-effect in the thermal subsystem. For each time instant, these values are transferred to the thermal system. The electrical power  $P_{el}$  generated by TEG is directly fed to the motor of the water pump. The volumetric flow rate  $\dot{V}$  provided by the water pump is given as an experimental determined function of electrical power  $P_{el}$  by a Simulink lookup table. The model is capable of simulating both, steady and transient states, of the cooling system. Therefore, open-circuit  $U_{oc}$  and load voltage  $U_L$ , load current  $I_L$ , electrical power  $P_{el}$ , and the

heat flow rates  $\dot{Q}$  by Peltier- and Joule-effect are simulated. The model architecture is scalable and easily adaptable to different applications.

## 4 Model validation

In order to validate the simulative results, a test bench of a self-sustaining cooling system, apart from the machine tool demonstrator, has been put into operation, Fig. 4. This allows the acquisition of experimental data, which is compared to the simulative results. The validation assesses the forecast accuracy of the model. In a volume flow controlled cooling systems, a constant outlet temperature  $T_{out}$  by varying induced heat flow rates  $\dot{Q}_{ind}$ , is a decisive parameter for a stable temperature profile in machine tool components. For this reason, special consideration is given to this parameter by assessing the applicability of a thermoelectric self-cooling system for LDD.

### 4.1 Test bench of a thermoelectric self-cooling systems

The test bench includes six TEG of typ TEG1-40-40-10/100, connected electrically in series and thermally in parallel. The temperature depending parameters of the TEG are determined previously by experimental investigations. The TEG are sandwiched between a copper heating plate with cartridge heaters inside and three water cooled cold plates. The induced heat flow rate  $\dot{Q}_{ind}$  is provided by an adjustable power supply. Based on spatial requirements the possible number of TEG in the LDD cooling system is set to 18 modules. Moreover, the maximal permanent induced heat flow rate  $\dot{Q}_{ind}$  to the designed cooling system is figured to  $\dot{Q}_{ind} \leq 1000$  W. As a result, the range of the induced heat flow rates is set to values of  $\dot{Q}_{ind} = 50 - 330$  W for the test bench setup. The heating plate, the TEG, and the cold plates are completely insulated from the environment. Therefore, it is assumed that the induced heat flow rate  $\dot{Q}_{ind}$  is completely dissipated by the cooling fluid. The closed cooling circuit consists of a gear pump, tubes, and a reservoir. To maintain a constant inlet temperature  $T_{in}$  ice cubes are added to the reservoir. Filled with water as coolant, an inlet temperature of approx.  $T_{in} \approx 2$  °C can be set independently of the outlet temperature  $T_{out}$ . Nevertheless, despite the above-mentioned measure, the inlet temperature  $T_{in}$  displays varying values of  $\pm 1$  K during the experiments. Therefore, the temperature differences between measuring points and coolant temperature at the inlet  $T_{in}$  are applied for the validation of the model. The procedure for data acquisition and the utilized hardware has been described in detail in previous research [12].

## 4.2 Results and analysis

The output parameters used to determine the prediction accuracy of the model are the heat source  $T_{hs}$  and coolant temperature at the outlet  $T_{out}$  as difference to the inlet flow temperature  $T_{in}$ , respectively. Further outputs are defined as the temperature difference between the outer surface of the TEG  $T_h - T_c$ , the electric power  $P_{el}$  generated by TEG, and the volumetric flow rate  $\dot{V}$ . These parameters are of relevance for the performance and operability of the designed cooling system.

- The temperature difference  $T_{hs} - T_{in}$  to prevent overheating of the electric coil inside the primary part of the LDD.
- The temperature difference between the outer surface of the TEG  $T_h - T_c$  which determines the electric power  $P_{el}$  and thus the operating ability of the water pump during steady-state and starting conditions.
- The inlet- and outlet temperature difference  $T_{out} - T_{in}$ , which should be maintained at a constant value even with varying heat flow rates  $\dot{Q}_{ind}$ .
- The volumetric flow rate  $\dot{V}$  as a value providing the cooling capacity.

All of them measured and simulated once the system reaches the steady state at induced heat flow rates of  $\dot{Q}_{ind} = 50, 75, 100, 175, 200, 250, 300$  and  $330$  W, Fig. 5.

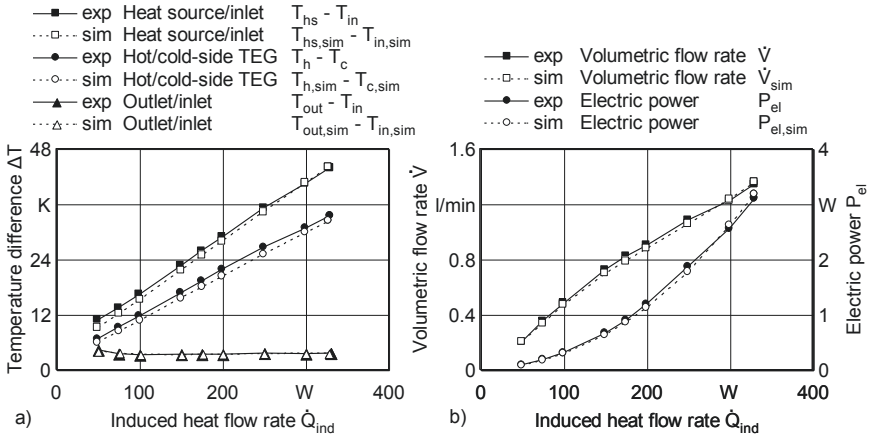


Fig. 5. Experimental and simulated values for steady-state conditions for different heat flows  $\dot{Q}_{ind}$ : (a) Temperature differences; (b) Volumetric flow rate  $\dot{V}$  and generated electrical power  $P_{el}$

The results show that the difference between heat source and inlet temperature  $T_{hs} - T_{in}$  increases with rising heat flow rates  $\dot{Q}_{ind}$ . The maximum deviation between measured and simulated values is stated to  $\Delta T = 1,7$  K at a heat flow

rate  $\dot{Q}_{ind} = 50$  W, which corresponds to a deviation of 15,7 %. Likewise, the temperature difference  $T_h - T_c$  between the hot/cold-side of the TEG also increases. The maximum deviation between measured and simulated values is stated to  $\Delta T = 1,4$  K at a heat flow rate  $\dot{Q}_{ind} = 200$  W, which corresponds to a deviation of 6,4 %. Determined by temperature difference  $T_h - T_c$ , rising values of electrical power  $P_{el}$  generated by TEG and volumetric flow rate  $\dot{V}$  can be observed for increasing heat flow rates  $\dot{Q}_{ind}$ . At a heat flow rate  $\dot{Q}_{ind} = 175$  W, the maximum deviation of the volumetric flow rate  $\dot{V}$  is obtained to be 4,8 %. Referring to the introduction, the studied thermoelectric self-cooling system is capable to provide a demand-oriented volumetric flow rate  $\dot{V}$ , which increases with rising thermal losses. As a consequence, the required cooling capacity  $P_c$  is supplied by these adaptive system-characteristics, which enables to maintain a constant outlet temperature  $T_{out}$  during varying heat flow rates  $\dot{Q}_{ind}$ . This adaptive system behavior is proved by measured and simulated values of the temperature difference  $T_{out} - T_{in}$  between outlet and inlet of the cold plates. The results show for each induced heat flow rate  $\dot{Q}_{ind}$  approx. constant temperature differences between inlet and outlet  $T_{out} - T_{in}$ , Fig. 5a. The maximum deviation between measured and simulated values can be stated to  $\Delta T = 0,3$  K and 6,9 % at a heat flow rates  $\dot{Q}_{ind} = 50$  W. As mentioned, the model is also capable of representing transient states of the system. To assess the transient prediction accuracy of the main outputs, a starting process of the cooling system at the test bench is investigated, Fig. 6.

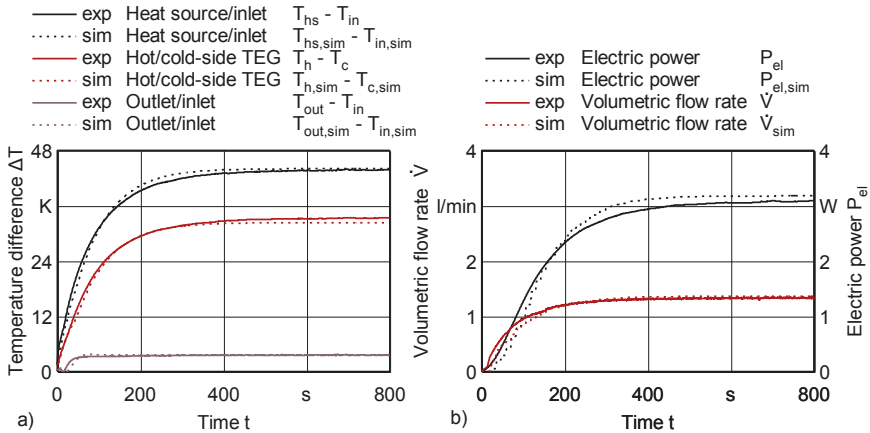


Fig. 6. Simulated and experimental values for the starting process of the pump with a heat flow rate of  $\dot{Q}_{ind} = 330$  W: (a) Temperature differences; (b) Volumetric flow rate  $\dot{V}$  and electrical power  $P_{el}$

Therefore, the test bench is cooled down by external power to a steady-state temperature of approx.  $T \approx 2^\circ\text{C}$ , which corresponds to the reservoir  $T_{\text{res}}$ . A difference between the outlet and inlet temperature  $T_{\text{out}} - T_{\text{in}}$  of nearly  $\Delta T \approx 0^\circ\text{K}$  is displayed as starting condition in Fig. 6(a). A heat flow rate  $\dot{Q}_{\text{ind}} = 330 \text{ W}$  is induced by the cartridge heaters to the heating plate. The results show that the electric power  $P_{\text{el}}$  rises as the temperature difference  $T_h - T_c$  between the hot/cold-side of the TEG also increases. The difference between the outlet and inlet temperature  $T_{\text{out}} - T_{\text{in}}$  of the coolant stagnated for approx.  $t \approx 20 \text{ s}$  at the starting value of  $\Delta T \approx 0^\circ\text{K}$ . The electrical power  $P_{\text{el}}$  generated by TEG is not sufficient to operate the water pump, so that there is no coolant flow in the circuit. At the time  $t \geq 20 \text{ s}$  the water pump is operating and supplies the cooling system with rising volumetric flow rate  $\dot{V}$ . It can be observed that the difference between outlet and inlet temperature  $T_{\text{out}} - T_{\text{in}}$  becomes constant, before all other outputs reach steady-state conditions. This behavior underlines the adaptive supply of volumetric flow rate  $\dot{V}$  and cooling capacity  $P_c$ . Finally, the five output parameters reach the steady state condition. The model is also capable to simulate the thermoelectric behavior during variable heat flow rates  $\dot{Q}_{\text{ind}}$ . As soon as the system has reached the steady state, the induced heat flow rate  $\dot{Q}_{\text{ind}}$  has been abruptly changed by an adjustable power supply in order to simulate a process related thermal load profile. Induced heat flow rates of  $\dot{Q}_{\text{ind}} = 330, 175, 250$  and  $330 \text{ W}$  are investigated. The experimental and simulative results of steady-state and transient conditions are displayed in Fig 7.

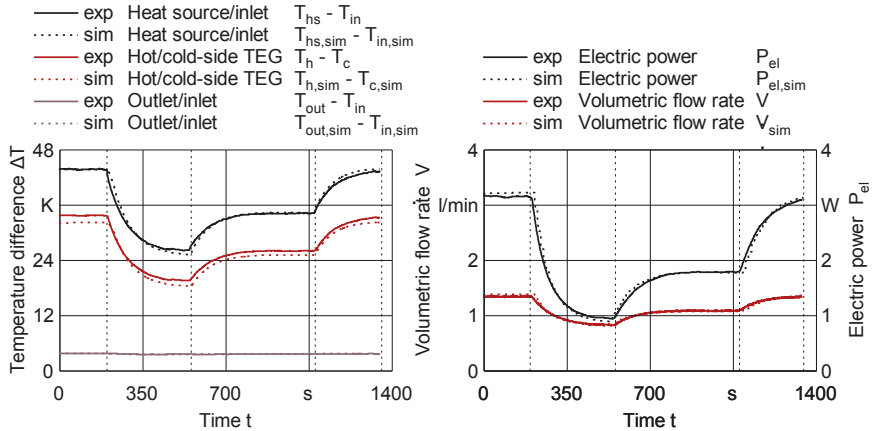


Fig. 7. Simulated and experimental values for steady-state conditions with 330, 175, 250 and 330 W of heat flow  $\dot{Q}_{\text{ind}}$ : (a) Temperature differences; (b) Volumetric flow rate  $\dot{V}$  and electrical power  $P_{\text{el}}$

These investigations prove that the model simulates the transient state of the cooling system with high accuracy. The simulated values of the output parameters agree sufficiently with the experimental data, even for changing thermal loads.

For all induced heat flow rates  $\dot{Q}_{ind} \geq 75$  W, the prediction accuracy of the thermoelectric model for steady-state and transient conditions is found to be higher than 90 %. Thus, the model is accurate enough to be used as a powerful tool for analyzing and development of water flow thermoelectric self-cooling-systems.

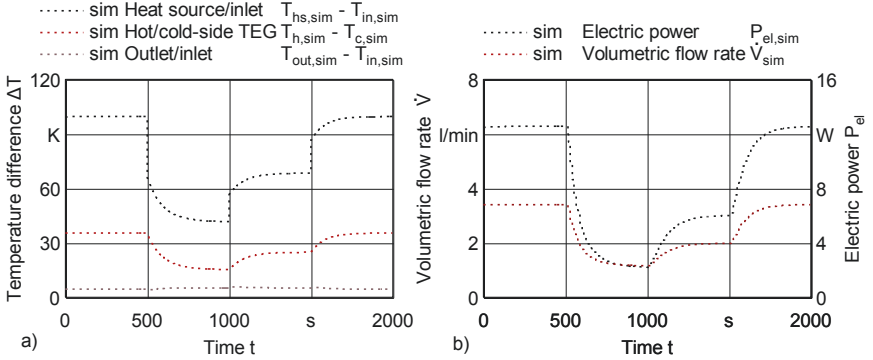


Fig. 8. Simulated and experimental values for steady-state conditions with  $\dot{Q}_{ind} = 1000, 400, 700$  and 1000 W: (a) Temperature differences; (b) Volumetric flow rate  $\dot{V}$  and electrical power  $P_{el}$

Therefore, the model is transferred and scaled-up to the developed design of a self-cooling system for integration in the presented machine tool demonstrator equipped with LDD. In contrast to the previous simulations, an ideal water pump is modeled. The simulated results of the thermal system behavior with variable induced heat flow rates of  $\dot{Q}_{ind} = 1000, 400, 700$  and 1000 W are displayed in Fig 8. It can be seen, that the temperature difference  $T_{hs,sim} - T_{in,sim}$  between inlet and electric coil inside the primary part of the LDD is varying and results in high maxima at heat flow rates of  $\dot{Q}_{ind} = 1000$  W. Due to the described demand-oriented supply of volumetric flow rate  $\dot{V}$ , the difference between outlet and inlet temperature  $T_{out} - T_{in}$  of the cold plate shows slight variations of  $\Delta T = \pm 1$  K, Fig 8.

The results indicate that the thermoelectric generators can provide sufficient energy to operate a pump in a decentralized fluid circuit of a cooling system with reasonable cooling capacity  $P_c$ . Due to the adaptive characteristics by self-regulated supply of volumetric flow rate  $\dot{V}$ , the suggested approach indicates promising prospects to maintain the outlet temperature  $T_{out}$  of machine tool components on constant values without external energy consumption. Therefore, the approach is promising to further reduce on energy consumption of the cooling

fore, the approach is promising to further reduce on energy consumption of the cooling systems in machine tools. Research efforts must be spent to experimental investigations regarding the thermoelectric behavior of the scaled-up cooling system in the machine tool demonstrator. Furthermore, there are challenges in lowering the temperature difference  $T_{hs,sim} - T_{in,sim}$  between electric coil and the inlet to prevent overheating of the primary part of LDD. As mentioned above, the simulated values can be assessed as critical for a continuous operation of the LDD. To reduce this temperature difference  $T_{hs,sim} - T_{in,sim}$ , solutions must be found to decrease the total thermal resistance between electric coil and coolant flow.

## 5 Conclusions

To prevent thermo-elastic deformations of precision related machine tool components, a cooling system ensuring an uniform temperature distribution, by dissipating induced thermal losses, is required. Machine tools subjected to high productivity and accuracy are faced with the challenge of suffering from high-energy consumption and thermal losses influencing the accuracy negatively. To reduce the required energy demand, thermoelectric self-cooling systems are presented. The transferability of a thermoelectric self-cooling system from a downsized test bench to the application in a machine tool equipped by LDD has been investigated. The goal was to investigate the model-based prediction ability of the thermoelectric behavior, especially the operability of a pump in a water cooling circuit without external energy supply.

The comparison of simulative and experimental determined data indicates a high prediction accuracy of the developed model. Therefore, the model is accurate enough to use it as a powerful tool for analyzing and design of water flow thermoelectric self-cooling-systems. The model was applied to predict the thermoelectric behavior of the concepted self-cooling system for linear direct drives. The simulative results show that the developed cooling system is able to maintain a fluid outlet temperature of a linear motor with only minor variations. Supplied by thermoelectric generators, the pump in the water cooling circuit provides a demand-orientated volumetric flow rate  $\dot{V}$  without external energy consumption. Based on the simulative model, the presented approach indicates prospects to increase the energy efficiency of machine tool components, which have substantial thermal losses and must be tempered due to thermal stability requirements.



## Acknowledgements

*This research is supported by the German Research Foundation (DFG). The title of the research project is "Konzepte zur energieautarken Kühlung von Lineardirektantrieben" (UH 100/195-1).*

Supported by:



## 6 References

- [1] IEA - International Energy Agency: Key World Energy Statistics 2017. Paris, 2017.(Accessed: 21.09.17).
- [2] EIA: Industrial sector energy consumption. (2016), S. 113 - 126. (Accessed: 22.09.17).
- [3] The European Parliament and the Council of the European Union. Directive 2009/125/EC of the European Parliament and of the Council of 21 October 2009. Establishing a framework for the setting of ecodesign requirements for energy-related products. Official Journal of the European Union L 285 (2009) S. 10 - 35. (Accessed: 21.09.17).
- [4] The European Parliament and the Council of the European Union. Directive 2010/30/EU of the European Parliament and of the Council of 19 May 2010. On the indication by labelling and standard product information of the consumption of energy and other resources by energy-related products. Official Journal of the European Union L 153 (2010) S. 10 - 12. (Accessed: 21.09.17).
- [5] The European Parliament and the Council of the European Union. Directive 2012/27/EU of the European Parliament and of the Council of 25 October 2012. On energy efficiency, amending Directives 2009/125/EC and 2010/30/EU and repealing Directives 2004/8/EC and 2006/32/EC. Official Journal of the European Union L 315 (2012) S. 1 - 56. (Accessed: 21.09.17).
- [6] Züst, S.; Züst, R.; Schudeleit, T.; Wegener, K.: Development and Application of an Eco-design Tool for Machine Tools. Procedia CIRP 48 (2016) S. 431 - 436.
- [7] Shabi, L.; Weber, J.; Weber, J.: Analysis of the Energy Consumption of Fluidic Systems in Machine Tools. Procedia CIRP 63 (2017) S. 573 - 579.
- [8] Wegener, K.; Mayr, J.; Merklein, M.; Behrens, B.-A.; Aoyama, T.; Sulitka, M.; Fleischer, J.; Groche, P.; Kaftanoglu, B.; Jochum, N.; Möhring, H.: Fluid elements in machine tools. CIRP Annals 66 (2017) S. 611 - 634.
- [9] Altintas, Y.; Verl, A.; Brecher, C.; Uriarte, L.; Pritschow, G.: Machine tool feed drives. CIRP Annals - Manufacturing Technology 60 (2011) S. 779 - 796.
- [10] Mohammadi, A.; Züst, S.; Mayr, J.; Blaser, P.; Sonne, M. R.; Hattel, J. H.; Wegener, K.: A methodology for online visualization of the energy flow in a machine tool. CIRP Journal of Manufacturing Science and Technology (2017).

- [11] Shabi, L.; Weber, J.; Weber, J.: Model-based Analysis of Decentralized Fluidic Systems in Machine Tools. In: Proceedings of the 15th Scandinavian International Conference on Fluid Power, Schweden, 07.06. - 09.06.2017.
- [12] Uhlmann, E.; Salein, S.: Energieautarke Kühlung von Lineardirektantrieben. *wt Werkstattstechnik Online* 107 (2017) 5, S. 359 - 365.
- [13] Uhlmann, E.; Salein, S.: Konzepte zur energieautarken Kühlung von Lineardirektantrieben. *Zeitschrift für wirtschaftlichen Fabrikbetrieb* 111 (2016) 7-8, S. 411 - 415.
- [14] Martínez, A.; Astrain, D.; Rodríguez, A.: Experimental and analytical study on thermoelectric self cooling of devices. *Energy* 36 (2011) 8, S. 5250 - 5260.
- [15] Martínez, A.; Astrain, D.; Rodríguez, A.: Dynamic model for simulation of thermoelectric self cooling applications. *Energy* 55 (2013) S. 1114 - 1126.
- [16] Kiflemariam, R.; Lin, C.-X.: Numerical simulation of integrated liquid cooling and thermoelectric generation for self-cooling of electronic devices. *International Journal of Thermal Sciences* 94 (2015) S. 193 - 203.



# System Modelling and Control Concepts of Different Cooling System Structures for Machine Tools

*J. Popken, L. Shabi, J. Weber, J. Weber*

Institute of Fluid Power IFD, Technische Universität Dresden, 01062 Dresden, Germany

**Abstract.** The current problem with the existing cooling structure of machine tools is that a central fixed pump supplies a constant cooling volume flow to cool all the components of the machine tools, which does not match the individual temperature development of the components: Due to the different amounts of heat introduced (power losses) by the machine components, an inhomogeneous temperature field is generated within machine tools, which leads to a thermo-elastic deformation of their structure. This deformation is responsible for the displacement of the Tool Center Point (TCP) of the machine tools. Consequently, the machine's accuracy during the production process is reduced.

The main target of this paper is to study the thermal behavior of the existing cooling system structure of a demonstration machine with the aid of an experimental investigation in order to develop a network-based simulation model and to introduce new control concepts for different cooling system structures.

Firstly, the paper presents the cooling system design of the demonstration machine and the experimental investigation, which are carried out. Furthermore, a network-based model of the existing cooling system is developed and validated against the measured data. Finally, the validated system model is used to study new control concepts of different cooling system structures in order to ensure a uniform temperature distribution to the machine tool at minimal energy consumption.

Peer-review under responsibility of the International Scientific Committee in the person of the Conference Chair Prof. Steffen Ihlenfeldt.

**Keywords:** Network simulation; Control concepts; Machine tool; Cooling system; Thermo-elastic deformation

---

## 1 Introduction

Due to the different heat input (power losses) of the machine components, an inhomogeneous temperature field is generated within the machine tool structure. Previous research projects such as [1, 2, 3] mainly focused on the energy

demand of the machine tool and its main drives, reducing the energy consumption of auxiliary units by developing more efficient components and control strategies. The thermal behavior, the effectiveness, and the design of the cooling system of a machine tool has not yet been described in detail. Therefore, a detailed analysis of the existing cooling system structures and their effectivity is carried out by sub-project (A04) of the research project SFB/TR96, Thermo-energetic design of machine tools. At the end, the objective is to increase the efficiency of the machine tools and to provide a uniform temperature distribution.

The main target of this paper is to show the deficit, not demand-oriented supply, of the existing cooling system structure of a demonstration machine with the aid of an experimental investigation. The investigation will help obtain more information concerning the effectivity of the cooling system. This makes it possible to derive new optimization approaches with new control concepts. So, the temperature development of each component of the machine tool can be controlled individually. Preliminary investigations in phase 1 of SFB/TR96 were carried out by the demonstration machine type Scharmann DBF630. The research activities of this demonstration machine have shown that the cooling is not sufficiently adjusted to the process and to the individual demand of the machine components [4, 5]. With the optimization of the design and the operation mode of the cooling system the heat introduced within the machine structure can be controlled more efficiently in order to reduce thermo-elastic deformations and the necessary energy demand.

#### Nomenclature

$B$	Flow coefficient	$\text{m}^3/\text{s}/\text{Pa}^{0.5}$
$c$	Specific heat capacity of fluid	$\text{J}/(\text{kg}\cdot\text{K})$
$e$	Control deviation	K
$K'$	Equivalent bulk modulus	Pa
$n$	Number of components	-
$p$	Pressure	Pa
$p_0$	Supply pressure	Pa
$\dot{p}_0$	Change of supply pressure	$\text{Pa}/\text{s}$
$\dot{Q}_H$	Heat flow	W
$T$	Temperature	K
$U_{max}$	Maximal voltage signal	V
$V_{L,0}$	Line volume between pump and valves	$\text{m}^3$
$\dot{V}$	Volume flow	$\text{m}^3/\text{s}$
$y_i$	Relative valve spool position	-
$\rho$	Fluid density	$\text{kg}/\text{m}^3$

## 2 Cooling system design of the demonstration machine

The next selected demonstration machine for the experimental investigation is type DMU80 eVo linear and is used mainly for high speed cutting (HSC). Detailed information about the demonstration machines (DBF630 and DMU80) can be found in [6]. The cooling system of DMU80, as shown in Fig. 1, simultaneously cools 13 components. Here, a fixed displacement pump 1 supplies the cooling medium (45 l/min at 4.5 bar) to the motor spindle 2, all the axis drives (3, 5, 7, 8), the housing of the B and C axes 4 as well as the rails of X, Y, and Z (6, 9-12). The electrical cabinet is not cooled directly by the cooling system but by a separate cooling unit. Moreover, the cooling unit 13 of DMU80's cooling system is not integrated in the return flow; it is mounted directly to the tank as bypass flow. A mixture of water and 30 % Glysantin® (G48®) is used as cooling medium. Furthermore, a three-way-valve 14 is placed into the return flow side. This valve is used as a diverting valve, with a defined setting as a part of the heated backflow it is introduced directly to the inlet side of the pump, and the remaining fluid flows back to the tank [7]. The controller of the three-way-valve adjusts the flow to the tank or to the inlet side of the pump so that the temperature on the pump inlet side always stays at 25 °C, with only a minimal deviation.

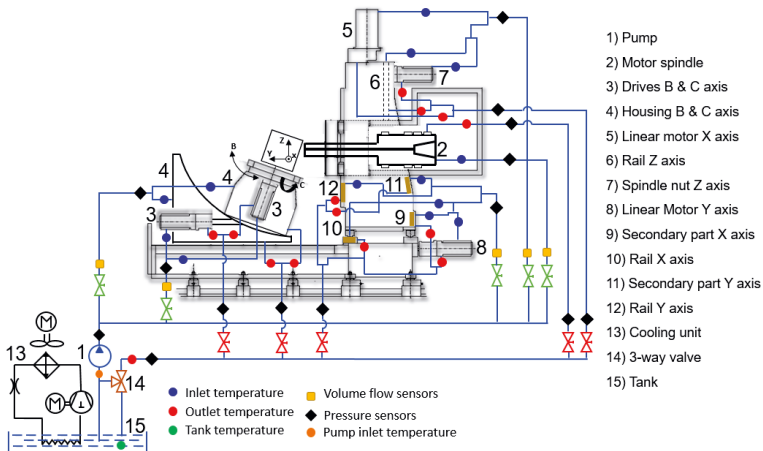


Fig. 1. Schematic of cooling system in DMU 80 eVo linear

In order to investigate the effectivity of the existing cooling system and to derive a statement about the thermal behavior of the components to be cooled, machine measurements of the cooling system of DMU80 are carried out. For

this purpose, several sensors, as shown in Fig. 1, are used to measure the temperature, pressure, and flow rate development. The test process being considered for the experimental investigation consists of four sub-processes: warm up process, idle process, setup process, and manufacturing process. The results of the idle process are shown in this paper, which is carried out in a period of 830 s. The idle process of the DMU80 is based on the ISO 230-3 [8], where typical load cycles are considered. Detailed information about the idle process can be found in [6]. Fig. 2 shows the temperature development of the cooling medium exemplified by the four components of the demonstration machine.

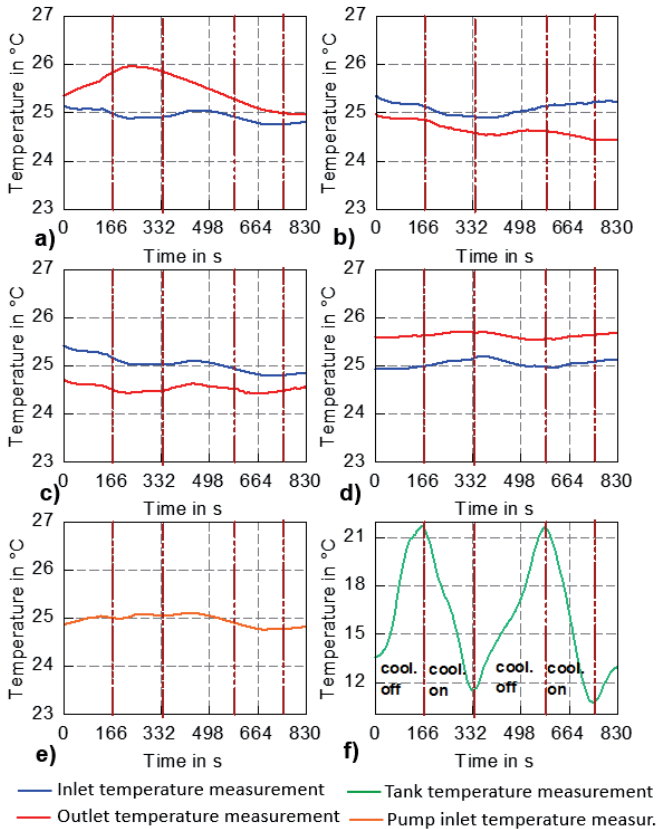


Fig. 2. Temperature characteristics in the idle process of the DMU80 eVo linear a) Motor spindle b) Drive B axis c) Spindle nut Z axis d) Secondary part X axis e) Pump inlet temperature. f) Tank

The effect of the ineffective cooling of the components, not demand-oriented supply, can be seen here. Over the entire process time, the cooling medium

inlet temperature of the drive B axis and spindle nut Z axis is higher than the outlet temperature. So the cooling medium is cooled while the components are warmed up. Another component, such as motor spindle or the secondary part X axis, are cooled during the test process. Further, the temperature characteristics of the components are not directly influenced by the state of the cooling unit, in spite of the two-point temperature control of the cooling unit. This can be traced back to the three-way-valve (Fig. 1, pos. 14) that is placed into the return flow side of the cooling system. As shown in Fig. 5 e, the valve adjusts the sucked in cooling medium from the tank and from the return flow so that the cooling medium always has a constant temperature of 25 °C with a small deviation of  $\pm 0.1 - 0.3$  °C according to the registered measurement.

### 3 System modeling and validation

The methodology of the model development in Fig. 3 is based on thermo-hydraulic network modeling. For the hydraulic and thermodynamic domain, the laws of the electrical engineering, such as rules of Kirchhoff's circuit laws and the laws for series and parallel connection of resistance, can be used. Detailed information about the modeling methodology can be found in [5, 9 tab. 1].

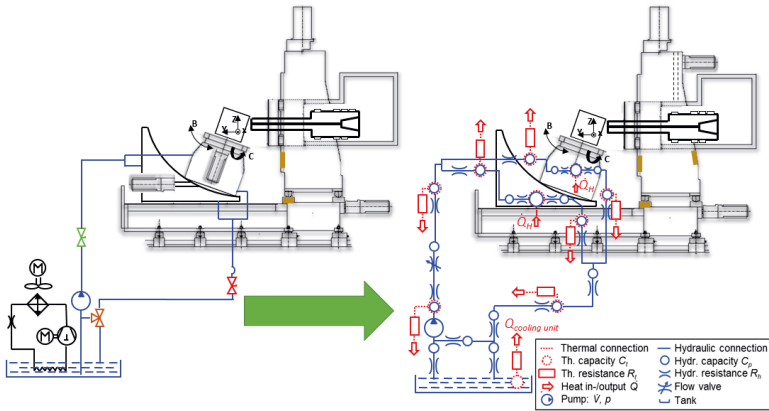


Fig. 3. Methodology of the thermo-hydraulic network modeling

With the aid of the measured temperatures ( $T$ ), volume flow ( $\dot{V}$ ), and pressure drops ( $\Delta p$ ) of each component, the heat flow ( $\dot{Q}_H$ ) of the respective component is calculated in Fig. 4 with the aid of (Eq. 1) as a heat source in the simulation model.

$$\dot{Q}_H = \dot{V} \cdot [c \cdot \rho \cdot (T_{outlet} - T_{inlet}) + (p_{outlet} - p_{inlet})] \quad (\text{Eq. 1})$$



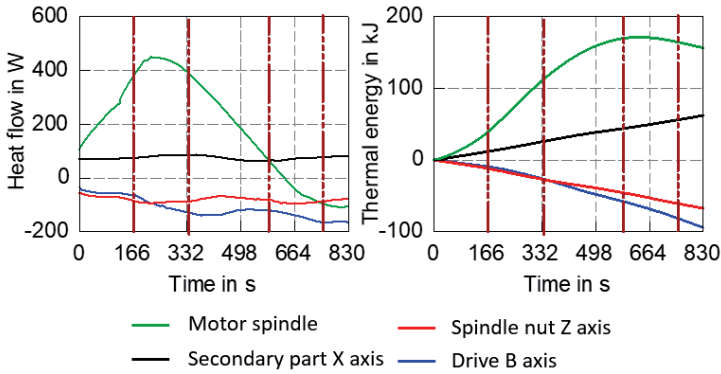


Fig. 4. Heat flow and thermal energy in the idle process of DMU80 eVo linear

For the model-based study of the cooling system, a domain-crossing system simulation with SimulationX (ESI ITI GmbH) is carried out. Table 1 and Fig. 5 show a direct comparison of the simulation and measurement of the idle process of the DMU80. The simulation model developed shows a high accuracy of the thermal (see Fig. 5) and hydraulic quantities (see Table 1) of the components under consideration. As mentioned above, the current cooling system includes a constant supply unit (pump), so in the evaluation of the hydraulic quantities it is easy to see that the cooling system is characterized as a stationary system. On the contrary, the temperature profile of the components shows fluctuations over the entire process time. Therefore, the simulation model can be validated and will be used to improve the current structure of a cooling system as well as to develop process- and demand-oriented control strategies.

Table 1. Comparison of hydraulic quantities in the idle process both in simulation and measurement

Sub-systems	Measured pressure [bar]	Simulated pressure [bar]	measured flow [l/min]	simulated flow [l/min]
Motor spindle	3.3	3.4	9.3	9.2
Drives B & C axis	3.3	3.3	7.3	7.4
Housing B & C axis	3.3	3.4	9	9.1
XZ axis	3.4	3.4	7.3	7.4
XY axis	3.3	3.1	10.9	10.9
Pump	4.5	4.6	43.8	44

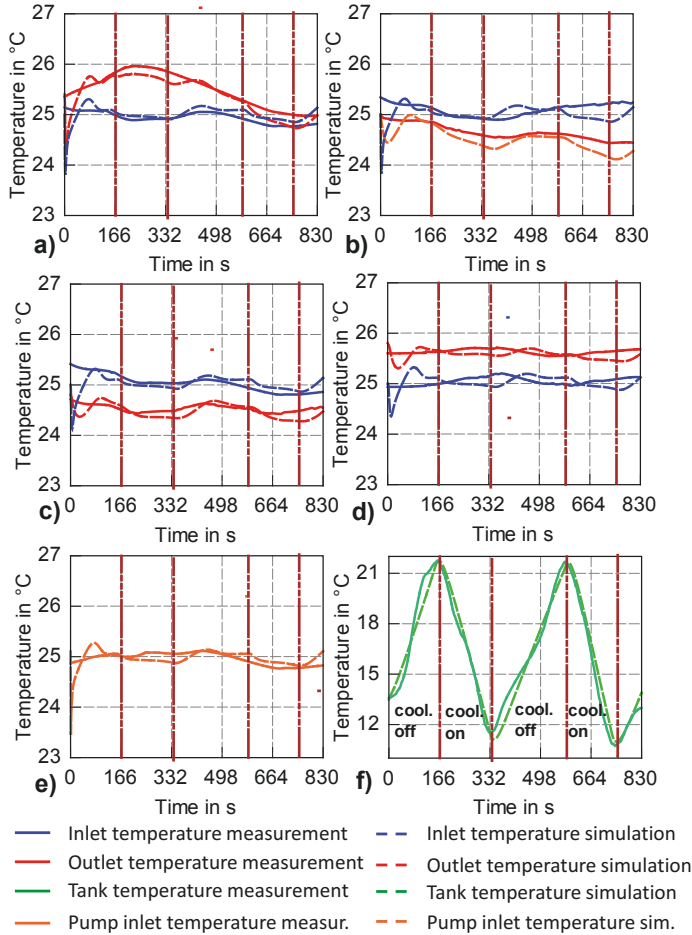


Fig. 5. Comparison of temperature development simulation and measurement in the idle process a) Motor spindle b) Drive B axis c) Spindle nut Z axis d) Secondary part X axis e) Pump inlet temperature f) Tank

## 4 Control concepts of different cooling system structures

The previous and current studies of the cooling systems for two demonstration machines (DBF630 and DMU80) indicate that the supplied cooling volume flow does not match the temperature development of the individual components. In order to counter the deficits of the current cooling system structure of machine tools, it is necessary to think about new concepts and structures to optimize

their thermal behavior and effectivity. Controlled cooling systems based on the temperature development of the components enable an appropriate flow rate supply with an individually targeted temperature control at low energy consumption. Fig. 6 shows three new structures of a cooling system that can be applied for a demand-oriented supply. The new structures will be evaluated in regard to minimal pressure loss, minimal hydraulic performance of the pumps, and uniform temperature development. The following sections explain the control concepts of new cooling systems.

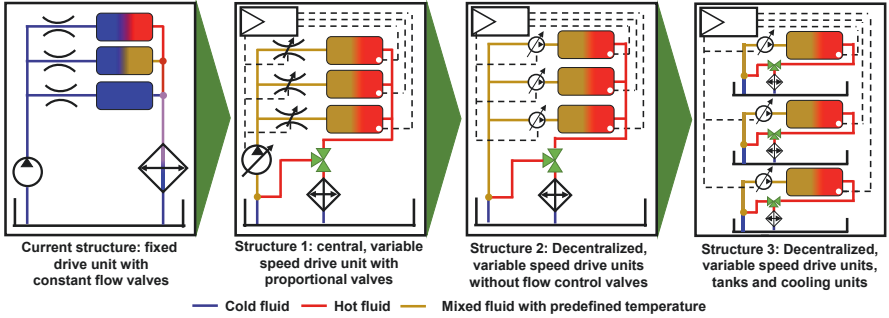


Fig. 6. New concepts of a cooling system

#### 4.1 Central, variable speed drive unit with proportional valves

Contrary to the current cooling system structure with a central, fixed speed drive and constant flow valves, controllable proportional valves are used in the cooling structure shown in Fig. 7. With the help of these valves, it is possible to adjust the demand-orientated flow based on the temperature development of the components. The control system of a cooling system compares the actual temperature with the required temperature of each component and according to the control algorithm, adjusts the proportional valves and the variable speed drive unit. The actual temperature is the fluid temperature on the outlet of the component. If the temperature development of the component does not exceed a predefined limit, the associated proportional valves will remain closed. The cooling unit remains in the two-point temperature control and regulates the middle temperature of the cooling medium in the tank. In addition, the control system adjusts the pump speed so that the sum of required flow rates of all the components is ensured [10]. The flow rate through a proportional valve can be calculated using the equation:

$$\dot{V} = B(y_i)\sqrt{p_0 - p_i} \quad (\text{Eq. 2})$$

The change of supply pressure is described by the equation:

$$\dot{p}_0 = \frac{K'(p_0)}{V_{L,0}} \left( \dot{V}_{pump} - \sum_{i=1}^n \dot{V}_i \right) \quad (\text{Eq. 3})$$

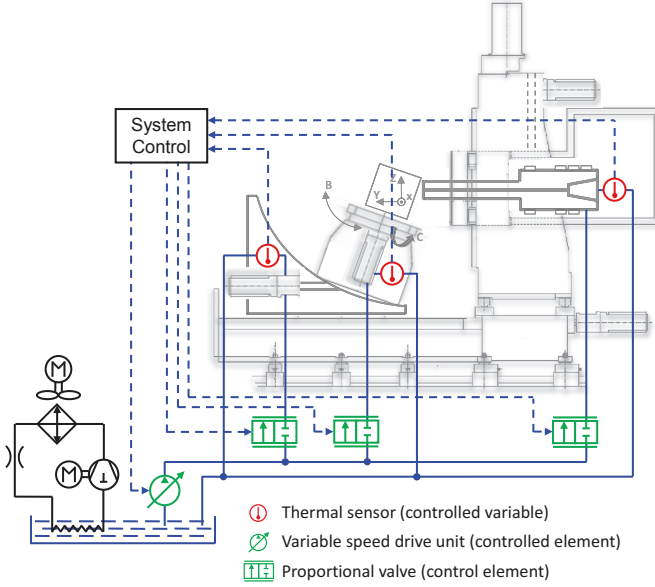


Fig. 7. Cooling structure with central, variable speed drive unit and proportional valves

Eq. 2 and Eq. 3 show the dependence of the individual flow rates of the components. Due to these correlations of the individual cooling circuits, the system considered is a so-called Multiple-Input-Multiple-Output System (MIMO system) and has cross-couplings. This means that one control element simultaneously influences several control variables. Fig. 7 shows that the cooling system has one more control element than control variables. The considered structure of the cooling system is over-determined because one degree of freedom is required to control one control variable. In the following, three approaches to solve the problem of this control strategy will be introduced:

#### A) Definition of a constraint

The over-determinacy in a control system can be eliminated by a control-based definition of constraint between several control elements. Fig. 8 illustrates a control concept which uses the definition of a constraint. The PI-controller compares the actual temperature with the targeted temperature and delivers a voltage signal from 0 to 10 V to adjust the valves. The output voltage signal

from the controller is transferred to the proportional valve and to the stored characteristic map. This characteristic map describes the correlation of Eq. 2. At the proportional valve, the pressure drop is measured. With the information of the pressure drop and output signal of the PI-controller, the volume flow rate in the characteristic map is determined. The flow rates of all the components are added, and the sum is converted to the input voltage signal of the variable speed drive unit.

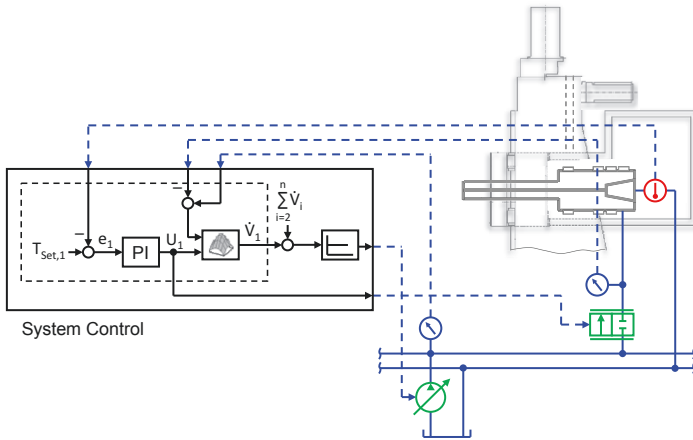


Fig. 8. Control concept with a control-based constraint

### B) Removal of control element from the active control loop

The next, selected approach to reduce the number of degrees of freedom is carried out by the removal of a control element from the active control loop. The feedback controller adjusts the control elements which are involved in the control loop. The removed control element from the active control loop is controlled separately or assigned with a predefined value. Fig. 9 shows the control concept with the removed control element.

From an energetic point of view, the proportional valve of the component with the highest thermal load will be completely open, and the remaining valves are adjusted by the controller. Consequently, the minimal pressure losses are achieved in the cooling system [10]. The variable displacement pump regulates the temperature of the component with the highest load. The temperature of the other components is controlled by the remaining proportional valves. With regard to the control strategy shown in Fig. 9 the output voltage signal of PI-controllers of the proportional valves are compared with each other, this way, the maximal output voltage signal is determined and the component with the

highest load is identified. The system control assigns the maximal output voltage signal ( $U_{max}$ ) to the proportional valve of the component with the highest load. At the same time the temperature deviation of the component with the highest load is assigned to the PI-controller of the variable speed drive unit.

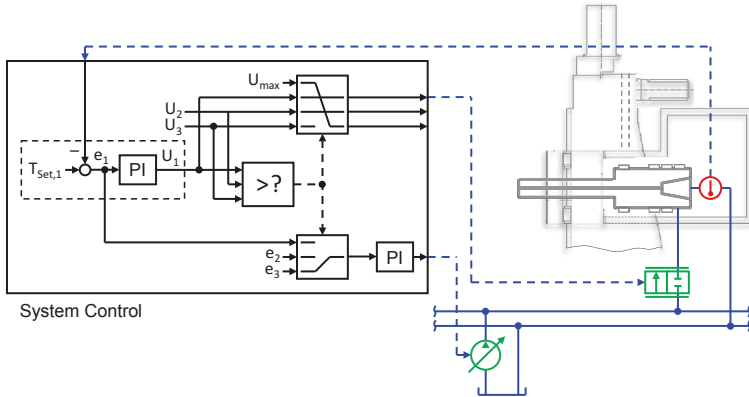


Fig. 9. Control concept with removal of a control element

### C) Definition of an additional control variable

The last approach that can be applied to avoid the over-determinacy of the cooling structure considered is the definition of an additional control variable in Fig. 10. A possible control variable is the input voltage signal (or opening) of the proportional valves of the component with the highest load.

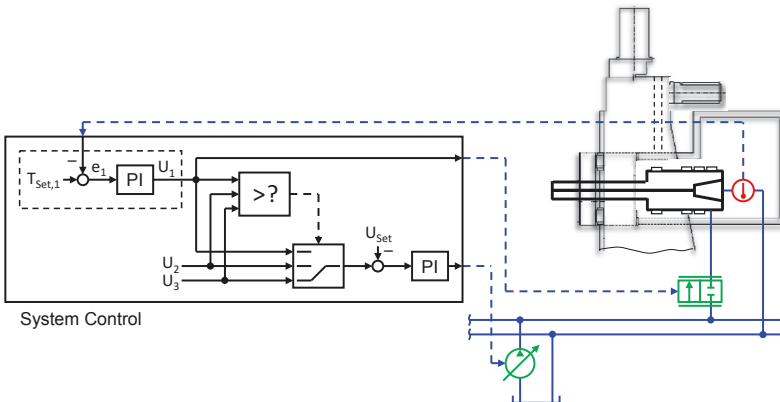


Fig. 10. Control concept with an additional control variable

With this control concept, all proportional valves are adjusted by PI-controllers. The system control determines the highest delivered output voltage signal from

the PI-controllers and compares this signal with the predefined targeted voltage signal in the control unit. A PI-controller processes the voltage deviation and transfers the output signal to the variable displacement pump. For example, the voltage signal can be regulated to 98% of  $U_{max}$  in order to generate small throttle losses. A complete valve opening (100% of  $U_{max}$ ) is not useful because the stability of the control loop cannot be guaranteed.

## 4.2 Decentralized networked pumps

In the cooling structure shown in Fig. 11, the components are supplied with individual variable displacement pumps and a common tank and cooling unit. Flow or proportional valves to parallelize the flow rate are not necessary for this cooling concept. The feedback controllers of each component compare the actual temperatures with the targeted temperatures and adjust the pump speeds on the basis of the temperature development. Each pump delivers a demand-oriented flow rate of the cooling medium. If the temperature of a component decreases below a predefined limit, the pump will become inactive.

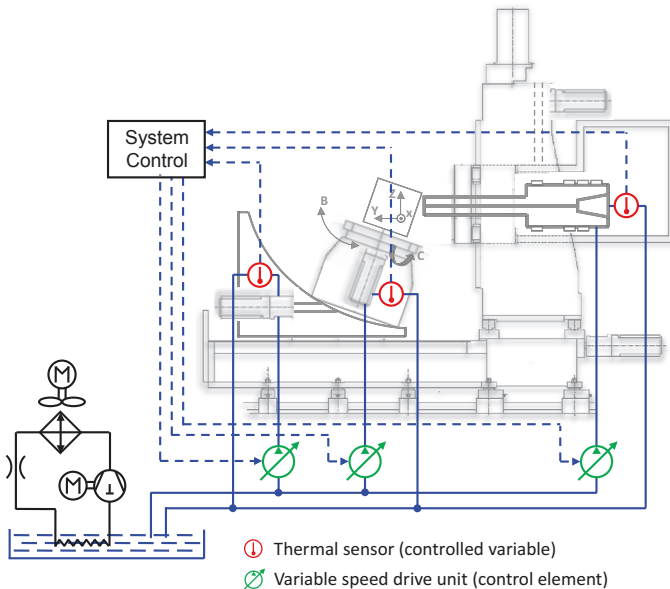


Fig. 11. Cooling structure with decentralized, variable speed drive units without flow control valves

Due to the individual supplies of each component with the decentralized pumps, the circuits operate independently. Therefore, this system consists of

several independent Single-Input-Single-Output control systems (SISO system). Consequently, each temperature can be regulated by a PI-controller. The I-term of the controller eliminates any remaining control deviation of the P-term.

## 5 Summary

During different production processes, e.g. drilling, cutting, or milling, a part of the electric and mechanical energy (energy losses) is converted to thermal energy. Insufficient cooling of the machine tools by a constant fixed drive unit with invariable flow valves leads to temperature fluctuations within the machine structure. Finally, a thermo-elastic deformation occurs and the machine's accuracy during the production process is reduced.

The experimental investigations of the cooling system of two different machine tools [4, 5] show the deficit of the existing current cooling system. It could be shown that the machine components are not purposefully cooled with the current cooling structures, and that the cooling is adjusted insufficiently in reference to component demand and process requirement. Therefore, the investigation and evaluation of the new cooling concepts is of great importance.

Different temperature control concepts for cooling system structures are discussed in this paper. Thereby, the focus is on the cooling structure with a central variable speed drive unit in combination with proportional valves to distribute the flow rates, and on overcoming the over-determinacy of this cooling structure. In the future, the described control concepts will be refined in order to evaluate the controller stability, high control precision in a steady state, and insensitivity to dynamic influences. Due to the cross-coupling of the system, the dynamic behavior of the control concepts is difficult to describe. Thus, a follow up investigation of the dynamic behavior is necessary.

### **Acknowledgements**

*The research activities presented are part of the project "Thermo-energetic description of fluid systems" (Ref. No. CRC/TR 96, A04). The authors would like to thank the German Research Foundation (DFG) for financial support.*



## 6 References

- [1] Brecher, C., 2012. Effizienzsteigerung von Werkzeugmaschine durch Optimierung der Technologien zum Komponentenbetrieb-EWOTek, Apprimus Verlag, Aachen.
- [2] Denkena, B., Garber, T., 2013. NCplus Prozess und wertschöpfungsorientiert gesteuerte Werkzeugmaschine, PZH Verlag, Aachen.
- [3] Götze, U., Koriath, HJ., Kolensikov, A., Linder, R., Paetzold, J., Scheffler, C., 2010. Energetische Bilanzierung und Bewertung von Werkzeugmaschinen, Tagungsband Energieeffiziente Produkt- und Prozessinnovationen in der Produktionstechnik eniPROD, Chemnitz.
- [4] Weber, J., Weber, J., 2014. Thermo-Energetic Analysis of the Fluidic Cooling Systems in Tooling Machines. 9th International Fluid Power Conference, Aachen, March 24-26, 2014.
- [5] Shabi, L., Weber, J., Weber, J., 2017. Model-based Analysis of Decentralized Fluidic Systems in Machine Tools, In: 15th Scandinavian International Conference on Fluid Power, SICFP'17, Linköping, Sweden, June 7-9, 2017.
- [6] Shabi, L., Weber, J., Weber, J., 2017. Analysis of the Energy Consumption of Fluidic Systems in Machine Tools. The 50th CIRP Conference on Manufacturing Systems, Taiwan, May 3th - 5th, 2017.
- [7] Sauter Group Product brochures valves and drives, P100014406 -V2, [www.sauter-controls.com](http://www.sauter-controls.com); 30.11.2016; 13:55.
- [8] International standard ISO 230-3. Test code for machine tools, part 3: Determination of thermal effects. Second edition 2007-08-15.
- [9] Weber, J., Weber, J., 2013. Thermo-energetic analysis and simulation of the fluidic cooling system of motorized high-speed spindles. SICFP2013, Linköping, Sweden June 3th-5th, 2013.
- [10] Finzel, R., 2011, Elektrohydraulische Steuerungssysteme für mobile Arbeitsmaschinen, Shaker Verlag, Aachen.

# The electric drive as a thermo-energetic black box

*S. Winkler, R Werner*

Faculty of Electrical Engineering and Information Technology,  
Technische Universität Chemnitz, 09107 Chemnitz, Germany

**Abstract.** Electric drives in machine tools can generate several kW of power losses. Hence the modelling of drive losses and the resulting heating is essential for determining the thermally induced displacement of a machine tool. The present study examines the specifications necessary for the modeling and the requirements of the motor model to the input parameters, for example their temporal resolution. Not all parameters of the motor, in particular the slot geometry, are sufficiently known. Therefore it is shown which assumptions to the parameter estimation can be made and how these affect the accuracy of the model.

Peer-review under responsibility of the International Scientific Committee in the person of the Conference Chair Prof. Steffen Ihlenfeldt.

*Keywords:* Electrical motor; Losses; Thermal model

---

## 1 Introduction

The losses in the electrical drives of a machine tool lead to heat flows. A part of these heat flows are transferred into the machine structure. This results in thermo elastic deformations which impair the machining accuracy. The knowledge of the heat input by the drive motor is therefore essential for an effective correction of the machining error. Therefore a motor model is required. This model must be able to describe both the power losses as well as the temperature distribution and the heat flows inside of the motor. The problem is the modeling of the inner structure, since its geometry is generally not published by the manufacturer. Nevertheless it will be shown how motor models can be derived. Furthermore these models can adequately approximate the motor temperature with a small computational effort.

## 2 Fundamentals of the motor model

The motor model is created using the method of the heat source networks, cf. [1,2,6]. In this case, network nodes are assigned to the essential motor compo-

nents. Power losses are fed to the nodes and the nodes have a thermal capacity in relation to the ambient temperature as a thermal reference potential. The relevant heat flows in the motor are represented by heat transfer between the respective nodes. The calculated node temperature is the difference to the ambient temperature and corresponds to the mean temperature of the respective motor component.

For the resulting motor model some simplifications can be made.

- The motor is evenly heated by the rotation of the shaft and is therefore rotationally symmetrical.
- Due to the geometry of the slots, the heat flow of the windings mainly flows to the teeth.
- Since all slots or teeth are tempered by the rotational symmetry, they can be considered to be connected in parallel.
- In a first approximation, the motors are mirror-symmetrical in the axial direction.
- In the air gap between the stator and the rotor, the heat transfer is based on Taylor-Couette flow.

In machine tools, asynchronous motors are generally used as spindle drives and permanent-magnet synchronous servomotors as feed drives. The main difference between these two types of motors is the rotor. Asynchronous motors have a laminated rotor with a so-called squirrel cage inserted in the slots. In a servo motor, the rotor usually consists of solid steel, which is covered with surface magnets made of neodymium-iron-boron.

In result there are two different models for the two motors. The model for asynchronous motors is shown in Fig. 1. The model for synchronous servomotors is shown in Fig. 2.

The essential task is to parameterize the heat capacities and heat transfers of these models. The procedure in the following section provides an adequate approximation for configuring the main dimensions of standard motors. For motors with comparable dimensions as often used in machine tools, the approximation also gives sufficiently accurate values. The procedure is not suitable, for motors with very different size ratios compared to standard motors, such as torque motors.

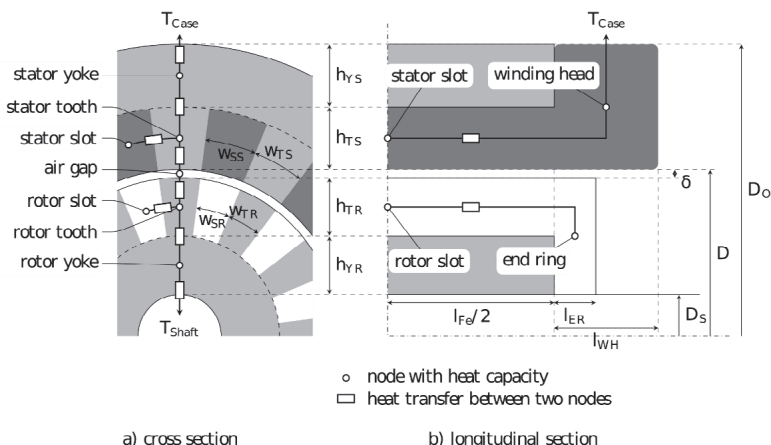


Fig. 1. Thermal model for asynchronous motors

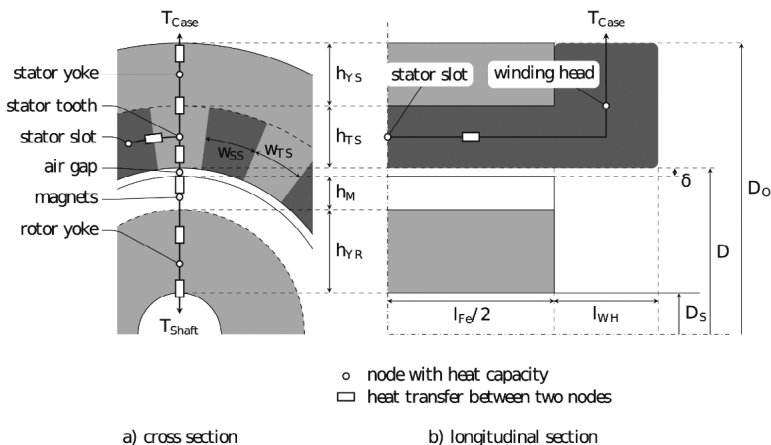


Fig. 2. Thermal model for synchronous servo- motors

### 3 Parameterization of the motor model

#### 3.1 Motor dimensions

For the model parameterization, the main dimensions of the stator and rotor are required. If these are not given, they must be estimated from given data, such as the case diameter. From a comparison of the data from various manufacturers (cf. [3,5]), the following geometric conditions could be determined

with reference to the outer stator diameter  $D_O$ . This comparison includes both spindle motors and standard motors.

- Case diameter  $D_C = 1.15 \cdot D_O$
- Inner stator diameter  $D = 0.65 \cdot D_O$
- Length of the core  $l_{Fe} = 0.89 \cdot D_O$
- Length of the winding head  $l_{WH} = 0.21 \cdot D_O$
- Shaft diameter  $D_S = 0.4 \cdot D_O$  for spindle motors,  $D_S = 0.225 \cdot D_O$  for standard motors
- Length of the air gap  $\frac{\delta}{\text{mm}} = 0.25 \cdot \sqrt[4]{\frac{P_N}{\text{kW}}} \geq 0.2\text{mm}$ , according to [4]

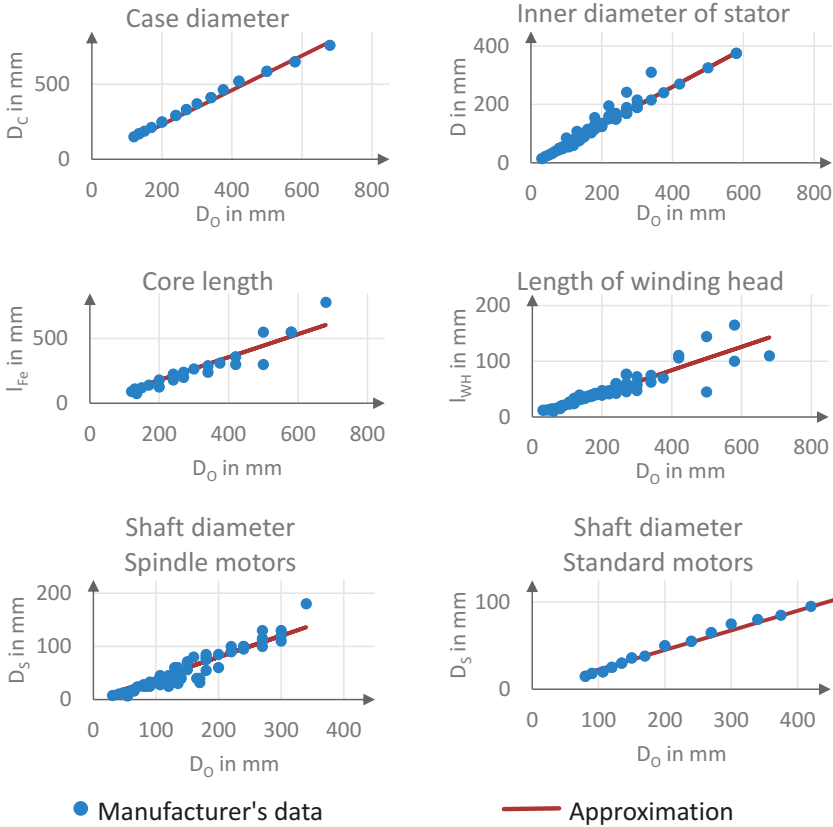


Fig. 3. Approximated dimensions of a rotating motor as a function of the outer stator diameter

Fig. 3 shows the dimensions given by the manufacturers together with derived estimates. With these estimations the slot geometry can be derived.

When designing the slot geometry, it is essentially sufficient to provide enough space to accommodate the winding and to ensure that the core is subjected to a uniform magnetic load. In general, the following ratios for the slot geometry (see Fig. 1 and Fig. 2) can be derived therefrom.

- In the stator, the yoke is as high as the teeth or the slots.
  - $h_{YS} = h_{TS} = h_{SS} = \frac{D_0 - D}{4}$
- The stator slots are approximately as wide as the stator teeth.
  - $w_{SS} = w_{TS} = \frac{(D + h_{SS}) \cdot \pi}{2 \cdot N_S}$
- For asynchronous motor conditions apply in the rotor similar to the stator
  - $h_{YR} = h_{TR} = h_{SR} = \frac{D - D_S - 2 \cdot \delta}{4}$
  - $w_{SR} = w_{TR} = \frac{(D - h_{SR} - 2 \cdot \delta) \cdot \pi}{2 \cdot N_R}$
- For rotors in servomotors other conditions apply by the magnets
  - Height of magnets  $h_M = 0.1 \cdot \frac{D - D_S - 2 \cdot \delta}{2}$
  - Height of rotor yoke  $h_{YR} = 0.9 \cdot \frac{D - D_S - 2 \cdot \delta}{2}$

As a final point to determine the slot geometry the number of slots is decisive. The number of slots per pole and strand  $q$  should preferably be greater than 2, cf. [4]. At the same time, the tooth width should be as large as possible, so that there are no complications in production. Therefore in most cases  $q = 3$  is chosen as a compromise. This leads to a

- Number of stator slots of  $N_S = 36$ .

The number of rotor slots in an asynchronous motor should differ from the number of stator slots. High-speed spindle motors are usually equipped with a

- Number of rotor slots of  $N_R = 32$

### 3.2 Material parameters

An electric motor is composed of different materials. In addition to pure substances such as the squirrel cage made of copper (for spindle motors) and aluminum (for standard motors) or the magnets made of NdFeB, whose values are described in the literature, the material mixtures in the winding and in the core are of particular importance.

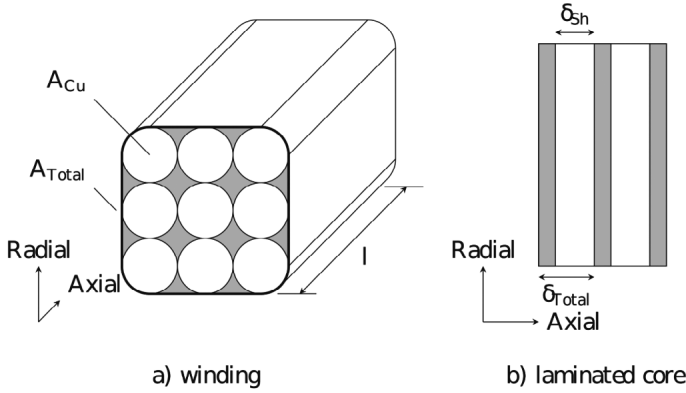


Fig. 4. Construction of the winding and the core

The core is a series connection of the thermal resistors  $R_{th}$  (compare Eq. 1) in the axial direction. The winding in axial direction, as the core in radial direction, is a parallel connection of the thermal conductances  $L_{th}$  of the pure substances (compare Eq. 2). In the radial direction, the heat of the windings must flow alternately through copper and insulation. For this, only conditionally valid approximations can be found, cf. [1].

$$R_{th,res} = \sum_i \frac{l_i}{\lambda_i \cdot A} \quad (\text{Eq. 1})$$

$$L_{th,res} = \sum_i \frac{\lambda_i \cdot A_i}{l} \quad (\text{Eq. 2})$$

With typical values (see [4]) for

- the slot filling factor  $\varphi_W = \frac{A_{Cu}}{A_{Total}} = 0.45$  and
- the stacking factor  $\varphi_{Fe} = \frac{\delta_{Sh}}{\delta_{Total}} = 0.95$

the material parameters shown in Table 1 are obtained.

Table 1. Material parameters of mixtures in electrical motors

	Winding axial	Winding radial	Core axial	Core radial
Thermal conductivity in $\frac{W}{m \cdot K}$	171.16	0.86	2.28	42.76
Heat capacity in $\frac{J}{kg \cdot K}$	391.4		470	
Density in $\frac{kg}{m^3}$	4564		7650	

### 3.3 Loss Distribution

In addition to the heat capacities and heat transfers, a decisive factor is how the different losses that are generated in a motor are divided as input variables to the individual model nodes.

The winding losses  $P_{V,W,S}$ , which are caused by the current flow, are assigned to the stator slots and the winding head. This applies to both types of motors. Which proportion of the losses is produced in the slots and in the winding head depends on the length of the winding. The length of the winding in the slots corresponds to the core length. The length of the winding head is calculated in accordance with [4]

$$l_{WH} = 1.3 \cdot \frac{D \cdot \pi}{2 \cdot p} + \left( 0.03 + 0.02 \cdot \frac{U_N}{kV} \right) m \quad (\text{Eq. 3})$$

This results in the relative winding head length

$$\varphi_{WH} = \frac{l_{WH}}{l_{WH} + l_{Fe}}. \quad (\text{Eq. 4})$$

In asynchronous motors, the winding losses  $P_{V,W,R}$  also occur in the rotor. This results in about 90% in the rotor slots and about 10% in the end ring.

The core losses  $P_{V,Fe}$ , which arise due to the change in the magnetic field in the core, are equally divided between the stator teeth and the stator yoke for both types of motors. This assumption is justified, since the induction in the teeth is higher than in the yoke. This results in more losses in a certain volume. However, the effect is offset by the smaller volume.

In the air gap, only the air friction losses  $P_{V,R,Air}$  are relevant.

The excess losses  $P_{V,Z}$  are mostly caused by harmonics in the air gap field and, therefore, attributed to the rotor teeth for asynchronous motors and the magnets for synchronous motors.

Table 2. Input values for the thermal models

Nodes for both motor models	Input value
Stator slots	$P_{V,W,S} \cdot (1 - \varphi_{WH})$
Winding head	$P_{V,W,S} \cdot \varphi_{WH}$
Stator teeth	$0.5 \cdot P_{V,Fe}$
Stator yoke	$0.5 \cdot P_{V,Fe}$
Air gap	$P_{V,R,Gas}$
Rotor yoke	0

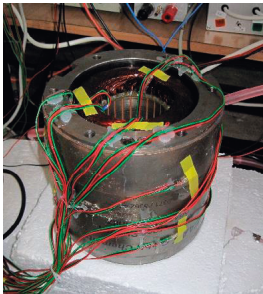


Nodes only for asynchronous motors	Input value
Rotor slots	$0.9 \cdot P_{V,W,R}$
End ring	$0.1 \cdot P_{V,W,R}$
Rotor teeth	$P_{V,Z}$
Nodes only for servomotors	Input value
Magnets	$P_{V,Z}$

## 4 Comparison of simulation and measurement

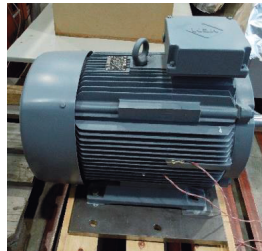
The accuracy of the created models was verified by measurements.

A first measurement was carried out with a water-cooled 30kW motor spindle whose rotor was removed, cf. Fig. 5a. A supply with direct current also ensured that only winding losses occur in the windings. This makes it possible to check the model in a simplified form.



a) 30kW motor spindle without rotor

Known Dimensions
Case Dia.
$D_C = 190\text{mm}$
Case Length
$l_C = 138\text{mm}$
Stator Dia.
$D_O = 130\text{mm}$
Core Length
$l_{Fe} = 100\text{mm}$



b) 22kW standard motor

Known Dimensions
Case Dia.
$D_C = 320\text{mm}$
Case Length
$l_C = 355\text{mm}$

Fig. 5. Motors used for model verifications

The spindle stator has four measuring points, at the stator slots, at the winding head, the case temperature and the average temperature of the cooling water. Except for the case temperature, the model can follow the measured values very well at all measuring points, cf. Fig. 6. The cooling is a boundary condition for the motor model. The heat transfer to the cooling water is thus greatly simplified in the model and is designed to follow the cooling water temperature. This results in the case temperature, which is calculated too low.

A measurement for checking the complete motor model was performed with an air-cooled 22kW standard asynchronous motor, cf. Fig. 5b. The average winding temperature and the case temperature served as measuring points.

To measure the winding temperature, the motor had to be switched off for about 30s. During this time the fan was not working, this led to a brief rise in

the case temperature. The standstill times are much smaller than the thermal time constant of the motor, so they were not considered in the model and therefore cannot be seen in the graph of the simulated temperature, cf. Fig. 7.

The complete model was calculated without knowledge of the internal motor geometry and without measuring calibration. The temperature deviation is up to 5K higher than with the simplified model. Though the model can follow the motor temperature quite well. And, if it should be necessary, it is quite possible to increase the model's accuracy by a measurement trim.

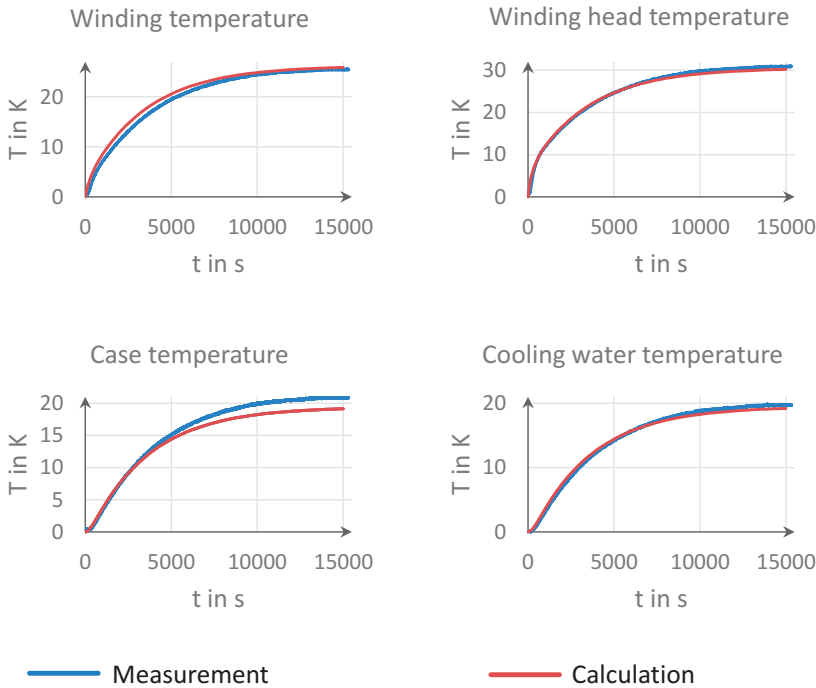


Fig. 6. Comparison of measurement and simulation for the simplified model

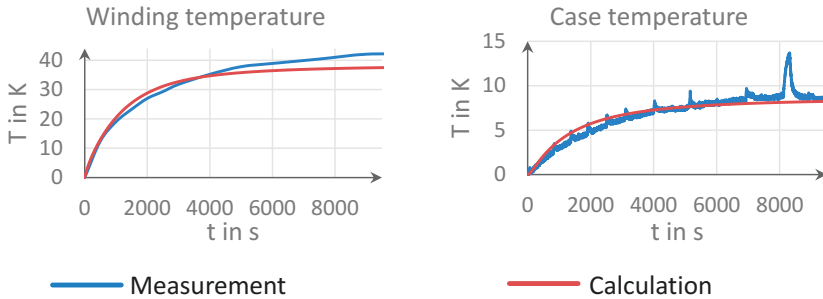


Fig. 7. Comparison of measurement and simulation for the complete model

## 5 Summary

In this article, a large number of motors were analyzed with regard to their geometry data. It turned out that the essential motor dimensions can be determined in good approximation by fixed ratios. This makes it possible to develop geometrically similar yet freely scalable models for each type of motor. Taking into account the thermal properties of some mixtures of materials frequently found in electric motors, it is possible to develop sufficiently accurate heat source networks with some easily determinable main dimensions and without knowledge of the internal motor geometry. These heat source networks are suitable both for the drives in machine tools as well as for standard motors.

### Acknowledgements

*The authors would like to thank the German Research Foundation (DFG) for financial support within the Collaborative Research Centre Transregio 96.*

## 6 Literature

- [1] Gotter, G., 1954. Erwärmung und Kühlung elektrischen Maschinen. Berlin, Springer
- [2] Kessler, A., 1964. Zur Theorie des Wärmequellennetzes. Archiv für Elektrotechnik 49, 109-123
- [3] KMMP, Kurt Maier Motor-Press GmbH [online]. Available: <http://www.kmmp.de> [Accessed 25 Jul. 2015]
- [4] Müller, G., Vogt, K., Ponick, B., 2008. Berechnung elektrischer Maschinen. Wiley VCH
- [5] Sycotec GmbH & Co. KG, sycotec.eu [online]. Available: <http://www.sycotec.eu/> [Accessed 25 Jul. 2015]
- [6] Wiedemann, E., Kellenberger, W., 1967. Konstruktion elektrischer Maschinen. Berlin, Heidelberg, Springer

# Thermal error compensation on linear direct drive based on latent heat storage

*I. Voigt<sup>a</sup>, S. Winkler<sup>b</sup>, R. Werner<sup>b</sup>, A. Bucht<sup>c</sup>, W.-G. Droschel<sup>a,c</sup>*

<sup>a</sup>Institute for Machine Tools and Production Processes IWP, Technische Universität Chemnitz, 09107 Chemnitz, Germany

<sup>b</sup>Faculty of Electrical Engineering and Information Technology, Technische Universität Chemnitz, 09107 Chemnitz, Germany

<sup>c</sup>Fraunhofer Institute for Machine Tools and Forming Technology IWU, Nöthnitzer Straße 44, 01187 Dresden, Germany

**Abstract.** Linear motor feed drives induce time variable heat losses that cause thermoelastic deformations in the surrounding machine structure. Consequently, unsteady displacement fields arise leading to decreased position accuracy. In order to compensate for thermal errors of the tool center point position, latent heat storage can be used to provide a smoother temperature response of the machine tool. The proposed approach considers paraffin-based phase change materials infiltrated in aluminum foam structures. Performance and efficacy of the realized compensation component are numerically and experimentally validated.

Peer-review under responsibility of the International Scientific Committee in the person of the Conference Chair Prof. Steffen Ihlenfeldt.

**Keywords:** Thermal error compensation; Linear direct drive; Machine tools; Latent heat storage; Phase change materials

---

## 1 Introduction

Linear motors are increasingly used as feed drives in machine tools as they provide high feed rates and good position accuracy. However, as a consequence of the high dynamic characteristics of linear motors the heat input from the motor into the machine structure strongly varies in time leading to unsteady temperature fields. The resulting thermoelastic deformations reduce the machine accuracy and hence necessitate improved methods for thermal management.

Thermal issues in machine tools are the main cause of geometrical errors of machined workpieces (up to 75%, [1]) and have numerously been addressed in literature. Most approaches for reducing the thermal induced error are com-

pensation methods that consider error prediction through modelling and measurement. By applying these methods, the position of the axes can be adjusted by the predicted value. Comprehensive reviews of different compensation methods are given in [2-4].

A novel approach for compensation of thermal induced errors is to use phase change materials that exhibit high thermal capacity during phase transition. By applying these materials to machine structures the thermal inertia can efficiently be increased. Temperature changes thereby can be reduced and a smoother temperature response of the structure can be obtained in a certain temperature range. Recent studies demonstrate the potential of this approach [5].

Table 1. Thermal storage properties in the temperature range from 32 °C to 37 °C for structural steel, aluminium and the paraffin-based phase change material RT35HC (manufacturer's data Rubitherm).

Material	Structural Steel	Aluminium	RT35HC
Density [kg/m³]	7856	2700	880
Specific heat capacity [kJ/kg K]	0.5	0.9	2
Latent Heat [kJ/kg]	-	-	209
Relative storage mass	87.6	48.7	1
Relative storage volume	9.8	15.9	1

In contrast to sensible heat materials, phase change materials show almost no change in temperature while storing or releasing heat. During phase transition, phase change materials exhibit high energy density enabling thermal management solutions. Typical applications for phase change materials are temperature control in buildings, photovoltaic systems and thermo-regulation in textiles [6-9]. Table 1 demonstrates the thermal storage properties for different materials. As shown, in comparison with structural steel and aluminium in the temperature range from 32 °C to 37 °C the thermal capacity for one unit of volume of paraffin-based phase change material RT35HC is higher by a factor of 9.8 and 15.9, respectively.

In this study, the proposed method for compensation of thermal errors on linear direct drives is exemplified through an experimentally examined latent heat storage unit added to a linear motor. The thermal losses of the linear motor are used as heat sources upon loading of the primary part and temperature profiles of the adjacent structure are measured. Additionally, a finite element model is used to calculate the temperature field of the motor.

## 2 Thermal losses of linear motors

Linear motors, like all other electric motors, produce different losses. The losses are divided into four categories due to their causes.

- **Winding losses** – These losses are caused by the electric current in the motor windings:

$$P_{V,W,S} = m \cdot R_{Str} \cdot I_{Str}^2. \quad (\text{Eq. 1})$$

- **Core losses** – The core losses occur in the ferromagnetic motor components and are caused by the change in the magnetic field. Two effects play a role. Firstly, the hysteresis losses required for aligning the magnetic domains in the iron are significant. On the other hand, the change of the magnetic field induces eddy currents whose power must be applied in addition. The core losses, similar to the motor voltage, are dependent on the strength of the magnetic field and the frequency. They can therefore be described by the simplified equation

$$P_{V,Fe} = \frac{U^2}{R_{Fe}}. \quad (\text{Eq. 2})$$

The core losses are represented by the iron loss resistor  $R_{Fe}$ .

- **Friction losses** – Frictional losses occur between moving parts of the motor, i.e. at the bearing points and in the air gap between the primary and the secondary part. They are dependent on the occurring friction force, the coefficient of friction between the parts and the travel speed:

$$P_{V,R} = f(v). \quad (\text{Eq. 3})$$

- **Excess losses** – The excess losses have different causes including the motor geometry and the development of the magnetic field within the motor. Since the current feed of the motor also has a significant influence on the excess losses, these can be assumed to be proportional to the square of the current. Studies have shown that the additional losses are about 10% of the winding losses.

$$P_{V,Z} = 0.1 \cdot P_{V,W,S} \quad (\text{Eq. 4})$$

The determination of the electrical losses requires the calculation of the RMS-values of current and voltage. Since a linear motor cannot be operated in stationary work points due to the limited travel distance, the calculation of the RMS-values is only inaccurate due to the required temporal integration.

The current and voltage must therefore be replaced by quantities for which no integration is required.

The current can be substituted with the motor force, which is proportional to the RMS-value of the current.

$$F_M = k_F \cdot I_{Str} \quad (\text{Eq. 5})$$

The voltage can, in principle, be substituted by the speed. However, this is not necessary for the motor used here. As a so-called ironless motor, this motor does not have any ferromagnetic components which are exposed to alternating magnetic fields and consequently does not generate any core losses.

### 3 Thermal error compensation through latent heat storage

The thermal losses outlined above lead to varying thermoelastic deformations of linear motors and adjacent components. This chapter describes the integration of a latent heat storage unit into a linear direct drive and conducted experiments with the objective of thermally stabilizing the feed drive structure.

#### 3.1 Design of the test rig

Experiments were performed on a three-phase synchronous motor with an ironless forcer and U-shaped stators with opposing magnets. The primary part is connected to a carriage moved on two parallel guide rails. The test rig is shown in Fig. 1.

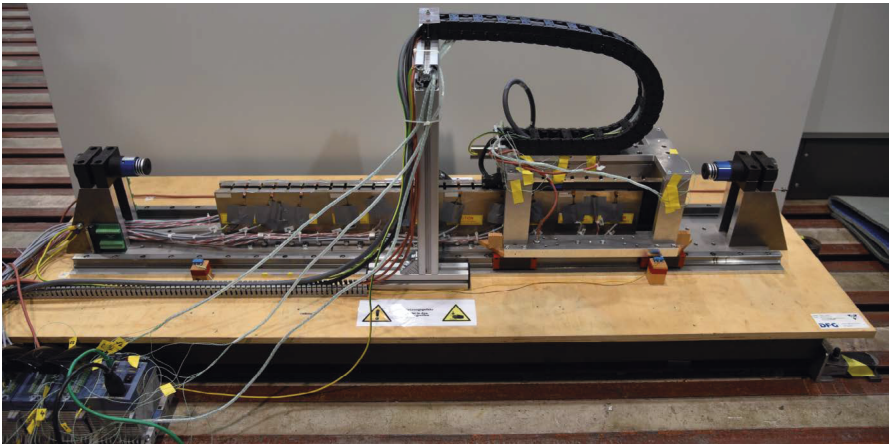


Fig. 1. Test rig with linear motor, data acquisition equipment and carriage with heat storage unit.

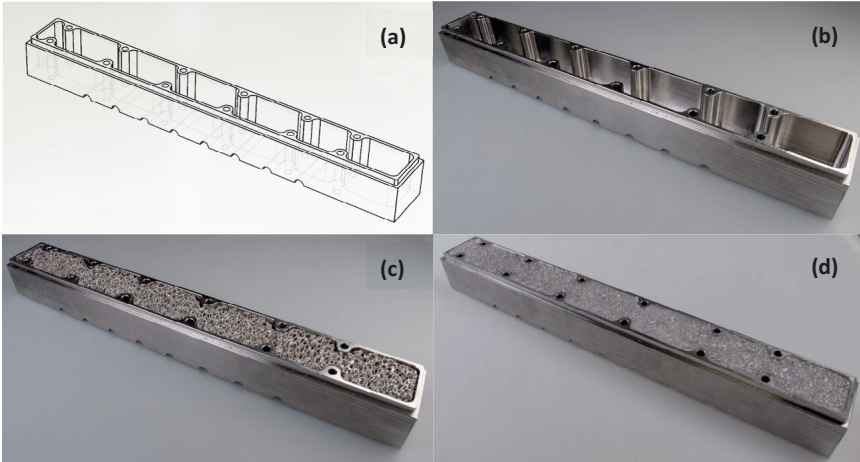


Fig. 2. (a) CAD model of storage container; (b) fabricated storage container; (c) container filled with aluminium foam; (d) storage unit infiltrated with phase change material.

In order to efficiently reduce thermal fluctuations in the feed drive, a latent heat storage container was fabricated allowing for bolted connection to the primary part being the principal heat source (Fig.2). The dimensions of the container are 37 mm x 42 mm x 360 mm. As latent heat storage medium the paraffin-based, commercially available phase change material RT35HC with a liquid-solid phase transition between 33 °C and 37 °C and a latent heat capacity of melting or fusion of 209 kJ/kg was used.

Due to the low thermal conductivity of the phase change material, it is used in combination with open cell aluminium foam. To fit the storage, the foam was sawn and pressed into the steel body. Finally, the storage container was heated in an oven and filled with the phase change material in liquid state. The mass of the infiltrated phase change material amounts to approximately 225 g.

After solidifying of the phase change material at room temperature, the storage was sealed and integrated into the test rig between the primary part and the carriage.

### 3.2 Experimental examination

To evaluate the thermal behaviour of the compensation component, 20 type-K thermocouples were attached to the surfaces of the primary part, the latent heat storage unit and the carriage. The positions of the measurement points



are illustrated in Fig. 3. Sensor data were recorded using the data logger Yokogawa MW100 with 10-Channel universal input module.

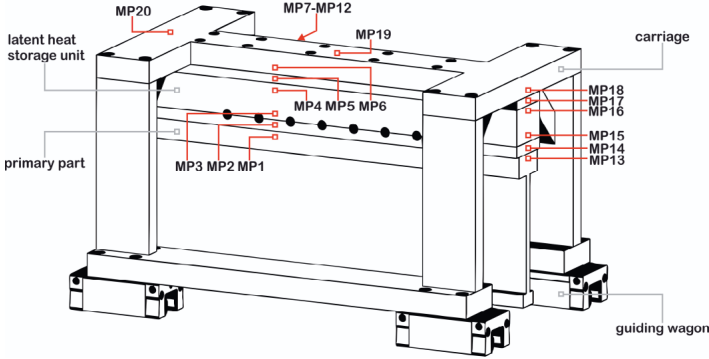


Fig. 3. Schematic representation of measuring point (MP) positions on primary part, heat storage and carriage. MP7-MP12 are symmetrically attached to MP1-MP6 on the backside of the linear motor.

The linear motor was thermally loaded by applying direct current to the primary part. A long-term heating with approximately 110 W power input was applied as well as short-term heating at around 500 W with subsequent cooling.

#### 4 Computational modelling of the thermal behaviour

In order to estimate the thermal behaviour of the test rig outlined above, a thermal finite element model is used. The underlying differential equation to be solved is Fourier's Law

$$k \left( \frac{\partial^2 T}{\partial x^2} + \frac{\partial^2 T}{\partial y^2} + \frac{\partial^2 T}{\partial z^2} \right) + Q = \rho c \frac{\partial T}{\partial t} \quad (\text{Eq. 6})$$

with the isotropic thermal conductivity  $k$ , inner heat-generation rate per unit volume  $Q$ , material density  $\rho$ , heat capacity  $c$  and temperature  $T$ . The latent heat storage unit is modelled using the reduced material model proposed by Drossel et al. [10]. Hence, an equivalent density and an equivalent thermal conductivity for the storage composite are applied. The increased thermal capacity during phase transition is considered by defining the temperature dependent enthalpy curve of the phase change material (Fig. 4)

$$H(T) = \int \rho c \, dT. \quad (\text{Eq. 7})$$

As shown in Fig. 4, half symmetry was applied. The surfaces in the symmetry plane exhibit adiabatic boundary conditions

$$\left. \frac{\partial T}{\partial x} \right|_{x=0} = 0. \quad (\text{Eq. 8})$$

On all remaining exterior surfaces  $\omega_{\text{conv}}$  with the normal direction  $n$  convection boundary conditions for a difference between the surface temperature  $T_s$  and the fluid temperature  $T_f$  are defined:

$$k \left. \frac{\partial T}{\partial n} \right|_{\omega_{\text{conv}}} = h(T_s - T_f). \quad (\text{Eq. 9})$$

The heat transfer coefficient  $h$  is hereby calculated as a function of the dimensions, orientation and temperature of the corresponding surfaces by the formulae given in [11]. The secondary part of the linear motor is assumed to be thermally decoupled and therefore not modelled. Heat radiation effects are considered negligible. Contact heat resistances between the different components are obtained approximately by measuring the temperature differences between contacting parts in steady-state.

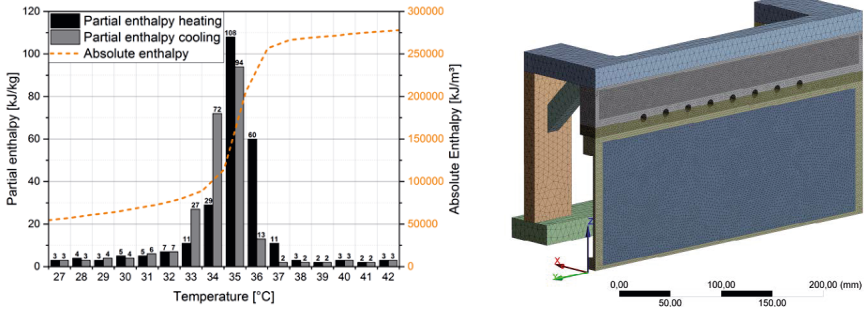


Fig. 4. Left: Partial enthalpies of RT35HC (manufacturer's data Rubitherm) and enthalpy curve for storage compound material model. Right: meshed finite element model.

The heat input was calculated based on the findings of Chapter 2. A constant heat input is used in the model by averaging the time-dependent heat losses in order to avoid high time resolution required for solving.

The platform used for executing the simulations is commercial FEA code ANSYS.

## 5 Results

Fig. 5 demonstrates the thermal responses of the primary part, storage unit and carriage to a nearly constant heat input of 110 W for approximately 14400 s. The effect of fusion and solidification of the phase change material can be observed in the reduced temperature increase during heating for about 30 min

starting at 1800 s and reduced temperature decrease during cooling for about 60 min starting at 17000 s.

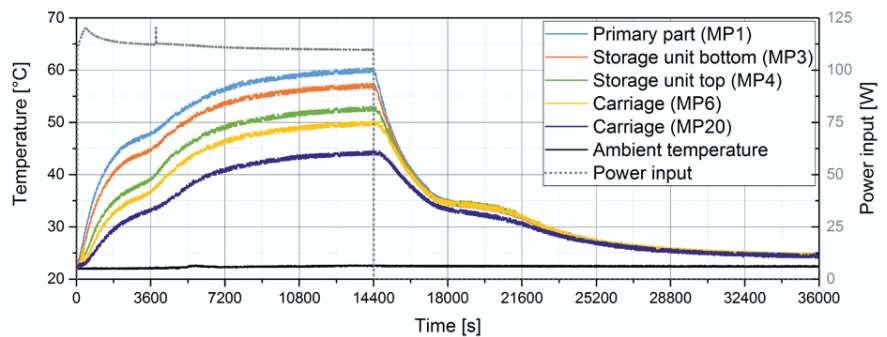


Fig. 5. Experimentally determined temperatures of selected measuring points. The motor was loaded with approximately 110 W for 14405 s and cooled through free convection.

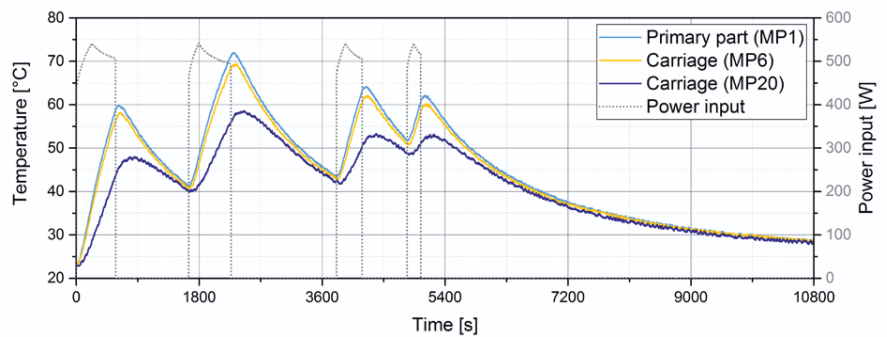


Fig. 6. Measured temperature curves on primary part and carriage during four load cycles (500 W) and subsequent passive cooling without latent heat storage unit.

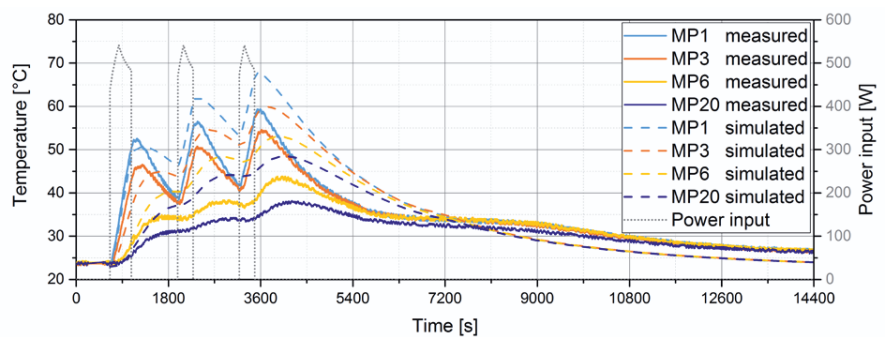


Fig. 7. Experimentally and numerically obtained temperature profiles for selected measuring points with three load cycles applied at approximately 500 W.

The temperature measurement was then conducted considering alternating load with repeating, short-duration power inputs and subsequent passive cooling. Testing without the latent heat storage unit resulted in maximum temperatures of forcer and carriage of 70 °C (Fig. 6).

Similar load cycles were applied with the latent heat unit added to the feed drive. While the temperature profiles of the components exhibit values up to 60 °C, the carriage does not exceed 45 °C (Fig. 7). The compensation unit hence significantly enhances the thermal inertia of the test rig through the heat capacity of the container and the latent heat of the phase change materials.

Fig. 7 also illustrates the results of the thermal finite element model in comparison with the experimental data for various measuring positions. The simulated temperature profiles exhibit deviations from the measured temperatures of up to 30%. The assumptions made in the model appear to be too restrictive for precise prediction of the thermal behaviour of the underlying assembly. Possible causes for the high deviations may be unconsidered forced convection effects and the rough estimation of the thermal contact resistances as well as the simplifications made by the reduced material model for the compound of aluminium foam and phase change material. Also, the heat transport between primary and secondary part is to be accounted for in future investigations.

## 6 Conclusion

A thermal error compensation method using phase change materials has been presented. Numerical and experimental investigations were conducted in order to demonstrate the efficacy of the developed component. It could be shown that by adding a latent heat storage unit between the primary part of the linear motor and the carriage the temperature change in time during heating and cooling is effectively decreased during phase change. The numerical model was found to be in poor agreement with the temperature curves obtained experimentally. Further efforts will be required to enhance the accuracy of the proposed model.

Consequently, passive compensation components using latent heat storage are a convenient approach for reducing thermal fluctuations by increasing thermal inertia in a certain temperature range. However, the effect of the proposed passive compensation method is limited due to the permanent connection between the latent heat storage unit and the heat source. While an increased thermal capacity of machine tools in the presence of varying thermal loads is favourable, it may not always be appreciated, e.g. during warm-up phases.

Hence, the aim for prospective investigations is to enhance flexibility of the concept by providing a variable thermal connection between heat releasing and heat storing machine components using adaptronic solutions.

### **Acknowledgements**

*The authors would like to thank the German Research Foundation (DFG) for financial support within the Collaborative Research Centre Transregio 96.*

## **7 References**

- [1] Mayr, J., Jedrzejewski, J., Uhlmann, E., Donmez, M. A., Knapp, W., Härtig, F., Wendt, K., Moriawaki, T., Shore, P., Schmitt, R., Brecher, C., Würz, T., Wegener, K., 2012. Thermal issues in machine tools. *CIRP Annals - Manufacturing Technology* 61, 771-791.
- [2] Ramesh, R., Mannan, M. A., Poo, A. N., 2000. Error compensation in machine tools – a review, Part II: thermal errors. *International Journal of Machine Tools and Manufacture* 40, 1257-1284.
- [3] Möhring, H.-C., Brecher, C., Abele, E., Fleischer, J., Bleicher, F., 2015. Materials in machine tool structures. *CIRP-Annals - Manufacturing Technology* 64, 725-748.
- [4] Li, Y., Zhao, W., Lan, S., Ni, J., Wu, W., Lu, Bingheng, 2015. A review on spindle thermal error compensation in machine tools. *International Journal of Machine Tools and Manufacture* 95, 20-38.
- [5] Voigt, I., Drossel, W.-G., Winkler, S., Werner, R., Bucht, A., 2017. Thermische Modellierung von Lineardirektantrieben und aktive Steuerung der Wärmeströme unter Einsatz von Latentwärmespeichern. *Thermo-Energetische Gestaltung von Werkzeugmaschinen*, 5. Kolloquium des SFB/TR 96, Chemnitz, Tagungsband, 261-276.
- [6] Mehling, H., Cabeza, L. F., 2008. *Heat and cold storage with PCM*. Berlin: Springer.
- [7] Griffiths, P. W., Eames, P. C., 2007. Performance of chilled ceiling panels using phase change material slurries as the heat transport medium. *Applied Thermal Engineering* 27, 1756-1760.
- [8] Browne, M. C., Norton, B., McCormack, S. J., 2015. Phase change materials for photovoltaic thermal management. *Renewable and Sustainable Energy Reviews* 47, 762-782.
- [9] Mondal, S., 2008. Phase change materials for smart textiles – An overview. *Applied Thermal Engineering* 28, 1536-1550.
- [10] Ohsenbrügge, C., Marth, W., Navarro y de Sosa, I., Drossel, W.-G., Voigt, A., 2016. Reduced material model for closed cell metal foam infiltrated with phase change material based on high resolution numerical studies. *Applied Thermal Engineering* 94, 505-512.
- [11] Verein Deutscher Ingenieure, 2010. *VDI Heat Atlas*. Berlin: Springer.

# Industrial relevance and causes of thermal issues in machine tools

*M. Putz<sup>a,b</sup>, C. Richter<sup>b</sup>, J. Regel<sup>a</sup>, M. Bräunig<sup>a</sup>*

<sup>a</sup>Institute for Machine Tools and Production Processes IWP, Technische Universität Chemnitz,  
09107 Chemnitz, Germany

<sup>b</sup>Fraunhofer Institute for Machine Tools and Forming Technology IWU, Reichenhainer Str. 88,  
09126 Chemnitz, Germany

**Abstract.** Regarding extensive research activities on the thermal behavior of machine tools, the question arises as to what relevance is given to thermal issues in industry. The answer comes from 75 small to very large machine tool manufacturers and mainly larger production companies from Europe and Asia. In contrast to machine users, machine manufacturers rate thermal failure higher than geometrical, static and dynamic manufacturing defects, even though production companies attribute a share of up to 50% to the thermally caused portion of scrap production. Users rate the relevance of thermal defects of workpiece, tool and machine tool for manufacturing accuracy to be almost identical. The assessments are based on their own experiences from the daily operation as well as on experimental investigations. The paper describes comprehensively the relevance of thermal errors. In addition, the occurring areas and methods for localization are explained. Finally, the causes and the conflict to energy-saving measures are clarified.

Peer-review under responsibility of the International Scientific Committee in the person of the Conference Chair Prof. Steffen Ihlenfeldt.

**Keywords:** Workpiece; Cutting tool; Machine tools; Thermal error; Thermal behavior; Machining accuracy; Modelling; Analysis; Design; Investigation; Temperature; Cutting

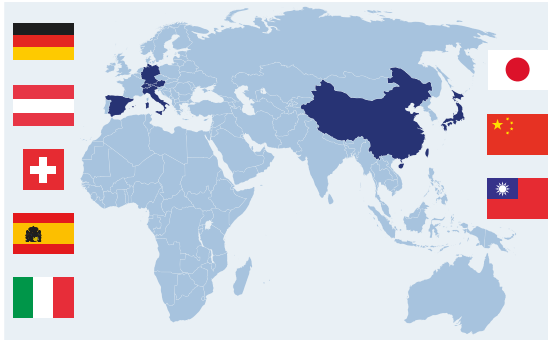


Fig. 1: Countries of the surveyed enterprises

## 1 Introduction

Machine tools have a production value of several billion USD [20]. The main requirement of machine tools is the production of workpieces with a defined accuracy. At the same time, ensuring the required accuracy is by no means a trivial task. The manufacturing accuracy can be decisively influenced, starting from the design with knowledge of the accuracy-determining properties up to the installation and production conditions of the user.

The geometry of the components is temperature-dependent. Each material has the property of deformation under thermal influence. This is caused by several power losses at different locations, which induces heat into the structure in varying degrees of time. So far a prediction of the displacement (thermal error) at the tool center point (TCP) of the machine tool due to thermal influences has only been possible to a limited degree.

The relevance of thermal defects is described in research papers [5]. Using the models developed in those investigations, not only is parameter identification possible, but also compensation and correction approaches are proposed in order to master the thermal error. In various publications, it has been found that up to 75% of geometrical errors in workpieces can be traced back to thermal influences [9]. Bryan summarizes the most important results categorically in [3] and writes about a thermal error of 70% in production, caused by the thermo-elastic deformation in the machine structure, the workpiece and the tool. According to [21], thermal shifts can contribute more than 50% to the total error. In [6], a point-of-effect deviation of up to 100  $\mu\text{m}$  is described in a process-appropriate evaluation. In [18] the thermal error is described as reaching

up to 60  $\mu\text{m}$  in the tool alone. It is possible to measure 30  $\mu\text{m}$  on the workpiece [10]. This small excerpt gives only a small insight into the absolute deformations which are recorded in experimental investigations. A comparative evaluation is not effective because of different assumptions and boundary conditions. The thermal error is initially strongly dependent on the geometry, the material properties, and the temperature gradients caused by the released power dissipation.

In the survey, a total of 55 manufacturers from 8 countries (see Fig. 1) including the three countries with the largest share of world production (China, Germany and Japan) [20] and 20 machine tool users from Germany were questioned about the relevance, causes and consideration of thermal errors. The answers regarding the relevance and causes were analyzed in this paper. The consideration of thermal errors is described in [14]. A distinction was made between small (SE), medium-sized (ME), large (LE) and very large (VLE) enterprises, with reference to the recommendation of the European Commission [4] (see Fig. 2). The differentiation to VLE is necessary in order to obtain statements regarding mass production.

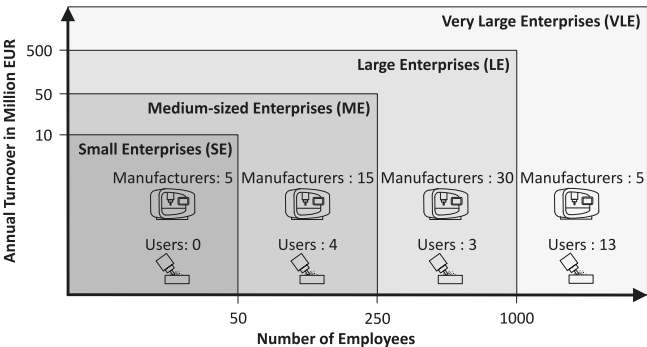


Fig. 2: Enterprises surveyed by enterprise size

The answers of the manufacturers and users are now compared and evaluated. Both regional differences are taken into account as well as different opinions, depending on the size of the company. Users were also asked about the need for new machines. The answers range from less than one machine to more than 20 machines per year (see Fig. 3).



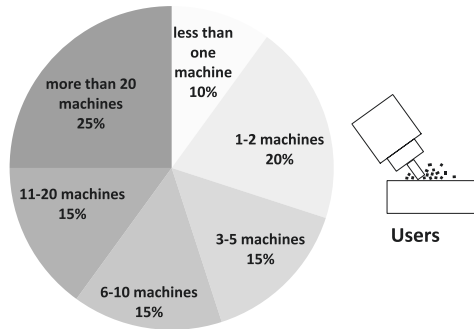


Fig. 3: Need for new machines per year

## 2 Relevance of thermal error

In order to find an answer to the question regarding the relevance of thermal errors in machine tools, it is helpful to draw a comparison of different errors which contribute to the total accuracy, although a comparison using the absolute size is hard to do. While geometrical errors have a low time dependency and are altered by subsidence and wear effects, static errors are load-induced deformations which occur during tool operation. The dynamically caused production error is shows up in the surface shape of the workpieces and has time constants in fractions of a second. The aim of the survey is to generally assess the significance of the thermal error. The results may also be interpreted as a measure of the error frequency.

### 2.1 Assessment of the size of thermal error

Every enterprise was asked about the proportion of thermal errors regarding the total accuracy (geometrical, static and dynamic errors). The proportion was rated as low, comparable and dominating. Overall, a dominant position is attributed to the thermal error. The manufacturers and users, however, are not fully in agreement. While manufacturers tend to describe a dominant thermal error on average, users qualify this statement by assigning higher relevance to the other errors (see Fig. 4).

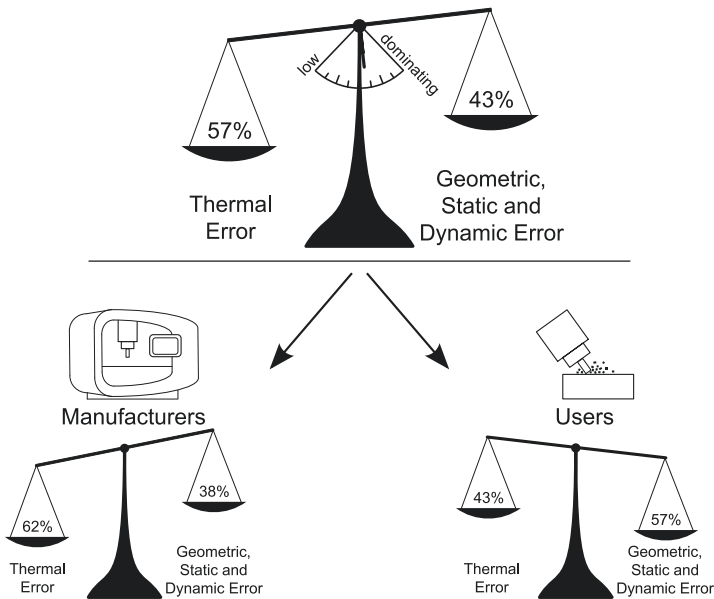


Fig. 4: Assessing the size of the thermal error compared to the total error for all companies

Significant differences are evident between very large manufacturers and medium-sized users. Three large manufacturers describe the thermal error as dominant and two large manufacturers describe it as comparable. In comparison, three medium-sized users rate the thermal error as comparable, and one user of this category believes that the thermal error is low. A large manufacturer from Italy rated the error as relevant when precision machining is necessary. In Germany, a large enterprise distinguishes between wet processing and minimum quantity lubrication. In Germany, one large company distinguishes between wet machining and minimum quantity lubrication. In this case, a dominant influence of the thermal error is described. A very large manufacturer from Japan produces machine tools from its point of view of high geometrical accuracy and good static and dynamic stiffness, and thus concludes that thermal defects dominate.

As a direct consequence of a thermal error, a share of waste production is observed. Users have to cope with very different challenges in production, which is the reason why no consistent statement can be made about the specific share of thermal errors in the cross-company production of NIO parts. However, it is specified to be up to 50%.

## 2.2 Basis of assessment

More than half of the manufacturers refer to research and development results in their assessment of the subject matter, the majority of which applies only to medium-sized and large enterprises. Small manufacturers have no knowledge from research and development. A significant proportion of companies rely on their own experience from daily operations, especially users (see Fig. 5). 67% of the manufacturers receive concrete customer feedbacks and try to meet these demands or to comply with them.

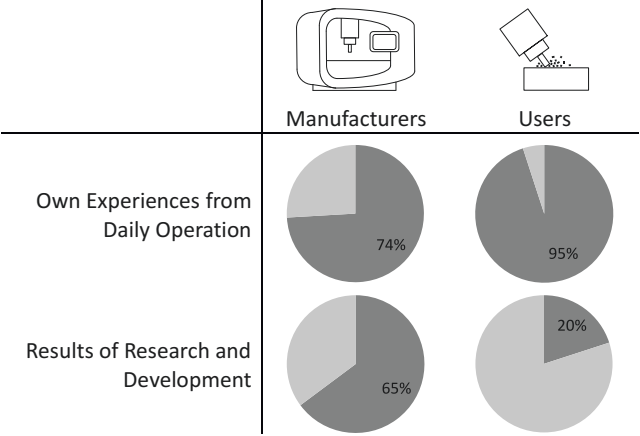


Fig. 5: Reference of the assessment

## 2.3 Localization of the thermal error

The temperature fields and the displacements in the respective components are described in scientific papers [18, [16, [7], [13]. Often it is difficult to make a general statement about the respective thermal errors of the total error. The research areas, however, initially show a corresponding relevance.

The users were asked in which area errors occurred during the machining process. The list of options included the machine tool structure, the tool and the workpiece. The machine tool structure has the largest error, but the tool and the workpiece also have a thermal error that is not negligible. Overall they differ only marginally (see Fig. 6).

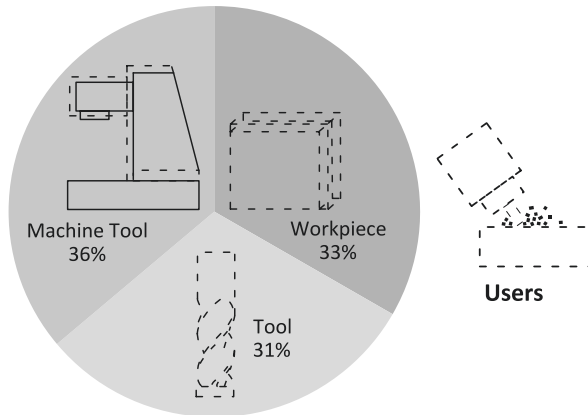


Fig. 6: Relevant areas of the thermal error, users' view

The assessment is contradictory to some extent, for example, the tool has been rated as low and as dominant. As mentioned above, companies are often evaluating using experiences from daily operations. A general description for all applications is only possible to a limited extent due to different production processes and ambient conditions. For example, a user notes that the errors have a dependence on the tool cooling.

## 2.4 Methods of determination

The companies examine thermal errors with experimental and simulation-based methods. The manufacturers use these methods significantly more in the design phase than they are later used by the user. The larger the manufacturer, the more often investigations are carried out. Experimental investigations always have priority (see Fig. 7).

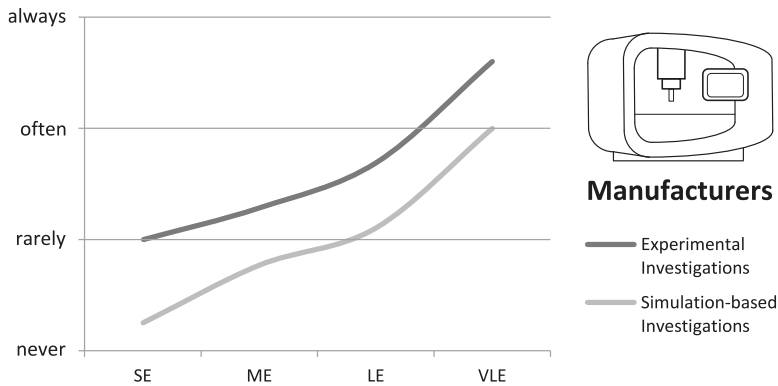


Fig. 7: Methods of the investigations for different enterprise sizes by manufacturers

In Asia significantly more experiments are also conducted and in Germany simulation models are used relatively rarely to determine the thermal errors, compared to the average manufactures. Only few users are represented in these two disciplines, and almost never resort to the selected methods. Only medium-sized and very large enterprises indicate that they perform experiments, albeit rarely. In principle, manufacturers show significantly higher expenditure in this aspect than users.

If thermal investigations are carried out, the company's own departments are mainly active (see Fig. 8). Only a few companies from the European area out-source thermal investigations to external service providers. Research facilities are rather in demand. Between 20% and 33% of the companies carry out thermal investigations in cooperation with a research institute. In Asia, cooperation with a research facility is very rare, while approximately one third of the companies in Germany and Europe are consulting a research facility for addressing their thermal errors.

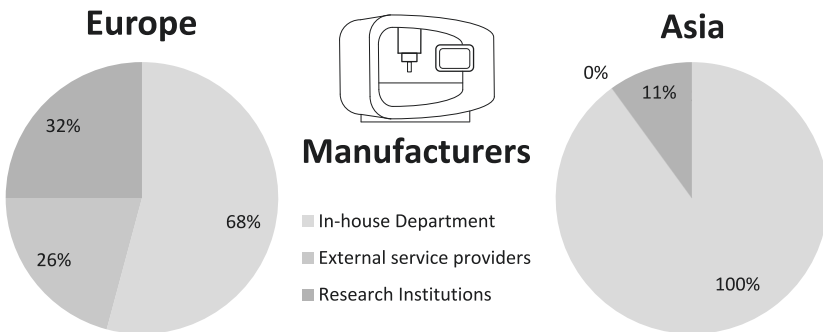


Fig. 8: Location of the thermal investigations in Europe and Asia

Regarding the objectives pursued with the investigations, 42% of the companies state that they are used to compare current and future assemblies. Furthermore, it is possible to estimate the thermal behavior of the machine. As a result, compensatory measures can be derived from these findings, an essential objective which 73% of the companies agree to. 56% of the companies use the results obtained as a basis for correction on the control side. Moreover, problems that can be estimated by the customer can be avoided by means of experimental and simulation-based investigations. As a consequence, it is described that the performance of the machines can be increased, which in turn results in competitive advantages. Furthermore, concrete optimizations can be made in the process from the data obtained. There were no significant differences for the users, so only the manufacturers' responses are listed.

### 3 Causes of thermal errors

In [3] relevant influences on the thermal behavior were described. These include heat fluxes from process and drives, interaction with the environment and tempering equipment, human influence and the thermal storage capacity of components. In the papers [11, [12], the environmental conditions are the subject of the investigations and described as influential parameters. The quantification of the power losses from process and machine components and the temperatures acting in these areas are described in numerous publications, which is an extract of current research [8, [15, [17, [2, 1, [19].

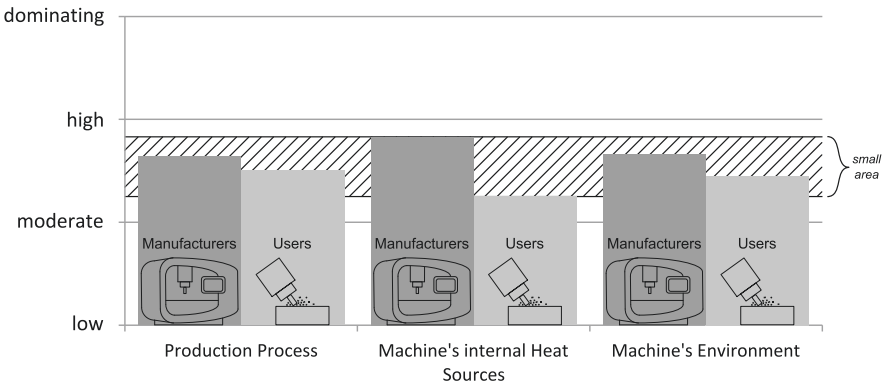


Fig. 9: Influence on the thermal error

The survey was limited to three main areas. These are the production process involving the chips and the influence of the coolant, the internal sources of the machine such as, for example, the power losses from main and secondary drive

as well as from mechanical drive and guide elements, and thirdly, the influence of the environment on the machine. Relating to the relevance of these different thermal influences, the manufacturers and users are largely in agreement. Fig. 9 provides a detailed description of the evaluation for manufacturers and users.

All three areas have an influence on the thermal behavior and can lead to a thermal error in the machine structure. The manufacturers generally measure a slightly higher relevance to each category within a small range (see Fig. 9). The greatest disagreement between manufacturers and users is evident in the internal heat sources of the machine. While manufacturers tend to believe that power dissipation is dominant within the machine, users expect greater impact from the process as well as the machine environment. In particular, large users assume an increased relevance from the environment. There are only marginal differences.

4 Energy efficiency and thermal stability in conflict

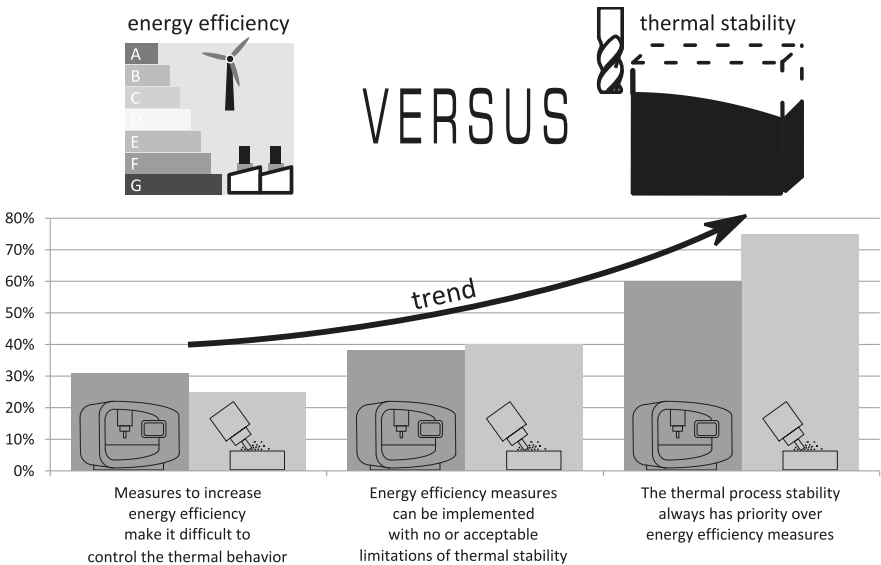


Fig. 10: Thermal stability and energy efficiency in conflict

The use of warm-up programs is an essential way to reduce manufacturing inaccuracies due to thermal influences. Users have a clear position here, with process stability being the priority for 3 out of 4 companies compared to energy efficient measures. Here the manufacturers are generally more willing to im-

plement measures of efficient energy savings, even if significantly more companies are of the opinion that the process stability must be ensured in any case.

Manufacturers and users are in agreement when it comes to energy saving measures (see Fig. 10). According to their assessment, these measures are mainly used at the expense of thermal stability. Only 40% of the companies believe that energy efficiency measures can be achieved with or without acceptable thermal stability constraints. For almost 30% of the companies, measures to increase energy efficiency, such as the reduction of electrical power supplied, such as controlled pumps, standby operation and the shutdown of secondary consumers, make the control of thermal behavior more difficult. In the machine, transient thermal states are favored, which influence the design of the structure in a time-invariant manner and make the production quality more difficult.

## 5 Summary

It has become apparent that there is now a great deal of experience in the industry regarding the thermal behavior of machine tools, and the topic is no longer taken lightly. The thermal error in machine tools is significantly greater than the geometrical, static and dynamic error. The proportion of thermal errors in the waste production can be as high as 50%. The manufacturing process, internal heat sources and the environment influence the thermal behavior in equal proportions. Regarding the topic of energy efficiency, a uniform picture is emerging between users and manufacturers. From the companies' point of view, energy saving measures are predominantly employed at the expense of thermal stability. Therefore 75% of all companies prioritize process stability.

*Acknowledgements: The authors thank the German Research Foundation (DFG) for the support within the Collaborative Research Center SFB Transregio 96 "Thermo-energetic Design of Machine Tools", subproject A01 and B09.*



## 6 References

- [1] Aggarwal, S., Nešić, N., Xirouchakis, P., 2013. Cutting torque and tangential cutting force coefficient identification from spindle motor current. *The International Journal of Advanced Manufacturing Technology*, 65:81-95.
- [2] Brecher, C., Fey, M., Neus, S., Shneor, Y., Bakarinow, K., 2014. Influences on the thermal behavior of linear guides and externally driven spindle systems. *Production Engineering*, 9(1):133-141.
- [3] Bryan, J., 1990. International status of thermal error research. *CIRP Annals - Manufacturing Technology*, 39(2):645-656.
- [4] Commission of the European Communities, Official Journal of the European Union, 2003. Commission Recommendation concerning the definition of micro, small and medium-sized enterprises, K(2003) 1422
- [5] Großmann, K., 2015. Thermo-energetic Design of Machine Tools, A Systemic Approach to Solve the Conflict between Power Efficiency, Accuracy and Productivity Demonstrated at the Example of Machining Production. Springer International Publishing, Switzerland.
- [6] Großmann, K., Jungnickel, G., 2006. Prozessgerechte Bewertung des thermischen Verhalten von Werkzeugmaschinen. TU Dresden.
- [7] Klocke, F., Lung, D., Puls, H., 2013. FEM-Modelling of the thermal workpiece deformation in dry turning. 14th CIRP Conference on Modeling of Machining Operations (CIRP CMMO), 8:240-245.
- [8] Komanduri, R., Hou, Z.B., 2001. Thermal modeling of the metal cutting process - Part III: temperature rise distribution due to the combined effects of shear plane heat source and the tool-chip interface frictional heat source. *International Journal of Mechanical Sciences* 43:89-107.
- [9] Mayr, J., Jedrzejewski, J., Uhlmann, E., Donmez, M.A., Knapp, W., Haertig, F., Wendt, K., Moriwaki, T., Shore, P., Schmitt, R., Brecher, C., Wuerz, T., Wegener, K., 2012. Thermal issues in machine tools. *CIRP Annals - Manufacturing Technology*, 61(2):771-791.
- [10] Neugebauer, R., Drossel, W.-G., Ihlenfeldt, S., Richter, C., 2012. Thermal Interactions between the Process and Workpiece. *Procedia CIRP*, Volume 4, pp.63-66.
- [11] Neugebauer, R., Harzbecker, C., Nestmann, S., 2001. Optimization of thermal behavior of machine tools with separated machine bed components. *Production Engineering*, 8:137-140.
- [12] Neugebauer, R., Ihlenfeldt, S., Zwingenberger, C., 2010. An extended procedure for convective boundary conditions on transient thermal simulations of machine tools. *Production Engineering*, 4(6):641-646.
- [13] Neugebauer, R., Ihlenfeldt, S., Zwingenberger, C., Glänzel, J., Richter, C., 2014. Modeling of Thermal Interaction between Environment and Machine Tool. *Thermo-energetic Design of Machine Tools*, pp.111–124.

- [14] Putz, M., Richter, C., Regel, J., Bräunig, M., 2018. Industrial Consideration of thermal issues in machine tools. *Journal of Machine Engineering*.
- [15] Putz, M., Schmidt, G., Semmler, U., Dix, M., Bräunig, M., Brockmann, M., Gierlings, S., 2015. Heat Flux in Cutting: Importance, Simulation and Validation. *Procedia CIRP* 31, 15th CIRP Conference on Modelling of Machining Operations, 334-339.
- [16] Schindler, S., Zimmermann, M., Aurich, J.C., Steinmann, P., 2014. Finite Element Model to Calculate the Thermal Expansions of the Tool and the Workpiece in Dry Turning. 6th CIRP International Conference on High Performance Cutting, HPC2014, 14:535-540.
- [17] Schulz, H., Schmitt, T., 1994. Model-Based Determination of Heat Generation in the Mechanical Structure of High Speed Drive Systems. *Production Engineering*, 1/2:89-92.
- [18] Semmler, U., Bräunig, M., Drossel, W.-G., Schmidt, G., Wittstock, V., 2014. Thermal Deformations of Cutting Tools: Measurement and Numerical Simulation. *Production Engineering – Research and Development* 8(4):543-550.
- [19] Uhlmann, E., Hu, J., 2012. Thermal modelling of an HSC machining centre to predict thermal error of the feed system. *Production Engineering*, 6:603-610.
- [20] Verein Deutscher Werkzeugmaschinenfabriken e.V., 2013. Deutsche Werkzeugmaschinenindustrie Daten und Fakten 2014.  
[http://www.vdw.de/bin/load\\_file\\_inter.pl?p\\_bereich=wirtschaft&p\\_paket\\_id=11&p\\_do\\_k\\_id=10000181&p\\_typ=doc&p\\_sprache=d](http://www.vdw.de/bin/load_file_inter.pl?p_bereich=wirtschaft&p_paket_id=11&p_do_k_id=10000181&p_typ=doc&p_sprache=d)
- [21] Weck, M., McKeown, P., Bonse, R., Herbst, U., 1995. Reduction and Compensation of Thermal Errors in Machine Tools. *CIRP Annals - Manufacturing Technology* 44(2):589-598.



## **Approaches considering environmental conditions**



# Clustering by optimal subsets to describe environment interdependencies

*J. Glänzel<sup>a</sup>, R. Unger<sup>b</sup>, S. Ihlenfeldt<sup>a,c</sup>*

<sup>a</sup>Fraunhofer Institute for Machine Tools and Forming Technology IWU,  
09126 Chemnitz, Germany

<sup>b</sup>Faculty of Mathematics, Technische Universität Chemnitz, 09107 Chemnitz, Germany

<sup>c</sup>Institute of Machine Tools and Control Engineering IWM, Technische Universität Dresden,  
01062 Dresden, Germany

**Abstract.** The paper copes with the problem of finding an optimal subset of interpolation points out of a given large set of computed values, arising from a finite element simulation. This simulation computes environment data, which are on their part input data for finite element simulations of machine tools.

For machine tool manufacturers it is still a seriously problem that the machine works imprecisely and produces scrap if environmental values like temperature changes. The change of the environment boundary conditions contribute to the phenomenon through sunlight or cold draught owing to open doors of the machine hall or factory. Resulting thermo-elastic effects on the tool center point are one of the major reasons for positioning errors in machine tools.

A genetic search algorithm for clustering relevant heat transfer coefficient values over the geometric surface through computational fluid dynamics (CFD) simulations will be described. These values are the input data for a developed thermo-elastic correction algorithm.

Peer-review under responsibility of the International Scientific Committee in the person of the Conference Chair Prof. Steffen Ihlenfeldt.

*Keywords:* Optimal subset problem; Radial Basis Functions; FEM; CFD

---

## 1 Introduction

The paper copes with the problem of finding an optimal subset of interpolation points out of a given large set of computed values, arising from a finite element simulation to establish a thermo-elastic correction algorithm for increasing the workpiece quality in production processes.

The quality of workpiece is depends on by the thermo-elastic behavior of the machine tool during the production process. Machine tool deformations occur due to waste heat from motors and frictional heat from guides, joints and the tool, while coolants act to reduce this influx of heat. Additional thermal influences come from the machine tool's environment and foundation. This leads to inhomogeneous, transient temperature fields inside the machine tool which displace the tool center point (TCP) and thus reduce production accuracy and finally the product quality [1]. Next to approximation strategies such as characteristic diagram based correction as in [8] and structure model based correction shown in [4], the most reliable way to predict the TCP displacement is via structure-mechanical finite element (FE) simulation. A CAD model of a given machine tool serves as the basis for this approach. On it a FE mesh is created. After establishing the partial differential equations (PDEs) describing the heat transfer within the machine tool and with its surroundings, FE simulations are run in order to obtain the temperature fields of the machine tool for specified load regimes. Using linear thermo-elastic expansion, the deformation can then be calculated from each temperature field and the displacement of the TCP read from this deformation field, see [6]. The accuracy of this latter approach depends on the correct modelling of the heat flux within the machine tool and the exchange with its surroundings. In order to calculate the correct amount of heat being exchanged with the environment, one may use known parameters from well-established tables. However, if the surrounding air is in motion or otherwise changing, computational fluid dynamics (CFD) simulations are required to accurately determine these transient parameters. This two-step approach makes realistic thermo-elastic simulations particularly complicated and time-consuming. Negative aspect of this approach is the very computing time intensive CFD simulation. Some methods aiming at real-time thermo-elastic simulations based on model order reduction must therefore rely on the inaccurate predetermined parameter sets [5]. This could be supported if all the necessary CFD simulations could be run in advance and supplied to the thermo-elastic models when they are needed.

Nevertheless, the whole output of this CFD simulations is too much amount of data for an effective computation of the correction steps. Therefore, a reduction of this data is desirable wherefore the ideas of this paper comes up.

This paper starts by introducing an interpolation method with radial basis functions (RBF) and the description of the optimal subset finding problem. After that a solution algorithm for solving this optimal subset problem is developed, based on the idea of genetic algorithms. In the numerical examples the potency of this algorithm is shown in some benchmark examples, where the optimal solution is

known. Afterwards it is also demonstrated that the algorithm works for practical relevant datasets too.

## 2 Radial Basic Function

The basic principle in the use of radial basis functions is solving an interpolation problem for  $m$  arbitrary sample points  $x_1, x_2 \dots x_m$  in  $R^d$  with given values  $w_1, w_2 \dots w_m$  in  $R$  to find a function  $f : R^d \rightarrow R$ , fulfilling the interpolation condition

$$f(x_i) = w_i \quad \text{for } i = 1 \dots m \quad (1)$$

The first step is to find an ansatz for (1). A function  $\eta_i: R^d \rightarrow R$  is a radial basis function if a function  $\phi : R \rightarrow R$  exists, which satisfies  $\eta_i(x) = \phi(|x - x_i|)$  for a fixed point  $x_i \in R^d$ . Commonly used types of RBF ansatz functions with the structure  $\phi(r)$  with  $r = ||x - x_i||$  are Gaussian, multiquadric, polyharmonic spline function, for more details see [12].

One possibility is the usage of a simple polyharmonic spline, which reads  $\phi(r) = r$ . Other variations, especially for large data sets are RBFs with compact support, e.g. the "Wendland functions" [2]. These basic functions are characterized through a sparse interpolation system.

A usual ansatz for an interpolation function is described by

$$f(x) = \sum_{i=1}^m \beta_i \phi_i(x) \quad (2)$$

Inserting condition (1) in (2) we get linear equations

$$f(x_i) = \sum_{j=1}^m \beta_j \phi_j(x_i) = w_i \quad \text{for } i = 1 \dots m \quad (3)$$

which can be written as a linear system by

$$\underline{\Phi} \underline{\beta}^{RBF} = \underline{w} \quad (4)$$

The components of (4) are defined by the system matrix  $\Phi := [\phi_j(x_i)]$  for  $i, j = 1 \dots m$ , the vector  $\underline{\beta}^{RBF} = [\beta_1, \beta_2 \dots \beta_m]^T$  of the unknown coefficients and the right hand side  $\underline{w} = [w_1, w_2 \dots w_m]^T$ . The system matrix  $\Phi$  is obviously symmetric. In



[2], it is shown that  $\Phi$  is positive definite for a vast variety of RBFs. The only disadvantage of this RBF ansatz is that a large number of sample points are needed to get a sufficiently exact approximation of a constant or linear function. One possible way to cope with this is to add a polynomial part  $p(x)$ .

$$f(x) = \sum_{i=1}^m \beta_i^{RBF} \phi_i(x) + p(x) \quad (5)$$

The d-variate polynomial  $p \in \pi_n(R^d)$  of maximum degree n is defined as

$$p(x) = \sum_{j=1}^k \beta_j^{POLY} p_j(x) \quad (6)$$

with  $k = \dim(\pi_n(R^d))$  and basis polynomials  $p_j$  for  $j = 1 \dots k$ . Consequently, this ansatz has  $(m + k)$  unknown coefficients, while the interpolation system (1) consists of only m equations. Therefore, an added condition is imposed by

$$\sum_{j=1}^m \beta_j^{RBF} p(x_j) = 0 \quad \text{for all } p \in \pi_n(R^d) \quad (7)$$

The result is a linear matrix system of dimension  $(m + k)$

$$\begin{bmatrix} \Phi & P \\ P^T & 0 \end{bmatrix} \begin{bmatrix} \underline{\beta}^{RBF} \\ \underline{\beta}^{POLY} \end{bmatrix} = \begin{bmatrix} \underline{w} \\ \underline{0} \end{bmatrix} \quad (8)$$

A simple and good choice for  $\pi_n(R^d)$  are linear polynomials, e.g.

$$\begin{aligned} p_1(x) &= x_1 \\ p_2(x) &= x_2 \\ &\dots \\ p_d(x) &= x_d \\ p_k(x) &= 1 \end{aligned} \quad (9)$$

where  $x$  in  $R^d$ ,  $k=d+1$  and  $x_i$  is the i-th component of  $x$ . The solution vector  $\underline{\beta} = [\underline{\beta}^{RBF}, \underline{\beta}^{POLY}]^T$  of eq. (8) contains the coefficients for the whole interpolation function.

$$f(x_i) = \sum_{i=1}^m \beta_i \phi_i(x) + \sum_{j=1}^k \beta_{(m+j)} p_j(x) \quad (10)$$

### 3 The Optimal Subset Problem

The CFD-simulation in Ansys computes the values of heat transfer coefficients (HTC), velocity vectors or other characterizing values in a huge number of nodes on the surface of the computed domain. Because of very large number of nodes it is desirable for fast evaluations, to reduce this number of nodes but keep the accuracy up. In the paper this is done by choosing a 'good subset' with a fixed size  $m$  of node values which will be used to build an interpolation function, based on radial basis functions. The mathematical formulation for choosing these optimal nodes for the interpolation can be done in the following way.

Given a set  $V = \{1, 2, \dots, N\}$  which corresponds with the nodes  $x_1, x_2, \dots, x_N$  of the finite element simulation and its computed HTC values  $w_1, w_2, \dots, w_N$  in these nodes (see chapter 5). Furthermore, define a number  $m < N$  and a weighting function

$$\xi : S \subset V \rightarrow \mathbb{R}_0^+ \quad \text{with} \quad |S| = m \quad (11)$$

which maps a  $m$ -sized subset  $S$  to a real number greater or equal zero. The „Optimal Subset Problem“ is minimizing this weighting function  $f$  as

$$\min_{\substack{S \subset V, \\ |S| = m}} \xi(S) \quad (12)$$

In our application the weighting function  $\xi$  itself is a function, calculating the interpolation error which occurs when the  $m$  node values of  $S$  are used to build the radial basis interpolation function  $f_S$  like in equation (10), evaluate it in all  $N$  nodes of the set  $V$  and compare the interpolated values with the given values  $w_i$ . Possible error measures are the sum of squares

$$\xi(S) := \sqrt{\sum_{i=1}^N (f_S(x_i) - w_i)^2} \quad (13)$$

or a pointwise computed maximum error

$$\xi(S) := \max_{i=1 \dots N} |f_S(x_i) - w_i| \quad (14)$$

Clearly the value of  $\xi(S)$  is (up to small round off errors) zero if  $m = N$  that is  $S = V$ , but it becomes greater than zero for  $m < N$ .

The challenge is now to find out the optimal subset  $S$  that leads to the minimum of Eq. (11). For very small sets  $V$  and small numbers  $m$  this can be done by computing all possible subsets  $S \subset V$  and compare the values of Eq. (11), but in all

practical relevant cases this becomes impossible due to the combinatorial explosion. The number of different subsets  $S \subset V$  of size  $m$  is given by the binomial coefficient  $N$  over  $m$ , which is defined as

$$\binom{N}{m} := \frac{N!}{m!(N - m)!} \tag{15}$$

some values are shown in the following table 1.

Table 1. Some values for  $N$  over  $m$

N	m	N over m
64	5	7624512
64	6	74974368
64	7	6·10^8
64	20	1.9·10^16
8065	100	2.6·10^232

The subset problems, belonging to the first three lines with 64 over 5, 64 over 6, 64 over 7 are computationally explicit by a full search and will be used in the section 5.1 as a benchmark value, because they provide the global minimum of the weighting function Eq. (11). The case 64 over 20 is not computable by a full search with reasonable effort and it will be used to show the minimization algorithm works. The last line with 8065 over 100 is a practical use case, the immense number of different subsets makes it impossible for all times to perform a full search by the computation of all cases, but the example in section 5.3 will show how the minimization algorithm works also in this case.

In the next section an optimization algorithm for finding the optimal subset will be developed.

### 4 Genetic Algorithms

The minimization of a function is a widely used technique for solving optimization problems. Depending on the properties of the function which is to be minimize (continuity, differentiability, ...) many effective algorithms exist for such classes of functions.

Nevertheless, the challenge of our minimization problem Eq. (12) is, that our weighting function is not continuous, moreover it is defined over a discrete set. All algorithms, depending on gradients are not applicable for such a problem. However, there exist one widely used technique for such problems, it is the class of genetic algorithms. The basic idea of this algorithms is to duplicate the selection of the fittest in natural evolution processes.

A solution candidate is seen as an individual, a bulk of individuals is seen as population and the population is developed from one generation to the next generation by annihilating individuals with poor fitness, selecting individuals with good fitness for reproduction and creates a new generation.

In principle, after fixing a population size  $p$ , a genetic algorithm consists of the following steps:

- 1. Initial population:** Generating the initial population by randomly creation of  $p$  individuals.
- 2. Assessment:** Perform a rating of all individuals by evaluating the fitness function for each one.
- 3. Stopping criterion:** Use the best individual as solution if the best fitness value reaches a given threshold, or if it not changes over a fixed number of generations.
- 4. Reproduction:** Annihilate individuals with poor fitness, use individuals with good fitness for reproduction to create a new generation.
- 5. Mutation:** Mutate some new generated individuals with a (small) probability. This mutation step offers the inclusion of new solution candidates to the population.
- 6. Loop to next generation:** Go to step two.

Especially for the reproduction step, there exist many different variants for the selection of parent individuals and their reproduction. For a more detailed introduction to genetic algorithms, see for example [3] or [8]. In our adoption of the algorithm, the important steps from above are done in the following way.

- 1. Initial population:** In our use case the individuals are subsets  $S \subset V$  of node numbers, i.e. integers out of  $\{1, 2 \dots N\}$ , such that the initial population is generated as a family of  $p$  random subsets  $S \subset V$ .
- 2. Assessment:** The assessment of each individual is done by setting up the RBF interpolation system with these basis nodes corresponding to the individuals set  $S$ , evaluate this system in all  $N$  nodes, compare the interpolated values with the given values like given in equation (8) and use the result as fitness value. Please

note, that these settings perform a minimization, such that best fitness value is zero.

**4. Reproduction:** During the reproduction step a small number of individuals with the best fitness values, e.g. the elite are transferred unchanged to the new population. The remaining individuals of the new population are created by mixing individuals out of the upper half of the population. For two parent sets  $S_1$  and  $S_2$  this is done by taking  $m$  elements out of  $S_1 \cup S_2$  to create a new individual.

**5. Mutation:** The mutation step is performed by changing some elements of the newly created set  $S$  to a random value out of  $\{1, 2 \dots N\}$ .

## 5 Numerical Examples

As numerical examples, three different use cases will be considered, see figure 1. In the first example, a benchmark to the optimization algorithm is established, because of the moderate number of different subsets it is possible to do a full search and find the optimal solution exactly to compare it with the solution found by the optimization algorithm.

The next two examples consider practical use cases, where the optimization algorithm works to find an optimal subset. Comparison with a full computed example is impossible.

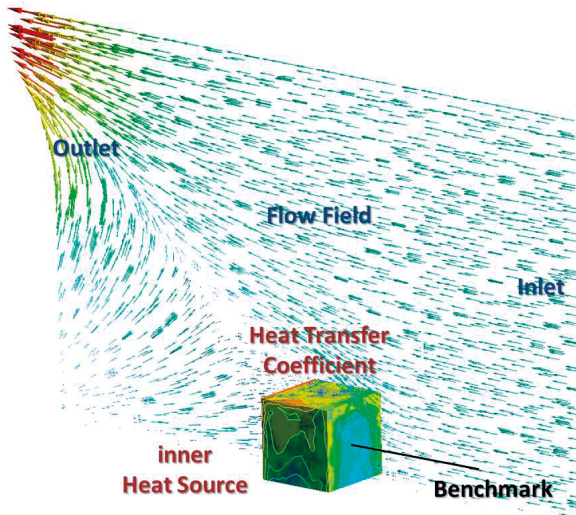


Fig. 1. Calculating of the HTC over the cube surface

In the example, a simple cube with one heat source inside is streamed in by a flow field of cool air. This simulation is done with Ansys-CFX. As the benchmark, values of the computed HTC over the front surface inside the flow field are used. The 64 HTC values are used as benchmark values and the challenge is to find a subset of  $m$  nodes together with a RBF interpolation function (see Eq. (14)) which minimizes the interpolation error, measured like in Eq. (13).

### 5.1 Benchmarks Examples with $N=64$ , $m=5$

This example is constructed for benchmarking the optimization algorithm in comparison with a known global minimum. This global minimum is computed by the assessment of all 64 over  $m$  cases for  $m = 5$ .

The exact numbers of how many different subsets exist in this case are given in table 1. The original Ansys data are shown in figure 2.

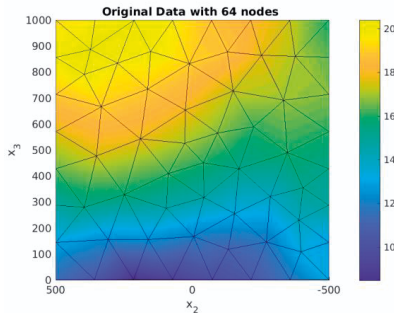


Fig. 2. Original mesh data with 64 nodes.

In table 2 the best six sets with their interpolation-error are shown. Moreover, for an illustration that there really exists 'good and bad sets' in table 2 the set with the largest error up to sets producing not a number results are given in the last line too. The corresponding nodes to this set are located all on a straight line on the right boundary of the domain by  $x = 500$ . Therefore, the interpolation with this set is one of the worst variants.

Table 2. Best six sets and the worst one (without NaN) for  $m=5$

Set S	Interpolation-Error	Set S with $ S =5$
1	4.180556e+00	13 16 45 48 61
2	4.268491e+00	18 29 45 48 61
3	4.291127e+00	2 18 45 48 61
4	4.301570e+00	3 15 45 48 61
5	4.344761e+00	1 18 45 48 61
6	4.346238e+00	13 20 45 48 61
<b>Bad Set S</b>		
7	1.771360e+04	42 56 59 60 61

When running the genetic algorithm for solving the optimization problem it runs after about 800 generations into the global minimum. For the evolution of the best error over the generations, see figure 3.

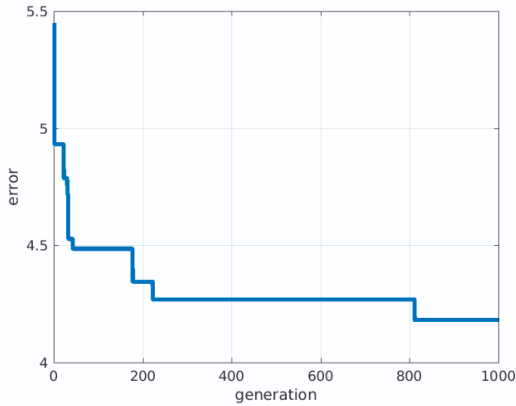


Fig. 3. Evolution of the error over the generations for  $m=5$ .

The resulting interpolation with this optimal set  $S = \{13, 16, 45, 48, 61\}$  is shown in figures 4a and 4b. The location of the interpolation centers of this five radial basis function is marked in figure 4a with the number placed on the center position.

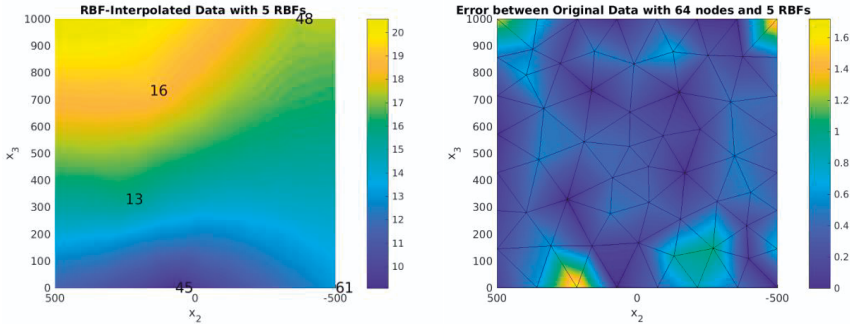


Fig. 4. Example with  $N=64$  and  $m=5$ ; (a) Interpolation with 5 RBFs (b) Interpolation-error with 5 RBFs.

## 5.2 Use case with $N=64$ , $m=20$

In this example, the algorithm chooses 20 nodes out of 64 to create the interpolation system. For the evolution of the best error over the generations, see figure 5. It can reduce the interpolation error to 1.7308 by using the subset  $S = \{5, 8, 11, 13, 19, 24, 25, 34, 35, 36, 38, 42, 45, 49, 54, 57, 58, 59, 61, 63\}$ , see figure 6 for the spatial distribution of this nodes.

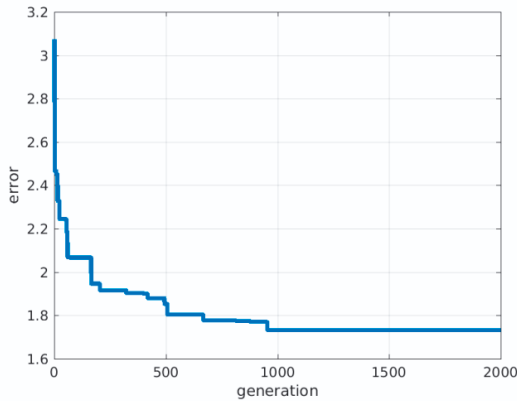


Fig. 5. Evolution of the error over the generations for  $m=20$ .



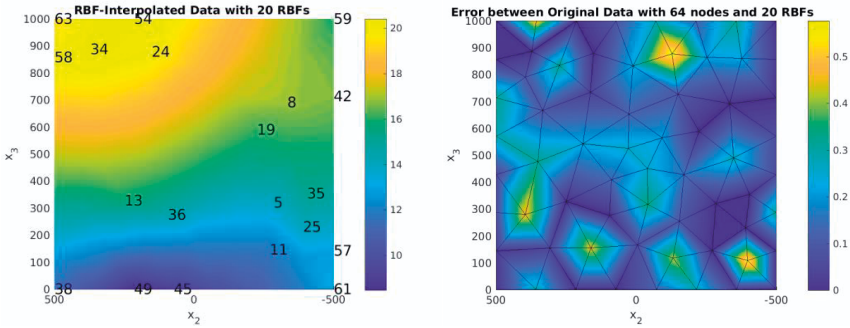


Fig. 6. Example with  $N=64$  and  $m=20$ ; (a) Interpolation with 20 RBFs (b) Interpolation-error with 20 RBFs.

### 5.3 Practical Example with $N=8065$ , $m=100$

In this numerical example, the computation of a heat transfer coefficient values on the Auerbach ACW machine with 8065 nodes are used as input data. Again, a heat source as drive-motor is located in the upper flange, the simulation computes the heat transfer coefficients, induced by a frontal air flow on the surface of the column.

In a project of the Collaborative Research Center (CRC) "Transregio 96" the influence of the environment of machine tools is done by parametrization through characteristic diagrams. The goal is the decoupling of the flow simulation and structural mechanical simulation by using characteristic diagrams for boundary condition definition (see [13], [14]). One constraint in the usage of characteristic diagrams is the selection and reduction of input data.

The first step is therefore to reduce the high number of input data, in this case the HTC's in 8065 nodes to a moderate number of values, which is done by the optimal subset selection of this paper.

This input data are shown in figure 7a. The corresponding interpolation with  $m = 100$  RBFs is shown in figure 7b, the interpolation centers of this 100 RBFs are marked with red balls. The evolution of the best error and the final interpolation error are shown in figure 8.

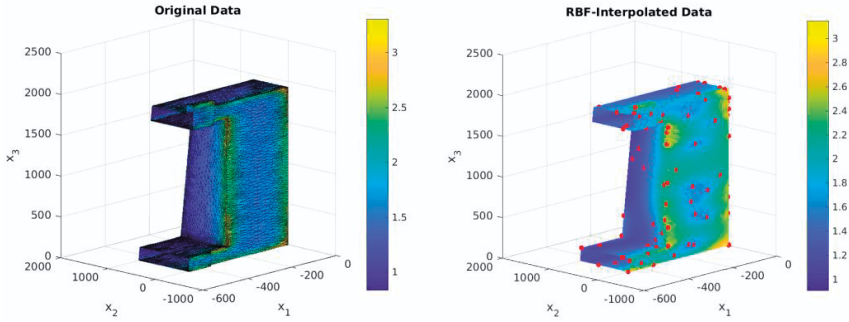


Fig. 7. Example with  $N=8065$  and  $m=100$ ; (a) Original mesh with 8065 nodes  
(b) Interpolation with 100 RBFs.

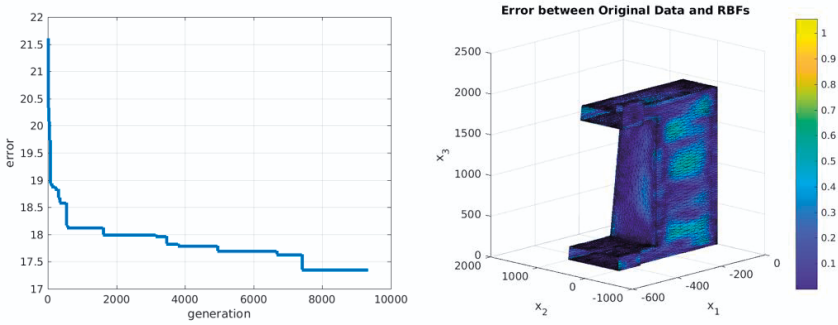


Fig. 8. Example with  $N=8065$  and  $m=100$ ; (a) Evolution of the error (b) Interpolation-error.

## 6 Conclusion and Outlook

This paper presents an efficient clustering approach for characteristic values out of the fluid simulation to describe the environment interdependencies of machine tools. The fluid simulation calculates a field of HTC around the surface of the machine component as characteristic values. Subsequently, interpolate this field for the following steps to find an optimal subset of nodes by using the RBF theory.

The implementation is ensued through a genetic algorithm. Some numerical use cases present the functionality of the developed method. The last part shows the result for an optimal subset of characteristic values on a realistic component of a machine tool.

Finally, the planned work is to use the developed method for the numerical calculation of a whole working day in a factory hall.

Therefore, many time-intensive fluid simulations are necessary and produce many data like heat transfer coefficients, temperature values, flow directions and velocities. The aim of the method, described in the paper is to assign this method for handling this big data of characteristic values for each time step and reduce it to the significant values.

#### Acknowledgements

*This research is being supported by the German Research Foundation in the context of the Collaborative Research Centers Transregio 96, subproject B09.*



## 7 References

- [1] Bryan, J., 1990. International status of thermal error research. CIRP Annals Manufacturing Technology.
- [2] Buhmann, M., D., 2004. Radial Basis Functions. Cambridge University Press.
- [3] Coley, D., A., 1998. An Introduction to Genetic Algorithms for Scientists and Engineers. World Scientific Publishing Co., Inc., River Edge, NJ, USA.
- [4] Grossmann, K., et al., 2015. Challenges in the development of a generalized approach for the structure model based correction. Applied Mechanics and Materials, 794:387-394.
- [5] Ihlenfeldt, I., et al., 2014. Modelling of thermal interaction between environment and machine tool. Thermo-energetic design of machine tools, pages 111-124.
- [6] Mayr, J., et al., 2009 Compensation of thermal effects on machine tools using afdem simulation approach. 9th International Conference and Exhibition on LASER Metrology, Machine Tool, CMM and Robotic Performance.
- [7] Narendra, P., M., K. Fukunaga, K., 1977. A branch and bound algorithm for feature subset selection. IEEE Trans. Comput., 26(9):917-922.
- [8] Naumann, C., et al., 2015. Characteristic diagram based correction algorithms for the thermo-elastic deformation of machine tools. Proceedings 48th CIRP Conference on Manufacturing Systems.
- [9] Ridout, M., S., 1988. [Algorithm AS 233] An improved branch and bound algorithm for feature subset selection. Applied Statistics, 37:139-147.
- [10] Sivanandam, S., N., Deepa, S., N., 2007. Introduction to Genetic Algorithms. Springer Publishing Company, Incorporated, 1st edition.
- [11] Somol, P., Pudil, P., Kittler, J., 2004. Fast branch & bound algorithms for optimal feature selection. IEEE Trans. Pattern Anal. Mach. Intell., 26(7):900-912, 2004.
- [12] Unger, R., 2009. Obstacle Description with Radial Basis Functions for Contact Problems in Elasticity. Preprint CSC 09-01 TU Chemnitz.

- [13] Glänzel, J., Ihlenfeldt, S., Naumann, C., Putz M., 2016. Decoupling of fluid and thermo-elastic simulations on machine tool using characteristic diagrams. Proceedings CIRP Conference on Intelligent Computation in Manufacturing ICME, Ischia (Italien).
- [14] Glänzel, J., Ihlenfeldt, S., Naumann, C., 2017. Effiziente Quantifizierung der Konvektion durch Entkoppelte Strömungs- und Strukturmechanische Simulation, Beispielhaft am Maschinenständer. In: 5. Kolloquium SFB/TR96, Chemnitz.



# Using meta models for enclosures in machine tools

F. Pavliček<sup>a</sup>, D. P. Pamies<sup>a</sup>, J. Mayr<sup>b</sup>, S. Züst<sup>a</sup>, P. Blaser<sup>a</sup>, P. Hernández-Becerro<sup>b</sup>,  
K. Wegener<sup>a,b</sup>

<sup>a</sup>Institute of Machine Tools and Manufacturing IWF, ETH Zürich, Leonhardstrasse 21,  
8092 Zürich, Switzerland

<sup>b</sup>Inspire AG, Technoparkstrasse 1, 8005 Zürich, Switzerland

**Abstract.** One of the crucial input parameters in thermo-mechanical simulation of machine tools is the heat transfer coefficient ( $h$ ). The heat transfer coefficient depends on many parameters, for example the nearby environment. The machine housing insulates the surface of the machine tool from the room environment. Therefore, the enclosure has to be taken into account to precisely determine the heat transfer coefficients. This paper presents how the enclosure can be efficiently considered in thermo-mechanical simulations of machine tools by means of meta models. The meta models are integrated in finite element simulations describing the boundary condition.

Peer-review under responsibility of the International Scientific Committee in the person of the Conference Chair Prof. Steffen Ihlenfeldt.

**Keywords:** Meta models; Heat transfer coefficient; Enclosures; Machine tools; Thermal simulation; Fluid simulation;

## 1 Introduction

According to Mayr *et al.* [5] up to 75% of the workpiece errors are caused by thermal errors of machine tools. In the thermal effects diagram Bryan [1] showed that different external and internal heat sources lead to these errors in machine tools. Simulations and measurements of external heat sources are shown by Mayr *et al.* [6]. They analyze how environmental changes affect thermal displacements in the frequency domain. An example of an internal heat source is the heat produced by rotation of the table. This heat source affects the machine temperature due to thermal conduction, convection and radiation. It is well known how to treat the heat transfer via conduction in a thermal finite element (FE) simulation of the machine tool. However, convection and radiation within the room enclosures are also significant, but often neglected. For the FE simulation the heat transfer coefficient  $h = \frac{Q}{A \cdot \Delta T}$ , where  $Q$  is the thermal power,  $A$  is the area and  $\Delta T$  is the temperature difference be-

tween the surface and the fluid, is necessary as an input parameter for the boundary conditions. However, the heat transfer coefficient on the walls of the machine tool depends on the thermal mechanisms and air circulations in the enclosure of the machine tool.

To analyze these effects time consuming computational fluid dynamics (CFD) simulations are required. The combination of a CFD simulation on a whole machine tool with the FE simulation of the same machine tool would lead to a drastically increased model complexity and unbearable computation times. Another way is the description of the enclosures with a meta model that can be easily implemented in the FE simulation of the machine tool.

Because the heat transfer coefficient is on the one hand an important boundary condition for the thermal FE simulation, as Grossmann [2] mentioned, and on the other hand complicated to measure there have been attempts to determine it efficiently. For example, Neugebauer *et al.* [7] show a method for adapting the heat transfer coefficient in a time variable simulation as a function of the surface orientation. Even though they reached their aim to gain the heat transfer coefficient in a fast way they mention that there is still a method needed to describe the heat transfer coefficient in enclosures, because their approach uses correlations for infinite surfaces.

To gain more information about natural convection in enclosures studies like the ones of Martyushev *et al.* [4] or Kuyper *et al.* [3] can be analyzed. In both studies an enclosure with a single heated wall is considered. Even though these studies are very helpful to get a better understanding of the thermal mechanisms, the full application of the thermal FE simulation of machine tools is still missing.

An approach to develop meta models for FE simulations from CFD simulations is presented by Pavliček *et al.* [8]. To this end, variations of the input parameters (e.g. temperatures) of the CFD simulation model are carried out and the heat transfer coefficient of the enclosure surfaces is gained as an output parameter. Out of these variations a least square fit is carried out to obtain the meta model. Here, this approach is applied and enhanced for a working room enclosure of a five-axis machine tool. The air circulation is analyzed via CFD simulations and the simulated temperatures are compared to temperature measurements. It is shown how a simplified enclosure can be used instead of the complex real working room enclosure. Then, the meta model describing the heat transfer coefficient on the surface of the machine tool, depending on the temperature changes during the working process, is developed and discussed.

## 2 Enclosures in machine tools

An important enclosure in machine tools is the working room, as shown in Fig. 1 of a five-axis machine tool. The table and the C-axis are highlighted in red, because they are the most important heat source in this enclosure. For a FE simulation of this machine tool the heat transfer coefficient on the surfaces of the working enclosure is needed as an input parameter. The heat transfer coefficients depend on the temperatures of the table, the C-axis, the environment and the cutting fluid tank that is directly beneath the machine table.

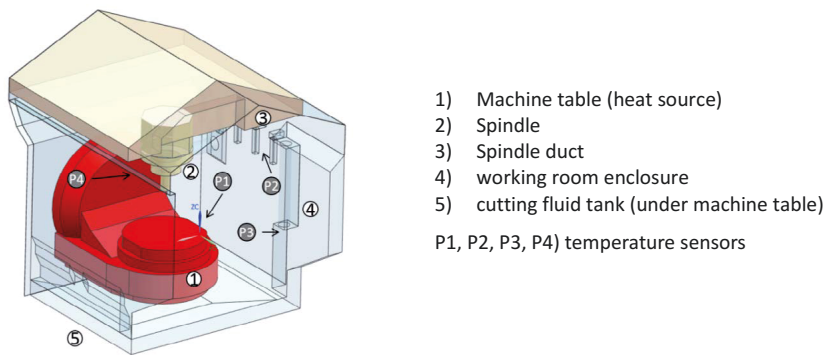


Fig. 1. Model and elements of the machine tool for simulation and measurements.

### 2.1 Measurements

To analyze the working room enclosure, measurements are performed over 36 hours using the procedure shown in Fig. 2. The measurements start with a heating phase of 6 hours, with the table rotation at 1200 rpm. The heating time ensures that the machine tool reaches steady state. Earlier experiments showed that the steady state is reached within this time. During the following cooling phase the machine is in NC-hold. After that, a break of 12 hours follows, with the machine completely turned off, before the same procedure is performed again on the next day. During the break the machine tool can reach a homogeneous temperature distribution but as the measurements showed the thermal memory can still be seen.

Heating 6 h	cooling 6 h	break 12 h	heating 6 h	cooling 6 h
----------------	----------------	---------------	----------------	----------------

Fig. 2 The measurement procedure for temperature measurements of the machine tool.

During the heating and the cooling phase the power consumption of the machine's C-axis is measured, which is shown in Fig. 3. The power consumption during the heating phase is around 8 kW. This power is converted to heat which



is partly extracted by the cooling system. The excess heat leads to temperature changes within the enclosure. The interruptions in the measurement occur, when the machine is stopped to measure the displacements at the tool center point (TCP) that are not shown in this work. During the cooling phase the power consumption is mostly zero, but the interruptions for the TCP-displacement measurements can be seen as well.

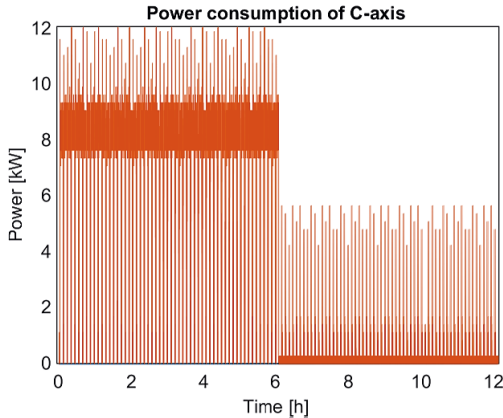


Fig. 3. The power consumption over time of the C-axis during heating and cooling phase.

Figure 1 shows the positions of four temperature sensors in the working enclosure. The sensors P1, P2 and P3 are attached to the right wall of the enclosure and the sensor P4 is on the shield of the C-axis. Figure 4 shows the results of the temperature measurement during heating and cooling phase for two days. Therefore the measurements have different initial temperatures. Light (dark) colors correspond to the first (second) measurement. As a result of the earlier measurements, the machine starts warmer on the second day. The C-axis reaches a maximum temperature of nearly 30 °C and is the main heat source within the enclosure. It can be seen that the temperatures on the wall show a slower and lower temperature rise compared to shield of the C-axis. The reason for the ripples in the profiles during the heating phase is that the C-axis stops rotating in defined time intervals for the above mentioned displacement measurements. Thus, the forced convection caused by the rotation of the axis is paused. This causes the temperature at the sensor positions to rise immediately. This effect is more pronounced for sensor P4 because it is located close to the rotating table and also connected to the heat source by thermally highly conducting metallic material.

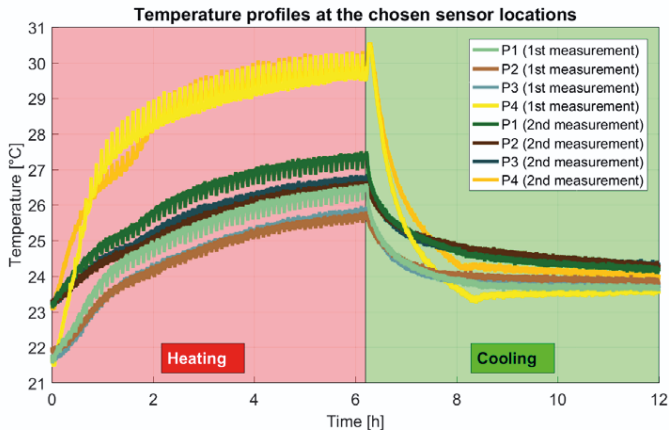


Fig. 4. Temperature profiles at the sensor positions shown in Fig. 1 during heating and cooling phase.

A comparison between the temperature measurements in Fig. 4 and the power consumption measurements in Fig. 3 show that the temperature needs time to react to the power input. That is why the power consumption is constant and the temperature measurements show a temperature change during the heating phase. The same situation occurs during the cooling phase. For that reason, the temperature is used as an input parameter in the meta model instead of the power consumption.

## 2.2 Fluid simulation

To analyse the temperature measurements in the working enclosure a CFD simulation considering convection, conduction and radiation is performed. The table and C-axis are defined as the heat source of the enclosure with a temperature of 30 °C. The ambient temperature is set to 22 °C as during the measurements. The simulation is carried out as a steady state simulation to save computational time, as transient simulations would last for more than two weeks. Apart from that the changes of the thermal behavior in the enclosure and the walls are slow. This allows enough time for the fluid to reach a (quasi) steady state and justifies CFD simulations in steady state. The results of the velocity stream lines are plotted in Fig. 5. As the enclosure is nearly symmetric to the middle plane that goes through the centre of the C-axis, the air velocity is analysed on this plane. The coloring of the streamlines scales with the velocity as shown in the legend. The hot air rises at the back of the machine table and forms stream cells as it reaches the top of the enclosure. Stream cells can be observed at expected locations inside the enclosure.

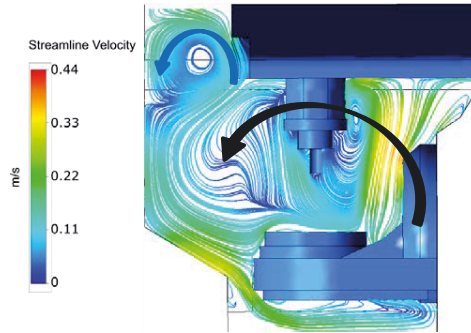


Fig. 5. Steady state streamlines of the air inside the enclosure.

The highest air velocity is reached above the heat source where the air rises up to the spindle stock and, thereafter, the upper surface of the working enclosure. The main air circulation is illustrated by the black arrow and another smaller air circulation occurs in the upper left corner of the enclosure (see blue arrow). The symmetry of the air flow in the enclosure is illustrated in Fig 6. The flow particles start at the heat source and move along their corresponding streamlines for 5 s with 0.1 s time steps. For each time step, a ball is drawn whose color corresponds to the velocity as shown in the legend. Again, it can be observed that air rises at the back of the machine table. It shows that the air rising up from the machine table flows symmetrically to the left and the right wall of the enclosure. This knowledge is important, when the simplified enclosure is defined.

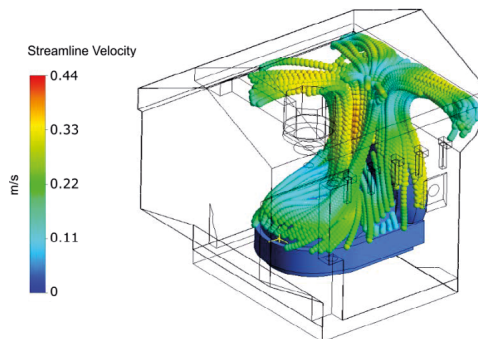


Fig. 6. Simulation of the particle flow and streamline in the enclosure.

## 2.3 Comparison

The measurement results in Fig. 7 confirm that the machine tool is warmer at the second day of the measurements as all temperatures reach higher values in the steady state. The steady state temperatures of the two measurements are

plotted as bars. The simulated temperatures at the corresponding sensor positions are shown as dots and reproduce the measurements very well.

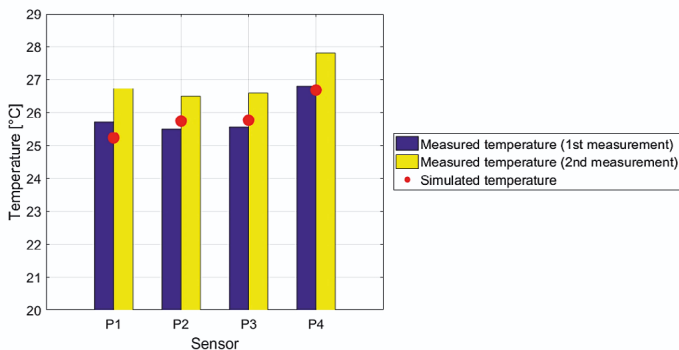


Fig. 7. Simulated versus measured steady state temperatures for the four temperature sensors.

Building up a CFD model of a real enclosure, as it was done here in detail, is very time consuming. An easier way is to use a simplified enclosure that represents the most important thermal mechanisms of the analyzed enclosure, as outlined in chapter 3.

### 3 Simplified enclosure

Figure 8 shows a simplified enclosure that covers the dominant thermal effects, considering conduction, convection and radiation, of the machine's working enclosure. Only the main dimensions of the enclosure and the heat source are considered. The velocity field in Fig. 8 shows the strong air circulation similar to the simulation of the original working enclosure in Fig. 5 and Fig. 6. The heat source is shown in red and the grey slide shows the plane on which the air velocity [m/s] on the right picture is plotted.

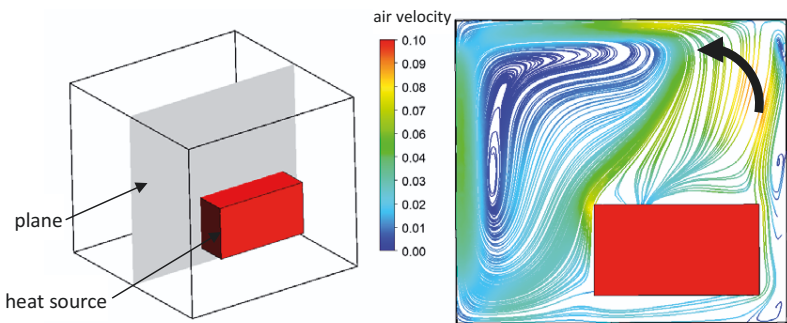


Fig. 8. Sketch of the simplified enclosure.

The main difference is that the less pronounced air circulation in the upper left corner (blue arrow in Fig. 5) is missing, due to the simplified shape of this enclosure. Therefore, some disagreement between the simulated and the physical values of the heat transfer coefficient is expected in this region. The advantages of the simplified enclosure are that it takes less time to build the model, that it has a reduced calculation time and therefore allows faster determination of the heat transfer coefficient.

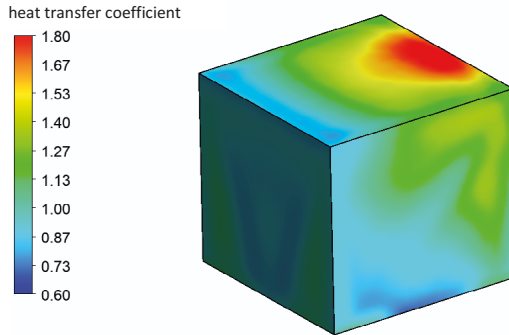


Fig. 9. Heat transfer coefficient [ $\text{W}/\text{m}^2\text{K}$ ] on the surfaces of the enclosure.

The heat transfer coefficient is analysed on all surfaces of the enclosure, as depicted in Fig. 9. It can be seen that the heat transfer coefficient is not homogeneous over the whole surface. It reaches its maximum above the heat source, where the air rises up. As the boundary condition for the whole upper surface is needed in the FE-simulation the average value as well as the maximum value is taken into account. The minimum value is also evaluated but as already mentioned it has to be used with care in the FE-simulation due to the missing smaller air circulation that occurs in the real enclosure due to the small geometry in the upper left corner (blue arrow in Fig. 5).

#### 4 Meta model

The meta model is developed as described in the approach of Pavliček *et al.* [8]. For this specific enclosure three influence parameters have to be considered. The first one is the temperature of the heat source  $T_{hs}$  that changes with time, as illustrated by Fig. 4. This temperature is continuously measured during the process. The same holds for the second parameter  $T_e$ , the temperature of the environment that changes with the cycle of the day and the year or with the opening of the shop floor door. The third parameter is the aforementioned temperature of the cooling fluid  $T_f$  in the tank within the structure. Fig. 10

shows the domain of definition for the meta model. The meta model is exemplarily shown for the upper surface (highlighted in blue).

considered parameters:

- temperature heat source  $T_{hs}$   
→ from 24 °C to 30 °C
- temperature environment  $T_e$   
→ from 16 °C to 35 °C
- temperature fluid  $T_f$   
→ from 18 °C to 32 °C

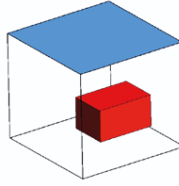


Fig. 10. Varied parameters to gain a meta model for the enclosure.

The meta model for the average heat transfer coefficient  $h$  is described by

$$h = b_1 + b_2 \cdot T_{hs} + b_4 \cdot T_e + b_6 T_f + b_3 \cdot T_{hs}^2 + b_5 \cdot T_e^2 + b_7 \cdot T_f^2 + b_8 \cdot T_{hs} \cdot T_e + b_9 \cdot T_{hs} \cdot T_f + b_{10} \cdot T_e \cdot T_f \quad (\text{Eq. 1})$$

where the temperatures have to be filled in K and the unit for  $b_1$  is  $\frac{W}{m^2K}$ ,  $b_2$ ,  $b_4$  and  $b_6$  is  $\frac{W}{m^2K^2}$  and  $b_3$ ,  $b_5$ ,  $b_7$  to  $b_{10}$  is  $\frac{W}{m^2K^3}$ . In general, the average heat transfer coefficient of a surface is sufficient as an input parameter for the FE simulation.  $b_1$  is a zero balancing factor. The influence of the three temperatures  $T_{hs}$ ,  $T_e$  and  $T_f$  are considered with linear terms and with polynoms of second order in accordance to the theory of convective heat transfer. Furthermore a combination of two of them is considered with respect to the radiation. The model terms are weighted with constant parameters, computed using least squares. For the least square fit the simulation model is varied with the input parameters shown in Fig. 10. The model parameters for the upper surface are listed in Table 1. For the other walls the parameters  $b_1$  to  $b_{10}$  have different values, but are obtained in a similar manner.

Table 1. Coefficients for computing the heat transfer coefficient of the upper surface.

$b_1$	$b_2$	$b_3$	$b_4$	$b_5$	$b_6$	$b_7$	$b_8$	$b_9$	$b_{10}$
$-2.6 \cdot 10^3$	-0.178	0.003	1.655	$10.0 \cdot 10^{-4}$	15.748	-0.022	-0.002	-0.004	-0.005

Meta models can easily be implemented in the FE simulation of the entire five-axis machine tool. As it is of general use it can also be used for other working room enclosures with comparable dimensions. In the future work this meta model could be further generalised so that also enclosures with different dimensions can be described.

This paper shows that the simplified enclosures accurately describe the basic thermal mechanisms in the real enclosure, such that they can replace a CFD simulation of the real enclosure. In addition, it is not needed to simulate a simplified enclosure of a similar geometry, as the model can be transferred to other working room enclosures.

### **Acknowledgements**

*The authors thank the Machine Tool Technologies Research Foundation (MTTRF), the Swiss Federal Office for Professional Education and Technology (CTI) and the Swiss National Science Foundation (SNF) for their support.*

## **5 References**

- [1] Bryan J. International Status of Thermal Error Research, 1990. Annals of the CIRP, pp. 645-656.
- [2] Grossmann K. Thermo-energetic Design of Machine Tools. Springer International Publishing Switzerland, pp. 111-124, 2015.
- [3] Kuypers R, Meer T V D, Hoogendoorn C and Henkes R., 1993. Numerical study of laminar and turbulent natural convection in an inclined square cavity. International Journal of Heat and Mass Transfer, pp. 2899–2911.
- [4] Martyushev S, Miroshnichenko I and Sheremet M. Influence of the Geometric Parameter on the Regimes of Natural Convection and Thermal Surface Radiation in a Closed Parallelepiped. Journal of Engineering Physics and Thermophysics, pp. 1522–1529, 2015.
- [5] Mayr J, Jedrzejewski J, Uhlmann E, Alkan Donmez M, Knapp W, Härtig F, Wendt K, Moriawaki T, Shore P, Schmitt R, Brecher C, Würz T, Wegener K. Thermal Issues in Machine Tools. CIRP Annals Manufacturing Technology, pp. 771-791, 2012.
- [6] Mayr J, Ess M, Pavliček F, Weikert S, Spescha D, Knapp W, Simulation and measurement of environmental influences on machines in frequency domain, CIRP Annals - Manufacturing Technology, 2015, Cape Town, South Africa
- [7] Neugebauer R, Ihlenfeldt S, Zwingenberger C. An extended Procedure for Convective Boundary Conditions on Transient Thermal Simulations of Machine Tools. Production Engineering Research and Development 6:641–646, 2010.
- [8] Pavliček F, Dietz F, Blaser P, Züst S, Mayr J, Weikert S, Wegener K, An approach for developing meta models out of fluid simulations in enclosures of precision machine tools, 31st ASPE Annual Meeting, 2016, Portland, Oregon, USA

# Model Order Reduction of Thermal Models of Machine Tools with Varying Boundary Conditions

*P. Hernández-Becerro<sup>a</sup>, J. Mayr<sup>a</sup>, P. Blaser<sup>b</sup>, F. Pavliček<sup>b</sup>, K. Wegener<sup>b</sup>*

<sup>a</sup>Inspire AG, Technoparkstrasse 1, 8005 Zürich, Switzerland

<sup>b</sup>Institute of Machine Tools and Manufacturing IWF, ETH Zürich, Leonhardstrasse 21, 8092 Zürich, Switzerland

**Abstract.** The numerical models describing the thermal behavior of machine tools lead to large systems of equations, which are computationally expensive. Efficient models by means of Model Order Reduction (MOR) aim at reducing the dimension of the system, enabling their use in applications requiring multiple evaluations, such as design optimization and compensation. The main contribution of this work is an efficient traceability of variable parameters defining the behavior of the system in the reduced models. This enables the model to represent sudden variations of boundary conditions, such as the application of a cooling fluid to the structure of the machine.

Peer-review under responsibility of the International Scientific Committee in the person of the Conference Chair Prof. Steffen Ihlenfeldt.

*Keywords:* Model Order Reduction (MOR); Thermal error model; Machine tool

## 1 Introduction

An approach for the characterization of thermal behavior of machine tools is to create physical models based on the heat transfer and elasticity equations. These models provide a great flexibility to test the feasibility of design modifications and are a useful tool to optimize the performance of the machining system. In comparison to other modeling approaches, they can be created at early stages of the design phase when the physical system is still not available.

The physical thermal error models are based on the discretization of the partial differential equations, which describe the heat transfer coupled to the mechanical response. Mian et al. [1] considered the environmental effects in a thermal Finite Element Method (FEM) model of a three-axis vertical milling machine. The authors stated that the initial state of the machine is usually unknown and therefore there is always a discrepancy between the first hours of the simulation and the measured values. Further work on the topic of thermal models of machine tools was carried out by Jedrzejewski and Kwasny [2]. Their thermal



model, based on the FEM, was combined with dynamic models aiming at a holistic simulation of the machine tool. Mayr [3] used a Finite Difference Element Method approach (FDEM) in order to compute efficiently the thermal error of machine tools. The temperature field was calculated by means of Finite Difference Method, while the associated mechanical displacements were computed with FEM. In his work, Mayr proposed a substructure approach of the system output, reducing the computational effort to compute the tool center point (TCP) displacements and orientation errors. The thermal errors were calculated for the whole working volume for linear and rotary axes. The component and location errors were derived from the simulated thermally induced volumetric errors in the working space. This work was continued by Ess [4], developing a software package, called Virtual Machine Prototype (VMP), which connected the axes through models representing different machine tool elements. The solution of the thermo-mechanical problem was performed by FEM. The software provides a large library of machine elements, such as thrust bearings or ballscrews, which are described by models accounting for the thermal conductivity, heat losses and mechanical stiffness. VMP allows the computation of the thermal response of machine tools taking into consideration the movement of the axes given by a numerical control (NC) code. A comprehensive review of the thermal error models of machine tools was conducted by Mayr et al. [5].

One disadvantage of full thermal error models of machine tools is their high computational effort, linked to the evaluation of the discretized partial differential equations. One alternative is the creation of surrogate models which reduce the computational time while maintaining the accuracy of the prediction. This enables the real time simulation of the model as well as its applicability for situations where the model needs to be evaluated a large number of times, such as parameter identification, design optimization and compensation. Projection-based reduced models are a type of surrogate models which decrease the computational effort by projecting the full model in a lower dimensional space. The main advantage of the model order reduction (MOR) is the ability to trace the dynamical evolution of the system while retaining the system structure, as explained by Benner et al. [6].

Analogously to dynamical systems, Bueno et al. [7] presented the concept of thermal modal analysis of a machine tool. Zhu et al. [8] developed a modal analysis for different machine tool parts, in order to find the optimal location of the sensors for thermal error compensation. With the information of the optimal temperature sensor locations, the authors created a position-dependent

thermal error model of the positioning error of the Z-axis, based on polynomial regression.

Galant et al. [9] developed a reduced thermal model of a milling machine column. The transformation matrices for the projection into a Krylov subspace were handled by Arnoldi process. In order to deal with the variable position of the heat load due to the movement of the machine tool axis, the guideways were divided in discrete positions. For each segment a reduced system was computed. Lang et al. [10] studied the reduction of models with moving thermal loads, applying their results to the same study case of Galant et al. They compared two reduction methods to deal with the parametric dependency of the system matrices due to the movement of the axis. They introduced the concept of switched linear approach (SLS). Similarly to Galant et al., they divided the guideways into different segments and computed the reduced system matrices by balanced truncation for each discretized position of the axis. As an alternative to the SLS approach, Lang et al. considered the structural variability as a continuous parameter, described by an affine representation. The projection matrices were calculated using the iterative rational Krylov algorithm (IRKA), considering information at different sampling points of the parameter space. Different reduction approaches for thermo-mechanical models of machine tools with moving axes were reviewed by Naumann et al. [11].

The effect of the cutting fluid on the machine tool accuracy has gained relevance both in industry and academia. Bryan [12] included the cutting fluid in his thermal effect diagram as an external influence. Mayr et al. [13] measured the thermally induced errors of a rotary table with and without the influence of the cutting fluid, concluding that it is necessary to include these effects in compensation strategies. Hernández-Becerro et al. [14] and Blaser et al. [15] conducted further measurements on the effect of the cutting fluid on the performance of a 5-axis machine tool by means of a precision level and a thermal test piece respectively.

The original contribution of this paper is the application of reduction algorithms to the case of suddenly varying boundary conditions, representing the introduction of cooling fluid or supply of cutting fluid into the working space. In Section 2, the parametric dependency of the system and the reduction algorithm with switching boundary conditions are presented. Section 3 describes the thermo-mechanical model and the results of the reduced system are compared to the full system in time and frequency domain. Finally, in Section 4 the conclusions and outlook of the work are provided.

## 2 Model Order Reduction with switch boundary conditions

The system obtained from the FEM discretization of the physical model can be expressed by the state-space representation.

$$\begin{aligned}\frac{dT(t)}{dt} &= \underline{\underline{A}}(t, \underline{p}) \cdot \underline{T}(t) + \underline{\underline{B}}(t, \underline{p}) \cdot \underline{u}(t) \\ \underline{y}(t) &= \underline{\underline{C}}(t, \underline{p}) \cdot \underline{T}(t)\end{aligned}\tag{1}$$

$\underline{\underline{A}}(t, \underline{p}) \in \mathbb{R}^{n \times n}$  is the system matrix representing the dynamics of the system,  $\underline{\underline{B}}(t, \underline{p}) \in \mathbb{R}^{n \times m}$  is the input matrix and  $\underline{u}(t)$  is the input vector, which describes the thermal loads. The thermally induced position and orientation errors at the TCP relative to the workpiece,  $\underline{y}(t)$ , are provided by the output matrix  $\underline{\underline{C}}(t, \underline{p})$ . The state-space representation of thermal error models of machine tools is described in detail by Mayr et al. [16]. The vector  $\underline{p}$  represents in the Equation 1 a set of parameters that define the model, e.g. the position of the machine tool axes. The focus of this work is the parameters representing the convective boundary conditions defining the heat exchange between the machine tool and the surrounding fluid domain. This heat exchange is described as proportional to the temperature difference between the fluid ( $T_{fluid}$ ), which can be the surrounding air or a cooling fluid, and the surface ( $T_s$ ), expressed as

$$\dot{q} = h \cdot (T_s - T_{fluid})\tag{2}$$

where the proportionality constant  $h$  is the heat transfer coefficient (HTC). The convective heat transfer between the environment and the structure is caused by natural convection. The temperature difference between the wall and the air creates variations of the fluid density, originating a buoyancy force that leads to a macroscopic fluid motion enhancing the heat transfer. The values of the HTC can be estimated by means of empirical formulas, Computational Fluid Dynamic (CFD) simulations or meta modeling techniques, as presented by Pavliček et al. [17]. The introduction of fluid media in the working space by an external device and the movement of the axes rapidly alter the heat exchange between the fluid and the machine, transitioning to forced convection. This leads to a sudden change of the HTC on the affected area, enhancing the heat transfer. The parameter describing the convection affects the system  $\underline{\underline{A}}(t, \underline{p})$  and the output matrix  $\underline{\underline{B}}(t, \underline{p})$  of Equation (1). Considering the change between dry and wet cutting in the thermo-mechanical model results in a linear time-variant (LTV)

system, as the HTC needs to be traced and updated at different times during the simulation.

In order to reduce the computational effort, a reduced model of the system described in Equation (1) is created. However, the time-dependency of the system and the output matrices due to varying boundary conditions restricts the direct use of well-established projection-based MOR for linear time-invariant (LTI) systems. In order to represent this time dependency, this work uses an approach based on interpolating local reduced matrices.

The variation of the HTC can be represented in many situations as a switch between two linear systems. This is the case of cooling fluid applied to some structural part of the machine or the introduction of cutting fluid to the working space. Therefore, a switch linear system can be created considering the reduction of two LTI systems,

$$\underline{\underline{\hat{A}_i}} = \underline{\underline{W_i}}^T \cdot \underline{\underline{A_i}} \cdot \underline{\underline{V_i}} \quad \underline{\underline{\hat{B}_i}} = \underline{\underline{W_i}}^T \cdot \underline{\underline{B_i}} \quad (3)$$

where  $\underline{\underline{V_i}}$  and  $\underline{\underline{W_i}}$  are the projection matrices in order to compute system of order  $r \ll n$ . The subscript  $i$  represents the two states of the machine, i.e. external cooling on or off. When the coolant is applied, the system matrices switch representing the sudden change of the boundary conditions. During the switch an interpolation between the two systems is required in order guarantee the existence of a solution of the differential equations. However, the system matrices cannot be directly interpolated given that they are in different generalized coordinate systems. This problem can be overcome with a congruence transformation, as explained by Panzer et al. [18], where the two system are expressed in terms of the same generalized coordinates. Thus the interpolation can be performed directly between the reduced system matrices.

### 3 Thermo-mechanical model with switching boundary conditions

In this paper, the thermal behavior of a vertical 5-axis machining center with a swiveling and rotary axis is studied. The kinematic configuration according to ISO 10791-1:2015 is:

$$V [w \ C2' \ B' \ b \ [Y1 \ Y2] \ X \ [Z1 \ Z2] \ (C1) \ t]$$

The structure of the machine tool is shown in Figure 1(a). This work focuses on developing a reduced model of a single part of the machine tool assembly. The thermo-mechanical model concentrates on the saddle of the body of the X-axis,

illustrated in Figure 1(b). The part is meshed in commercial FEM software with a total number of nodes  $n = 39211$ . The body is exposed to the environment, affecting all the surfaces depicted in blue in Figure 1(b). The front side of the body, depicted in green, is exposed to a cooling fluid, leading to a sudden change of boundary conditions. The rest of the boundary conditions represent the machine elements, namely the guideways, ballscrew nuts as well as the thrust bearings. The contact conductivities for these machine elements are obtained from models available in the literature, for instance Grossmann and Jungnickel [19]. Finally, the heat input of the drive is also included as thermal loads.

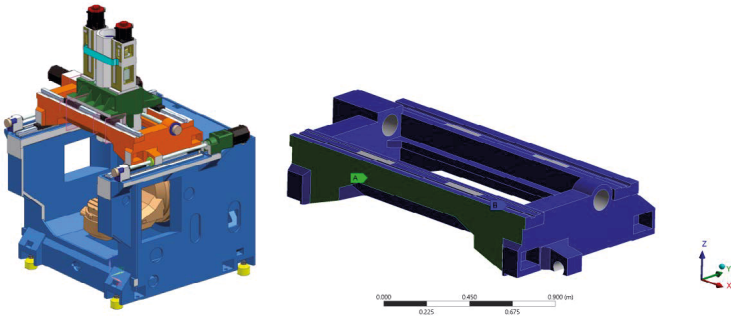


Fig. 1. (a) Left: CAD model of the machine tool under study; (b) Right: Geometry of the saddle of the X-axis. In blue surfaces exposed to the environment. In dark green surfaces exposed to cooling fluid

The reduction of the system is performed by means of Block Arnoldi. The order of the reduced system is  $r = 120 \ll n$ , which is selected so that the maximum error of the transfer function at any of the combinations of the inputs and outputs does not exceed 8%. In order to validate the reduction method the relative errors between transfer function of the original and reduced system for the different combinations of inputs and outputs are depicted in Figure 2. The vertical line points out the frequency corresponding to a periodicity of 24 h, which is one of the main excitation frequencies in an uncontrolled environment. The maximum errors of the transfer functions lay in a lower frequency range. Thus errors lower than 8% are expected in the transient simulation.

The reduction method for varying boundary conditions is further validated in a time-domain simulation. The environmental temperature, depicted in Figure 3 (a), is obtained from measurements in the workshop, in order to achieve a more realistic numerical validation capturing the typical frequency spectrum of the environment surrounding the machine. Different time-varying contact temperatures are also introduced for the machine elements and a constant heat

flux for the drive is considered. The numerical integration of the full and reduced system is performed over 80 h with variable time-step. The sudden change of the boundary condition by introducing the cooling fluid is performed after 40 h. The temperature of the fluid is also shown in Figure 3 (a). In this transition an interpolation between the local reduced matrices is performed, as explained in the previous section.

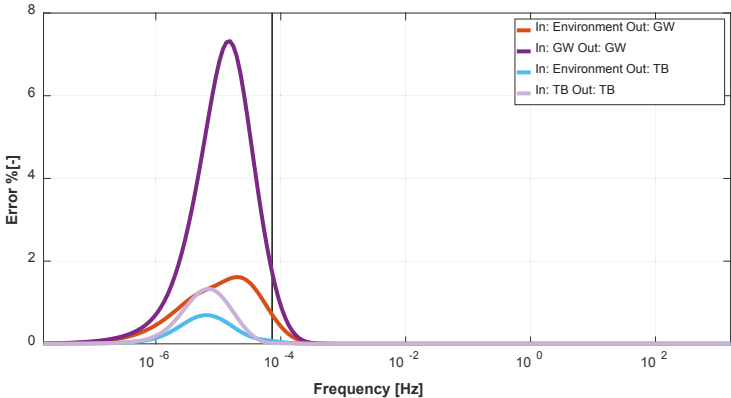


Fig. 2. Relative error (%) in frequency domain for several combinations of inputs (In) and Outputs (Out) for the full and reduced (Red.) system. Guideway (GW), Thrust Bearing (TB)

The temperature values of the reduced and the full system are displayed in Figure 3 (a). The displayed temperatures are evaluated on the guideway and thrust bearing. The Figure 3 (b) shows that the relative error between the reduced and the full system remains below 0.25%. While the full system requires 6 h 25 min for the time integration, the elapsed time for the transient simulation of the reduced system is lower than 2 min. During the initial time steps and after the sudden change of the boundary condition larger relative errors are observed. This can be attributed to a combined effect of the reduction method and the adaptive time-step integration method.

The Figure 4 depicts the calculated displacements of the full and reduced system on the guideway. In addition, Figure 4 shows the relative errors, which are during the transient simulation in an acceptable range. The maximum value of the error, found after 10 h, is associated with small displacements and thus divisions by values close to zero during the calculation of the relative error.

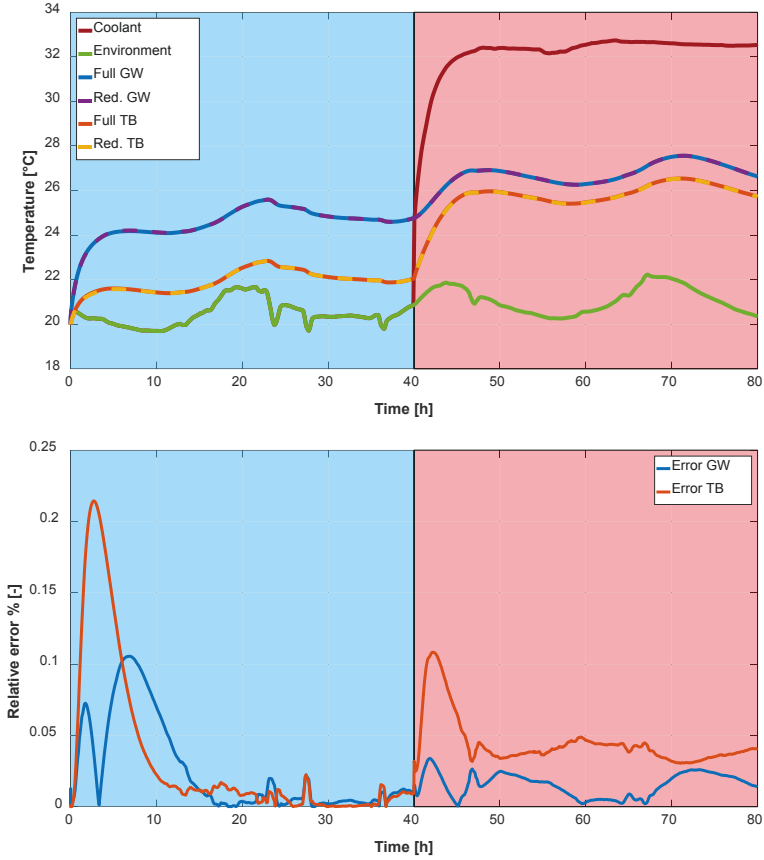


Fig. 3. (a) Up: Environment and coolant temperature. Average temperature on the guideway (GW) and thrust bearing (TB) comparing full to reduced system (Red.). The left side (blue color) represents coolant off and the right side (red color) represents coolant on; (b) Down: temperature relative error (%) in time-domain.

## 4 Conclusions and outlook

This work deals with the efficient calculation by means of projection-based MOR of thermo-mechanical models with sudden changes of the boundary conditions. This is shown for the study case of the effect of the introduction of the cooling fluid in the thermal response of a machine tool part. The developed reduction method shows its validity to simulate the effect of the sudden changes of boundary conditions, considerably reducing the computational cost. Further

work will extend this approach to the whole machine tool assembly, combining the studied effect with other parametric dependencies, such as the variation of the TCP-position of the machine tool.

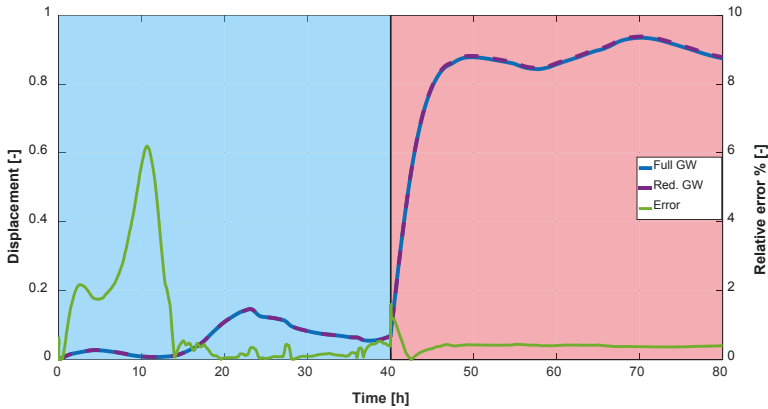


Fig. 4. Left: Normalized sum of the average displacement on the guideway (GW) in time domain comparing full to reduced system (Red.); Right: Displacement relative error (%) in time-domain.

### Acknowledgements

*The authors would like to thank the Swiss Federal Office for Professional Education and Technology (CTI), the Swiss National Science Foundation (SNSF) and the Machine Tool Technologies Research Foundation (MTTRF) for their financial support.*

## 5 References

- [1] Mian, N. S., Fletcher, S., Longstaff, A. P., Myers, A., 2013, Efficient estimation by FEA of machine tool distortion due to environmental temperature perturbations, *Precision Engineering*, 37/2:372–379.
- [2] Jedrzejewski, J., Kwasny, W., 2015, A step towards the holistic modelling of the HSC machining centre and the efficient compensation of its errors, *International Journal of Computer Integrated Manufacturing*, 28/1:126–136.
- [3] Mayr, J., Weikert, S., Wegener, K., 2007, Comparing the Thermo-Mechanical-Behavior of Machine Tool Frame Designs Using a FDM-FEA Simulation Approach, *Proceedings of the 22nd ASPE Annual Meeting*, /1:17–20.
- [4] Ess, M., 2012, Simulation and Compensation of Thermal Errors of Machine Tools, Diss. ETH No. 20300, /20300.
- [5] Mayr, J., Jedrzejewski, J., Uhlmann, E., Alkan Donmez, M., Knapp, W., et al., 2012, Thermal issues in machine tools, *CIRP Annals - Manufacturing Technology*, 61/2:771–791.



- [6] Benner, P., Gugercin, S., Willcox, K., 2015, A survey of model reduction methods for parametric systems, *MPI Magdeburg Preprints*, MPIMD/13–14:1–36.
- [7] Bueno, R.; Arzamendi, J; Almandoz, J., 1997, Thermal modal analysis of machine-tools, *Integrated Design and Manufacturing in Mechanical Engineering*, pp. 307–315.
- [8] Zhu, J., Ni, J., Shih, A. J., 2008, Robust Machine Tool Thermal Error Modeling Through Thermal Mode Concept, *Journal of Manufacturing Science and Engineering*, 130/6:61006.
- [9] Galant, A., Beitelschmidt, M., Großmann, K., 2016, Fast High-Resolution FE-based Simulation of Thermo-Elastic Behaviour of Machine Tool Structures, *Procedia CIRP*, 46:627–630.
- [10] Lang, N., Saak, J., Benner, P., 2014, Model Order Reduction for Systems with Moving Loads, 68/2020:1–10.
- [11] Naumann, A., Lang, N., Partzsch, M., Beitelschmidt, M., Benner, P., et al., 2016, Computation of thermo-elastic deformations on machine tools a study of numerical methods, *Production Engineering*, 10/3:253–263.
- [12] Bryan, J., 1990, International Status of Thermal Error Research (1990), *CIRP Annals - Manufacturing Technology*, 39/2:645–656.
- [13] Mayr, J., Gebhardt, M., Massow, B. B., Weikert, S., Wegener, K., 2014, Cutting fluid influence on thermal behavior of 5-axis machine tools, *Procedia CIRP*, 14:395–400.
- [14] Hernández-Becerro, P., Blaser, P., Mayr, J., Weikert, S., Wegener, K., 2017, Measurement of the effect of the cutting fluid on the thermal response of a five-axis machine tool, in *Laser Metrology and Machine Performance XII*.
- [15] Blaser, P., Hernández-Becerro, P., Mayr, J., Wiessner, M., Wegener, K., 2017, Thermal errors of a large 5-axis machine tool due to cutting fluid influences - Evaluation with thermal test piece, in *32nd ASPE Annual Meeting*.
- [16] Mayr, J., Ess, M., Pavliček, F., Weikert, S., Spescha, D., et al., 2015, Simulation and measurement of environmental influences on machines in frequency domain, *CIRP Annals - Manufacturing Technology*, 64/1:479–482.
- [17] Pavliček, F., Dietz, F., Blaser, P., Züst, S., Mayr, J., et al., 2016, An approach for developing meta models out of fluid simulations in enclosures of precision machine tools, in *31st ASPE Annual Meeting*.
- [18] Panzer, H., Mohring, J., Eid, R., Lohmann, B., 2010, Parametric Model Order Reduction by Matrix Interpolation, 58:475–484.
- [19] Grossmann, K., Jungnickel, G., 2003, Instationäres thermoelastisches Verhalten von Vorschubachsen mit bewegtem Wälzkontakt. *Inst. für Werkzeugmaschinen und Steuerungstechnik, Lehrstuhl für Werkzeugmaschinen*.

# Effectiveness of modelling the thermal behaviour of the ball screw unit with moving heat sources taken into account

*J. Jedrzejewski, Z. Kowal, W. Kwasny, Z. Winiarski*

Wroclaw University of Science and Technology, 27 Wybrzeze Wyspianskiego st.,  
Wroclaw 50-370, Poland

**Abstract.** This paper deals with the precise modelling of the thermal behaviour of the ball screw unit in the machine tool feed drive. The problem is discussed for the lathe centre. The serious consequences of thermal errors arising in the ball screw unit for the precision of positioning the lathe assemblies in controllable axes Z and X are highlighted. The factors, especially the ball screw preload and moving heat sources, having a bearing on the thermal errors are described. Using an FE model, integrating thermal and force deformations, the significant effect of moving heat sources is demonstrated and the thermal positioning error characteristic along the ball screw is determined.

Peer-review under responsibility of the International Scientific Committee in the person of the Conference Chair Prof. Steffen Ihlenfeldt.

**Keywords:** Ball screw; Thermal behavior modelling; Positioning error

---

## 1 Introduction

The speed and precision of positioning the machine tool assemblies slidable in the controllable axes, ensuring the optimum shaping of the tool path, is vital for increasing the productivity of machining processes. The deformations occurring in the controllable axes and in the load-bearing structure of the machine tool bodies affect this precision in a complex way, depending on the thermal loads, the static loads and the dynamic loads. The deformations contribute to positioning errors, which are subject to minimization and compensation. The two activities are based on the accurate identification of error components and their correlations and on the possibly most faithful holistic modelling and numerical simulation of the behaviour of the errors under time- and space-variable loads in operating conditions.

The holistic modelling and simulation of errors is the basis for generating error correcting and compensating functions [1]. The improvement of the operational properties of linear controllable axes based on ball screws (which owing to

their simple design and low cost commonly used in feed drives) has been the subject of numerous studies. The most important of them are:

- experimental investigations of ball screw power losses and heating up in operating conditions and of positioning errors [2,3,4,5],
- modelling the thermal deformations of ball screws under the assumption of a trapezoidal distribution of the heat flux generated in the nut and measuring the distribution of temperature along the ball screw by means of thermocouples [6] or using infrared thermography [7],
- modelling deformations, using a model and the simulation of a moving heat source, on the basis of the trace of power losses in the ball screw unit's motor [8], and through attempts to renumber discretization nodes in FEM [9]. Unfortunately, the latter approach turns out to be too slow to be employed in machine tools with the current feed rates. Similar attempts for a moving headstock were made in [10].

The principal limitations of the holistic modelling of ball screw positioning errors are its complexity, inadequate knowledge of the interactions between loads and deformations and the demand for very high computing power of the generally available computers. As a result, incomplete models are used in application research. This paper presents an analysis of the modelling of the thermal behaviour of the ball screw unit, using as an example an idling lathe centre and the ABAQUS software.

Moving heat sources at high feed rates, static loads, thermal loads and dynamic loads, ball screw and bearing preloads in the ball screw supports and a variable work cycle are taken into account in the modelling, which goes significantly beyond the range of model research to date.

## **2 Discussion of deformations and load influencing on ball screw positioning error**

Positioning errors in the controllable axes of the lathe centre are the sum of the ball screw pitch error and the deformations of: the ball screw itself, the rolling screw-nut joint, the bearing sets and the front and back supports of the ball screw and the bed, expressed by their static, thermal and dynamic displacements. In order to forecast the deformations for an assumed feed mechanism work cycle one must identify the deformation generation mechanisms and take them into account in the simulation models. In thermal deformation models the mechanism of the thermal load caused by a moving heat source is particularly complex. The load changes over time with the operating conditions of the

ball screw unit and depends on the variable friction forces on the slideways and on the variable feed motion dynamics. This is accompanied by variable heat transfer conditions which need to be taken into account in the computational models.

It was found difficult to model the transfer of the tractive force effects on the assemblies of the whole mechanical structure of the feed drive. The tractive force comprises the friction forces on the slideways, the forces of inertia of the shifted masses and the resistances to motion in the nut and in the ball screw bearings and depends on the feed motion direction and the instantaneous value of ball screw tension.

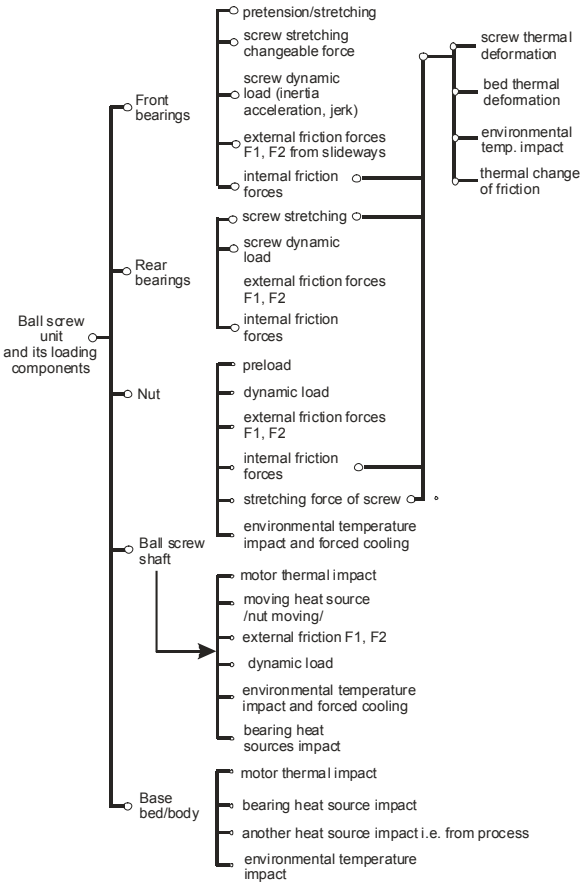


Fig. 1. Ball screw unit load components.

Figure 1 shows in detail the components of the load acting on the ball screw unit subassemblies, which have a direct and indirect bearing on positioning precision. Research on the accurate modelling of friction in rolling joints and the modelling of contact deformations [11] and heat transfer in such joints continues to be conducted.

Each component of the ball screw unit structure is assigned force loads having a direct or indirect bearing on the intensity of the heat sources active in the structure of the ball screw unit or are directly heat loads. For such loads as the ball screw preload and the friction force also the factors determining them in operating conditions are shown (column two). Column three contains thermal factors which influence some load components presented in column two. The mathematical relations describing the loads need to be very precise in order to accurately model thermal loads and deformations. For example, the power losses arising in the screw-nut joint used to be modelled under considerable simplifications, whereby it was impossible to precisely determine their instantaneous values at dynamically changing tractive force values. Also the omission of the effect of bed deformations, which by causing displacements of the ball screw supports change the magnitude of the static loads and the thermal loads, was a gross simplification in earlier research. The thermal loads include the heat generated in the screw-nut joint and in the screw support bearings, as well as the heat transmitted to/from the environment.

### **3 Ball screw thermal behaviour modelling assumptions annuerical simulation**

The subject of the holistic modelling was the lathe centre structure, with a special focus on the feed drive based on the ball screw in the principal longitudinal axis Z and in axis X of the carriage. A geometrical model of this structure is shown in Fig. 2. One can see the location of the two feed mechanisms and the places in which the power losses and the deformations included in the modelling of positioning errors occur.

In both the axes the feed cycle includes: a dwell time of minimum 2 s, a run up (starting, accelerating and a jerk) to a speed of 0.5 m/s, running at this speed over a distance of 400 mm (0.57 s) for the Z-axis and over a distance of 200 mm (0.17 s) for the X-axis, and braking. The two ball screws: Z with a diameter of 36 mm and X with a diameter of 32 mm were pretensioned by respectively 50  $\mu\text{m}$  and 30  $\mu\text{m}$ , which resulted in the simultaneous additional axial loading of bearing sets A and B of both the ball screws and in deformations of the supports and the bed. External nut load  $F_a$  during the work cycle, which together with

the nut preload determined the instantaneous value of power losses in the screw-nut unit, was evaluated.

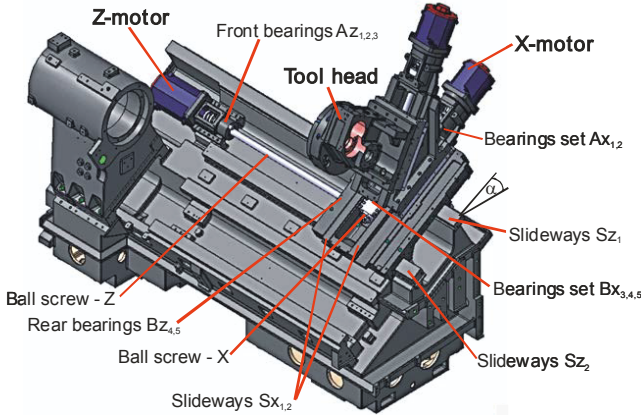


Fig. 2. Geometrical model of turning centre main structure bodies.

The instantaneous value of this load is determined by the sum of the forces acting on the nut at a given work cycle instant:

$$F_a = m \cdot g \cdot \sin \alpha \pm \mu \cdot m \cdot g \cdot \cos \alpha \pm m \cdot a + F_c \text{ [N]} \quad (\text{Eq. 1})$$

where:  $m$  – the total mass of the assemblies shifted,  $g$  – the acceleration of gravity,  $\alpha$  – the angle of inclination of the drive axis,  $\mu$  – the coefficient of friction on the slideways,  $a$  – acceleration/deceleration in feed motion,  $F_c$  – a component of the cutting force along the drive axis.

In the considered case, the cutting forces were not taken into account. Depending on the work cycle phase, the angle of inclination of the ball screw and the direction of movement, there can occur different combinations of force  $F_a$  components. For the constant motion velocity phase, for example, this will be only the sum of the friction forces on the slideways and the gravitational forces (if  $\alpha \neq 0$ ). The maximum value of external ball screw nut load  $F_{amax}$ , allowable for the considered lathe design, was used to select nut preload  $F_p$  (2) and the latter was used to determine the moment of friction in the screw-nut joint ( $T_d$  (3)) [12]:

$$F_p = \frac{F_{amax}}{2.8} \text{ [N]} \quad (\text{Eq. 2})$$

$$T_d = \frac{K \cdot F_p \cdot L}{2000 \cdot \pi} \text{ [N]} \quad (\text{Eq. 3})$$

$$T_d = \frac{K \cdot F_p \cdot L}{2000 \cdot \pi} \text{ [N]} \quad (\text{Eq. 3})$$

where:  $K$  - a preload torque coefficient,  $L$  - the lead, mm.

The loading of the nut preloaded with external force  $F_a$  results in the additional loading of half of the balls (force  $F_A$ ) and simultaneously in the partial unloading of the other balls (force  $F_B$ ) (Fig. 3). In the case of the uniform motion phase, this has little effect on the moment of friction in the nut since the additional loading of one part of the nut is almost counterbalanced by the unloading of its other part. However, this can be important during the starting and braking phases when due to the strong dynamic forces some of the balls can be completely unloaded. The stiffness characteristics shown in Fig. 3 were taken into account in the modelling of the moment of friction in the nuts of the considered drives of the X and Z axes in order to increase the accuracy of friction moment evaluation and to regain control over the total unloading of some of the balls in the rolling nut.

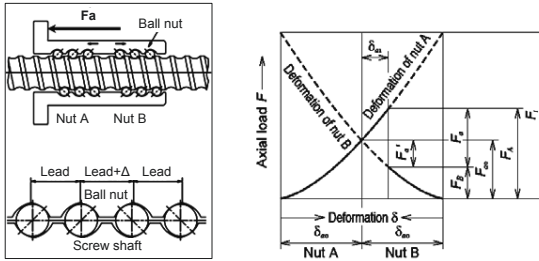


Fig. 3. Stiffness of ball screw-nut assembly [12].

By introducing to formula (2) in the place of  $F_{a\max}$ , instantaneous values of external force  $F_a(t) = F_A(t) + F_B(t)$  obtains from formula (3) instantaneous values of friction torque in the nut, by external force  $F_a$  acting on the preloaded nut. They are the sum of the friction torque in the uploaded zone  $T_A(t)$  and the friction torque in the unloaded  $T_B(t)$  zone, generating instantaneous power losses  $P(t)$ .

The heating up and thermal deformations of the ball screw are determined by the friction moment caused jointly by the nut's preload  $F_p$  and its external load  $F_a$ , generating instantaneous power losses  $P(t)$ .

$$P(t) = \frac{(T_A(t) + T_B(t))}{9.55} \cdot n \text{ [W]} \quad (\text{Eq. 4})$$

$T_B(t)$  – instantaneous value of friction torque in the unloaded zone by  $F_B$  force  
 $n$  – the instantaneous rotational speed.

The nut power losses in axes Z and X determined in the above way are shown in Fig. 4. The different shapes of the power loss graph for the two controllable axes are due to the different loads occurring during the to-and-back motion. In the case of axis X, the inclination of the slideways and the resulting large moment of inertia at acceleration and small at deceleration are the contributing factors. For the travel up the losses are clearly larger than for the travel down towards the spindle.

For machine tool, including ball screw unit, convective heat exchange coefficients have been applied, defined by analytic formulas - both for movable and non- movable components, available in literature eg. [13]. Heat exchange between joined components has been modelled through contact thermal resistance. Heat exchange on other surfaces or between non-contacting elements has been modelled by the use of cavity radiation method or radiation to ambient method.

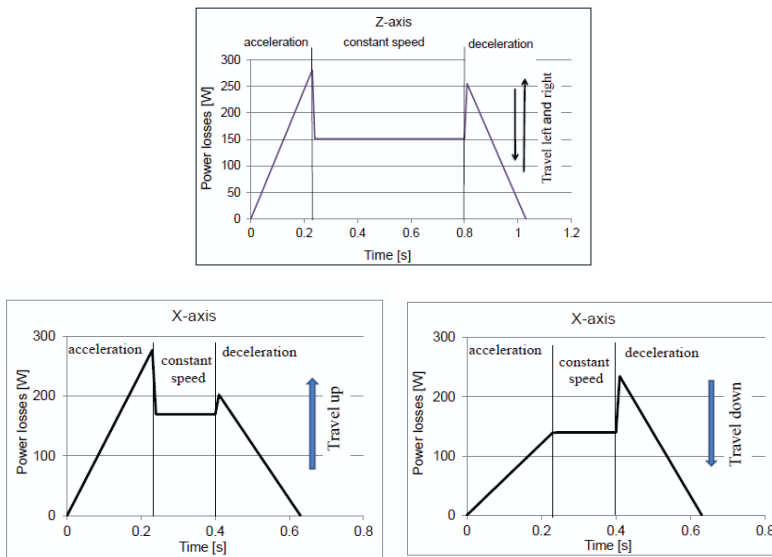


Fig. 4. Nut/screw power losses in Z and X axis.

The predicted power losses in the nut-ball screw assembly and in the bearing sets were used to simulate the variation in temperature in the Z-axis screw-nut joint during the assumed feed drive work cycle (Fig. 5). In over 3 second cycle



(3.06s), presented in the upper part of the Figure, the work lasted 1.06 s and the break 2 s, during which the screw temperature was decreasing. This is clearly visible in the inset in the bottom right corner of the figure and confirms the need to include in the model such phenomena as drive run up, braking and standstill.

The temperature measured on the nut enclosure exceeds the values calculated using the FE model already after 100 s of drive operation, with the differences amounting to 1.5 K. This can be ascribed to the fact that, besides the heat generated in the screw-nut joint, also the air collecting in the only partially open spaces (very difficult to model in such structurally complex objects as the machine tool equipped with various partitions and housings) is a contributing factor.

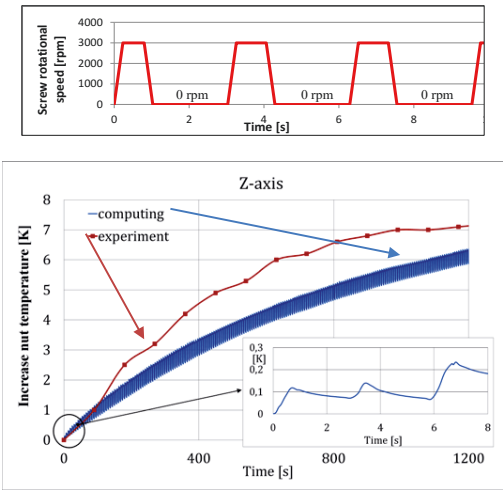


Fig. 5. Comparison of computed and measured ball screw nut temperatures during operation of drive Z.

As mentioned earlier, the increase in nut temperature during to-and-fro motion depends to a considerable extent on the duration of the breaks between the cycles. In the example shown in Fig. 5, when the break duration is increased from 2 s to 20 s, the increase in nut temperature after 1200 s does not exceed 1°C while the increment in screw length near the rear bearing support decreases from 15  $\mu\text{m}$  to about 1  $\mu\text{m}$ .

The experimental and computing results indicate the FE model is sensitive to changes in power losses and heat transfer conditions in ball screw and nut and

can be used to simulate nut displacements/elongations resulting from the action of the moving heat source which the nut is.

The nut's preload (50  $\mu\text{m}$  in the Z-axis) and dynamic load, taking into account the moment of inertia of the carriage being shifted and the friction forces determined by the mass of the carriage and the variable coefficient of friction on the slideways coated with plastic (TURCITE), have a bearing on the instantaneous tension of the ball screw during the performance of work cycles. Also changes in the location of the ball screw supports on the bed together with changes in the temperature of the bed itself and in ambient temperature (at an appropriate time lag) have an effect on the instantaneous tension of the ball screw. Therefore the accurate modelling of the ball screw unit should take into account the thermal elongations of the ball screw, the direction and value of the tractive force due to inertia, friction and cutting forces, as well as the thermal deformations of the bed and the resulting displacements of the ball screw supports, and the variation in ambient temperature due to the different inertia of the heating up/cooling of the lathe assemblies with the rise/fall of ambient temperature, as illustrated by the diagram shown in Fig. 6. In the considered case, the spindle tip reacts most quickly (after 40 min) to changes in ambient temperature, followed by the points located on the outer surface of the bed (after 120 min) and lastly, the ball screws (after 280 min). The repeatable one-minute spindle work cycle with a short break of 10 s, used in the measurements can be treated as continuous operation for over two days during which the only variable factor was the ambient temperature.

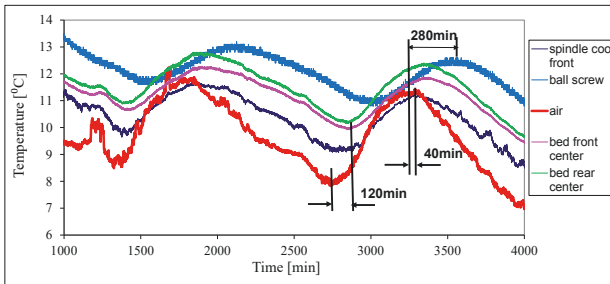


Fig. 6. Effect of long-term variation in ambient temperature on temperature of lathe assemblies for spindle running.

Considering the importance of the moving heat source, i.e. the connection of the carriage with the slideways (e.g. the top and bottom bed slideways in axis Z), one should take into account the oblique location of the slideways, resulting in different pressures, which affects the friction forces, the temperatures and

the displacements. Also important is the degree of simplification adopted in the modelling of heat generation in slideway systems. Figure 7 shows simulated temperature distributions on the bed slideways in direction Z, using the precise model (the upper curve) and the simplified model (the bottom curve). As one can see, quite different temperature distributions along the considered slideways were obtained. The simplified model took into account only average pressures on the surface of the slideways, whereas the precise model took into consideration all the static and dynamic loads acting on the top and side surfaces of the slideways, as well as the clearances in the joints. The considerably higher temperatures of the bottom guide are mainly due to the function which it performs in the machine tool – this guide carries all the gravitational forces of the assemblies being shifted, i.e. the longitudinal slides and the carriages together with the X and Y axes drives. The presented simulation results convincingly argue for precise modelling since the adoption of too drastic model simplifications can lead to erroneous conclusions.

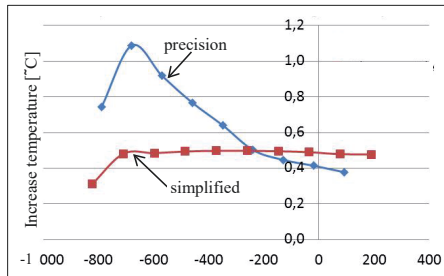


Fig. 7. Upper guide temperature in Z axis simulated using respectively precise and simplified model.

Figure 8 shows how temperature changes in selected points on respectively the left and right guide during successive feed cycles. After 30 minutes (1800 s) the temperature difference between the two guides amounted to about 1.5°C. The variation in temperature on the guides during the work cycles is similar to the variation in the temperature of the nut, despite the different heat capacity of the guides and the ball screw unit.

This is shown in Fig. 9 where in the short time interval of 20 s one can see (besides the different heating up of the guides) the drive work cycle consisting of a carriage run up, uniform motion, braking and a break. Figure 10 shows the displacements of the bed guides in directions X and Y caused by the drive operation in the X-axis. Since in precision lathes the resulting errors directly affect machining precision they deserve attention.

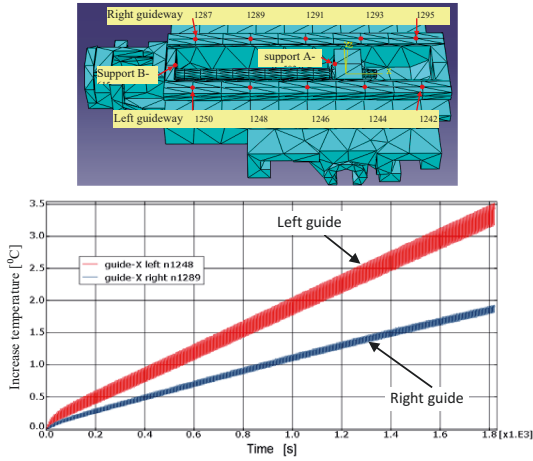


Fig. 8. Location of mesh nodes on guides of drive X (upper) and variation in temperature of left and right guide of drive X (lower).

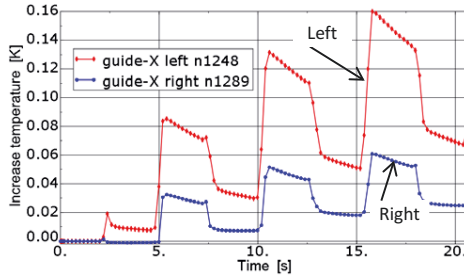


Fig. 9. Detailed characteristic of guide-X initial transient temperature from 0 to 20s operating time.

The degree of positioning error reduction owing to ball screw preloading depends on the value of the preload and on the position of the considered point on the length of the working ball screw, i.e. on the position of the nut (Fig. 11). The position of the nut in which the smallest positioning error will occur is the position close to the left ball screw support (point 5067) while the largest errors will occur when the nut is close to the other ball screw support (point 1512). The results shown in the figure were obtained for the drive work cycle (a one second-long run and a two second-long break) presented in Fig. 5.

The considerations presented in this paper give a nearly full picture of the factors having a bearing on positioning accuracy and how they affect the latter. The factors should be taken into account when modelling errors contributed by the ball screw unit.

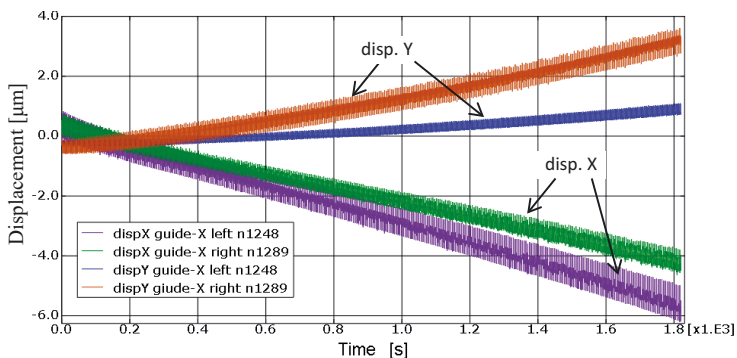


Fig. 10. Transient displacements of left and right guide-X on direction X and Y.

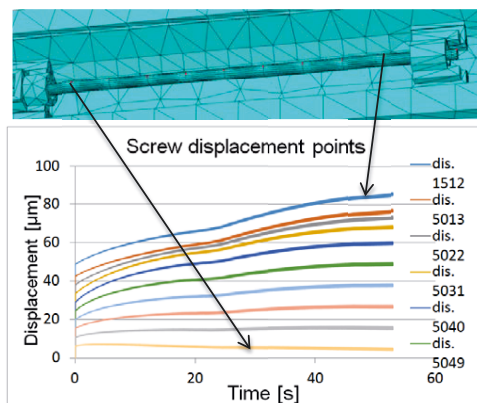


Fig. 11. Resultant axial screw nut displacement in Z direction during runtime.

## 4 Conclusions

From the presented results of the research on the modelling of the thermal behaviour of the assemblies of the lathe centre ball screw unit for the assumed work cycle one can draw the following conclusions:

1. In order to model the thermal errors in the positioning of machine tool drives one must use in the computational analyses a model of moving heat sources which integrates the phenomena of thermal and force loads.
2. The thermal error of positioning the nut/carriage largely depends on the ball screw preload.
3. For a long period of execution of work cycles the effect of ambient temperature, changing the spacing of the ball screw bearing supports and the state

of the thermal deformations of both the screw and the nut, should be taken into account.

4. In order to precisely determine positioning errors one should take into account the effect of the deformations of the slideways.
5. The resultant displacements of the nut during drive running, determined through precise modelling and numerical simulations, can be the basis for compensating errors in the controllable feed axes.

#### **Acknowledgements**

*The authors express their thanks to Doosan Infracore Co. for making it possible to test the model and for financially supporting this research.*

## **5 References**

- [1] Jedrzejewski, J., Kwasny, W., 2017, Development of machine tools design and operational properties. *Int J Adv Manuf Technol*, 93:1051–1068.
- [2] Altintas, Y., Verl, A., Brecher, C., et al, 2011, Machine tool feed drives, *CIRP Annals – Manufacturing Technology*. 60/2: 779-796.
- [3] Winiarski, Z., Kowal, Z., Kwasny, W., Ha, J.Y., 2010, Thermal model of the spindle drive structure. *Journal of Machine Engineering*, 10/4: 41-52.
- [4] Verl, A., Frey, S., 2010, Correlation between feed velocity and preloading in ball screw drives. *CIRP Annals –Manufacturing Technology*, 59/1: 429-432.
- [5] Winiarski, Z., Kowal, Z., Jedrzejewski, J., Kwasny, W., 2017, Precise modelling of machine tool drives with ball screw thermal behavior. *Journal of Machine Engineering*, 17/1: 31-45.
- [6] Wu, C.H., Kung, Y.T., 2003, Thermal analysis for the feed drive system of a CNC machine centre. *International Journal of Machine Tools & Manufacture*, 43: 1521-1528.
- [7] Heisel, U., Koscsak, G., Stehle, T., 2006, Thermography-based investigation into thermally induced positioning errors of feed drives by example of a ball screw. *CIRP Annals –Manufacturing Technology*, 55/1: 423-426.
- [8] Kim, S.K, et al, 1997, Real-time estimation of temperature distribution in a ball-screw system. *International Journal of Machine Tools and Manufacture*, 37: 451-464.
- [9] Gleich, S., 2007, Approach for simulating ball bearing screws in thermal finite element simulation. *Journal of Machine Engineering*, 7/1: 101-107.
- [10] Grochowski, M., jedrzejewski, J., 2006, Modelling headstock motion influence on machine tool thermal behavior. *Journal of Machine Engineering*, 6/2: 124-133.
- [11] JEDRZEJEWSKI, J., MACIOLKA, P., 2017, Evaluation of different approaches to 3d numerical model development of the contact zone between elementary asperities and flat surface, *Journal of Machine Engineering*, 17/4: 40-53.

- [12] NSK, 2002, Precision machine components. Catalogue, No.E9008a 2011 Z-9, NSK Motion & Control.
- [13] BUCHMAN, K., JUNGNICKE, G., 1978, Die Wärmeübertragung an Be-und Verarbeitungsmaschinen, PWR Wroclaw, ITMiA, 20, 279, (in Polish).

## **Thermal robust sub-assemblies**

---





# Analyzing and Optimizing the Fluidic Tempering of Machine Tool Frames

*A. Hellmich, J. Glänzel, A. Pierer*

Fraunhofer Institute for Machine Tools and Forming Technology IWU,  
09126 Chemnitz, Germany

**Abstract.** Thermal stabilization of frame structures by integration of demand-oriented fluidic temperature control systems offers considerable potential concerning the minimization of thermo-elastic displacements and energy requirements. Additionally, by using high performance concrete, completely new possibilities for the design-wise integration of channel structures arise during casting. Thus, heat removal can be further improved by means of fluidic circuits adapted locally to the heat sources. The paper describes a developed high performance concrete (HPC) machine tool frame with integrated fluidic fluidic circuits. A special focus is laid on modeling the structure and developing a suitable control methodology, identifying required parameters and deriving possibilities for optimization.

Peer-review under responsibility of the International Scientific Committee in the person of the Conference Chair Prof. Steffen Ihlenfeldt.

**Keywords:** Machine tools; Machine frame; Fluidic tempering system; Network-based simulation; Control methodology

---

## 1 Introduction

The aim of the research, presented in this paper is to optimize the tempering capabilities in high performance concrete (HPC) machine frames. Special focus is laid on the balance of thermal and energetic issues. The optimization criterion is to achieve the best possible thermal stability of the machine frame and therewith to ensure a high manufacturing accuracy with minimal energy costs. Factors, influencing the thermal condition, are time-variant thermal loads as well as the resulting, very complex, three-dimensional heat flows in the machine frame.

The most promising approach for tempering the machine frame is to integrate demand dependent fluid circuits into the machine frame and to equip them with a situationally adaptable control strategy. This approach offers a large po-

tential for optimization in terms of minimizing thermal induced errors or bulges with affordable energy consumption. However, a methodology for the optimal dimensioning and integration of the fluid circuits as well as the control methodology is not yet available. Hence, research activities were initiated to investigate influence factors and to derive tools and methods towards a transferable design methodology for tempering machine tool frames.

Subsequently to the state of the art in tempering of machine structures, the course of action and main research aspects are introduced in section three. In the following section, the main aspects of the ongoing research, subdivided into the aspects test object, fluidic tempering system and implemented sensors are presented. The control strategy is discussed in chapter 5. The paper is finalized by a section 6, comprising a conclusion and an outlook.

## 2 State of the Art

Thermal aspects of machine tools are an important field of ongoing research. Thermo-elastic errors are considered to be „the most often by the specific machine behavior induced errors of the manufactured part“[1]. Hence a significant number of universities and research organizations are carrying out fundamental research, focusing on machine tools and surrounding components. The Collaborative Research Center CRC/TR 96 plays an important role with the specialization on modeling of the thermal behavior of machine tools and developing component solutions under the focus of interplay of thermal behavior and energy efficiency [2]. A remarkable potential of improvement is seen in considering productivity and energy efficiency in a holistic way by adjusting the fluidic tempering systems depending on the specific thermal load input. Due to changes within the fluidic tempering system, thermal losses of the drive and the production process, a constant adjustment of the cooling strategy is required to ensure a suitable production accuracy ([12], [15] and [16]).

The proposed approach intends to beneficially influence the temperature field, the third aspect of the thermo-elastic functional chain (see Fig. 1, [2]). If the temperature field is controlled in an appropriate manner, the position displacement can be reduced.



Fig. 1. Thermo-elastic functional chain, influencing the temperature field ([2])

Thermal measurements on machine tools repeatedly show that, despite a thermo-symmetric design on machine structures, imbalanced thermal loads occur. Reasons for this behavior can be found in asymmetrically mounted drives, external heat sources (solar radiation, waste heat etc.) or of spatially varying processes in the work space. To compensate these effects and the resulting Tool Center Point (TCP)-displacement, an active removal of the heat flow is required. One possible approach is the integration of fluidic circuits into active components and passive structures and a control strategy, aiming for the temperature level of the surrounding structure.

In the areas of forming technology, the viability of this approach was proven [3]. Based on polymer concrete frame structures, a fluidic tempering system was developed with the aim on reducing displacements, induced by thermal loads [17]. For this manner simple prismatic shapes were measured under well-defined thermal loads, leading to a model description and an autonomic fluidic tempering system, operated by a centralized controller. With this approach it was possible to reduce the deviation of the guiding from  $\pm 35 \mu\text{m}$  to  $\pm 2 \mu\text{m}$  [17].

Besides the removal of thermal loads, a second focus has to be laid on the energy efficiency of the installed fluidic tempering systems. Auxiliary units require a significant part of the overall energy demand of a machine tool [4]. Thereof, the coolant system is the main energy consumer [5] and should be investigated concerning the potential to increase energy efficiency. Pump systems usually comprise a pump, equipped with an electric drive, power electronic- and mechanical components as well as tubes. Those components and/or their sub-systems were optimized in several preceding research projects such as ([6], [7], [9], [10] and [19]). For example the utilization of energy efficient drives and/or pumps it was possible to reduce the energy consumption of the systems [[11], [14]]. Further enhancement of the energy efficiency was realized by a demand-dependent control strategy ([8] and [13]) and friction optimized components [18]. However, those energy efficient components were not yet considered in terms of designing an energy efficient and situationally optimal overall tempering system.

The state of the art shows a possible improvement of the thermal behavior and most importantly a reduction of deviations by integrated cooling mechanisms. A number of simulations and some practical experiments were carried out. Also the potential for higher energy efficiency of (fluidic) components was shown. However the presented solutions were not yet integrated into one holistic de-

sign approach for a machine frame. Also the combination of thermal stabilization with the parallel aim on high energy efficiency was not yet investigated.

### 3 Course of action and main research aspects

The main research aspect is to develop a methodology to design and put into operation an overall tempering system for machine tools under accuracy and energy efficiency requirements, which are competing objectives.

As displayed in Fig. 2 , those objectives can only be reacted to with hardware, in particular the machine frame and the fluidic tempering circuits. However, no design principle was developed yet for this case. The proposed methodology is to extend the viewpoint by a software level, because software, in terms of simulation is able to link the hardware aspects with the design objectives and to create an optimal solution, comprising hardware and, again software in terms of a control strategy.

Underlying research questions to be answered are the optimal placement of hardware components like fluid circuits (centralized vs. decentralized), temperature and flow rate sensors and the choice of a cooling unit. Software-related questions are the overall cooling strategy (desired fluid temperature above or below environment temperature), the control strategy (controller structure and parameters) of the fluid channel control loops as well as the question whether separate control loops have to be linked by means or multi-input multi-output control. Concerning these questions, a combined investigation of fluidic tempering system and its energy demand is of highest importance, because installed power to reach a certain cooling effect and the connected energy consumption of the fluidic tempering system interfere with each other [12] has to be developed.

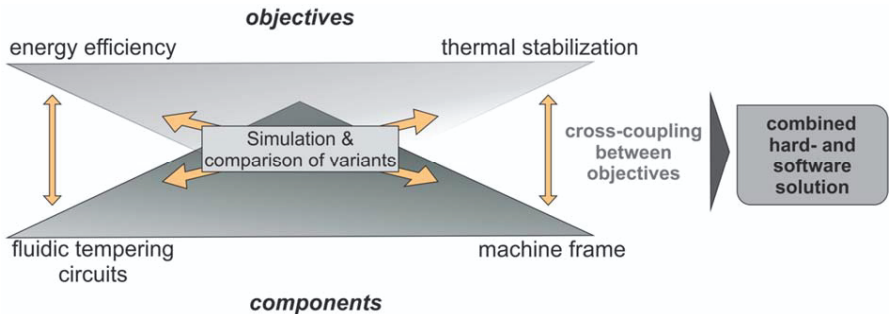


Fig. 2. Holistic approach for optimal tempering of machine frames.

The course of action in the research topic comprises 7 parts:

- design and realization of an experimental HPC machine frame with integrated (not yet optimized) fluidic circuits and fluidic tempering system,
- domain specific modelling of the machine frame (finite elements method, FEM), the fluidic system (Computational Fluid Dynamics, CFD) and the control system (network simulation),
- validation of the simulation models based on experiments with subsequent measurement of temperature fields and displacements,
- model order reduction and combination of the domain specific models into a comprehensive network model,
- sensitivity analysis and comparison of variants for developing the control strategy, sensor and fluid channel placement,
- design and realization of an optimized HPC machine frame with integrated fluidic circuits and fluidic tempering system and
- derivation of generally valid design principles for machine frame tempering.

Detailed information concerning the research questions of simulation (FEM, CFD) are given in [21]. This paper mainly addresses the HPC machine frame with its overall appearance and the integrated fluid circuits as well as sensors. Also, research questions concerning the control strategy (single loop modes interlinkage of control loops) are discussed and findings are displayed.

## **4 Thermal stabilized machine frame**

The test machine structure for the research comprises a of a five axis parallel kinematic head, coupled with an autarkic linear test rig (see Fig. 3). The test rig is realized as HPC machine frame with integrated temperature sensors and fluidic circuits.

### **4.1 Basis structure of the demonstrator machine**

The particular machine, used for research in this paper was designed as manufacturing unit to be mounted on a test rig, comprising friction optimized hydrodynamic sliding rails, changeable ball screws and two chip conveying screws. Hence, four drives are mounted to the thermally robust machine tool frame, made from HPC with a weight of 18 tons. The appearance of the machine frame is fixed to the greatest extend.

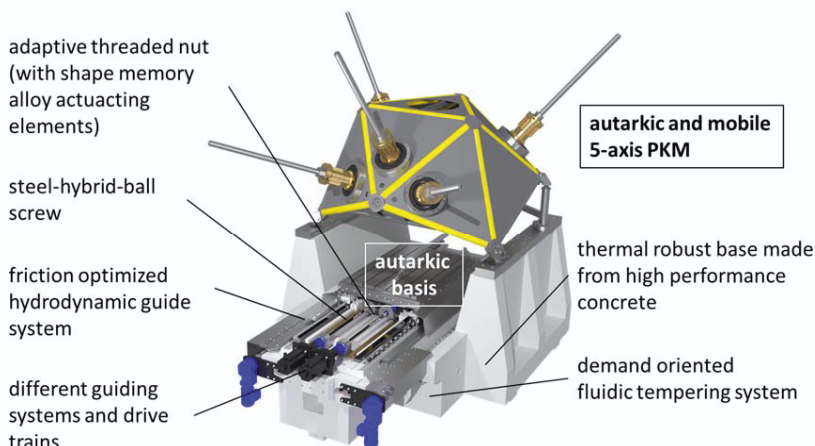


Fig. 3. HPC machine frame with a five axis parallel kinematic.

However, concerning research possibilities, parameter variations and an examination of variants for designing an optimal tempering/fluidic tempering system, several boundary conditions and parameters can be alternated:

For experimental investigation, production sequences, heat losses by the drives and moved components (bearings, ball screw nut, guiding systems) as well as thermal loads from the process itself can be induced into the machine frame, leading to unwanted thermal induced displacements. Furthermore asymmetric thermal loads can be induced by external heat sources, such as heating foils. These variable input factors will influence the temperate field in the machine frame. To quantify this, several temperature sensors were integrated.

## 4.2 Sensors

A suitable temperature measurement strategy is the key for modelling the thermal behavior of machine structures as well as the design of a tempering methodology. In the given machine tool frame, 23 internal thermo-sensors are integrated. The position of these sensors was consciously chosen along the path from the heat sources (e.g. guiding system) and heat sinks (fluidic circuits). Hence, the quantification of temperature distribution inside the frame and the armoring were installed. Fig. 4 shows the sensor placement and indicates that both side bars of the frame contain three thermo-sensors each to extract the influence of external heat sources such as radiation by sunlight each,

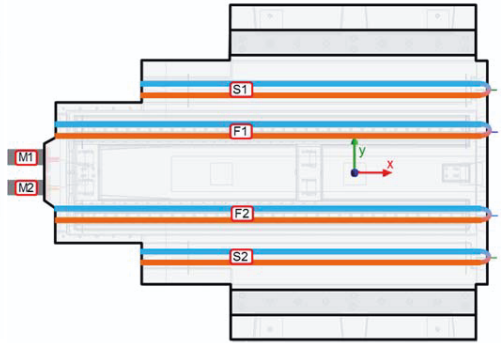
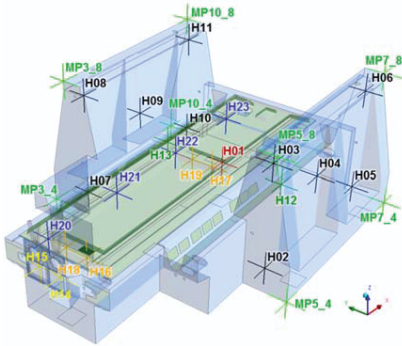


Fig. 4. Overview of the sensors inside the machine frame.

Fig. 5. Fluidic tempering system of the machine frame.

whereas an asymmetric sensor placement layout was used under the chip conveyor circuits due to the symmetric construction of the machine bed.

For easier data processing the temperature sensors of the machine frame were divided into following areas and logically attached to the integrated fluidic circuits (see Fig. 5):

- Fluidic circuit S1: Temperature sensors 7, 8, 9, 10, 11, 13
- Fluidic circuit S2: Temperature sensors 2, 3, 4, 5, 6, 12
- Fluidic circuit F1: Temperature sensors 1, 18, 19, 20, 21, 22, 23
- Fluidic circuit F2: Temperature sensors 1, 16, 17
- Fluidic circuit M1: Temperature sensor 15
- Fluidic circuit M2: Temperature sensor 16

The high number of installed thermo-sensors gives a good opportunity to exactly observe the thermo-mechanical behavior of the machine frame during production and under different load conditions. The measurement data provides essential information about the temperature field in the machine frame: Concerning the sensitivity analysis, the measurement values will be utilized to rate the performance of certain design solutions and parameter settings. Especially the deviation of the measured values will be an indicator for the performance of the fluidic tempering system. Subsequently, the design and implementation of the decentralized fluidic tempering system can be carried out.



### 4.3 Fluidic tempering System

Attached to the HPC machine tool, a fluidic tempering system, comprising a surge tank with recuperator and pump and six individually controllable fluidic circuits was realized. The circuits are intended to temper the guiding system, the chip conveyers and the main drives with two fluid circuits each (see Figure 3). Furthermore a fluidic-air-cooling is utilized. The system is composed of a controlled ventilator and a constant pump. The pump, conveying a water-glycol-mixture, can be enabled or disabled by the programmable logic controller (PLC) of the machine controller.

The cooling power of fluidic tempering system is controlled by a PID-controller, regulating the ventilator speed of the fluidic-air-cooling system via an analog voltage signal (0..10 V). The controller reads the environment temperature  $T_{\text{environ}}$  and the temperature of the coolant after the heat exchanger  $T_{\text{inflow}}$  via two temperature sensors as input values.

With these hardware premises, the fluidic tempering system can control the cooling power in two different modes:

1. The coolant temperature  $T_{\text{inflow}}$  at the central inflow-point of the fluidic circuits can be regulated to a fixed absolute set-point value.
2. The coolant temperature  $T_{\text{inflow}}$  can be tempered to a fixed difference, relative to the environmental temperature  $T_{\text{environ}}$ . Hence a constant heat flow  $dQ/dt$  is dissipated from the coolant when the flow rate  $dV/dt$  of the pump is also constant.

Six electromotive controlled flow-valves were installed to regulate the coolant inflow into each fluidic circuit of the machine frame. The valve stroke is set via an analog voltage signal (0..10 V) by the programmable logic controller of the machine tool. For overload protection of the pump, bypass throttles were installed in each fluidic circuit which retains the circulation of the coolant when the electromotive controlled flow-valves are nearly closed. To measure the flow rate of the coolant into the fluidic tempering system, flow sensors with built-in PT1000 temperature sensors from Huba Control were installed and connected to the PLC. The mentioned influencing factors contribute to the matrix of variable parameters on which a sensitivity analysis will be carried out. The outcome of this analysis will be information, which parameters need to be optimized due to their influence to the overall performance and energy efficiency of the fluidic tempering system.

Ostensibly, the paper focusses on the thermal homogenization of the machine bed. The on top mounted five axes parallel kinematic is separately tempered.

This ensures a thermal decoupling of machine structure and machine bed. Hence, the heat input through the contact of tool and workpiece is negligible. Consequently, the main heat inputs to the machine bed can be expected at the chip conveyor and the feed drives.

## 5 Control approach

The given hardware premises offer the possibility for a demand-actuated control concept. For tempering the HPC-machine frame, each of the fluid circuits must be equipped with a separate temperature controller, influencing the specific volumetric flow rate in the specific circuit. Therewith it will be possible to react to asymmetric or imbalanced temperature input to the machine frame adequately. Utilizing the integrated temperature sensors, the system behavior and separately controllable actuators, different control strategies will be examined and compared to each other.

However, designing and setting up such a control strategy has to meet a large number of requirements. No universal paradigms or designing rules are present so far. In consequence, knowledge has to be built up. This is done based on system simulations on the basis of MATLAB® Simulink® and SimulationX®.

### 5.1 Single loop control

For initial experimental investigations the control loops for each fluidic circuit are automated separately. A flexible and scalable controller software was implemented into the PLC of the machine tool to control the tempering of the machine frame and to record time-series of its thermal behavior. Input signals for this controller software are the sensor signals of all above mentioned temperature and flow-rate sensors, associated with the fluidic tempering system and machine frame. Controller outputs are the valve stroke of the electromotive flow-valves at the inflows of the fluidic circuits.

For each cooling circuit the type of control strategy, the acquisition of the actual value for the temperature control and the set-point can be selected via a human machine interface (HMI). As actual value for the temperature control  $T_{in}$ , single temperature sensors (i.e. reflow temperature of fluidic circuit or temperatures measured inside the machine frame) or an aggregated signal (i.e. averaging, weighted linear combination and minimum/maximum) of multiple temperature sensors can be chosen.

The following control strategies are available:

1. Open loop control of valve stroke (manual mode), where the flow-valve is opened to a fixed value without any further temperature or flow regulation
2. Closed loop control with a two-point on-off-control. Thereby a hysteresis function opens the valve to a predestinated stroke if the input temperature is less then a given lower set-point boundary  $T_{\min}$  and closes the valve if the input temperature  $T_{\text{in}}$  exceeds the given upper set-point boundary  $T_{\max}$ .
3. Closed-loop flow-rate PID-control. Thereby the flow-rate is regulated by a PID-Controller to a fixed set-point without any regard to temperature sensor signals.
4. Closed-loop temperature PID-control. Thereby the temperature is regulated to a fixed set-point.
5. Closed-loop cascade temperature PID-control with subordinate PID-control of the flow-rate.

The control takes also the non-linear valve characteristic between valve stroke and volumetric flow-rate into account and linearizes its characteristic by applying an inverse static valve model. Based on the variety of control approaches, experiments can be carried out.

An additional possibility to further enhance the variety of investigation is given by a network model, representing the machine frame and the control strategy.

and Fig. 7 depict the principal control structure of one cooling circuit with a simplified hydro-thermal SimulationX® model for the on-off (case 2) and cascade temperature (case 5) control.

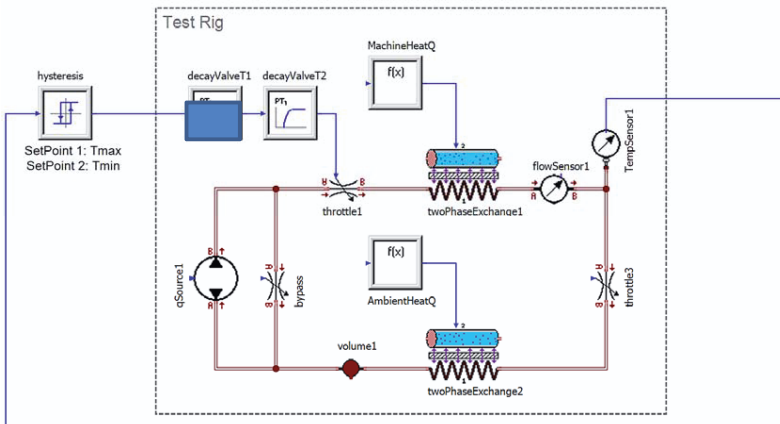


Fig. 6. Two-point control to control the fluidic circuits.

In both figures the reflux temperature is controlled as main control variable. But as already mentioned also other temperature signals can be selected as input value on demand. The model yet simplifies the fluidic circuit as lumped parameter model, comprising the constant pump, bypass throttle, volume and flow resistance of coolant as well as the heat transfer from the machine frame to the coolant and the dissipation of excess heat flow from the coolant to the environment at the air-cooled heat exchanger. Fig. 6 shows the two-point on-off control. First findings show a continuous oscillation within a boundary window around the designated set-point. This is due to the switching work principle of the relay controller. However, this operation mode is ideal for online system identification, because the system is only excited with step functions and simultaneously kept on a controlled temperature level [20].

Fig. 7 depicts the closed-loop cascade temperature control with subordinated flow control. The control structure comprises two interconnected control loops. By deactivating the inner flow-control and linking the PID-output to the valve the control structure is in the single-loop temperature control mode. By deactivating the outer temperature control, the cooling circuit is operated in the flow-controlled mode. Based on the simulations, it could be shown, that the temperature controller regulates the system to a fixed set-point by generating an auxiliary set-point for the subordinated and faster PID-control of the flow-control loop. In comparison to the single-loop control the control system is faster, more accurate and more robust against disturbances. All sensor signals, set-points and the command signals of the flow-valves are accessible via an open OPC-interface. Hence, the prototypic development of advanced control strategies with external tools (i.e. Matlab/Simulink® or LabView®) is facilitated.

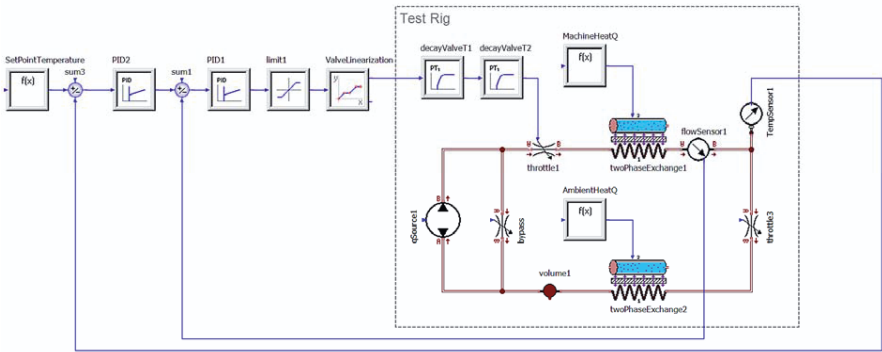


Fig. 7. Closed-loop cascade temperature PID-control.

Furthermore, the controller software was prepared to provide a multitude of interface variables at the summation points of the controller set-points and PID outputs. Through these interfaces advanced controller set-point with cross-coupling of the separated fluidic circuits to multi-variable or to inject of feed-forward signals (i.e. from an inverse plant model) are possible. The necessity of cross-coupling the implemented, yet independent single loop control approaches will be discussed in the following section.

## 5.2 Control strategy based on decentralized, liked controllers

A first step towards an integrated model, comprising the mechanical structure, the fluidic behavior and the control engineering is presented. Fig. 8 shows the basic scheme for the observation of different control loops with shared manipulating value. Furthermore the maximum amount of manipulating value for all loops is limited. To investigate the functionality of the control loops separately and in combination, they were simulated with different time behaviors of the heat input, representing eight hours of heating and twelve hours of cooling down. Values were prepared to reflect different locations in the machine frame (see Fig. 9). E. g. this could be a position close to the drive (heat input-spot 1) and on in the center of the machine frame (heat input-spot 2). The PI-controllers of loop 1 and loop 2 are tuned accordingly to provide comparable controlled values. With unlimited manipulating value the loops work sufficiently (see Fig. 10). However, in the application the provided overall supply of cooling fluid is limited.

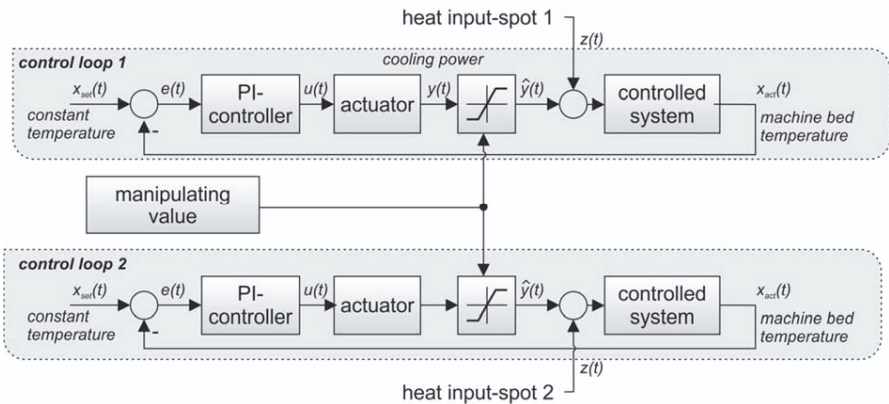


Fig. 8. Scheme of control loops with shared source of manipulating value.

This was modelled as well, in a first stage without reciprocative influence of the control loops. As presented in Fig. 12, loop 1 is working properly. It is also visible that the cooling power is not sufficient after approx. 2 h in each cycle, leading to an abrupt increase of the controlled value. It varies in a range of > 5 K.

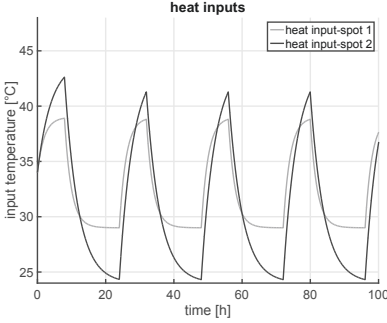


Fig. 9. Time behavior of the heat input.

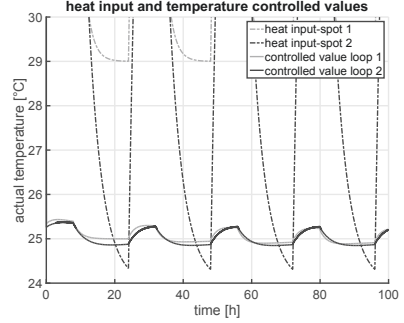


Fig. 10. Functionality of the temperature control.

A more powerful cooling unit would be one expedient to the insufficient control behavior but is not feasible due to energy efficiency. Another alternative is to link the loops with each other and share information of the required cooling power with the aim of a harmonized consumption for each loop. In simulation the general operability shall be presented in a first step. An additional block is included in simulation, distributing the provided amount of cooling power following equations (1) to (3) in Fig. 11. Here the input is formed by the desired manipulating values  $y_{11}$  and  $y_{12}$  of the control loops 1 and 2. A weighting factor  $f_{weight}$  is calculated based on those values, providing information for a harmonized distribution of the maximum available manipulating value  $y_{tot}$ . In the last step new saturation boundaries  $y_{11\_bound}$  and  $y_{12\_bound}$  are computed as input for the saturation blocks, limiting  $y_{11}$  and  $y_{12}$  and leading to the limited manipulating values if the dedicated loops 1 and 2  $\hat{y}_{11}$  and  $\hat{y}_{12}$ .

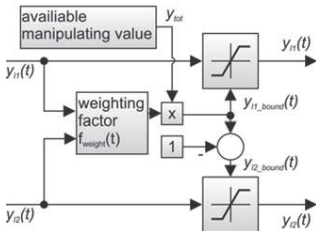


Fig. 11. Scheme for harmonized distribution of manipulating value

$$f_{weight}(t) = \frac{y_{11}(t)}{(y_{11}(t) + y_{12}(t))} \quad (1)$$

$$\hat{y}_{11}(t) = \max \left\{ \frac{f_{weight}(t) \cdot y_{tot}}{y_{11}(t)} \right\} \quad (2)$$

$$\hat{y}_{12}(t) = \max \left\{ \frac{(1 - f_{weight}(t)) \cdot y_{tot}}{y_{12}(t)} \right\} \quad (3)$$

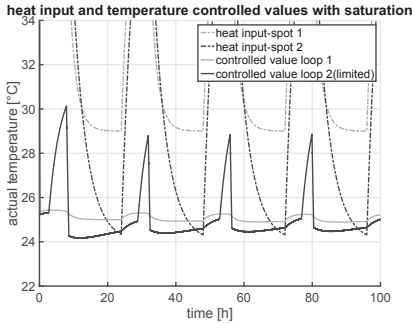


Fig. 12. Deterioration of the control behaviour with limited manipulating value.

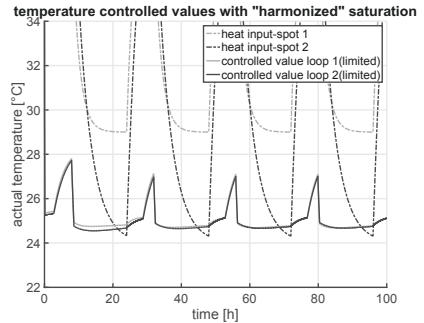


Fig. 13. Improved controller performance due to harmonized limitation of manipulated values.

If the manipulating values are negative, the equations have to be adjusted accordingly. Fig. 13 shows the positive effect of the “harmonized limitation”. Both controlled values oscillate similarly, but with a range of only 2,5 K. Hence, it is proven that the chosen approach is beneficial. Although the simulation was carried out for two control loops, the methodology is also expandable for a larger number of loops and fluid circuits respectively.

For the experiments, approaches will be examined subsequently. However, it was shown, that the linkage of control loops is necessary for the suitable tempering of complex structures with multiple fluidic circuits. Based on further experiments, an optimal control strategy will be developed. It will subsequently be implemented into intelligent sub-components, such as micro-valves, which can be regarded as cyber-physical-systems.

## 6 Conclusion and Outlook

The objective of the research field, presented in this paper, is to develop a tempering methodology for HPC machine frames in order to reduce the thermally induced position deviations with tolerable energy demand. Seven research aspects to achieve this goal are introduced, whereas the paper focusses on the introduction of the hardware basis and initial findings concerning the control strategy. In particular, the machine frame, the fluidic tempering system with fluidic circuits and the included thermo-sensors are presented. For experimental variations, a flexible and scalable controller software is implemented to control the tempering of the machine frame and to record long-term time-series of its thermal behavior. Additionally, the currently implemented single loop controller strategies are shown with first simulative results. Furthermore, simulations show the necessity of an overall control strategy with interlinked

components due to a limitation of provided manipulating values. Also one approach to harmonize the control behavior of two loops was presented. Parallel to the realization of the machine frame and implementation of the controller structure, FE and CFD simulations were carried out. They are topic of a separate paper [21].

Subsequent research steps are couple and combine the simulation models (FE and CFD). Therefore, a fast computable network-based model will be created and enable for calculating varying operating parameters and design principles. Based on the consideration of variants, an optimal structure and placement of the fluidic circuits and temperature sensors will be derived. Also the control strategy will be investigated based on variations of control structures and controller parameters.

#### **Acknowledgements**

*The presented research activities are part of the transfer project T02 "Robust and thermo-energetically optimal tempering of machine tool frames with fluidic tempering systems" (Ref. No. CRC/TR 96, T02). The authors would like to thank the German Research Foundation (DFG) and all project partners including HYDAC Cooling GmbH, FRAMAG Industrieanlagenbau GmbH and METROM Mechatronische Werkzeugmaschinen GmbH for the financial support.*



## **7 References**

- [1] Wegener K., 2014. Innovative Werkzeugmaschine –Präzision, Produktivität, Effizienz, Tagungsband Industrie 4.0 – die intelligente Fabrik der Zukunft; 259-269
- [2] Großmann, K., 2015. Thermo-energetic Design of Machine Tools A Systemic Approach to Solve the Conflict Between Power Efficiency, Accuracy and Productivity Demonstrated at the Example of Machining Production, Springer Verlag,
- [3] Gebauer M, Hund R, Kotzian M, Malek R, Mueller B, Polster S., 2014. Ressourceneffiziente Blechwarmumformung durch innovative Werkzeugtemperierung mittels laserstrahlgeschmolzener Werkzeugaktivkomponenten. Ergebnisse Innovationsallianz „Green Carbody Technologies“. Stuttgart: Fraunhofer Verlag;. S. 88-91.
- [4] Neugebauer R., 2014. Energieeffiziente Produkt- und Prozessinnovationen in der Produktionstechnik. Ergebnisse des sächsischen Spitzentechnologieclusters. TU Chemnitz
- [5] Neugebauer R, Frieß U, Paetzold J, Wabner M, Richter M, 2009. Approach for the Development of Energy-Efficient Machine Tools, XXI CIRP Conference Knowledge Based Manufacturing". Karpacz, Poland
- [6] Abele E., Kuhrke B., Rothenbücher S., 2010. Energieeffizienz von Werkzeugmaschinen maximieren. Maschinenmarkt, (9):26-29.



- [7] Augenstein E., Nelles J., Wurm A., 2012 Energieeffiziente Kühlsysteme für Werkzeugmaschinen. wt Werkstattstechnik Online, 102(5):306-311.
- [8] Bosch Rexroth AG (Hrsg.), 2010. Bedarfsgerechte Regelung hilft beim Stromsparen – Energieeffiziente Fluid-technik für Werkzeugmaschinen. Fluid, 43(5):10–12.
- [9] Brecher C., 2012. Effizienzsteigerung von Werkzeugmaschinen durch Optimierung der Technologien zum Komponentenbetrieb. EWOTeK. Aachen: Apprimus Verlag.
- [10] Denkena B., Möhring H.-C., Hackelöer F., Hülsemeyer L., Dahlmann D., Augenstein E., Nelles J., Grigoleit A., 2011. Effiziente Fluidtechnik für Werkzeugmaschinen. wt Werkstattstechnik Online, 101(5):347-352.
- [11] Eun I-U., 1999. Optimierung des thermischen Verhaltens von elektrischen Linearmotoren für den Einsatz in Werkzeugmaschinen [Dissertation]. RWTH Aachen.
- [12] Gebhardt M., Wegener K., 2013. Temperatureinfluss auf Werkzeugmaschinen. Institut für Werkzeugmaschinen und Fertigung, ETH Zürich; Zürich; Bericht.
- [13] Haubner, F. G., 2002. Bauteilbelastungsgeregeltes Kühlsystem für verbrauchsoptimierte Verbrennungsmotoren. Dissertation, RWTH Aachen.
- [14] Michel, S. Schulze, T., Weber, J., 2014. Energy-efficiency and thermo energetic behaviour of electro-hydraulic compact drives. 9th International Fluid Power Conference, Aachen.
- [15] Knapp W., 2013. Temperatureinfluss und Werkstücktoleranzen. Schweizer Maschinenmarkt. Vogel Business Medien, URL: [http://www.maschinenmarkt.ch/fertigung\\_production/mess\\_und\\_prueftechnik/artic-les/397140/](http://www.maschinenmarkt.ch/fertigung_production/mess_und_prueftechnik/artic-les/397140/).
- [16] Neugebauer R., Drossel W.-G., Ihlenfeldt S., Richter C., 2012. Thermal interactions between the process and workpiece. 3rd CIRP Conference on Process Machine Interactions. Nagoya, Japan.
- [17] Schneider M. Das „intelligente“ Mineralgussbett. VDI-Z Integrierte Produktion 155 Nr. 3; 2013
- [18] Neugebauer R., Hirsch A., Kolouch M., Zhu B., 2012. Optimierung der Schmiernutenform in hydrodynamischen Gleitführungen. Konstruktion, 64(11/12):71-74.
- [19] NN., 2010. Pumpen und Pumpensysteme für Industrie und Gewerbe. Ratgeber Deutsche Energie-Agentur GmbH (dena). Berlin.
- [20] Hang, C.C.; Aström, K.J.; Wang, Q.G. 2002: Relay feedback auto-tuning of process controllers - a tutorial review, Journal of Process Control, 12, S. 143-162,
- [21] Weber J, Glänzel J, Shabi L, Weber J, 2017. Combined and fast computable thermal models for situationally optimal tempering of machine components, to be published, 1st Conference on Thermal Issues in Machine Tools, Dresden, Germany

# Thermo-mechanical interactions in hot stamping

*L. Penter<sup>a</sup>, N. Pierschel<sup>b</sup>*

<sup>a</sup>Institute of Machine Tools and Control Engineering IWM, Technische Universität Dresden,  
01062 Dresden, Germany

<sup>b</sup>Fraunhofer Institute for Machine Tools and Forming Technology IWU, Reichenhainer Str. 88,  
09126 Chemnitz, Germany

**Abstract.** Manual, mechanical die spotting is a significant time and cost factor in the manufacturing business of forming tools. This particularly applies to warm forming, since the mechanical and geometrical properties of the part strongly depend on the tool's cooling performance. An even distribution of the contact pressure between tool and blank is key to a uniform cooling behavior, and hence, a homogenous micro structure of the formed part.

This paper presents the current developments on transitioning the spotting of hot forming tools into virtual production environment in order to reduce manual labor and lower costs. It specifically elaborates on numerical predictions of spotted tool surfaces under the influence of elastic tool and machine deformations, and furthermore, it explains the aspect of the temperature induced tool expansion and contraction.

Since the character of heat transfer from workpiece to tooling mainly depends on the contact pressure on the tool surface, a correct numerical prediction of the tool's actual surface evens the path for a virtual try-out in the future.

Peer-review under responsibility of the International Scientific Committee in the person of the Conference Chair Prof. Steffen Ihlenfeldt.

*Keywords:* Hot stamping; Virtual die spotting; Machine-process interaction

---

## Nomenclature

$h_C$	thermal contact conductance coefficient
$p_N$	normal contact pressure
$\alpha$	coefficient of thermal expansion
$\epsilon_T$	true strain
$\sigma_T$	true stress

# 1 Direct hot stamping

Direct hot stamping is a hot forming process, which uses the advantage of low forming resistance of special steels at high temperatures and their microstructural transformation towards high strength when quenched above a certain cooling rate. A typical material for hot stamping is 22MnB5 steel. The steel blank is heated above 900 °C for a complete transformation to an austenitic microstructure. Then, the red-hot blank is transferred to the stamping tool and directly formed into its final shape (Figure 1). Once the tool is closed, the quenching process enables superior mechanical properties due to phase transformations to martensite. The steel possesses a yield strength up to 1500 MPa [5].

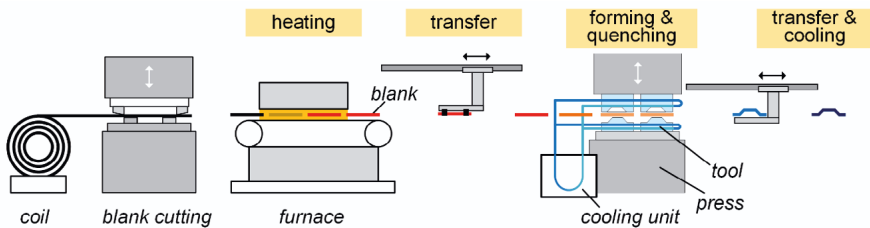


Fig. 1. Process chain of direct hot stamping

## 1.1 Hot stamping tools

Hot stamping tools are usually designed for hydraulic single action presses with or without die cushion. Since the friction coefficient between hot steel and the tool surfaces during hot stamping is high ( $\mu$  equals 0.4), toolmakers usually rely on spacers for fixed gaps between blankholder and die surface rather than directly applying a blankholder force. That way, the die cushion of the press needs to generate enough force to ensure that the spacers touch the opposite side. The same principle applies to the tool's punch and die to accomplish a fixed die clearance. Punch and die are usually equipped with cooling channels.

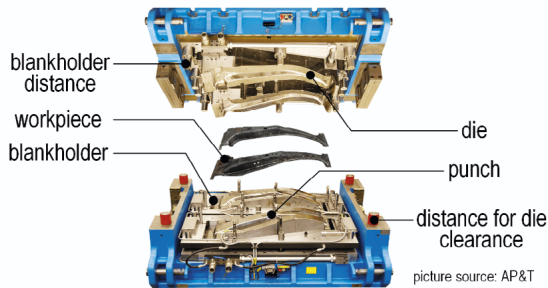


Fig. 2. Typical tool set-up for direct hot stamping

## 1.2 Die spotting of hot stamping tools

A defined martensitic microstructure after quenching is key in generating superior mechanical properties of hot formed parts. Since the formation of martensite depends on the cooling rate of the part, which is a result of the temperature gradient [6] and of the normal contact pressure [1], the punch, die, and workpiece must perfectly fit each other. In cold forming, toolmakers apply blue die spotting ink on the surface of the tool or the workpiece for locating local high spots. As of today, there is no die spotting ink for high temperatures on the market. Therefore, toolmakers of hot forming tools use indirect methods for locating high-pressure zones. One example is an optical measurement of the part's temperature directly after the forming process. Local hot spots indicate areas of lower normal contact pressure since there is also a lower heat flow in these zones. In conclusion, the toolmaker will manually remove tool material in the colder areas, which correspond to local high spots, and therefore, to a better thermal conductance. Die spotting of hot stamping tools takes many iterations and is a large cost factor in the tool development phase. Two of the main reasons for this extensive tool try-out are mechanical deflections of the press and the tool due to large process forces during quenching and the thermal expansion of the tool during the process ramp-up to a steady state temperature.

## 1.3 Mechanical tool and machine deformation under process load

In hot stamping, the forming forces are relatively low but the quenching step needs high pressure between upper and lower die for a sufficient heat flow. The mechanical interaction between press and process lead to elastic deformations of the forming tool and entail negative effects on the pressure distribu-

tion between tool and workpiece. Since the heat flow depends on the contact pressure, the elastic deformations of the tool and the press finally affect the cooling rate, and as a result, the mechanical properties of the workpiece. In order to compensate for global deformations of the press table, toolmakers emboss the lower die. This applies to both cold and hot forming.

### 1.4 Thermo-mechanical tool and machine expansion

An additional difficulty in hot stamping are thermal tool expansions and contractions, which also affect the part geometry and the mechanical properties due to their influence on the normal contact pressure, and therefore, on the thermal contact conductance and the part's microstructure (Figure 3). This is particularly hard to address during tool try-out since the toolmaker cannot manipulate the die's surface in the thermal steady state of the serial hot stamping process but needs the tool to cool back down to lower temperatures. As for today, there is no evidence that thermal deformations of the press, caused by radiation from the blank, are of significance for the quality of the hot stamped part.

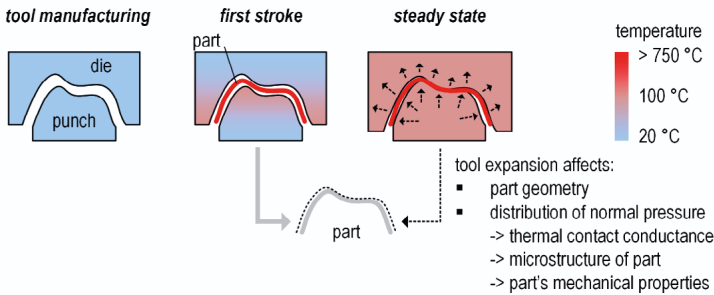


Fig. 3. Tool expansion affecting the part's geometry and mechanical properties

### 1.5 Simulation of hot stamping

The typical simulation chain (Figure 4) comprises the blank heating and transport to the tool, calculation of the blanks deformation due to gravitational forces, die closing and quenching [3]. The major fields for the simulation are the thermal tool design, the thermo-mechanical process simulation and the metal-lurgical transformation.

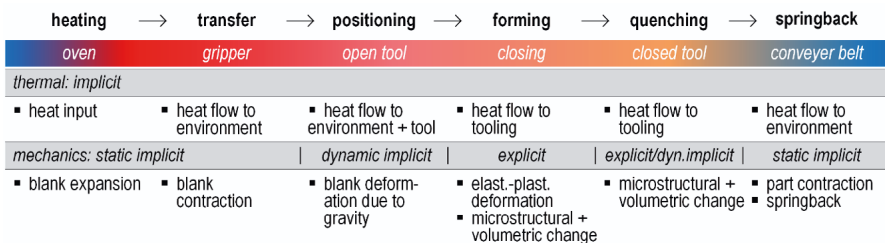


Fig. 4. today's simulation chain for hot stamping process design

So far, tool and press deformation as well as thermal expansion of the tool are excluded from this simulation chain, which is one of the reasons for manual die spotting. The following chapters discuss how to implement these properties into the FE process model, how the implementation affects the simulation results, and how to integrate them into the tool development process.

## 2 Set-up for virtual experiment

### 2.1 Blank material and contact formulation

22MnB5 is the typical material used in hot stamping and was, therefore, applied in the following analysis. In a first step an elastic-visco-plastic material model was implemented. The material model accounts for temperature dependent true stress – true strain curves (Figure 5 left) The heat flow from work-piece to tool depends on the thermal contact conductance and is expressed as a function of the normal interface pressure (Figure 5 right). All parameters were obtained from [7].

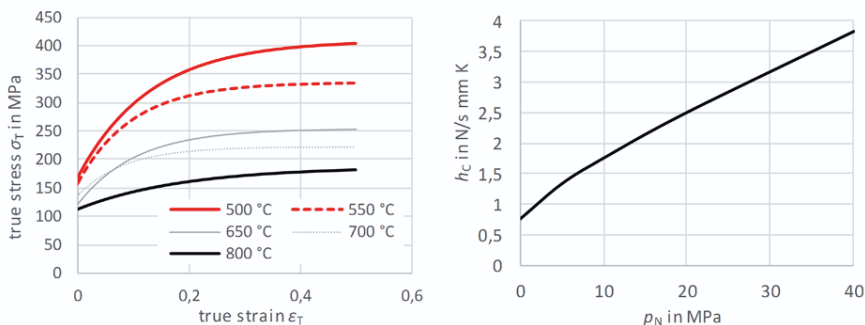


Fig. 5. material properties (according to Numisheet 2008 benchmark)

## 2.2 Hot stamping tool

The experimental tool was designed for a single action press with die cushion (Figure 6). Since the hot metal has a high friction value and the material's yield stress is very low, there is a fixed gap between die and blankholder to ensure an easy material flow into the cavity.

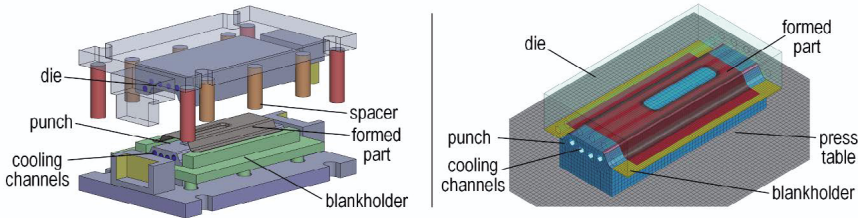


Fig. 6. left: CAD model of hot stamping tool; right: FE-Modell with elastic tools and press table

Spacers separate die and punch as well. The height of the spacers is adjusted during tool try-out to tune the pressure distribution. Punch and die are equipped with cooling channels to guarantee a thermal steady state.

## 3 Simulation of tool deformation under process load

In order to compensate for elastic tool and press deformations, their elastic properties were implemented into the process simulation. Since that will entail significant increases in computation time, the simulation strategy needs to be as efficient as possible. Since the blank shows only little residence during the forming stage, the tool can be considered as rigid. Once upper and lower die touch, the pressure on the formed part increases (quenching phase 1), which causes the real tool and press to deform. Due to process-machine interactions, these deformations affect the surface pressure between tool and workpiece, and hence, influence its cooling rate. For that reason, the tool model switches into elastic mode for the initial quenching phase. Since the acting press force remains the same over the course of the quenching process, the deformation of the tool and the press will not change. It is a fair assumption, that the tool can now be considered as rigid again. Therefore, the deformed tool surface mesh from simulation stage C is mapped on the thermo-mechanical process model in simulation stage D. This procedure saves a significant amount of computation time.

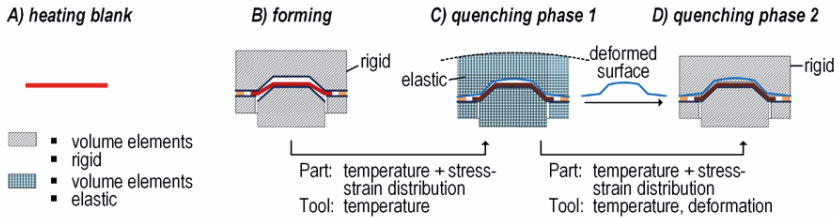


Fig. 7. strategy for considering tool elasticity during hot stamping

In order to guarantee an appropriate heat flow from the workpiece to the tool a normal surface pressure between 15 and 20 MPa is desirable. For the test workpiece with a projected surface area of 92000 mm<sup>2</sup> the machine has to provide 1840 kN of press force.

In order to reduce simulation time for this principle investigation, a 40 mm slice of the tooling was modeled. For further reduction of computation time, the tool surface was modeled with fine shell elements and tied to coarsely meshed volume elements, which represent the tool structure. Since this method was separately suggested for both thermal [4] and elastic [2] simulations, it was applied in the thermo-mechanical quenching simulation (Figure 8). In order to deform realistically, the FE punch sits on an elastic surrogate model of the press table with a thickness of 400 mm (Figure 8). Now, it is possible to calculate the influence of the elastic tool deformation on the actual heat flow from work-piece to tooling.

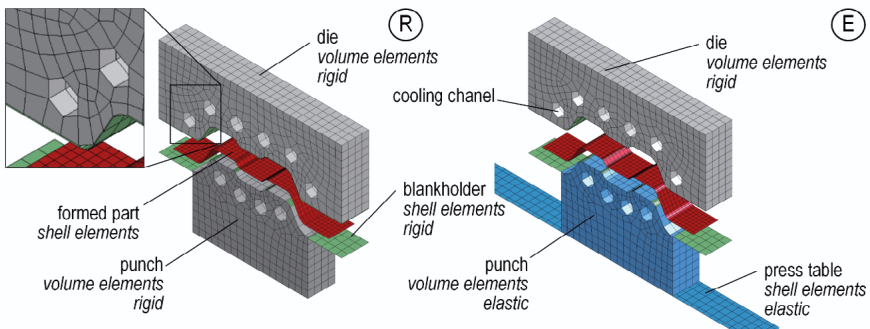


Fig. 8. rigid and elastic tool model

Since the punch in the model deforms under quenching load, the surface pressure between punch and die reduces and entails a lower thermal conductance. The consequences are visible in the part temperature, shown in Figure 9.



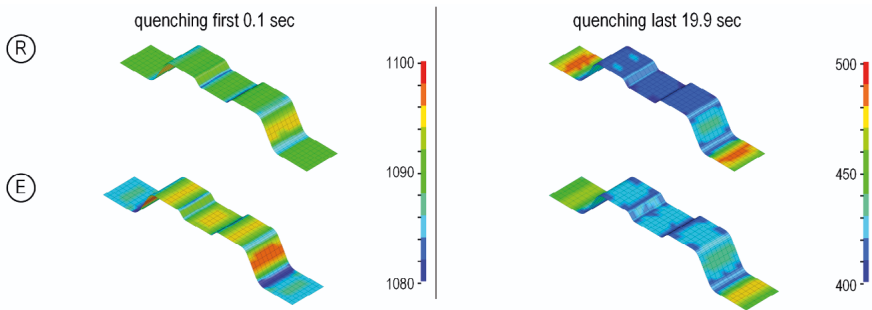


Fig. 9. Tool deformation affecting the part temperature

Not only is there a difference in the final part temperature, but also the temperature gradient (cooling rate) is lower in the process model with elastic punch compared to the process model with rigid punch (Figure 10). Since the microstructural transformation depends on the cooling rate, there is a significant risk of predicting incorrect part properties with rigid tool surfaces.

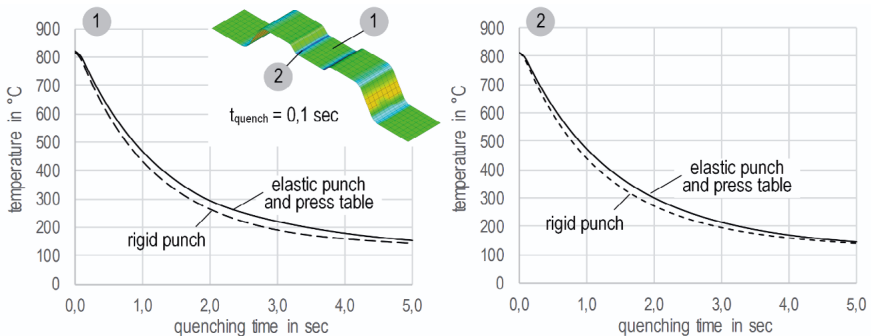


Fig. 10. temperature in the part during quenching phase 2: left: part center, right: part radius

## 4 Tool expansion and contraction

Since mechanical die spotting requires manual labor, the tool must cool down well below steady state process temperature to be accessible for the worker. This temperature difference yields in a thermal expansion of both the upper and lower die. The regular strategy to compensate for this geometrical change in the shop floor is to adjust the surfaces iteratively based on information of the resulting part temperature after quenching.

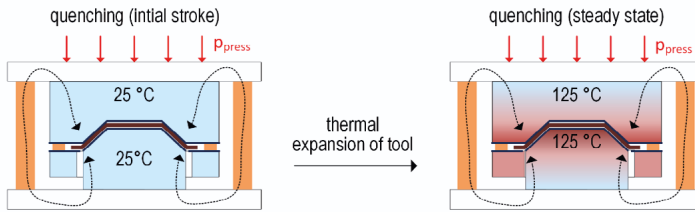


Fig. 11. influence of tool expansion on part shape and mechanical properties

The simulation shows, that the contact pressure between tool surface and quenched part increases with the tool temperature (Figure 12). The contact pressure rises until the reaction force exceeds the set load of the press, the tool would lift and the spacers would not touch anymore. In the example, the temperature difference is only 25 K. The tool expands by 20  $\mu\text{m}$  in Z direction, which causes a contact pressure growth by 30 MPa in the flat middle area of the part. According to Figure 5, the thermal contact conductance coefficient would multiply by 4. Based on this simulation, the toolmaker would need to remove a significant amount of material on the upper and lower die to guarantee the correct closing behavior under process temperature.

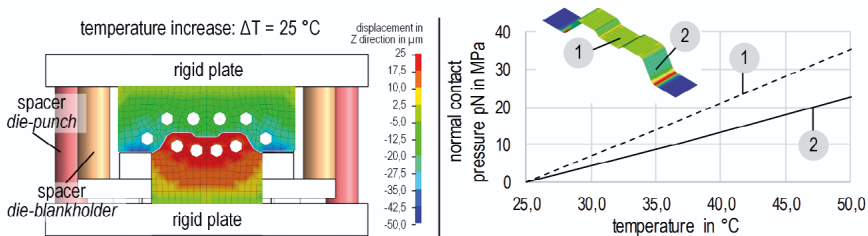


Fig. 12. Influence of thermal expansion on the contact pressure between die and blank

The simplification of rigid tool and machine parts obviously causes a larger increase of contact pressure than observed in reality.

## 5 Tool deformation and expansion

Since in reality tool deformation and thermal expansion and contraction superimpose, the correct prediction of the tool surfaces through virtual try-out requires the computation of both effects at the same time. For that reason, the elastic properties of the press table and press slide were implemented into the quenching model (Figure 13). The results of the elastic simulations suggest a slightly lower growth of contact pressure during tool warming.

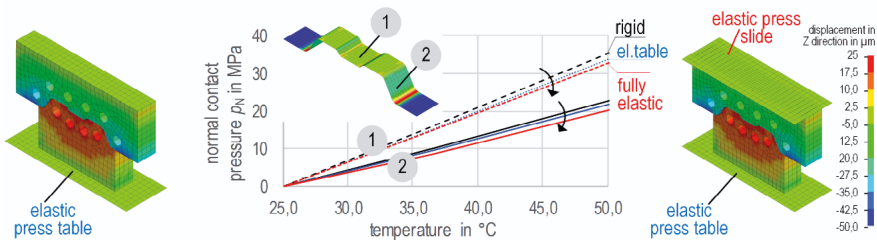


Fig. 13. Influence of tool expansion and deformation on the contact interface pressure

## 6 Future work for virtual tool try-out

Future goal is to compensate for mechanical deformations and for thermal induced changes of the tool geometry before the physical production of the tool, and hence, reduce try-out cycles and overall try-out time. In order to do so with a minimum of computation power, the workflow (Figure 14) starts with a process simulation with rigid tools and a steady state temperature distribution. The first phase of quenching will be simulated with elastic tools and mounting plates; the steady state temperature field will be mapped on the tool structure. Now, the tool's surfaces are embossed by the amount of deformation under quenching load. The last step of the compensation method is to compute the contraction of the tool.

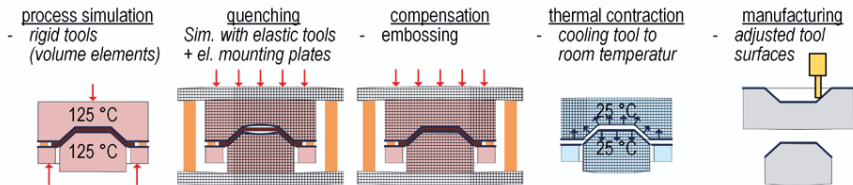


Fig. 14. Future workflow for virtual compensation for thermal and mechanical deformations

As a next step, the quenching model will be extended to compute the micro-structural evolution based on LS-DYNA material model 244. Another key to the compensation is an accurate representation of the tool surface. Since the surface pressure of FE models shows a strong dependency on the individual mesh size, the element type and the contact formulation, alternative methods like NURBS-based finite elements must be investigated in future research.

## 7 References

- [1] Caron, E. ; Daun, K. ; Wells, M. : Experimental Characterization of Heat Transfer Coefficients During Hot Forming Die Quenching of Boron Steel. In: Metallurgical and Materials Transactions B 44B (2013), S. 332–343
- [2] Haufe, A. ; Lorenz, D. ; Roll, K. ; Bogon, P. : Concepts to take elastic tool deformations in sheet metal forming into account. In: 10th International LS-DYNA Conference. Detroit, 2008
- [3] Hochholdinger, B. ; Hora, P. ; Grass, H. ; Lipp, A. : Simulation of the Press Hardening Process and Prediction of the Final Mechanical Material Properties. In: 8th International Conference and Workshop on Numerical Simulation of 3D Sheet Metal Forming Processes, 2011
- [4] Lorenz, D. : Simulation of Thermo-Mechanical Forming Prozess in LS-DYNA. In: 9. LS-DYNA Forum, 2010
- [5] Naganathan, A. ; Penter, L. : Hot stamping. In: Altan, T. (Hrsg.) ; Tekkaya, E. (Hrsg.): Sheet Metal Forming - Processes and Applications. ASM International, 2012. – ISBN 978–1–61503–844–2, Kapitel Hot Stamping, S. 133–154
- [6] Salomonsson, P. ; Oldenburg, M. ; Åkerström, P. ; Bergman, G. : Experimental and numerical evaluation of the heat transfer coefficient in press hardening. In: Steel Research International 80 (2009), S. 841–845
- [7] Shapiro, A. B.: Using LS-Dyna for hot stamping. In: 7th European LS-DYNA Conference, 2009



## **Approaches considering cutting processes**

---



# Experimental analysis of the heat flux into the grinding tool in creep feed grinding with CBN abrasives

*C. Wrobel, D. Trauth, P. Mattfeld, F. Klocke*

Laboratory of Machine Tools and Production Engineering WZL, RWTH Aachen University,  
Steinbachstr. 19, 52074 Aachen, Germany

**Abstract.** This paper presents an experimental investigation regarding the heat flux into a the electroplated CBN abrasive wheel in creep feed grinding of 100Cr6 (1.3505, AISI 5210) and minimum quantity lubrication. For the first time, the influence of the heat flux into the grinding wheel on the thermal tool center point displacement is analysed by measuring the maximum temperature in the subsurface of the grinding wheel using embedded thermocouples.

Peer-review under responsibility of the International Scientific Committee in the person of the Conference Chair Prof. Steffen Ihlenfeldt.

*Keywords:* Thermal error; Grinding; Energy; Topography; Super abrasive

---

## 1 Introduction

In a machine tool, a large number of energy transformation processes take place during the machining of workpieces. Each of these energy transformation processes involves energy dissipation in the form of heat. The heat spreads out into the machine structure by radiation, conduction and convection. If the heat exceeds a critical value, a thermal displacement of the tool center point (TCP) can occur. As a result, the machining accuracy decreases. In order to reduce the thermal error in machine tools, compensation measures (e.g. tempering of structural parts) or corrective measures (e.g. prediction of the thermal TCP-displacement) are needed [1]. The development and design of these measures requires precise knowledge of all heat sources as well as their resulting temperature fields, which are relevant for the thermal TCP displacement.

In grinding, the cutting energy induced by the spindle and workpiece drive is almost entirely converted into heat [2]. Thus, the grinding process is one major heat source in the machine tool. The cutting energy converted into heat within the contact zone is partitioned between the components tool, workpiece, chips



and cooling lubricant. The partitioning of the heat varies depending on the design of these components, the cooling strategy and the process control.

Most of the investigations regarding heat flux partitioning in grinding focus on the heat flux into the workpiece to predict the occurrence of thermal damage in the workpiece external zone [3]. Although there has been an enormous progress in numerical simulation of grinding in the present past, well summarized by Brinksmeier et al. [4] and Altintas et al. [5], the prediction of the heat flux partitioning in grinding is still based on the analytical moving heat source theory by Jaeger [6]. The most recent and most detailed heat flux partitioning models for grinding are the grain contact models by Demetriou and Lavine [7] and Ju et al. [8]. In those models the consideration of the heat fluxes into the grinding tool, cooling lubricant and chip, however, are only of methodological interests to improve the quantitative prediction quality of the heat flux into the workpiece. First investigations regarding the temperature field in the grinding tool were carried out by Gu et al. [9] and by Kundrák et al. [10]. Both studies use finite element analysis (FEA) to simulate the temperature field of the grinding wheel. Due to different assumptions and simplifications of the implemented heat flux partitioning models and boundary conditions, the FEA simulations led to significant different temperature fields inside of the grinding tool. Since the results of FEA simulations have not been validated by experimental studies yet, it is still unknown, if the heat flux into the grinding wheel influences the thermal TCP displacement.

This paper presents an experimental investigation focusing on the temperature field inside of an electroplated CBN grinding tool in creep feed grinding of 100Cr6 (1.3505, AISI 5210) and minimum quantity lubrication (MQL). For this purpose, a measuring system was developed, which is implemented inside the grinding wheel carrier and measures temperatures of the workpiece surface within the contact zone and inside of the grinding tool at different radial depths during grinding.

## 2 Design of experiment

The experimental investigations were carried out on the flat grinding machine Blohm Profimat MT608. In continuation to previous research [11], CBN of the grain type ABN300 and a mean grain diameter of  $d_g = 151 \mu\text{m}$  was selected for the electroplated grinding wheel. The grinding wheel had an outer diameter of  $d_s = 400 \text{ mm}$  and a grinding wheel width of  $b_s = 15 \text{ mm}$ . The minimum quantity lubrication was operated with a lubricant flow  $q_f = 6.48 \text{ ml/min}$ . The workpieces

made of out 100Cr6 (1.3505, AISI 5210) had a length of  $l_w = 100$  mm, a height of  $h_w = 10$  mm and a width of  $b_w = 15$  mm. The width of cut  $a_p$  was set to 15 mm. The specific material removal rate  $Q'_w$  was varied between 2.5 mm<sup>3</sup>/mm and 5 mm<sup>3</sup>/mm at a constant depth of cut  $a_e = 0.25$  mm. The grinding parameters and workpiece geometry led to grinding time of 10 s and 5 s per grinding stroke. The grinding tests were examined in down and up grinding for both specific removal rates. In total, four test points were investigated. Each test point consisted four grinding strokes in series on the same workpiece. After each grinding stroke, the experiment was paused until grinding wheel and workpiece were cooled down again to ambient temperature of  $T_0 = 23$  °C. In addition, all test points were repeated once. The grinding tests were first carried out in down grinding, subsequently in up grinding. Before the test started, the grinding wheel was ground in by an intermittent pendulum grinding process with a depth of cut of  $a_e = 5$  µm, a workpiece speed of  $v_w = 25$  m/min, a grinding wheel circumferential speed of  $v_s = 60$  m/s and a specific material removal  $V'_w = 1000$  mm<sup>3</sup>/mm.

During grinding, the grinding force was measured by a force measuring system 9255C of Kistler. The temperature field inside of the grinding wheel was measured by a newly developed measuring system. Additionally, imprints of a defined location on the grinding wheel topography were made after the grind-in-process as well as after the down und up grinding tests. The grinding wheel topography imprints were evaluated with a 3D-Laser-Scanning-Microscope Keyence VKX-150.

### 3 Design of the grinding wheel temperature measurement system

The objective of the developed measuring system was to detect the temporal development of the temperature field inside the grinding tool in order to conclude the influence of the heat flux of the grinding process into the grinding tool on the thermal TCP displacement. The concept of the system was inspired by the research of Brinksmeier [12] and Sakakura et al. [13] and has been developed in cooperation with FOS Messtechnik. The measurement system itself is implemented inside of the grinding wheel carrier, which is made of steel. The design of the measurement system in its basics is presented in Fig. 1. It consists of two opposing measurement chambers to avoid unbalance. Each measurement chamber includes one high-speed infrared sensor, two thermocouples and one transmission unit with a programmable microprocessor. The transmission of measurement data takes place wirelessly to a receiver unit. Due to the integrated programmable microprocessor, it is possible to use different configu-

rations of measurement to achieve different objectives using the same sensor network. The measuring chambers are sealed against infiltration of coolant lubricant by glass-fiber covers, which are permeable to signal transmission.

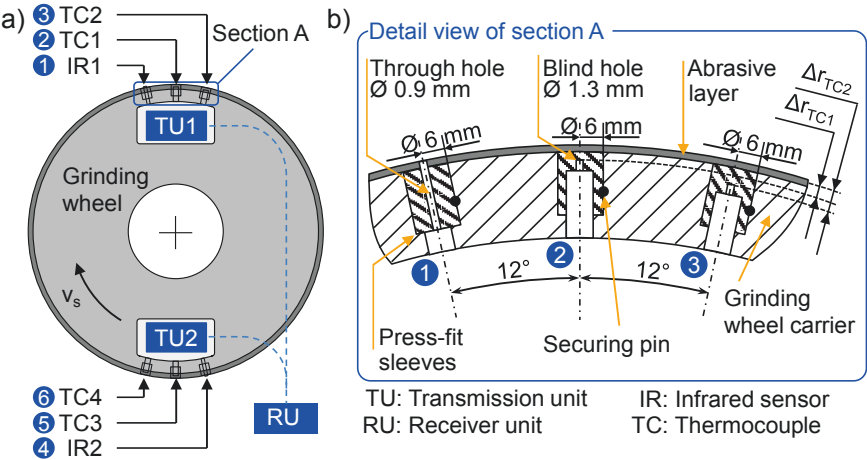


Fig. 1. Concept of the in-process-measurement system of the grinding wheel

Figure 1.b presents a detail view of the design of the measuring points of one measuring chamber. The high-speed infrared sensor is installed at position 1. The objective of the infrared sensor is to measure the surface temperature in the contact zone. For this purpose, the infrared radiation of the workpiece surface is directed into the interior of the grinding wheel through a through hole by a glass fiber. There, the infrared radiation is converted to an analog signal by the infrared sensor head at a sampling rate of 1 MHz. At Position 2 and position 3, the inner temperature of the grinding wheel carrier is measured by thermocouples of type K, which are placed in blind holes. The blind holes have different depths, so that measurements of the temperature field of the grinding wheel carrier takes place at different radial distances to the abrasive layer. The radial distances to the abrasive layer  $\Delta r_{TC}$ , used during the grinding test, are listed in Tab. 1. The thermal contact between the grinding wheel carrier and thermocouple is supported by a mechanical pre-suspension of sensor head and a thin film of heat-conducting paste. The thermal contact of each thermocouple was tested before and after the grinding tests by applying an electrical voltage between grinding wheel carrier and thermocouple.

Table 1. Measuring depth of the thermocouples inside the grinding wheel

Measuring Point	Radial distance to abrasive layer $\Delta r_{TC}$ ( $\mu\text{m}$ )
TC1	0,15
TC2	0,25
TC3	0,5
TC4	1

Due to the restricted accessibility for manufacturing the blind holes from inside of the grinding wheel carrier at simultaneously achieving high precision for the hole depth, the blind holes are first inserted externally into sleeves using 180°-drills. Subsequently, the sleeves are pressed into the grinding wheel carrier from the outside. The pressed-in sleeves are secured each with a securing pin against slipping out and allow the usage of grinding wheel circumferential speeds  $v_s$  up to 100 m/s. Before the grinding wheel carrier was electroplated with CBN, the circumferential surface of the carrier was ground cylindrical once again to remove minimum excesses of the sleeves.

The microprocessor of the measuring systems was programmed to measure the workpiece surface temperatures in the contact zone and the temperatures inside of the grinding wheel carrier at each revolution. The measurement starts when the infrared sensor exceeds a threshold value of  $T_{IR,start} = 200\text{ }^{\circ}\text{C}$  at the beginning of the contact zone. Subsequently, the infrared sensor detects  $n_{meas} = 200$  temperature signals at a sampling rate of  $f_{meas} = 1\text{ MHz}$ . This results to a recorded distance of  $\Delta l_{meas} = 12\text{ mm}$  at a grinding wheel circumferential speed of  $v_s = 60\text{ m/s}$ , given by

$$\Delta l_{meas} = \frac{n_{meas}}{f_{meas}} \cdot v_s \quad (\text{Eq. 1})$$

The contact length  $l_g$  between grinding wheel and workpiece can be approximated through the grinding wheel diameter of  $d_s$  and the depth of cut of  $a_e$  by

$$l_g = \sqrt{a_e \cdot d_s} \quad (\text{Eq. 2})$$

This leads to a contact length of  $l_g = 10\text{ mm}$  for the present study, which is smaller than the measured distance  $\Delta l_{meas}$ . Thus it is ensured, that the expected high temperatures at the end of the contact zone are included in the measurement sequence. After the measurement sequence, the microprocessor determines the maximum temperature of the recorded data and evaluates the temperatures of the two thermocouples of the respective measurement chamber. Finally, the three temperature data are transmitted to the receiver station. The

# 4 Results

Figure 2 shows the maximum temperature rise at the measuring points of the thermocouples TC1 - TC4 inside the grinding wheel carrier as a function of the examined test points. The temperature rises of the initial and repetition test are shown separately, which will be important in the later analysis of the results. Furthermore, the sequence of experiments is given by the number in the upper right corner of each diagram. Within one test point, the maximum temperature rises from each of the four grinding strokes were arithmetically averaged. The standard errors of the calculated arithmetic mean values are added to the diagrams.

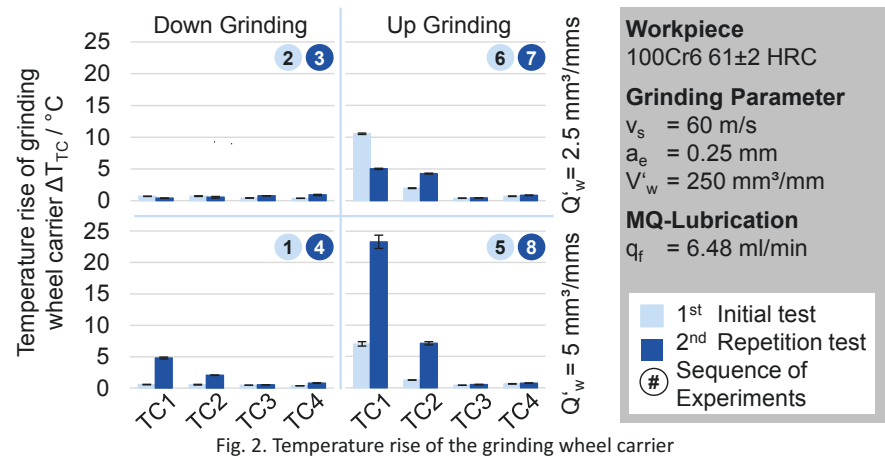


Fig. 2. Temperature rise of the grinding wheel carrier

The results show that at TC1 and TC2 the maximum temperature rise increases with increasing specific material removal rate  $Q'_w$ . Additional, up grinding led to higher temperature rises than down grinding at TC1 and TC2. This confirms experimentally the conclusions on the influence of the grinding mode on the heat flux into the grinding tool, first drawn by Guo and Malkin [14] on the base of analytical modelling. In contrast to this, the thermocouples at TC3 and TC4 measure almost independent of the examined test point a maximum temperature rise between 0.4 - 0.9 °C. A radial temperature gradient, as it would be expected according to the temperature rises at TC1 and TC2, was not detected. One reason for this is that according to the programming of the microprocessor the thermocouples are evaluated at the time although they are physically not at the same angular position since they are implemented in different sleeves. However, the quantity of the measured temperature rises led to the result, that the influence of the heat flux into the grinding wheel on the thermal TCP dis-

placement is negligible in the examined grinding test. Since the contact length  $l_g$  was less than 1 % of circumference of the used grinding wheel, it is assumed that the heat flux introduced into in the grinding wheel within the contact zone is removed by convection, due to the long cooling phase outside of the contact zone.

Another finding can be concluded from the sequence of experiments in Fig. 2. The low standard errors indicate that the four grinding strokes run in series for each test point had a high reproducibility. On the other hand, however, the temperatures rises, measured at TC1 and TC2, increase qualitatively from the fourth experiment onwards with increasing test number. In particular the results show, that the repeat test led to significant different temperature rises. Thus, the application behavior of the grinding wheel changed over the grinding test. The reason for the unstable application behavior of the grinding tool is attributed to wheel surface clogging as a result of insufficient removal of the chips. The cause-effect relationships between wheel surface clogging and the temperature field inside the grinding wheel can be deduced from the grinding force measurements and the grinding wheel topography imprints.

Figure 3 presents the maximum measured specific grinding forces, divided into their tangential and normal components, using an analog data-layout like Fig. 2. The specific grinding force data show, that in down grinding normal and tangential force components both decreased with increasing test number, which is equal to an increasing material removal. In the subsequent up grinding tests, the behavior of the development of the specific grinding force changed. Here the specific grinding force components increased with increasing test number.

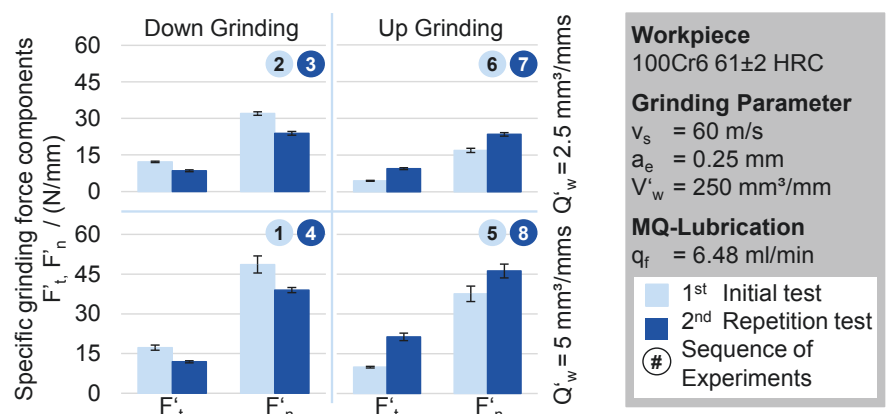


Fig. 3. Specific grinding force components

In addition to this, Fig. 4 shows the evaluation of the grinding wheel imprints taken before test point 1, after test point 4 and after test point 8. The decrease of the grinding force in down grinding indicates that the grinding wheel topography has been exposed to high mechanical load. Because of this, microfracturing occurred at the cutting edges and individual grains broke out (see Fig. 4.b). At the beginning, this caused to new sharp cutting edges so that the grinding force sank. However, the continuous mechanical loss of grain material also led to a constant reduction of the surface roughness of the abrasive layer. By this, the chip removal from the contact zone was further and further inefficient, which is critical in the case of MQL. Additionally, the grain density of the abrasive layer was reduced because of the grain break-outs. As a result the number of kinematic cutting edges  $N_{\text{kin}}$  decreased, which caused an increase of the chip thickness  $h_{\text{cu}}$  in order to maintain the material removal rate  $Q'_w$ .

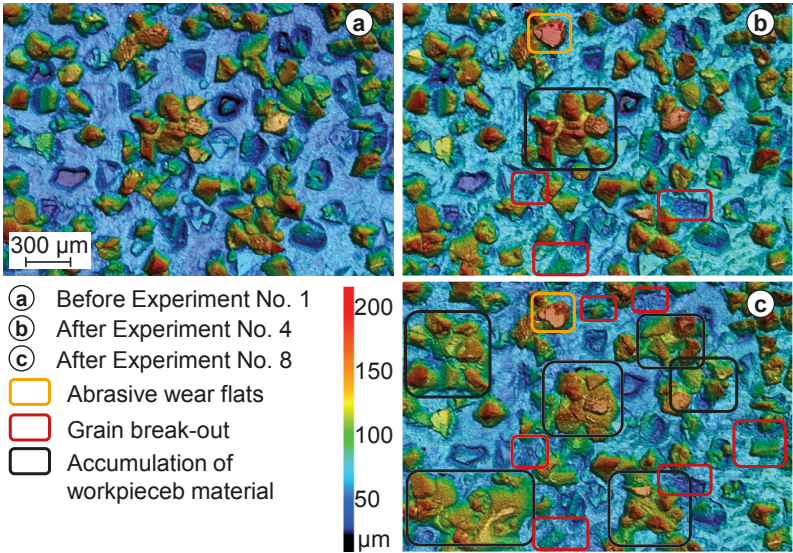


Fig. 4. Topography of the grinding tool at different stages of the experimental investigations

Thicker chips with simultaneously reduced chip removal caused the grain interspaces of the grinding wheel topography to become more and more clogged with remaining chips. The clogging of the grinding wheel topography led to the effect that material removal rate  $Q'_w$  had to be provided by a continuous further decreasing number of exposed cutting edges. As a result, the increasing specific cutting load of the remaining cutting edges caused the surrounding clogging of workpiece material to melt. Subsequently during the cooling phase outside of the contact zone, the melted workpiece material solidified again and

formed accumulations around the grains. As the experiment progressed, the accumulations grew and formed big conglomerates of grain and workpiece material on the grinding wheel topography (see Fig. 4.c). The conglomerates caused a local concentrated heat transfer into the grind wheel and resulted in hot spots at the abrasive layer. The hot spots were detected by TC1 and TC2 due to their short radial distance to the abrasive layer. Since TC3 and TC4 did not detect any significant changes in temperature rises, it is assumed that due to the high thermal conductivity of steel the hot spots equalize very quickly within the external zone of the grinding wheel carrier by diffusive heat transfer.

## 5 Conclusions

This study presented a newly developed in-process-temperature measurement system, which can be used to analyze if the heat flux into the grinding wheel needs to be taken into account to predict the thermal TCP displacement.

The results of the grinding tests showed, that the measurement system is able to detect reasonable temperature rises within the subsurface of the grinding tool. Furthermore, the measurement system was able to recognize an unstable process behavior of the grinding tool by detecting anomalous temperature rises of the grinding wheel carrier. The latter result reveals a high potential for the use of the measuring system as an assistance system for tool lifetime and process stability monitoring for grinding applications with electroplated grinding tools.

The experiments showed that in deep grinding of 100Cr6 with a CBN grinding wheel and MQL the temperature increased at a depth of 1 mm inside the grinding wheel carrier was less than 1 °C at a grinding time of 5 s. This suggests that in the present case, the heat flux into the grinding tool will only have a subordinate role for thermal TCP displacement. It is assumed, that the heat input into the grinding wheel within the contact zone was dissipated to the ambient by convection, due to the long cooling phase outside of the contact zone.

Consequently, particular in grinding it is necessary to take account of both, the heat input within the contact zone by the cutting process and the heat dissipation to ambient by convection, in order to analyze and determine its impact on the thermal TCP displacement. For this purpose, in further research the measurement system will be expanded by a continuous measurement of the grinding wheel carrier temperatures and the influence of the heat dissipation to the ambient by convection will be examined.



## Acknowledgements

*The authors would like to thank the German Research Foundation (DFG) for the support of the depicted research within the project SFB/TR 96-A03.*

## 6 References

- [1] Pereira, P.H., Giacomo, B. Di, 2008, Thermal error evaluation and modelling of a CNC cylindrical grinding machine. *Metrologia*, Vol. 45, No. 2, P. 217-22
- [2] Malkin, S., Guo, C., 2007, Thermal analysis of grinding. *CIRP Annals*, Vol. 56 (2), P. 760-82
- [3] Jermolajev, S., Heinzl, H., Brinksmeier, E., 2015, Experimental and Analytical Investigation of Workpiece Thermal Load During External Cylindrical Grinding, *Procedia CIRP*, Vol. 31, P. 465-70
- [4] Brinksmeier, E., Aurich, J., Govekar, E., Heinzl, C., Hoffmeister, H.-W., Klocke, F., Peters, J., Rentsch, R., Stephenson, D., Uhlmann, E., Weinert, K., Wittmann, M., 2006, Advances in Modeling and Simulation of Grinding Processes, *CIRP Annals*, Vol. 55 (2), P. 667-96
- [5] Altintas, Y., Kersting, P., Biermann, D., Budak, E., Denkena, B., Lazoglu, I., 2014, Virtual process systems for part machining operations. *CIRP Annals*, Vol. 63 (2), P. 585-605
- [6] Jaeger, J.C., 1942, Moving Sources of Heat and the Temperature at Sliding Contacts, *Proc. R. Soc. New South Wales*, Vol. 76 (3), P. 203-24
- [7] Demetriou, M.D., Lavine, A.S., 2000, Thermal Aspects of Grinding: The Case of Upgrinding. *Journal of Manufacturing Science and Engineering*, Vol.122, P. 605-11
- [8] Ju, Y., Farris, T.N., Chandrasekar, S., 1998, Theoretical Analysis of Heat Partition and Temperatures in Grinding. *Journal of Tribology*, Vol. 120, P. 789-94
- [9] Gu, R.J., Shillor, M., Barber, G.C., Jen, T., 2004, Thermal analysis of the grinding process. *Mathematical and Computer Modelling*, Vol. 39 (9-10), P. 991-1003
- [10] Kundrák, J., Markopoulos, A.P., Karkalos, N.E., 2017, Numerical Simulation of Grinding with Realistic Representation of Grinding Wheel and Workpiece Movements: A Finite Volumes Study. *Procedia CIRP*, Vol. 58, P. 275-80
- [11] Rasim, M., 2016, Modellierung der Wärmeentstehung im Schleifprozess in Abhängigkeit von der Schleifscheibentopographie. Dissertation RWTH Aachen
- [12] Brinksmeier, E., Wilkens, A., Giese, E., 2009, In-Process temperature measurement during grinding. 3rd Vienna Int. Conference Nano Technology, Vienna, Austria
- [13] Sakakura, M., Ohnishi, T., Shinoda, T., Ohashi, K., Tsukamoto, S., Inasaki, I., 2012, Temperature distribution in a workpiece during cylindrical plunge grinding, *Prod. Eng. Res. Devel.*, Vol. 6 (2), P. 149-55
- [14] Kohli S., Guo, C., Malkin, S., 1995, Energy Partition to the Workpiece for Grinding with Aluminum Oxide and CBN Abrasive Wheels. *J. Eng. Ind.*, Vol. 117 (2), P. 160-68

# Development of multidimensional characteristic diagrams for the real-time correction of thermally caused TCP-displacements in precise machining

*M. Putz<sup>a,b</sup>, C. Oppermann<sup>a</sup>, M. Bräunig<sup>b</sup>*

<sup>a</sup>Fraunhofer Institute for Machine Tools and Forming Technology IWU,  
09126 Chemnitz, Germany

<sup>b</sup>Institute for Machine Tools and Production Processes IWP, Technische Universität Chemnitz,  
09107 Chemnitz, Germany

**Abstract.** In the present paper the development of characteristic diagrams of cutting processes which relate the Tool Center Point (TCP) displacement to thermal tool load is explained. The heat fluxes in the system workpiece –chip –tool are estimated by means of FEA (finite element analysis) in order to achieve multidimensional dependencies as function of the cutting parameters. The approach allows the real-time correction of tool paths within the machine tool control crucial in precise machining operations. Model verification and result comparison with cutting experiments have been realized.

Peer-review under responsibility of the International Scientific Committee in the person of the Conference Chair Prof. Steffen Ihlenfeldt.

**Keywords:** FEA; Model verification; TCP-displacement; Thermal error; Characteristic diagram; Heat source; Temperature measurement; Thermal displacements; Machine Tools

## 1 Introduction

### Nomenclature

$a_e$	Cutting width	$a_p$	Cutting thickness
$d$	Tool diameter	$f_z$	Feed per tooth
$L_s$	Supported tool length	$L_u$	Unsupported tool length
$V_c$	Cutting speed	$Q$	Heat
$\alpha$	Heat transfer coefficient	$\rho$	Density
$\gamma$	Rake angle	$\vartheta$	Temperature

Nowadays dry machining operations play an increasing role in manufacturing due to environment, health care and economical requirements. These exigencies stand in contradiction to minimization of tool wear caused by high process temperatures and tool deformations caused by these high temperatures.

In precise machining operations controlling the introduced heat is important to keep the tool center point (TCP) displacements constant and exactly known [1,2]. For the estimation of these thermal deformations in tool and clamping devices heat generation, partitioning and temperature distribution in machining has to be well known.

## 2 Correction approach

The authors have developed a combined numerical / analytical / experimental approach for the estimation of heat distribution and resulting deformations in milling operations as an interrupted cutting process [3-6], an overview is shown in Fig. 1. This procedure is based on relevant investigation about generated heat ([7] among others), its measurement ([8] among others), heat fluxes and their partitioning in tool, workpiece and chips ([9,10], among others) and analytical solution ([13] among others).

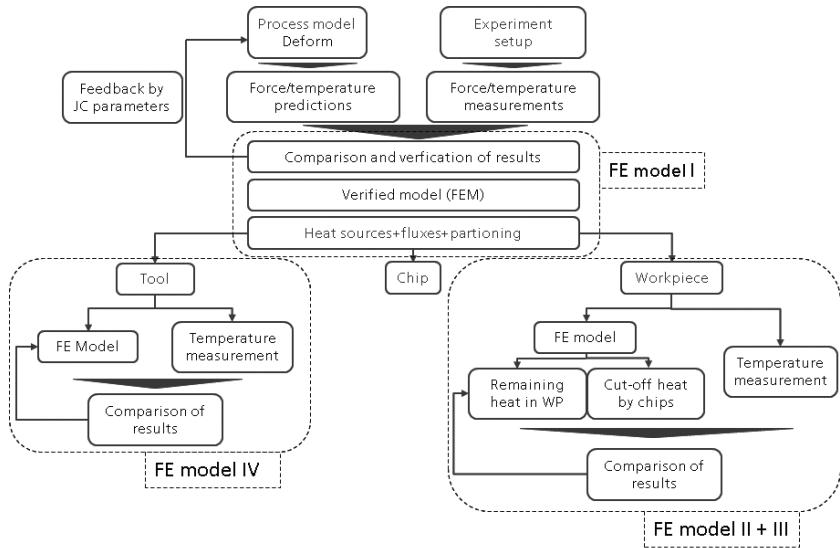


Fig. 1. Workflow

In the present work this simulative modus operandi is executed for a variety of different cutting conditions, like cutting speed, feed rate, tool geometry, cutting process, machined material etc. with the aim of developing a multidimensional characteristic diagram for the real-time correction of TCP displacements. The analytical and experimental model verifications are no longer executed.

## 2.1 Operating conditions as first part of diagram domain

Different operating conditions are variables for the characteristic diagram to be developed. These independent variables serve as input and are chosen according to relevant operations in industrial applications [12, 13].

A milling operation has been investigated, variations realized are:

- Cutting speed  $v_c$ : [50; 100; 200; 300] m/min
- Feed rate per tooth  $f_z$ : [0.05; 0.1; 0.2] mm/tooth
- Rake angle  $\gamma$ : [-5; 0; 5; 10]°
- Cutting width  $a_e$ : [1; 2; 3; 4] mm
- Cutting depth  $a_p$ : [2; 5; 10; 20] mm
- Workpiece material: [structural steel, cast iron; nitriding steel, heat treatment steel, heat resisting steel, 2000 series aluminum alloy, 7000 series aluminum alloy]
- Cutting operation: [down-milling, up-milling]

First, each variable has been varied based on the basic configuration (down-milling,  $v_c=100$  m/min,  $f_z=0.1$  mm/tooth,  $a_e=3$  mm,  $a_p=5$  mm, workpiece material: structural steel (S235JR)), keeping all variables constant. In order to have a densely defined characteristic diagram afterwards all meaningful cross variations, i.e. most of all possible combinations of the variables, have been realized. Of course not all of the over 9000 possible combinations can be simulated. Some industrially applied configurations, e.g. negative clearance angles can be simulated, but would provoke numerically high efforts, so they are not investigated. But nevertheless it is shown that a wide range of possible cutting operations can be taken into account predicting the resulting TCP displacements.

For the process simulation a primary processing time of 77 s has been used, where the tool is in engagement. Afterwards a cooling of 11 s as secondary processing time is added. These concrete operation times have been taken from former cutting experiments [4] whose measurements served for the calibration and verification of the models.

## 2.2 Tool geometry as second part of diagram domain

Additionally to the operation conditions the tool geometry has been varied to investigate its influence on the TCP displacement. Due to the long and slim geometry of the tool the TCP displacement is designated through its axial elongation. The basic geometry with three cutting inserts, unsupported length  $l_u = 62$  mm, supported length  $l_s = 40$  mm and diameter  $d = 20$  mm is shown in Fig. 2.

In case of the unsupported length, which is more relevant for the temperature distribution and therefore for the corresponding displacement field, the basic length has been scaled by the factor 2/3 in both senses, which corresponds best to commercially available tools. The diameter has been doubled and bisected.

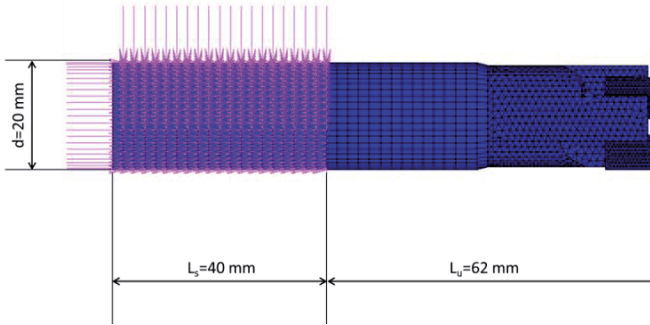


Fig. 2: Tool geometry, with supported length  $L_s$ , unsupported length  $L_u$  and diameter  $d$

Variations realized are:

- Unsupported length  $l_u$ : [42; 62; 93] mm
- Diameter  $d$ : [10; 20; 40] mm

Furthermore a variation of shaft and insert material would be reasonable, but due to the broad number of variations in operation conditions this aspect could not be investigated.

### 2.3 Simulation procedure

Because the experimental model verification, mainly done by FE (finite element) model II and III (see Fig. 1), has already been realized in [3-5] and analytically been proved in [6] in this work only the heat flux partitioning in Deform® is fulfilled. The main result, the heat flux into the tool, is taken as input parameter for FE model IV, where the prediction of the thermo elastic expansion within MSC.Marc® takes place. After several purely thermal simulations within MSC.Marc® a linear correlation between heat flux and axial elongation could be determined, shown exemplarily for  $d = 20\text{ mm}$  in Fig. 3. This is appropriate because of the linearity of the estimated thermo elastic expansion  $\Delta L$  and its corresponding linear thermal expansion coefficient  $\alpha$  (see Eq. 1) as a linear approximation of the calculation of the Taylor series of the exponential function and the heat as the volume integral over  $\rho$ ,  $c_p$  and  $\Delta\vartheta$  (see Eq. 2). Though the expansion coefficient is not constant for temperature variation. This correlation is only valid for the considered tool geometry.

$$\Delta L = \alpha \cdot L_0 \cdot \Delta \vartheta \quad (\text{Eq. 1})$$

$$Q = \int^V \rho \cdot c_p \cdot \Delta \vartheta \, dV \quad (\text{Eq. 2})$$

with  $\Delta L$ =expansion length,  $\alpha$ =thermal expansion coefficient,  $L_0$ = initial length,  $V$ =tool volume,  $\Delta \vartheta$ =temperature difference,  $Q$ = heat,  $\rho$ = density and  $c_p$ =heat capacity

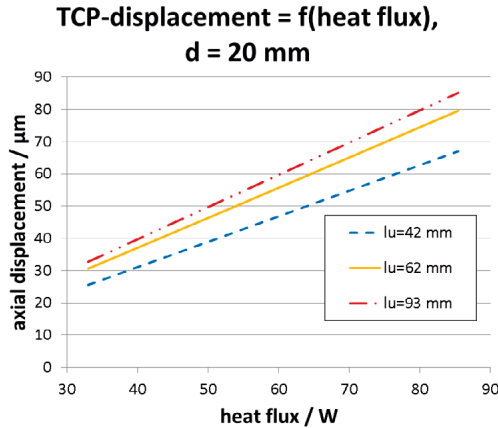


Fig. 3: Correlation Heat flux – TCP displacement for unsupported lengths  $L_u$ =[52; 62; 93] mm and tool diameter  $d$ =20 mm

## 2.4 Results

The resulting TCP displacements are shown in the following diagrams. Due to clarity aspects and shortage of space not all results can be presented.

The first diagram, Fig. 4, shows the TCP displacement as function of cutting speed and feed per tooth for the basic geometry and workpiece material, where the color code corresponds to certain ranges at the ordinate. In Fig. 5 a) the same diagram is shown for a long and slim tool and in Fig. 5 b) for a short and compact tool. The shape of all three diagrams stays the same, only the absolute value of the displacement varies. This results from the same tool, as a matter of principle (peripheral milling cutter with three inserts), which has only been scaled. Completely different tools would have different shapes.

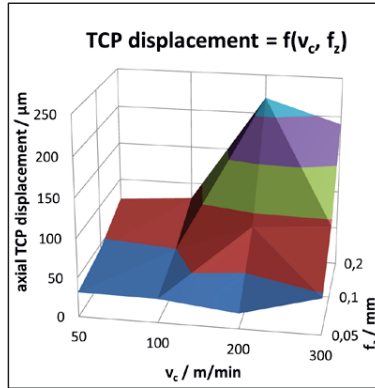


Fig. 4: TCP displacement for basic configuration  $l_u=62$  mm and  $d=20$  mm

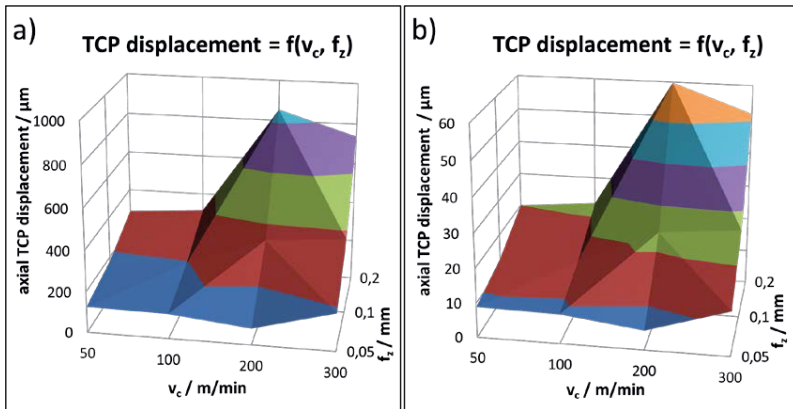


Fig. 5: TCP displacement variations for a)  $l_u=93$  mm and  $d=10$  mm, b)  $l_u=42$  mm and  $d=40$  mm

The steep rise at cutting speed  $v_c=100$  m/min results less relevant when taking into account the non-constant spacing on the abscissa. Nevertheless for low cutting speeds a big amount of heat is conducted into the workpiece due to the sufficiently high heat conduction, for higher cutting speeds the heat conduction begins getting too slow and more heat flows into the tool. The decrease at cutting speed  $v_c=200$  m/min can be explained by the higher ratio of the cutting heat source staying in the chip and being cut of in the consecutive engagement. With rising cutting speed the chip thickness is decreasing because of the lower local yield stress due to higher material temperatures. The heat is concentrating due to the low heat conduction. Although higher strain rates result in an increase of yield stress, the contribution of the temperature in yield stress decrease is bigger.

The differing absolute values can be explained thermodynamically with the different amount of heat which can be accumulated. The inserted heat  $Q$ , provoked by the cutting heat source, stays the same. While the volume  $V$  increases and material parameters  $\rho$  and  $c_p$  are constant the temperature change  $\Delta\theta$  and the resulting expansion  $\Delta L$  must consequently decrease, and vice versa, see Eq. 1 and 2.

As written in chapter 2.1 the effect of much more variables on the TCP displacement than only cutting speed  $v_c$  and feed per tooth  $f_z$  has been investigated. Fig. 6 to Fig. 12 represent certain dependencies between TCP displacement and geometry of the cutting edge, cutting conditions and tool material, among others. All diagrams are valid for the basic tool geometry of  $l_u=62$  mm and  $d=20$  mm. For different tool geometries the shape of the diagrams stays the same, only absolute values differ, as described in the diagrams before. For clarity aspects the dependence is only shown two-dimensionally.

The low displacement values for cutting speed  $v_c = 50$  m/min are resulting from the fact that no real comma shaped chip is developing, the material is compressed in front of the cutting face.

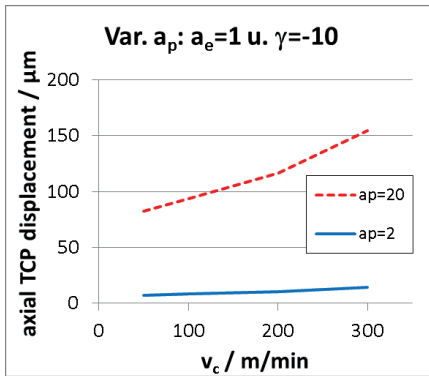


Fig. 6: TCP displacement for rake angle  $\gamma=-10^\circ$  and cutting width  $a_e=1$  mm for cutting thickness  $a_p=[2; 20]$  mm

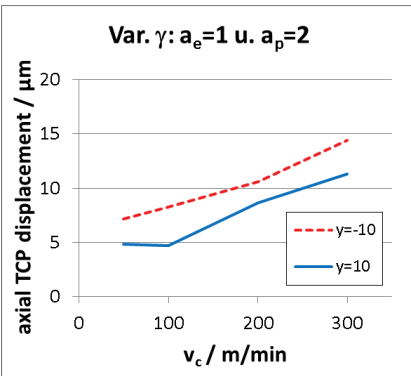


Fig. 7: TCP displacement for cutting width  $a_e=1$  mm, cutting thickness  $a_p=2$  mm and rake angle  $\gamma=[-10^\circ; 10^\circ]$



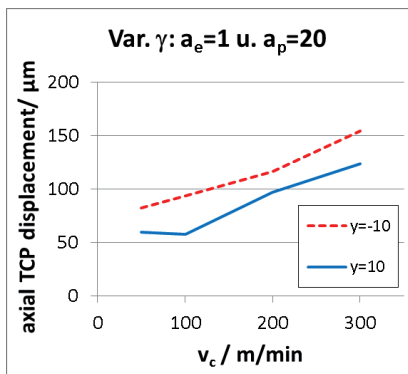


Fig. 8: TCP displacement for cutting width  $a_e=1$  mm, cutting thickness  $a_p=20$  mm and rake angle  $\gamma=[-10^\circ; 10^\circ]$

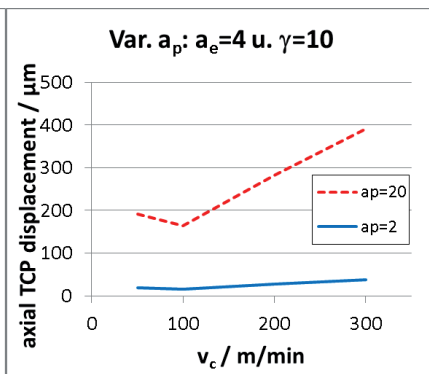


Fig. 9: TCP displacement for rake angle  $\gamma=10^\circ$ , cutting width  $a_e=4$  mm and cutting depth  $a_p=[2; 20]$  mm

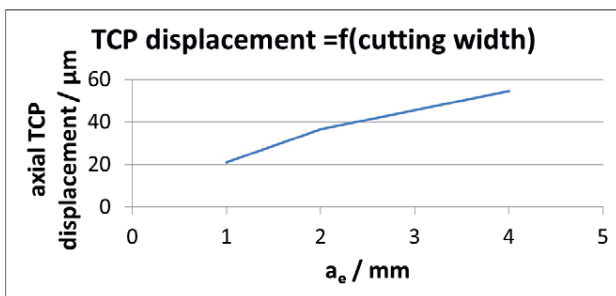


Fig. 10: TCP displacement dependent on cutting width  $a_e$

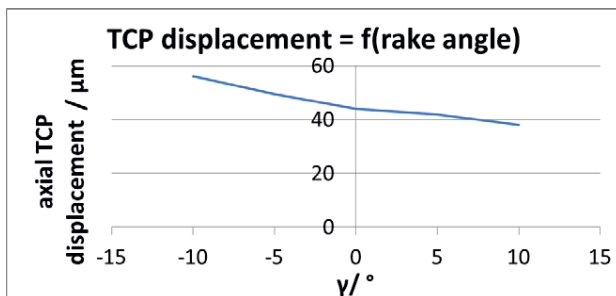


Fig. 11: TCP displacement dependent on rake angle  $\gamma$

The decreasing TCP displacement in case of increasing rake angles (see Fig. 11) is explained by the smaller cutting heat source due to easier material flow and

less compression in front of the cutting face, as already explained with increasing cutting speeds.

Instead a decrease of the rake angle, getting even negative, results again in a compression of the material, provoking higher cutting heat sources and therefore higher TCP displacements.

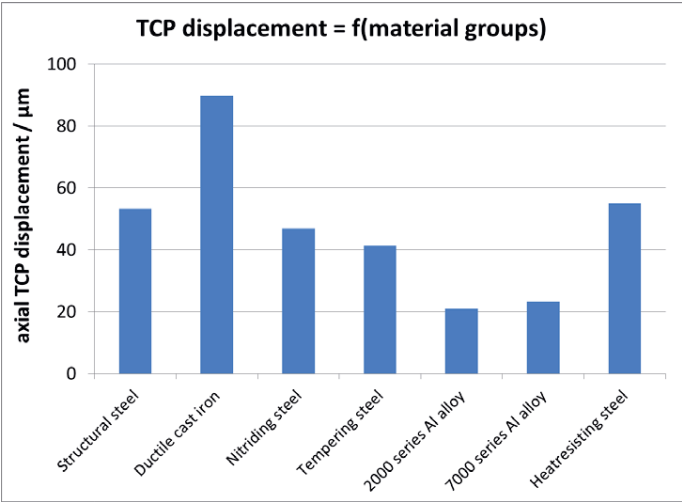


Fig. 12: TCP displacement dependent on material groups

The dependence of TCP displacement on material groups of the machined workpiece is related to thermal issues like heat conduction, heat capacity and thermal expansion. This very complex correlation cannot be simplified more.

### 2.5 Summary

The actual work has shown the application of a numerical approach for the prediction of tool expansion due to the generated heat in cutting operations. In former works [3] the exactness of these approaches has been proved with an error less or equal 10 %, so the contribution of the works is relevant especially in case of precise machining.

The TCP displacements here calculated and stored in the machine control as characteristic diagrams can solve thermally induced inaccuracies, especially necessary in case of precise machining. The domain of the characteristic maps can be refined and adapted to other ranges of operation conditions. The only limitation of this approach is the necessity of all thermal and mechanical material parameters for the exact numerical representation.

## Acknowledgements

*The authors thank the German Research Foundation (DFG) for the support within the Collaborative Research Center SFB Transregio 96 “Thermo-energetic Design of Machine Tools”, sub-project A01.*

## 3 References

- [1] Neugebauer R., 2012. Werkzeugmaschinen – Aufbau, Funktion und Anwendung von spanenden und abtragenden Werkzeugmaschinen. Springer, Berlin, Heidelberg
- [2] Großmann K. (Ed.), 2015. Thermo-energetic Design of Machine Tools, Lecture Notes in Production Engineering, Springer
- [3] Putz M., Oppermann C., Semmler U., Bräunig M., Karagüzel U., 2017. Consistent simulation strategy for heat sources and fluxes in milling. 10th CIRP ICME, Procedia CIRP, 62, 239-244.
- [4] Putz M., Schmidt G., Semmler U., Oppermann C., Bräunig M., Karagüzel U., 2016. Modeling of heat fluxes during machining and their effects on thermal deformation of the cutting tool, 7th CIRP HPC, Procedia CIRP, 46, 611-614.
- [5] Putz M., Schmidt G., Semmler U., Dix M., Bräunig M., Brockmann M., Gierling S., 2015. Heat Flux in Cutting: Importance, Simulation and Validation. 15th CIRP CMMO, Procedia CIRP, 31, 334-339.
- [6] Putz, M., Oppermann, C. Bräunig, M, Karagüzel, U., 2017. Heat sources and fluxes in milling: Comparison of numerical, analytical and experimental results, 16th CIRP CMMO, Procedia CIRP, 58, 97-103
- [7] Shaw M.C., 1984. Metal Cutting Principles, Clarendon Oxford.
- [8] Davies MA, Ueda T, M'Saoubi R, Mullany B, Cooke AL (2007) On The Measurement of Temperature in Material Removal Processes. CIRP Annals - Manufacturing Technology 56(2): 581-604
- [9] Takeuchi Y., Sakamoto M., Sata, T., 1982. Improvement in the working accuracy of an NC lathe by compensating for thermal expansion. Precision Engineering, 4(1), 19-24.
- [10] Blok H., 1938. Theoretical study of Temperature Rise at Surfaces of Actual Contact Under Oiliness Lubricating Conditions, Proceedings of the General Discussion on Lubrication and Lubricants, The Institution of Mechanical Engineers, London, 222–235.
- [11] Stephenson G., Ardmore, M. P. Advanced Mathematical Methods for Engineering and Science students, Cambridge University Press, London, 1990, 192
- [12] König, W., 1990. Fertigungsverfahren Band 1,2, VDI-Verlag, Düsseldorf
- [13] Tönshoff, H. K., 1995. Spanen – Grundlagen – Springer Lehrbuch, Springer Verlag, Berlin, Heidelberg, New York

# Measurement of Near Cutting Edge Temperatures in the Single Point Diamond Turning Process

*E. Uhlmann<sup>a,b</sup>, D. Oberschmidt<sup>b</sup>, S. Frenzel<sup>a</sup>, J. Polte<sup>b</sup>*

<sup>a</sup>Institute for Machine Tools and Factory Management IWF, Technische Universität Berlin,  
10587 Berlin, Germany

<sup>b</sup>Fraunhofer Institute for Production Systems and Design Technology IPK,  
10587 Berlin, Germany

**Abstract.** Thermomechanical and chemical wear mechanisms influence the contact region between diamond tool and workpiece during ultraprecision(UP)-machining. The measurement of near cutting edge temperatures in the single point diamond turning process provides the opportunity of a holistic consideration of diamond tool wear to complement existing temperature models. For this reason thin film thermocouple arrays has been designed, fabricated and integrated in a diamond tool, which were used for cutting tests and process simulations. Hence, a connection between process temperatures and diamond tool wear could be identified.

Peer-review under responsibility of the International Scientific Committee in the person of the Conference Chair Prof. Steffen Ihlenfeldt.

*Keywords:* Thin film thermocouples; Single point diamond turning; Temperature measurement; Sensor integration

---

## 1 Introduction

Cutting temperatures affect tool wear, surface integrity and accuracy in ultra-precision processes. The aim of this paper is the expansion of the basic knowledge of near cutting edge temperatures in single point diamond turning processes. This goal should be achieved through the integration of thin film thermocouple (TC) arrays into the diamond tool. This approach combines an experimental and numerical process analysis and therefore provides a pragmatic technology for process monitoring.

### 1.1 State of the Art: temperature measurements in UP-machining

The embedded TC was first patented by H. Verbeek in DRP No. 359477. The tool-chip-TC was introduced shortly thereafter by SHORE [1], GOTTWIEN [2], HERBERT [3] and substantially optimized by BOSTON ET AL. [4]. Measured and

predicted temperatures near the cutting zone differ broadly from room temperature to several hundred Kelvin at certain UP-processes [5, 6, 7, 8]. MORIWAKI ET AL. [5] investigated the effect of cutting heat on the machining accuracy in UP diamond turning. Temperature differences of  $\Delta\vartheta = 280.65\text{ K}$  were measured in the tool shank between a new and a worn tool after cutting Aluminium and Copper for a path length  $l_c = 200\text{ km}$  of. UEDA ET AL. [6] performed temperature measurements by using infrared radiation two-colour pyrometer directly inserted under the single crystal diamond. The maximum temperature during turning varied between  $\vartheta_{Al} = 190\text{ }^{\circ}\text{C}$  and  $\vartheta_{Cu} = 220\text{ }^{\circ}\text{C}$ . For material removal processes in general DAVIES ET AL. [9] reviewed temperature measurement methods, e.g. resistance methods, thermocouple and spectral radiation thermometry.

## 1.2 Characteristics of Thermocouples

Thermocouples are passive sensors based on the thermoelectric effect [10]. If there is a temperature gradient between the connection point and the free conductor ends, the material-dependent velocity of the electrons  $v_e$  differs in each of these materials. The result is a measurable thermoelectric voltage per degree Celsius in the range of  $5\text{ mV}/^{\circ}\text{C} \leq U_t/^{\circ}\text{C} \leq 100\text{ mV}/^{\circ}\text{C}$  (see Fig. 1).

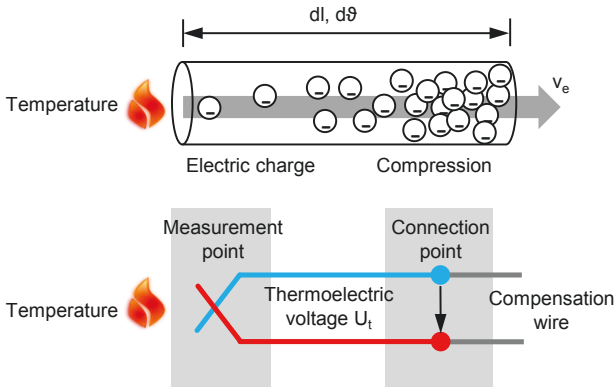


Fig. 1. Functional principle of thermocouples.

Thin film TCs are generally used for time-resolved temperature measurements. TCs have an extremely low mass  $m$  and heat capacity  $Q$  because of their low layer thickness in the range  $100\text{ nm} \leq s \leq 1,000\text{ nm}$ . This results in a low thermal time constant in the range of  $t = 10\text{ ns}$  [10]. However, the selection and interpretation of the thin film TC-measurement has a high complexity.

## 2 The sensor integrated diamond tool

The sensor design for the production of an integratable thin film TC array depends on the process-related and spatial conditions of the diamond tool. The final sensor layout has been designed for both production and measurement purposes. With the extension of the number of measuring points it is possible to detect two-dimensional temperature fields in contrast to point-like temperature measurements with an one-channel TC. Therefore, an 8-channel sensor design was provided for the experimental setup. Challenges for manufacturing the thin film TC array were

- resist edge roundings depending on the coating temperature,
- geometric precision of the structure alignment,
- lithography parameters and coating adhesion on different substrate materials and
- the particle-free TC fabrication.

### 2.1 Fabrication of thin film thermocouple arrays

The TCs are produced by a combined PVD coating and photolithography process (lift-off process, see Fig. 2). The cleaning procedure for the substrate preparation comprises the cleaning in an ultrasonic bath (US) in acetone, isopropanol and distilled water, carried out in a clean room ISO7 according to EN ISO 14644. The aim of the substrate masking (step 2 – 4 and 7 – 9) is to create a structure - the essential design feature - which is characterized by two crossing TC paths. These are generated in two iterative process loops. For the lift off process (step 6 and 11) a negative resist was used.

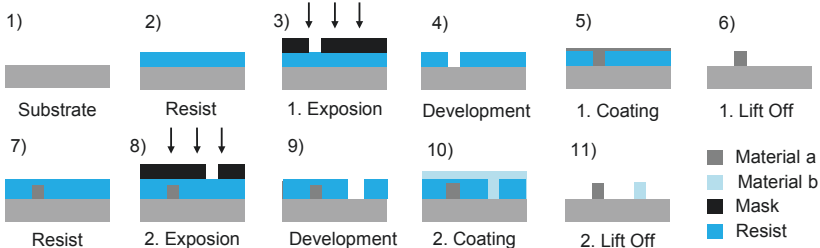


Fig. 2. Conceptual fabrication of thin film TCs.

For the fabrication of TCs from Ni/NiCr (k-type TC) and high temperature resistant W/WRe (c-type TC), the magnetron sputtering process was performed (step 5 and 10). The DC/HF magnetron sputtering, carried out on a LH Z400

from LEYBOLD-HERAUS, Cologne, is suitable for temperature-sensitive lift-off processes due to the low thermal loads in the range of  $50\text{ }^{\circ}\text{C} < \vartheta < 150\text{ }^{\circ}\text{C}$ . The layer thickness of the TC path is between  $100\text{ nm} \leq s \leq 300\text{ nm}$ . To finish, acetone lifts the non-exposed areas after coating (step 6 and 11). A final version of a successfully fabricated k-type thin film TC on aluminum oxide substrate is shown in figure 3.

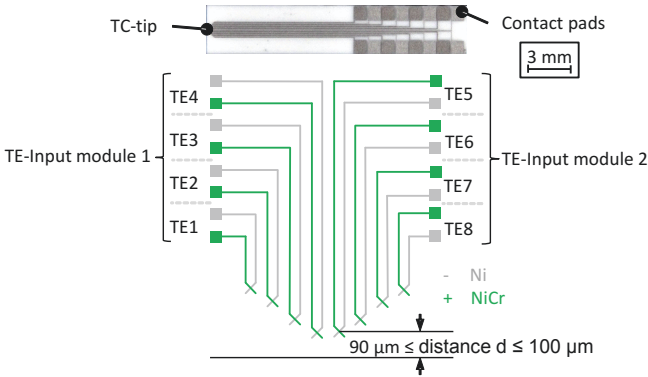


Fig. 3. Characteristics of a fabricated k-type thin film TC on aluminum oxide substrate.

## 2.2 Integration in the diamond tool

Generally, a solid holder and connecting system are crucial for reliable TC-temperature measurements. As it is necessary to change the diamond, a tool fixture has been designed to provide a reproducible connection. The diamond and the TC are mounted to each other by a force-locked connection (see Fig. 4).

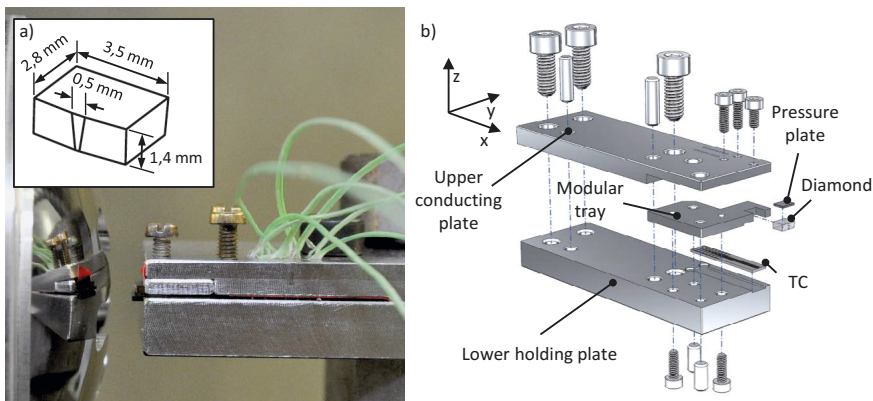


Fig. 4. (a) Experimental setup and the diamond insert; (b) exploded view of the modular holding system.

The tool holder has a modular design, which allows clear and reproducible positioning of the diamond and the TC. The diamond thickness varies between  $0.5 \text{ mm} \leq s \leq 1.4 \text{ mm}$ . The distance of the TC-tip to the cutting edge measures between  $262 \text{ } \mu\text{m} \leq d_z \leq 272 \text{ } \mu\text{m}$  in z-direction and in y-direction between  $0.5 \text{ mm} \leq d_y \leq 1.4 \text{ mm}$ . The TC-calibration was performed according to the guidelines of the NATIONAL INSTITUTE OF STANDARDS AND TECHNOLOGY (NIST).

### 3 Experimental temperature measurements

The acquisition of the experimentally obtained TC-temperature data requires a measurement chain, which is exemplary shown in figure 5.

In fact, the signal transmission is carried out exclusively with corresponding TC material until the signal reaches the input module. First the thermoelectric voltage, which is an analog signal produced by the TC, needs to be amplified. The integrated analog amplifier produces a high level output from a TC signal by combining a cold-junction compensation with a precalibrated amplifier. The amplified signal is converted to a digital signal in the analog input module and transferred to the data acquisition system (DAQ). The DAQ-system operates and coordinates the timing, synchronization and data transfer between the input module and an external host computer. Finally, the digital measurement data can be processed with the graphical programming system LABVIEW, USA. Overall the sampling rate per TC of the introduced measuring chain is  $t_s \approx 70 \text{ ms}$ .



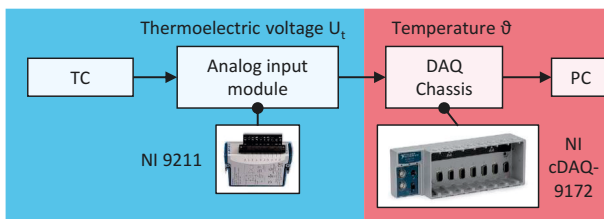


Fig. 5. Temperature measurement chain for thin film TCs.

## 4 Temperature distribution during cutting

### 4.1 Measured temperatures during cutting

The experimental setup was carried out on the ultra-precision machine tool Nanotech®350 FG from MOORE NANOTECHNOLOGIES, USA. Natural (MND), CVD and HTHP facet diamond tools have been investigated in a continuous SPDT process. As a result the outer TCs measured a stronger temperature gradient  $\Delta\vartheta$  than the inner TCs (see fig. 3). This is caused by the compressed air, but is unavoidable to prevent the jamming of chips in the diamond tool holder. Both the chip jamming and the compressed air influence the thin film TC-temperature measurement significantly. The experimental results show that the cutting temperature  $\vartheta$  increases with increasing depth of cut  $a_p$  (see Fig. 6a). However, a continuous temperature rise in relation to higher depths of cut  $a_p$  could not be observed. Based on the average thin film TC temperature data for cut  $n = 3$  and  $n = 10$ , it can be shown that the cutting temperature  $\vartheta$  increases with increasing cutting time  $t$  (see Fig. 6b). Summarizing the experimental results, it was not possible to provide an explicit statement about an exact three-dimensional temperature field as well as the diamond surface temperature. The reason is the insufficient thermal insulation of the cutting edge due to the intervention on the tool holder system.

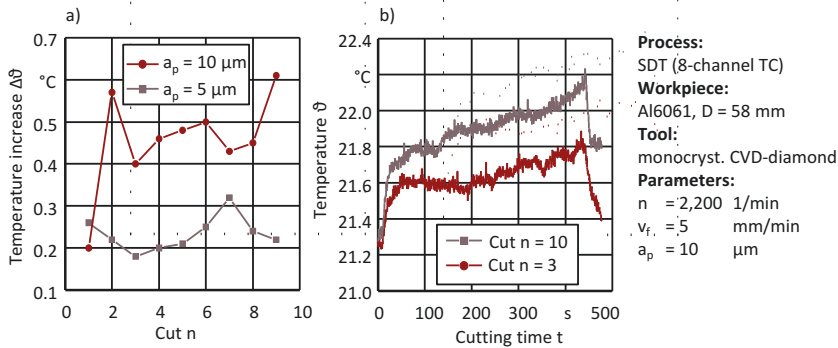


Fig. 6. Experimental thin film temperature data regarding (a) Impact of depth of cut  $a_p$ ; (b) cutting time  $t$  on the cutting temperature  $\theta$ .

## 4.2 Modelling of the cutting temperatures on the cutting edge

Two 3D-FEM-simulations were performed to determine the maximum temperatures  $\vartheta_{\max}$  at the diamond cutting edge. In order to consider both thermal and cutting processes in a FEM-simulation, a mechanical and a thermal FE simulation have been implemented with ANSYS WORKBENCH and DEFORM-3D. The temperature profile is characterized by the very high thermal conductivity  $\lambda$  of the diamond. The isotherms, in distance to the cutting edge, depict temperature differences of  $\Delta\vartheta = 1.0 \times 10^{-3}$  °C whereas near cutting edge isotherms are notable condensed (see Fig. 7). The temperature gradient  $\partial\vartheta/\partial z$  reaches its maximum in the area of the cutting edge. The simulations were performed for diamond tools with a height of  $0.8 \text{ mm} \leq 1.1 \text{ mm}$  as well as the materials Al6061 and OFHC-Cu on the basis of table 1. Generally, the cutting temperature difference  $\Delta\vartheta$  of OFHC-Cu ( $\Delta\vartheta = 0.750 \text{ K}$ ) is higher than of Al6061 ( $\Delta\vartheta = 0.029 \text{ K}$ ). At high cutting velocity  $v_c$  (+) the thin film TC measures a significantly higher cutting temperature of OFHC-Cu ( $\vartheta_{\text{Cu}} = 21.632$  °C) than of Al6061 ( $\vartheta_{\text{Al}} = 21.326$  °C). On the contrary the cutting temperature of OFHC-Cu ( $\vartheta_{\text{Cu}} = 20.882$  °C) is lower than of Al6061 ( $\vartheta_{\text{Al}} = 21.297$  °C) with regard to lower cutting velocity  $v_c$  (-) under the same conditions.

Table 1. Simulated parameter set (DoE)

Parameter	Maximum +	Minimum -
Feed velocity $v_f$ [mm/min]	5	2.5
Cutting speed $v_c$ [m/min]	400	200
Depth of cut $a_p$ [ $\mu\text{m}$ ]	5	2.5

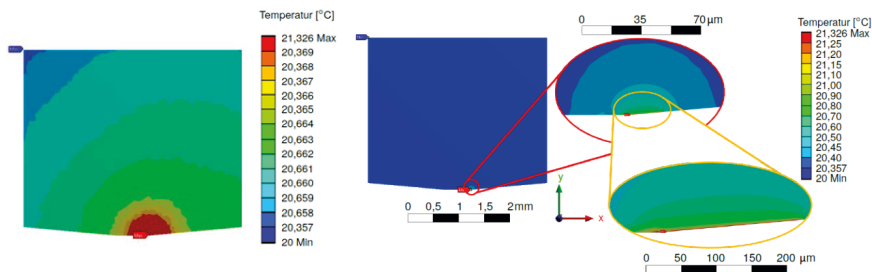


Fig. 7. Simulation results for the material Al6061; left: isotherms in the stationary temperature profile; right: stationary temperature profile of the diamond tool in the area of the cutting edge

## 5 Outlook: process monitoring

The use of thin film TCs is mainly suitable for manual process control during SPDT. Unfortunately an automated process control cannot be implemented without complex intervention in the machine control and a process-critical time delay. However, a user interface could be programmed using LabVIEW, which allows temperature warnings and partly automated zero point determination to be implemented using the thin film thermocouple signals (see Fig. 8). For example, whenever the experimentally determined critical temperature  $\vartheta$  is exceeded, a visual signal lights up to inform the machine operator about a process correction or a tool change.

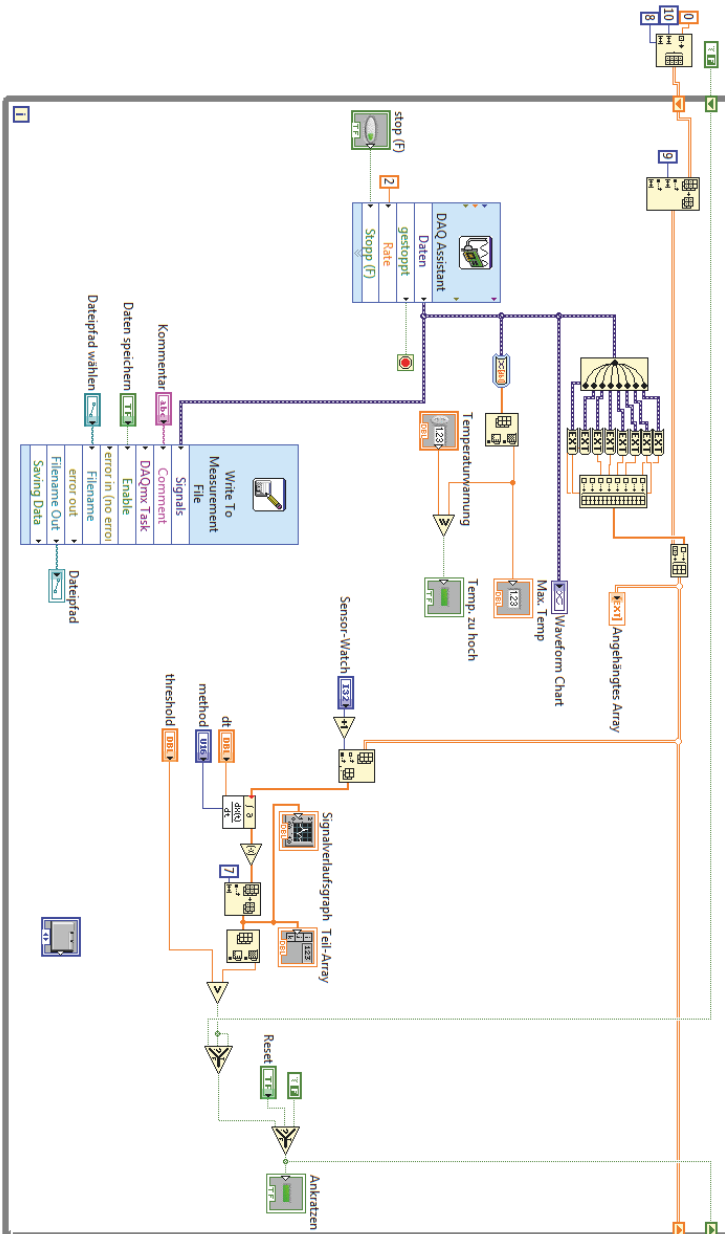


Fig. 8. Block-diagram of the LabVIEW-Program

## 6 Conclusion

Within the scope of a public funded research project a thin film TC field (k-type: Ni/NiCr) was integrated into a UP-diamond tool and used experimentally for SPDT processes.

Two major effects could be identified in the cutting experiments. With regard to the depth of cut  $a_p$ , it could be shown that the cutting temperature  $\vartheta$  increases per thin film TC with increasing cutting depth  $a_p$ . Furthermore, it was possible to show the cutting temperature  $\vartheta$  increases with increasing cutting time  $t$ . The performed SPDT experiments with 8-channel thin film TCs confirmed that the compressed air had a significant influence on the cutting temperature  $\vartheta$  near the cutting edge and thus on the temperature measurement data itself. As a result further investigations with different experimental setup regarding the air cooling will be performed. The peripheral arranged TCs showed a bigger temperature difference  $\Delta\vartheta$  than the centrally arranged TCs. However, it was not possible to determine a three-dimensional temperature field as well as the temperature of the diamond surface. The thermal insulation of the cutting edge, which is crucial for this purpose, could not be achieved under the circumstances.

In summary, the maximum temperature difference  $\Delta\vartheta_{\max}$  measured with the wire TC ( $\Delta\vartheta_{\max} = 0.338$  K) is 7 % smaller than the simulated temperature difference  $\Delta\vartheta_{\max} = 0.363$  K. The distance from the wire TC to the diamond edge was  $d = 1.1$  mm. The first cut using the thin film TCs with a cutting distance  $x = 20$  mm and (+++)-parameters produced a maximum temperature difference  $\Delta\vartheta_{\max} = 0.29$  K. The distance from the nearest thin film TC to the diamond edge was  $d = 100$   $\mu\text{m}$ . Therefore the measured maximum temperature difference is 20 % smaller than the temperature difference of the simulation.

### Acknowledgements

*The authors wish to acknowledge for the financial support provided for this fundamental research project by the GERMAN RESEARCH FOUNDATION (DFG).*

## 7 References

- [1] Shore, H., 1924. Tool and Chip Temperatures in Machine Shop Practice. M.I.T., M.A. thesis.
- [2] Gottwein, K., 1925. Die Messung der Schneidentemperatur beim Abdrehen von Flusseisen. Maschinenbau 4, p. 1129 – 1135.

- [3] Herbert, E. G., 1926. The Measurement of Cutting Temperatures. Proc. Inst. Mech. Eng., 1, p. 289 – 329.
- [4] Boston, O. W., Gilbert, W. W., 1935. Cutting temperatures developed by single point turning tools. Trans. Of the American Soc. Of Met., 23:703.
- [5] Oberschmidt, D., 2009. Mikrofräsen mit zylindrischen Diamant-Schaftfräs Werkzeugen. Berichte aus dem Produktionstechnischen Zentrum Berlin. Hrsg.: Uhlmann, E. Stuttgart: Fraunhofer IRB.
- [6] Moriwaki, T., Horiuchi, A., Okuda, K., 1990. Effect of Cutting Heat on Machining Accuracy in Ultra-Precision Diamond Turning. CIRP Annals – Manufacturing Technology, Volume 39, Issue 1, p. 81 – 84.
- [7] Ueda, T.; Sato, M.; Nakayama, K., 1998. The temperature of a single crystal diamond tool in turning. CIRP Annals – Manufacturing Technology, Volume 47, Issue 1, p. 41 – 44.
- [8] Shimada, S., Inamura, T., Higuchi, M., Tanaka, H., Ikawa, N., 2000. Suppression of tool wear in diamond turning of copper under reduced oxygen atmosphere. CIRP Annals – Manufacturing Technology, Volume 49, Issue 1, p. 21 – 25.
- [9] Davies, M. A., Ueda, T., M'Saoubi, R. M., Mullany, B., Cooke, A. L., 2007. On The Measurement of Temperature in Material Removal Processes. CIRP Annals - Manufacturing Technology, Volume 56, Issue 2, p. 581 – 604.
- [10] Fraden, J., 2010. Handbook of Modern Sensors - Physics, Design and Application. New York u. a.: Springer.



# Investigation of Heat Flows during the Milling Processes through Infrared Thermography and Inverse Modeling

*T. Helmig<sup>b</sup>, T. Augspurger<sup>a</sup>, Y. Frekers<sup>b</sup>, B. Döbbeler<sup>a</sup>, F. Klocke<sup>a</sup>, R. Kneer<sup>b</sup>*

<sup>a</sup>Laboratory of Machine Tools and Production Engineering WZL, RWTH Aachen University, Steinbachstr. 19, 52074 Aachen, Germany

<sup>b</sup>Institute of Heat and Mass Transfer WSA, RWTH Aachen University, Augustinerbach 6, 52056 Aachen, Germany

**Abstract.** Quantifying the heat flow into the tool and subsequently into the tool clamping is of paramount importance for accurately predicting the thermal behavior of the manufacturing process. Yet there is a lack of methods for measuring these heat flows and as well for determining them and their dependence on the process parameters. The heat flow acts as a thermal boundary condition on a resulting transient temperature field within the cutting tool, thus, posing a so-called inverse problem. Experimental investigations by means of infrared thermography are conducted for a milling process, in order to measure this transient temperature field and using it to calculate affiliated heat flows into the tool, applying transient temperature models or thermodynamic considerations.

Peer-review under responsibility of the International Scientific Committee in the person of the Conference Chair Prof. Steffen Ihlenfeldt.

*Keywords:* Milling; Transient heat flow; Tool; Measurement; Infrared thermography

---

## 1 Introduction

Milling is a manufacturing process, which requires the consideration of both, mechanical and thermal mechanisms for an effective and efficient process design with regard to tool wear, workpiece quality and process times [1]. The entire capability of the milling process depends on the thermo-mechanical conditions and affiliated state variables of the cutting process in order to meet economical as well as quality-related requirements. In their interaction, these state variables constitute the prevailing thermal and mechanical stresses on the tool, as well as on the workpiece, leading to geometrical and structural modifications. Adverse modifications of the interacting materials, in form of tool wear and surface property modifications may subsequently impair the tool's or workpiece's functionality [2]. Due to the kinematics of the milling process, specifically interruption and the varying uncut chip thickness, the heat flow into



the tool fluctuates, causing transient temperature fields and cycling material strains [3, 4, 5]. These tool material strain cycles may cause comb cracks and other tool wear phenomena, depending on the occurring amplitude and frequency [6].

Thus, knowledge of the state variables' dependence on the process parameters is an essential part of an economic and knowledge-based process design for high-quality manufacturing. Although sophisticated models exist for steady-state processes, like turning [7], which explore the connection between the thermal state variables like temperature fields and process parameters, processes under transient thermal conditions are not yet fully understood.

For such dynamic processes, prediction or measurement of heat partitioning from the cutting zone into the chip, workpiece and tool is also currently not possible. However, heat partitioning is a necessary input variable for many subsequent models regarding simulation of temperature fields, tool wear and surface integrity. The generated heat is conducted from the tool into the tool clamping and further, into the motor spindle, where additional heat is generated, the amount of which is dependent on the process. Thus, the process influences the temperature field throughout the machine, which in turn leads to tool center point deflection and impedes the accuracy of the process as a whole [8]. Models capable of predicting these characteristics are in demand, as well as methods to measure the thermal conditions in the milling process in order to provide empirical data and validate the former. Finally measuring or predicting the thermal state of the milling process enables monitoring or control strategies.

Regarding measurement approaches for interrupted cutting processes, the state of art reveals a persisting deficit in methods for the efficient measurement of temperature fields in the milling process, specifically at relevant areas within the cutting zone. Despite extensive efforts, past studies did not succeed in providing a consistent understanding of the time-variant thermal conditions in the milling process. A combined spatial and temporal investigation of temperature fields within the tool has not yet been investigated comprehensively. For the inverse determination of heat flows, only punctual temperature measurements were considered [4, 5, 9]. This is due to difficult accessibility of the cutting zone for measurement, particularly for experiments with a rotating tool.

In this paper, the heat flow into the tool was investigated for a circumferential milling process of AISI 1045. A measurement setup is presented for gaining in-

sight into the transient temperature field, which develops during the milling process. Further, methods for quantifying and predicting the heat flow into the tool during the cutter engagement on the basis of these temperature fields are described. Similar studies conducted for a steady-state cutting process with constant heat generation and no temporal temperature changes show good agreement between predicted temperature and measured temperature data [10]. Going further, for this paper, a rotating milling tool is tracked throughout the cutting process by means of infrared thermography in order to determine time-variant heat flow into the tool under transient thermal conditions.

## 2 Experimental setup

For the observation of transient temperature fields in the dry circumferential milling process of AISI 1045, a machine setup was chosen, for which the feed movement was carried out by the workpiece, enabling lateral observation of the end mill's end face by the infrared camera (see Fig. 1). The infrared camera is triggered at distinct tool rotation angles through the rotational spindle encoder signal. The tool was characterized by diameter  $d = 20$  mm, rake angle  $\gamma = 6^\circ$ , clearance angle  $\alpha = 12^\circ$ , cutting edge rounding  $r_\beta < 5$   $\mu\text{m}$ , no helix angle and

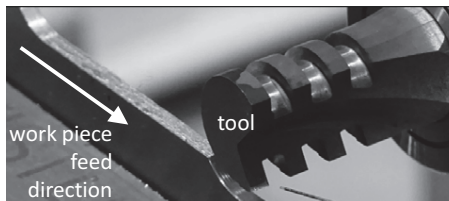


Fig. 1. Experimental setup of a circumferential milling process of AISI 1045

10 % cobalt tungsten carbide as tool material. In order to increase the emissivity of the cutting tool and minimize measuring errors through reflected radiation stemming from chip and work piece, it is painted black prior to the measurement. The rotating tool remained on a stationary position, fed by a workpiece with a thickness of  $w = a_p = 3$  mm during the entire experiment. For capturing images at defined cutter rotation angles, the high speed infrared camera (FLIR X6580sc) was synchronized to the spindle rotation encoder. It has a digital indium antimonide focal plane array detector, consisting of  $640 \times 512$  individual pixels observing the temperature field at 670 Hz with a spatial resolution of  $32.6$   $\mu\text{m}/\text{Pixel}$ . With this frequency and the aforementioned cutting parameters, the camera was able to record one cutter engagement of the tool on 10 separate frames at different tool rotation angles, which constituted the basis of

the following numerical and analytical evaluations. An example for the captured frames is given in Fig.2.

The presented experiment consisted of 18 successive cutter engagements, during which the tool and work piece heated up considerably, thus, undergoing transient thermal behavior.

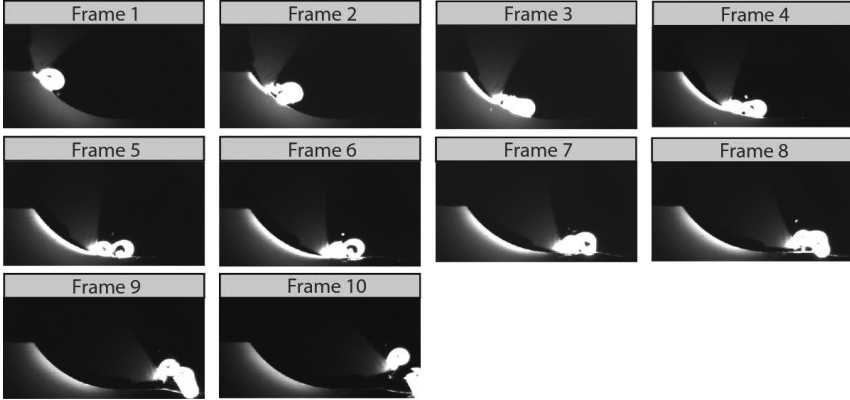


Fig. 2. Recorded IR imagery for one exemplary cutter engagement

The heat flow was calculated on the basis of the lateral temperature field at the tool end face, assuming that that heat flows principally in radial direction, due to the notched tool geometry depicted in Fig. 1.

The heat flux into the tool results in a temperature gradient at the boundary between tool, chip and work piece, which is defined by Fourier's law:

$$\dot{q}'' = -\lambda \frac{\partial T}{\partial x} \quad (1)$$

Here,  $\lambda$  represents the thermal conductivity of the material. However, determining the heat flow into the tool solely by evaluation of the recorded temperature gradients may yield significant errors. This is due to the inverse nature of the posed problem, by which the heat flow, which is the cause of a temperature distribution, is attempted to be quantified by a temperature measurement [11]. As a result, even minor measurement errors are propagated and thereby yield inaccurate results. This issue is further increased by the transient nature of the investigated problem. In order to solve this inverse problem, a numerical method for obtaining heat flow predictions from the measurement data is presented in the following chapter.

### 3 Numerical quantification of the heat flow into the tool

Before building the numerical model, first the tool needed to be tracked during the recorded milling process in order to extract the relevant temperature information. For this purpose, an edge detection algorithm has been utilized, which determined the gradients in image contrast at transition from ambience to tool surface. Since this algorithm also detected edges of the workpiece and chips, which are not part of the investigations presented in this work, these edges were filtered out. The remaining edges were fitted to a template of the unaffected tool edge. The template was rotated and translated until the highest agreement between detected edges and template was achieved, ensuring the correct bounding of the area of interest. This process is illustrated by Fig. 3 and was conducted for each infrared image obtained during the cutter engagements.

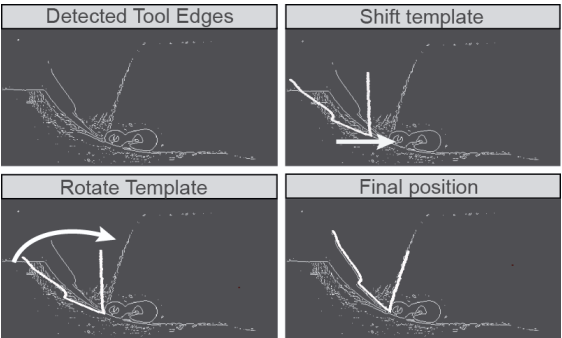


Fig. 3. Edge detection algorithm

The heat flow into the tool mainly occurred at the tool tip at the tool-chip contact zone. Thus only a small area of the tool is affected by the heat flow, and thereby needs to be investigated (Fig. 4). Using the Edge detection algorithm, all recorded frames are cropped and fitted, establishing a series of temperature maps for the tool area of interest.

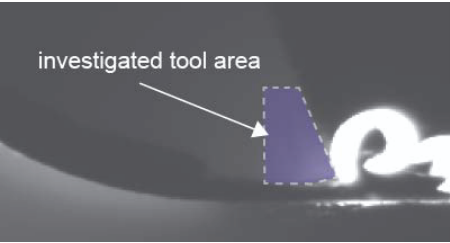


Fig. 4. Considered part of the tool

The aforementioned thermal model then was built for this region of interest. The model is based on the transient, two-dimensional heat transfer equation (Eq. 2), for which  $\rho$  represents the density and  $c$  the thermal capacity of the material.

$$\rho c \frac{\partial T}{\partial t} = \frac{\partial}{\partial x} \left( \lambda \frac{\partial T}{\partial x} \right) + \frac{\partial}{\partial y} \left( \lambda \frac{\partial T}{\partial y} \right) \quad (2)$$

Spatial terms are implemented with central differences and are discretized with the same spatial resolution as the IR-camera images provide (32.6 $\mu$ m edge length). Temporal terms are implemented, using an implicit time step scheme. The temperature data of the first considered video frame is used as the initial temperature condition.

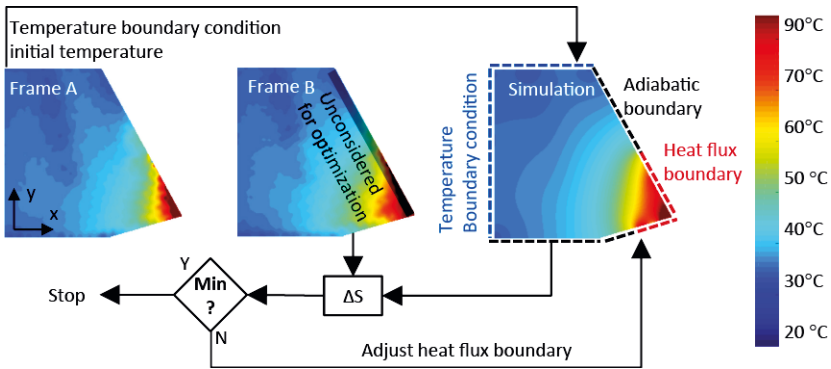


Fig. 5. Iteration procedure for deriving the heat flux boundary

The model contains certain simplifications of the actual experimental set up. This includes, that heat loss into the surroundings, either through convection or radiation, is negligible in comparison to the heat conducted through the tool. Additionally, the heat conduction is assumed to be two-dimensional, i.e. the temperature distribution perpendicular to the image plane (z-coordinate) is assumed to be homogeneous. Material properties, such as density 14.306 g/cm<sup>3</sup>k, heat capacity 223 J/kgK and heat conductivity 65.33 W/mK are provided by the supplier and are assumed to be constant within the observed temperature range.

The unknown heat flow into the tool influences the thermal model as a thermal boundary condition (Neumann boundary). For quantifying this boundary condition, an algorithm is employed, utilizing a least square approach:

$$\Delta S = \sum (T_{sim}(x, y) - T_{Meas}(x, y))^2 \quad (3)$$

An illustration of this algorithm is shown in Fig.5, for which Frames A and B represent two subsequent images. Similar methods have been published by [12, 13], which quantify heat transfer coefficients between contacting interfaces (Robin boundary).

Within this algorithm, the heat flux boundary is iteratively changed from one iteration step to the next, resulting in new simulated temperature distributions ( $T_{sim}$ ). This is done, until the simulated temperature best matches the measured temperature of Frame B ( $T_{meas}$ ), thereby achieving a minimum value of  $\Delta S$ . This procedure is conducted for every set of subsequent frames within the measurement (Fig.2).

As heat flux into the tool only occurs within the vicinity of chip and work piece at the front of the tool, additional boundary conditions are necessary for simulating the temperature field. For this, two different sets of boundaries are chosen. To the back of the tool, temperature boundary conditions (Dirichlet boundaries) are implemented, for which values are taken directly from the measured temperature field of Frame A. Along the rake face and the clearance face, adiabatic boundaries were assumed [10].

In order to achieve best possible results, the temperature measurements need to be as precise as possible. Utilizing infrared thermography in this context involves, that if a hot chip emitting considerable thermal radiation moves through the field of view, it implies abrupt temperature increases on the tool. This can be especially challenging when considering temperatures along the tool's rake face. Due to this fact, the area near the rake face is taken out of consideration for the optimization algorithm (see Fig.5, Frame B).

## 4 Empirical modeling of the heat flow into the tool

In addition to the proposed numerical modeling of heat fluxes, an alternative empirical approach was also carried out. This approach is based on results of an orthogonal cutting experiment of AISI 1045, for which a tool micro-geometries similar to the previously shown milling experiments was used (Fig 6a). The heat input into the tool  $Q_{tool}$  was determined by observing the lateral tool face, using the IR-camera, before and immediately after the cutting process, assuming that the visible temperature field extends over the depth of cut  $a_p = 3$  mm. At the boundaries of the field of view no temperature rise was observed, so the visible temperature field represented the planar internal energy rise of the tool's lateral face.

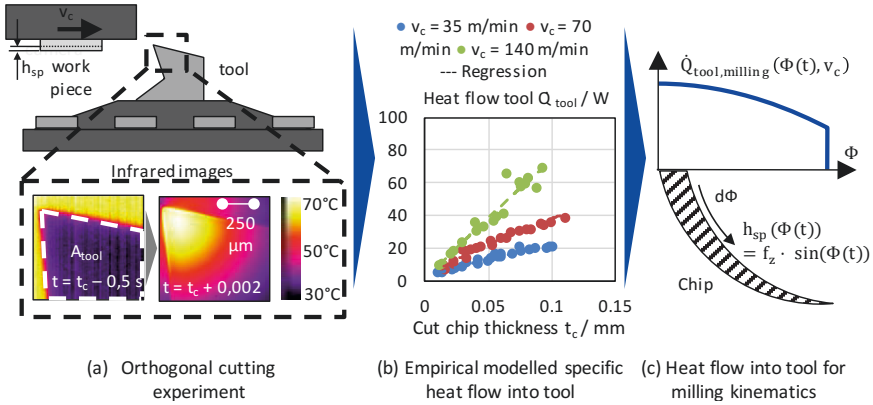


Fig. 6. Empirical modeling of the heat flow into the tool

In the center of the tool and the workpiece, a temperature maximum is expected, as it is typical for such symmetric heat conduction problems. The tool depth further extends the cutting depth by 0.4 mm and a temperature rise also presumably occurs in the remaining volume. These effects contribute to the assumption of a minimal estimation regarding the heat input into the tool, which is determined by the change of internal energy from before to after the cut. The internal energies were calculated by the use of the temperature measurements before and after the cut, for which material properties and tool geometry are known parameters:

$$Q_{tool} = U_{tool,after} - U_{tool,before} = \rho c_p A_{tool} a_p (T_{after} - T_{before}) \quad (4)$$

Hereby,  $A_{tool}$  represents the chosen control volume, in which a temperature change is observed after the cut. As for the numerical evaluation, the material properties are assumed to remain constant within the considered temperature range.

This investigation was conducted for different chip thicknesses  $t_c$  and cutting speeds  $v_c$ , yielding a set of results, for which a regression analysis was performed (Fig. 6b). The regression of the specific heat input into the tool was further used in order to calculate the heat flow into the tool for the circumferential milling process, which is characterized by a varying uncut chip thickness, as well as interrupted cutting (Fig. 6c). Therefore, the analytical description of the uncut chip thickness  $t_c$  in the milling process together with the empirically determined specific heat input per length and depth of cut  $q_{l_c, a_p}(t_c(\Phi), v_c)$  provided an empirical model for the heat flow into the tool over the cutter rotation for any combination of the parameters cutting velocity  $v_c$ , feed per tooth  $f_z$  and radial engagement  $a_e$ .

Under these assumptions the heat input into the tool depending on the cutter rotation angle  $\Phi$  was calculated by:

$$Q(\Phi) = a_p \cdot \frac{d}{2} \cdot \int_{\Phi_{st}}^{\Phi_{ex}} q_{l_c, a_p}(t_c(\Phi), v_c) d\Phi \quad (5)$$

$$t_c(\Phi) = f_z \cdot \sin(\Phi) \quad (6)$$

Respectively the time variable heat flow  $\dot{Q}(t)$  during the contact can be calculated by:

$$\dot{Q}(t) = \frac{dQ(\Phi)}{d\Phi} \cdot \frac{d\Phi}{dt} = a_p \cdot \frac{d}{2} \cdot q_{l_c, a_p}(t_c(\Phi), v_c) \cdot \frac{d\Phi}{dt} \quad (7)$$

Classical investigations in orthogonal cutting commonly focus on the forces and chip formation. The proposed methodology in contrast also considers the thermal domain of the process. Thereby, it enables investigation of the heat flow distribution in the cutting process for different workpiece material and tool material combinations, as well as for different parameters and tool geometries. It may also be further extended to temperature fields within the workpiece and the chip, by integrating additional temperature measurements.



# 5 Results

The results for the numerical and the empirical method are shown in Fig.7, for the first and the last of 18 subsequent cutter engagements.

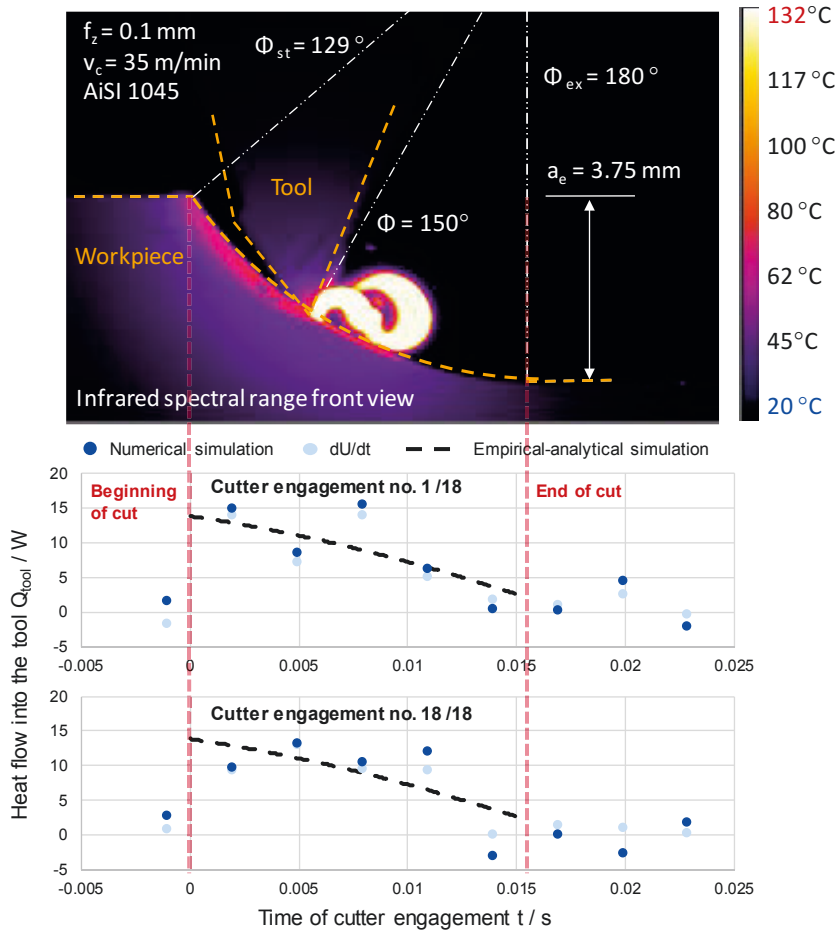


Fig. 7. Heat flow into the tool during the cutter engagement

For additional validation of both methods, the results also include the change of internal energy ( $dU/dt$ ), calculated by the temperature difference between two subsequent frames within the investigated tool area. All three results are in good accordance and show a decreasing heat flux with uncut chip thickness. As the tool exits the workpiece at a cutter rotation angle  $\Phi = 180^\circ$ , the heat flow

reduces to approximately zero. In this context, negative values indicate that the amount of heat flow being conducted out of the computational domain is higher than the heat flow transferred into the tool from the chip, which is welded to the tool after the cut. The results indicate a peak heat flow of around 15 W into the tool declining to zero within 0.015 seconds. This transient heat flow over time can be used for further analytical temperature models, for example for the model of STEPHENSON [4] solving the partial differential equation by means of on GREENS functions. The model is able to predict a transient volumetric temperature field  $T(x, y, z, t)$  in the tool approximated by a semi-infinite corner as the result of a transient heat flow  $\dot{Q}_{\text{tool}}(t, x, y)$  into the volume.

## 6 Conclusions

In the presented paper, two different methods are shown for quantifying transient heat flows into the tool for the milling process. Both methods use temperature measurement data obtained by an infrared camera. For the first method, the tool temperature is reconstructed within a numerical model, for which the heat flow boundary condition into the tool is iteratively varied, in order to find optimal agreement between the numerical simulation and the measurement. The second method constructs the heat low into the tool by empirical data, derived from orthogonal cuts and thermodynamics calculations for the kinematics of the milling process. Both methods show to be in good agreement with each other and also with a direct evaluation of the change of internal energy. With the developed methods, a thermal prediction of the milling process, which is connected to tool wear surface integrity and manufacturing precession is achievable.

### Acknowledgments

*The authors wish to thank the German Research Foundation (DFG) for funding the transregional Collaborative Research Center SFB/TR 96 Thermo-Energetic Design of Machine Tools”.*

## 7 References

- [1] Klocke, F.: Manufacturing Processes, 2011
- [2] Brinksmeier, E.; Gläbe, R.; Klocke, F.; Lucca, D. A.: Process Signatures – a Alternative Approach to Predicting Functional Workpiece Properties. In: Procedia Engineering, 2011, pp.44–52

- [3] Yellowley, I.; Barrow, G.: The influence of thermal cycling on tool life in peripheral milling. In: *International Journal of Machine Tool Design and Research*, No. 1, 1976, pp.1–12
- [4] Stephenson, D.; Ali, A.: Tool Temperatures in Interrupted Metal Cutting. *Journal of Manufacturing Science and Engineering*, No. 2, 1992, pp.127
- [5] Sato, M.; Tamura, N.; Tanaka, H.: Temperature Variation in the Cutting Tool in End Milling. In: *Journal of Manufacturing Science and Engineering*, No. 2, 2011, pp.21005
- [6] Okushima, K.; Hoshi, T.: Thermal Crack in the Carbide Face-Milling Cutter. 1st Report, Results Obtained from the Fundamental Cutting Experiments; *Bulletin of JSME*, No. 17, 1962, pp.151–160
- [7] Komanduri, R; Hou, Z.B.: Thermal modeling of the metal cutting process. *International Journal of Mechanical Sciences* 2000; 42, No.9, pp 1715-1752
- [8] Grossmann, K.: *Thermo-energetic Design of Machine Tools*, Lecture Notes in Production Engineering, Springer International Publishing, 2015
- [9] Jiang, F.; Liu, Z.; Wan, Y.; Shi, Z.: Analytical modeling and experimental investigation of tool and workpiece temperatures for interrupted cutting 1045 steel by inverse heat conduction method. In: *Journal of Materials Processing Technology*, No. 6, 2013, pp.887–894
- [10] Augspurger, T.; Brockmann, M.; Frekers, Y.; Klocke, F.; Kneer, R.: Experimental Investigation of Thermal Boundary Conditions During Metal Cutting; *Procedia CIRP*, 2016, pp.119–122
- [11] Alifanov, O.; *Inverse Heat Transfer Problems*, 1994
- [12] Fieberg, C.; Kneer, R.: Determination of thermal contact resistance from transient temperature measurements. *International Journal of Heat and Mass Transfer* 2008; 51 (5-6):1017-23
- [13] Burghold, E.; Frekers, Y.; Kneer, R.: Determination of time-dependent thermal contact conductance through IR-thermography. *International Journal of Thermal Sciences* 2015; 98: 148-55.

# Thermally induced displacements of machine tool structure, tool and workpiece due to cutting processes

*O. Horejš, M. Mareš, J. Hornych*

Research Center of Manufacturing Technology RCMT, Czech Technical University in Prague,  
Horská 3, Prague, 128 00, Czech Republic

**Abstract.** A thermal error model for software compensation of machine tools is usually established from air cutting (AC) experiments. However, the accuracy of the AC model in real machining applications is often questioned. This paper describes experimental results of cutting process impact on thermally induced displacements of machine tool structure, tool and workpiece in a dry milling process. A series of tests were carried out on a 5-axis milling machine. Experimental results confirmed high impact of the cutting process on thermally induced displacements between the workpiece and the tool. It is also shown that real-time thermal compensation algorithms based on experimental data under load-free rotation of the spindle have a very poor estimation quality.

Peer-review under responsibility of the International Scientific Committee in the person of the Conference Chair Prof. Steffen Ihlenfeldt.

*Keywords:* Machine tool; Cutting process; Thermal error; Real-time compensation; Milling

---

## 1 Introduction

Challenges for machining include greater and greater material removal rates coupled with an increase in the use of difficult-to-machine materials, as well as environmentally-friendly dry or MQL machining. These trends lead to a large (and variable) heat input into the machine structure causing thermo-elastic displacements of the machine tool, the tool, the workpiece and clamping devices [1]. Up to 75% of the overall geometrical errors of machined workpieces can be induced by thermal effects. Therefore, this topic is the focus of significant recent research activities [2].

Software compensation of thermally induced displacements at the tool center point (TCP) is one of the widely employed techniques to reduce machine tool thermal errors due to its cost-effectiveness and ease of implementation. Although real-time software compensations of thermal errors exist, the majority

of these models only presume machine tools under load-free rotation of the main spindle (air cutting - AC) without any reference to rough machining. The machining process is completely neglected in spite of the fact that the machining process represents a significant heat source and consequently an essential cause of workpiece inaccuracy. Application of the air cutting (AC) thermal error model for software compensation of machine tools would be acceptable in finishing or low power processes. However, rough machining requires high torques and much electrical power, which dissipate into intense heat. The result is obvious: due to the strong heat development of the spindle, even at a low speed level, the TCP displacement is high [3]. The high complexity of the machine tool – tool – workpiece system thermal behaviour result in difficulties in how to address the phenomenon with robust and reliable approaches which could successfully be implemented into the machine tool control system. Generally, there are two main aspects of the cutting process that affect machining accuracy from the thermal point of view.

Firstly, power of the main spindle and feed drives increase during the cutting process, especially in the case of rough machining. Thermal distortion under spindle loading conditions was investigated using a stressing unit in [4]. A robust compensation of thermo-dependent machine tool deformations due to spindle load in consideration of rough machining was developed based on tests with the stressing unit [3].

Secondly, the cutting process itself is a very problematic heat source. A certain amount of heat generated by the cutting process is always transferred into the tool, machined workpiece, chips and coolant. Further, it dissipates through the tool chuck into the spindle, and through the workpiece and the clamping system into the machine table. Despite the fact that it is very difficult to determine heat partition ratios of these components depending on cutting conditions [5], researchers developed a myriad of analytical or numerical methods and performed multifaceted experiments to understand the heat generation, partitioning and temperature distribution in machining [6].

In [7] it is shown that the thermal error rapidly increases at the moment when wet cutting with a coolant becomes dry cutting. The temperature rise of the spindle housing and the thermal growth of the spindle under four different air cutting and cutting conditions were tested in [8]. The result showed that the predictive accuracy of the AC model (MRA and ANN model) is unacceptable in real cutting applications. In [9] a general approach to fast and robust dynamic modelling of thermally induced displacements at the TCP based on transfer functions (TF) was presented. This approach was successfully applied to 3 dif-

ferent machine tool structures [10]. The tested TF models proved their ability to significantly reduce thermal errors at the TCP independently of the machine tool structure. However, the models developed were designed based on testing under load-free rotation (AC models).

The compensation model was extended to the real cutting process description based on measured spindle power for a 3-axis vertical milling centre under rough machining [11]. The approach was applied to a 5-axis milling machine and the effectiveness of 3 compensation model structures during various cutting processes were tested in [12]. This paper is a continuation of research mentioned above focusing on evaluation of thermal displacements of the workpiece in comparison with thermal displacements of a 5-axis milling center and the cutting tool.

## 2 Experiment

In order to evaluate the impact of the cutting process on overall thermal displacements at the TCP, a series of cutting tests was carried out (Fig. 1).

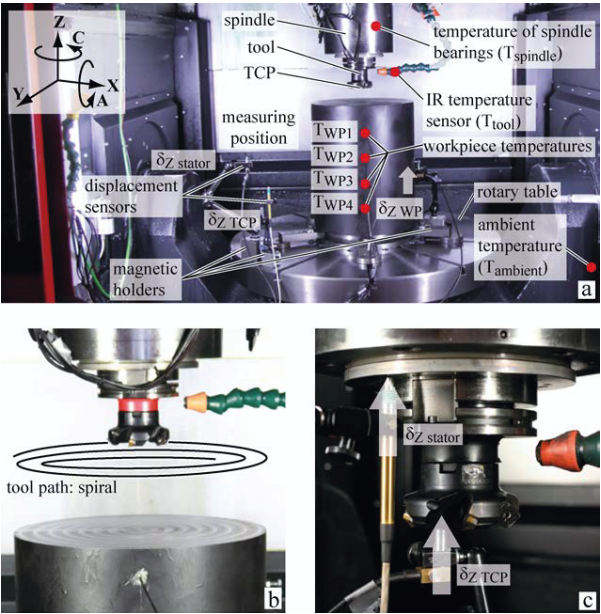


Fig. 1. (a) Experimental setup on 5-axis milling machine; (b) Cutting process; (c) Measuring position.

## 2.1 Experimental setup

Experiments were performed on a 5-axis milling centre with a 630 mm rotary table diameter. The experimental setup is shown in Fig. 1. The machine tool was equipped with a number of RTD temperature probes (Pt100, Class A, 3850 ppm/K) placed close to heat sinks and heat sources. Besides temperatures of the machine structure, ambient temperatures and non-contact measurement of the tool temperature  $T_{tool}$  was carried out using an infrared (IR) sensor (Optris CT- SF15-C1) aimed at the upper part of the cutting tool. The sensor and its cabling was safely covered in a flexi hose of a type commonly used for cooling liquid circuits. The thermal field of the workpiece was measured using an infrared camera and several RTD sensors placed inside the workpiece. The reason was to evaluate thermal deformation of the workpiece.

Additionally, thermal displacements were measured using 3 inductive contact sensors (only in the most affected Z direction) at the:

- machine tool frame (measured at the stator part of the spindle, further denoted as  $\delta_{Z\ stator}$ ),
- TCP ( $\delta_{Z\ TCP}$ ),
- workpiece ( $\delta_{Z\ WP}$ ).

The displacement sensors were mounted in magnetic holders attached to the machine tool table (see Fig.1). Thus, the demanded value of the tool thermal elongation ( $\delta_{Z\ tool}$ ) can be obtained with simplification by the difference between the two measured displacement elements:

$$\delta_{Z\ tool} = \delta_{Z\ TCP} - \delta_{Z\ stator} \quad (\text{Eq. 1})$$

Thereafter, the overall thermal displacement  $\delta_Z$  between the TCP and workpiece consist of three elements:

$$\delta_Z = \delta_{Z\ stator} + \delta_{Z\ tool} + \delta_{Z\ WP} \quad (\text{Eq. 2})$$

where  $\delta_{Z\ stator}$  is the machine tool frame thermal displacement (influence of feed drive activity, spindle bearings, removed material, ambient temperature etc.),  $\delta_{Z\ tool}$  is the cutting tool elongation (predominantly impacted by the cutting process) and  $\delta_{Z\ WP}$  is the workpiece thermal displacement. A programmable automation controller (PAC) NI CompactRIO was used for data acquisition.

Except for temperatures and displacements mentioned above, NC data such as effective power, electric current, torque, feed rate, etc. were recorded using profibus communication between the machine controller (Heidenhain, iTNC 530) and the PAC (sampling rate was 1 sec).

## 2.2 Experimental condition and approach

Altogether, 12 tests with different dry milling processes were carried out (finishing, semi-finishing and rough machining) to assess the impact on thermal displacement ratios of workpiece, the cutting tools and machine tool structure itself and to evaluate the AC model estimation quality during real machining.

The machine tool should be in a steady state with its surroundings as a precondition to initiate testing. All experiments include a load phase (cutting process) followed by a cool-down phase. The load phase of the testing consists of cycle repetition of two phases: cutting phase (Fig.1(b)) and measuring phase (Fig.1(c)). The cutting part means removal of one layer of workpiece material by following a specific tool path. The tool path was set up as a spiral to ensure approximately constant spindle load during the cutting process (Fig.1(b)). Face milling was chosen as the basis for measurement of cutting process influence. Medium-carbon steel 1.0503 (DIN C45) was applied as the workpiece material (cylindrical workpiece, diameter: 300 mm, original length: 400 mm). All tests were carried out without coolant (dry machining) according to the latest worldwide trend to save the environment and production costs (also to consider the most affected case from a thermal displacement point of view).

Three different cutters (with 3 different tool diameter  $D$ ) were used for: finishing process ( $D = 25$  mm), semi-finishing process ( $D = 63$  mm) and rough machining ( $D = 100$  mm).

As mentioned above, there was an effort to keep spindle power almost constant during cutting tests. Two cutters of identical type (diameter) were employed for the cutting tests. If the spindle power increased due to the tool wear during the cutting test, the cutter was replaced by the new one. A cutting process with an almost constant spindle power was stopped only to acquire thermal displacements with the help of 3 inductive contact sensors recording displacement ( $\delta_{Z \text{ stator}}$ ,  $\delta_{Z \text{ TCP}}$ ,  $\delta_{Z \text{ WP}}$ ) according to Fig.1(a) during the measuring part or due to changing the cutter (see above). The cutting and measuring parts were repeated in the load phase until supposed achievement of machine tool steady state with all active heat sinks and heat sources (from 4 hours up to 6 hours). The cooling phase followed with the permanent spindle placement in the measuring position (Fig.1(c)). The 5-axis milling centre was in a feed-drive-on mode during the cool-down phase. Each cutter was used for 4 different tests (12 tests in total) with a constant set of the cutting parameters (see Table 1): total number of teeth in cutter ( $z_n$ ), working engagement ( $a_e$ ), table feed ( $v_f$ ), spindle speed ( $n$ ) and chosen tool path. Experiments differed in changing of the



depth of cut  $a_p$  (from 0.1 mm to 3 mm). It results in changing of the average spindle power ( $P_{spindle}$ ) for each test (from 0.06 kW to 4.25 kW). Hence, one test for each process (finishing, semi-finishing and rough machining) is selected as a representative sample to discuss the experimental results. Cutting parameters for selected tests are summarised in Table 1.

Table 1. List of cutting conditions for steel cutting tests.

D [mm]	$z_n$	$a_e$ [mm]	$v_f$ [m/min]	$n$ [min <sup>-1</sup> ]	$a_p$ [mm]	Pspindle [kW]
25	3	18.75	764	2546	0.5	0.29
63	5	31.5	758	758	1.5	1.52
100	7	50	668	477	1.5	2.12

### 2.3 Experimental results and comparison with AC compensation model

Experimental results of cutting process impact on thermally induced displacements of the machine tool structure, the tool and the workpiece in a dry milling process are shown in Fig. 2 to Fig. 4. The graph on the left depicts time behaviour of temperatures used as inputs of the TF compensation model (see [12]). The graph on the right shows thermally induced displacements of the machine tool structure  $\delta_{Z\ stator}$  (the red curves), the cutting tool  $\delta_{Z\ tool}$  (the blue curves) and the workpiece  $\delta_{Z\ WP}$  (the brown curves) during finishing (Fig. 2), semi-finishing (Fig. 3) and rough machining (Fig. 4).

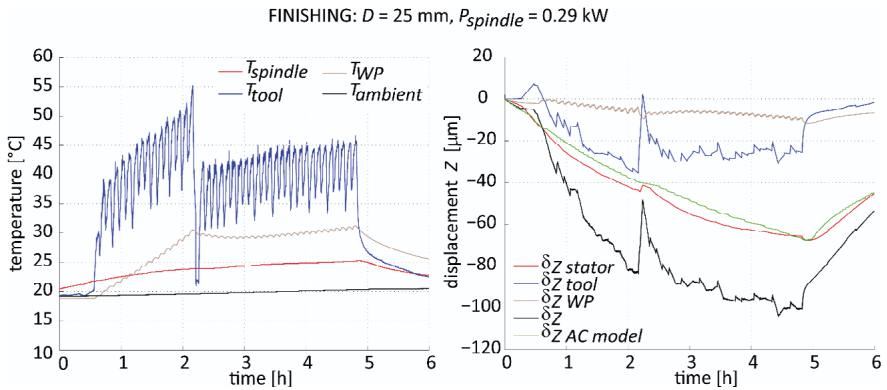


Fig. 2. Temperatures (left) and thermally induced displacements of the machine tool structure, cutting tool and the workpiece in Z direction during finishing (right).

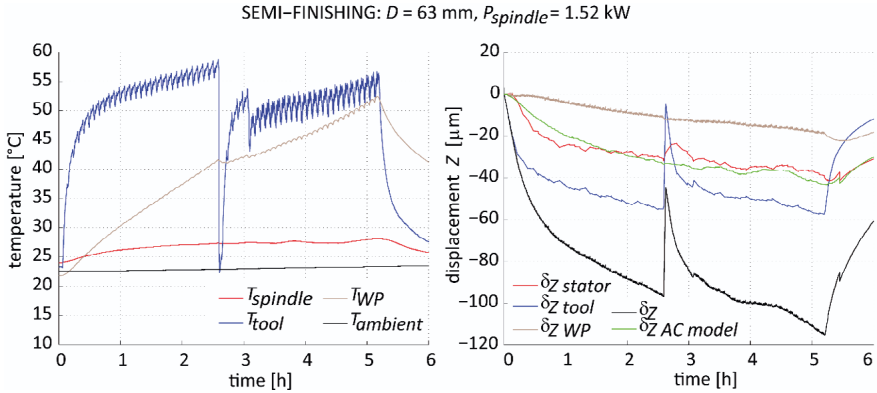


Fig. 3. Temperatures (left) and thermally induced displacements of the machine tool structure, cutting tool and the workpiece in Z direction during semi-finishing (right).

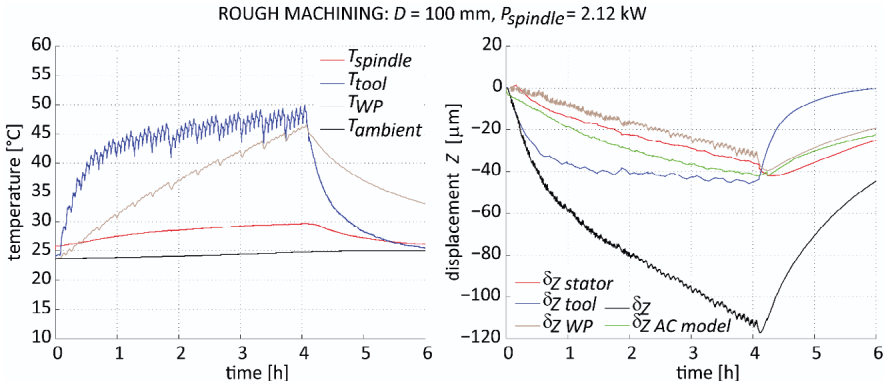


Fig. 4. Temperatures (left) and thermally induced displacements of the machine tool structure, cutting tool and the workpiece in Z direction during rough machining (right).

Furthermore, the graphs on the right (Fig. 2 to Fig. 4) depict the overall thermal displacement  $\delta_z$  between the TCP and workpiece (the black curves) calculated according to Eq. 2 and AC TF model prediction (see [12]) of thermally induced displacements of the machine tool structure in Z direction  $\delta_{z \text{ AC model}}$  (the green curve).

Two temperature probes were used for thermal error AC model inputs (for more details see [12]). These probes were namely  $T_{\text{spindle}}$  (temperature of spindle bearings) and  $T_{\text{ambient}}$  (temperature of the machine tool surrounding). Firstly, an AC TF model was implemented into the machine tool control system using profibus communication and PAC (an identical PAC which was employed for da-

ta acquisition during cutting tests). Thereafter, the compensation algorithm was converted to Python code as the Heidenhain machine controller allows object-oriented high-level programming using the Python OEM Process option. The AC TF model should approximate only part of the overall thermal displacement  $\delta_z$  which is thermally induced displacements of the machine tool structure  $\delta_{z\text{ stator}}$ . AC TF model approximation quality of the measured  $\delta_{z\text{ stator}}$  is quite high during dry milling process as seen by the comparison of green curves with red curves (see Fig. 2 to Fig. 4).

Maximal measured thermal displacements of the workpiece, the cutting tools and the machine tool structure at the end of cutting process (load phase) in Z direction are summarized in Table 2 for 3 the selected tests. Fig. 5 represents thermal displacement ratios of the workpiece, the cutting tools and the machine tool structure calculated based on maximal measured displacements in Table 2.

Table 2. Maximal thermal displacements of the workpiece, the cutting tools and the machine tool structure at the end of cutting process (load phase) in Z direction.

Thermal displacements [μm]	Finishing	Semi-finishing	Rough machining
Machine structure ( $\delta_{z\text{ stator}}$ )	66	39	36
Cutting tool ( $\delta_{z\text{ tool}}$ )	25	58	45
Workpiece ( $\delta_{z\text{ wp}}$ )	10	18	31
Overall displacement ( $\delta_z$ )	101	115	112

### 3 Summary and conclusion

A series of 12 tests were carried out to evaluate cutting process impact on thermally induced displacements of a machine tool structure, the cutting tool and the workpiece in a dry milling process. The impact of the cutting process was studied in 3 selected experiments (finishing, semi-finishing and rough machining) in detail. Thermal displacement ratios of the workpiece, the cutting tools and the machine tool structure were calculated based on maximal measured displacements (see Table 2) changes depending on the cutting process (resp. value of the average spindle power). In case of finishing ( $P_{\text{spindle}} = 0.29\text{ kW}$ ), thermally induced displacement of the machine tool structure  $\delta_{z\text{ stator}}$  (66%) is the dominant part the overall thermal displacement  $\delta_z$  in comparison with thermally induced displacement of the tool  $\delta_{z\text{ tool}}$  (25%) and the workpiece  $\delta_{z\text{ wp}}$  (9%) see Fig. 5. On the contrary, thermally induced displacement of the

tool  $\delta_{Z \text{ tool}}$  becomes the dominant part of the overall thermal displacement  $\delta_Z$  between the TCP and the workpiece if the average spindle power is increased, e.g. in case of semi-finishing test ( $P_{\text{spindle}} = 1.52 \text{ kW}$ ) thermally induced displacement of the tool  $\delta_{Z \text{ tool}}$  is 50% in comparison with the thermally induced displacement of the machine structure  $\delta_{Z \text{ stator}}$  (34%) and the workpiece  $\delta_{Z \text{ WP}}$  (16%) as shown in Fig. 5. In the case of rough machining ( $P_{\text{spindle}} = 2.12 \text{ kW}$ ) thermally induced displacement of the tool  $\delta_{Z \text{ tool}}$  is also the dominant part of the overall thermal displacement  $\delta_Z$  (40%).

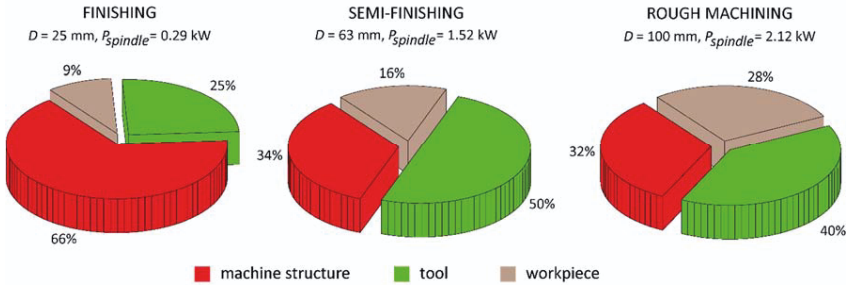


Fig. 5. Thermal displacements ratios of the workpiece, the cutting tools and the machine tool structure during tests in Z direction.

Thermally induced displacement of the workpiece  $\delta_{Z \text{ WP}}$  is the smallest part of the overall thermal displacement  $\delta_Z$  in all tests (see Fig. 5). Herein, it is necessary to mention that thermal displacement of the workpiece  $\delta_{Z \text{ WP}}$  was measured at the middle of the original length of the cylindrical workpiece. Thus, thermal displacement of the workpiece  $\delta_{Z \text{ WP}}$  could probably be even higher at the top of the workpiece than at the areas measured. Moreover, thermal displacements of the workpiece  $\delta_{Z \text{ WP}}$  are strongly dependent on the particular shape, mass and material of the workpiece itself (heat capacity of the workpiece). The results of the real-time thermal compensation algorithms based on experimental data under load-free rotation of the spindle (AC model) are in good agreement with measured displacements of the machine tool structure  $\delta_{Z \text{ stator}}$ . However, experimental results confirmed the high impact of the cutting process on overall thermally induced displacements between the workpiece and the tool  $\delta_Z$ . Consequently, AC model have a very poor estimation quality of thermal errors in real machining applications as seen by the comparison of green curves with black curves (see Fig. 2 to Fig. 4). The analysis of the experimental results show the compensation method of machine tool thermal errors should include cutting process effects to ensure robustness of the compensation algorithm during real cutting conditions.

## Acknowledgements

*This paper (Thermally induced displacements of machine tool structure, tool and workpiece due to cutting process) has received funding from the Technology Agency of the Czech Republic (Project TE01020075).*

## 4 References

- [1] Peters J., Bryan, J. B., Estler, W. T., Evans, C., Kunzmann, H., Lucca, D. A., 2001. Contribution of CIRP to the Development of Metrology and Surface Quality Evaluation during the last fifty years, CIRP Annals - Manufacturing Technology, 50/2, 471-488.
- [2] Mayr, J., Jedrzejewski, J., Uhlmann, E., Donmez, M.A., Knapp, W., Härtig, F., Wendt, K., Moriwaki, T., Shore, P., Schmitt, R., Brecher, C., Würz, T., Wegener, K., 2012. Thermal issues in machine tools. CIRP Annals - Manufacturing Technology, 61/2, 771-791.
- [3] Brecher, C., Wissmann, A., 2011. Compensation of thermo-dependent machine tool deformations due to spindle load: investigation of the optimal transfer function in consideration of rough machining, Prod. Eng. Res. Devel., 5, 565-574.
- [4] Brecher, C., Wissmann, A., 2009. Stressing Unit for Modelling of Thermal Behaviour of a Milling Machine," 12th CIRP Conference on Modelling of Machining Operations, Donostia - San Sebastian - Spain.
- [5] Karpat, Y., Özel, T., 2006 Predictive Analytical and Thermal Modeling of Orthogonal Cutting Process-Part II: Effect of Tool Flank Wear On Tool Forces, Stresses and Temperature Distributions, ASME Journal of Manuf. Sci. & Engr., 128/2, 445-453.
- [6] Putz, M., Oppermann, C., Semmler, U., Bräunig, M., Karagüzel, U., 2017. Consistent simulation strategy for heat sources and fluxes in milling. Procedia CIRP 62, 239-244.
- [7] Ramesh, R., Mannan, M. A., Poo, A. N., 2003. Thermal error measurement and modelling in machine tools: Part I. Influence of varying operating conditions, Int.J.Mach.Tools Manuf., 43/4, 391-404.
- [8] Chen, J.-S., 1996. A study of thermally induced machine tool errors in real cutting conditions, Int. J. Mach. Tools Manuf., 36/12, 1401-1411.
- [9] Horejš, O., Mareš M., Novotný, L., 2012. Advanced Modelling of Thermally Induced Displacements and Its Implementation into Standard CNC Controller of Horizontal Milling Center, Procedia CIRP, 4, 67-72.
- [10] Horejš, O., Mareš M., Hornych, J., 2014, A general approach to thermal error modelling of machine tools. Machines et usinage à grande vitesse (MUGV), Clermont Ferrand, France.
- [11] Horejš O., Mareš M., Hornych J., 2015. Real-time compensation of machine tool thermal error including cutting process. Journal of Machine Engineering, 15/3, 5-18.
- [12] Mareš M., Horejš O., 2017. Modelling of cutting process impact on machine tool thermal behaviour based on experimental data. Procedia CIRP, 58, 152-157.

## **Thermo-energetic analysis and modelling, shown by the example of spindles**

---



# A new calibration approach for a grey-box model for thermal error compensation of a C-Axis

*C. Brecher, R. Spierling, M. Fey*

Laboratory for Machine Tools and Production Engineering (WZL) of RWTH Aachen University, Steinbachstr. 19, 52074 Aachen, Germany

**Abstract.** Thermal errors cause significant geometrical errors on machined work pieces. This paper presents an approach to calibrate a simplified grey-box model under real workshop conditions, using control internal data as input datas. The calibration is performed with a new measurement approach for rotary axis, inspired by ISO 230-6 ETVE test. The model leads to an error reduction of a selected thermally induced error of a rotary axis with a maximum remaining error of 14  $\mu\text{m}$ .

Peer-review under responsibility of the International Scientific Committee in the person of the Conference Chair Prof. Steffen Ihlenfeldt.

*Keywords:* Machine tools; Thermal error; Modelling; Compensation; ETVE test; Rotary Axis;

---

## 1 Introduction

High-performance machine tools are an important competitive factor for the metal-working industry. The most important factors affecting the competitiveness are the productivity and the machining accuracy respectively part quality. These factors are determined by the static and dynamic behaviour of the machine structure, the dynamic behaviour of the control and drives and the geometric, kinematic and thermal behaviour of the system. The thermal influence causes up to 75% of the resulting geometrical work piece error. The phenomenological processes and possible compensation approaches are explained in the next paragraph along the thermo-energetic functional chain, see Figure 1. [1,2]

Different inner and outer heat sources and sinks, e.g. power losses of the drives and the workshop climate, lead to unsteady heat flows in the machine structure. This causes a transient temperature respectively displacement field, resulting in deviations of the Tool Centre Point (TCP) from its commanded position. For a model-based compensation approach of misalignments of the kinematics due to thermal causes, input data can be acquired at different points of the thermo-energetic functional chain, e.g. sensors integrated in the structure that measure



deviations, temperature sensors at representative points of the temperature field or control internal data that is phenomenologically related to the error source. A compensation model based on one of these different input data types then predicts the TCP drift. [3]

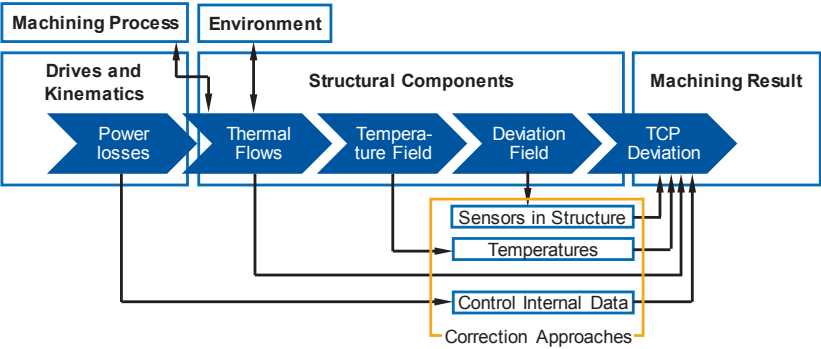


Figure 1: Thermo-energetic functional chain and correction approaches [4]

There is an increasing demand for five-axis machine tools producing high-precision parts in aerospace industry, medical engineering, process engineering and power engineering. The requirements concerning the geometric and thermal precision are high, as the machining of small areas of the work piece's surface may necessitate huge compensating movements of the kinematic in larger sections of the volume.

During the last years, several standards for measurement of thermal errors of machine tools have been developed, such as ISO 230-3 [5], ISO 10791-10 [6] and ISO 13041-8 [7]. Furthermore, five-axis accuracy is a topic for ongoing research efforts. Jatzkowski investigated the calibration of machine tools rotary axes with sequential multilateration and tracking interferometers [8]. Gebhardt compensates the thermal errors of rotary axes with a phenomenological model utilising temperature measurements and control internal data as input data [9,10]. Flore presents and validates a method to optimise the machining accuracy of five-axis machine tools with tracking interferometers [11].

This paper presents a phenomenological model of a rotation axis using control internal input data. The new aspect is the cost efficient and easy to use measurement method to determine the thermal deviation of the rotary axis. Existing measurement devices such as the R-Test [12] or inclination gauges are more expensive. The low price of the measurement equipment panders to a widespread application in industry. It is presented in the next chapter.

During the last years, efforts modelling the thermal behaviour of rotary axis have been made. Blazejewski et al. simulate the drift of a C-axis due to bearing and direct drive power losses with the finite element method [13]. Gebhart et al. use a phenomenological grey-box approach to model the thermal drift of a C-axis depending on the axis speed/power consumption and the environmental influence, using the R-Test to calibrate the model [9]. Abdulshahed et al. model a grey neuronal network for the thermal response of a Z- and a C-axis based on fibre bragg gratings measurement inputs. [15]. They use four laser displacement sensors and a test bar to measure the resulting axes displacement.

The key question is, what quality of calibration data can this measurement method provide under real workshop conditions, compared to other rotary axis measurement devices, for a simplified model, only using control internal data as an input? Chapter 3 explains the modelling approach and reviews the results of the model validation. The last chapter summarizes the results and gives an outlook.

## **2 Measurement setup and method**

The testing method presented in [14] is an extended variation of the ETVE test from ISO 230-3 [5], see Figure 2. The setup consists of five high precision mandrels on the table and a sensor mount, carrying five displacement sensors, attached to the spindle. All parts are made of invar to ensure a low thermal influence on the testing setup. The measurement setups enables an evaluation of the displacement in three directions, two angular errors and form errors of the table's surface. In addition, 28 environmental temperature sensors on five different height levels surround the demonstrator machine, but their data is only used to perform an environmental temperature logging, as prescribed for the ETVE test. The correct placement of environmental temperature sensors is time consuming and handicaps the correct application in industry [16].

The additional axes of a five-axis machine tool leads to a significantly higher number of geometric errors compared to a three-axis machine tool [11,17,18]. The orientational errors of an investigated rotary axis parallel to the spindle, in the notation according to ISO 230-1, are shown in Figure 2 [18].

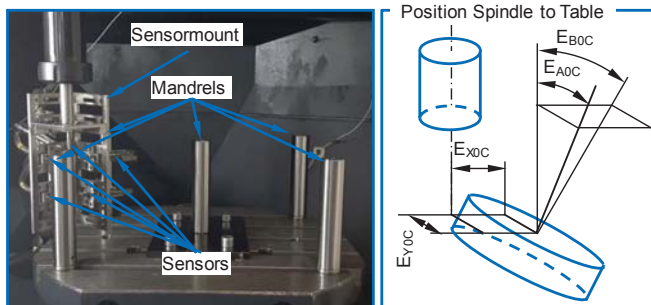


Figure 2: Measurement setup (left) [14] and geometrical errors of the table axis (right)

The measurement uncertainty of the measurement procedure has been determined by the Type A procedure with 50 iterations according to GUM [19] for every combination of mandrel and sensor individually. The uncertainty values show a range between  $0.8 \mu\text{m}$  and  $2.3 \mu\text{m}$  with an average of  $1.6 \mu\text{m}$ .

The demonstrator machine is a medium size machining centre with a [w C B b Y Z t] kinematics according to ISO 10791-6 Annex A [20], see Figure 3. This design with a work piece sided rotary tilt table and a tool sided three-axis serial kinematics is very common for five-axis machine tools [21]. The X- and Y-axis have direct drives and the table is actively cooled. The volume has a size of 400/350/375 (X/Y/Z).

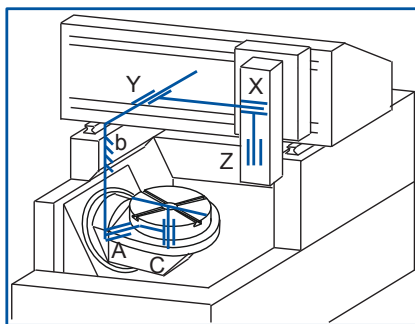


Figure 3: Machine kinematics with rotary-swivel table in [w C B b Y X Z t] configuration

Before every test run, the drives of the demonstrator machine have been in control for at least 24 hours. The test portfolio consists of three test runs for model calibration and one test run for its validation. The two-day calibration test runs consist of a load phase and a cool down phase. The thermal load is applied by an acceleration of the C-axis to a commanded speed followed by a deceleration. This pattern repeats twice per revolution. Every calibration test run started around

the same time of the day and its duration is slightly longer than one day. Thereby, possible environmental influences on the calibration are reduced, because the daily variation in the workshop climate is only contained with one full period in the plateau phase of every test. During the cool down phase, the machine stays in control and no additional load is applied. The effect of the load/cool down is measured every 15 minutes. As only the thermal effect is investigated, the results of the first measurement are subtracted from all other measurements. For an example of the deviations during a calibration measurement and the average of all monitored environmental temperature sensors  $T_{e\,mean}$ , see Figure 4.

The relative measurement between a mandrel and the sensor mount allows the determination of linear deviations in three directions. The angular drifts can be calculated by Equation 1 respectively Equation 2, the geometrical relation of the parameters is shown in Figure 4. The difference  $l_1-l_2$  is 50 mm.

$$B0C = \arctan\left(\frac{x_1 - x_2}{l_1 - l_2}\right) \quad (\text{Eq. 1})$$

$$A0C = \arctan\left(\frac{y_1 - y_2}{l_1 - l_2}\right) \quad (\text{Eq. 2})$$

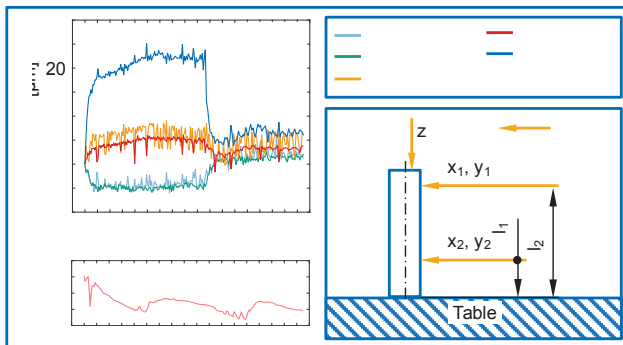


Figure 4: Calibration measurement example (left), arrangement of the sensors and mandrel (right)

The deviation in X- and Y-direction and the differences between the upper and the lower sensors are very small for all test runs, see Figure 4. The results for the angular errors additionally show a very bad ratio of calculated value to measurement uncertainty, due to the small measured differences of the upper and the lower sensor. Therefore, an abbe error compensation is not possible and this paper focuses on the significant deviations in Z [22]. As the differences between the

different Z-direction measurements are in the range of the measurement uncertainty, so the table surface is thermally stable. Only the error of the central mandrel is taken into account for the compensation of the whole table surface. To the author's opinion, the good thermal behaviour in X, Y and of the table surface is caused by the direct drives of these axes and the cooling system of the table. The measurements of position errors of the C-axis have an uncertainty of up to 12 µm. This measurement uncertainty is too high for model input data for compensation purposes.

### 3 Phenomenological modelling approach

The thermal behaviour causing deviations of machine tools has a delay characteristic [23]. The simplified phenomenological grey-box model presented in this paper is a first order delay element, Equation 3. The model relates the axis commanded speed  $u$  and the model displacement  $y$ , by the amplification factor  $K$  and the time constant  $T$ .

$$\frac{y}{u} = \frac{K}{1 + Ts} \quad (\text{Eq. 3})$$

The determined measurement uncertainties are taken into account by a Monte Carlo simulation of the input parameters [19]. The results are fitted by a least square algorithm. The influence of the uncertainties on the achieved maximum value of the calibration step responses are below one micrometre, therefore their influence is neglected.

The model is calibrated with the results of tests for commanded feeds of 5.000 °/min, 10.000 °/min and 15.000 °/min under workshop conditions. The cool down behaviour with no load of the calibration runs defines the models cool down properties. The model parameters for all commanded speeds that differ from the calibrated ones is interpolated linearly. Some of the chosen feeds were part of the model calibration, to see the prediction error of the model for the trained cases. Other feeds were not part of the calibration spectrum to be able to judge the models ability to predict these as well. The commanded feeds of the validation are shown in the bottom part of Figure 5.

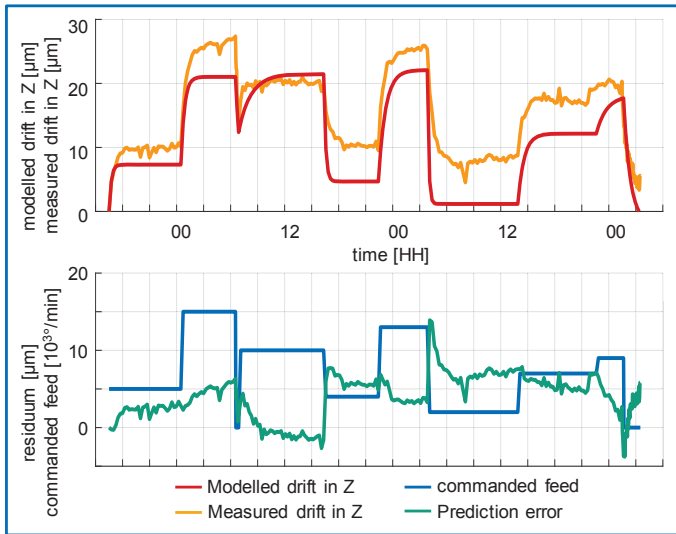


Figure 5: Modelled and measured drift in Z-direction (top), commanded feed and model error (bottom)

The prediction error of the model is displayed in the bottom diagram of Figure 5. For the load scenarios, that were part of the model calibration, the maximum prediction error of the model is 6  $\mu\text{m}$ . With respect to the calibration under workshop conditions this is an acceptable error. For the load sequences that were not part of the calibration, the maximum prediction error raises up to 14  $\mu\text{m}$ . It is caused by the insufficient prediction quality for small commanded feeds.

Additional research is necessary to determine, a better calibration spectrum for the model. Besides, an advanced model, that takes additional thermal influences into account, could enable a better prediction based on the measurements with the presented test setup under workshop conditions. Especially the environmental influence seems to cause prediction errors. In Figure 4 the plateau phase during the heat up procedure shows non-steady measurement results. In Figure 5 the model predicts no error at the end of the cycle, while the machine shows an error, indicating that it has a different thermal state than at the beginning of the cycle.

## 4 Conclusion and Outlook

This paper presents a delay element based approach for modelling of the thermal behaviour of a machine tool's rotary axis with control internal data as input data.

The calibration of the model is performed with a new, extended measurement method inspired by ISO 230-3's ETVE test. The test setup itself is a very cost efficient approaches for rotary axes.

The maximum model prediction error is 14  $\mu\text{m}$  during the validation run, this equals a reduction of the error of 50%. Especially small commanded feeds lead to prediction errors. The model's ability to reduce the thermal error of the machine is limited in case of low commanded feeds. But for high commanded feeds and the resulting huge deviations, the performance is appropriate with respect to the workshop condition calibration. Gebhardt et al. achieve a reduction from 90,1  $\mu\text{m}$  to 34,3  $\mu\text{m}$ , resp. 61,9%, for the C-axis drift in Z [9]. Abdulshahed et al. reduce the thermal error in Z of a C-axis from more than 80  $\mu\text{m}$  to  $\pm 8 \mu\text{m}$ , resp. 80%.

An optimised calibration test spectrum for low commanded feeds promises to enable a better performance of the prediction. In addition, an extension for the model to consider the environmental influence promises a smaller prediction error.

#### *Acknowledgements*

*The Authors want to thank the DFG (German Research Foundation) for the financial support. The represented findings result from the subproject B06 'Property model based compensation' of the special research field SFB/Transregio 96 Thermo-energetic design of machine tools.*

## **5 References**

- [1] C. Brecher, M. Weck, Werkzeugmaschinen Fertigungssysteme: Konstruktion, Berechnung und messtechnische Beurteilung, Springer Berlin Heidelberg, Berlin, Heidelberg, 2017.
- [2] J. Mayr, J. Jedrzejewski, E. Uhlmann, M. Alkan Donmez, W. Knapp, F. Härtig, K. Wendt, T. Moriwaki, P. Shore, R. Schmitt, C. Brecher, T. Würz, K. Wegener, Thermal issues in machine tools, CIRP Annals 61 (2) (2012) 771–791.
- [3] K. Großmann, Thermo-energetic Design of Machine Tools, Springer International Publishing, Cham, 2015.
- [4] C. Brecher, M. Wennemer, M. Fey, Temperaturstabile Werkzeugmaschine, Werkstatttechnik Online 104 (2014) 490–495.
- [5] ISO 230, Test code for machine tools - Part 3: Determination of thermal effects, 2nd ed., ISO copyright office, Genf 25.080.01, 2007.
- [6] ISO 10791, Test conditions for machining centres - Part 10: Evaluation of thermal distortions, 1st ed., ISO copyright office, Genf 25.040.10, 2007.

- [7] ISO 13041, Test conditions for numerically controlled turning machines and turning centres - Part 8: Evaluation of thermal distortions, 1st ed., ISO copyright office, Genf ICS 25.040.20, 2004.
- [8] P. Jatzkowski, Ressourceneffiziente Kalibrierung von 5-Achs-Werkzeugmaschinen mit Tracking-Interferometern, 1st ed., Apprimus-Verl., Aachen, 2011.
- [9] M. Gebhardt, Thermal behaviour and compensation of rotary axes in 5-axis machine tools, ETH Zurich, 2014.
- [10] M. Gebhardt, J. Mayr, N. Furrer, T. Widmer, S. Weikert, W. Knapp, High precision grey-box model for compensation of thermal errors on five-axis machines, CIRP Annals 63 (1) (2014) 509–512.
- [11] J. Flore, Optimierung der Genauigkeit fünfachsigter Werkzeugmaschinen, 1st ed., Apprimus Verlag, Aachen, 2016.
- [12] S. Weikert, R-Test, a New Device for Accuracy Measurements on Five Axis Machine Tools, CIRP Annals 53 (1) (2004) 429–432.
- [13] A. Blazejewski, W. Kwasny, J. Jedrzejewski, T.-W. Gim, Modelling thermal deformation of tilting rotary table with direct drive system, Journal of Machine Engineering 10 (4) (2010) 26–40.
- [14] C. Brecher, R. Spierling, F. Du Bois-Reymond, M. Fey, Thermo-elastic deformation of rotary axes, in: L. Blunt, W. Knapp (Eds.), Laser metrology and machine performance XII, euspens, Bedfordshire, 2017, pp. 111–121.
- [15] A.M. Abdulshahed, A.P. Longstaff, S. Fletcher, A. Potdar, Thermal error modelling of a gantry-type 5-axis machine tool using a Grey Neural Network Model, Journal of Manufacturing Systems 41 (2016) 130–142.
- [16] A. Wissmann, Steuerungsinterne Korrektur thermisch bedingter Strukturverformungen von Bearbeitungszentren, 1st ed., Apprimus Verlag, Aachen, 2014.
- [17] Dr. Johannes Heidenhain GmbH, Einfluss der Positionserfassung auf die Genauigkeit in der 5-Achs-Bearbeitung, Traunreuth, Germany, 2011.
- [18] ISO 230, Test code for machine tools - Part1: Geometric accuracy of machines operating under no-load or quasi-static conditions, 3rd ed., ISO copyright office, Genf 25.080.01, 2012.
- [19] JCGM 101:2008, Evaluation of measurement data — Supplement 1 to the “Guide to the expression of uncertainty in measurement” — Propagation of distributions using a Monte Carlo method, 1st ed., 2008, available at <https://www.bipm.org/en/publications/guides/gum.html> (accessed on 12.12.17).
- [20] ISO 10791, Test conditions for machining centres - Part 6: Accuracy of speeds and interpolations, 2nd ed., ISO copyright office, Genf 25.040.10, 2014.
- [21] Seng Khim T., L. Chin Keong, Modeling the Volumetric Errors in Calibration of Five-axis CNC Machine, in: S.I. Ao (Ed.), The 2010 IAENG International Conference on Industrial Engineering, the 2010 IAENG International Conference on Industrial Engineering - Human Factors and Ergonomics, the 2010 IAENG International Conference on



Operations Research, the 2010 IAENG International Conference on Scientific Computing, IAENG, Hong Kong, 2010.

- [22] J.B. Bryan, The Abbé principle revisited: An updated interpretation, *Precision Engineering* 1 (3) (1979) 129–132.
- [23] G. Jungnickel, *Simulation des thermischen Verhaltens von Werkzeugmaschinen*. Schriftenreihe des Lehrstuhls für Werkzeugmaschinen, Dresden, 2000.

# Investigation of passive torque of oil-air lubricated angular contact ball bearing and its modelling

*J. Kekula<sup>a</sup>, M. Sulitka<sup>a</sup>, P. Kolář<sup>a</sup>, P. Kohút<sup>a</sup>, J. Shim<sup>b</sup>, C.H. Park<sup>b</sup>, J. Hwang<sup>b</sup>*

<sup>a</sup>Research Center of Manufacturing Technology RCMT, Czech Technical University in Prague, Horská 3, Prague, 128 00, Czech Republic

<sup>b</sup>Korea Institute of Machinery & Materials KIMM, Daejeon 34103, Republic of Korea

**Abstract.** Angular contact bearings are most commonly used in high speed spindles. To increase higher speeds and bearing life, minimum quantity oil-air lubrication is used. Model providing reality close prediction of ball bearing heat generation is a main prerequisite for relevant simulating the spindle thermo-mechanical behaviour. A test rig for experimental research of ball bearing thermal behaviour and passive torque for grease and oil-air lubrication has been developed. Houpert frictional model have been implemented into the test rig complex thermo-mechanical model and verified. Torque models reliability for oil-air lubrication is evaluated.

**Keywords:** Angular contact ball bearing; Heat generation; Bearing torque; Oil-air lubrication

---

## 1 Introduction

Heat generated by the spindle ball bearings represents the main factor affecting the thermal and structural behaviour of the spindle under rotation. Heat generation strongly depends on the bearing lubrication. Improper lubrication can cause thermal instability particularly at high spindle speeds; bearing over lubrication can lead to elevated heat generation as well. Description of the angular contact bearing kinematics under rotation and force loading was introduced by Jones [1] and Harris [2]. Heat generation models have been proposed by Palmgren [4], Snare [5] or Harris [2]. Houpert contributed to the torque modelling by a more detailed description of the torque components [3].

### Nomenclature

T	temperature
U	dimensionless speed parameter
W	dimensionless load parameter
G	dimensionless material parameter
$d_m$	mean diameter of the bearing
E	reduced Young's modulus of elasticity
$R_x$	Hertzian radius of the curvature of the elastic contact
k	reduced radius ratio

r	radius of the relevant contact
D <sub>b</sub>	diameter of the rolling element
RPM	velocity of the inner ring
η	lubricant dynamic viscosity
ν	lubricant kinematic viscosity
ω	angular rotational velocity
α	current contact angle

## 2 Torque Models

Loss torque (heat) is generated in the contact point between the rolling elements and the race. Ball bearing torque models are developed with the aim of correctly describing the force and velocity distribution in the bearing. Torque models known up to now formulate three main components of the bearing torque: the rolling resistance, the viscous friction torque and the spinning contribution.

The most well-known is the Palmgren torque model [4]. This model is used also by Harris [2]. Different approach is used by Houpert [3] model, which adopts a detailed description of the contact between rolling elements and bearing race.

### 2.1 Palmgren/Harris Torque Model

As mentioned above, the total passive torque of angular contact ball bearing is composed from several components.

The first one is the rolling friction component which primarily depends on the contact forces in the bearing. This contribution is substantial at higher force loading of the bearing.

The second one is the viscous friction component. This is the most important component especially for the spindle ball bearings. The bearing lubrication has an essential impact to the total friction torque. The viscous Palmgren/Harris formula can be presented according to [6] as:

$$M_{v\ i,o} = 0,225 \cdot 1.10^{-3} \cdot (\nu(T_B) \cdot \omega)^{\frac{2}{3}} \cdot d_m^3 \quad (1)$$

Where  $i,o$  indexes indicate the inner or outer contact. The additional movement of the rolling element called as spinning arises from complex kinematic conditions in the bearing. This contribution is considered at the inner race only following the outer race control theory according to Jones [1].

The resulting torque at the inner ring is calculated as a sum of all of the partial components.

## 2.2 Houpert Torque Model

Houpert model [3] consist of similar components as Palmgren/Harris model, however the Houpert model introduces a more detailed modelling of the ball bearing internal forces, arising in the contact zone between the ball and race. The first force component called the *rolling resistance MER* is determined following the Snare [5] investigation. This resistance correspondences to the elastic hysteresis losses and the contact micro slip during the rolling process at the contact zone. The second force component, viscous resistance, is determined following the lubrication regime occurring in the contact between the ball and race. If a proper lubrication is established and a full film between the ball and the race is developed, EHL lubrication regime is considered. The EHL viscous force is determined by the formula (2), introduced in [9]:

$$FR_{EHL\ i,o} = 2,765 \cdot E^* \cdot R_{x\ i,o}^2 \cdot k_{i,o}^{0,35} \cdot U_{i,o}^{0,656} W_{i,o}^{0,466} \cdot G_{i,o}^{0,022}. \quad (2)$$

Total torque, as proposed by Houpert, is composed by MC and MP components. The first one is the curvature friction moment MC which is caused by the shape of the contact ellipse in space. The MP component is the friction moment due to pivoting effects. For both of the components the constant friction coefficient over the contact ellipse is considered.

Contribution of one rolling element to the overall rolling resistance acting on the shaft (inner ring rotates) is expressed by the following relationship according to [3], see Fig. 1:

$$dM_T = 2 \cdot (FR_i + FR_o) \cdot \frac{r_o \cdot r_i}{d_m} + \frac{MC_i \cdot r_o + MC_o \cdot r_i}{D_b} + \frac{MER_i \cdot r_o + MER_o \cdot r_i}{D_b} + \frac{MP_i \cdot \left(1 + \frac{D_b \cdot \cos \alpha_i}{d_m}\right)}{2} \cdot \sin \alpha_i \quad (3)$$

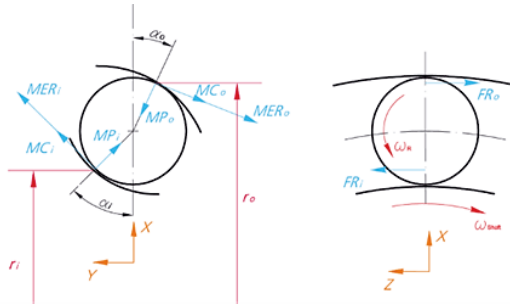


Fig. 1. Forces and moments acting on the rolling element

The final torque is determined by the sum of individual contributions of all of the rolling elements. The final bearing loss torque is determined as a product of the shaft angular velocity and the bearing passive torque.

### 3 Angular Contact Ball Bearing Kinematical Model

Ball bearing kinematical model represents the main prerequisite for a ball bearing torque modelling. In this study, a model of angular contact ball bearing based on Jones theory [1] is used, see Fig. 2 (a). Ball bearing model is a 2 DOFs axisymmetric model considering the outer ring control theory, see Fig. 2 (b). Gyroscopic effect is neglected. The ball bearing model calculates the actual bearing internal conditions resulting from the current speed, temperature and displacements of the outer structure.

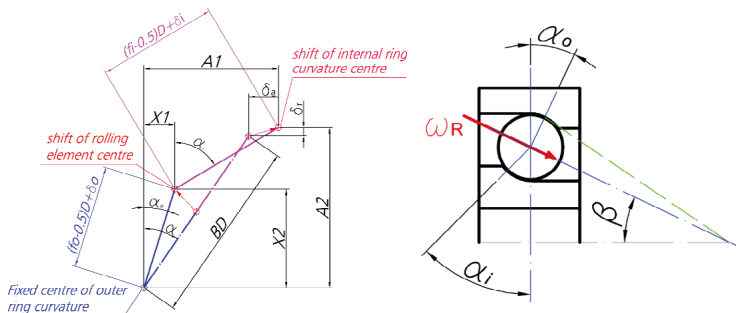


Fig. 2. (a) Internal bearing geometry; (b) Outer race control theory

### 4 Thermo-mechanical model

Spindle thermo-mechanical behaviour represents a complex problem with the closed loop interaction between the spindle, spindle bearings and the outer

structure. For describing the transient thermo-mechanical (TM) spindle behaviour, a closed loop simulation model can be used. The principle of the TM model is introduced in [8] and a scheme of model is presented in the Fig. 3 (a) together with the 2 DOFs axisymmetric finite element (FE) model used for structural solution (Fig. 3 (b)). The TM model takes into account the bearing configuration (number of bearings, “X” or “O” etc.) and type of preloading (rigid/spring). Based on the knowledge of the conditions from the previous step the update of the bearing internal conditions (angles, forces and velocities) is used as an input for the next computational step.

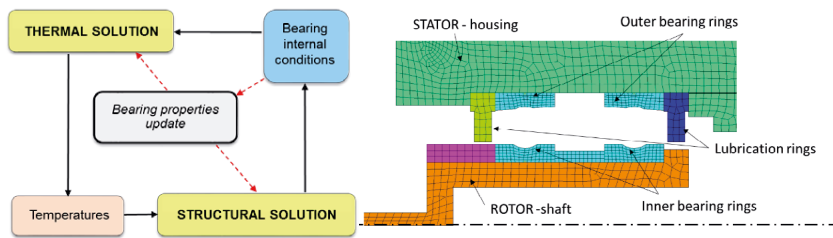


Fig. 3. (a) Scheme of the thermo-mechanical task; (b) FEM model of the bearings and test rig structure

Heat generated by the bearing is used as an input for the thermal and structural task by the TM model. Heat flux is divided uniformly between the bearing rings and rolling elements. Half of the heat flux is assigned to bearing rings (25 % to inner and 25 % to outer ring) and the 50 % of the overall heat flux is applied to the rolling elements.

## 5 Experimental Setup

Validation of the ball bearing torque models is performed by using a specialized test rig Fig. 4 (a). The structure consists of the electric motor (1) which is coupled through the rotational torque sensor (2) with the shaft and the examined bearings. Spring preloaded angular contact ball bearing are fitted in “X” arrangement in the housing (3).

Spring preloaded configuration was used in order to minimize the preload variation due to thermal deformation of the structure. Thanks to spring preloaded bearing design and relatively light preloading force it is possible to observe primarily viscous effects in the bearings. The housing structure allows measuring the temperatures of the bearing outer rings, temperatures of the structure and the surface temperatures as well. The preloading force is monitored by an in-

built force sensor. Oil-air lubrication by a VG68 oil is applied with the oil dosing according to the manufacturer recommendation as approx. 0,1 g/bear/hour. Also the grease lubrication of an open type bearing design was examined.

Angular contact ball bearings FAG B7214-E-T-P4S-UL with 25° contact angle were used. Preloading force was adjusted by spring preloading system to approx. 800 N.

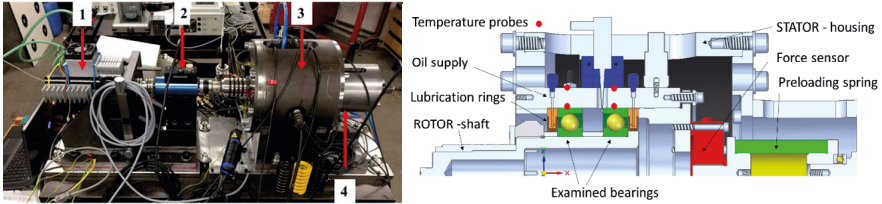


Fig. 4. Configuration of the test rig.

## 6 Results

Tests have been performed for speeds ranging from 2 000 to 10 000 rpm. Both the oil air and grease lubrication was considered. Each test starts from the room temperature and runs until a stable temperature of the structure is reached.

### 6.1 Experimental Data and Torque Model Comparison

Behaviour of the Harris and Houpert EHL torque models has been examined at stable temperatures, determined from experiments. The results for a single bearing without structure interaction can be seen in the Fig. 5. Average experimental temperatures of the bearing outer rings are marked at each speed level by vertical red lines.

It is obvious that both of the torque models return overestimated torque values, compared to the experimental data even if the real experimental temperatures of the bearing are applied. Harris model reveals drastic deviation of hundreds percent from the experiments; Houpert torque model gives more reasonable values, nevertheless still the torque prediction is higher than the experiments.

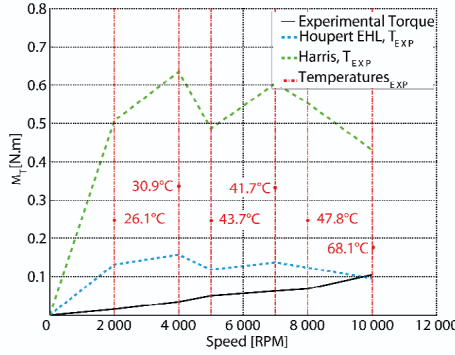


Fig. 5. Experimental data and torque models comparison, FAG B7214-E-T-P4S-UL, 800 N axial preload force; oil-air lubrication method, VG68 oil, without structure interaction;  $d_r = 0$  mm

## 7 Torque Model Modification

Based on the experiments, a correction of the Houpert model is proposed.

### 7.1 Houpert Torque Model Fit

Houpert torque model reveals only slight dependency on the speed, as can be seen from Fig. 5, despite a quite significant temperature rise. The biggest contribution to the final torque is generated by the viscous force component acting on the ball, computed according to the EHL theory by the equation (2(2)). The speed effect in the torque calculation is expressed by the dimensionless speed parameter  $U$ :

$$U_{i,o} = \frac{\eta_0 \cdot v_{m i,o}}{E^* \cdot R_{x i,o}} \quad (4)$$

The numerator is composed of the dynamic viscosity  $\eta_0$  and the mean relative speed  $v_m$  between the race and the rolling element at relevant contact. As the speed grows, the temperature is rising and the lubricant viscosity decreases. The final torque value calculated by the equation (2(2)) is most sensitive to the values of the parameter  $U$  exponent.

Therefore, the analysis has focused on an indirect fitting of the parameter  $U$  exponent value according to the measured data. An additive parameter  $\delta$  depending on the speed is proposed:



$$FR_{EHL\_H} = 2,765 \cdot E^* \cdot R_x^2 \cdot k^{0,35} \cdot U^{(0,656+\delta)} W^{0,466} \cdot G^{0,022} \quad (5)$$

Fit of the parameter  $U$  exponent correction value  $\delta$  for both the oil-air and grease lubrication is evaluated in Fig. 6. An approximately linearly decreasing dependency of the  $\delta$  parameter with the speed can be seen for both the oil air (O-A) and grease (G) lubrication.

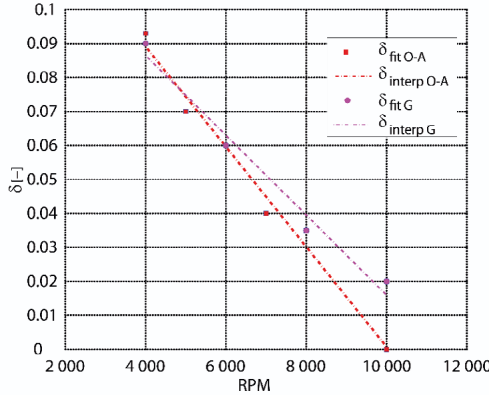


Fig. 6. Fit of the parameter  $U$  exponent correction value  $\delta$

$$\delta_{VG680\alpha} = -1.473 \cdot 10^{-5} \cdot RPM + 0.1480 \quad (6)$$

$$\delta_{VG22g} = -1.175 \cdot 10^{-5} \cdot RPM + 0.1335 \quad (7)$$

Simulation of the loss torque and comparison with the experiments is presented in Fig. 7. Calculation by using the original Houpert model and the real experimental values of speed, force and temperature for a single bearing without the structure interaction is shown by the magenta line. The same case, however using the corrected Houpert model is shown by the blue line. The black line corresponds to the corrected Houpert model implemented in the TM simulation model of the whole test rig structure. Experimental data is depicted by the green line. Temperatures of the bearing outer ring calculated by the TM simulation model (cyan line) are compared with the experimental data (red line).

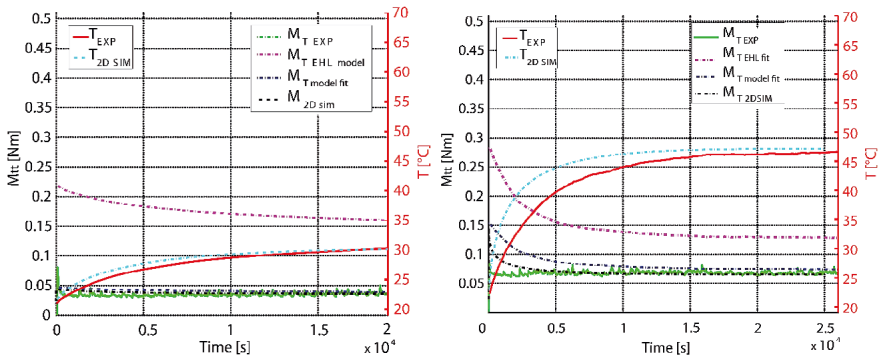


Fig. 7. Comparison of the Houpert torque model (magenta), updated model (blue) and experimental data (green); (a) 4 000 RPM; (b) 8 000 RPM, oil-air lubrication, VG68 oil, 800 N axial preload

List of the experimental data ( $MT_{exp}$ ) obtained by the original Houpert model ( $MT_H$ ) and the corrected Houpert ( $MT_{Hc}$ ) model for oil air lubrication is given in the Table 1.

Table 1. Experimental (oil-air) and simulation data comparison using the original and corrected Houpert model

Speed (RPM)	$MT_{exp}$ (RPM)	$MT_H$ (RPM)	error (%)	$MT_{Hc}$ (Nm)	error (%)
4 000	0,04	0,16	358,6	0,04	3,1
5 000	0,05	0,12	144,0	0,04	16,6
7 000	0,07	0,14	104,6	0,06	17,4
8 000	0,07	0,13	87,1	0,07	8,2
10 000	0,10	0,10	0,6	0,08	23,0

## 8 Conclusion

Experimental research of the Harris and Houpert ball bearing torque models for spindle bearings with oil air and grease lubrication has been performed by using a specialized test rig and spindle ball bearing with 25° contact angle. The torque models have been implemented into the test rig thermo-mechanical simulation model.

It has been demonstrated that both the Harris and Houpert model overestimates the torque prediction. A better behaviour is shown by the Houpert model, for which a correction providing a more accurate expression of the ball bearing speed effect has been proposed. Speed dependent correction of the Houpert EHL viscous force component is calculated for both the oil air and grease lubrication.

Effect of different ball bearing contact angles and lubrication amount, especially in the case of oil air lubrication, is a perspective of the next work.

### **Acknowledgements**

*The authors greatly acknowledge the support of the Sponsored research agreement between the Korea Institute of Machinery and Materials (KIMM) and Czech Technical University in Prague, Research Centre of Manufacturing Technology (RCMT)*

## **9 References**

- [1] Jones, A., B., 1960. A General Theory for Elastically Constrained Ball and Radial Roller Bearings Under Arbitrary Load and Speed Conditions. *Journal of Basic Engineering* 06/1960, 309-320. doi:10.1115/1.3662587.
- [2] Harris, T., A., Kotzalas, M., 2006. *Rolling Bearing Analysis* 5th edition. Essential Concepts of Bearing Technology. Taylor&Francis Group, LLC. ISBN-13: 978-0-8493-7183-7
- [3] Houpert, L., 2002. Ball Bearing and Tapered Roller Bearing Torque: Analytical, Numerical and Experimental Results. 57th STLE Annual Meeting, Houston 05/2002
- [4] Palmgren, A., 1959. *Ball and Roller Engineering*. SKF Industries
- [5] Snare, B., Rolling resistance in Bearing. *SKF Journal*. BBI 67 03 01
- [6] Jorgensen, B., R., Shin, Y., C., Dynamic of Machine Tool Spindle/Bearing Systems Under Thermal Growth. *Journal of Tribology* 10/97, vol.119, 875-882
- [7] Cao Y., Altintas, Y., Holkup, T. 2010. Modeling and comparison of high speed spindle systems with different bearing preload mechanisms. *CIRP -2nd International Conference, Process Machine Interactions*, UBC, Vancouver 01/2010
- [8] Cao Y., Altintas Y., A General Method for the Modeling of Spindle-Bearing Systems, *J. Mech. Des.* 126 (2004) 1089. doi:10.1115/1.1802311.
- [9] Houpert, L., 1987. Piezoviscous-rigid rolling and sliding traction forces. Application: the rolling element-cage pocket contact. *Proceedings of the 1986 ASLE/ASME conference*. Pittsburgh, *ASME Journal of Tribology*. Vol.109;1987.p.363-371

# Cooling strategy for motorized spindle based on energy and power criterion to reduce thermal errors

*A. Mathur, S. N. Grama, A. N. Badhe*

Dr. Kalam center for innovation, Bharat Fritz Werner Ltd.,  
Off Tumkur road, Bengaluru- 560022, India

## Extended abstract.

Thermal effects are one of the major reasons for dimensional inaccuracy obtained on a machined component. Thermal effects from a motorized spindle contribute largely to the distortions of the Tool Centre Point (TCP) from its reference position. Frictional losses at bearing region and electrical and magnetic losses at motor region are the main culprits for heat generation within a spindle. Though a chiller unit with Ambient temperature Tracing Strategy (ATS) is widely used to extract the generated heat from the spindle, significant amount of distortion is observed due to the unsynchronized dissipation of heat with respect to the generated heat. The present work relates to an improved control strategy, called Chiller Trigger Model (CTM), with respect to the chiller unit compressor on the basis of heat generation rate (power criterion) and the total heat generation (energy criterion). The principle idea of the strategy is to control the switching frequency as well as the switching duration of the compressor so that the amount of heat extraction is in accordance with the heat generation. The proposed strategy is analogous to a conventional proportional controller with the exception that the field variable is chosen as heat rate instead of temperature.

The core idea in the development of the control strategy is to minimize the thermal distortions by effective cooling. As the concept involves dissipating the generated heat in accordance with the generation, a pre-requisite of the model is to estimate them. For instance, the heat generated at the motor region is a function of the rated available power of the motor and the power used by the motor at that particular instant. In contrast to the motor, the heat generated at the bearing section is due to friction at the contact points of the bearing with the spindle. The generated heat is a function of the speed, preload, applied torque and type of lubrication used. Contrary to the generated rates, the dissipated heat is experimentally calculated by measuring the inlet and outlet coolant temperature from the spindle.

The underlying principle of CTM strategy is to control the ON and OFF switching of the chiller unit compressor so as to minimize the difference between the heat generation and the heat dissipation. CNC parameters such as spindle speed and load are computed using FOCAS (FANUC Open CNC API Specification) dynamically linked library files to estimate the real-time heat generation. The experimental setup for testing and validation of the model involves a stand-alone motorized spindle with around 19 temperature sensors affixed within and nearby the spindle. The thermal distortions are calculated using non-contact capacitive displacement sensors mounted on a fixture clamped at the front of the spindle face. Experiment is performed under no-load condition and the temperature readings and corresponding thermal displacements are measured. The displacements measured using the capacitive sensors are transformed to get the thermal expansion,  $\Delta z$ , yaw and pitch angles ( $\gamma_x$  and  $\gamma_y$ ) respectively. During experimentation, the displacements are measured at a higher frequency initially and later every 600 seconds (at 60, 60, 60, 120, 300 and every 600 seconds). The validation of the model is done by comparing the results of both ATS and CTM strategy obtained for the same experimental profile (Fig. 1).

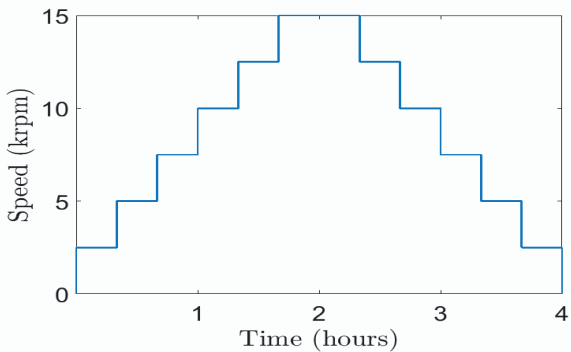


Figure 1: Speed profile for the experiment

The thermal distortion obtained for the aforementioned experimental profile for both ATS and CTM are shown in Fig. 2.

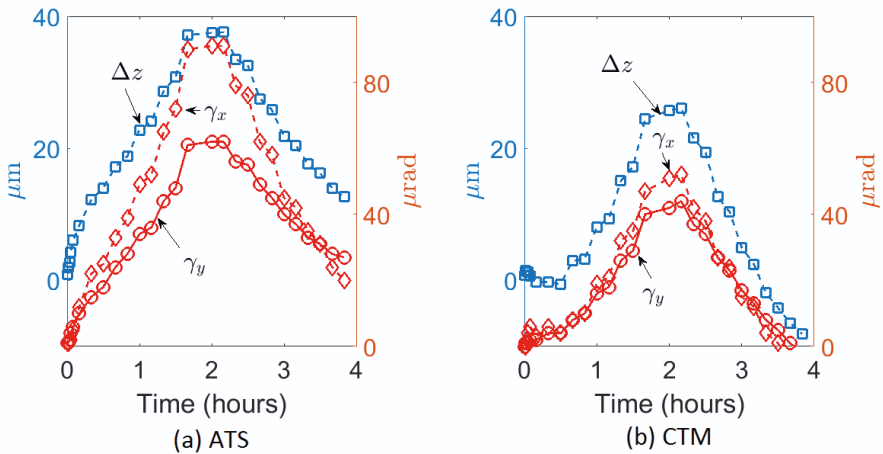


Figure 2: The thermal distortion observed when compressor is operated through CTM strategy (right) is much lower than the one during ATS strategy (left).

It is clear from the results that for the same experiment, a significant amount of reduction in thermal expansion and yaw and pitch angles is observed for CTM when compared with ATS. It is thus remarked that the proposed strategy fares better than the standard control strategy when thermal errors are important. It is important to note that although a power matching based cooling strategy has been developed in [1], the current method can be implemented on a traditional bath recirculation cooler unit with significantly lower cost.

### References:

[1] T. Liu, W. Gao, Y. Tian, D. Zhang, Y. Zhang, W. Chang, Power matching based dissipation strategy onto spindle heat generations, *Applied Thermal Engineering* 113 (2017) 499–507.



# Cooling Potential of Heat Pipes and Heat Exchangers within a Machine Tool Spindle

*B. Denkena, B. Bergman, H. Klemme, D. Dahlmann*

Institute of Production Engineering and Machine Tools IFW, Leibniz Universität Hannover,  
30823 Garbsen, Germany

**Abstract.** Heat losses of the motor and bearings lead to thermal loads on motor spindles and thus to machining inaccuracies, varying dynamic spindle stiffness and decreasing bearing life. The herein introduced novel cooling approach uses heat pipes and heat exchangers to dissipate heat from the shaft through air convection to decrease thermally induced influences on the spindle. This paper illustrates the implementation of the heat transfer devices into a spindle system and results of measurements on a prototype spindle. Finally, the concept's potential for reducing spindle displacement, system temperatures and the time to reach a thermally stable state is shown.

Peer-review under responsibility of the International Scientific Committee in the person of the Conference Chair Prof. Steffen Ihlenfeldt.

Keywords: Spindle; Cooling; Convection

---

## 1 Introduction

Current developments in motor spindles for applications in machine tools are pushed by demands for increasing torque and cutting speeds. As a result, the spindle designer is confronted with demands for higher power on the one side and consequently an increase in power losses on the other side. Thermal loads on motor spindles are particularly critical, as it is an accuracy determinative component. Thermal loads on a spindle system lead to following basic challenges [1]:

- Tribological stresses on bearings benefit wear. The lifetime of bearings is affected negatively.
- Heat losses within the motor can reduce its performance limit. Thus, it is not possible to use its entire electrical efficiency.
- A large portion of heat losses is conducted into the shaft. Thus, the shaft deforms thermoelastically so that manufacturing inaccuracies may occur.
- Thermoelastic elongation of the shaft leads to relative displacement between inner and outer bearing rings, thus to varying spindle dynamics.



In order to reduce these effects, jacket cooling of the spindle housing is commonly applied. However, jacket cooling decreases the temperature of the spindles static components disproportionally more than it reduces temperatures of the rotating parts. In case of bearings, this leads to a temperature gradient between inner and outer bearing rings, as the temperature of the inner ring is always higher. According to the applied bearing type and arrangement, this gradient affects the mechanical properties of the spindle system. In most spindle designs preloaded O-arrangements of at least two angular contact ball bearings are used when high axial and tilting stiffness is required. The bearing preload is set manually during the spindle assembly. As a result of centrifugal forces and thermally induced displacement of the spindle shaft the initial preload decreases. These correlations reveal that, for some applications where the spindle is subjected to high thermal loads, solely cooling of the spindle housing is not sufficient [1]. In order to increase the spindle durability and stiffness, additional cooling of the rotating system is necessary. Currently available cooling systems cool the shaft actively by supplying oil through a rotary feedthrough. However, the sealing technique is susceptible to leakage at high speeds and leads to significant additional system costs.

The herein presented concept suggests that passive heat transfer devices be utilized to reduce the shaft temperature. Heat is transferred from the heat sources with heat pipes (HP) to rotary heat exchangers (HE). A HP is a heat transfer device that combines the principles of both heat conduction and phase transition to transfer heat between two solid materials. Conventional jacket cooling is used to dissipate heat out of the spindle system. The first section of this paper covers the description of this approach. In the second section, results of experiments and simulations are presented that characterize the heat transfer behaviors of the applied HP and HE. Based on these findings a spindle prototype was designed, which is introduced in the following chapter. The paper ends with an experimental evaluation of the prototype.

#### Nomenclature

$\gamma_{HP}$	angle between heat pipe axis and shaft axis
$\lambda_{HP}$	heat conductivity of heat pipe
$\omega$	angular velocity
$\alpha_{eq}$	equivalent heat transfer coefficient
$A_{HE}$	heat exchanger surface
$A_{HP}$	heat pipe cross section
$dT$	temperature difference
$D_{th}$	thermally induced displacement
HE	heat exchanger
HP	heat pipe
$l_{ax}$	distance from shaft axis to heat pipe axis
$l_{Con}$	length of condensation zone
$l_{Ev}$	length of evaporation zone

$l_{HP}$	heat pipe length from middle of evaporation zone to middle of condensation zone
$n$	rotational speed
$\dot{Q}$	heat flow
$T_1$	low temperature
$T_2$	high temperature
$t_s$	time to reach a thermally stable state

## 2 State of the art and novel approach

Several approaches for cooling a motor spindle shaft with HP have been introduced in the past. Judd et al. [2] investigated the use of HP for bearing cooling within the center of a machine tool spindle shaft at a maximum rotational speed of 2.778 rpm. The condensation zone of the HP was cooled with ice and water. A temperature decrease of around 50% was achieved. The cooling effect was found to be negligible when environmental air was used instead. As the shaft center is usually used for mounting a clamping system, this idea is not feasible for applications in machine tools [3]. However, Gebert [1] reveals the potential of convective heat transport from the rotating to the static components of a machine tool spindle using the internal air. A similar approach is described in [4]. Groll et al. [5], Harano et al. [6] and Khanh [7] applied additional lamellar heat dissipators as a heat sink in the condensation zone of the HP, thereby improving the cooling effect of a central HP within a shaft of electrical machines. Groll et al. [8] and Hashimoto et al. [9] replaced the central HP with several HP revolving around the shaft axis. In [9], the HP has inclining condensation zones using centrifugal forces to support fluid return to the evaporation zone. At a maximum speed of 24.000 rpm, the maximum shaft temperature was decreased by around 40%. While numerous approaches for applications of fluid-less heat dissipation within shafts of electrical machines exist, no application specifically for machine tool spindles is known.

The herein described approach is based on the approaches of [5], [6], [7] and considers the potential, which is mentioned in [1]. A combination of highly conductive revolving HP and rotating lamellar HE dissipate heat out of the rotating system. The principle is illustrated in Fig. 1. The basic idea is to transfer heat from rotating heat sources, such as the inner bearings rings and the secondary part of the motor, to a heat sink, respectively into the HE system. Therefore, HP are integrated into the spindle shaft. The rotating fins of the HE are mounted onto the shaft. Heat is conductively transferred from the rotating side of the HE to the static side conductively through small air gaps. The static fins are thermally coupled to the spindle housing. Finally, heat is dissipated out of the spindle system using conventional jacket cooling. In the following sections, the cooling potential of this approach is described.

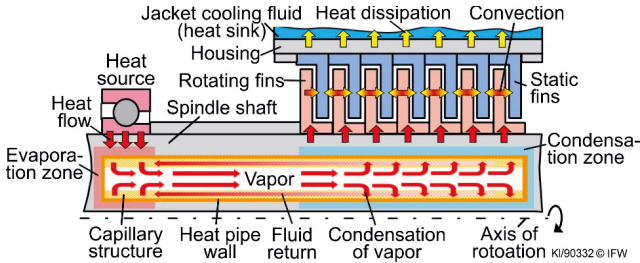


Fig. 1. Schematic drawing of heat dissipation from the shaft.

### 3 Determination of heat transfer characteristics

In order to evaluate the cooling potential within a motor spindle, HP and HE were implemented into a motor spindle. The adapted spindle design is described in chapter 4. ANSYS finite element (FE) software was used to evaluate the cooling potential of the novel approach. In order to obtain physical input values for the simulation, the heat conductivity of the applied HP was determined based on experiments. The heat transfer coefficient of HE was analyzed using FE-simulations. The applied model was validated experimentally.

#### 3.1 Heat conductivity of heat pipes

The determination of heat conductivity of HP can be done analytically, using fluid flow simulations, or experimentally. Detailed descriptions of these approaches can be found in [10]. However, model-based approaches have to consider a variety of correlations, as physical processes of heat transport within a HP are very complex. For this reason, a test bench for the evaluation of revolving HP was designed. In [9] and [11], it was found that centrifugal forces benefit the fluid return and increase heat conductivity. Consequently, the test bench allows the variation of the angle  $\gamma_{HP}$  between HP axis and shaft axis in two steps ( $0^\circ$  and  $1^\circ$ ). This way, the effect of centrifugal forces on the fluid return to the heating zone shall be investigated. A schematic illustration of the test arrangement can be seen in Fig. 2. The distance  $l_{ax}$  between HP axis and shaft axis is 58 mm. The length was chosen according to dimensions of the target spindle. Both lengths of condensation zone  $l_{con}$  and evaporation zone  $l_{ev}$  are 40 mm long. A 130 mm long copper alloy HP with 6 mm in diameter, sintered metal capillary structure (QY-SHP-D6-150 SA) and water as working fluid was used. It was assumed that the large capillary surface of a sintered structure benefits the evaporation of the fluid and thus the heat conductivity, as it is described in [10]. A heat flow  $\dot{Q}$  of 25 Watt is applied to the revolving HP using heat cartridges. Power is transmitted throughout a slip ring. The

temperatures  $T_1$  and  $T_2$  in the middle of the evaporation and condensation zones were measured using PT-100 sensors. The heat conductivity  $\lambda_{HP}$  was calculated according to the equation

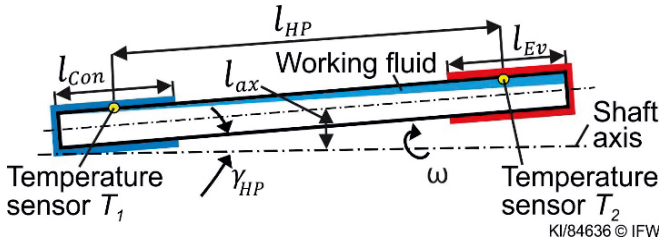


Fig. 2. Revolving heat pipe with nomenclature.

$$\lambda_{HP} = \frac{\dot{Q}}{(T_2 - T_1) \cdot A_{HP}} \cdot l_{HP} \quad (\text{Eq. 1})$$

where  $A_{HP}$  represents the cross section area of the HP and  $l_{HP}$  the length between the middle of evaporation and condensation zone. Hence,  $\lambda_{HP}$  provides an approximation for the combined fluid, wick and wall material conductivity. In Fig. 3, the heat conductivity is illustrated as a function of rotational speeds between standstill and 8.000 rpm for both investigated angles,  $0^\circ$  and  $1^\circ$ . The heat conductivity of the HP with  $0^\circ$ -orientation decreases digressively from a value of around  $3,2 \cdot 10^4 \text{ W}/(\text{m} \cdot \text{K})$  approximating a nearly constant value of around  $1,1 \cdot 10^4 \text{ W}/(\text{m} \cdot \text{K})$ . Forces on the revolving fluid lead to an accumulation of fluid on the outwardly directed inner wall of the tube [11]. This increases the thickness of the fluid film along the entire pipe. A decrease of conductivity is the result. According to [11], it is also assumed that for higher speeds, the conductivity will approximate a value of around  $1,1 \cdot 10^4 \text{ W}/(\text{m} \cdot \text{K})$ . The minimal conductivity of the HP with  $1^\circ$ -orientation is around  $1,0 \cdot 10^4 \text{ W}/(\text{m} \cdot \text{K})$  and can be determined at standstill. This is about a factor of three less than in case of a  $0^\circ$ -orientation. Without centrifugal forces, fluid return to the evaporation zone is caused only by capillary forced. At standstill, gravity acts against the capillary forces. At a speed between 3.000 and 5.000 rpm, centrifugal forces exceed gravity so that the conductivity increases up to a value of around 6.500 rpm followed by a digressive curve. The conductivity of the  $1^\circ$ -oriented HP at a speed of 8.000 rpm is about five times higher than the respective conductivity of the  $0^\circ$ -oriented HP. When the fluid film thickness increases in the evaporation zone, a larger surface available for evaporation is wetted, thereby resulting in an increase of conductivity. These effects are also described in [10] and [11]. However, in [12] it is shown that heat conductivity decreases when the fluid film thickness exceeds a certain value. It is assumed that

the heat conductivity of the examined HP decreases at a certain rotational speed. This effect has not been investigated, as it was not possible to apply higher speeds on the test rig.

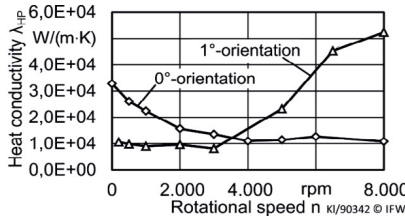


Fig. 3. Results of experimental heat pipe tests for 0°- and 1°-orientation.

### 3.2 Heat transfer coefficient

The heat transfer coefficient  $\alpha_{eq}$  between inner and outer HE fins was determined by applying the equation

$$\alpha_{eq} = \frac{\dot{Q}}{(T_2 - T_1) \cdot A_{HE}} \quad (\text{Eq. 2})$$

with average surface temperatures  $T_1$  and  $T_2$  at the static and rotating fin-air-interface, a definable heat flow  $\dot{Q}$  and the fin surface area  $A_{HE}$ . CFX-simulations were used to investigate the effect of geometrical parameters such as the air gap. Experiments were carried out to validate the simulation model. The simulation setup with the HE geometry is illustrated in Fig. 4. The validation of this model, a description of the test rig setup and analysis of parameters affecting the heat transport of the introduced HE system are presented in [13]. A comparison between the results of experiments and simulations with a 0,5 mm air gap revealed that the applied simulation model is valid up to a rotational speed of 14.500 rpm. For a 0,5 mm air gap, the heat transfer coefficient increases digressively starting from a value of 50 W/(m<sup>2</sup>·K) at standstill to 112 W/(m<sup>2</sup>·K) at 14.500 rpm. For a gap of 0,2 mm, the coefficient increases with increased rotational speed up to a maximum value of 280 W/(m<sup>2</sup>·K) at a speed of around 9.000 rpm. After this,  $\alpha_{eff}$  decreases to around 250 W/(m<sup>2</sup>·K). In fact, the coefficient itself does not decrease. Additional heat is generated as a result of increasing turbulences and fluid friction, respectively. This heat falsifies the calculation according to eq. 2 since the previously defined heat flow  $\dot{Q}$  increases. Consequently, the parameter  $\alpha_{eq}$  is introduced as an equivalent heat transfer coefficient considering additionally generated heat within eq. 2.

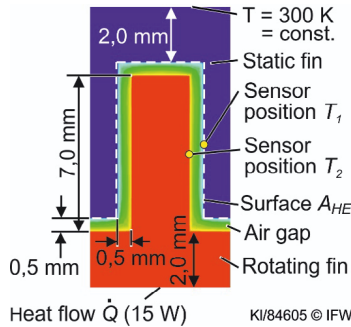


Fig. 4. Simulation setup with heat exchanger geometry (cross section).

## 4 Prototype design

Both, HP and HE were implemented into an FE-model of a spindle and simulated thermoelastically. Other parameters, such as the number, diameter and position of HP, geometry and material of HE, were analyzed iteratively. As a matter of these extensive analyses, only the final spindle design will be described in this chapter. A sectional view of the prototype spindle is illustrated in Fig. 5. In the spindle front, two angular contact ball bearings in an O-arrangement with an inner diameter of 70 mm are used. In the rear, a cylindrical roller bearing with an inner diameter of 60 mm is applied. The spindle is powered by an 11 kW asynchronous motor. Bearings are lubricated with oil-air-lubrication at a flow rate of 40 l/min for each bearing. The distance from the flange to the spindle nose is comparatively long (370 mm), as the spindle shall be applied for complex die and mold making. An overall number of 15 HP transfer heat from the bearings to a lamellar HE system with 13 fins in the middle of the fixed bearings. The motor heat is transferred to the spindle rear using 8 HP. The same type of the HP with a sintered capillary structure was used, as in the experiments before. The HP are inserted into the shaft with a clearance of 0,5 mm and thermal grease for better heat transfer.

A second HE with 10 fins is used in the rear. Each of the static sides of the HE and the stator side of the motor are chilled with one cooling jacket. No clamping system was considered, neither in the simulation model, nor in the experiments with the prototype in order to reduce manufacturing costs. In a first step, no externally acting moments and forces were considered, but only heat generation in the bearings and motor at idle speed.

However, additional forces and moments are considered to be low in die and mold making.

For the thermoelastic FE-model, heat losses in the bearings and motor were calculated according to commercially available bearing calculators and data sheets [14]. Values for the convection between cooling channels and its periphery were calculated using CFX simulations. Convection between rotating parts and air within the spindle was neglected. The FE-Model was used to evaluate the potential of the HE and HP. Therefore, the heat conductivity of the HP was varied between values of 5.000 and 50.000 W/(m·K). No significant reduction of spindle displacement was observed above a value of around 7.000 W/(m·K). Based on the previously described experimental results, no angulated HP are necessary for prototype manufacturing as a conductivity of 11.000 W/(m·K) is assumed to be reached in practice. The heat transfer coefficient of both HE was varied between values of 50 and 400 W/(m<sup>2</sup>·K). A significant effect of heat transfer between rotating and static fins on thermally induced displacement was observed [13]. The final spindle prototype was designed and manufactured with air gaps of 0,2 mm in the front and 0,3 mm in the rear.

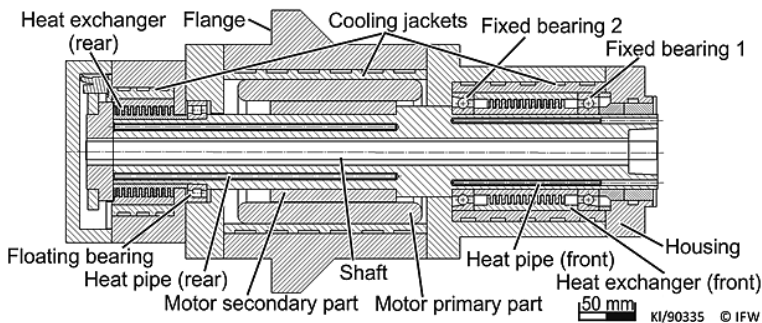


Fig. 5. Cross section of spindle prototype with heat pipes and heat exchangers.

These gap widths were chosen according to simulation results of the thermally induced relative displacement between rotating and static fins. Smaller gaps than 0,2 in the front and 0,3 mm in the rear were assumed critical concerning possible contact between both sides. However, it was found that the effect of HP within the thermal system is small compared to the effect of HE. Various design changes during the iterative spindle design optimization reduced, in particular, the temperatures of the fixed bearings. Thus, only little heat is transferred into the HP.

## 5 Experimental evaluation

A prototype spindle was manufactured according to Fig. 5. A second similar spindle without HP and HE was built to evaluate the cooling efficiency of the introduced cooling concept. The thermally induced displacement was measured with eddy current sensors. As target values, the displacements of the spindle nose (overall displacement) and housing nose were defined. The displacement of the flange was also determined as a reference. The shaft displacement was calculated as the difference between overall displacement and housing displacement. The measured displacements for both spindles are illustrated in Fig. 6 as a function of rotational speed. A significant reduction of displacement can be observed within the entire measuring range. At a maximum speed of 20.000 rpm, the overall displacement of the spindle with the novel cooling concept is 21,4  $\mu\text{m}$ . This is 12,2  $\mu\text{m}$  less than without extra shaft cooling. The housing displacement is nearly similar in both cases. As more heat dissipates into the housing when the novel concept is applied, the housing displacement slightly increases by about 0,2  $\mu\text{m}$ . Thus, it becomes clear that almost the entire reduction of displacement results from shaft cooling. Both spindles were equipped with PT-100 sensors on the surface of the outer bearing rings. The temperatures of the inner rings were measured with PT-100 sensors immediately after stopping the rotation abruptly after

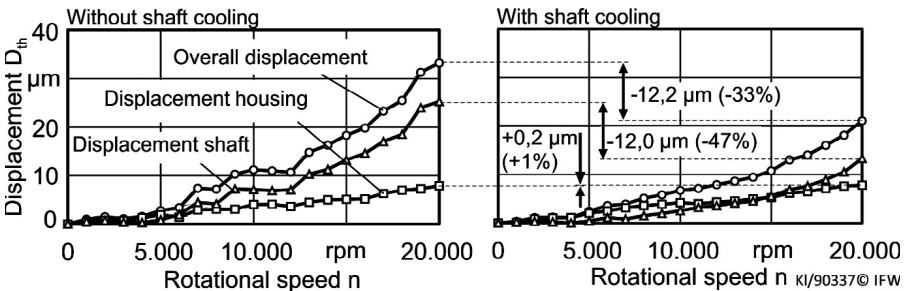


Fig. 6. Spindle displacement as a function of rotational speed with and without new cooling concept.

having reached a thermally stable state. The effect of shaft cooling on the temperature difference  $dT$  between inner and outer bearing rings is illustrated in Fig. 7 as a function of rotational speed. For both fixed bearings, a significant decrease of  $dT$  is achieved.  $dT$  at fixed bearing 2 is reduced from 12,4 K to 4,2 K (-66%) at a speed of 9.000 rpm. As this bearing is more affected by motor heat losses,  $dT$  is constantly higher than that of bearing 1. The reduction of  $dT$  at maximum speed is around 8 K for both fixed bearings. In case of the floating bearing,  $dT$  is



only slightly influenced when the new concept is applied as more heat is transferred from the motor to the back of the spindle. However, a decrease of around 2 K can be stated at speeds between 4.000 and 13.000 rpm. No reduction of  $dT$  can be stated at maximum speed.

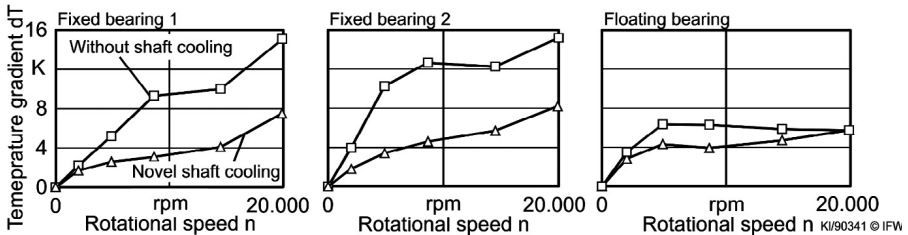


Fig. 7. Temperature differences between bearing rings as a function of rotational speed.

For both spindles, the required time to reach a thermally stable state  $t_s$  was measured. The time  $t_s$  is defined as the time at which the bearing temperatures decrease by no more than 0,1 K. The spindle with shaft cooling is thermally stable after around 15,7 min along all examined rotational speeds. Without shaft cooling,  $t_s$  was determined to 35,3 min. Consequently, an average of 56% of time is saved with the novel approach.

## 6 Conclusion

The herein introduced approach for fluid-less cooling of a motor spindle shaft leads to significant reduction of spindle displacement by 35% compared to a spindle without shaft cooling at a rotational speed of 20.000 rpm. The temperature gradient between inner and outer fixed bearing rings is reduced by around 50%. As heat is consciously transferred to the spindle back, the temperature of the floating bearing increases. However, the temperature gradient between the bearing rings is only slightly influenced. The required time to reach a thermally stable state was reduced by 56%. Consequently, the novel concept allows for the application of higher speeds or bearing preloads in comparison to a spindle without shaft cooling. This results in increased productivity, while maintaining required accuracy. In the future, experiments will be done to quantify the effect of reduced shaft temperature on the dynamic stiffness of the spindle. However, the experimental results show that it is not possible to equalize the temperatures of inner and outer bearing rings. For this reason, it is not yet possible to meet the high demands on temperature stability, as it can be achieved with current fluid-based shaft cooling concepts. Consequently, cooling of the shaft has to be further increased. For this reason, a more efficient use of the internal air for cooling purposes will be investigated in the future.

## 7 References

- [1] Gebert, K., 1997, Ein Beitrag zur thermischen Modellbildung von schnelldrehenden Motorspindeln, Dissertation, Technische Hochschule Darmstadt
- [2] Judd, R.L., Aftab, K., Elbestawi, M.A., 1994, An Investigation of the Use of Heat Pipes for Machine Tool Spindle Bearing Cooling. *International Journal of Machine Tools and Manufacture*, 34/7, pp.1031-1043
- [3] Postlethwaite, S.R., Allen, J.P., Ford, D.G., 1999, Machine Tool Thermal Error Reduction - An Appraisal, *Journal of Engineering Manufacture*, 213/1, pp.1-9
- [4] Kann, J.C., Schirle, N.B., 2003, Motor Shaft Having an Integral Heat Pipe, U.S. patent US6528909 B1
- [5] Groll, M., Kraus, G., Kreel, H., Zimmerman, P., 1973, Industrial applications of low temperature heat pipes, *Proceedings of First International Heat Pipe Conference*
- [6] Harano, K., Oyama, S., 1980, Rotary Electric Machine with a Heat Pipe for Cooling, U.S. patent US4240000 A
- [7] Khanh, D., 1995, Electric motor having internal heat dissipator, U.S. patent US5394040 A
- [8] Groll, M., Krähling, H., Münzel, W.D., 1978, Heat pipes for cooling of an electric motor, *Proceedings of Third International Heat Pipe Conference*, AIAA Report CP784
- [9] Hashimoto, R., Itani, H., Mizuta, K., Kura, K., Takahashi, Y., 1996, Heat Transport Performance of Rotating Heat Pipes Installed in a High-Speed Spindle, *Mitsubishi Heavy Industries Technical Review*, 33/2, pp.88-92
- [10] Faghri, A., 1995, *Heat Pipe Science And Technology*, Global Digital Press
- [11] Hassan, H., Harmand, S., 2016, Effect of Operating Parameters on the Heat Transfer and Fluid Film Thickness of Revolving Heat Pipe, *Heat Transfer Engineering*, 38/5, pp.538-548
- [12] Daniels, T.C., Al-Jumaily, F.K., 1973, Theoretical and experimental analysis of a rotating wickless heat pipe, *Proceedings of First International Heat Pipe Conference*, pp.1-12
- [13] Denkena, B., Dahlmann, D., Klemme, H., 2016, Investigations on Thermal Management of a Machine Tool Spindle by Using Lamellar Heat Exchangers, *Euspen SIG: Thermal Issues*, Presentation, Prag
- [14] Schaeffler Technologies AG & Co., 2016, Easy Friction, <http://bearinx-online-easy-friction.schaeffler.com>, viewed on Nov. 16th 2016



## **Control-integrated correction of thermal displacements**



# Structure model based correction of machine tools

*X. Thiem, B. Kauschinger, S. Ihlenfeldt*

Institute of Machine Tools and Control Engineering IWM, Technische Universität Dresden,  
01062 Dresden, Germany

**Abstract.** The structure model based correction approach utilizes physically based models (e.g. finite element models) for online compensation of thermo-elastic errors at machine tools. This approach requires only a few additional sensors because it uses control internal data. In this paper the structure model based correction approach is investigated on the basis of a machine tool with a serial kinematic and a complex structure. Methods for online parameter identification are adapted and integrated in the correction approach to improve the robustness and the accuracy of the correction model.

Peer-review under responsibility of the International Scientific Committee in the person of the Conference Chair Prof. Steffen Ihlenfeldt.

*Keywords:* Thermal error; Machine tool; Correction; Compensation; Structure model; Control; Online

---

## 1 Introduction

With increasing machining accuracy thermal errors become more and more important. Thermal error dominate the overall error of machine tools [1]. For a further improvement of the machining accuracy different methods are developed to reduce these thermal errors [2, 3]. Common counter measures, like cooling and temperature control of the machine, requires additional energy input. Therefore, the overall energy consumption of the machine is increased significantly [4]. Within CRC/Transregio 96 „Thermo-energetic design of machine tools“ different approaches [5] are researched to reduce the thermal error of machine tools without additional energy consumption while maintaining or increasing productivity. One of the investigated approaches is the structure model based correction of thermo-elastic errors at machine tools [6]. This correction approach utilizes physically based models, like finite element models (FE models), for online compensation of thermo-elastic errors at machine tools [7, 8, 9]. In [10] a modelling systematic is developed which reduces the time effort and necessary knowledge to create a FE based structure model.

## 2 Principle of structure model based correction

The Structure model based correction is classified at the thermo-elastic functional chain [11] in Fig. 1. Within the structure model the different parts of the thermo-elastic functional chain are modelled. The structure model starts at the technological loads which determine the thermal behavior of the machine (e.g. position  $\mathbf{x}$ , velocity  $\mathbf{v}$ , motor current  $\mathbf{I}$ ). Another necessary input information is the environmental temperature  $T_E$  which is needed to describe the environment in the model. Based on these loads power loss ( $\dot{Q}$ ) and thermal conduction ( $\mathbf{L}$ ) are calculated. These are the input information for a load step of the thermal model. In the thermal model the temperature field ( $\mathbf{T}$ ) of the machine is calculated. The deformation field ( $\boldsymbol{\varepsilon}$ ) follows the temperature field instantaneously. Therefore, the deformation field is calculated in a thermo-elastic model based on the temperature field. Finally, the thermal displacement ( $\Delta\mathbf{x}$ ) at the tool center point (TCP) is determined and corrected in the machine tool by an offset to the set point of the machine axes. To enable the correction the structure model has to be calculated in thermal real time. That means the deformation field have to be determined before significant changes occur (for machine tools usually in the time range of several minutes). Node models, rough FE models or FE models with reduced model order [12] usually fulfil this requirement.

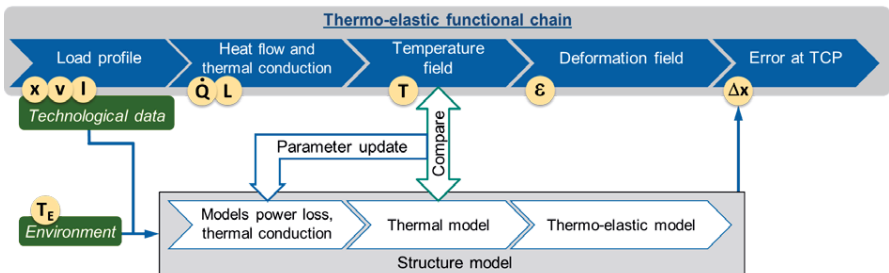


Fig. 1. classification of structure model based correction and parameter update at thermo-elastic functional chain

Some of the model parameters of the structure model are uncertain or change during operation. Therefore, the output of the different part models of the structure model can be compared to measurement values in order to optimize model parameters and improve model accuracy. The parameters of the models for power loss (heat sources) are usually uncertain [13] and have a significant effect on the resulting temperature field in the machine. The heat flow at the heat sources are difficult to measure that's why measured temperatures are

compared to the simulated temperatures and used to optimize the parameters (see Fig. 1). This paper focuses on the online parameter adjustment of power loss models as a part of the structure model based correction based on measured temperatures.

### 3 Model of demonstration machine

The machine in Fig. 2 is selected to demonstrate the correction approach and the online parameter adjustment. It is a three axes Cartesian serial kinematic in lightweight construction. The machine consists primarily of aluminum alloy plates which are clamped with the help of tie rods [14]. The Z-slide is driven by three ball screw drives and the X- and Y-slide by linear direct drives.

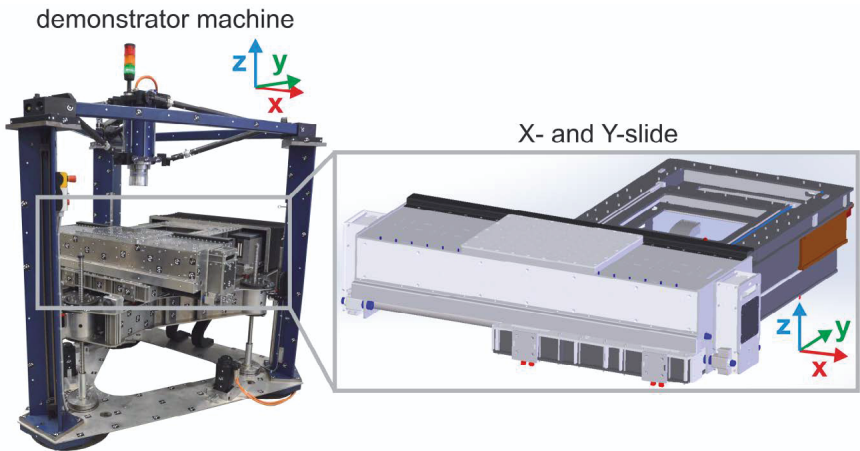


Fig. 2. on the left side demonstrator machine and on the right side CAD model of X- and Y-slide

To reduce the complexity of the structure model this paper focuses on the X- and Y-slide. Node models [8, 15] of X- and Y-slide are developed based on the CAD models (Fig. 2). Node models are network models with lumped parameters. The node models of the slides are pictured in Fig. 3. The lumped heat capacities are sketched as circles. The black lines represent the thermal conduction between the heat capacity. The heat sources in the structure are marked by orange flashes. Heat sources are the linear direct drives, the guides and the measurement amplifier integrated in the Y-slide. The measurement amplifiers are used for the temperature sensors integrated into the X- and Y-slide.

Node models are chosen due to their low computing power requirements. A fast computing model (thermal real time) is necessary to enable online correc-



tion of thermal errors. Additionally a fast model enables the use of optimization methods for parameter adjustment in parallel during machine operation. A rough model was developed with a small number of nodes. Therefore, the modelling effort was low. The relative movement between X- and Y-slide is considered in the model. The interfaces between the slides are the rolling element contact in the guides and the air gap in the linear direct drive between primary and secondary part. The X-axis position determines which heat capacities at the interface are connected to each other by thermal conduction.

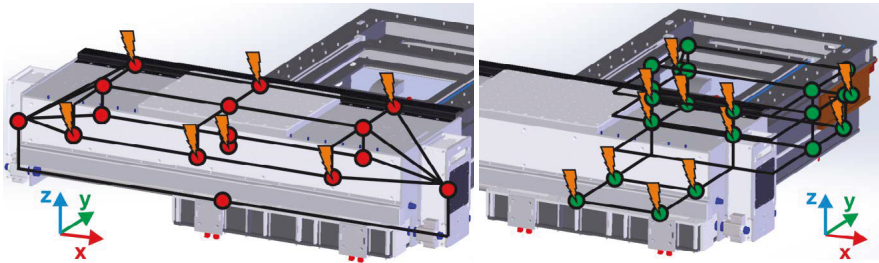


Fig. 3. (a) node model (red) and power loss (orange) X-slide;  
(b) node model (green) and power loss (orange) Y-slide.

## 4 Online parameter adjustment

The initial parameterization based on literature and datasheet differ from the exemplary behavior of the guides and drives. Therefore, the model is inaccurate and a parameter adjustment necessary [13]. Some of the model parameters change during operation due to for example changes in lubrication, wear and preload. That's why a cyclic online update of the parameters is required.

In the example of the X-slide the power loss in guides and linear direct drive has a decisive influence on the temperature field and the parameters are also uncertain. Therefore, these parameters are chosen for online parameter adjustment. The power loss in the components is adjusted by scaling factors under the assumption that the qualitative behavior of the power loss models meets the behavior of the exemplary components.

The parameters are adjusted by minimization of the least error squares between simulated and measured temperatures at chosen positions in the machine structure. For this optimization the same models are utilized as for the structure model based correction. Fig. 4 shows the flowchart for the online parameter adjustment. The steps are sketched chronologically from top to down. On the left side under "online structure model" the cyclical calculation of the

structure model to determine the correction value is pictured. The structure model is calculated every 10 s. The input information (technological loads and environmental temperature) are collected for 10 min and provided afterwards for the online parameter adjustment. Additionally, the simulated start temperature field at the beginning of this 10 min is provided. The measured temperatures at sensitive positions over this 10 min are also necessary to optimize the parameters. For the optimization a Matlab function based on the interior point method was used. The start value for the scaling factors is one. Assuming the correct value is near the initial parameterization. In every optimization step the lower boundary is 90 % and the upper boundary 110 % of the start value because the physical parameters cannot change rapidly. The termination criterions of the optimizer are set to: a step size below 0.01, a maximum of 30 transient model calculations and a maximum of 5 iterations of the optimizer. The model calculations and iterations are limited to prevent the optimizer from extensive and time consuming calculations. Finally, the determined new parameters (updated scaling factors) are provided for the correction model. At the same time the optimizer starts over with a new set of technological loads and the start temperature field of the previous 10 min. The scaling factors determined in the previous evaluation of the optimizer are used as start values. In order to keep the scaling factors within a plausible range, they are limited to 0.25 as lower boundary and 4 as upper boundary. It is assumed that the start values improve with every evaluation of the optimizer. If the optimization takes longer than 10 min, the input information of the optimizer is dropped until the optimization is completed.

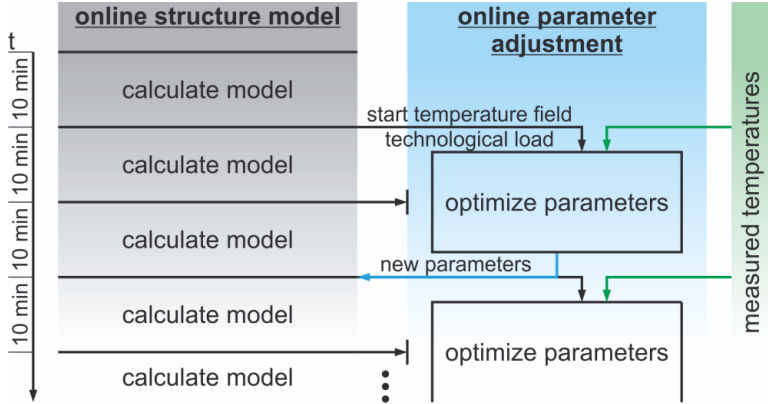


Fig. 4. flowchart for online parameter adjustment

## 5 Measurement setup

Temperature sensors are applied to the X- and Y-slide of the machine for the online parameter adjustment and for the verification of the results of the simulation with and without online parameter adjustment. The temperature sensors are Pt100 resistance sensors. As measurement amplifier Beckhoff bus terminals were used. In this way, the measured values are available in the machine control. The sensors are located near the heat sources and at which determine the thermal error at the TCP. The sensor positions are sketched in Fig. 5. The demonstrator machine was placed in a housing of aluminum profiles and perspex to stabilize the environmental temperature. Temperature fluctuations, e.g. due to an open hall door, are reduced. The environmental temperature sensor is mounted at the height of the X-slide at the machine frame.

During the experiments the X-slide moves cyclically between -200 mm and 200 mm. The middle position of the X-slide is at 0 mm. Therefore, a symmetrical thermal load is applied to the X-guides and the X-drive. The movement resp. the thermal load is applied for 10 min and followed by a displacement measurement cycle of approximately 1 min. The load cycle and the measurement cycle are repeated during a warm-up phase.

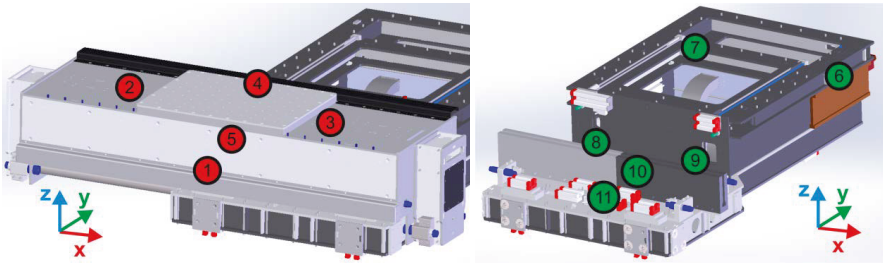


Fig. 5. (a) temperature sensors at X-slide; (b) temperature sensors at Y-slide

## 6 Results

The aim is to adjust the calculated power loss in guides and linear direct drives of the X-slides by scaling factors. Therefore, the temperature sensors near the heat sources are selected for optimization. The temperature sensor 1 (see Fig. 1) at the front plate is selected. This sensor is close to the guide and the measured temperature is dominated by the influence of the power loss due to friction at the guide. Sensor 5 is selected as second sensor for the optimization. This sensor is located at the top side of the primary part of the linear direct

drive. That's why the power loss in the drive has the greatest influence on the temperature measured at this position.

According to Fig. 4 the parameters are optimized for time steps of 10 min. Fig. 6 shows the temperature curves at some of the positions which are marked in Fig. 5 and the scaling factors for the power loss. The measured values are plotted in red and dashed. The simulated values without online parameter adjustment are plotted in blue and the simulated values with online parameter adjustment in green. The environmental temperature is plotted in black. In Fig. 6 (a) the values at sensor position 2 and 3 are nearly the same due to a symmetric thermal load. That's why the simulated values at 2 overlay the values at 3.

In the experiment, both warm-up and cool-down phases are included. In the first three hours the velocity is set to 0.75 m/s, the acceleration is set to  $2 \text{ m/s}^2$  and the jerk is set to  $500 \text{ m/s}^3$ . This load phase is followed by a phase while the axis stand still but the axes remain in position control. Afterwards a second load phase is conducted with a velocity of 0.75 m/s, an acceleration of  $4 \text{ m/s}^2$  and a jerk of  $500 \text{ m/s}^3$ . The doubled acceleration leads to a higher current in the drive and therefore to an increased power loss. The average velocity resp. power dissipation by friction is also increased. This phase is followed by a cool-down phase. During the cool-down phase the axis isn't in position control. The power loss in the drive and guides is zero.

The diagrams in Fig. 6 show that the characteristic thermal behavior is met by the rough simulation model with an initial parameterization already quite well. However, there is still a significant difference between measurement and simulation. To reduce this difference the online parameter adjustment is applied. Fig. 6 (b) and (d) show the results for the temperature sensors which are used for optimization. At Sensor 1 (Fig. 6 (b)) the online parameter adjustment lead to an increased accuracy of the simulated temperature but especially during the second load phase there are an oscillation around the measured value. The oscillation is caused by a fluctuation of the scaling factor for the power dissipation in the guides (Fig. 6 (f)). The initial scaling factor of one seems to be too small and needed to be increased. From the beginning of the cool-down phase on there is no power dissipation due to friction and the scaling factor doesn't affect the temperature. Therefore the scaling factors don't change significantly during cool-down phase. At sensor 5 (Fig. 6 (d)) the simulation without parameter optimization already meets the real temperature quite well and the online parameter adjustment doesn't lead to an improvement. The fluctuation of the scaling factor for the power loss in the primary part is smaller than for the pow-

er loss in the guides, due to the better initial parameterization. The overall accuracy of the thermal model is improved by the online parameter adjustment as the diagrams of the other sensors show.

In future works the stability of the online parameter adjustment should be improved by narrow boundaries for parameter variation, larger time steps for optimization and a better initial parameterization of the model. Approaches have to be developed to determine the minimal number of parameter to adjust and to select a minimal number of temperature measurement positions.

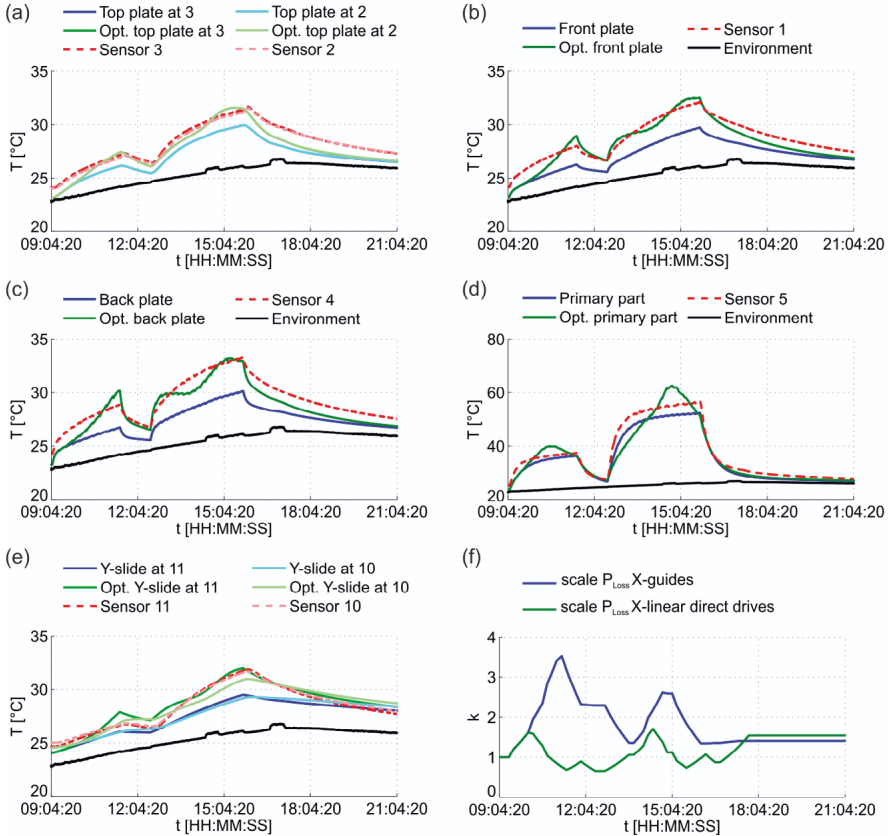


Fig. 6. simulated temperatures (with and without parameter optimization), measured temperatures (sensor numbering according to Fig. 5) and determined scaling factors for power loss in guides and drives of x-axis (f)

## 7 Summary

In conclusion the online parameter adjustment leads to a significant improved accuracy of the thermal model. Even with a rough node model and an initial parameterization only based on literature and datasheets the essential thermal behavior of the machine could be described. This approach could be useful if parameters change during the operation e.g. due to wear and changes in lubrication. Deficiencies of the model can be partially compensated by this approach too. However, the approach still needed to be improved, especially to improve the stability.

### **Acknowledgements**

*This research was funded by the German Science Foundation (DFG) within the CRC/Transregio 96 “Thermo-energetic design of machine tools”, project B07.*

## 8 References

- [1] Wegener, K., Weikert, S., Mayr, J., 2016. Age of Compensation – Challenge and Chance for Machine Tool Industry. *IJAT* 10, 609–623.
- [2] Mayr, J., Jedrzejewski, J., Uhlmann, E., Alkan Donmez, M., Knapp, W., Härtig, F., Wendt, K., Moriwaki, T., Shore, P., Schmitt, R., Brecher, C., Würz, T., Wegener, K., 2012. Thermal issues in machine tools. *CIRP Annals - Manufacturing Technology* 61, 771–791. doi:10.1016/j.cirp.2012.05.008
- [3] Ramesh, R., Mannan, M., Poo, A., 2000. Error compensation in machine tools — a review. *International Journal of Machine Tools and Manufacture* 40, 1257–1284. doi:10.1016/S0890-6955(00)00010-9
- [4] Weber, Juliane, Weber, Jürgen, Shabi, L., Lohse, H., 2016. Energy, power and heat flow of the cooling and fluid systems in a cutting machine tool, in: Volume 46. Presented at the 7th CIRP Conference on High Performance Cutting HPC 2016, Chemnitz, pp. 99–102.
- [5] Großmann, K. (Ed.), 2015. *Thermo-energetic Design of Machine Tools*, 1st ed, Lecture Notes in Production Engineering. Springer International Publishing, Cham.
- [6] Thiem, X., Mühl, A., Großmann, K., 2014. Structural model-based correction of thermo-elastic machine tool errors, in: *Thermo-Energetic Design of Machine Tools*, Lecture Notes for Production Engineering. Berlin u.a., pp. 185–198.
- [7] Ess, M., 2012. *Simulation and Compensation of Thermal Errors of Machine Tools*. ETH Zurich.
- [8] Gebhardt, M., 2014. Thermal behaviour and compensation of rotary axes in 5-axis machine tools. doi:10.3929/ethz-a-010103980

- [9] Moriwaki, T., 1988. Thermal Deformation and Its On-Line Compensation of Hydrostatically Supported Precision Spindle. *CIRP Annals - Manufacturing Technology* 37, 393–396. doi:10.1016/S0007-8506(07)61662-X
- [10] Maier, T., 2014. Modellierungssystematik zur aufgabenbasierten Beschreibung des thermoelastischen Verhaltens von Werkzeugmaschinen. Technische Universität München, München.
- [11] Großmann, K., 2012. Thermo-Energetische Gestaltung von Werkzeugmaschinen. *ZWF Zeitschrift für wirtschaftlichen Fabrikbetrieb* 307–314.
- [12] Galant, A., Beitelschmidt, M., Großmann, K., 2016. Fast High-Resolution FE-based Simulation of Thermo-Elastic Behaviour of Machine Tool Structures. *Procedia CIRP* 46, 627–630. doi:10.1016/j.procir.2016.04.020
- [13] Kauschinger, B., Schroeder, S., 2015. Uncertain Parameters in Thermal Machine-Tool Models and Methods to Design their Metrological Adjustment Process. *Applied Mechanics and Materials* 794, 379–386. doi:10.4028/www.scientific.net/AMM.794.379
- [14] Ihlenfeldt, S., Müller, J., Merx, M., Peukert, C., 2017. Innovatives mechatronisches Systemkonzept für eine hochdynamische Werkzeugmaschine, in: Bertram, T., Corves, B., Janschek, K. (Eds.), *Mechatronik 2017*. Dresden, pp. 203–208.
- [15] Jungnickel, G., 2000. Simulation des thermischen Verhaltens von Werkzeugmaschinen (Schriftenreihe des Lehrstuhls für Werkzeugmaschinen), Lehre Forschung Praxis. TU Dresden Institut für Werkzeugmaschinen und Steuerungstechnik, Dresden.

# Optimal temperature probe location for the compensation of transient thermal errors

*G. Aguirre, J. Cilla, J. Otaegi, H. Urreta*

IK4-IDEKO, Arriaga 2, Elgoibar 20870, Spain

**Abstract.** Thermal error compensation is a cost-effective means of improving machine tool accuracy. The effectiveness and robustness of the method depends greatly on the location of the thermal probes, mainly when transient behaviour is relevant, such as in milling machines, where spindle speed and position in workspace are changing frequently and the machine never reaches thermal equilibrium. The influence of temperature probe location on the error compensation of a heavy duty milling machine and the relevance of finding optimal locations will be discussed, looking at both experimental and simulation data.

Peer-review under responsibility of the International Scientific Committee in the person of the Conference Chair Prof. Steffen Ihlenfeldt.

*Keywords:* Thermal error compensation; Thermal key points; Thermal imaging

## 1 Introduction

Thermal effects are considered to be the main factor affecting machine tool accuracy [1], thus receiving strong research interest for many years [2]. A variety of phenomena related to temperature variations can occur concurrently during a machining process:

- Heat losses in motors and guiding elements increase the temperature of the machine structure around them, creating thermal gradients.
- Variations in ambient temperature, leading to a more homogeneous warming of the machine structure.
- Cooling fluids circulating within the machine aim to extract heat from the machine hot spots, but may affect other areas on their way.
- Heat generated in the cutting process in the tool and workpiece. It will, on the one hand, warm up the part and the tool, and this can lead to errors, and on the other hand, the hot chip and the cooling fluid can reach other parts of the machine and produce local temperature gradients.



The relevance of each effect and the way to deal with them varies within the range of machine tool types, dimensions, applications, etc. They can be grouped in four main approaches:

1. Design for minimal thermal distortions: Minimize the effects of temperature variations by isolating heat sources from the structure, designing symmetrical structures, using low thermal expansion materials, etc.
2. Temperature control: Minimize temperature variations by circulating temperature controlled fluids in critical areas of the machine.
3. Software compensation: A simulation model estimates in real time thermally induced errors and compensates them via CNC.
4. Process planning: Perform critical operations when machine is expected to achieve highest accuracy, e.g. after sufficient warm-up time.

The first two approaches are in general preferred, providing the most robust way to accuracy, but they typically lead to more complex and expensive solutions. The fourth approach is valid in many machines which work in continuous operation (e.g. many grinding machines) and are stabilized in a reasonable time (i.e. less than one hour).

Our case of interest is large heavy duty multitasking milling machines, which can operate several spindle heads rating up to tens of kW. Here design variations and temperature control solutions are applied within possible, but are not enough to eliminate errors generated by the high heat losses in the spindle. Process planning is limited due to frequent tool and spindle head and speed variations, which keep the machine almost always far from a steady state.

Finally, software compensation has a great potential for improving machine accuracy at low cost, but the main challenge is to obtain a robust model for all working conditions from limited testing time. Most solutions are based on models that estimate thermal growth from temperature probes embedded at selected positions in the machine. Alternatives based on process data (e.g. spindle speed and power) alone, or combined with temperature probes have been developed, but robustness can be here a major issue.

In the following, temperature probe based thermal error compensation is discussed, with the main focus on how to deal with transient effects and the importance of the location of the temperature probes. In Section 2, thermal compensation strategies, looking at mathematical models and strategies for choosing the locations for thermal probes are reviewed. In Section 3, transient thermoelastic effects are discussed using a simple 1D model. In Section 4, the anal-

ysis is extended to experimental results from a milling machine. Finally, in Section 5 conclusions are drawn and future work is discussed.

## 2 Thermal compensation strategies

A wide range of compensation models have been proposed in the literature. The simplest approach, and also probably the most popular in practice, is the use of multivariable linear regression models (see (Eq. 1),

$$\partial X = \sum_{i=1}^n k_i T_i \quad (\text{Eq. 1})$$

where  $\partial X$  is the thermal growth,  $T_i$  are the  $n$  temperature signals and  $k_i$  the model coefficients. This model structure is claimed to have a stronger physical basis than others, since it is similar to the general expression for thermal growth for an element, shown next in one dimension,

$$\partial X = \alpha LT \quad (\text{Eq. 2})$$

where  $\alpha$  is the coefficient of thermal expansion and  $L$  is the length. The thermal growth of the machine can be thus seen as a combination of the thermal growth of  $n$  lumped masses, each with temperature  $T_i$ , and  $k_i$  representing  $\alpha LT$ . This mathematical similarity does not however ensure that the resulting model has a physical base, since this will depend on the location of the temperature probes and the experimental identification process.

Regression models are static and their accuracy is highly dependent on the location of the temperature probes (as it will be discussed later). A variety of alternatives have been developed to overcome these limitations, from transfer functions [3,4] to neural networks [5,6], support vector machines [7,8] among others.

Due to their simplicity and physical basis, linear regression models will be used in this paper to facilitate understanding the relevance of thermal probe location on the compensation of thermal errors.

The selection of the locations of the temperature sensors for the compensation of thermal errors has been a key aspect in the development of thermal compensation solutions. Some general criteria based on engineering judgement have been used proposed, such as placing sensors close to heat sources, but this does not always lead to the optimal model, as it is discussed in Section 3.

A wide variety of alternative methods have been proposed, from clustering techniques, thermal modal analysis, proper orthogonal decomposition, grey correlation, etc. [9–11]

### 3 Simulation of transient thermoelastic effects

The relevance of temperature probe location on error compensation models will be first discussed with a simple 1-D model. The beam is discretized in 10 elements as shown in the next figure, with a heat input  $Q$  and convection:

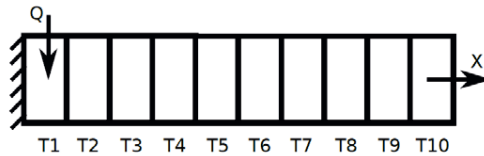


Fig. 1: 1D beam model

Simulation results are shown in Fig. 2. All results are normalized since correlation is based on the shape of the signals, not on the dimension. Temperatures are first normalized to the global maximum (a), and then to their own maximum value, and compared to the normalized displacement (b). A linear regression model is fit with each temperature, and the residual errors are shown in (c). The RMS error associated to each model is shown in (d).

The best correlation coefficient happens with T3, and it will thus give the best linear regression model based on a single temperature. The other temperatures detect the changes in displacement too early (T1 and T2) or too late.

The results show that the largest errors happen while temperature is changing fast, and they are small when temperature is stabilized. This demonstrates the special relevance of probe location for compensating transient effects. Compensation based on T1 and T2 could be improved with dynamic models that can lead with the lag between temperature and displacement, but this is out of the scope of this paper.

### 4 Experimental analysis

The concepts explained above have been further explored on real tests on a milling machine. The thermal growth of the spindle and ram due to the internal heat generated by its rotation has been analysed. A compensation model is first calibrated with a test following a certain spindle speed profile, and it is validat-

ed on a different profile. The influence of the number of sensor positions considered is then discussed.

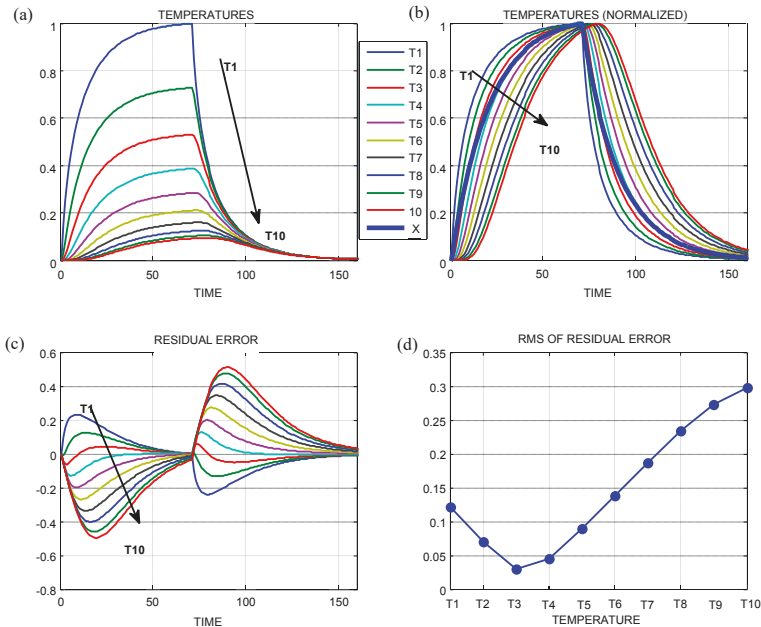


Fig. 2: Simulation results for 1D beam model

### 4.1 Experimental setup

Experiments have been performed on a 3 axis milling machine equipped with an automatic universal milling head (see Fig. 4). The tests are performed at a fixed machine position, following different rotating speed profiles. Tool displacement has been measured by three inductive sensors, and the temperature field on the surface of the spindle has been measured with a thermographic camera.

#### Spindle rotation speed

Two measurements have been performed, following different spindle speed profiles adapted from ISO 230-3. The duration of the test has been extended

considering the large size of the spindle, which leads to long stabilization times due to large thermal inertia.

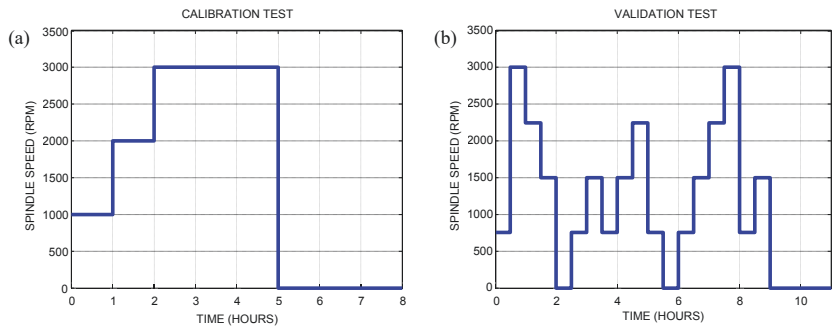


Fig. 3: Spindle speed profiles for (a) calibration test and (b) validation test

In the calibration test, the spindle is rotated for 5 hours looking for the stabilization at maximum temperature, and then the measurement continues for 3 more hours with no rotation, while spindle cools down. The validation test follows the pattern defined in ISO 230-3, with each period extended to 30 minutes due to the large thermal inertia of the spindle head.

Both tests lead to different temperature variation ranges and the transient behaviour is very different, which makes them suitable for the analysis of the robustness of the compensation models.

### Temperature measurement

The thermographic camera provides a large number of temperature measurement points. As shown in the next figure, 20 points distributed in the surface have been selected for further analysis in both tests.

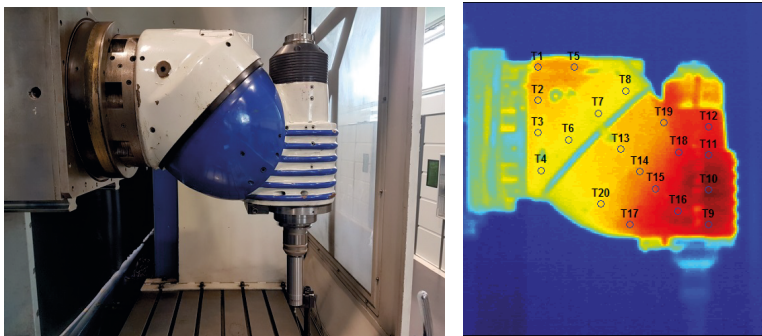


Fig. 4: (left) Spindle head under test; (right) Temperature measurement points on spindle

## 4.2 Test results

The results registered in the calibration and validation tests are presented in Fig. 5. Temperature and growth (in ram direction) results presented in the following are normalized to a common reference (maximum growth and temperature in calibration test) for both tests. When temperatures are shown as normalized, it means that each temperature has been normalized to its own variation range, so that signal shapes can be directly compared.

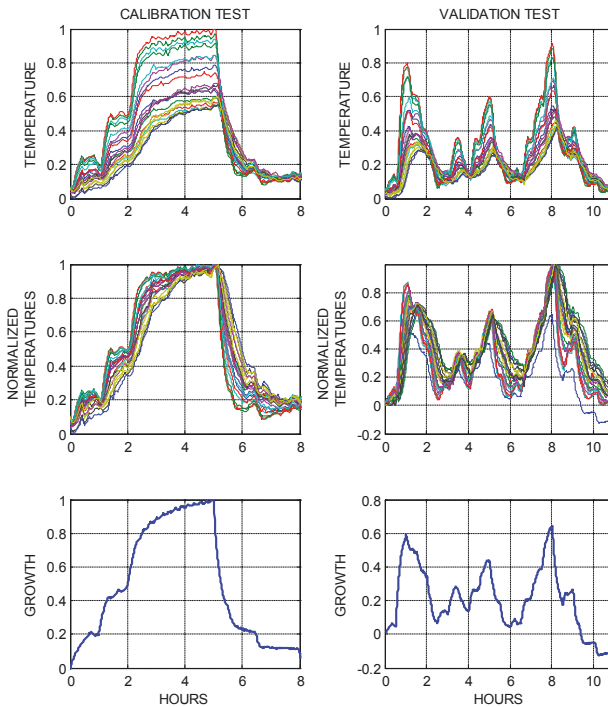


Fig. 5: Temperatures and growth in the calibration and validation tests

## 4.3 Compensation based on a single temperature input

As a first analysis, the influence of the temperature probe location on compensation models based on a single temperature probe has been analysed. A sepa-

rate model (see (Eq. 1)) has been fit and evaluated for each one of the 20 temperature points. The compensation error for each model on the same test and on the validation test are presented in Fig. 6.

A factor four variation between the errors (0.05 to 0.020) is observed in function of the temperature location in the calibration test, and a factor three in the validation test. The largest error is produced in transient thermal conditions, when it is most sensitive to the location of the temperature sensor. In stable thermal conditions, the compensation error is smaller, and less sensitive to the position of the sensor.

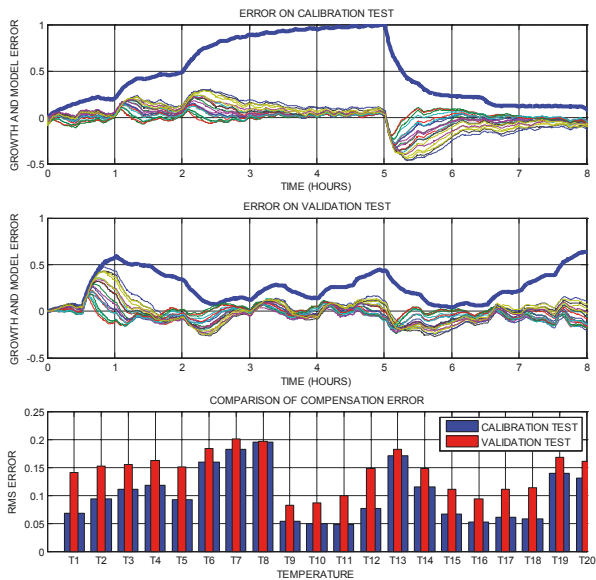


Fig. 6: Compensation error with model calibrated with a single temperature

#### 4.4 Compensation based on multiple temperature inputs

A further step in the search for the optimal compensation model is to use multiple temperature inputs. A forward stepwise regression algorithm is applied to fit multiple regression models (Eq. 1) using an increasing number of temperature measurements. The root mean square error of the fit is used to evaluate the quality of the model. Based on the same experimental data, the result of

this stepwise process is shown in Fig. 7. Only the ten first selected temperatures are shown for convenience.

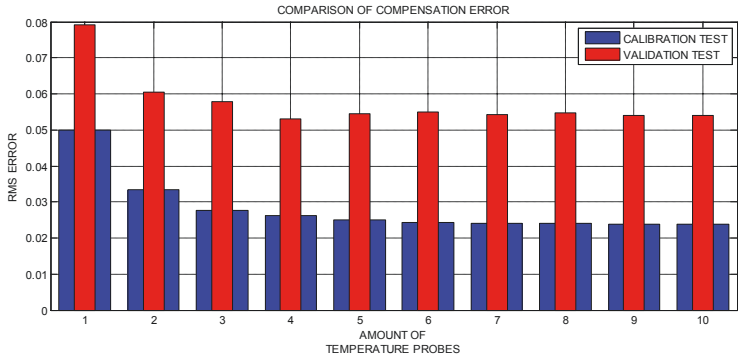


Fig. 7: Compensation error with stepwise fit models

The calibration of the model shows improvement up to the 7th temperature that is considered. Applied on the validation data, the same models show that the best result is obtained with 4 sensors. This illustrates the problem of over-fitting, where increasing the number of sensors is not always of advantage.

It is worth noting that the first four selected temperature probes are located on the hot point, near the spindle bearings (T9, T10, T11 and T15)

## 5 Conclusions

The influence of the location of the temperature sensors for the development of thermal error compensation models has been demonstrated, both based on simulation and experimental data.

- The location of the sensor is most critical when the machine is suffering fast temperature changes. In steady conditions, a wider range of sensor locations can lead to a good compensation.
- Model calibration using an increasing number of sensors reduces the residual error, but model robustness in extrapolation to different working conditions must be considered, and this will set a limit to the benefit of adding extra temperature sensors.
- The use of thermal imaging for the analysis optimization of thermal probe location has been validated.



## 6 References

- [1] Mayr J, Jedrzejewski J, Uhlmann E, Alkan Donmez M, Knapp W, Härtig F, et al. Thermal issues in machine tools. *CIRP Annals - Manufacturing Technology* 2012;61:771–91. doi:10.1016/j.cirp.2012.05.008.
- [2] Brewer W, Bryan JB, McClure E, Pearson J. Thermal effects on machine tool metrology. *ASME* 65 1965.
- [3] Horejš O, Mareš M, Novotný L. Advanced Modelling of Thermally Induced Displacements and Its Implementation into Standard CNC Controller of Horizontal Milling Center. *Procedia CIRP* 2012;4:67–72. doi:10.1016/j.procir.2012.10.013.
- [4] Brecher C, Fey M, Wennemer M. Correction Model of Load-Dependent Structural Deformations Based on Transfer Functions. *Thermo-energetic Design of Machine Tools*, Springer, Cham; 2015, p. 175–83.
- [5] Fletcher S, Abdulshahed AM, Longstaff AP. Robust prediction of machine tool thermal error using ANFIS-based modelling fusing temperature and displacement measurement, Prague, CZ: 2016.
- [6] Yang J, Shi H, Feng B, Zhao L, Ma C, Mei X. Applying Neural Network based on Fuzzy Cluster Pre-processing to Thermal Error Modeling for Coordinate Boring Machine. *Procedia CIRP* 2014;17:698–703..
- [7] Zhang ZP, Liu K, Guo F. Prediction of Machine Tool Thermal Error Compensation Based on SVMR and ARM11. *Applied Mechanics and Materials* 2015;740:120–6.
- [8] Jin C, Wu B, Hu Y, Cheng Y. Identification of thermal error in a feed system based on multi-class LS-SVM. *Frontiers of Mechanical Engineering* 2012;7:47–54.
- [9] Li Y, Zhao W, Lan S, Ni J, Wu W, Lu B. A review on spindle thermal error compensation in machine tools. *International Journal of Machine Tools and Manufacture* 2015;95:20–38.
- [10] Herzog R, Riedel I. Sequentially optimal sensor placement in thermoelastic models for real time applications. *Optim Eng* 2015;16:737–66.
- [11] Miao E, Liu Y, Liu H, Gao Z, Li W. Study on the effects of changes in temperature-sensitive points on thermal error compensation model for CNC machine tool. *International Journal of Machine Tools and Manufacture* 2015.

# Adaptive learning control for thermal error compensation on 5-axis machine tools with sudden boundary condition changes

*P. Blaser<sup>a</sup>, J. Mayr<sup>b</sup>, F. Pavliček<sup>a</sup>, P. Hernández-Becerro<sup>b</sup>, K. Wegener<sup>a</sup>*

<sup>a</sup>Institute of Machine Tools and Manufacturing IWF, ETH Zürich, Leonhardstrasse 21,  
8092 Zürich, Switzerland

<sup>b</sup>inspire AG, Technoparkstrasse 1, 8005 Zurich, Switzerland

**Abstract.** A system of differential equations is used to compute a thermal error prediction model based on temperature and machine states as well as on-machine measurements. The model can predict thermal displacements of the tool center point based on changes in the environmental temperature, load-dependent changes and boundary condition changes and states, like machining with or without cutting fluid. The information gained by the process-intermittent probing is used to adaptively update the model parameters, so that the model learns how to predict thermal position and orientation errors and to maintain a small residual error of the thermally induced errors of the rotary axis over a long time.

Peer-review under responsibility of the International Scientific Committee in the person of the Conference Chair Prof. Steffen Ihlenfeldt.

**Keywords:** Machine tool; Thermal error; Adaptive learning; On-machine measurement; Cutting fluid

## 1 Introduction and State of the Art

Precision manufacturing processes are strongly connected to the accuracy of their machine tools (MTs). There is an increasing demand for high precision 5-axis machined work-pieces, especially in the medical engineering and aerospace industries. According to Mayr *et al.* [1], thermal influences on MTs are one of the largest contributor to errors on machined workpieces. Bryan [2] summarized the sources that can cause thermal errors as following:

- Room environment
- Thermal memory from previous environment
- People
- Cutting process
- Machine

- Coolants

The influence of process and people is neglected since a long time by researchers. The focus of this research lies mainly on thermal tool centre point (TCP) errors regarding influences of the environmental temperature changes, running the main spindle and moving the linear axes. International standards developed regarding the aforementioned thermal errors on MTs are ISO 230-3 [3], ISO 10791-10 [4], and ISO 13041-8 [5]. The procedures described in the standards are used for measuring the thermal error of MTs under no load and finishing conditions. Missing links in these standards, depicted by Gebhardt *et al.* [6] or Ibaraki *et al.* [7], are measurement procedures for thermal errors regarding rotary and swivelling axes of 5-axis MTs. Furthermore not considered in the standards are influences of cutting fluids on the accuracy of MTs. Recent research activities showed that these influences have a significant impact on the thermal behaviour of MTs, e.g. by Mayr *et al.* [8], Hernández-Becerro *et al.* [9] and Blaser *et al.* [10].

A popular and successful method to model thermal errors on MTs is the phenomenological model approach which captures the relationship between the observed thermally induced errors and the thermal and losses related information, presented e.g. by Gebhardt *et al.* [11], Yang *et al.* [12], Mayr *et al.* [13] and Brecher *et al.* [14], just to name a few. Ideally the residual errors between the predicted errors and the actual MT will approach zero. However, the predicted system behaviour is always different from the physical one. Additionally, the actual machining conditions may be different from the machining conditions used to derive the empirical model, which leads to model uncertainties. Mou and Liu [15] stated that this can cause difficulties especially for small batch productions, where the sequence of manufacturing processes changes frequently as do the direction and rate of change of thermal effects. Due to statistical uncertainties, assumptions in the model and the constantly changing boundary conditions, the error models derived from pre-process calibration are not necessarily accurate enough in the long term. They need to be verified and updated iteratively as the MT is continually used.

Blaser *et al.* presented in [16] a new approach for an adaptive learning control (ALC) for thermal error compensation of rotary axes. Fig. 1 shows an illustration of the ALC concept. During a calibration phase, the TCP errors and current boundary and machining conditions obtained from various sensors are measured in a strict interval. After the regression model is obtained and the thermal error compensation starts, the TCP errors are measured with a reduced frequency to increase the productivity. The thermally induced errors are compared

to a defined tolerance band. If the deviations exceed this threshold a new set of model parameters is obtained with the data gather since a specific point in time, so that the parameters of the error model can be adapted to the present situation.

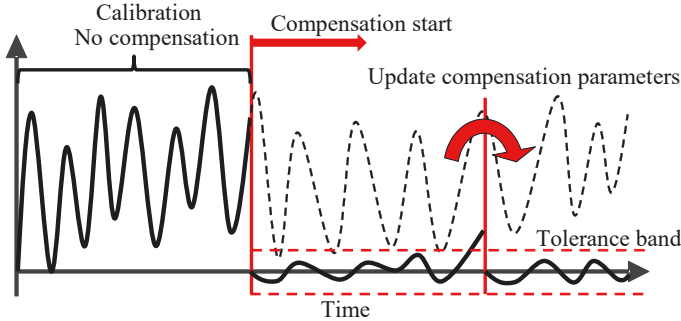


Fig. 1. Illustration of the concept of ALC for thermal error compensation [16]

This paper shows an extension of the previously mentioned thermal ALC, introduced by Blaser *et al.* [16], by including spontaneously changing boundary conditions to predict the thermal errors of a 5-axis MT under various machining states. In Section 2 the methodology of ALC compensation is described in detail, followed by Section 3, where the MT under investigation is presented. In Section 4, the extension of the phenomenological model for sudden boundary condition changes is introduced followed by Section 5, which demonstrates the practicability of the newly developed model in a 72 hour long experiment. This paper finalizes with a conclusion and a short outlook of future work.

## 2 Methodology of ALC for thermal error compensation

The goal of an adaptive thermal compensation is to reduce the thermally induced TCP-deviations and to enhance the long-term accuracy of the MT in both material removal as well as on-machine inspections. The extended procedure is capable of adapting the model parameters to changes in the process as well as fast and slow changes in the boundary conditions. This methodology is also able to adjust the on-machine measurement time intervals according to the predefined precision to ensure a high productivity at a constant uncertainty range of the phenomenological model, as described in [16].

Fig. 2 shows a schematic diagram of the methodology by Blaser *et al.* [16]. First, a measurement procedure is derived which is capable of identifying the thermal position and orientation errors of a rotary axis with a touch probe and a precision artefact mounted on the machine table. The axis error model used is based on the rigid body assumption and the use of homogeneous transformation matrices (HTM) to obtain the thermal displacements of the TCP relative to the workpiece position. The input of the HTM model are the predicted errors and the axis position of the MT and the output is an axes offset that shifts the axis origin in the opposite direction of the occurring thermal error.

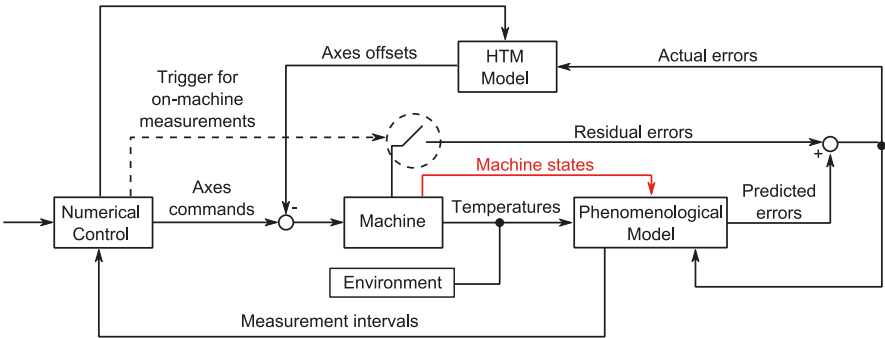


Fig. 2. Schematic diagram of thermal ALC for numerically controlled MTs. The dashed line represents the trigger for on-machine measurements which give access to the residual thermal errors only at discrete times. The measurement intervals are adaptively adjusted by the phenomenological model. The extension to the schematic of Blaser *et al.* [16] is seen in red.

A phenomenological model is developed to predict the thermal behaviour only by tracking multiple machine states as well as temperature sensor values on and around the machine structure. The extension of using machine states as input for the model is introduced to include cutting fluid conditions. The outputs of the phenomenological model, the predicted errors, are compared with the on-machine measurements obtained by the touch probe at discrete points in time. This comparison is used to periodically update the parameters of the thermal error model. To adapt to changing working conditions the approach is capable of alternating the NC-Code, with the use of a numerical control interface, to adjust the time intervals between on-machine measurements. This allows to dynamically adapting the amount of measurements to tradeoff between accuracy and productivity. The proposed on-machine measurement procedure only needs a few measurement points and allows a fast tracking of the

thermal TCP-deviations. The repeatability and the measurement uncertainty of this on-machine measurement cycle is presented by Blaser *et al.* in [16,17].

### 3 Machine Tool under Investigation

The kinematic chain of the MT under investigation, shown in Fig. 3, can be described in accordance with ISO 10791-2 [18] as:

$$V [w C2' B' b [Y1 Y2] X [Z1 Z2] (C1) t]$$

The rotary/swivelling axes unit of the MT consists of axes B and C2. The MT has two closed cooling circuits. One cooling circuit is used for the rotary and swivelling axis and one for the main spindle and the ball screws. The C2-axis of this MT can be used in turning mode with a maximum speed of 1'200 rpm. The coolant outlet flow, i.e. the flow of the coolant into the MT out of the chiller unit, of both cooling circuits, is controlled by the machine bed temperature. The MT is located in a standard non air conditioned shop floor. The linear axes are arranged in a box in box design. The rotary axes are driven by direct drives. The resolutions of the linear axes are 1  $\mu\text{m}$  and 1  $\mu\text{m}/\text{m}$  for the rotary axes. These resolutions are a limiting factor to the on-machine measurement and the compensation, as described in [16,17]. The cutting fluid is not temperature controlled and supplied to the machine by different pumps as described by Mohammadi *et al.* in [19]. This can lead to thermally induced errors, with small time constants, due to the fact, that a large volume of cutting fluid is brought into contact with the machine structure.

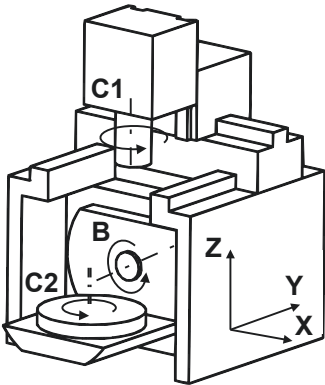


Fig. 3. Schematic of the 5-axis machine tool under investigation, adapted from [16]

## 4 Extension for Sudden Boundary Condition Changes

A system of differential equations, according to [20], is used to model the thermal position and orientation errors of the MT rotary axis C2.

$$\frac{d}{dt}\underline{y}(t) = \underline{p}_0 \cdot \underline{y}(t) + \underline{p}_1 \cdot u_1(t) + \underline{p}_2 \cdot u_2(t) + \underline{p}_3 \cdot u_3(t) + \underline{p}_4 \quad (\text{Eq. 1})$$

Equation (1) shows the ODE for a system of thermal position and orientation errors provoked by three different thermal loads.  $u_{1...3}(t)$  are input parameters and  $\underline{p}_{1...3}$  are the corresponding sensitivities with respect to the output  $\frac{d}{dt}\underline{y}(t)$ , where  $\underline{y}(t)$  is the overall thermal location error vector.  $\underline{p}_0$  defines the thermal inertias, the time lags for heating and cooling.  $\underline{p}_4$  is a zero balancing parameter that adjusts the mathematical zero of the equation to the physical system's zero.

To provoke a sudden boundary change, the influence of dry and wet cutting is investigated in this paper, by switching on or off the cutting fluid supply next to the spindle head, which delivers oil to the cutting zone. To determine the dynamics of the thermal influence of the cutting fluid one of the input parameters  $u(t)$  has to capture this behaviour. There are several options to do so, one is to only capture the discrete states of the MT cutting fluid supply, so that  $u(t) = \{0, 1\}$ . An alternative is to place a sensor in the machining room, that either measures the cutting fluid temperature when it is switched on or in the dry state captures the machining room temperature. For the experimental results in Section 5 the second method with a temperature sensor is chosen.

## 5 Experimental Results

To demonstrate the practicability of the ALC for sudden boundary condition changes on a real 5-axis MT, illustrated in Fig. 3, an experiment of 72 hours with random intervals of cutting fluid is carried out. The cutting fluid is supplied, through flexible ball socket joint tubes aiming at the machine table and the B-axis corpus. As additional thermal load the C2-axis is turning at different speeds. The speed profile and the cutting fluid states can be seen in Fig. 4, as well as the measured temperatures used as inputs for the phenomenological model.

A calibration of 12 hours is chosen in accordance to [16], during this phase a measurement is performed every 5 minutes. The first set of model parameters

is computed after the calibration phase and the compensation of thermal errors of the C2-axis starts. The measurement interval time is increased to 30 minutes. As a predefined threshold 10  $\mu\text{m}$  for the linear errors ( $E_{X0C}, E_{Y0C}, E_{Z0T}, E_{R0T}$ ) and 15  $\mu\text{m/m}$  for the angular errors ( $E_{A0C}, E_{B0C}, E_{C0C}$ ) is chosen. During the compensation and after each measurement, every error is compared against this threshold. If one error exceeds this boundary the measurement interval is decreased to 15 minutes for the next 2 hours. This is followed by a new parameter update, where all the gathered information from the start of the experiment is taken into account. After the phenomenological model is up-to-date, the measurement interval time is again increased to 30 minutes. If no error exceeds the threshold for more than 6 hours another parameter update is performed and the measurement interval is kept at 30 minutes.

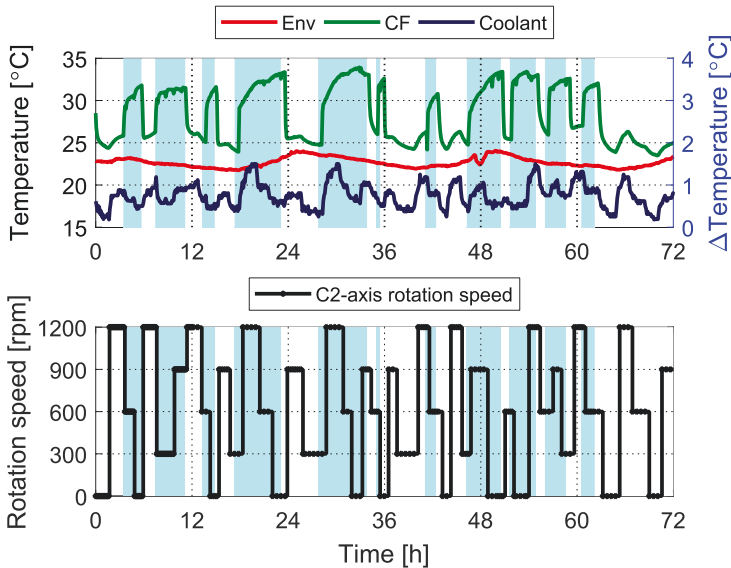


Fig. 4. Measurements of two temperatures, Environment (Env) and Cutting Fluid (CF), and one temperature difference, inlet and outlet of the C2-axes coolant (Coolant), over 72 hours, with varying rotational speed of the C2 axis and changes of cutting fluid states. The cyan areas depict the time intervals, where the cutting fluid supply was switched on.

Fig. 5 shows the experimental results of an ALC for thermal error compensation of a rotary axis C2 over a time interval of 72 hours. The four major error contributors of the rotary axis of the MT under investigation are depicted. It can be seen, that the compensated deviations, solid lines, stay most of the time inside the set thresholds. When one exceeds this limit, a parameter update is forced



and the error quickly returns back in the predefined margins, e.g.  $E_{Z0T}$  after 42 hours. The experiment shows, that sudden changes of the boundary conditions have no significant impact on the accuracy of the ALC for thermal error compensation.

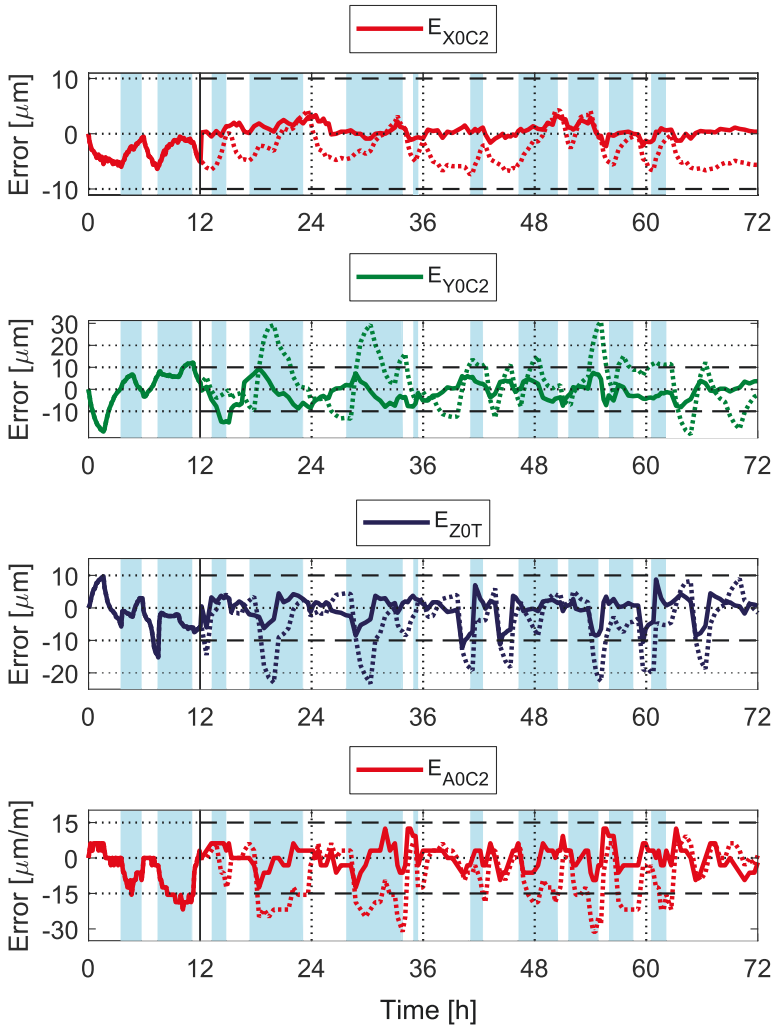


Fig. 5. Experimental results over 72 hours of an ALC for thermal error compensation of the rotary axis C2, under changing thermal loads. The cyan areas depict the time intervals, where the cutting fluid supply was switched on. The solid lines are the compensated deviations and the dashed ones the uncompensated. The black dashed lines illustrate the predefined thresholds.

## 6 Conclusion and Outlook

This work shows, that with a simple extension of an already existing ALC for thermal error compensation, sudden changes of the boundary condition, like cutting fluid on or off, can be compensated. The conducted experiment confirms, that with periodical model parameter updates the phenomenological model can adjust to suddenly changing boundary conditions and correct the predictions if they exceed a defined threshold of 10  $\mu\text{m}$  resp. 15  $\mu\text{m}/\text{m}$  for 72 hours.

Future work aims for developing more suitable model and parameter identification algorithms, to increase the prediction accuracy und to reduce the length of the calibration phase. In addition the thresholds should adapt over time, to enable tighter action control limits.

### Acknowledgements

*The authors would like to thank the Swiss Federal Office for Professional Education and Technology (CTI), the Swiss National Science Foundation (SNSF) and the Machine Tool Technologies Research Foundation (MTTRF) for their financial support.*

## 7 References

- [1] Mayr, J., Jedrzejewski, J., Uhlmann, E., Alkan Donmez, M., Knapp, W., Härtig, F., Wendt, K., Moriwaki, T., Shore, P., Schmitt, R., Brecher, C., Würz, T., Wegener, K., 2012, Thermal issues in machine tools, CIRP Annals - Manufacturing Technology, 61/2:771–791.
- [2] Bryan, J., 1990, International Status of Thermal Error Research, CIRP Annals - Manufacturing Technology, 39/2:645–656.
- [3] ISO 230-3:2007, Test code for machine tools — Part 3 : Determination of thermal effects, International Organization for Standardization ISO, Geneva, Switzerland.
- [4] ISO 10791-10:2007, Test conditions for machining centres—Part 10: Evaluation of thermal distortions, International Organization for Standardization ISO, Geneva, Switzerland.
- [5] ISO 13041-8:2004, Test conditions for numerically controlled turning machines and turning centres, Part 8: Evaluation of thermal distortions, International Organization for Standardization ISO, Geneva, Switzerland.
- [6] Gebhardt, M., Ess, M., Weikert, S., Knapp, W., Wegener, K., 2013, Phenomenological compensation of thermally caused position and orientation errors of rotary axes, Journal of Manufacturing Processes, 15/4:452–459.
- [7] Ibaraki, S., Ota, Y., 2013, Error calibration for five-axis machine tools by on-the-

machine measurement using a touch-trigger probe, *International Journal of Automation Technology*, 8/1:20–27.

- [8] Mayr, J., Gebhardt, M., Massow, B. B., Weikert, S., Wegener, K., 2014, Cutting Fluid Influence on Thermal Behavior of 5-axis Machine Tools, *Procedia CIRP*, 14:395–400.
- [9] Hernández-Becerro, P., Blaser, P., Mayr, J., Weikert, S., Wegener, K., 2017, Measurement of the effect of the cutting fluid on the thermal response of a five-axis machine tool, in *Laser Metrology and Machine Performance XII*.
- [10] Blaser, P., Hernández-Becerro, P., Mayr, J., Wiessner, M., Wegener, K., 2017, Thermal errors of a large 5-axis machine tool due to cutting fluid influences - Evaluation with thermal test piece, in *32nd ASPE Annual Meeting*.
- [11] Gebhardt, M., Schneeberger, A., Knapp, W., Wegener, K., 2013, Measuring, modeling and compensating thermally caused location errors of rotary axes, *The Proceedings of MTTRF Meeting*, pp. 19–24.
- [12] Yang, H., Ni, J., 2005, Adaptive model estimation of machine-tool thermal errors based on recursive dynamic modeling strategy, *International Journal of Machine Tools and Manufacture*, 45/1:1–11.
- [13] Mayr, J., Egeter, M., Weikert, S., Wegener, K., 2015, Thermal error compensation of rotary axes and main spindles using cooling power as input parameter, *Journal of Manufacturing Systems*, pp. 542–549.
- [14] Brecher, C., Esser, M., Witt, S., 2009, Interaction of manufacturing process and machine tool, *CIRP Annals - Manufacturing Technology*, 58/2:588–607.
- [15] Mou, J., Liu, C. R., 1995, An Adaptive Methodology for Machine Tool Error Correction, *Journal of Engineering for Industry*, 117/19:389–399.
- [16] Blaser, P., Pavliček, F., Mori, K., Mayr, J., Weikert, S., Wegener, K., 2017, Adaptive Learning Control for Thermal Error Compensation of 5-Axis Machine Tools, *Journal of Manufacturing Systems*, 44.
- [17] Blaser, P., Gebhardt, M., Mayr, J., Knapp, W., Wegener, K., 2014, Automatic compensation of thermally induced errors on five-axis machine tools, in *Euspen - Special Interest Group Meeting: Thermal Issues*.
- [18] ISO 10791-2:2001, Test conditions for machining centres -- Part 2: Geometric tests for machines with vertical spindle or universal heads with vertical primary rotary axis (vertical Z-axis), *International Organization for Standardization ISO*, Geneva, Switzerland.
- [19] Mohammadi, A., Züst, S., Mayr, J., Blaser, P., Sonne, M. R. M. R., Hattel, J. H. J. H., Wegener, K., 2017, A methodology for online visualization of the energy flow in a machine tool, *CIRP Journal of Manufacturing Science and Technology*, 19.
- [20] Mayr, J., Blaser, P., Knapp, W., Wegener, K., 2016, Compensation of cutting fluid influences on five axis machine tools, *Proceedings of MTTRF Meeting*, pp. 101–106.

# Hybrid Correction of Thermal Errors using Temperature and Deformation Sensors

*C. Naumann<sup>a</sup>, C. Brecher<sup>d</sup>, C. Baum<sup>b</sup>, F. Tzanetos<sup>b</sup>, S. Ihlenfeldt<sup>a,c</sup>, M. Putz<sup>a</sup>*

<sup>a</sup>Fraunhofer Institute for Machine Tools and Forming Technology IWU, Reichenhainer Str. 88, 09126 Chemnitz, Germany

<sup>b</sup>Fraunhofer Institute for Production Technology IPT, Steinbachstraße 17, 52074 Aachen, Germany

<sup>c</sup>Institute of Machine Tools and Control Engineering IWM, Technische Universität Dresden, 01062 Dresden, Germany

<sup>d</sup>Laboratory of Machine Tools and Production Engineering WZL, RWTH Aachen University, Steinbachstr. 19, 52074 Aachen, Germany

**Abstract.** Thermo-elastic deformations are one of the most significant sources of production inaccuracies in cutting machine tools today. There are numerous methods to model, monitor and correct or compensate these thermal errors in machine tools. Among the indirect correction methods count the characteristic diagram based correction and the correction based on integral deformation sensors (IDS). Both are briefly described and their strengths and weaknesses are discussed. Following this, ways of combining both methods to overcome their respective weaknesses are discussed. A hybrid correction method is proposed which uses characteristic diagrams to derive a relationship between online IDS measurements and the actual tool-center-point (TCP) displacement. Experiments carried out on a 3-axis machine tool demonstrate the effectiveness of both correction methods.

Peer-review under responsibility of the International Scientific Committee in the person of the Conference Chair Prof. Steffen Ihlenfeldt.

**Keywords:** Thermal Deformation; Characteristic Diagram; TCP Displacement; Correction; Integral Deformation Sensors; Machine Tools

---

## 1 Introduction

Thermo-elastic deformations are one of the most significant sources of production inaccuracies in cutting machine tools today [1]. Numerous methodologies have been developed over the course of the last decades to model, monitor and correct or compensate these thermal errors in machine tools. While some of the solutions promise big improvements of machine tool stability and accuracy, not all of them are applicable in daily production yet. The alternatives

most commonly used in today's industrial practice include thermally stable machine tool design, warm-up procedures, thermal conditioning with cooling systems and air conditioning of the production environment. The design of thermally stable machine tool structures can reduce the overall effect of temperature gradients, but it cannot completely eliminate all thermal errors. Strategies such as extensive warm-up procedures and thermal conditioning consume a lot of time and energy and thus increase the production costs and lower the productivity of the machine. The air conditioning of the production environment, though necessary to fulfill the environmental temperature constrictions in the standards [2], requires high investments.

On the other hand, mechatronic correction promises good results for several modeling techniques -[1], [3] and [4]-. This type of error correction introduces offsets to the machine tool axes' current position via the control unit of the machine. A model that uses sensor data as input calculates these correction values. Compared to purely simulation based correction models, sensor based methods are often much easier to implement and similarly effective. For the sensor-based correction, different approaches are usually pursued: correction based either on the direct measurement of the TCP displacement or the indirect estimation of the TCP displacement through measurement of other machine state variables and hybrid correction methods based on combinations of the former two.

The most forward approach is to directly measure the TCP displacement, e.g. with help of a test mandrel and displacement transducers or a 3D-probe and precision balls [2]. The advantage of this method is that the actual TCP displacement is measured directly, without the need for models. However, the obtained value is only valid in the moment of the measurement. Hence, the cyclic recalibration of machine tools is bound to be compromised between frequency of calibration and level of precision.

Indirect correction can solve this issue by using machine state variables like temperatures, machine control data or deformations. These variables feed a mathematical model that estimates the actual TCP displacement. Different approaches can be used to generate the mathematical model. Many of these can be categorized as phenomenological modeling techniques (see also [5]), where the relationship between state variables and TCP displacement is derived from experiments. Hence, the machine is put out of production to run experiments that train the models until a reliable outcome arises. The rest of the approaches can be classified as multi-physics modelling techniques, where models are generated a-priori with the help of knowledge about the system behavior. Howev-

er, the effectiveness of these methods depends on the quality of the mathematical models and their parameters.

The hybrid approach combines the advantages of two methods. Two types of hybrid correction methods have been investigated until now (see [3], Chapter 3.4): the combination of direct and indirect correction methods as well as the combination of sensor-based and sensorless correction methods. In the first type, an indirect model continuously generates correction values, which are recalibrated with direct TCP measurements. In the second type, a sensor-based approach corrects long-term thermal deformations, while sensorless methods using the internal data of the machine correct non-thermal but process-related errors that superimpose on thermal deformations, like sudden spindle shifts.

This paper combines the characteristic diagrams based on temperature sensors (Chapter 2) and the correction model based on deformation sensors (Chapter 3). Both models are sensor-based, indirect approaches, but they have advantages and drawbacks that complement each other, making them suitable for a hybrid correction strategy (Chapter 4). For example, the small installation space of the cross-slide of the test machine (Chapter 5) does not allow the installation of IDS. Hence, characteristic diagrams can be used to predict the deformation of this component. This enables an efficient correction that uses the practical strengths of both strategies and considers the influence of all machine tool components on the overall TCP displacement. Chapter 6 finally demonstrates the effectiveness of both correction methods.

## **2 Characteristic Diagram Based Correction**

Characteristic diagrams are continuous maps of a set of input variables onto a single output variable. They consist of a rectangular grid of support points along with kernel functions, which describe the interpolation in between. They are created by first discretizing each input variable in order to establish the grid, then choosing a type of kernel function adequate for describing the local dependency of the input variables on the output variable and finally calculating the parameters of the kernel functions for each support point based on training data from simulations or experiments, see [6]. The most common form of characteristic diagram uses multilinear interpolation between support points, where a scalar factor equal to the output value at the support point acts as a weight multiplied to the pyramid shaped kernel. Other types of kernels include polynomial kernels, wavelets, radial basis functions or B-splines. A more detailed description of characteristic diagrams and how they are calculated can be

found in [7]. Here Priber describes a method called “Smoothed Grid Regression” (SGR) which adds smoothing terms to the data fitting terms described above in order to fit sparse or defective data. SGR is the basis for the characteristic diagram based correction employed here.

In the course of the CRC/TR 96 project, improvements to the characteristic diagram computation were achieved by employing multigrid solvers to efficiently solve the large sparse linear systems of high dimensional characteristic diagrams. This was done by developing a partial differential equation (PDE) that mimicked the common location interpolation approach and using it to derive the linear system via the finite element method (FEM). The equation comprises a data fitting term plus a smoothing term. Its derivation along with a more detailed explanation can be found in [8], under chapter “Correction Algorithms and High-Dimensional Characteristic Diagrams”. While the common approach is limited to only five or six input variables due to limited memory, this new iterative solver can cope with ten or more variables, as was shown in [9] using simulation data from a machine tool column. This development is of paramount importance when complex machine tool structures are to be modelled.

Many trials have shown that multilinear interpolation, given a fine enough grid, is best suited for the thermo-elastic problems in machine tools. Not only are they sufficiently accurate and easy to calculate, they also require comparatively few parameters and limit the risk of overfitting, see [9]. Equally important as the choice of kernel function is the method of grid structuring. Available options include equidistant and variably spaced grids, transformed grids, substructure grids and sparse grids. [10] describes their use and compares their effectiveness using simulations on a machine tool column with a moving heat source. The comparison shows that substructure grids provide good estimations with few grid points if the training data plentiful und mostly error-free. If training data is limited or erroneous, however, the complex substructure grids are susceptible to overfitting and the simple equidistant grids perform best. Since the latter scenario is typical for most measurement data, equidistant grids were used in this paper.

### **3 Integral Deformation Sensors Based Correction**

The complexity of thermal issues in machine tools is evident. Several heat sources can influence the structure from anywhere within or outside the machine. These heat sources influence the structure with three mechanisms: the heat conduction, the heat convection and the heat radiation, each of them having a different degree of influence depending on several factors. These factors

include properties of the structure -e.g. the thermal properties of the materials used in each component or the area of the contact surfaces- as well as properties of the production environment -e.g. the ambient temperature and humidity-. Most of these properties are either unknown or bound with high uncertainties. Their calculation is then cumbersome, if not impossible as in many cases. To make matters worse, many heat sources are very difficult to gauge. Some examples are the process heat flowing in the workpiece and in the tool, the influence of the chips generated during the production process, as well as the influence of the cooling fluid used in the process. However, all of these influences lead to a deformation field, which can be thought of as a superposition of the individual deformations inflicted by each thermal effect on the structure.

Therefore, measuring the deformation field is the most practical way to attain the necessary information for a subsequent correction. The reason is that the deformation field is the cumulative effect of all thermal mechanisms, so it carries all information from all these sources. The remaining question at this point is how to measure the deformations of the machine tool structure.

A few researchers have investigated this question in the past. Bosetti et al. -[11] and [12]- have developed a methodology that uses a network of fiber-Bragg grating sensors. These sensors are mounted in a way that they build an FEM-like network of nodes (called reticular displacement measurement system – RDMS), thus measuring the relative deformation between nodes. In this way, the deformation field can be reconstructed with simple geometric relations. The drawback here is of course that it requires large areas of free surface to attach the sensors. Liu et al. -[13] and [14]- have also used fiber-Bragg grating sensors, although to measure the integral deformation of machine column instead. Mitsuishi et al. -[15]- have previously used the same concept of measuring the integral deformation of machine components, although they used long rods from invar-steel and strain gauges.

The concept of the integral deformation measurement is based on the nature of thermal influences. Heat flows from a colder to a warmer location. Assuming linear expansion, the elongation of a material block is proportional to the temperature difference along its length. The factor of proportionality depends on the geometry (original length  $l_0$ ) and the material (thermal expansion coefficient  $\alpha$ ) of the block. In order to make a better estimation of the thermal expansion, the temperature profile of the block would have to be integrated over the block length. A linear temperature profile would thus lead to a factor of proportionality that contains the block length in square. A quadratic temperature profile would lead to a block length in cube and so on. The concept of IDS



is thus measuring directly the integral elongation of the entire block, being the result of a specific temperature gradient in the direction of the elongation.

However, these values are only valid for one-dimensional temperature profiles and elongations. An additional temperature profile across the cross-section of a beam would lead to two more deformations: the transversal deflection  $\Delta y(x)$  and the inclination of the beam  $\theta(x)$ . It is thus evident, that more IDS are needed to estimate these values, since each IDS gives one-dimensional information (the integral elongation in one direction).

The mechanical constraints play here a vital role. A block with a fixed and a loose bearing on both ends of its lengthiest dimension will deform in a different way than a block that has one fixed and one free side in one of its dimensions. Therefore, a simple analysis of the thermo-mechanic constraints of the machine tool (relevant temperature gradients and expected bending lines due to mechanical constraints) lead to the proper positioning of the IDS.

Since the temperature fields along the machine components can be much more complex than a simple superposition of two temperature gradients in two directions, the IDS concept leads to intrinsic errors. The smaller the machine component, the more significant the deviation from simple temperature fields. Hence, the concept of measuring the integral deformation is a practice-oriented method that aims to bring the best possible results with the least effort. The concept can consider all significant modes of thermally induced deformations that are met in practice and is most suitable for bigger machine components, whose deformation is most detrimental due to the bigger lever arms.

## 4 Hybrid Correction using Temperature and Deformation Sensors

The main advantage of characteristic diagram based correction is that all it requires is a number of well-placed sensors and a large set of data, either experimental or from simulations. Once a characteristic diagram has been computed from this data, it is very easy to use and thus allows online TCP correction based on live sensor data [8]. The main disadvantages are that the effectiveness of characteristic diagram based correction depends strongly on the selection of input variables (sensor locations, etc.) and the quality of the training data. Also, the exponential increase of the computational effort limits the number of input variables to about twelve [6].

The main advantage of IDS based correction is that it measures the actual deformation of the machine tool structure online, which is the effect of all ther-

mal influences and hence includes more information than temperature sensors. It only remains to find the optimal positions for these sensors within the machine structure and develop a model that takes the most out of this information to predict the TCP displacement. However, each IDS gives a one-dimensional information, so the number of IDS increases with the level of accuracy of the prediction. This means that machine components with complex deformation behavior need more IDS to get enough information about their thermal state. At the same time, complex thermal deformation behavior characterizes smaller machine components, which have less available installation space to be outfitted with IDS.

Therefore, a suitable way to combine both methods is to use characteristic diagrams instead of the physical model to calculate the TCP displacement from the IDS data. This eliminates the drawbacks of physical modeling, while taking advantage of the upside of sensor-based correction. The downside is that it does not ensure robustness, since only a finite number of experimental data trains the characteristic diagrams. However, this hybrid method can still not anticipate the deformation of any component that cannot be outfitted with IDS.

To solve this issue, the information of temperature sensors can be added to the characteristic diagrams. These can be placed wherever the IDS cannot and thus complete the characteristic diagram based correction of the entire machine tool. The problem with this method is that the limited number of inputs for the characteristic diagrams, which means that for every additional temperature sensor one less IDS can be included.

Another considerable way is a modular correction method, where the IDS are used to calculate the deformation of all the large machine tool assemblies. For all smaller assemblies with more complex deformation behavior, the characteristic diagrams calculate their part based on simulations or temperature sensors. This method employs the strengths of both correction methods to minimize the overall effort for the implementation of an online correction. All large components are outfitted with IDS, which leaves more free variables for the inputs of the characteristic diagrams. Simultaneously, the higher computational effort of the characteristic diagrams is used for the more complex deformation behaviors, where it is needed, thus leading to a more efficient allocation of resources. However, the kinematic coupling of such an assembly-based modular model is more complicated and sets higher requirements concerning the real-time capability of the online correction. This method is not investigated in this work.

## 5 Experimental Setup

The experimental investigations were carried out on a 3-axis machining center, which is thermo-symmetric along its X-axis, see Figure 1. The machine is equipped with a system of twenty-four IDS and twenty-seven temperature sensors. The models investigated in this paper use only twelve of the deformation sensors (also designated in Figure 1a), since not all IDS are necessary to determine the deformation of this machine tool -[16] and [17]-.

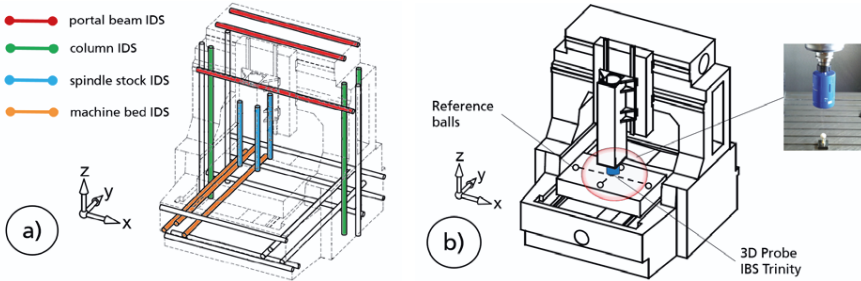


Fig. 1. Structure of demonstrator machine illustrated with a) Integral Deformation Sensors (IDS) and b) temperature sensors.

The setup for the external measurement of the TCP displacement is shown in Figure 1b. Four reference balls are mounted on the work piece carriage in the depicted cross configuration, in order to determine the dependency of the TCP-displacement across the workspace. A wireless probe is used to gauge the relative displacement between workpiece- and tool-side.

In order to introduce thermal loads, all three linear axes (X-, Y- and Z-) as well as the spindle were set to execute a repeated motion with 100 % feed rate (80 m/min) or 100 % spindle speed (18,000 rpm) for approximately two hours. This motion prescribes a Helix across the three-dimensional workspace with all axes moving almost to their full travel range. The machine enters then standby to cool down, while the control is still active. All measurements continue for an additional six hours during the cool-down phase. The thermal load was hence executed as to simulate finishing conditions according to [2], however the activation time of the heat sources has been reduced from four hours to two hours, which is considered sufficient to demonstrate the correction method. The TCP displacement was measured approximately every fifteen minutes with two measurements taken at each reference ball. The IDS and temperature sensors were recorded continuously with a sample rate of 2 Hz.

In metrology, it is vital to estimate the uncertainty of all measurements, otherwise they have no practical meaning. The uncertainty of the temperature sensors is  $\pm(0.3 + 0.005 \cdot T) ^\circ\text{C}$  according to [18] for class B type Pt100. The uncertainty of the measurement with the IDS is  $1 \text{ }\mu\text{m/m}$  according to [16]. The column IDS are 6.5 m long, the machine bed IDS are 2.2 m long, the portal IDS are 3.2 m long and the spindle stock IDS are 1 m long. Hence, the highest measurement uncertainty is  $6.5 \text{ }\mu\text{m}$  for the column IDS. The uncertainty of the direct measurement of the TCP-displacement is  $3.2 \text{ }\mu\text{m}$  as calculated in [19].

## 6 Test and Comparison of Correction Methods

The structure of the machine tool was modeled with eight blocks (Fig. 2): three blocks for the portal beam, one block for the columns, three blocks for the machine base and one block for the headstock. The four identified machine assemblies were modeled with simplifications according to the positions of the IDS in Fig. 1. The physical model has been set-up according to [16] and [20]. The physical model of the IDS approach calculates the displacement of the edges of the modeled blocks according to the recordings of the IDS, under the assumptions that their cross-sections remain even but not necessarily normal during the deformation and that deflections are small. The levers between the machine assemblies are also defined in order to calculate the effect of one block to another. Hence, the kinematic relationships have a significant influence on the overall prediction quality of the model.

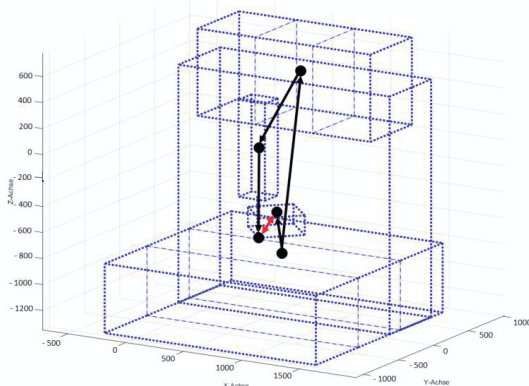


Fig. 2. Geometric-kinematic model of the demonstrator machine with kinematic vector chain (portal beam and machine base are modeled by segmented blocks; dashed lines distinguish block segments and dotted lines designate blocks; red double-sided vector indicates the distance between work-piece- and tool-side).

The kinematic chain of the machine components starts at the machine base, so that the model calculates all displacements with respect to the fixed machine base (Figure 2). The block segments of the machine base itself are kinematically linked in a way that simulates the mechanical constraints of its four fixing points, as it is described in [20]. The kinematic chain sets up vector relationships from each machine component to the next one in the following order: a) for the tool side: machine base, column, portal beam, headstock and tool; b) for the workpiece side: machine base, worktable and reference ball. Hence, the TCP displacement is calculated as the relative difference between tool- and workpiece-side. Their initial distance in the undeformed state is subtracted from the calculated distance in the deformed states. The cross-slide has no IDS, so it is not included in the model and its deformation is neglected.

The results of the IDS based correction are shown in Figure 3.

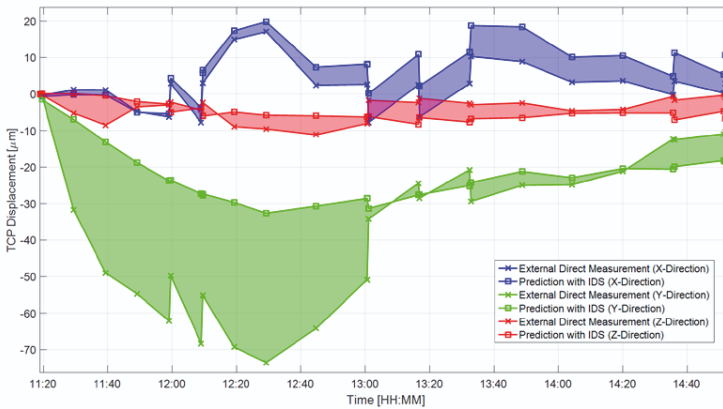


Fig. 3. Offline correction values for four different thermal loadings: a) X-axis, b) Y-axis, c) Z-axis and d) spindle loading.

It is evident that the deformation in y-direction could not be predicted with high accuracy. The reason for this is that there is missing information for two important machine components: the cross-slide and the spindle-motor. Both are components that cannot be outfitted with IDS, although they have a detrimental effect in the y-direction. The motor-spindle is the closest element to the tool, so it can significantly increase the dislocation. The cross-slide can also have a significant effect on this direction due to its long lever arm through the headstock.

The two first hybrid strategies described in Chapter 5 were tested using three-fold cross validation based on eleven experiments. The test was done once with

only using six temperature sensors as input and then once with only six IDS as input. For each test, twelve characteristic diagrams were computed, which is one for the x-, y- and z-displacement per reference ball. By including the x-, y- and z-TCP position as input dimensions into the characteristic diagrams, all four balls (and the rest of the workspace) could be done at once, so that only three characteristic diagrams would be needed. This was not done here because only measurement data from the four discrete positions was gathered and therefore any interpolation between them was pointless since it could not be verified.

Figure 4 shows the measured displacement of the test data in y-direction and the y-displacement estimated by the corresponding two characteristic diagrams.

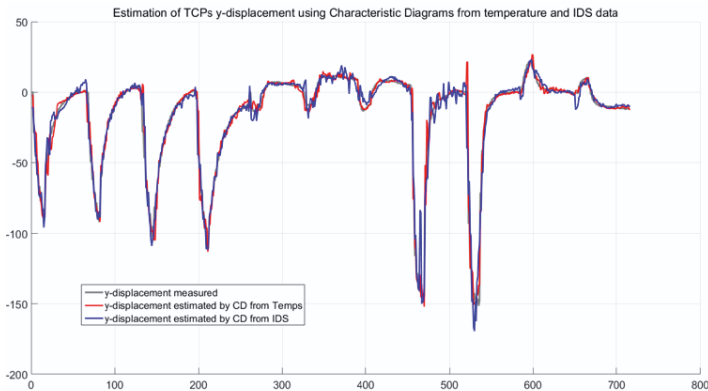


Fig. 4. Comparison of estimated and measured y-displacement using characteristic diagrams from temperature (red) and IDS data (blue).

It is apparent, that the hybrid strategy using characteristic diagrams trained by IDS recordings are performing much better than the physical model of the IDS based correction. The test shows that both temperatures and IDS work similarly well as input data for characteristic diagrams. The remaining characteristic diagrams (for the 11 other cases) performed equally well. Several consecutive tests revealed that using IDS as input was on average slightly better than using temperatures, in the sense that there occurred fewer large error peaks such as the one at recording 570. The reason for this is that temperature sensors are identifying local deformations and IDS are indicating global deformations, since their length spans entire assemblies. Therefore, a combination of both as inputs for characteristic diagram based correction promises the best results.

The data include some error, because the displacement was assumed zero at the start of each of the eleven experiments, while the actual thermal state may

not have been equal. Further improvements to the correction method could be achieved mainly through an optimal choice of input variables. Here the selection was done through trial-and-error, aided by experience.

## 7 Summary and Outlook

The paper gives an overview on the state of the art in thermal error correction and compensation. Among the indirect correction methods, the focus in this paper lies on the characteristic diagram based correction and the correction based on IDS. A review of both illuminates their strengths and weaknesses, which leads to a discussion of strategies to combine both methods and achieve a better allocation of resources.

Experiments on a machine tool were carried out to demonstrate and compare the effectiveness of the considered strategies. A hybrid correction, which uses characteristic diagrams that are trained by IDS as well as temperature measurements, is shown to perform much better than the physical model. The characteristic diagrams based on temperature sensors perform as well as with IDS inputs. However, the required optimal selection of input variables will be further investigated in future research. Last but not least, a modular correction strategy is expected to have an even better performance, not only in accuracy but also in the level of computational and model-training effort as well as in robustness, and will be also tested in future research.

### *Acknowledgements*

*This research was funded by a German Research Foundation (DFG) grant within the Collaborative Research Centers (CRC) /Transregio (TR) 96, which is gratefully acknowledged.*

## 8 References

- [1] J. Mayr, J. Jedrzejewski, E. Uhlmann, M. A. Donmez et al., Thermal issues in machine tools, CIRP Annals - Manufacturing Technology, Volume 61, Issue 2, 2012, pp. 771-791
- [2] ISO 230-3. Test code for machine tools - part 3: Determination of thermal effects. 2007.
- [3] P. Turek, J. Jedrzejewski, W. Modrzycki, Methods of machine tool error compensation. Journal of Machine Engineering, Volume 10, Issue 4, 2010.
- [4] K. Grossmann et al., Thermo-Energetic Design of Machine Tools, Lecture Notes in Production Engineering, Springer, 2015.
- [5] J.S. Chen, J. Yuan, J. Ni, Thermal Error Modelling for Real-Time Error Compensation, International Journal for Advanced manufacturing Technology, Volume 12, 1996, pp. 266-275

- [6] C. Naumann, U. Priber, 2012, Modellierung des Thermo-Elastischen Verhaltens von Werkzeugmaschinen mittels Hochdimensionaler Kennfelder, Proceedings Workshop Computational Intelligence.
- [7] U. Priber, 2003, Smoothed Grid Regression, Proceedings Workshop Fuzzy Systems.
- [8] X. Thiem et al. Implementation and Demonstration of Characteristic Diagram as well as Structure Model Based Correction of Thermo-Elastic Tool Center Point Displacements. In: Journal of Machine Engineering, Volume 16, Issue 3, 2016, pp. 88-101.
- [9] S. Ihlenfeldt, C. Naumann, U. Priber, I. Riedel, 2015, Characteristic diagram based correction algorithms for the thermo-elastic deformation of machine tools, Proceedings 48th CIRP Conference on Manufacturing Systems.
- [10] S. Ihlenfeldt, C. Naumann, M. Putz, J. Glänzel, Optimized Grid Structures for the Characteristic Diagram Based Estimation of Thermo-Elastic Tool Center Point Displacements in Machine Tools, Journal of Machine Engineering, 2017.
- [11] Biral F., Bosetti P., Oboe R., Tondlini F., A new direct deformation sensor for active compensation of positioning errors in large milling machines. AMC '06, Istanbul, Turkey, 2006, pp. 126-131.
- [12] Bosetti P., Bruschi S., Enhancing positioning accuracy of CNC machine tools by means of direct measurement of deformation. International Journal of Advanced Manufacturing Technology, Volume 58, Issue 5-8, 2012, pp. 651-662
- [13] Zhou Z.-D., Gui L., Tan Y.-G., Liu M.-Y., Liu Y., Li R.-Y., Actualities and development of heavy-duty CNC machine tool thermal error monitoring technology. Chinese Journal of Mechanical Engineering, Volume 30, Issue 5, 2017, pp. 1262-1281
- [14] Liu Y., Liu M., Yi C., Chen M., Measurement of the deformation field for machine tool based on optical fiber-Bragg grating sensors. International conference on innovative design and manufacturing. Montreal, Quebec, Canada, 2014.
- [15] Mitsuishi M., Warisawa S., Hanayama R., Development of an intelligent high-speed machining center. CIRP Annals – Manufacturing Technology, Volume 50, Issue 1, 2001, pp. 275-280.
- [16] C. Wenzel, M. Klatte, Structurally Integrated Sensors, in: K. Großmann (Ed.), Thermo-energetic Design of Machine Tools, Springer International Publishing, Cham, 2015, pp. 209–221.
- [17] C. Brecher, M. Klatte, C. Wenzel, Application of Machine Integrated Deformation Sensors, in: Proceedings of the 11th International Lamdamap Conference, Huddersfield, Bedfordshire, United Kingdom, 2015, pp. 8–17.
- [18] DIN EN 60751; Industrial platinum resistance thermometers and platinum temperature sensors. 2009
- [19] C. Brecher, M. Klatte, F. Tzanetos, Analysis of spatial and temporal dependencies of the TCP-dislocation measurement for the assessment of the thermos-elastic behavior of 3-axis machine tools, in: 12<sup>th</sup> International Conference and Exhibition on Laser Metrology,



Coordinate Measuring Machines and Machine Tool Performance, Bristol, Gloucestershire, UK, 2017, pp. 122–132.

- [20] C.Brecher, J. Müller, M. Klatte, M. Riedel, F. Tzanetos, Funktionsprinzip der messtechnisch basierten Korrektur thermischer Verlagerungen am Versuchsträger MAX. 5. Kolloquium zum SFB/TR96: Thermo-Energetische Gestaltung von Werkzeugmaschinen – Modellierung und Simulation, Dresden, Germany, 2017, pp. 241-259.

## **Technical and analytical measurement issues**

---



# Optimal sensor placement based on model order reduction

*P. Benner<sup>a</sup>, R. Herzog<sup>b</sup>, N. Lang<sup>b</sup>, I. Riedel<sup>b</sup>, J. Saak<sup>a</sup>*

<sup>a</sup>Max Planck Institute for Dynamics of Complex Technical Systems,  
Computational Methods in Systems and Control Theory, 39106 Magdeburg, Germany

<sup>b</sup>Faculty of Mathematics, Technische Universität Chemnitz, 09107 Chemnitz, Germany

**Abstract.** In this paper, we consider optimal sensor placement problems for thermo-elastic solid body models. More precisely, the temperature sensors are placed in a near-optimal way, so that their measurements allow an accurate prediction of the thermally induced displacement of the tool center point (TCP) of a machine tool under thermal loading. An efficient calculation is based on a low-dimensional approximation of the thermal field. Different model order reduction methods are compared with respect to the accuracy of the estimated TCP displacement and the optimized sensor locations.

Peer-review under responsibility of the International Scientific Committee in the person of the Conference Chair Prof. Steffen Ihlenfeldt.

*Keywords:* Optimal sensor placement; Model order reduction; Thermo-elastic model

---

## 1 Introduction

This paper is concerned with an optimal sensor placement problem for thermo-elastic solid body models. The goal is to place temperature sensors in a near-optimal way so that their measurements allow an accurate prediction of the thermally induced deformation at a particular point of interest (POI) in real time. Our main motivation and example used throughout the paper is to predict the deflection of the tool center point (TCP) of a machine tool under thermal loading.

Sensor placement problems for problems with partial differential equations (PDEs) are difficult optimization problems due to their large scale and the intricate structure of the objective, which normally involves the estimator covariance matrix of the quantity estimated. In the current application the restriction of the sensor locations to lie on the surface of the machine column imposes further constraints. In our approach we exploit the particular structure of thermo-elast-

tic models. While the evolution of the temperature  $T$  is relatively slow, the deformation  $u$  is instantaneous. Moreover, we can neglect the mechanically induced heat sources, so that the coupling is  $T \rightarrow u$  is uni-directional and time independent.

In the optimal sensor placement problem, our objective is to choose sensor locations in such a way that the measurements will contain the maximum amount of information with regard not to the reconstruction of the temperature field itself, but rather with regard to the subsequent prediction of the thermally induced displacement at a point of interest. In order to reduce the complexity of the placement problem we apply model order reduction (MOR) for the temperature. In this paper we compare four model order reduction techniques, namely the Proper Orthogonal Decomposition (POD), Balanced Truncation (BT) and two different Moment Matching (MM) approaches. For details about the MOR methods we refer the reader to [1], [2]. The focus of this paper is to compare the results of the sensor placement for these different methods.

Model order reduction techniques are frequently used in sensor placement problems involving PDEs. A detailed literature overview can be found in [2], [7]. In [7] a POD based sensor placement approach using detailed information about the heat loads is described. The present paper is an extension of that work and we compare different MOR techniques including POD.

The paper is organized as follows. In the next section we state the thermo-elastic model. The sequential placement strategy is described in detail in section 3. Numerical experiments are provided in section 4 which allow a comparison of the MOR techniques in the context of sensor placement problems.

Nomenclature		
$\rho$	density	(7250 kg/m <sup>3</sup> )
$c_p$	specific heat at constant pressure	(500 J/(kg K))
$\lambda$	thermal conductivity	(46.8 W/(K m))
$T_{ref}$	ambient temperature	(20 °C)
$\alpha$	heat transfer coefficient	(0 to 12 W/(K m <sup>2</sup> ))
$\nu$	Poisson's ratio	(0.3)
$E$	modulus of elasticity	(114·10 <sup>9</sup> N/m <sup>2</sup> )
$\beta$	thermal volumetric expansion coefficient	(1.1·10 <sup>-5</sup> 1/K)

## 2 Thermo-elastic forward model

We denote the solid body on which we consider the thermo-mechanical displacement problem by  $\Omega$  and its surface by  $\Gamma$ . In our application  $\Omega$  is the machine column shown in Figure 1. We consider the linear heat equation,

$$\begin{aligned}
\rho c_p \dot{T} - \operatorname{div}(\lambda \nabla T) &= 0 & \text{in } \Omega \times (0, t_{\text{end}}) \\
\lambda \frac{\partial T}{\partial n} + \alpha(x)(T - T_{\text{ref}}) &= r(x, t) & \text{on } \Gamma \times (0, t_{\text{end}}) \\
T(\cdot, 0) &= T_0 & \text{in } \Omega
\end{aligned} \tag{1}$$

The boundary conditions represent a simple model for the free convection occurring at the surface  $\Gamma$ , and the heat transfer coefficient may vary across the surface. The right hand side  $r(x, t)$  represents thermal loads, e.g., due to electric drives.

Here  $T_{\text{ref}}$  denotes the ambient temperature. We discretize (1) by standard linear Lagrangian finite elements in space; see, e.g., [4], [6]. Then the temperature field at the finite element nodes at any given time is represented by a vector  $T \in \mathbb{R}^{n_{th}}$ .

The linear elasticity model is based on the balance of forces,

$$-\sigma(\varepsilon(u), T) = f \text{ in } \Omega \tag{2}$$

We employ an additive split of the stress tensor  $\sigma$  into its mechanically and thermally induced parts. Together with the usual homogeneous and isotropic stress-strain relation, we obtain the following constitutive law, see [3]:

$$\begin{aligned}
\sigma(\varepsilon(u), T) &= \sigma^{el}(\varepsilon(u)) + \sigma^{th}(T) \\
\sigma^{el}(\varepsilon(u)) &= \frac{E}{1+\nu} \varepsilon(u) + \frac{E\nu}{(1+\nu)(1-2\nu)} (\varepsilon(u))I \\
\sigma^{th}(T) &= \frac{-E}{1-2\nu} \beta(T - T_{\text{ref}})I
\end{aligned} \tag{3}$$

Herein,  $\varepsilon$  denotes the linearized strain tensor  $\varepsilon(u) = \frac{1}{2}(\nabla u + \nabla u^T)$  and  $I$  the  $3 \times 3$  identity tensor. Moreover,  $E$  and  $\nu$  denote Young's modulus and Poisson's ratio, respectively. In order to simplify the notation, we consider from now on the temperature relative to the constant  $T_{\text{ref}}$ , i.e., we write  $T$  instead of  $T - T_{\text{ref}}$ . For the numerical treatment of (2)-(3), the same finite element discretization as for the thermal model (1) with the discrete dimension  $n_{el} = 3n_{th}$  is used. Note that in the remainder there are no external forces induced in the system, i.e.,  $f = 0$  holds.

### 3 Optimal sensor placement

With the sensor placement problem we seek to choose optimal positions of temperature sensors on the surface  $\Gamma$ . The goal is to reconstruct from these measurements the temperature field  $T$  as an intermediate quantity, and subsequently to predict the displacement  $u(x_{TCP})$  at the point of interest, i.e., the tool center point. As was mentioned in the introduction such placement problems are challenging for a number of reasons. In the following subsections, we reduce the complexity of the problem step by step so that it becomes tractable.

#### 3.1 Displacement estimation

Our first step to make the problem tractable is to apply model order reduction to the temperature state space, i.e. we generate a matrix  $V \in \mathbb{R}^{n_{th} \times r}$  with  $r \ll n_{th}$  such that the reduced temperature field  $\hat{T}$  is a good approximation of the original temperature field  $T$ , i.e.  $T \approx V\hat{T}$ . The particular choice of the matrix  $V$  depends on the model order reduction technique to be applied, an overview over different MOR methods can be found in [1]. Exploiting the linearity of the elasticity equation (3) we can express the elasticity field in terms of the reduced temperature field  $\hat{T}$ ,  $u = ST \approx SV\hat{T}$ . Herein,  $S$  is the solution operator for the elasticity equation. Then the displacement at the point of interest is

$$u(x_{TCP}) = C_u u \approx C_u SV\hat{T} \in \mathbb{R}^3 \quad (4)$$

with an observation matrix  $C_u \in \mathbb{R}^{3 \times n_{el}}$ , mapping the entire displacement field to the displacement of the POI. To estimate the TCP displacement (4) from temperature measurements, we first estimate the reduced temperature field  $\hat{T}$ . This estimation will be instantaneous, i.e., at any given moment in time we estimate the temperature field using only measurements from that same time instance. Therefore we suppress the dependence on time in our notation. The estimation of the reduced temperature field is achieved by solving the least squares problem

$$\underset{\hat{T} \in \mathbb{R}^r}{\text{Minimize}} \frac{1}{2} \sum_{i=1}^{n_{sensors}} \left( \sum_{j=1}^r \hat{T}_j v_j(x_i) - \tilde{T}_i \right). \quad (5)$$

Here  $\tilde{T}_i$  denotes the  $i$ -th temperature measurement, acquired at location  $x_i$  on the surface  $\Gamma$ , where  $i = 1, \dots, n_{sensors}$ . We restrict these locations to the nodes of the finite element mesh. Notice that each row of the reduced basis matrix  $V$

corresponds to one degree of freedom in the finite element space for the temperature. Since we are using linear Lagrangian elements each row in  $V$  is associated with a FE node. Hence we can identify the  $j$ -th column of  $V$  with a function  $v_j$ . This justifies the notation  $v_j(x_i) = V_{ij}$ .

Next let  $X = [x_1, \dots, x_{n_{sensors}}]$  be the vector of all sensor positions selected. Then the solution of the linear least-squares problem (5) given by the normal equation

$$J(X)^T J(X) \hat{T} = J(X)^T \tilde{T}. \quad (6)$$

Here  $J(X)$  denotes the Jacobian of the residuals w.r.t. the unknowns (the components of the reduced temperature  $\hat{T}$ ) and  $\tilde{T}$  is the vector of measurements  $[\tilde{T}_1, \dots, \tilde{T}_{n_{sensors}}]$ . The solution of (6) is unique if  $J(X)$  has full rank, which we assume. To ensure this, it is necessary to have  $n_{sensors} > r$ . The solution of (6) gives us an estimator  $\theta_{\hat{T}}(X)$  for the reduced temperature and using the relation (4) an estimator for the TCP displacement  $u(x_{TCP})$ , which is given by

$$\theta_{u(x_{TCP})}(X) = C_u S V \theta_{\hat{T}}(X) = C_u S V (J(X)^T J(X))^{-1} J(X)^T \tilde{T}. \quad (7)$$

### 3.2 Covariance of the estimator

In order to judge the quality of the estimator we consider the covariance matrix of  $\theta_{u(x_{TCP})}(X)$ . We assume the measurement errors to be independent identically distributed random variables with normal distribution  $N(0, \sigma^2)$ , i.e., with zero mean and variance  $\sigma^2$ . This means that the measurements  $\tilde{T}$  are multivariate normally distributed with associated covariance matrix  $Cov_{\tilde{T}} = \sigma^2 I$ . The estimator  $\theta_{\hat{T}}(X)$  for the reduced temperature field is a linear transformation of the measurements  $\tilde{T}$ , thus its covariance can be written as

$$\begin{aligned} Cov_{\hat{T}}(X) &= (J(X)^T J(X))^{-1} J(X)^T Cov_{\tilde{T}} J(X) (J(X)^T J(X))^{-1} \\ &= \sigma^2 (J(X)^T J(X))^{-1} \mathbb{R}^{r \times r}. \end{aligned}$$



Analogously we obtain the covariance of the estimator  $\theta_{u(x_{TCP})}(X)$  for the TCP displacement from

$$Cov_{u(x_{TCP})}(X) = \sigma^2 C_u S V (J(X)^T J(X))^{-1} (C_u S V)^T \in \mathbb{R}^{3 \times 3}. \quad (8)$$

Notice that the covariance  $Cov_{u(x_{TCP})}(X)$  does not depend on the current thermal state of the machine. However it does depend on the sensor positions selected (encoded in  $X$ ) as well as on the choice of the reduced-order basis matrix  $V$ .

### 3.3 Optimal sensor placement strategy

The precision of a linear least-squares estimator can be judged from the eigenvalues of its covariance matrix, see for instance [5] or [8].

Large eigenvalues of  $Cov_{u(x_{TCP})}(X)$  point to a high sensitivity of  $u(x_{TCP})$  w.r.t. perturbations in the temperature measurements. For this reason it is our goal to choose sensor positions  $X$  such that the covariance becomes small in a sense to be defined.

This results in the optimal sensor placement problem

$$\begin{aligned} & \text{Minimize } \Psi_D \left( Cov_{u(x_{TCP})}(X) \right) \\ & \text{subject to } X = [x_1, \dots, x_{n_{sensors}}] \subset \Gamma. \end{aligned} \quad (9)$$

Here  $\Psi_D(Cov) = \ln(\det(Cov))$  denotes the D-optimality criterion, which measures the volume of the uncertainty ellipsoid for the estimate of  $u(x_{TCP})$ , according to [9].

Due to the fact that problem (9) is in general hard to solve, we will reduce the complexity of the problem in the following. On the one hand, taking the constraints  $x_1, \dots, x_{n_{sensors}} \in \Gamma$  literally would require a parametrization of a complicated surface such as the one depicted in Figure 1. As mentioned previously we therefore restrict the potential sensor positions to the vertices to the FE nodes to overcome this difficulty. This amounts to the selection of a finite but possibly large set  $\Gamma_{finite} \subset \Gamma$  of feasible sensor locations.

Finding globally optimal solutions of (9) with the constraints  $x_1, \dots, x_{n_{sensors}} \in \Gamma_{finite}$  would require the solution of a large combinatorial problem. While in principle this can be achieved for sizable problems using sophisticated branch-

and-bound algorithms, see for instance [10], we proceed differently here and replace the simultaneous placement by a sequential (greedy) placement of one sensor at a time. As observed in [7] this will lead to slightly suboptimal solutions but it makes the overall problem tractable. In addition the sequential placement strategy allows us to determine the total number of sensors required for a desired target precision on the fly.

Owing to the sequential placement approach we need to solve a series of sub-problems of the form

$$\underset{x_i \in \Gamma_{finite}}{\text{Minimize}} \Psi \left( Cov_{u(x_{TCP})}(x_1, \dots, x_{i-1}; x_i) \right). \quad (10)$$

Here  $x_1, \dots, x_{i-1}$  are the locations of the sensors already placed and  $x_i$  is the currently sought position of the  $i$ -th temperature sensor. We refer the reader to [7] for further details.

## 4 Numerical results

The following numerical experiments are based on the geometry of the prototypical Auerbach ACW 630 machine column shown in Figure 1. The material constants are given in the introduction. Notice that the heat transfer coefficient varies over different parts of the boundary, which are classified according to the orientation of the outer surface normal, see Figure 1. The machine column experiences the influence of two heat sources. One source originates from an electric drive mounted on the top of the machine column (surface part  $\Gamma_{r1}$ ) while the other source represents the ball screw nut driving the horizontal movement of the column ( $\Gamma_{r2}$ ), see Figure 1.

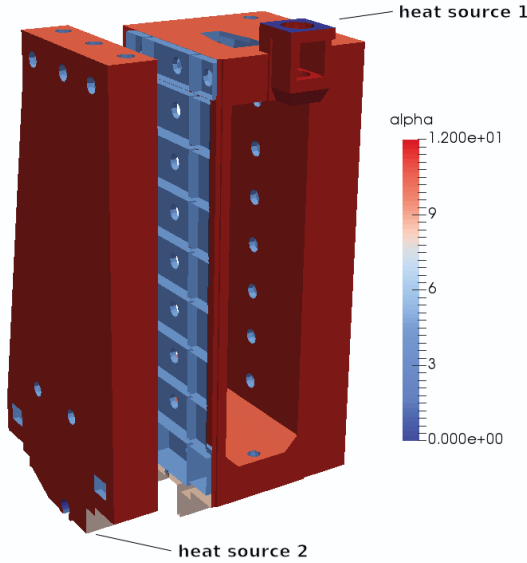


Fig. 1. Heat sources and boundary conditions.

The method described in section 3 was applied using four different MOR method, which are POD, BT as well as two variants of MM (Padé and IRKA) using a model size of  $r = 20$ . The resulting 30 optimal sensor positions can be seen in Figure 2. In the case of POD most of the sensors are placed near to the heat sources, the reason for this phenomenon is that the projection subspace associated with the basis matrix  $V$  is based solely on simulations of the thermal model (1), so the heat sources will strongly influence the computed subspace. By contrast, the projection matrices  $V$  computed from the BT and the two MM procedures are set up independently of the thermal loads and initial condition. Therefore the final sensor locations are spread out more evenly across the machine column's surface. Despite its smaller physical extension, it can be observed that the heat source located at the lower part of the machine column attracts a significant amount of sensors. This is quite intuitive since even small deformations at the base of the machine column will naturally be transferred up along the height of the column and thus may have a sizable influence on the displacement of the TCP.

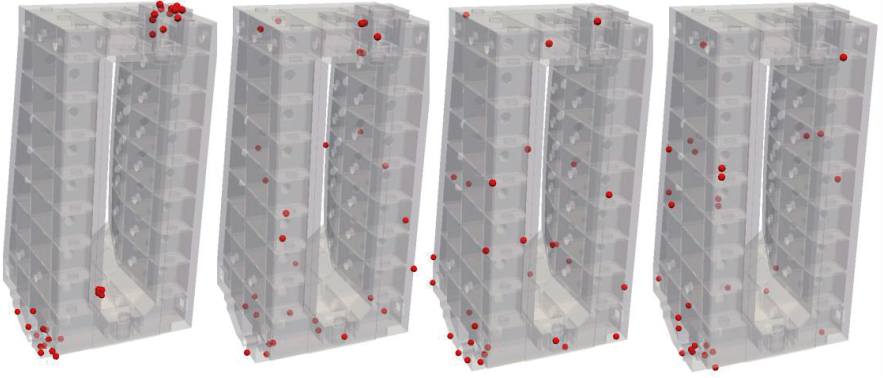


Fig. 2. Optimal sensor locations for the different MOR methods (from left: POD, BT, Padé, IRKA).

To achieve a comparison of the quality of the estimation using the four MOR variants we used simulated values as measurements from a simulation of the full model with thermal loads

$$r(x, t) = \begin{cases} 6700 \text{ W/m}^2 & \text{if } x \in \Gamma_{r1} \quad \text{and } 0s \leq t \leq 2400s \\ 2700 \text{ W/m}^2 & \text{if } x \in \Gamma_{r2} \quad \text{and } 0s \leq t \leq 2400s \\ 2700 \text{ W/m}^2 & \text{if } x \in \Gamma_{r2} \text{ and } 2400s \leq t \leq 4800s \\ 6700 \text{ W/m}^2 & \text{if } x \in \Gamma_{r1} \text{ and } 4800s \leq t \leq 7200s \\ 0 & \text{else} \end{cases}$$

and initial temperature  $T_0 = T_{ref}$ . Figure 3 shows the evolution of the simulated TCP deflection, compared to its estimated position based on the 30 optimally placed sensors (in the sense of the approach in section 3) with reduced bases of dimension 20. The TCP displacement estimate was then obtained from solving the least-squares problem (5) using disturbed measurements. The estimated displacements are quite accurate except for Padé (Figure 3 left) and the relative errors of the estimation are similar for all four MOR methods (Figure 3 right).

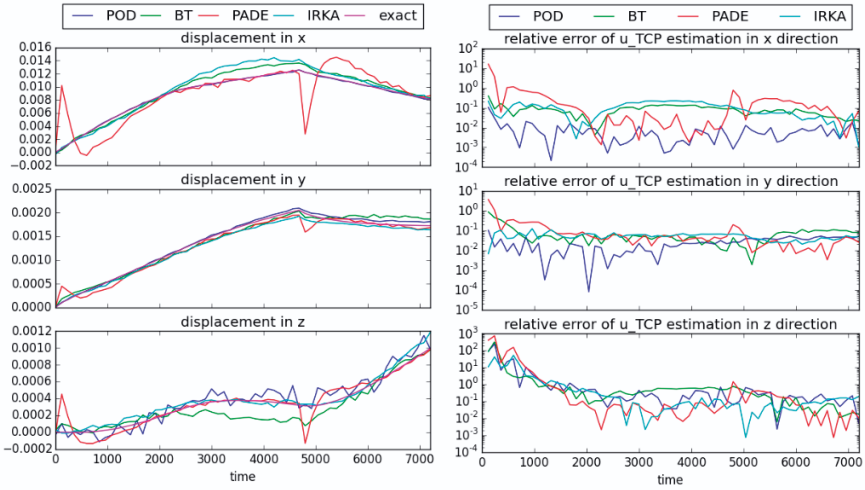


Fig. 3. Comparison of the exact (simulated by the full model) TCP displacement with the estimates (left) and the corresponding relative errors (right).

## 5 Conclusion

In this paper we revisited an optimal sequential placement strategy for temperature sensors in order to predict thermally induced mechanical deformations from temperature measurements. To make the sensor placement procedure tractable, we applied model order reduction either to the temperature equation alone, or to the full thermo-mechanical model. The main focus of this paper was to compare the performance of different MOR methods w.r.t. the sensor placement objective and the prediction quality of the induced displacement estimation using simulated measurements at the optimized sensor positions.

### Acknowledgements

*This work was supported by two DFG grants within the Special Research Program SFB/Transregio 96 (Thermo-energetische Gestaltung von Werkzeugmaschinen), which is gratefully acknowledged.*

## 6 References

- [1] Antoulas, A.C., 2005. Approximation of Large-Scale Dynamical Systems. SIAM Publications.
- [2] Benner, P., Herzog, R., Lang, N., Riedel, I., Saak, J., 2017. Comparison of model order reduction methods for optimal sensor placement in thermo-elastic models. Preprint.

- [3] Boley, B.A., Weiner, J.H., 1960. Theory of thermal stresses. John Wiley & Sons Inc.
- [4] Braess, D., 2007. Finite elements. Cambridge University Press, Cambridge.
- [5] Fedorov, V.V., Hackl, P., 1997. Model-oriented design of experiments. Springer-Verlag 125.
- [6] Grossmann, C., Roos, H.-G., Stynes, M., 2007. Numerical treatment of partial differential equations. Springer-Verlag.
- [7] Herzog, R., Riedel, I., 2015. Sequentially Optimal Sensor Placement in Thermoelastic Models for Real Time Applications. Optimization and Engineering 16/4, 737-766.
- [8] Seber, G.A.F., Wild, C.J., 2005. Nonlinear Regression. John Wiley & Sons.
- [9] Uciński, D., 2005. Optimal measurement methods for distributed parameter system identification. CRC Press.
- [10] Uciński, D., Patan, M., 2007. D-optimal design of a monitoring network for parameter estimation of distributed systems. Journal of Global Optimization 39/2, 291-322.



# Workpiece temperature measurement and stabilization prior to dimensional measurement

*N. S. Mian, S. Fletcher, A. P. Longstaff*

Centre for Precision Technologies (CPT), University of Huddersfield, Queensgate,  
Huddersfield HD1 3DH United

**Abstract.** In- or close-to-process dimensional measurement of workpieces allows rapid detection of production errors, which allows responsive corrections. The time required for the component to reach thermal stability before measurement is a more sensitive issue than for post-process coordinate metrology in a measurement laboratory. The traditional approach of waiting for a nominal, empirically selected duration with the component “soaking” in the environment results in considerable inefficiencies. Similarly, surface temperature measurement can have significant uncertainty due to sensor accuracy, deployment and the correlation to the core component temperature. This research analyses surface temperature methods and then utilizes finite element analysis to predict the timespans required by a component to stabilise using different boundary conditions in order to optimise the quality process.

Peer-review under responsibility of the International Scientific Committee in the person of the Conference Chair Prof. Steffen Ihlenfeldt.

*Keywords:* Temperature; Thermal; CMM; Workpiece; Time; Soaking; Temperature stabilization

---

## 1 Introduction

It is well known that temperature affects increase uncertainty in manufacturing and coordinate metrology. There are techniques employed in industry to reduce such affects and specific inspection system, infrastructure and methods are employed to either control temperature variation or reduce its influence on the results. In manufacturing industry it is common that the production process is not temperature controlled or that it adds heat to the workpiece, requiring that it then be soaked in a controlled environment prior to measurement. There is plenty of associated literature including reviews [2] and ‘Guide to dimensional measurement equipment’ [3] which also highlights the importance of temperature soaking prior to dimensional inspection. Similarly, there has been



work targeting non-standard environment i.e. measuring in manufacturing environments where temperature control is not available. Kruth et al [1] have mentioned the effects of temperature variations during the measurement process on the CMMs and highlighted the usefulness of acquiring soaking procedures to avoid errors in CMM measurements.

In-process or close-to-process dimensional measurement of workpieces, perhaps using on machine probing or a co-located measurement system like a Renishaw Equator or CMM, allows rapid detection of production errors. This is becoming increasingly popular as it increases efficiency and allows responsive corrections. As time-savings are sought, the time required for the component to reach thermal stability before measurement is a more sensitive issue than for post-process coordinate metrology in a measurement laboratory where time constraints or temperature monitoring systems are more available. One option is to monitor the temperature of the workpiece during the process, then post-process measurement could be performed immediately afterwards. Muller [4] used a fast pyrometer to achieve this during turning operations. However, for complex multi-axis milling, access to the tool and component surfaces is often not possible.

Considering the persistent need for either differential compensation or workpiece stabilisation, this research analyses surface temperature methods and then utilizes finite element analysis to predict the timespans required by a component to stabilise using different boundary conditions in order to optimise the quality process.

## **2 Workpiece temperature measurement**

In order for measurements to be made rapidly at temperatures other than 20°C, differential expansion compensation is simple to apply, and automatic on most CMM systems. However, significant uncertainty can arise from thermal contact resistance between the sensor and surface, the difference between the surface temperature reading and the bulk temperature affecting the particular characteristics being measured, sensor accuracy and material properties. In this work, we assume the uncertainty in the expansion coefficient for the materials is relatively low, either because the material properties are well known, or this property has been calibrated by an appropriate laboratory.

## 2.1 Digital temperature sensor module

While most CMMs use PT100 sensors having a typical accuracy of  $\pm 0.1^{\circ}\text{C}$ , they are not often used on manufacturing equipment and require signal conditioning electronics. Low cost alternatives include thermocouples and direct-to-digital sensors. Thermocouples can have good accuracy but not usually in affordable systems and still require additional signal conditioning units for absolute accuracy. They also require individual cables for each sensor. If we consider simple manual inspection tables or on-machine measurement, then simple connection, communication and low cost are significant considerations. Direct-to-digital semiconductor sensors have the significant advantage of providing data direct through serial communication, which also provides a significant reduction in cabling requirements when multiple sensors are in use, and compatibility with cost effective wireless solutions. The main disadvantage relates to them not having the same accuracy specifications, although they do lend themselves to calibration using low order/quadratic equations and this method was therefore applied. For this work, DS18B20 sensors from Maxim Integrated were tested. These use a 1-wire bus, enabling 100s of sensors on a single loom. They have an OEM accuracy specification of  $\pm 0.5^{\circ}\text{C}$ , but experience shows that this is conservative and mainly consists of absolute error with some smaller non-linearity occurring over the temperature range ( $-10^{\circ}\text{C}$  to  $85^{\circ}\text{C}$ ). In order to be comparable with standard CMM type sensor performance, the target for the calibration is  $\pm 0.1^{\circ}\text{C}$ .

### 2.1.1 Sensor calibration

It is standard practice to calibrate sensors in a low uncertainty comparator such as a dry or wet block calibrator with a high accuracy reference (in this case a FLUKE CHUB E4 1529 controller with a four wire secondary standard thermistor was used). In this work an alternative calibration was considered that did not require such hardware, just a good reference probe (accuracy ideally an order of magnitude better than the target specification). An important reason for this is that a dry or wet block calibrator has a deep well into which the sensors and reference probe are inserted in order to remove or reduce the influence of conduction through the cable. This may not be a problem for some sensors that use differential connection to cancel wire resistance and self-heating etc., but in our experience, the effect is significant with these digital sensors. The issue here is the difficulty to implement the sensor with same controls therefore nullifying the calibration in the application. In addition, the readings from the sur-

face of a workpiece needs to represent the temperature of the target material therefore the effect of the interfacial fluid (heat transfer compound was used in this case to reduce air content), level of pressure and gradients within the sensor itself (convection from the sensor or housing) should be included in the calibration process.

Considering the first problem of conductance down the cable, an intermediate miniature circuit board (very simple direct connection of three wires) was used to connect the sensors to the cable, reducing the cross sectional area and therefore heat transfer. This was embedded into a bespoke aluminium housing along with two sensors as shown in Fig. 1. The holes for the sensors provided an interference fit and heat transfer compound was used to fill any remaining gaps (the sensor is not perfectly cylindrical). The sensors were located very close to the bottom measuring surface to minimise thermal gradient and hysteresis. Aluminium was chosen because it is more resistant to corrosion from coolant and the effect of variation in conductance compared to copper was negligible for the <1mm of interface material. Two sensors were used to provide a level of averaging to compensate a little for the limited resolution of the digital sensors (0.0625°C).

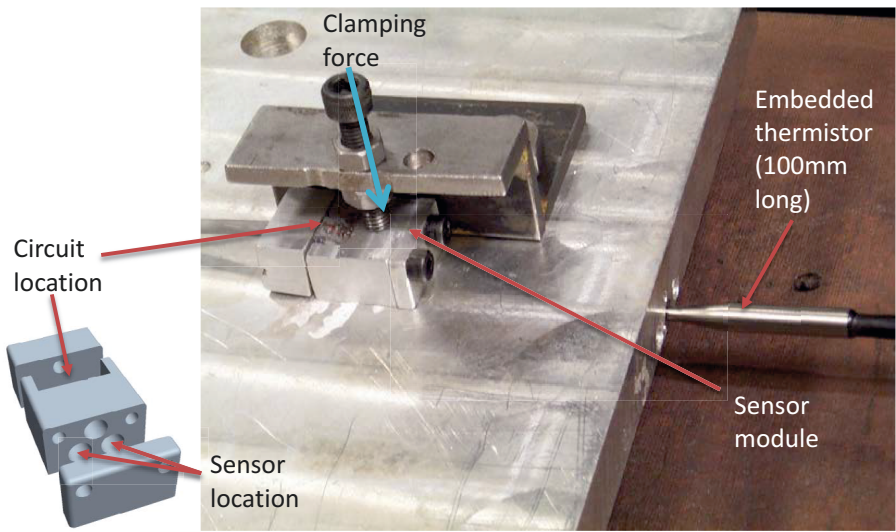


Fig. 1. Experimental setup for the surface mounted sensor calibration

An aluminium plate with good quality machined surface (Surface finish value Ra of 0.5µm to 0.8µm) was used as a representative workpiece into which the

100mm reference thermistor was embedded approximately 5mm below the surface to give an accurate core reading. The temperature range applied to the workpiece was between 21 °C and 51 °C and the results of uncalibrated and calibrated measurements are shown in Fig. 2a and Fig. 2b respectively, with the residual error for pre and post calibration provided in Fig. 3 and Fig. 4 respectively. The uncalibrated sensors readings are lower, in an absolute value sense, and the range of error is reduced from 0.6°C to within +/- 0.1°C with averaging of the two sensors.

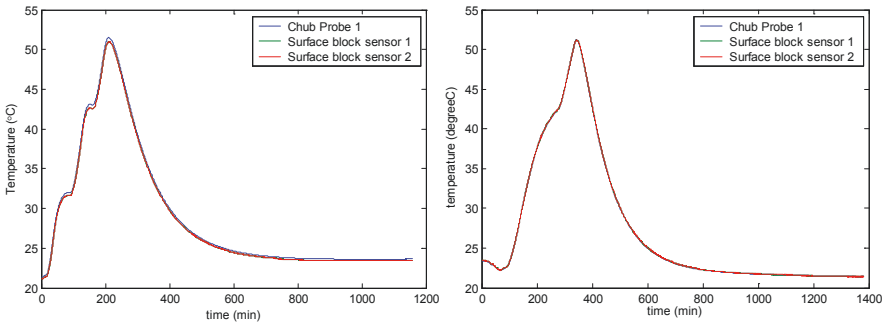


Fig. 2. (a) Temperature profile for sensor calibration (b) Post calibration validation check

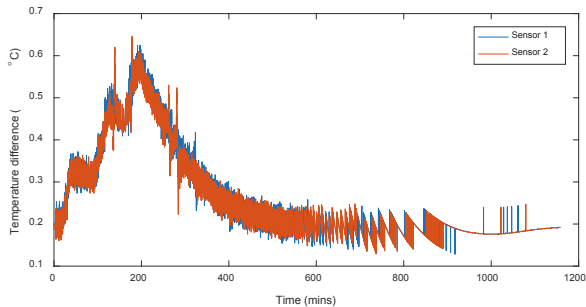


Fig. 3. Sensor module temperature difference compared to reference

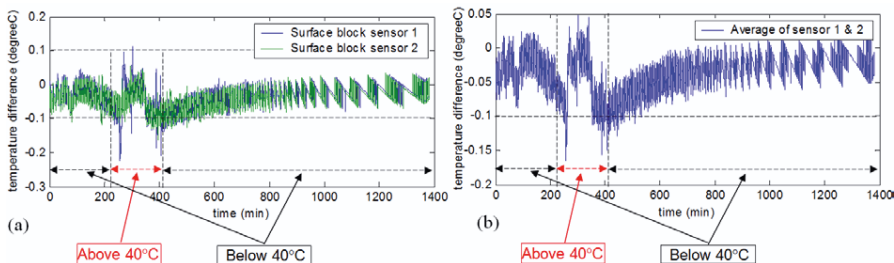


Fig. 4. (a) Temperature differences of sensors 1 and 2 against the thermistor (b) Difference using average of sensors 1 and 2

These results were comparable with previous tests performed on the same DS18B20 sensors when embedded inside the workpiece. But this is not a practical solution in most cases. So far no tests have been performed on other materials where lower conductivity could increase the uncertainty in the surface sensor reading compared to the bulk temperature.

### 2.1.2 Comparison with CMM PT100

A further comparison was made between the new digital sensor module and a Zeiss Prismo CMM PT100 sensor during a similar workpiece cooling scenario to see how the new calibration compares to such an application specific sensor. Fig. 5 shows the measured temperature data from the digital sensors 1 and 2 as well as the CMM sensor (PT100 type). The comparison is made only for temperature below 40°C as the CMM temperature sensor does not produce any meaningful result for temperature above 40°C (default to 20°C). The difference between the digital temperature sensor measurements against the CMM sensor is shown in Fig. 6.

The digital sensor readings are shown to vary between 0 to 0.2°C relative to the CMM sensor. As can be seen from Fig. 6, some of the comparison data from the graph is missing as the CMM inadvertently stopped measuring because the number of programmed measurement loops had been reached. This does not affect the measurement trend significantly as the measurement was able to be restarted later.

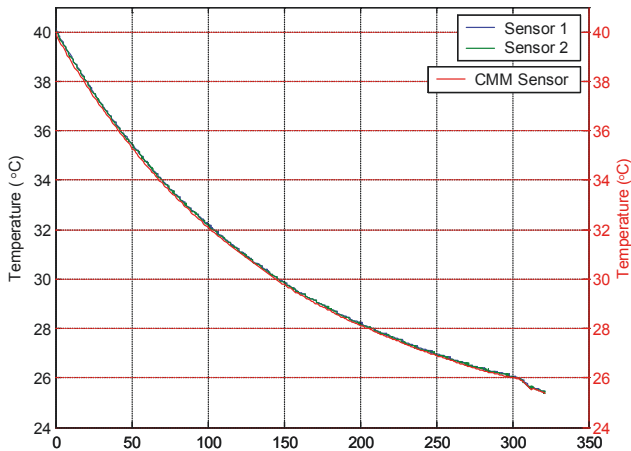


Fig. 5. Temperature profile measured by the CMM sensor (PT100) and the digital sensors

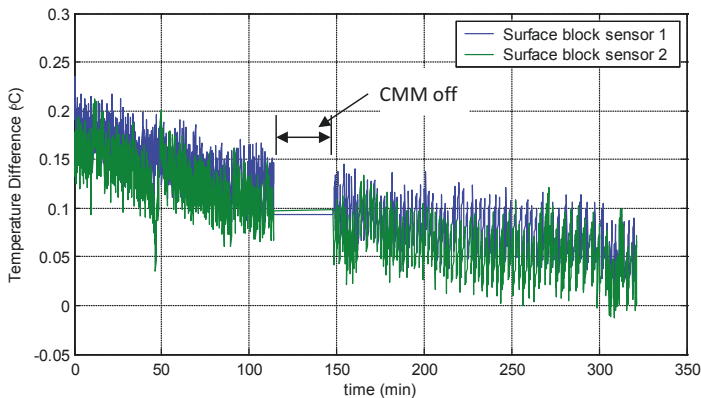


Fig. 6. Temperature difference between the CMM sensor (PT100) and the digital sensor module

## 2.2 Simulated cooling for error prediction using FEA

Following the previous workpiece tests, a larger workpiece was designed that would provide greater thermal gradients and a large void to consider the influence of trapped air (Air pocket) on cooling and its influence on the accuracy of Finite Element Analyses (FEA). To reduce weight, the material used was Aluminium. Each face of the cube has the circle diamond square features of the NAS979 standard to generate simple characteristics. Fig. 7 shows the cube and the location of the temperature readings and probing. For this FEA work and

comparison of cooling effects, just the circle diameter on the top was considered. The side features showed negligible difference for longer cooling times associated with natural convection. It is likely that forced convection (using, for example, cooling fans) and conduction from the base will increase the likelihood of significant thermal gradient.

The following simulations represent a circumstance where a component has had work performed on it and has an elevated temperature of 30°C and therefore requires soaking/cooling prior to inspection. As mentioned previously, using simulation to estimate required cooling times is sometimes applied, but uncertainties exist in the boundary conditions. Convective heat loss is often the primary heat transfer mechanism and a value of 6W/m<sup>2</sup>/K based on previous research by Mian [5] was applied to the outer surfaces. This is an average for different surface orientations and actual values would vary from surface to surface. For this comparison it has sufficient accuracy.

While there are many articles on thermal contact conductance theory, modelling and experiments, no literature was found regarding contacting surfaces of aluminium and granite. In order to reduce uncertainty in contact conductance between the bottom surface to a fixture or the CMM bed (a related topic also being researched but outside the scope of this paper), the cube is supported sparsely (surface contact less than 30mm<sup>2</sup>) to minimise conduction.

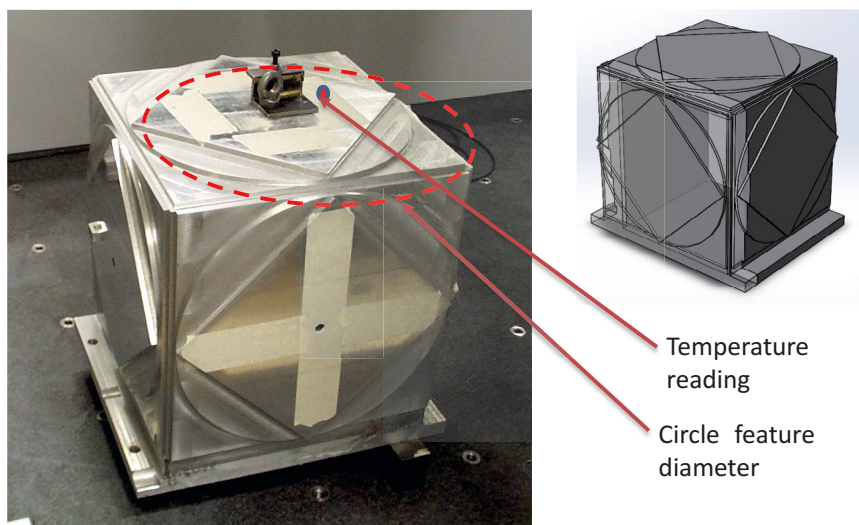


Fig. 7. Five sided aluminium test workpiece

Fig. 8 shows the temperature of the top of the cube for two simulations, one using just convective heat loss to an infinite sink from all exposed surfaces, and the second using a cubic model of air inside the workpiece, with heat transfer across the boundary set to the same as natural convection. The initial condition sets the air to be the same as the ambient ‘sink’ temperature (22 °C).

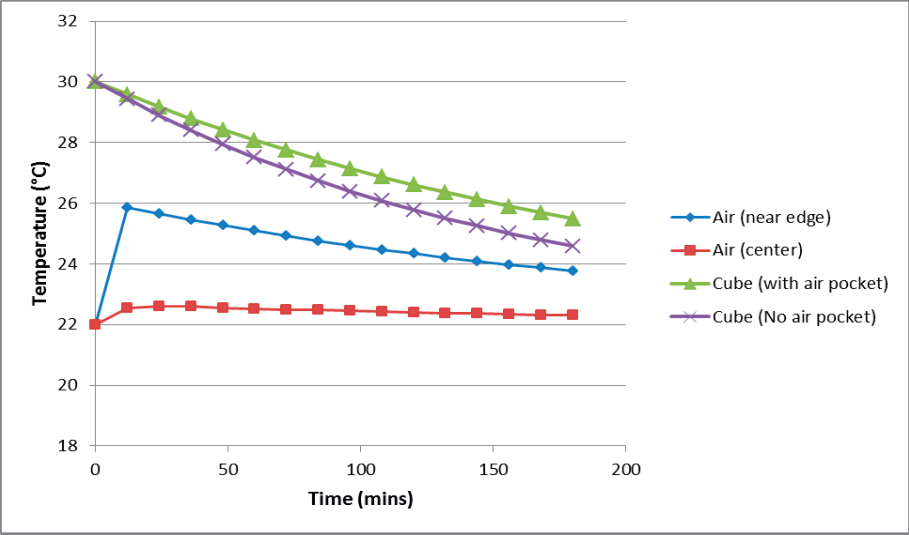


Fig. 8. Simulated temperature of the cube with and without air pocket

Comparing the simulation results with the measured temperature on the CMM, we see that the air pocket results in Fig. 9 show good correlation to within just 0.1°C. The deviation with just convection on all exposed surfaces is 0.9°C (based on the trace in Fig. 8).

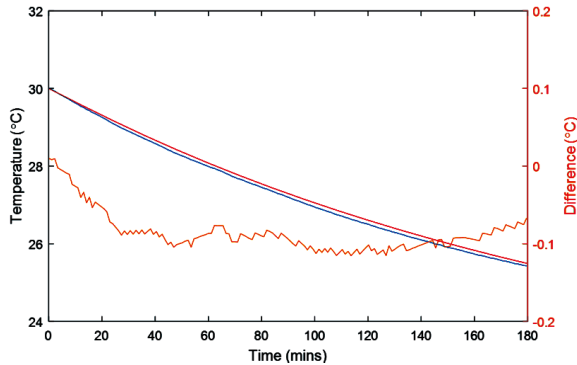


Fig. 9. Comparison between simulated and measured temperature during natural cooling of cube



The effect of the different cooling conditions on the dimensional readings is shown in Fig. 10. Considering a target temperature of 22°C, the difference in prediction is almost 45 minutes.

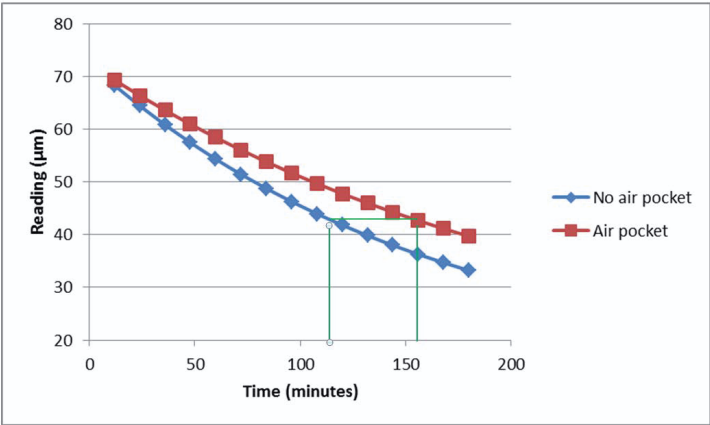


Fig. 10. Deviation in circle diameter from nominal (300mm) during cooling with and without air pocket

### 3 Conclusions

In order to reduce the uncertainty of dimensional measurement of manufactured components at temperature other than 20 °C, the measurement of the temperature using surface mounted sensor is convenient but is subject to uncertainty and availability of affordable and easy to use sensors compatible with general inspection tables and on-machine measurements. A simple sensing module comprising two direct-to-digital temperatures sensor was calibrated and tested to achieve an accuracy approaching typical CMM specification of +/- 0.1 °C. Where soaking of the workpiece is required for thermal stabilisation/cooling, then simulations can provide predictions for the transient behaviour i.e. cooling times and the effect on the dimensional result. Good results within 0.2°C were simulated when the air pocket was considered correctly in the FEA model.

#### Acknowledgements

*The authors gratefully acknowledge the UK’s Engineering and Physical Sciences Research Council (EPSRC) funding of the Future Metrology Hub (Grant Ref: EP/P006930/1).*

## 4 References

- [1] Kruth, J.-P., et al., Interaction between workpiece and CMM during geometrical quality control in non-standard thermal conditions. *Precision Engineering*, 2002. 26(1): 93-98.
- [2] Claverley, J.D. and R.K. Leach, A review of the existing performance verification infrastructure for micro-CMMs. *Precision Engineering*, 2015. 39: 1-15.
- [3] Royce, R., Guide to Dimensional Measurement Equipment. November 2015, Rolls-Royce plc.
- [4] Muller, B., Renz, U., 2003. Time resolved temperature measurements in manufacturing. *Measurement* 34, 363–370.
- [5] Mian, N.S., Fletcher, S., Longstaff, A., Myers, A., Efficient thermal error prediction in a machine tool using finite element analysis. *Measurement Science and Technology*, 2011. 22(8): 085-107
- [6] Mian, N.S., Fletcher, S., Longstaff, A., Myers, A., The significance of air pockets for modelling thermal errors of machine tools, in *Laser Metrology and Machine Performance X*, L. Blunt and W. Knapp, Editors. 2013, EUSPEN: Bedfordshire, UK. p. 189-198
- [7] E. E. Marotta and L. S. Fletcher. "Thermal Contact Conductance for Aluminum and Stainless-Steel Contacts", *Journal of Thermophysics and Heat Transfer*, Vol. 12, No. 3 (1998), pp. 374-381.



# Measurement of test pieces for thermal induced displacements on milling machines

*H. Höfer, H. Wiemer*

Institute of Machine Tools and Control Engineering IWM, Technische Universität Dresden,  
01062 Dresden, Germany

**Abstract.** Within Collaborative Research Centre (CRC) “Transregio 96”, a test piece was developed to demonstrate the effectiveness of correction and compensation solutions on milling machines. Therefore the test piece can map the thermal proportion of the displacements. This paper focus on the used measurement strategy and the measurement results on three different coordinate measuring machines (CMM) are evaluated. In doing so, various influences on the measurement result are considered. The objective is a sturdy measurement strategy to achieve comparable measurement results independently from the used coordinate measuring machine.

*Keywords:* Machine tool; Thermal error; Test piece; Evaluation Strategies; Measurement

---

## 1 Introduction

Within the CRC “Transregio 96” a test piece was developed to illustrate the thermally induced error during the process of a milling machine [1]. For this paper test pieces were milled for a load case which represents the period from the balanced state to the thermal steady state of the milling machine [2]. In order to ensure a general application of the developed measuring method, a sturdy measurement strategy is required, which can be executed on different coordinate measuring machines CMM’s. For testing the selected measurement strategy, the test piece was measured by three CMM’s. This article deals with the boundary conditions for achieving accurate, comparable and efficiently recorded results and presents the results of the evaluation. For this purpose, relevant influences on the measuring uncertainty are shown. In an accredited measuring laboratory, the measurement uncertainty according to [3] was determined using the method “Virtual Coordinate Measuring Machine” (VCMM) [4], [5].

## 2 State of the art

For the measurement of test pieces on coordinate measuring machines, there are numerous publications which deal with influences on measurement uncertainty and measurement process suitability. For this work the question arises which conditions must be fulfilled so that the investigations of the test pieces on three different coordinate measuring machines leads to comparable results with low measurement uncertainties? The complete measurement result consists of estimated value of a measured variable  $y$  and the specification of the extended uncertainty  $U$  ( $U = k \cdot u(y)$ ) [6]. In addition to measurement uncertainty, there is also the question of the measurement process suitability. This involves the comparison of the measurement uncertainty of a measuring system with the required dimensional tolerance on the test piece [7] [8]. Fig. 1 shows various influences on the measurement result. A distinction is made between factors of the measuring system (Fig. 1, bottom) and all other influences. The separation makes it possible to specify the measurement uncertainty for the measuring system independently of the specific application. In [9] and [10] examples are shown which illustrate that the way the operator of CMM defines the measurement strategy can have a clear influence on the value and uncertainty of the results of coordinate measurements.

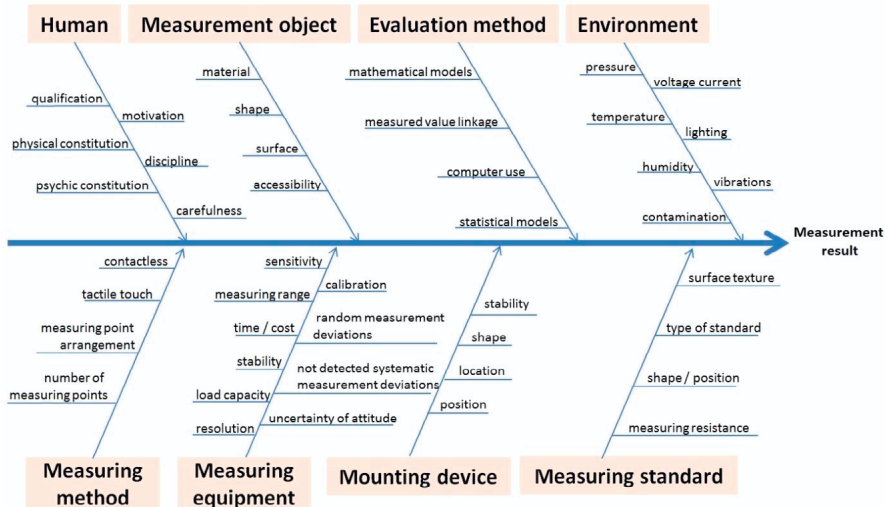


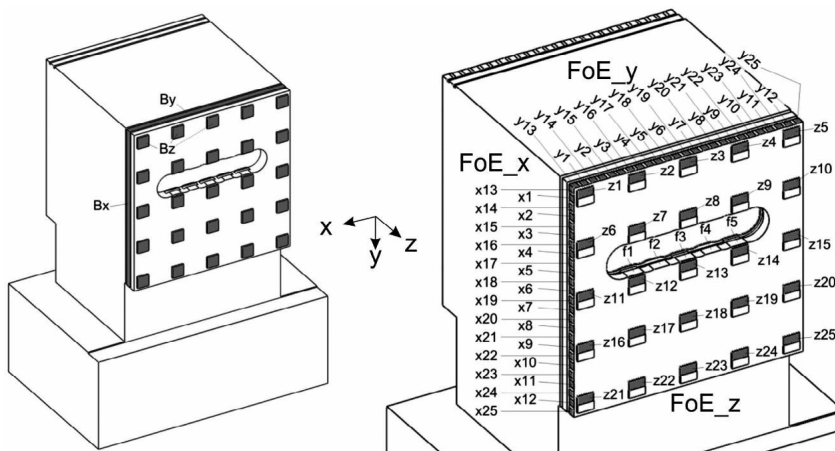
Fig. 1: Influences on the measurement result in the measurement process

For the characterization of the accuracy of CMM, general limits are often given, e.g. Maximum Permissible Error (MPE) [11]. However, the measurement uncertainty must be related to the specific measurement task [12]. With the “Guide to the Expression of Uncertainty in Measurement” (GUM) [3] exist a standard method for determining the measurement uncertainty. The basis is a mathematical model function which describes the dependence of the measuring result from the influencing factors. The standard method according to GUM is often not applicable for complex measurement tasks with many influencing variables. In [13] three methods for determining the task-specific measurement uncertainty of coordinate measurements according to GUM are described. This involves the numerical simulation by VCMM, the measurement of calibrated workpieces as well as the measurement uncertainty budget or uncertainty balance sheet. An overview of the simulation of measurement uncertainty is given by [14]. For the measurement of the test piece in this work, an examination of the measurement uncertainty based on the VCMM was carried out in the accredited laboratory in Dresden. It exist no general method for determining a robust measurement strategy for the test piece. A procedure for measurement of the test piece must still be found.

### **3 Influences on the measurement result**

#### **3.1 Measuring object**

The object is a test piece (Fig. 2) designed for the measurement on a CMM. The thermally induced errors can be mapped on defined small surfaces on the test piece. The test piece thus becomes the bearer of the measured variable, the thermally induced displacement. The 25 surfaces per axis direction are close to one another and accessible with the measurement sensor. The test piece consists of the material AlCuMg1 (EN AW 2017-A). At the beginning of the milling process, the reference surfaces Bx, By, Bz (Fig. 2 left) are created. At defined times the forming surfaces x1 to x25, y1 to y25 and z1 to z25 are created. The nominal distance between the reference surfaces and the forming surfaces is 0.2 mm for the forming surfaces 13 to 25 in X and Y direction, respectively 0.3 mm for all over forming surfaces (Fig. 2).



reference surface Bx, By, Bz forming surface (FoE) x1-x25, y1-y25, z1-z25

Fig. 2: Geometry of the test piece

### 3.2 Measuring method and measuring equipment

The measurement is done unidirectional and uniaxial. The measurement length  $L$  is 0.2 or 0.3 mm. The CMM has a Maximum Permissible Error (MPE) of  $0.5 + L$  [mm] /  $600 \mu\text{m}$ . However, this is the volumetric length measurement deviation for bidirectional single-axis measurements according [11]. Table 1 show CMM's used at the three measuring stations.

Table 1: Technical data of coordinate measuring machine

	Dresden (DD)	Chemnitz (CH)	Koeln
Type CMM	Leitz PMM	Zeiss Prismo	Zeiss Prismo
Measuring software	Quindos	Callypso	Callypso
probe ball diameter	2 mm	2 mm	2 mm
Orientation test piece	lying	standing	lying
Maximum Permissible Error	$0,5 + L/600 \mu\text{m}$	$0,5 + L/500 \mu\text{m}$	$0,5 + L/500 \mu\text{m}$
Contact force	3,5 N	0,1 N	0,1 N

In order to observe further influences during the measurement, the measurement uncertainty  $U$  ( $k=2$ ) was determined at the laboratory in Dresden using the VCMM method. The evaluation of the task-specific measurement uncertainty with VCMM in X, Y, and Z results  $U(k=2) = 1 \mu\text{m}$ . The main contributors in the

VCMM method are the ambient conditions in the measurement room, the geometrical errors of the CMM, the touch probe system and the roughness influence of the test piece. The influence of roughness on the uncertainty of the measuring point determined with VCMM is around 0.6  $\mu\text{m}$ . For determining this influence, three straight lines with at least 20 touch points are measured on the test piece. The length of the lines was 0.2 mm. From the measured coordinates of the touched points a balance line is determined as well as the standard deviation of the coordinates related to the balance line. From the three standard deviations, the mean standard deviation  $s_W$  is determined. On a measurement standard, the standard deviation  $s_N$  is determined in the same way. From both quantities, the uncertainty amount resulting from the roughness of the test piece is determined as follows (1)[15]:

$$U_{roughness} = 2 \cdot \sqrt{s_W^2 - s_N^2} \quad (1)$$

Random roughness measurements on the surface of the test piece revealed a roughness of  $R_z = 2 - 3 \mu\text{m}$ . For a simple estimation of the uncertainty component on the measuring point, the VCMM recommends (2) [4]:

$$U_{roughness} = R_z/2 \quad (2)$$

However, this estimation does not take into account the filter effect of the probe ball. The uncertainty component of the roughness of 0.6  $\mu\text{m}$  determined by VCMM measurement is thus approximately 50% of the estimated value of 1 to 1.5  $\mu\text{m}$  determined by the roughness parameter  $R_z$  for this measurement task. The uncertainty component of the CMM geometry is very low because of the small dimensions and the measurement length of the test piece.

### 3.3 Evaluation method

The reference surfaces Bx, By and Bz define the coordinate system of the test piece for the measurement on the CMM. Therefore 5 points on these three surfaces are touched. For getting the results at least one touch point must be selected for all surfaces. However, on this way no statement on the quality of the surfaces is possible. At the first test pieces on a milling machine, it is thus recommended to use 5 touch points on the reference and forming surfaces. Fig 3 shows the nominal position of the touch points on the forming and reference surfaces.



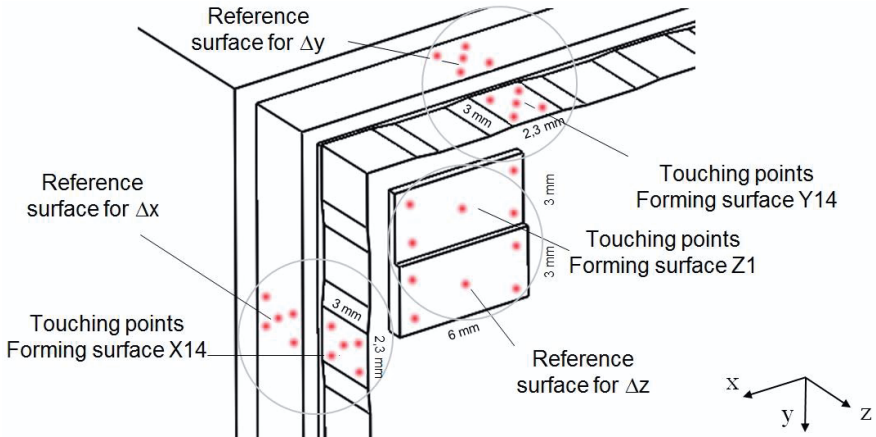


Fig 3: Position of the 5 touch points on the forming and reference surface of the test piece

4 touch points are located in the corners, one point in the center of the surfaces. Each of these surfaces and the associated area of the reference surface are touched with 5 points, called 5-point-measurement. With the 5 measuring points, the measuring software calculates correction planes according to the method of the least square error. The associated center of gravity is formed for each correction plane. The geometry error of the 75 forming surfaces ( $25 \times \Delta x$ ,  $25 \times \Delta y$ ,  $25 \times \Delta z$ ) follows as the difference between the center of gravity of the forming surface and the reference surface reduced by distance  $s_{\text{nominal}}$  (3) :

$$\Delta = (S_{\text{forming surface}} - S_{\text{reference surface}}) - s_{\text{nominal}} \quad (3)$$

Compared to the 5-point-measurement, a clear time saving can be achieved with the 1-point measurement. In the 1-point measurement, only the center point on the surfaces is evaluated. The decision whether a 1-point-measurement is sufficient can decide in the 5-point-measurement by detecting the shape deviation of the surfaces. In order to assess the surface quality of the milled surfaces, the difference between the minimum and maximum value of the correction plane is evaluated. In addition, the difference of results between the 5-point and 1-point-measurement are compared. For larger shape deviation and the differences, an adaptation of the process parameters during milling is necessary. The procedure for the measurement is documented in a test instruction. So the measurement can be carried out independently of the location and provides comparable results. The surfaces must be checked for impurities in advance. If necessary a cleaning in ultrasonic bath is recommended. It is also necessary to visually check

whether the surfaces have good surface quality. The edges of the surfaces must be free of burrs to avoid contact with the probe ball

3.4 Environment

The measurements are carried out in an air-conditioned room. The room temperature is usually 20 degrees Celsius and is kept constant to +/- 0.2 K. The boundary conditions for temperature, humidity, and vibrations are based on [16]. The test piece must be in the measuring room for several hours. The milling machine is in a hall with temperatures between 19 and 21 degrees Celcius.

4 Methodology of experiments

Fig. 4 shows the axis arrangement of the milling machine.

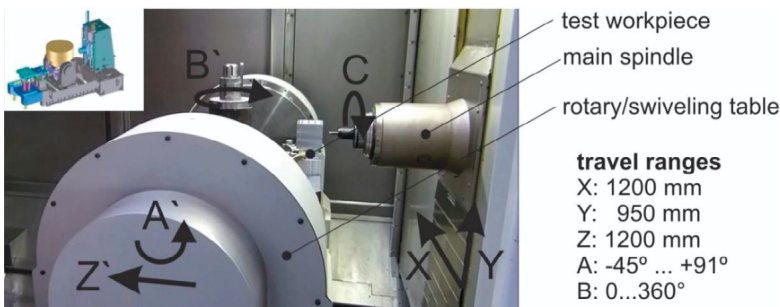


Fig. 4: Axis arrangement of the milling machine [17]

The thermal load of the milling machine is achieved by accelerating the main spindle and the translational feed axes X, Y and Z based on the motion sequence in Fig. 5.

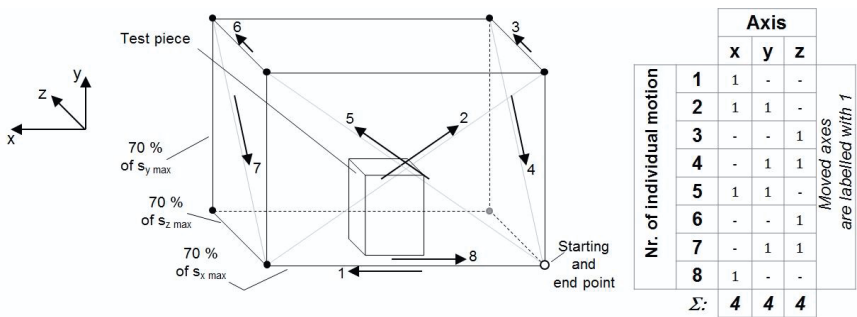


Fig. 5: Motion sequence of translational feed axes [17]

The load of the feed axes occurs at two power levels. The power level 1 is based on the average power of a representative milling process for the selected milling machine. The power level 2 corresponds to the rapid traverse movement of the axes with maximum axis acceleration. The sequence of movements follows the pattern 2x power level 1, 1x power level 2 and again 1x power level 1. This movement cycle lasts 148 seconds (Fig. 6). The rotational speed of the spindle has also different levels and takes each one 60 seconds. The level is based on the recommendations in [18]. The spindle is accelerated around each of these levels.

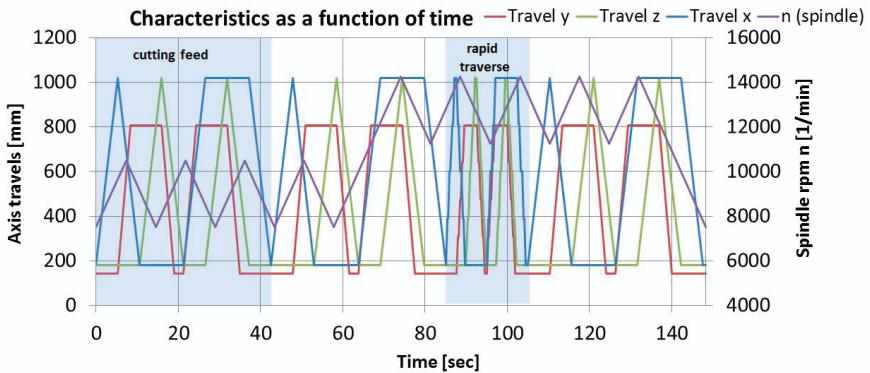


Fig. 6: Movement cycle for warm up the machine tool [17]

The movement cycle is repeated as often as desired to specifically heat the milling machine between the machining of the forming surfaces on the test piece. The time periods in the investigations are six times 10 min, 20 min, 30 min and 40 min. This results in a total examination time of 600 min. In this time the 25 forming surfaces in X-, Y- and Z-direction on the test piece are milled.

## 5 Measurement results

Fig. 7 to Fig. 9 show the displacement curves of the X-, Y- and Z-axes of the milling machine measured at the three locations in Dresden, Chemnitz and Köln. These are the results of investigations by the same thermal load over 10 hours, carried out on the milling machines on 12.11.2015 and 13.11.2015. The displacement curves are specified in machine coordinates. The measured values result from the 5-point-measurement on the test piece. As reference point, the first measuring point is selected. The displacement value at the first measuring point is subtracted from all other measured values. A state of thermal persistence is not noticeable in the displacement processes after 10 hours because the deformation behavior of the axes X, Y, Z and the main spindle with different time constants is

superimposed on the thermally induced displacement. Although the same load profile is used on both days, the absolute displacement in the X direction on 13.11.2015 is about 3  $\mu\text{m}$  less than on 12.11.2015 (Fig. 7). In the Y direction (Fig. 8) is the displacement on 12.11.2015 ca. 2  $\mu\text{m}$  less than on 13.11.2015. In the Z-direction these differences are not recognizable. This can be explained by the thermal behavior of the main spindle in the Z direction (Fig. 9), which has a significantly stronger effect than thermal influences from other components in the Z direction. It turns out both days, the same trend of displacement curve in all three directions. But at the beginning, especially at the first measuring point, there are major differences. The machine is switched on directly at the beginning of the investigation. There is no lead time before starting the investigation. At the beginning of the measurement, the machine was without processing for 20 hours. The hall temperature fluctuates on both days only less than 1 Kelvin. Even under these conditions it can't be guaranteed that exactly the same starting conditions can be assumed and thus comparable shifts are to be expected. One way to approximate the starting conditions of the machine would be a lead time of 1 hour. Also, the clamping of the milling tool directly after switching on the machine and the subsequent milling of the first shape element can lead to a distinction at the beginning. The requirements on the operating condition of the machine at the beginning of milling will be stronger analyzed in further work. This article focuses on the results of surveying on the CMM.

The differences between the measurement results at the three locations are very low for both investigations although the measurements were not carried out under exactly the same conditions. The test pieces were clamped differently. In Dresden and Köln the test piece stood parallel to the X-Z-plane, in Chemnitz the test piece has located parallel to the X-Y-plane during the measurement. In Chemnitz and Köln were used different positions of the touch points on the surfaces in Z-direction. These were 1 mm next to the touch points using in Dresden. The reasons were micro impressions on the surfaces in Z-directions that have formed in Dresden due to excessive probing force. Because this is a differential measurement between two surfaces, this influence is negligible. The measurements at old and new measuring points in Chemnitz led to the same results. And also the subjective influences of the operator at the settings in the measuring software are not the same. The analysis confirms that despite the differences at the measurement sites comparable results are ensured by the chosen measurement process. Of course, measurement conditions will be prescribed for future measurements. The magnitude of the thermally induced error in the X-direction (Fig. 7) is in the range of the positioning accuracy of the milling machine. Random errors can therefore influence the result more strongly. In X-direction (Fig. 7) a

thermal persistence condition is not recognizable even after 10 hours. After the increase in the displacement during the first 3 h, a decrease of the displacement follows and it is almost returned to the initial state after 10 h. This is the result of two opposing thermal time constants in the machine.

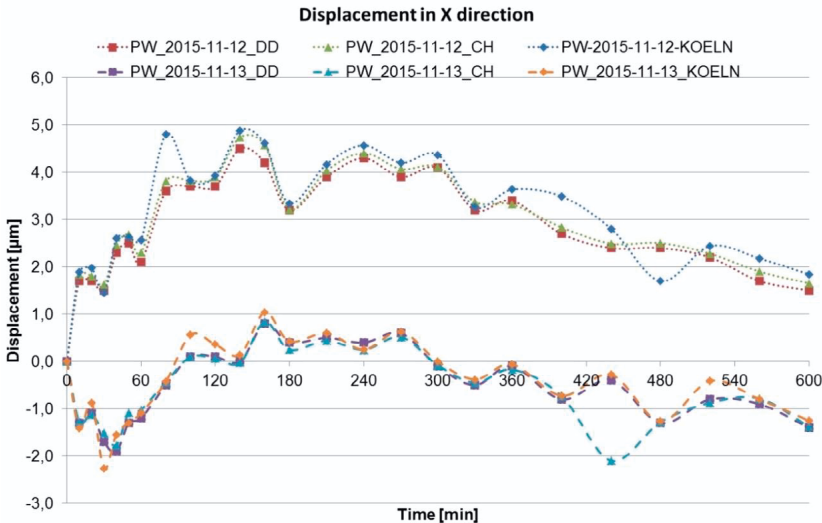


Fig. 7: Thermal displacement in the X-direction

In the Y-direction (Fig. 8) a thermal persistence is reached after approx. 5 h but there are different influences in the persistence condition visible. Here dominates one thermal time constant. After 6 h the results from 13.11.2015 shows a ripple of  $\pm 1 \mu\text{m}$  in the state of persistence. This shows the influence of the machine cooling system in the axes. This influence is less recognizable on 12.11.15. However the displacement on 12.11.2015 decreases again by approx.  $1.5 \mu\text{m}$  after 7 h. The hall temperature decreases by 0.5 K on 12.11.2015. This behavior is very low in the investigation on 13.11.2015. On this day the hall temperature increases by 0.5 K. The reason for this decrease on 12.11.2015 is yet unknown. The measurement on 12.11.2015 started 4 pm, on 13.11.2015 it started 1 pm. Both measurements end at night. In the Z direction (Fig. 9), there are hardly any differences between the two investigations. The course is the result of at least two independent thermal shifts. Within the first hour, a thermally induced extension of the main spindle follows by a maximum of  $22 \mu\text{m}$ . Then a very slow decrease of the shift takes place within 8 hours.

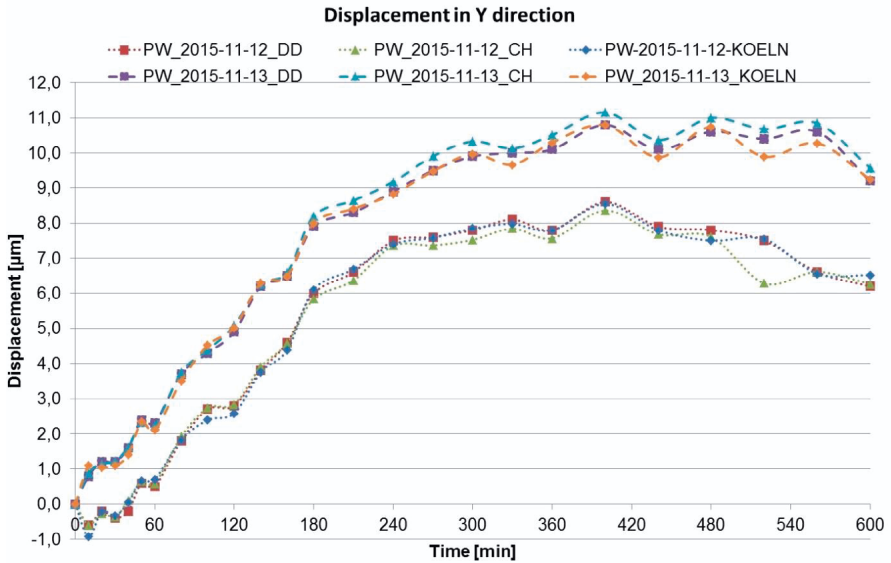


Fig. 8: Thermal displacement in the Y-direction

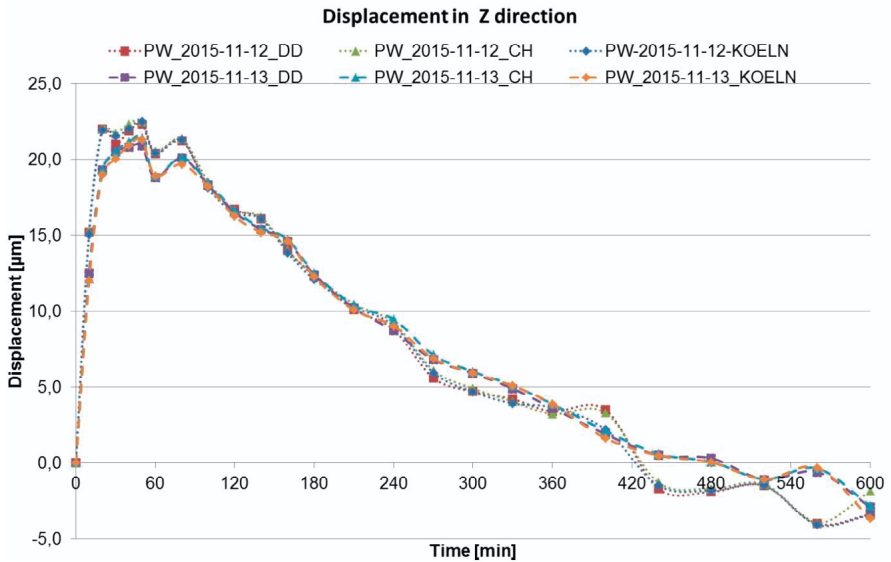


Fig. 9: Thermal displacement in the Z-direction

## 6 Outcomes and outlook

In the present paper, the results of the two investigations on a test piece were presented. The test pieces were measured at three locations. It has been shown that the influences on the measuring process have only a minor influence on the measuring result and thus a measurement can be carried out independently of the location. Furthermore, it was shown how the measurement sequence can be made more time-efficient due to the number of touch points on the test piece. The first results for the examined milling machine suggest that accuracy and reproducibility can be ensured despite measurement at different locations.

### Acknowledgement

*The activities executed in the project were financed by the German research Association DFG within the scope of the Collaborative Research Centre CRC "Transregio 96" on "Thermo-energetic design of machine tools". The authors are grateful to the DFG for funding. The authors also thank the Fraunhofer Institute for Machine Tools and Forming Technology IWU in Chemnitz and the Institute for Manufacturing Engineering of the TU Dresden for their support in the execution of explorations and experiments.*

## 7 References

- [1] L. Neidhardt, H. Höfer, H. Wiemer. Prüfwerkstück zum Nachweis von thermisch bedingten Verlagerungen an Fräsmaschinen – Konzept und erste Erfahrungen. ZWF 109 (2014) 11, p. 814-818
- [2] H. Höfer, H. Wiemer. Generation of motion sequences for thermal load of machine tools. In: Production Engineering, vol. 11, pp 75-83, 2017, Springer, Berlin
- [3] ISO/IEC Guide 98-3: Uncertainty of measurement - Part 3: Guide to the expression of uncertainty in measurement, International Organization for Standardization, Genf, 2008
- [4] F. Wäldele, H. Schwenke. Automated Calculation of Measurement Uncertainties on CMMs – Towards Industrial Applications. In: tm - Technisches Messen, Oldenbourg Industrieverlag, 69 (2002), pp. 550-557
- [5] ISO/TS 15530-4: Geometrical Product Specifications (GPS) - Coordinate measuring machines (CMM): Technique for determining the uncertainty of measurement - Part 4: Evaluating task-specific measurement uncertainty using simulation, 2008
- [6] DIN 1319-4: Grundbegriffe der Messtechnik – Teil 4: Grundlagen der Messtechnik, Auswertung von Messungen, Messunsicherheit, 1999
- [7] VDI 2617-8: Genauigkeit von Koordinatenmessgeräten-Kenngrößen und deren Prüfung – Teil 8: Prüfprozesseignung von Messungen mit Koordinatenmessgeräten, 2017
- [8] ISO 14253-1: Geometrical product specifications (GPS) - Inspection by measurement of workpieces and measuring equipment - Part 1: Decision rules for proving conformity or nonconformity with specifications, 2013

- [9] A. Weckenmann, M. Knauer, H. Kunzmann. The Influence of Measurement Strategy on the Uncertainty of CMM-Measurements. In: Annals of the CIRP – Manufacturing Technology, Volume 47, Issue 1, 1998, pp. 451-454
- [10] H. Li, X. Chen, H. Wang et al.. Comparison of the influences of CMM measurement strategies on uncertainty evaluation. In Proceedings: SPIE 9903, Seventh International Symposium on Precision Mechanical Measurements, 2016
- [11] ISO 10360-2: Geometrical product specifications (GPS) - Acceptance and reverification tests for coordinate measuring machines (CMM) - Part 2: CMMs used for measuring linear dimensions, 2010
- [12] R. G. Wilhelm, R. Hocken, S. Schwenke. Task Specific Uncertainty in Coordinate Measurement. In: CIRP Annals – Manufacturing Technology, Volume 50, Issue 2, 2001, pp. 553-563
- [13] M. Hernla et.al.. Aufgabenspezifische Messunsicherheit von Koordinatenmessungen. In: Technisches Messen, Volume 77 (2010) 11, pp. 607-615
- [14] T. Kistner, A. Gabbia, D. Imkamp. Messunsicherheit durch Simulation: Stand der Technik und neue Entwicklungen für die Koordinatenmesstechnik in der industriellen Produktion. In Proceedings: 18. GMA/ITG-Fachtagung Sensoren und Messsysteme, 2016
- [15] L&W GmbH. Bestimmung des durch Werkstückrauheit verursachten zusätzlichen Unsicherheitsbeitrages. In: Qualitäts-Management-Handbuch, Ausgabe 01, 20.11.2015, chapter 13.16.
- [16] VDI/VDE 2627: Measuring rooms, Classification and characteristics, Planning and execution, 2015
- [17] H. Höfer, H. Wiemer. Generation of motion sequences for thermal load of machine tools. In: Production Engineering, vol 11, pp 75-83, 2017, Springer, Berlin
- [18] ISO 230-3: Test code for machine tools – Part 3: Determination of thermal effects. Geneva, Switzerland, 2007





# Model reduction for thermally induced deformation compensation of metrology frames

*J. van den Boom*

ASML Netherlands B.V., P.O. Box 324, 5500 AH Veldhoven, The Netherlands

**Abstract.** When wafers are exposed the change of heat load will introduce thermo-mechanical drifts of the metrology frames in lithography systems. These deformations lead to a decrease in positioning accuracy of the system affecting key performance indicators such as focus and overlay. To deal with these drifts compensation techniques are considered. Interpretation and implementation of low-order controllers is more straightforward, therefore, they are favored over complex high-order controllers. Real-time implementation of these low-order strategies ask for an approach where the high-order model for the thermo-mechanical behavior is reduced before controller synthesis is performed. Several model reduction techniques are investigated to arrive at the best reduced-order system model. This model is evaluated on prediction performance and usability.

*Keywords:* Model order reduction; Control

---

## 1 Introduction

Nowadays, machine tools are confronted with increasing attention to errors induced by thermal effects due to e.g. increasing powers and decreasing error margins. This is also valid for the measurement systems in lithography machines, where the allowed displacement by thermally induced deformations is in the sub-nanometer order. During operation these thermal errors has to be compensated. Active compensation of control techniques are needed which firmly rely on state-of-the-art model-based control designs, requiring an accurate description of the system (plant). Controller design methods such as Linear Quadratic Gaussian (LQG) or  $\mathcal{H}_\infty$  produce controllers of order at least equal to that of the plant, and usually higher because of the implementation of weights [1]. The implementation of these high-order controllers requires often more real-time control computational effort and hardware than simpler alternatives. Often reduction techniques are applied to sufficiently accurate reduce either the order of the model at the start of the controller design or the order of the controller after the design. Reduced order models (ROM) are also applicable for

advanced observer design for point-of-interest (POI) estimation and actuator/sensor placement where the optimal location need to be calculated.

In this paper, the focus is on model order reduction for a system, a metrology frame, with a moving heat load, with the goal to derive a ROM accurate enough for controller design. The modelling error is considered in terms of temperature difference over time between a Finite Element (FE) model and the ROM. The induced deformation and positioning error are not considered in this paper. This will be a next step in thermally induced deformation compensation. The system, a metrology frame, where model reduction techniques will be applied to, is introduced in Section 2. In Section 3 model order reduction techniques are discussed. The paper is finalized with the results and an outlook in Section 4.

## **2 Metrology frame**

Since 2000, ASML is producing the TWINSCAN lithography platform. This machine, see Figure 1 for an example, is applied in chip manufacturing to expose wafers. A wafer is a silicon disk which can contain hundreds of chips. The TWINSCAN design with two wafer stages allows for non-stop parallel processing: exposing/imaging one wafer while measuring another.

The position of the wafer in relation to the wafer stage and the wafer height map is determined exceedingly accurately at the measurement side of the machine. After the measurement the stage with the wafer moves from the measurement towards the projection side where the wafer is exposed. The heart of this machine is the metrology frame. It connects the sensors that determine the position of the stages with respect to the projection lens (and other sensors) to the lens [2]. Therefore a thermally induced deformation of the metrology frame between the lens and sensors or between sensors results in a measurement error, affecting performance. This leads to specifications for thermal drift during measure or exposure in sub-nanometer order.

During operation mostly changes in the heat load towards this frame lead to thermo-mechanical drifts. Changing loads are caused by transmission losses in the projection lens or the fast movement of the wafer stages for example. Active temperature control is a manner to mitigate these moving heat loads on the metrology frame.



Fig. 1. NXT1970Ci TWINSKAN Lithography platform

Often the starting point for controller design is a high order transient FE simulation. This is also the case here. The metrology frame is modeled as a C-shaped Aluminum frame with some features, like holes. The dimension of the system is approximately  $1 \times 10^5$ . It is a Multi-Input Multi-Output (MIMO) model with four different convective heat transfer coefficients and a moving heat source with a prior known trajectory. The temperature of all the nodes are outputs of this system. The next step is to reduce the model order of this system with a moving heat load.

### 3 Model order reduction

There are various manners to describe a system with a moving load, and, accordingly different approaches to reduce them.

One approach is to model the system with moving loads as a set of Linear Time-Invariant (LTI) subsystems; one system per load position. For this linear switched systems well-known reduction methods, like balanced truncation, can be applied.

Another possibility is to represent moving loads as Linear Time-Varying (LTV) systems, in which only the input and/or output matrices are time-dependent.

Model reduction can be done based on balanced truncation [4]. The drawback of this method is the high computational effort for systems of orders  $\gg 10^3$ . In [5] a reduction method is described for systems with only time-varying input and output matrices. This two-step approach consists of a low-rank approximation of the time-dependent input matrix via linear least squares minimization followed by standard model reduction techniques to result in a LTI system with a modified input.

A third alternative is to consider the position of the load as a time-dependent parameter of the system model. This results in a linear parameter varying (LPV) system, in which only the input and/or output matrix depend on a time-varying parameter. In [6] an overview of parametric model order reduction methods approaches (pMOR) is given.

In our case a high-dimensional LTV system, represented in descriptor state space notation, is considered.

$$\begin{aligned} E\dot{x}(t) &= Ax(t) + B(t)u(t), \\ y(t) &= Cx(t), \end{aligned} \tag{Eq. 1}$$

where  $E, A \in \mathbb{R}^{n \times n}$  and  $C \in \mathbb{R}^{q \times n}$  are time-independent system ces,  $B(t) \in \mathbb{R}^{n \times m}$  is a time-dependent input matrix, describing the position of the moving heat load at time  $t$ .  $x(t) \in \mathbb{R}^n$  is the state vector, and  $u(t) \in \mathbb{R}^m$ ,  $y(t) \in \mathbb{R}^q$  represent the inputs and the outputs of the system respectively.

The two-step approach, presented in [5], is applied to derive a reduced-order description for the metrology frame. For this reduction method has been, because it straightforwardness and the fact that this approach is limited to systems where the trajectory of the moving load is known a priori, which is the case in our problem.

First the time-variability of the input matrix is shifted to the input variables through a low rank optimization of  $B(t)$  by  $B(t) \approx \mathcal{B}\tilde{B}(t)$  and introduction of a new input  $\tilde{u}(t) = \tilde{B}(t)u(t)$  Equation 1 is transformed to:

$$\begin{aligned} E\dot{x}(t) &= Ax(t) + \mathcal{B}\tilde{B}(t)u(t), \\ y(t) &= Cx(t), \end{aligned} \tag{Eq. 2}$$

where  $\mathcal{B} \in \mathbb{R}^{n \times \tilde{m}}$  with  $\tilde{m} \ll n$  is a constant matrix and  $\tilde{B}(t) \in \mathbb{R}^{\tilde{m} \times m}$ .

After this the resulting MIMO LTI system is reduced by MIMO-IRKA [3], since this procedure is very fast and applicable to high-order models. The reduced order model is then given by Equation 3.

$$\mathbf{W}^T \mathbf{E} \mathbf{V} \dot{x}_r(t) = \mathbf{W}^T \mathbf{A} \mathbf{V} x_r(t) + \mathbf{W}^T \mathbf{B} \tilde{\mathbf{B}}(t) u(t), \quad (\text{Eq. 3})$$

$$y_r(t) = \mathbf{C} \mathbf{V} x_r(t),$$

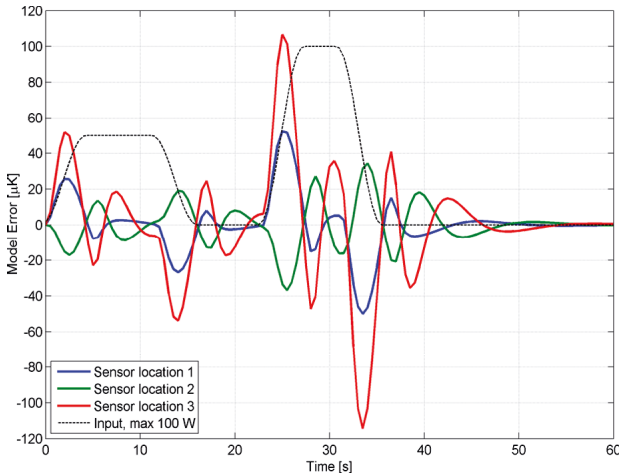
with the projection  $\mathbf{W}$  matrices and  $\mathbf{V}$ .

## 4 Results and Outlook

In Figure 2 the relative error between original (FE) and reduced model for three different nodes (possible sensor locations) on the metrology frame is shown.

Fig. 2. results for the metrology frame with moving heat source at expansion point  $s=0$

This is the result of MOR where the system is reduced to 100 nodes using the two step approach. From the small error can be concluded that the ROM is good in predicting the behavior of the full order model. The order of the re-



duced system still seems high for to perform controller synthesis with.

An application of model order reduction for a LTV system has been shown in this paper. In this case the approach of using time-independent projection matrices has been sufficient for a low error between FE model and ROM, but not to reduce model order sufficiently. More research is needed when complex techniques with time-dependent projection matrices are used. Within the frame work of the advanced thermal control consortium (ATC) ASML is contributing to the research on parametric model order reduction methods.

## 5 References

- [1] Skogestad, S., Postlethwaite, I., 2007. Multivariable feedback control analysis and design. John Wiley & Sons LTD. 2<sup>nd</sup> edition
- [2] Box, S., 2008. Design and temperature control for nanometre precision. Mikroniek nr. 3, 13-16.
- [3] Antoulas, A.C., 2005. Approximation of large-scale dynamical systems. Society for Industrial and Applied Mathematics.
- [4] Sandberg, H., Rantzer, A., 2004. Balanced truncation of linear time-varying systems. IEEE Transactions on automatic control. 49(2), 217-229.
- [5] Stykel, T., Vasilyev, A., 2016. A two-step model reduction approach for mechanical systems with moving loads. Journal of computational and applied mathematics. 297, 85-97.
- [6] Benner, P., Gugercin, S., Willcox, K., 2015. A survey of projection-based model reduction methods for parametric dynamical systems. SIAM review. 57(4), 483-531.

# Local Heat Transfer Measurement

*A. Kuntze, S. Odenbach, W. Uffrecht*

Institute of Fluid Mechanics ISM, Technische Universität Dresden, 01062 Dresden, Germany

**Abstract.** This contribution presents a thermoelectric sensor with a measurement area of approximately  $1.2 \text{ mm}^2$  to determine heat transfer coefficients (HTC) for stationary as well as moving metallic machine components surrounded by fluid flow. The sensor is based on the temperature rise or over temperature method, which is applied locally.

This setup enables sensor designs capable of measuring at high centrifugal acceleration - tested at up to  $25500g$  - with high resolution versus temperature and HTC. Results of an experimental investigation at a rotating free disc with a diameter of  $400 \text{ mm}$  running at up to  $11000 \text{ rpm}$  are presented. The experimental work demonstrates the compatibility of the sensor setup with the telemetry systems also developed and designed at TU Dresden.

The measurements are compared to known, published Nusselt-Reynolds correlations. Conditioned by the local measurement method with small heating element area, the determined HTC are higher compared to HTC measurements based on uniform temperature distribution. The reason for the shifted result is the different history of the thermal boundary layer when comparing local measurements to global ones.

The usage of the local measurement method features high resolution, low measurement uncertainty in terms of local heat transfer, telemetry compatibility and very low backlash onto the thermal conditions compared to entirely heated parts, but many researchers or machine designers use conventional HTC or Nu-Re-correlations, which are based on measurements for uniformly heated surfaces. Thus, research on the translation/calibration of the shift caused by different measurement approaches (local vs. global) is required. Therefore, experiments on incompressible flat plate flow and rectangular channel flow investigate the transferability of the local measurement results towards wall shear stresses and heat transfer coefficients valid for surfaces with uniform temperature distribution.

Peer-review under responsibility of the International Scientific Committee in the person of the Conference Chair Prof. Steffen Ihlenfeldt.

**Keywords:** Heat transfer; Wall shear stress; Telemetric measurements



# 1 Introduction

Heat transfer coefficients (HTC) is needed for the development of efficient rotating machines, but the determination of reliable HTC at fast rotating components is a great challenge. This results from the difficulty of measuring accurate temperatures and HTC for metallic components with high conductivity using telemetric instrumentation.

HTC is the proportionality factor between heat flux and the temperature difference. The HTC is usually determined from the heat flux and a temperature difference between wall temperature and predefined reference temperature. Several techniques are commonly used. The contribution by Uffrecht et al. [1] provides a good overview of the different methods for heat flux and heat transfer measurements, respectively.

Each method has its own benefits and drawbacks. Common problems with these measuring methods are (1) heat flux sensors act as a thermal barrier to the object and/or (2) induce significant heat into the component to be examined. Therefore, a significant backlash on the thermal and fluid dynamical situation is caused. Additionally, an appropriate reference temperature is difficult to choose and/or measure. All these difficulties become even worse under the circumstances of fast rotating components at high centrifugal forces.

The work reported here presents a telemetry-compatible sensor to determine the HTC in fast rotating environmental conditions by use of the over-temperature method. It also fulfills the requirement for a simple, robust and cost-effective technology. The next section briefly describes the measurement method to determine the local HTC. The performance of the setup is shown through experiments using a rotating free disk, which runs at up to 11000 rpm.

Conditioned by the small heating area of the sensor, the local HTC are higher and do not compare to HTC based on uniform temperature situations. Furthermore, the local HTC can also be calibrated as wall shear stress. In this respect, the results can be used twice. For this purpose, additional flow experiments have been performed in a rectangular channel and at a flat plate. Sensor calibrations were carried out, based on channel flow and measured wall shear stresses with Reynolds-analogy yielding global HTC. Subsequently, the evaluation of the sensor is done at a turbulent flat plate flow. The objective of the contribution is to exhibit that the local HTC can be evaluated for wall shear stresses and as HTC in uniform temperature situations, with some limitations.

### Nomenclature

A	Calibration coefficient [-]
$A_t$	Cross-section of heating element [ $m^2$ ]
a	Thermal diffusivity [ $m^2/s$ ]
$a_2$	Calibration coefficient [-]
B	Calibration coefficient [-]
$C_f$	Dimensionless friction value [-]
h	Channel height [m]
k	Thermal conductivity [W/mK]
l	Sensor length [m]
$Nu_x$	Local Nusselt Number [-]
Pr	Prandtl Number [-]
$P_{th}$	Thermal Heating Power
$R_0$	Calibration Coefficient [ $\Omega$ ]
$R_{th}$	Electrical resistance of thermistor [ $\Omega$ ]
$R_\alpha$	Thermal resistance representing HTC [K/W]
$R_c$	Thermal resistance of insulation [K/W]
$Re_{dh}$	Hydraulic Re-Number $Re=(\rho u_d h/\mu)$
$Re_x$	Local Re-Number $Re=(\rho u x/\mu)$
T	Temperature [K]
$T_0$	Reference Temperature = 298.15K
$T_1$	Temperature of thermistor [K]
$T_W$	Wall or surface temperature [K]
u	Velocity [m/s]
x	Length [m]
$\alpha_{calib}$	Calibrated HTC [W/( $m^2K$ )]
$\alpha_{ch}$	HTC channel correlation [W/( $m^2K$ )]
$\alpha_s$	Measured HTC at the sensor [W/( $m^2K$ )]
$\alpha_{Pl}$	HTC flat plate correlation [W/( $m^2K$ )]
$\mu$	Dynamic viscosity [kg/(ms)]
$\nu$	Kinematic viscosity [ $m^2/s$ ]
$\tau_W$	Wall shear stress [Pa]

## 2 Experimental Work

### 2.1 Description of the sensor setup

The entire measuring method was already presented more detailed in Uffrecht et al. [1], [2] and briefly outlined in this section. The utilized HTC sensor consists of a small NTC thermistor with an electrical resistance  $R_{th}$  of approximately 10 k $\Omega$  at 25°C, which is flush-mounted into the surface of the component to be examined. The thermistor and its electrical collection are insulated thermally from the surface. Calibration of the resistance vs. temperature was conducted in a range between 15°C and 120°C by steps of 5 K using a WIKA temperature calibrator and a Keithley Model 2000 multimeter. The uncertainties of the temperature calibration and of the digital multimeter are, respectively,  $\pm 0.1K$  and  $\pm 1\Omega$  in the 100k $\Omega$  range. The fit function used is the following [3]:

$$T = \left\{ \frac{1}{T_0} + \frac{1}{B} \left[ \ln \frac{R_{th}}{R_0} + a_2 \left( \ln \frac{R_{th}}{R_0} \right)^2 \right] \right\}^{-1}. \quad (\text{Eq.1})$$

The fit coefficients  $B$  and  $a_2$  are obtained by curve fitting. The reference temperature  $T_0$  is 298.15K and  $R_0$  is the electrical resistance at  $T_0$ .

$R_{th}$  is part of a half bridge along with a constant resistor  $R_a$ , and the obtained signal is connected to an analog-digital converter (ADC). The sensors are operated at low heating power supplied by a changeable bridge voltage. Therefore, it is assumed that the thermal heating power has no effect on the fluid flow.

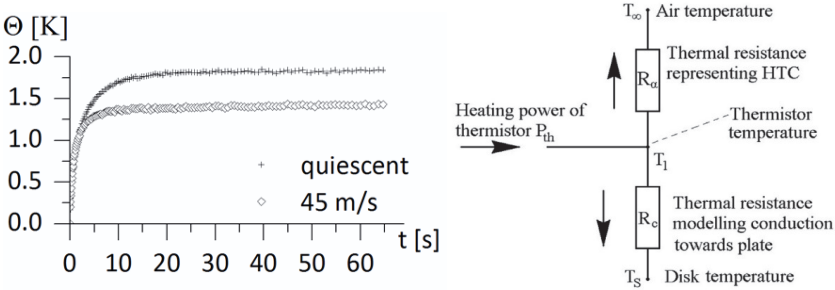


Fig. 1. (a) Thermal settlement curves of HTC in a quiescent environment and overflow at a velocity of 45 m/s (b) Thermal measurement circuit with heating power, thermal resistance  $R_\alpha$  representing HTC and conductive resistance  $R_c$  modeling the losses towards the disk.

The determination of thermal resistances into the fluid and substrate is made by a stationary thermal model with lumped parameters according to Fig. 1(b) and [2]:

$$P_{th} = \theta \left( \frac{1}{R_\alpha} - \frac{1}{R_c} \right) \quad (\text{Eq.2})$$

$P_{th}$  is the thermal heating power,  $R_c$  the thermal resistance into substrate and  $\theta$  is the over-temperature. Thermal resistance into the fluid  $R_\alpha$  is defined by [2]

$$R_\alpha = \frac{1}{A_t \alpha_s} \quad (\text{Eq.3})$$

where  $\alpha_s$  is the heat transfer coefficient at the cross-sectional area  $A_t$  of the heating element. The thermal resistance describes the heat conduction towards the substrate. It is determined under quiescent conditions with the assumption that  $R_\alpha \gg \infty$ . Fig. 1 (a) shows the measured over-temperature curves

under quiescent conditions and with overflow at 45m/s.  $R_c$  is assumed to be constant for all subsequently forced convection measurements.

The thermistor starting temperature  $T_0$  is detected after the electrical settlement. The supplied heating power and the resulting temperature ramp are recorded until thermal equilibrium is reached. The over-temperature  $T_1 - T_0$  is taken from the stationary temperature  $T_1$  and starting temperature  $T_0$ .

## 2.2 Results from rotating free disc

The measurements in this section were carried out in [1] and show the suitability of the sensor setup according to the (telemetric) applicability at operating conditions found within industrial machinery. Fig. 2 shows a Nu-Re-plot based on HTC-measurements for different revolving speeds at a rotating free disk. Sensors of the same sort as described in the previous section were embedded into the surface of a rotating disk measuring HTC using an identical measurement circuit and control as used for the continuation of the work presented here. The results were compared with correlations by Dorfman [4].

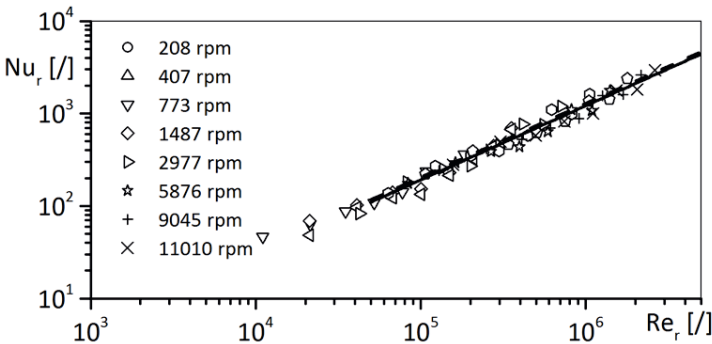


Fig. 2. Results at rotating free disk by Uffrecht [1], calibrated Nusselt-number  $Nu_r$  versus Reynolds number  $Re_r$ , black solid line corresponds to the turbulent correlation by Dorfman [4]

The test rig consisted of a free disk at a spindle, mounted onto a concrete base and driven by an electrical motor with frequency converter. The disk was instrumented with 8 HTC sensors, different pressure tabs for fast and slow response as well as 14 thermistors embedded directly into the disk surface for temperature measurement. All instrumentation in the rotor rig was operated by an in-house developed telemetry system. More information about the test rig, instrumentation, measurement setup and discussion are presented in Uffrecht et al. [1].

### 2.3 Rectangular channel flow and flat plate flow

Following are shown the current measurements according the transferability from local HTC  $\alpha_s$  to wall shear stress  $\tau_w$  as well as HTC for components with uniform temperature distribution. A comprehensive survey of wall shear measuring methods and its calibration are given by Naughton et al. [5], Fernholz et al. [6] and Scott [7]. Thermal electrical sensors that rely on wall shear stress exploit the dependence of heat transfer at a heating element within the viscous boundary layer. A relationship between the rate of the heat transfer from the element and the wall shear stress  $\tau_w$  was derived as follows, e.g. Goldstein [8]:

$$Nu_l = \frac{\alpha_s l}{k} = A \left( \frac{l^2}{\mu a} \tau_w \right)^n, \quad (\text{Eq.4})$$

where  $l$  is the stream-wise length of the sensor,  $\mu$  is the dynamic viscosity and  $a$  is the thermal diffusivity. The HTC  $\alpha_s$ , as described in the prior section, is expressed as non-dimensional  $Nu_l$ -number where  $k$  is the thermal conductivity of the fluid. This relation, established as “classical theory” for  $n=0.33$ , applies only for specifically geometric dimensions and neglects the heat conduction into the substrate.

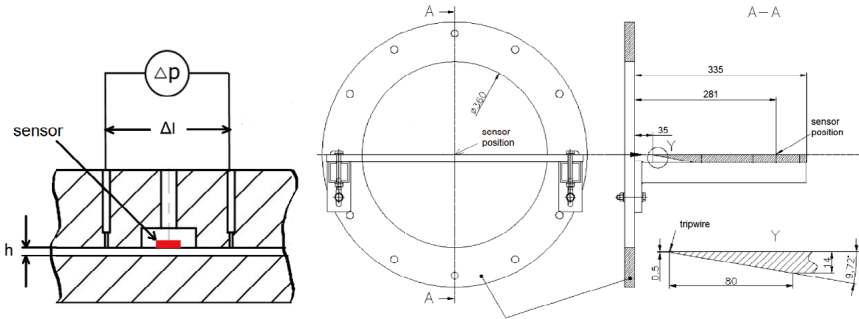


Fig. 3. (a) Scheme determining of the wall shear stress in a 2D channel flow according eq. (6); (b) Wind tunnel test setup with exit plane of the nozzle and flat plate with sensor position as sectional view

Calibration in a rectangular channel flow with an adjustable height is conducted to achieve the correlation between wall shear stress and local HTC according Fig. 3 (a). The channel is made of an aluminium alloy, and the air flow is supplied by an in-house compressed air system. The test section has a length of 713 mm and a width of 760 mm. The channel height  $h$  is adjusted by shims initially. Afterwards, once a fully developed laminar flow exists, the effectively channel

height is determined by measuring the volume flow  $Q$  and the stream-wise pressure drop  $dp$  along the channel by using a relationship for small gaps [9]

$$Q = \frac{h^3 w}{12\mu} \frac{dp}{dx}, \quad (\text{Eq.5})$$

where  $w$  is the channel width,  $\mu$  is the dynamic viscosity of the fluid,  $dp$  is the pressure drop and  $dx$  the pressure tap spacing. The wall shear stress is calculated subsequently by using [9]:

$$\tau_w = \frac{h}{2} \frac{dp}{dx}. \quad (\text{Eq.6})$$

Fig. 4 (a) shows the measured wall shear stresses as a dimensionless friction drag coefficient  $c_f = 2\tau_w/(\rho u^2)$  versus  $Re_{dh}$  for the channel flow. Mass flow is varied in the range of 0.012 and 0.1 kg/s, which corresponds to shear stresses of 0.47 Pa and 16 Pa respectively. The values are in good agreement with the laminar correlation until  $Re \approx 3500$  (dashed correlation line), considering measurement uncertainty. Above that value, the system transitions into the turbulent flow regime. The solid line corresponds to the turbulent correlation which is valid for channel flows  $Re_{dh} > 10^4$ . These values yield the reference values for the calibration.

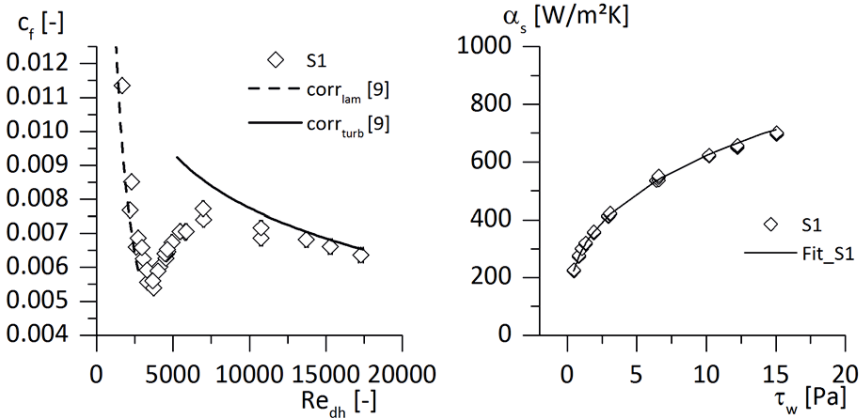


Fig. 4. (a) Dimensionless friction drag value versus  $Re_{dh}$  number for the rectangular channel flow; (b) Relation between local HTC at the heating element and wall shear stresses by measuring the pressure gradient according to (Eq.6)

The HTC sensor, called S1, is a thermistor with a cross-section of  $A_t=1.2\text{mm}^2$  which operates in a thermally insulated substrate consisting of pertinax and glue. Heating power is approximately 5.5mW and a bridge operating voltage of 6.5V DC for following results.

Fig. 4 (b) depicts the correlation between the local HTC and wall shear stress for the sensor. The determined coefficients are  $A=1.667$  and  $n=0.3216$  (Eq.4). The coefficient  $n$  fits almost to the “classical theory” by [8]. As long as the temperature boundary layer is still inside the viscous sublayer of the velocity, the assumptions of the “classical theory” are fulfilled for the validity of laminar and turbulent flow.

Measurements are conducted in a wind tunnel with a low turbulence free jet, see Fig. 3(b). The examination of the free jet quality and details of the test rig design may be found in Uffrecht et al. [1]. A plate is attached perpendicular to the exit plane of the nozzle to build a forced convection at the flat plate setup. A trip wire is fixed at the leading edge to ensure fully turbulent flow. The sensor is positioned at  $x=0.281\text{m}$  downstream of the leading edge of the plate. Jet velocity is varied between 15 and 45 m/s and measured using a Pitot-probe.

## 2.4 Results

Firstly, the results of the wall shear stresses are depicted versus local  $Re_x$  in Fig. 5 (a). The wall shear stress is obtained by measuring  $\alpha_s$  and using the calibration function according (Eq.4).

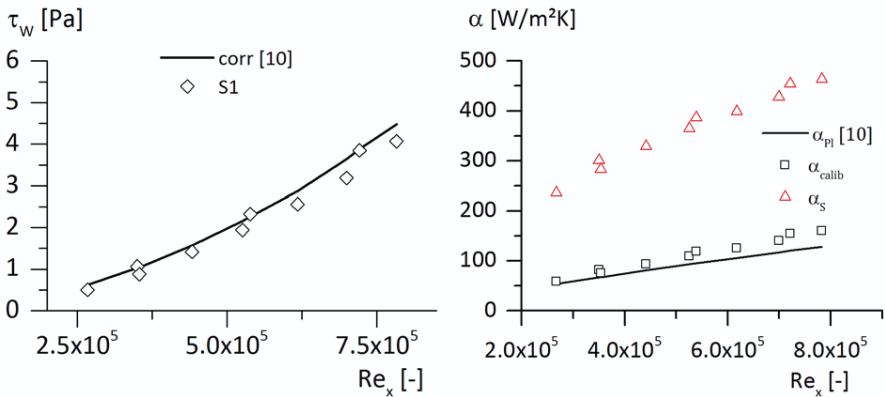


Fig. 5. (a) Wall shear stresses are determined by measuring HTC versus local  $Re_x$ -number compared to the turbulent flat plate correlation according (Eq.7); (b) Heat transfer coefficient versus local  $Re_x$ -number from measurement, correlation and calibration

The black solid line indicates the correlation for a turbulent flat plate Oertel jr. [10]:

$$c_f = \frac{2\tau_w}{\rho u^2} = 0.058 \left( \frac{u x}{\nu} \right)^{-0.2}, \quad (\text{Eq.7})$$

where  $\rho$  is the density of the fluid and  $Re_x=ux/\nu$  is the local Reynolds-number are composed of the free jet velocity  $u$ , the sensor position  $x$  and the kinematic viscosity  $\nu$ . At low  $Re_x$  the wall shear stresses are in good agreement with the correlation. With increasing  $Re_x$ , a shift of  $\tau_w$  arises, perhaps because the sensor is not mounted exactly flush with the wall.

Next the local HTC values are compared to the global HTC, i.e. the HTC for uniform temperature distribution  $\alpha_{ch}$ , which are calculated for the channel flow based on known wall shear stresses by using the Reynolds analogy [10]:

$$Nu_{dh} = \frac{c_f}{2} Re_{dh} Pr^{1/3}, \quad (\text{Eq.8})$$

where  $Nu_{dh} = \alpha_{ch} d_h / k$  and  $Re_{dh} = u d_h / \nu$  are based on the hydraulic diameter  $d_h = 2h$ . The thermal conductivity is  $k$  and  $Pr$  is the Prandtl-number. The channel velocities  $u$  are obtained from a mass flow meter in the air supply and the known channel cross-sectional area.

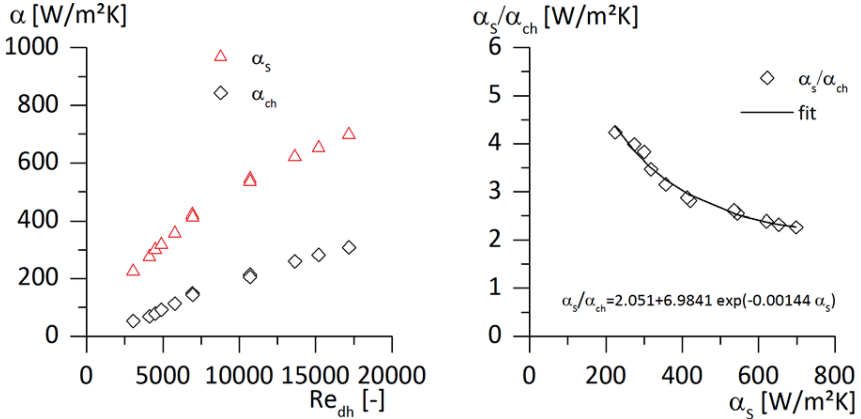


Fig. 6. (a) Measured HTC versus  $Re_{dh}$  compared with HTC from correlation according (Eq.8); (b) Ratio of measured HTC to correlation HTC (according (Eq.8)) versus measured HTC.



Fig. 6 (a) shows the measured HTC  $\alpha_s$  compared to the HTC at uniform temperature distribution  $\alpha_{ch}$  by using the Reynolds-analogy according to (Eq.8) versus  $Re_{dh}$ . The measured HTC  $\alpha_s$  are significantly higher compared to  $\alpha_{ch}$ .

Similar investigations were conducted by Mocikat and Herwig [11], [12]. They used film sensors with a heating area of 130 mm perpendicular to the flow and 3 mm in flow direction. These sensors were glued onto a cylinder with a 46mm diameter which was positioned in a wind tunnel. They also measured higher local HTC compared to HTC at a uniform temperature distribution and discuss the reasons. They state additionally a constant of 0.28, the so-called “tac-factor”, under three certain boundary conditions for translation from local to global HTC. The first condition requires forced convection, and the second demands a fully turbulent flow. The third condition requires reproducible temperature step changes.

Fig. 6 (b) depicts the ratio of  $\alpha_s$  and  $\alpha_{ch}$ , which corresponds to the reciprocal of the “tac-factor” by Mocikat and Herwig [11], [12]. In contrast to their work, the ratio is not a constant here and can be fitted by an exponential function. The second condition requiring a fully turbulent flow might not be fulfilled completely and may explain the discrepancy. The measurements presented here do not exceed the transitional range of the channel flow very much.

Assuming a saturation towards a constant for large Reynolds-numbers or fully turbulent condition, an exponential fit with saturation is applied (Fig. 6 (b)). Thus, an extension of the experiments towards higher Reynolds-numbers is planned for future work to check the saturation assumed.

Furthermore, the translation to global HTC for flat plate flow is discussed in Fig. 5 (b). The HTC correlation for fully turbulent plate flow is obtained by inserting (Eq.7) in (Eq.8), [10]:

$$Nu_x = \frac{\alpha_{Pl} x}{\lambda} = 0.029 Re_x^{0.8} Pr^{1/3} , \quad (Eq.9)$$

$Nu_x$  and  $Re_x$  are determined for the sensor position  $x=0.281m$ . Fig. 5 (b) shows the measured HTC  $\alpha_s$  as well as the calibrated HTC  $\alpha_{calib}$  versus  $Re_x$  compared to  $\alpha_{Pl}$  (Eq.9). The translation of  $\alpha_s$  delivers the calibrated HTC  $\alpha_{calib}$  by using the exponential calibration function in Fig. 6 (b) with  $\alpha_{calib}=\alpha_{ch}$ . The  $\alpha_{calib}$  values match the correlation with acceptable accuracy (15%) within the range of the measurements (Fig. 5 (b),  $\alpha_{calib}$ ,  $\alpha_{Pl}$ ).

### 3 Conclusion

This study investigates the relationship of HTC measurements using the over-temperature method applied locally to wall shear stresses and HTC at parts heated uniformly. Formerly, experiments at a rotating free disk show the compatibility to a telemetry system for operation with moving parts suffering high centrifugal forces. Therefore, a further investigation of the sensor and the measurement method is indicated and promises an extension of its application area.

Correlations of local HTC and wall shear stresses as well as local HTC and global HTC are presented. The correlations are based on experiments using rectangular channel flow. This setup enables wall shear stress determination based on pressure gradients.

Within the boundaries of the range investigated, the transferability of the local HTC measurements to wall shear stresses shows uncertainties below 10 %. The transferability of the local HTC measurements to Nu-Re-correlations for turbulent flat plate flow shows uncertainties below 15 %. This is a good result considering that the sensor were calibrated using a different flow case, rectangular channel flow. Furthermore, the rectangular channel flow had not yet reached fully turbulent Reynolds numbers. Thus, the possibility of determining the global HTC as well as the wall shear stresses by measuring the local HTC is shown. The sensor as well as the measurement method, including telemetry operation, have a great potential for future applications.

#### **Acknowledgements**

*The present study was conducted within the project COOREFLEX Turbo 3.2.1 of AG Turbo. It is funded by the Federal Ministry for Economic Affairs and Energy of the Federal Republic of Germany and MAN Diesel & Turbo SE. The responsibility for the content lies solely with its authors.*

### 4 References

- [1] Uffrecht, W., Heinschke, B., Caspary, V., Odenbach, S., 2015. Measurement of heat transfer coefficients at up to 25,500 g – A sensor test at a rotating free disk with complex telemetric instrumentation. International Journal of Thermal Sciences.
- [2] Uffrecht, W., Günther, A., Caspary, V., 2012. Electro-thermal measurement of heat transfer coefficients, in: Proc. Of ASME Turbo EXPO Copenhagen, GT2012-68144, 2012.

- [3] Bernhardt, F., 2004. Technische Temperaturmessung: physikalische und meßtechnische Grundlagen, Sensoren und Meßverfahren, Meßfehler und Kalibrierung, Springer Verlag Berlin, Heidelberg
- [4] Dorfman, L.A., Hydrodynamic Resistance and the Heat Loss of Rotating Solids, Oliver and Boyd, Edinburgh, 1963.
- [5] Naughton, J.W., Sheplak, M., Modern developments in shear-stress measurements, Progress in Aerospace Sciences 38, 521-527, 2002
- [6] Fernholz, H.H., Janke, G., Schober, M., Wagner, P.M., Warnack, D., New developments and applications of skin-friction measuring techniques, Meas.Sci.Techol., 7, 1396-1409, 1996
- [7] Scott, M.A., The need for a shear stress calibration standard, 24<sup>th</sup> AIAA Aerodynamic Measurement Technology and Ground Testing Conference; Portland, OR, USA, 2004-2302
- [8] Goldstein, R.J., 1996. Fluid Mechanics Measurement, 2<sup>nd</sup> edition, (Taylor & Francis, New York).
- [9] Fox, R.W., McDonald, A.T., Introduction to Fluid Mechanics, 8<sup>th</sup> edition, Wiley, 2011
- [10] Oertel jr., H., Prandtl-Essentials of Fluid Mechanics, Springer Verlag, 2010
- [11] Mocikat, H., Herwig, H., 2007. An advanced thin foil sensor concept for heat flux and heat transfer measurements in fully turbulent flows. Heat Mass Transfer 43, 351 – 364
- [12] Mocikat, H., Herwig, H., 2008. Heat transfer measurements in fully turbulent flows: basic investigations with an advanced thin foil triple sensor. Heat Mass Transfer 44, 1107-1116

# Thermal error compensation of 5-axis machine tools using a staggered modelling approach

*J. Mayr<sup>a</sup>, T. Tiberini<sup>b</sup>, P. Blaser<sup>b</sup>, K. Wegener<sup>b</sup>*

<sup>a</sup>inspire AG, Technoparkstrasse 1, 8005 Zurich, Switzerland

<sup>b</sup>Institute of Machine Tools and Manufacturing IWF, ETH Zürich, 8092 Zurich, Switzerland

**Abstract.** Thermal errors on machine tools are one of the main contributors to geometrical errors of machined workpieces. The sources of thermal machine tool errors can be divided into internal and external influences. This paper presents a staggered compensation approach that is modelling the thermal machine tool errors by the error sources, modelled stepwise on top of each other. It is shown that with the approach a reduction of up to 90 % of the arising thermal machine tool errors, measured on a 5-axis precision milling machine, can be achieved.

Peer-review under responsibility of the International Scientific Committee in the person of the Conference Chair Prof. Steffen Ihlenfeldt.

**Keywords:** Machine tools; Cutting fluid; Thermal error; Compensation; Environment

---

## 1 Introduction

Modern manufacturing processes are strongly connected to the abilities of machine tools. Basically three axis machine tools are therefore used for producing parts with low tolerances with geometrically defined cutting edges, like milling. Nevertheless, there is an increasing demand on high precision five-axis machined workpieces. Examples are found in the medical engineering, power engineering and aerospace industries.

In [1] it is shown that thermal influences on machine tools belong to the largest errors sources acting on machined workpieces. In accordance to Bryan [2] the error sources of geometrical workpieces errors of machined workpiece induced by thermal effects are:

- Heating or cooling influences by the room environment
- Heating or cooling influences by coolants
- Effects of people
- Heat generated by the machine
- Heat generated by the (cutting) process

- Thermal memory

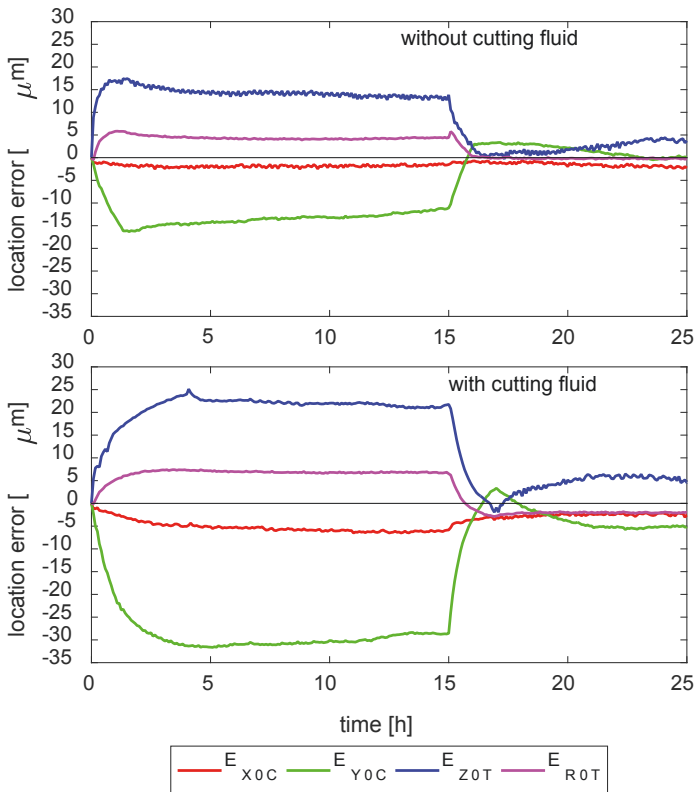


Fig. 1. Translational errors with and without cutting fluid influences measured during a C-axis operation of 15 h warm-up at 600 rpm and 10 h cool-down phase at standstill with R-Test setup [7].

International standards developed for evaluation of thermal errors on machine tools are ISO 230-3 [3], ISO 10791-10 [4], and ISO 13041-8 [5]. The evaluation procedures described in the standards are used for measuring of the thermal error under no load or finishing conditions. A missing link in the standards are influences of cutting fluids on the accuracy of machine tools. Mayr et al. [6] show an investigation of thermal errors induced by cutting fluid influences on a 5-axis machine tool. In [7] the arising linear thermal location errors, described in Table 1, with and without cutting fluid supply for a five axis machine tool during a 15 hours warm-up cycle and a 10 hours cool down cycle are shown, Fig.1. During the warm-up cycle the machines rotary table C is rotating with 600 rpm interrupted by measurements. During the measurements the cutting fluid supply is also stopped. During the cool-down the machine tool is in NC-hold, inter-

rupted only by the measurement cycles. During cool down no cutting fluid is supplied. As illustrated in Fig. 1 the influences of the cutting fluid on the thermal errors are significant.

In [9] the error sources acting on the temperature field of machine tools and its components are distinguished in internal and external error sources. This distinguishing is necessary as countermeasures are strongly different. In [10] a compensation approach using the environmental temperature as model input used for compensating 5-axis machine tools is presented. In [8] the approach is extended to compensate the thermal location error of the machine tool arising due to internal influences when running the machine tool’s rotary table.

Table 1. Thermal location errors of a vertical rotary axis C analysed in this paper [8].

Thermally induced location errors of a vertical C-axis		
Error	Unit	Description of the error
$E_{X0C}$	$\mu\text{m}$	Position error of C in X-axis direction
$E_{Y0C}$	$\mu\text{m}$	Position error of C in Y-axis direction
$E_{Z0T}$	$\mu\text{m}$	Position error of the table surface in Z-axis direction
$E_{A0C}$	$\mu\text{m/m}$	Orientation error of C in A-direction; squareness of C to Y
$E_{B0C}$	$\mu\text{m/m}$	Orientation error of C in B-direction; squareness of C to X
$E_{C0C}$	$\mu\text{m/m}$	Zero angle error of the C-axis
$E_{R0T}$	$\mu\text{m/m}$	Radius error of the table

In this paper a staggered modelling approach for compensating thermal location errors of 5-axis machine tools is presented. In section 2 the modelling approach is explained. In section 3 the implementation via a cyber-physical system integration in a real machine tool setup is described. In section 4 the compensation results are shown and discussed. The paper ends with a conclusion and outlook in section 5.

## 2 Staggered modelling approach

To model the thermal errors a system of differential equations according to [11] is used. The basic structure of the differential equation for computing a single thermal error  $y$  provoked by one single thermal load  $u$  is:

$$\frac{dy}{dt} = p_1 \cdot y(t) + p_2 \cdot [u(t) + p_3] \quad (\text{Eq. 1})$$

In Eq.(1)  $p_1, \dots, p_3$  are constant parameters where  $p_1$  defines the thermal inertias, the time lags for heating and cooling,  $p_2$  is the sensitivity of the input parameter  $u(t)$  with respect to the output  $\frac{dy}{dt}$  and  $p_3$  is a zero balancing parameter that adjusts the mathematical zero of the equation to the measurement scale's or physical system's zero. The constant parameters  $p_1, \dots, p_3$  are derived from measurements using least square fitting.

In a first step the machine tools environmental variation error (EVE) is validated. The measurements carried out with the machine tool in NC-hold in a non-air-conditioned environment are used to derive a first set of model parameters, Eq.(2). If necessary the machine tool axes are moved during the measurement performing a measurement cycle. The input of the model for compensating the EVE influence chosen is the hall temperature in °C. The model derived is capable to compensate the machine tool's thermal location errors induced by environmental influences.

$$\frac{d}{dt} y_{EVE}(t) = \underline{p}_1 \cdot \underline{y}_{EVE}(t) + \underline{p}_2 \cdot [u_{EVE}(t) + p_3] \quad (\text{Eq. 2})$$

After creating the model it is used for compensating the environmental influences acting on the machine tool. A second error source, the cutting fluid influences are induced and a second set of parameters,  $p_4, \dots, p_6$ , are derived from the measurements of the arising thermal location errors  $y_{CF}$

$$\frac{d}{dt} y_{CF}(t) = \underline{p}_4 \cdot \underline{y}_{CF}(t) + \underline{p}_5 \cdot [u_{CF}(t) + p_6] \quad (\text{Eq. 3})$$

using the same fitting procedure. The input used for modelling the cutting fluid influence,  $u_{CF}$ , the cutting fluid supply temperature is chosen. Deriving the second set of parameters the model is extended to consider both thermal error sources by superpositioning both models:

$$\frac{d}{dt} y_{mod}(t) = \frac{d}{dt} y_{EVE}(t) + \frac{d}{dt} y_{CF}(t) \quad (\text{Eq. 4})$$

The model of Eq.(4) is used for compensating the machine tool thermal errors induced by EVE and cutting fluid influences. A third thermal error source, the influences of moving the machine tool axis, is induced. According to [8] the axis cooling power is used as input  $u_{int}$  for modelling the thermal location errors

arising by internal influences. With the measurements a third set of parameters,  $p_7, \dots, p_9$ , are derived.

$$\frac{d}{dt} \underline{y}_{int}(t) = \underline{p}_7 \cdot \underline{y}_{int}(t) + \underline{p}_8 \cdot [u_{int}(t) + p_9] \quad (\text{Eq. 5})$$

The model of Eq.(4) is extended by superpositioning the cutting fluid influences of Eq.(5) to model the total thermal location error  $\underline{y}_{tot}$ :

$$\frac{d}{dt} \underline{y}_{tot}(t) = \frac{d}{dt} \underline{y}_{EVE}(t) + \frac{d}{dt} \underline{y}_{CF}(t) + \frac{d}{dt} \underline{y}_{int}(t) \quad (\text{Eq. 6})$$

$$\begin{aligned} \frac{d}{dt} \underline{y}_{tot}(t) = & \underline{p}_1 \cdot \underline{y}_{EVE}(t) + \underline{p}_2 \cdot [u_{EVE}(t) + p_3] + \underline{p}_4 \cdot \underline{y}_{CF}(t) + \underline{p}_5 \\ & \cdot [u_{CF}(t) + p_6] + \underline{p}_7 \cdot \underline{y}_{int}(t) + \underline{p}_8 \cdot [u_{int}(t) + p_9] \end{aligned} \quad (\text{Eq. 7})$$

The second and third step for modelling the cutting fluid influences and internal load influences could also be performed vice versa. In Fig. 2 the procedure is illustrated for a machine tool with rotary axis.

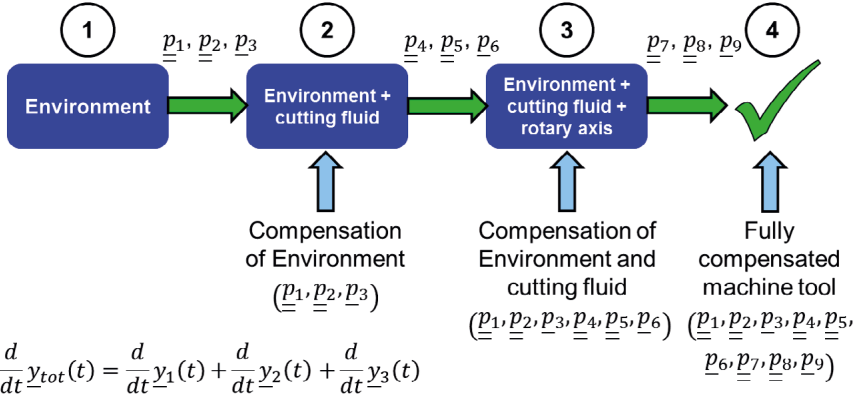


Fig. 2. Staggered modelling approach for deriving a compensation model capable for reducing the thermal errors induced by environmental, cutting fluid, and rotary axis influences.

The modelling approach is capable of deriving a model to compute the thermal machine tool location errors divided in influences and axis. Vice versa for each error source and each axis a new measurement becomes necessary.

An approach estimating the modelling uncertainty using the least square residual of the error fitting is given in [11]. For the machine tool under investigation,



Gebhardt [13] investigated the required measurement time for the machine tool under investigation giving a required measuring time of about 40 h.

### 3 Test setup

The machine tool under investigation is a vertical 5-axis milling machine. A schematic illustration of the kinematic structure of the milling machine, the used measurement setup R-Test and the cutting fluid supply is given in Fig. 3. The swiveling axis B and the rotary axis C of the machine tool are serial arranged on the workpiece side. The kinematic chain of the vertical machine tool can be described in accordance with ISO 10791-1:2015 [12] as:

$$V [w C2' B' b [Y1 Y2] X [Z1 Z2] (C1) t]$$

To evaluate the thermal location errors of the rotary axis C of the machine tool the R-Test discrete measurement setup is used. At four axis positions, 0°, 90°, 180° and 270°, the thermal machine tool errors in X-, Y- and Z- direction are measured and the thermal location errors are evaluated in accordance to [13]. The measurement uncertainty of the R-Test discrete setup is given in [8] with  $U(k = 2) = 1.7 \mu\text{m}$ .

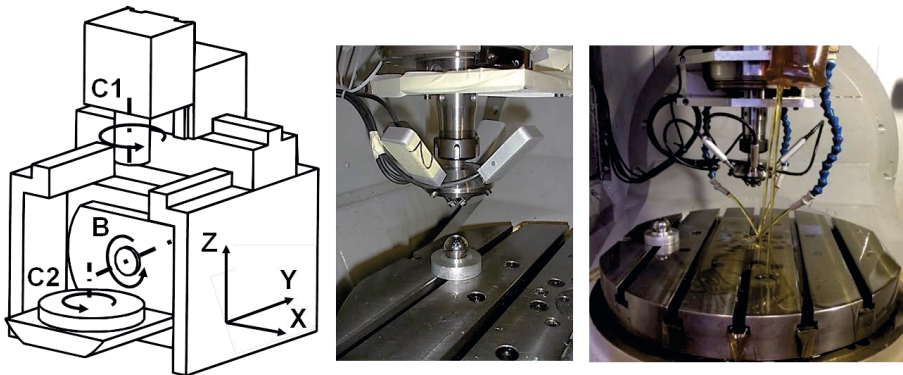


Fig. 3. a) Schematically representation of the kinematic milling machine under investigation [13]; b) R-Test measuring device used on the machine tool [8]; c) cutting fluid supply on the machine tool under investigation during the measurements

The compensation model derived for the machine tool is used to compensate the machine tool's thermal location errors online. For safety reason the computations are performed on an external PC connected to the internet. The PC communicates with the machine tool's control using FANUC FOCAS2 interface. During the measurements the compensation movements are performed by off-setting the machine tool's coordinate system.

#### 4 Compensation of cutting fluid influences

The compensation approach is used on the 5-axis machine tool illustrated in Fig. 3. Fig. 4 shows the thermal location errors induced by environmental influences, cutting fluid and internal load on a compensated machine tool compared to an uncompensated machine tool. The internal load is induced by a randomly generated pattern of the rotational speed of the rotary axes of the machine tool. The automatic random NC-code generator [8] used build an arbitrary speed profile avoiding overcompensation of the machine tool.

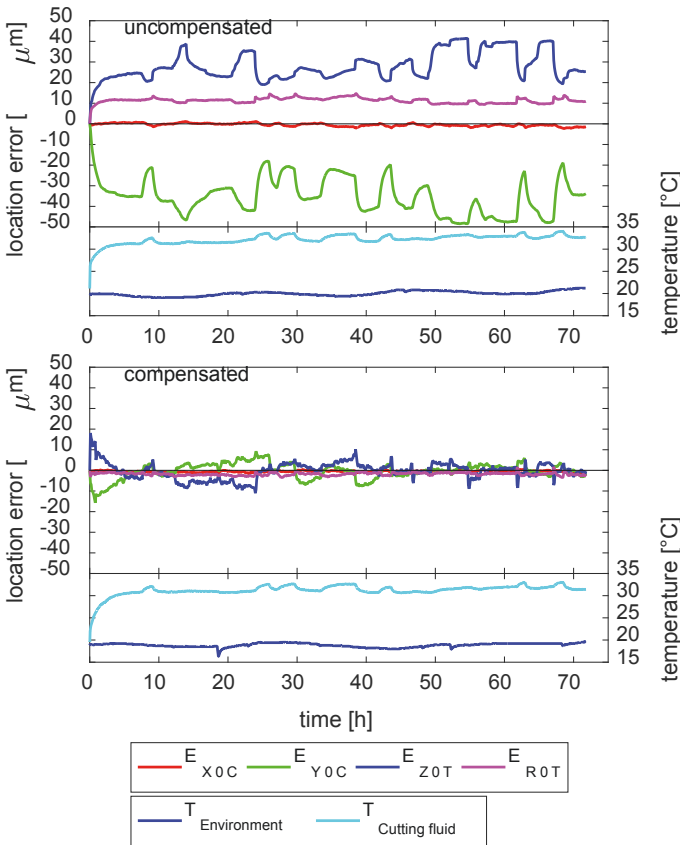


Fig. 4. Measured thermal location errors  $E_{X0C}$ ,  $E_{Y0C}$ ,  $E_{Z0T}$  and  $E_{R0T}$  induced by environmental influences, cutting fluid and internal load on uncompensated (upper diagram) and compensated (lower diagram) machine tool using the model of Eq. 7. In the lower boxes of the diagrams the temperature of the cutting fluid and the environmental temperature are given

In Table 2 the measurement evaluations comparing both the uncompensated and compensated machine tool for three quality criteria, peak value  $P_V$ , mean value  $M_V$  and quadratic deviation from mean value  $Q_M$  are given. The R-Test discrete measurements show that with the approach, depending on the quality criteria used, more than 90 % of the thermal errors arising by the error sources environmental influences, cutting fluid and internal load, can be compensated.

Table 2. Thermal location errors for investigation of rotary axis relative reduction for the quality criterion peak value ( $P_V$ ), arithmetic mean ( $M_V$ ), the quadratic deviation to the mean value ( $Q_M$ ).

Error		$P_V [\mu\text{m}],$ $[\mu\text{m}/\text{m}]$	$M_V [\mu\text{m}],$ $[\mu\text{m}/\text{m}]$	$Q_M [\mu\text{m}^2],$ $[\mu\text{m}^2/\text{m}^2]$
$E_{VOC}$	uncompensated	49	-35	73
	compensated	25	-0.2	15
	<b>improvement [%]</b>	<b>49</b>	<b>99</b>	<b>80</b>
$E_{ZOT}$	uncompensated	42	28	44
	compensated	29	-0.3	16
	<b>improvement [%]</b>	<b>30</b>	<b>99</b>	<b>64</b>
$E_{ROT}$	uncompensated	15	11	1.7
	compensated	5	-2	0.5
	<b>improvement [%]</b>	<b>65</b>	<b>84</b>	<b>71</b>
$E_{AOC}$	uncompensated	38	16	80
	compensated	41	-4	62
	<b>improvement [%]</b>	<b>-9</b>	<b>75</b>	<b>23</b>

Measurements for a single influence on a single axis as the rotary table of the machine tool requires a measurement time of about 3 days. For one single axis a total measurement time of about 10 days is required to get the full compensation model. About 20 days are required to derive the model for the rotary/swivelling axis unit with this approach.

## 5 Conclusion

In this paper a new approach for compensating machine tool's thermal errors is presented. The approach is based on a staggered modelling procedure. As several internal and external thermal error sources can cause equal thermal loca-

tion errors of machine tools the system for a single error becomes a multiple input single output system. In thermal error compensation up to now no prediction models, e.g. which can be derived from CAD data, are in a usable small model size to be able to run online on the machine tool's control. Deriving the compensation model from measurements is still often the only possible way for a proper quality and long term stability.

In this paper a model is presented that is capable to predict the thermal errors arising by changing environmental conditions, environmental variation error (EVE), cutting fluid influences and internal loads. Each error source acting on each single axis is thereby investigated separately to understand the effects in more detail. These single error source for a single axis measurements are modelled using a phenomenological grey box model, for which the model parameters are derived using a least square fitting. The model always starts with the investigation of the behaviour of changing environmental conditions. Once the model is derived it is running on the machine tool online compensating these influences.

The environmental influences can then be neglected for the next investigation, e.g. the machine tool's sensitivity to cutting fluid influences. As the model derived from the second investigation is not influenced by environmental conditions for compensating both environmental conditions and cutting fluid influences the models can be superpositioned. Further models, like the compensation model for the internal load, can be added in a same manner.

The approach introduced is a robust approach as the error sources are separated from each other. The approach can be used for all machine tool axis and spindles. Nevertheless the big issue to be solved is still the measurement time. Investigations on a single thermal error of a machine tool usually requires several days. With the machine tool investigated for the rotary axis C the total measurement time is about 10 days to derive the compensation model.

Future work is therefore focusing on reducing the measurement and setup time by process-intermittent probing, on investigation of the long term stability and developing new approaches for simultaneous estimation of all model parameters.

#### **Acknowledgements**

*The authors would like to thank the Machine Tool Technologies Research Foundation (MTTRF) and the Swiss Federal Office for Professional Education and Technology (CTI) for their financial support.*

## 6 References

- [1] Mayr, J., Jedrzejewski, J., Uhlmann, E., Donmez, A., Knapp, W., Härtig, F., Wendt, K., Moriawaki, T., Shore, P., Schmitt, R., Brecher, C., Wuerz, T., Wegener, K., 2012. Thermal issues in machine tools, *Annals of the CIRP* 61/2, 771–791
- [2] Bryan, J., 1990. International status of thermal error research. *Annals of the CIRP* 39/2, 645-656.
- [3] ISO 230-3:2007. Test code for machine tools - part 3: Determination of thermal effects. International Organization for Standardization, Geneva, Switzerland
- [4] ISO 10791-10:2007. Test conditions for machining centres - part 10: Evaluation of thermal distortions, Geneva, Switzerland
- [5] ISO 13041-8:2004. Test conditions for numerically controlled turning machines and turning centres - part 8: Evaluation of thermal distortions. Geneva, Switzerland
- [6] Mayr, J., Gebhardt, M., Massow, B., Weikert, S., Wegener, K., 2014. Cutting fluid influence on thermal behavior of 5-axis machine tools. *Procedia CIRP* 14, 395 - 400
- [7] Mayr, J., Blaser, P., Knapp, W., Wegener, K., 2016. Compensation of cutting fluid influences on five axis machine tools. *Proceedings of the MTTRF 2016 Annual Meeting*, 1 - 6
- [8] Mayr, J., Egeter, M., Weikert, S., Wegener, K., 2015. Thermal error compensation of rotary axes and main spindles using cooling power as input parameter. *Journal of Manufacturing Systems* 37/2, 542-549
- [9] Wegener, K., Weikert, S., Mayr, J., 2016, Age of Compensation – Challenge and Chance for Machine Tool Industry, *International Journal of Automation Technology*, 609 – 623
- [10] Mayr, J., Egeter, M., Weikert, S., Wegener, K., 2015. Shop floor conditions versus precision on 5-axis machine tools. *Laser Metrology and Machine Performance* XI, 308-318
- [11] Gebhardt, M., Mayr, J., Furrer, N., Widmer, T., Weikert, S., Knapp, W., 2014. High precision grey-box model for compensation of thermal errors on five-axis machines. *CIRP Annals – Manufacturing Technology* 63/1, 509 - 512
- [12] ISO 10791-1:2015. Test conditions for machining centres -- part 1: Geometric tests for machines with horizontal spindle (horizontal Z-axis), Geneva, Switzerland
- [13] Gebhardt, M., 2014. Thermal Behaviour and Compensation of Rotary Axes in 5-Axis Machine Tools, Diss. ETH Nr.: 21733

# Design of a Photogrammetric Measurement System for Displacement and Deformation on Machine Tools

*M. Riedel<sup>a</sup>, J. Deutsch<sup>b</sup>, J. Müller<sup>b</sup>, S. Ihlenfeldt<sup>a,b</sup>*

<sup>a</sup> Fraunhofer Institute for Machine Tools and Forming Technology IWU,  
01187 Dresden, Germany

<sup>b</sup>Institute of Machine Tools and Control Engineering IWM, Technische Universität Dresden,  
01062 Dresden, Germany

**Abstract.** For the characterisation of the thermo-elastic machine state the measurement of the displacement at the Tool Centre Point (TCP) and the deformation of the machine assemblies at a large number of measuring points on moving objects are necessary. One approach is the use of photogrammetric methods. In this article an extended photogrammetric method for the measurement of the deformation and the displacement on a test rig is presented. The main focus is on the model based design and operation, the realization of a measurement setup as well as initial experimental investigations on a machine tool.

Peer-review under responsibility of the International Scientific Committee in the person of the Conference Chair Prof. Steffen Ihlenfeldt.

*Keywords:* Measurement-based correction; Monte-Carlo-Simulation; 6DOF-Measurement

---

## 1 Introduction

One important task of the Collaborative Research Centre 96 “thermo-energetic design of machine tools” is the development of new methods to measure the thermo-elastic deformation of machine modules and the resulting error at the TCP [1]. Our new approach is to use machine-integrated cameras and high accuracy photogrammetric methods. In previous tests the 6 degrees of freedom (6 DOF) that define the pose of the TCP were measured to get information of the displacement. This was performed on an existing experimental setup and an uncertainty (1 sigma) up to 5  $\mu\text{m}$  (position) and up to 15  $\mu\text{m}/\text{m}$  (orientation) for the error at the TCP could be achieved [1][2][3].

Now it is required to expand the method in such a way, that both - TCP-error and the deformation of the body - can be measured simultaneously. The measurement setup shall be tested and optimized in a model based simulation be-

fore it gets installed on a test rig. For this purpose the experimental machine “MAX” is as test rig available, which is a cartesian 3-axis machine (Z, Y, X) with three additional rotational degrees of freedom (U, V, W) to allow the correction of thermo-elastic errors.

The aim of this article is to present a model based photogrammetric measuring system for displacement and deformation at the test rig. The most important part of the system is the combination of classical photogrammetric models with the geometric-kinematic model of the machine. The article describes the measurement setup, the measuring model, the simulation based verification and the installation of the system on the test rig.

## 2 Photogrammetric Measurement Model

Photogrammetry allows the detection of spatial coordinates from object points or position and orientation from 3D-objects based on 2D-images of an object [12]. State of the art (Fig. 1) are 6DOF systems with low accuracy up to 250  $\mu\text{m}$  [4][5], stereo vision with medium accuracy up to 80  $\mu\text{m}$  [6] or systems based on bundle block adjustment with high accuracy up to 3  $\mu\text{m}$  + 7  $\mu\text{m}/\text{m} \cdot \text{l}$  dependent of the object-size (l) [7].

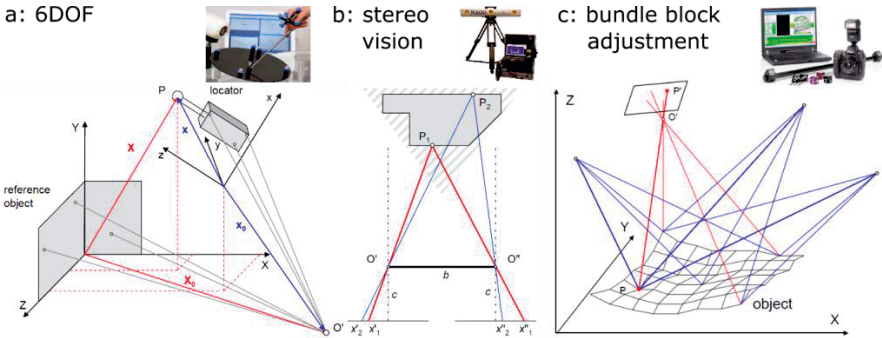


Fig. 1. Photogrammetric systems: a: 6DOF systems [4][12], b: stereo-vision systems [6][12] and c: bundle block adjustment systems [7][12].

For the measurement at the test rig these three methods are insufficient, because they neither reach the needed accuracy nor are they suitable for real-time measurement of moving parts. To obtain these characteristics, the methods must be adapted for this purpose as follows.

The test rig (Fig. 2, left) is equipped with a photogrammetric system which consists of cameras and markers. Therefore the measuring points on the machine are signalized by circular paper targets, which can be easily and precisely de-

tected in the optical images [12]. The images conserve the current position of the machine, so the coordinates (IC) of the targets as well as their uncertainties  $u(IC)$  are calculated by image measurement (Fig. 2, left). Because of the variable kinematic structure the geometrical setup and the set-position at any time must be known.

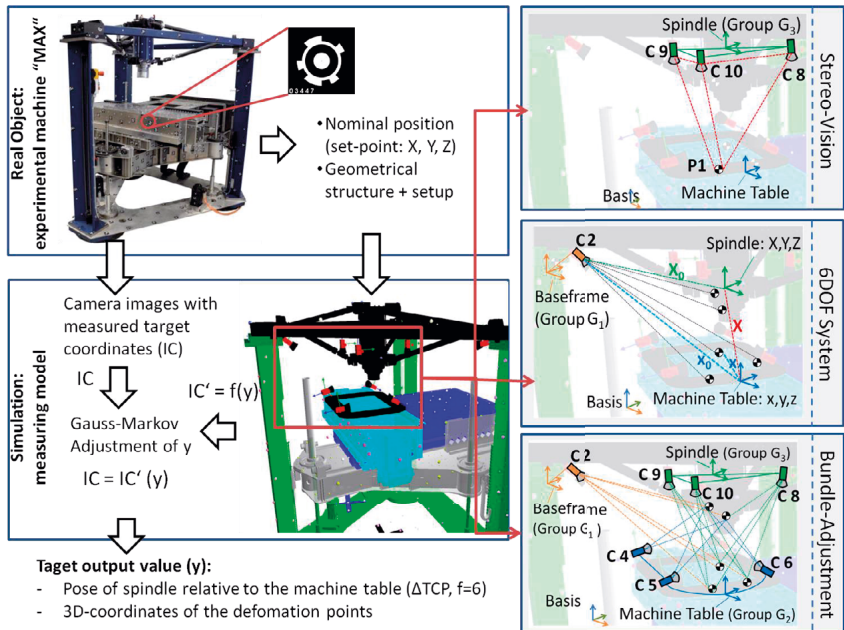


Fig. 2. Test rig Max, measuring model and submodules.

For the calculation of the deviation and deformation at the measurement points we use a parametric 3D-Model (Fig. 2, middle), a so called measuring model. It simulates the image coordinates of the targets in the camera image ( $IC'$ ), depending on the set-point. The measuring model can be interpreted on the one hand as a geometric model of the measuring setup, that considers the kinematic structure as well as rigid bodies and the time-dependent deformation state. On the other hand the model includes the photogrammetric camera model. To get best results the model integrates a mixture of the classical photogrammetric methods (Fig. 2 right). There are parts of a 6DOF system (Fig. 2, centre right), stereo vision (Fig. 2, top right) and bundle block adjustment (Fig. 2, bottom right).

The output parameters ( $\vec{y}$ ) of the model are the 6DOF at the TCP as deviation of the spindle relative to the rigid table and the 3D-coordinates of the signaled



parts on the deformed machine modules. Moreover output parameters contain all estimated results during calibration, such as the inner and outer orientation of the cameras. The model parameters ( $\vec{y}$ ) are estimated by an adjustment (Gauss-Markov). So the collated simulated position represents the actual-state of the machine which includes the target state and the errors (Eq. 1). Therein the partial deviation is described by  $A = \frac{\partial f(y)}{\partial y}$ .

$$IC - IC' = A * \vec{y} \quad (\text{Eq. 1})$$

### 3 Measurement Model Design

In order to achieve a good measurement of deformation and pose, an expedient design for the setup is indispensable. The setup should be simulated prior to the installation to verify that it meets all measurement requirements. It is known that the assemblies and the baseframe of the machine are no rigid bodies. For that it is necessary that all relevant objects in any position are in the field of the view of at least two cameras. For that reason the setup is made up in three groups of cameras ( $G_1 - G_3$ ), each positioned in different parts of the system with different fields of view (Fig. 3). In total 615 targets are affixed all over the test rig to obtain a high number of measuring points.

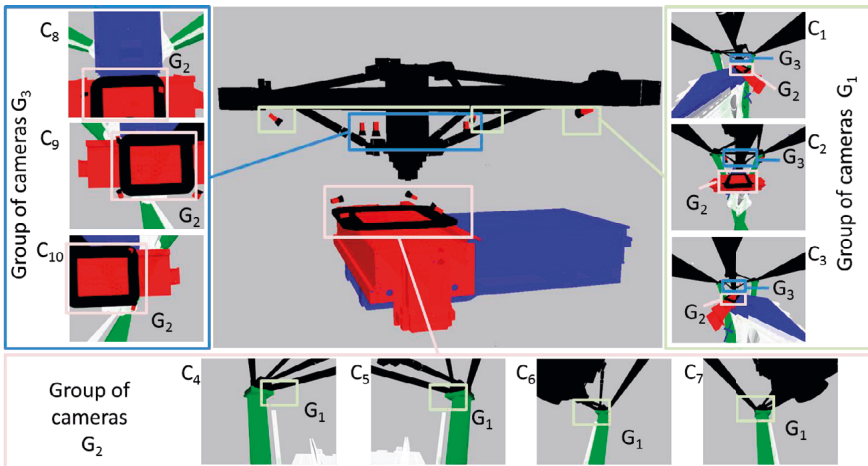


Fig. 3. Position and field of view of all three groups of cameras.

Camera group  $G_1$  monitors the entire structure and can directly detect the displacement of the baseframe as well as the displacement of the spindle relative to the table. At the same time the baseframe itself is subject to deformation,

which means that the outer orientation (position and orientation) of these three cameras can change and have to be verified in every measurement.

The cameras of group  $G_2$  are installed at the machine table. They monitor the  $G_1$ -cameras and can detect the displacement of the table relative to the machine frame. Finally group  $G_3$  is installed near to the spindle head and view on the machine table with cameras and targets of Group  $G_2$ .

Through the arrangement of the cameras and targets, it is possible to determine the displacement of the table relative to the spindle, the outer orientation of the three cameras of the group  $G_1$  and the deformation of the assemblies with one image set of all cameras.

#### 4 Simulated Accuracy of the Measuring Setup

The measurement model is the basis to analyze the system and allows to estimate the statistical uncertainty of the determined displacement of the TCP by the Gauss-Markow-Method and by the Monte-Carlo-Simulation [9]. Since no measured values can be presented yet, estimated values of the input variables ( $x$ ) and their standard uncertainties ( $u(x)$ ) have to be estimated first. Those values form the simulation basis and are taken from results of the image measurement.

$$\Delta TCP = \bar{y} \pm U \quad (\text{Eq. 2})$$

On this basis, estimated values of the output parameters ( $y$ ), the combined standard uncertainty  $u_c(y)$  and the theoretical uncertainty  $U$  of the output variables can be determined from Eq. 2. Via the factor ( $k$ ), the confidence range for the theoretical uncertainty  $U$  is described, usually with  $k = 2$  and with a confidence level of 95 % (Eq. 3).

$$U = k \cdot u_c(y) \quad (\text{Eq. 3})$$

It can be performed under the condition, that there is a sufficiently high number ( $l = 1000$ ) of sets of statistically normal distributed estimates of the input values (Eq. 4).

$$\bar{y} = \frac{1}{l} \sum_{j=1}^l \vec{f}(x_{1,j}, x_{2,j}, \dots, x_{i,j}) \quad (\text{Eq. 4})$$

Moreover the standard uncertainty  $u_c(y)$  of the simulated output variables ( $y$ ) must be determined using the uncertainty propagation law (Eq. 5) [10]. Uncertainties of input values can be derived from the data sheets of the used measurement systems or from experience. The factor  $c_j$  denotes the sensitivity coef-

ficient and is calculated as  $c_j = \frac{\partial f}{\partial x_j}$ . It can also be interpreted as a transfer factor between the input and the output variable.

$$u_c(y) = \sqrt{\sum_{j=1}^i c_j^2 \cdot u(x_j)^2} \quad (\text{Eq. 5})$$

Because this method is only a numerical representation of the probability distribution of the model output, an overlap interval must be defined for determining the confidence level. The effective degrees of freedom serve this purpose (Eq. 6). The quotient  $v_j$  describes the number of available simulation runs, where  $v_j = i - 1$ . With  $v_{eff} \gg 50$  the simulation can be assumed as empirical significant.

$$v_{eff} = \frac{u_c^4(y)}{\sum_{j=1}^M \frac{u_j^4(y)}{v_j}} \quad (\text{Eq. 6})$$

This extended uncertainty includes both random and systematic influences. According to [11] "the physical interpretation of the extended uncertainty is not quite simple" [11]. But in comparison to the propagation law this approach provides more realistic results, since it takes into account a greater number of uncertainties. Therefore, it is used for the design of the measuring systems.

In the first step, the input variables ( $\vec{IC}$ ) are determined for the simulation using the (pre-parameterized) model at the defined pose of the table to estimate the measurement uncertainties. Assuming a Gaussian distribution, the input variables get randomized with a Gaussian noise and then they are introduced into the model as an artificial noisy input signal ( $\vec{IC}'$ ), so that the output variable ( $\Delta TCP'$ ) is calculated (Fig. 4).

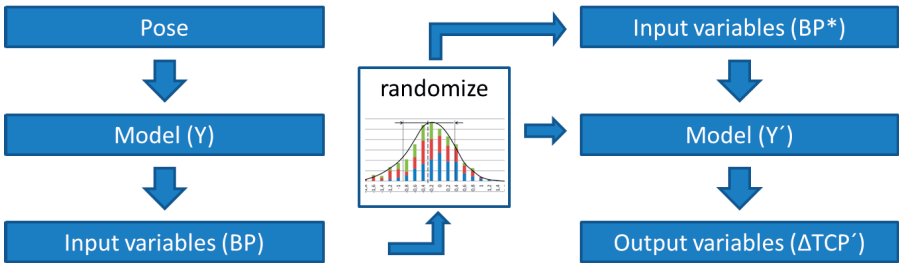


Fig. 4. Procedure of the Monte-Carlo-Simulation.

For the photogrammetric measurement, a measurement uncertainty  $u(IC)$  of the image coordinates of less than  $\pm 0.025$  pixels by an ellipse diameter of more than 10 pixels can be assumed [12]. Converted to an uncertainty of the object, this is about 6  $\mu\text{m}$ . In addition to the pure numerical value of a variable to be determined, the measurement model also provides a model-internal uncertainty based on the error propagation in the Gauss-Markov model (Table 1).

According to [12], this is very optimistic since it only takes into account the variation of the input variables. For this reason, Monte Carlo simulation is proposed in order to take into account external influences. The distribution of the simulated TCP displacement and inclinations are shown in Figure 5. The normal distribution of the output quantities is clearly visible.

Table 1. Mean value of the internal uncertainty as well as statistical distribution of the simulation results.

	$\Delta X$ [ $\mu\text{m}$ ]	$\Delta Y$ [ $\mu\text{m}$ ]	$\Delta Z$ [ $\mu\text{m}$ ]	$\Delta U$ [ $\mu\text{m}/\text{m}$ ]	$\Delta V$ [ $\mu\text{m}/\text{m}$ ]	$\Delta W$ [ $\mu\text{m}/\text{m}$ ]
Model-intern uncertainty:	0.281	0.334	0.065	0.008	0.008	0.005
Mean value of simulation:	0.017	-0.086	-0.015	-0.064	0.007	0.014
Standard deviation ( $1\sigma$ ):	0.530	0.590	0.263	0.371	0.367	0.299
Range:	3.272	3.587	1.576	2.274	2.190	1.974

The statistical parameters of the simulation show a standard deviation of 0.6  $\mu\text{m}$  for the position and a standard deviation of 0.4  $\mu\text{m}/\text{m}$  for the inclination. The range is maximally 3.6  $\mu\text{m}$  and 2.3  $\mu\text{m}/\text{m}$ , respectively (Table 1).

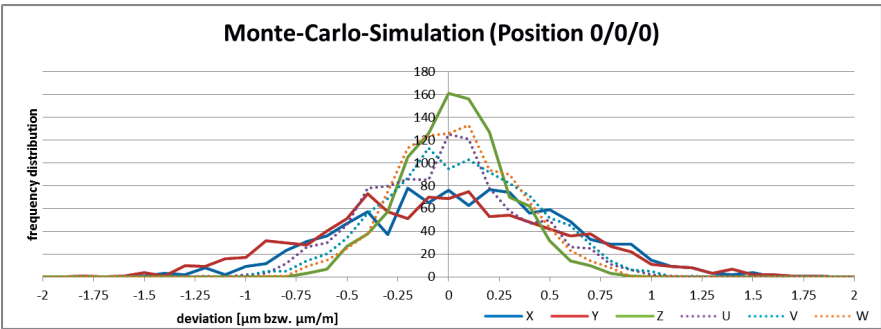


Fig. 5. Frequency distribution of the position and orientation of the TCP in the case of noisy image measurements.

The extended uncertainty for the photogrammetric measurement at the described structure can be quantified with a confidence interval of 95 % for the position of less than 1.8  $\mu\text{m}$  and for the orientation of less than 1.8  $\mu\text{m}/\text{m}$ . The control value  $v_{\text{eff}}$  indicates a good statistical certainty (Table 2).

In this calculation only the uncertainties of the image measurement were considered and the uncertainty of all other model parameters determined during the measurement system calibration were neglected. However, these can be estimated on the basis of prior learning and experience.

Table 2. Results of the Monte-Carlo-Simulation.

	$\Delta X$ [μm]	$\Delta Y$ [μm]	$\Delta Z$ [μm]	$\Delta U$ [μm/m]	$\Delta V$ [μm/m]	$\Delta W$ [μm/m]
Mean value (y)	0.017	-0.086	-0.015	-0.064	0.007	0.014
Uncertainty (95%)	1.570	1.666	1.713	1.707	1.707	1.695
$V_{eff}$	$5.4 \cdot 10^5$	$6.1 \cdot 10^5$	$6.4 \cdot 10^5$	$6.4 \cdot 10^5$	$6.4 \cdot 10^5$	$6.4 \cdot 10^5$

For example, the uncertainty of the target coordinates can be approximated to  $u \approx 5 \mu m$  with the aid of the spatial resolution. This uncertainty of the calibration parameters is recorded as a variation variable in addition to the uncertainty of the image measurement. The statistical characteristics of the simulated TCP displacements and inclinations are summarized in Table 3.

Table 3. Statistical distribution of the simulation results.

	$\Delta X$ [μm]	$\Delta Y$ [μm]	$\Delta Z$ [μm]	$\Delta U$ [μm/m]	$\Delta V$ [μm/m]	$\Delta W$ [μm/m]
Mean value:	0.148	0.103	0.012	0.121	-0.173	0.126
Standard deviation (1σ):	4.119	5.389	2.302	3.835	3.091	2.889
Range:	28.259	34.829	14.493	23.675	21.493	15.269

In this case, the uncertainty exceeds the uncertainties calculated with constant calibration parameters by a factor of 10 (see Table 1). Furthermore, the results do not correspond to an ideal Gaussian distribution. Here, more simulation runs would have been useful but were not performed due to high simulation effort.

These values represent a "worst case" scenario in which the calibrated parameters of the model change abruptly. Although this is not possible in reality, the comparison of standard deviation with and without inclusion of model parameters can be used as a criterion for the interpretation of the camera system. For practical purposes, this simulation means that the calibration parameters of the measuring system must be kept up to date or permanently checked. A check of the measurement is already provided and implemented via the control variables of the Gauss-Markov model (standard deviation).

# 5 Realisation of Measurement Setup

With the measurement model the precision of the measurement of the deviation and deformation is simulated and got good results for the proposed, optimized setup. Based on this optimized setup the test rig gets equipped with cameras and measuring targets to put the measurement into praxis. Currently the configuration of the measurement setup is tested. As explained above, it consists of three camera groups, each with a different field of view to cover the complete working area. As a first step the camera group  $G_3$  close to the head of the spindle gets implemented.

For this group of cameras it is important to ensure that the position and orientation of the cameras within the group relative to one another as well as relative to the spindle do not change during the measurement. For that reason the cameras are mounted on a frame made of carbon-fiber-reinforced-polymer CFRP (Fig. 6, middle). This strong and light material can cover the requirement of high rigidity and low deformation due to temperature.

The resolution of the cameras and the lens focal length are selected in such a way that the local resolution on the measurement object for all cameras is approximately 0.25 mm/pixel. This ensures a homogeneous distribution of the measurement uncertainties in the entire working area of the machine. In Figure 6 the camera's field of view is shown. In comparison to Fig. 2 it gets evident that the simulation has estimated the positions very well. As this is the first group to be installed, the expected group  $G_2$ -cameras cannot yet be detected in these images.

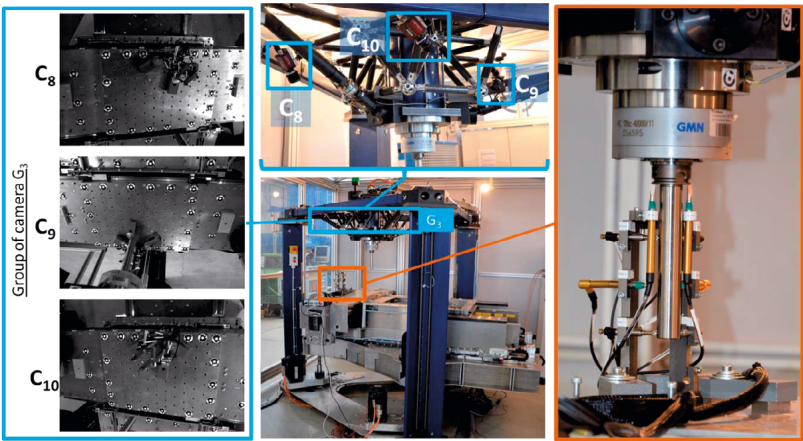


Fig. 6. Configuration of camera group  $G_3$  and dial indicators as reference system

Moreover a set of dial indicators (Fig. 6, right) is installed in the middle of the machine table (according to [13]). This allows to compare the results of the non-contact photogrammetric methods with the results of direct measurement. There are three sensors in the X and Y direction, two sensors in the Z direction. All sensors are tested in a first test run of the machine to proof reproducibility and thus the suitability of the dial indicators to act as a reference (results see Fig. 7 left).

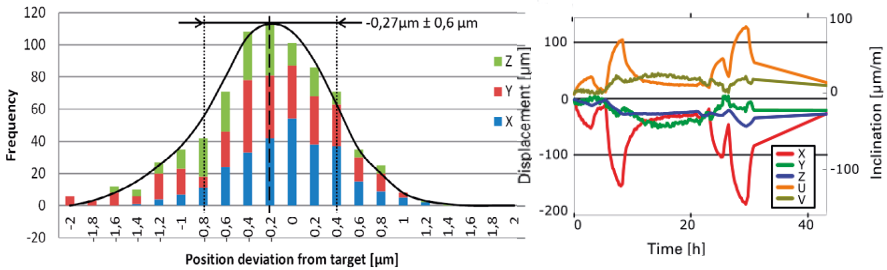


Fig. 7. Left: Deviation of measured position of dial indicators; right: Results of displacement and inclination of the TCP measured with dial indicators.

The results represent a worst-case scenario, because they have been obtained by repeated movement to different positions from different directions. In that way all possible errors were introduced to the system. Nevertheless the mean value of deviation is  $-0,27\mu\text{m} \pm 0,6\mu\text{m}$ . That proofs that dial indicators have a finite accuracy based on real measurements.

Then the indicators were used to measure displacements directly on the TCP. Therefore the machine runs two complete load cycles to see the development of the deviation over a longer period of time. Particularly X- and U- direction are noticeable in Figure 7 right. The more heat generated by the movement of the machine, the greater the deviation gets.

## 6 Summary

An approach for the measurement-based detection of thermo-elastic deformation and displacement of the TCP uses photogrammetry methods, these enables position measurement close to the TCP of the machine. The structure of the measuring setup and the mathematical model were presented. The model was examined using the Monte-Carlo-simulation for better interpretation of the approach. It simulation results shows that the described measuring setup can be used for the complete position measurement with a simulated uncertainty of  $1.8\mu\text{m}$  (deviation) and  $1.8\mu\text{m/m}$  (inclination).

Thus the first group of simulated cameras is realised and physically installed at the test rig. The images cover the entire working area and detect measuring targets with good resolution. In addition a reference system, consisting of eight dial indicators, is installed. Those provide good reproducibility and have captured a set of data that show the influence of the temperature on the derivation of the TCP clearly. This proves as well that the planned measuring system performs well so the next step is to install the two other groups of cameras.

## 7 References

- [1] K. Großmann (2012). Thermo-energetische Gestaltung von Werkzeugmaschinen, Eine Übersicht zu den Zielen und Vorgehen im SFB/Transregio 96, ZwF, vol. 5, pp. 307-314.
- [2] K. Großmann, J. Müller, M. Merx, M. Riedel (2015). Experimental Analysis of the Thermo-Elastic Behaviour of Machine Tools by Means of Selective Thermography and Close-Range Photogrammetry. In: K. Großmann (ed.), Thermo-energetic Design of Machine Tools, Switzerland: Springer International Publishing, pp. 247-261.
- [3] X. Thiem, M. Riedel, B. Kauschinger, J. Müller (2016). Principle and verification of a structure model based correction approach, Procedia CIRP 46 ( 2016 ), pp. 111 – 114.
- [4] Axios 3D Services GmbH (2014). Datenblatt Optisches Messsystem CamBar B2 C8. [online] Available at: [http://www.axios3d.de/Doc/datasheet/Datenblatt\\_CamBarB2C8.pdf](http://www.axios3d.de/Doc/datasheet/Datenblatt_CamBarB2C8.pdf) [Accessed 06.01.2017].
- [5] T. Luhmann (2009). Precision potential of photogrammetric 6DOF pose estimation with a single camera. single camera ISPRS Journal of Photogrammetry and Remote Sensing 64 (2009), pp. 275-284.
- [6] NDI Measurement Sciences (2018). PRO CMM Overview. [online] Available at: <https://www.ndigital.com/msci/products/procmm/> [Accessed 02.01.2018].
- [7] Aicon 3D Systems (2018). AICON MoveInspect DPA. [online] Available at: <http://aicon3d.com/en-GB/products/moveinspect-technology/aicon-moveinspect-dpa> [Accessed 02.01.2018].
- [8] M. Riedel, J. Müller, M. Klatte, F. Tzanetos (2017). Funktionsprinzip der messtechnisch basierten Korrektur thermischer Verlagerungen am Versuchsträger MAX, in: Brecher, C. (Ed.), Thermo-energetische Gestaltung von Werkzeugmaschinen –Modellierung und Simulation, reprogress GmbH, Dresden, pp. 241-259.
- [9] JCGM 101 (2008). Evaluation of measurement data – Supplement 1 to the "GUM" – Propagation of distributions using a Monte Carlo method
- [10] JCGM 100 (2008). Evaluation of measurement data – Guide to the expression of uncertainty in measurement (ISO/IEC Guide 98-3:2008)
- [11] DIN ISO 21748:2014-05. Leitfaden zur Verwendung der Schätzwerte der Wiederholpräzision, der Vergleichpräzision und der Richtigkeit beim Schätzen der Messunsicherheit



- [12] T. Luhmann, S. Robson, S. Kyle, J. Boehm (2014). Close-Range Photogrammetry and 3D Imaging. 2nd edition, Walter de Gruyter GmbH, Berlin/Boston
- [13] ISO 230-3:2007. Test code for machine tools – Part 3: Determination of thermal effects

# Thermography on machine tools

*M. Riedel<sup>a</sup>, J. Deutsch<sup>b</sup>, J. Müller<sup>b</sup>, S. Ihlenfeldt<sup>a</sup>*

<sup>a</sup> Fraunhofer Institute for Machine Tools and Forming Technology IWU, Nöthnitzer Straße 44,  
01187 Dresden, Germany

<sup>b</sup>Institute of Machine Tools and Control Engineering IWM, Technische Universität Dresden,  
01062 Dresden, Germany

**Abstract.** A basis for the adjustment of thermo-elastic models is the measurement of temperatures at a large number of measuring points. For this purpose, the thermography can be used. However, the determination of the emission coefficients and the measurement on large moving parts are problematic. The difficulty lies in the geometrical assignment of the measuring points to the moving assemblies and in the localization of image points. The article describes a measuring system based on a combination of thermography and photogrammetry for measuring temperatures at moving assemblies. The main points of the contribution are the functional principle, structure and an exemplary application.

Peer-review under responsibility of the International Scientific Committee in the person of the Conference Chair Prof. Steffen Ihlenfeldt.

*Keywords:* Thermography; Photogrammetry; Calibration

---

## 1 Introduction

The achievable accuracy of workpieces is highly influenced by thermally induced deviations in the machine tools, which has to be considered when correction models are generated. To estimate the thermic state of the machine and the correlated thermal error at the Tool Centre Point (TCP), it is necessary to obtain values by direct measurement of temperature and deviation. This can be done by measurement of deviations at the TCP or the deformation of the assembly. However, the measurement especially on large and moving machine parts is difficult, so that normally it is preferred to obtain values of temperature on a high number of measurement points.

To get an idea of the field of temperature among the group of components, usually Pt100-sensors are attached directly on the surface of the assembly. Therefore a test carrier is equipped with a measuring setup consisting of 20 material- and 10 ambient temperature sensors (Fig. 1). To ensure a high accuracy

of measurement, all sensors are calibrated previously at a reference temperature. The required equipment is available at the Institute of Machine Tools and Control (IWM), so that sensors and measurement chain has an accuracy of about 1/10 Kelvin in a range from 10 °C to 100 °C.

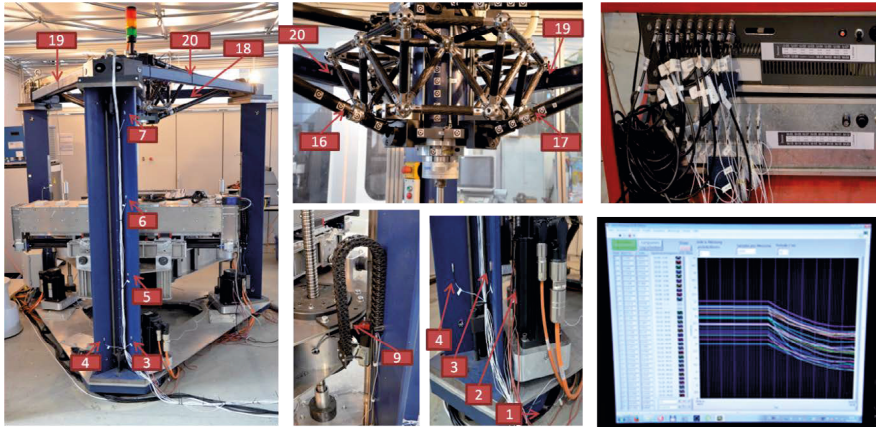


Fig. 1. Measurement of temperature: conventional sensors (PT100) and measurement software require a high effort for setup.

In spite of the fact, that local temperature can be recorded at a high accurate level, there are just a restricted number of captured measurement points because the setup requires a high amount of equipment and the installation is time intensive. When concerning moving assemblies a rather rigid connection of signal or power cables (cable length between 5m up to 10m) from measurement point to the measuring amplifier is problematic or even impossible to install. That means a significant loss of flexibility because all relevant points of measurement should be decided in advance, in order to prevent subsequent and cumbersome retrofitting.

That is why there appear to be particular challenges in the use of contact temperature sensors, especially when configuring and monitoring machines, e.g. adjusting parameters of given models or analyzing weaknesses in the process. A possible method to avoid those disadvantages is to use contact thermometer (resistor type), but those require a long time for acquisition of data, in which the thermal state of the machine has possibly already changed.

An alternative method is to use thermography, which is characterized by good reaction times and is able to detect the whole visible outer surface of the test object, instead of only a few measuring points. In addition the sensor allows

free motion of the machine. Taking the data sheet of typical thermal cameras in account, it seems as if the resolution of measurement is sufficient (Table 1).

Table 1. Comparison of resolution in different thermal cameras.

	Optris PI 400 (t)	Infratec (t)
Geometrical resolution [pixel]	382x288	1024x768
Thermal resolution at 25 °C [K]	0.04	0.02
System uncertainty (range)	±2K	±1K

Infrared radiation is part of the electromagnetic spectrum, that extends to a wavelength range from 1µm to 20 µm. Infrared thermography is based on the fact that any object emits electromagnetic radiation. By determining the radiation intensity, the temperature of that emitting body can be calculated. Moreover the radiation intensity depends on the material and its characteristics (Fig. 2 left).

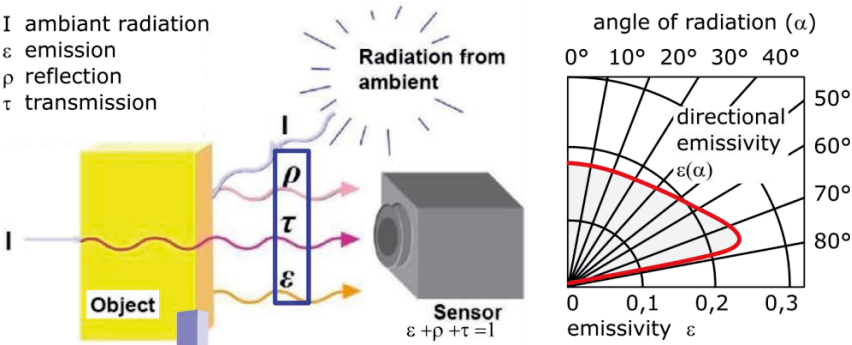


Fig. 2. left: Components of infrared radiation [1]; Right: Emissivity of metal [2].

The detected radiation is affected by reflection of vicinity, what leads to the difficulty to distinguish the emission component from the reflection- and transmission component of the radiation ([1],[11]). Typical emission coefficients in dependence on the angle are shown in Fig. 2 right. Therefore the low emission coefficient for typical materials without coating used in mechanical engineering gets evident, as well as the high dependence on the angle ([2], [8], [9]).

One solution is to stick targets made of paper onto the object, whose emission coefficient differs significantly from metal. To this end, a method is presented in [4] of how emission coefficients can be determined for different types of paper used for the target (cf. Table 2).

Table 2. Emission coefficients of different types of paper [4].

Type of paper	Emissivity min	Emissivity max
Herma 4379	0.890	0.942
Herma 4698	0.887	0.956
Labelmedia	0.897	0.938
Herma 4458	0.890	0.940

In addition, the extent to which the emission coefficient is dependent on the angle and temperature was investigated [3]. The results in Fig. 3 show that observation angles until 55° achieved temperature coefficients, defined as  $T_{th}(\varepsilon=1)/T_{tactile}$ , around 1 with slight fluctuations, which remain in tolerance range. That means the calculated temperature from the thermal images ( $T_{th}$ ) correspond well to the measured temperature of the sensors ( $T_{tactile}$ ). In this range, the emissivity of the targets can be regarded as known (0.9-0.94) for temperatures between 20°C-70°C, as well as independent on the observation angle.

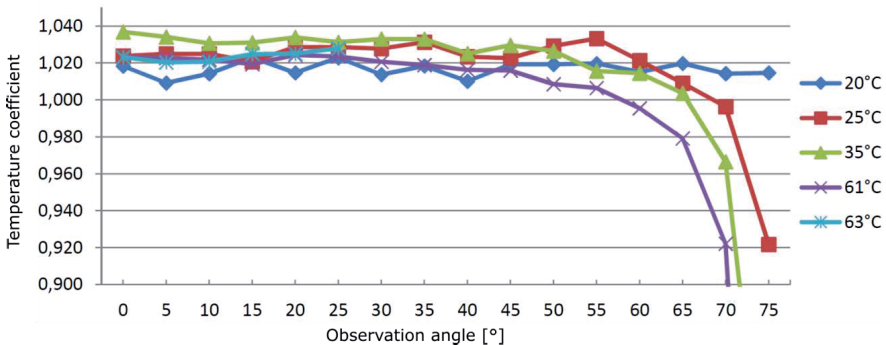


Fig. 3. Emissivity in dependence of temperature and angle [3]; Temperature coefficient is defined as  $T_{th}/T_{tactile}$ .

An evaluation of the temperature uncertainty under shop floor conditions is described in [5]. There the difference between calibrated tactile temperature sensors and the thermographic measurement is compared. The dataset has 80 pictures from different viewpoints at the object. In these case an uncertainty range of 0.5 ... 0.2 K is possible.

These findings will be taken into account for further experiments, but in practice other difficulties of thermography become apparent. As a matter of fact the contrast of the thermal images is often not sufficient for further analysis [5]

and the reflection of the thermal camera leads to errors in the image. In purposes of illustration, an object is equipped with self-adhesive paper targets with high emission coefficients ( $\epsilon > 0.9$ ), as are customary in photogrammetry (Fig. 4a).

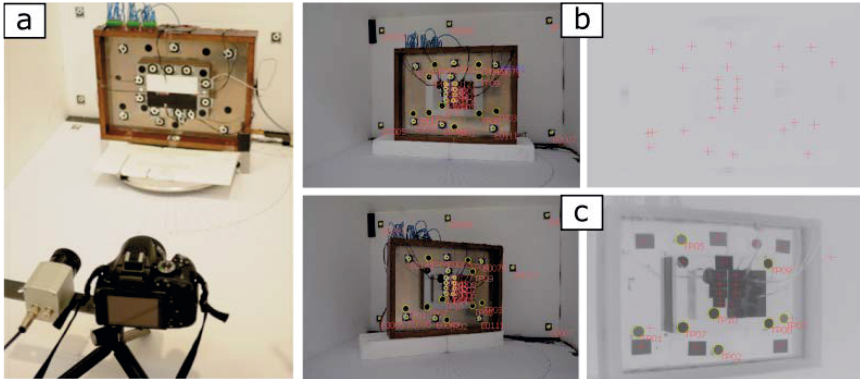


Fig. 4. (a) Thermal and optical camera in temperature measurement setup; (b) cold object in optical and thermal image; (c) heated object in optical and thermal image.

Then the object is photographed with a thermal and an optical camera in cold and heated state to compare both images (Fig. 4 b+c). The different properties are clearly visible, since in the thermogram almost no texture can be seen, but in visible spectral range shapes and targets are detected easily.

## 2 Principle of selective thermography

It is a good idea to link the strengths of both measurement methods: The selective thermography allows to measure temperature fields in a non-contact manner with high resolution and minimum equipment by using thermal and optical camera in combination.

With photogrammetry methods spatial coordinates of all measurement points can be determined precisely. Afterwards those positions are transferred to the thermal image to get the result of the temperature measurement at the correct point in the picture [5]. Therefore it is obligatory that the relative position and orientation of the optical and the infrared camera are known, which can be figured out by prior calibration on a test panel, as shown in Fig. 5. The test panel for calibration consists of coded and uncoded paper targets, scale bars and heatable target plates. Those can be detected with sufficient contrast in the optical as well as in the thermographic image (Fig. 5, right).

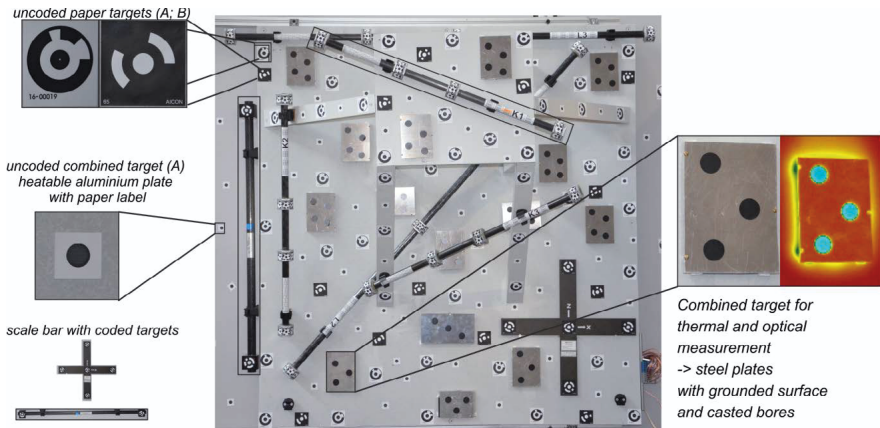


Fig. 5. Test panel for calibration with (un-) coded targets, scale bars and combined targets for optical and thermal camera (right).

In an image set of approximately 10 images, the test panel is recorded from different directions and therein the circular target's outlines are measured. Based on that measurement, on the one hand, the relative orientation of both cameras (TMY in Fig. 6) and on the other hand the internal orientation, e.g. the distortions of the optics, can be calibrated. This is calculated by a bundle block adjustment ([6], [10]). The remaining residuals are normally under 0.5 pixels in both cameras. With a minimal target diameter of 10 pixel in the optical camera and 5 pixels in the thermal camera we can measure the temperatures at the right position in thermal image.

To obtain information about the third dimension out of a 2D-image is typically difficult. Usually a forward intersection is used to obtain this information, if in both images reliable texture is available. But normally the difference between the thermal radiation and the visible surface texture is too high for stable results. So another approach is needed.

The intercept theorem allows the calculation of the object's spatial coordinates within the coordinate system of the optical camera (Eq. 1 and Fig. 6).

$$Z = \frac{c_{opt} * DM}{2 * a_{opt}}, X = \frac{x_{opt} * DM}{2 * a_{opt}}, Y = \frac{y_{opt} * DM}{2 * a_{opt}} \quad (\text{Eq. 1})$$

It can be assumed that the used target's diameter in object space (DM) is known. Moreover measurement in image space has given information about the target's position ( $x_{opt}$ ,  $y_{opt}$ ) as well as the semi-major axis ( $a_{opt}$ ) of the ellipse. As a good approximation, the calculated ellipse centre corresponds to the required centre of the circular target, what means that the relation between the

major-axis of the ellipse and the diameter of the circular target is valid. With the relation in Eq. 1, the internal orientation of both cameras determined during camera calibration and their relative orientation, the coordinates can be projected into the thermogram. This allows the temperature to be calculated when the emission coefficient is known.

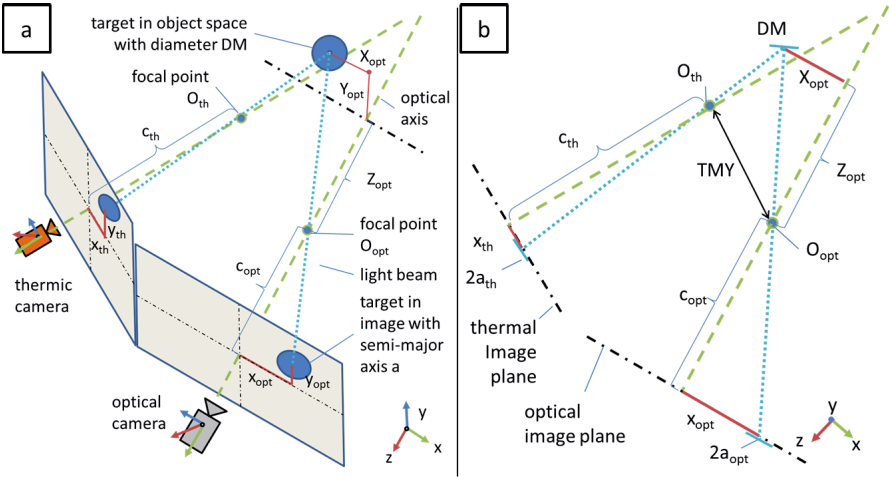


Fig. 6. Intercept theorem for estimation of distance, a: Schematic setup in 3D is transferred to b: mathematical scheme of setup in 2D.

### 3 Fields of application for selective thermography

If cameras are calibrated in terms of the geometric imaging model, selective thermography can be used for a variety of practical applications. The method allows to position targets as desired and to adapt them to changing ambient conditions. The greatest advantage therefore lies in the gained flexibility, which is enabled by a quick and simple experimental setup. No long cables affect motion range, what makes it an appropriate method for acquisition of temperature data on moving assemblies [7].

At the IWM experiments have been carried out on a rigid and on a moving carrier to test selective thermography. The results for the heating of a spindle sleeve are shown in Fig. 7. It shows position measurement (Fig. 7 right) and its transfer into the thermogram, which calculates and displays the temperature of the spindle sleeve at these spots. Typical features of a thermogram remain, for example the load cells can be seen as light green fields on the outer arms of the



carrier, as well as the reflection of the thermal camera and camera man are seen as a red area on the spindle head.

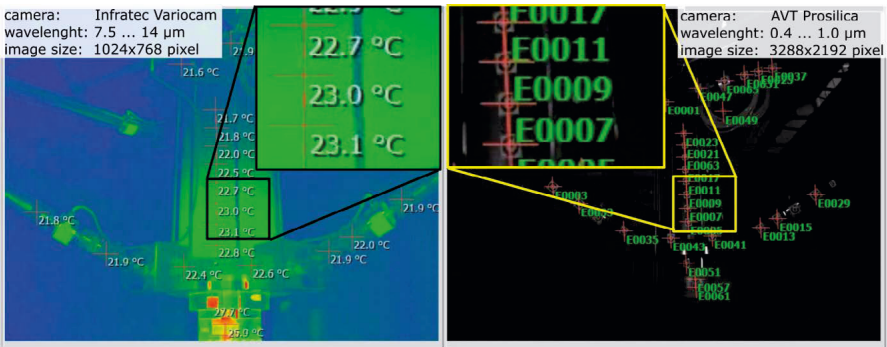


Fig. 7. Heating of a spindle sleeve, Right: Photogrammetric measurement of the position on 26 targets, Left: Transfer of positions to thermogram with measurement of temperature at those locations.

During the experiment both cameras are mounted on a tripod that is moved vertically up and down. In this way, a relative movement between cameras and object is forced in order to test the stability of the measurement. However, the relative movements do not distort either the position or the temperature measurement. The same result is obtained by the test which carried out measurements on a moving object with a hand-held camera.

#### 4 Summary

Compared to the PT100 temperature sensors described at the beginning, selective thermography proves to be a flexible measuring method, which enables non-contact metrological determination of temperature fields with high structural resolution and minimal instrumentation effort. In addition, it is easy to be applied to large components or to moving assemblies and achieves good results.

The approach uses methods of photogrammetry for locating the temperature measuring points, while the actual temperature is measured by means of thermography. As a result an uncertainty of 0.5...0.2 Kelvin can be reached, which means a lower result compared to PT 100 sensors. Nevertheless there appear to be application scenarios for which selective thermography can be a better or a quicker choice. That may be an application for fundamental behavioral analysis, a weak point analysis or an elaboration of parameters for correction models. For any application with a larger uncertainty requirement the selective thermography is a verified mean.

## 5 References

- [1] Optris GmbH: Grundlagen der berührungslosen Temperaturmessung. Last access: 28.09.2017, [http://www.optris.de/tl\\_files/pdf/Downloads/Zubehoer/IR-Grundlagen.pdf](http://www.optris.de/tl_files/pdf/Downloads/Zubehoer/IR-Grundlagen.pdf)
- [2] G. Koscsák (2007): Ermittlung des stationären thermischen Verhaltens von Vorschubachsen mit Kugelgewindetrieb mit Hilfe der Verarbeitung thermografischer Messdaten. PhD Thesis, University of Stuttgart, 2007
- [3] C. Whynalec (2013): Vergleichende Untersuchung von Marken für die selektive Thermografie an WZM, Interdisziplinäre Projektarbeit. TU-Dresden
- [4] M. Drui (2014): Genauigkeit der selektiv thermografischen Temperaturmessung, Großer Beleg. TU Dresden
- [5] K. Großmann, A. Galant, M. Merx, M. Riedel (2014): Methodology for the efficient Analysis of thermal and thermo-elastic Behaviour of Machine Tools. In: Advanced Materials Research Vol. 1081. Switzerland: Trans Tech Publications, pp. 395-402
- [6] T. Luhmann, J. Ohm, J. Piechel, T. Roelfs (2010): Geometric Calibration of Thermographic Cameras. In: International Archives of Photogrammetry, Remote Sensing and Spatial Information Sciences, Vol. XXXVIII, Part 5, Commission V Symposium, Newcastle upon Tyne, UK, pp. 411-416
- [7] K. Großmann, J. Müller, M. Merx, M. Riedel (2015): Experimental Analysis of the Thermo-Elastic Behaviour of Machine Tools by Means of Selective Thermography and Close-Range Photogrammetry. In: K. Großmann (ed.), Thermo-energetic Design of Machine Tools, pp. 247-261. Switzerland: Springer International Publishing
- [8] U. Heisel, G. Koscsák, T. Stehle (2006): Thermography-Based Investigation into Thermally Induced Positioning Errors of Feed Drives By Example of a Ball Screw. Annals of the CIRP Vol. 55/1/2006
- [9] J. Mayr, et al. (2012): Thermal issues in machine tools. CIRP Annals - Manufacturing Technology 61 (2012) 771–791
- [10] S. Lagüela, H. González-Jorge, J. Armesto, P. Arias (2011): Calibration and verification of thermographic cameras for geometric measurements. Infrared Physics & Technology 54 (2011) 92–99
- [11] S. Marinetti, P. G. Cesaratto (2012): Emissivity estimation for accurate quantitative thermography. NDT&E International 51(2012) 127–134



# Test piece for thermal investigations of 5-axis machine tools by on-machine measurements

*M. Wiessner<sup>a</sup>, P. Blaser<sup>a</sup>, S. Böhl<sup>a</sup>, J. Mayr<sup>b</sup>, K. Wegener<sup>a</sup>*

<sup>a</sup>Institute of Machine Tools and Manufacturing IWF, ETH Zürich, 8092 Zurich, Switzerland

<sup>b</sup>inspire AG, Technoparkstrasse 1, 8005 Zurich, Switzerland

**Abstract.** Thermal errors evaluation of two 5-axis machine tools with thermal test pieces is presented. The measurements of two thermal testpieces are performed on-machine with a touch trigger probe. The thermal deformations in X-, Y-, Z-, and B-direction as well as thermal material expansion errors of the test piece can be calculated. A comparison with coordinate measuring machine results and an R-Test shows a good conformity of the evaluated thermal errors. The on-machine measurements can be performed automatically and provide fundamental knowledge for thermal characterization of the machine tool, this lays the basis for autonomous manufacturing.

Peer-review under responsibility of the International Scientific Committee in the person of the Conference Chair Prof. Steffen Ihlenfeldt.

**Keywords:** Thermal error; Machine tool; Test piece; On-machine measurement

---

## 1 Introduction

In the past years 5-axis machine tools became more important in industrial applications for precision manufacturing of complex workpieces. This is driven especially by the requirements of aero-space industry and mold and die manufacturing. With the help of precise 5-axis machine tools, new products and optimized machining strategies became possible. For example, workpieces can be machined on up to five sides without additional clamping and the inclination of the tool can be optimised to current cutting conditions. The accuracy of 5-axis machine tools depends mostly on the geometrical position and orientation errors and the error motions of the machine tool axes. Mayr et al. [1] described the thermal influences on position and orientation errors and motion errors of machine tools.

E.g. standards like ISO 10791-10 [2] evaluation of thermal distortions, ISO 13041-8 [3] for turning machines and ISO 230-1 [4] for geometric accuracy of

machines deal with the evaluation of errors of machine tools under no load or finishing conditions, which can be detected by measuring devices. To evaluate machine tools with chipping loads, test pieces were developed from which examples are given for NC machine tools in ISO 10791-7 [5]. Several facets and segments are featured on the workpieces. Besides ISO other societies like the German NC Gesellschaft [6] or the Association of German Engineers (VDI) [7] developed test pieces for machine tools.

Up to now there is no standard for thermal test pieces, despite the fact that these are crucial for industrial improvements concerning thermal issues on machine tools. Currently new test pieces, which are able to capture the thermal errors of 5 axis machine tools are in development. A geometrical test piece design was extended by Ibaraki and Ota [8] to measure thermally induced errors by motions of rotary axes. Three different test pieces were manufactured every 25 minutes in order to measure the thermal effects directly with a touch probe system on the machine. Höfer and Wiemer [9] developed a compact test piece for the evaluation of the thermally induced translational displacements of the tool centre point (TCP). The test piece consists of several reference surfaces and the thermal load was induced by rotation of the spindle as well as several axes movements. Given the fact that shop floors do not have the possibility to test their machine tools regularly for thermally induced errors with special measuring equipment, a high demand for a simplified measurement procedure is claimed by Wiessner *et al.* in [10]. The proposed analysis method of thermal errors on machine tools with a thermal test piece in combination with an automatic on machine measurement as explained in this paper, is not only a change for industry to evaluate their machines fully autonomously without expensive measurement equipment but also a next step to new standardization in this field.

## 2 Experimental Setup

### 2.1 Thermal test piece and test cycle

The thermal test piece, shown in Figure 1 and described in detail in [11], has 9 functional surfaces in orthogonal to Z to determine the deviations in Z-direction and the B-respectively A-axis errors. For the X- and Y-deviations as well as the thermal material expansion error of the test piece itself, 36 facets are milled on the outer cylindrical face with a distance of 97.5 mm to the centre. Two nominal parallel and opposed facets are needed to measure the errors in different

directions. This enables the evaluation of 9 deviations in two axes directions. One of the 9 deviations in each direction is used as reference which leads to 8 available points in time which is in conformity to a four hours warm-up cycle, described in ISO 230-3 [12], and a four hours cools down cycle. The test piece is pre-milled to keep the cutting forces low and during the test cycle the functional facets and surfaces are milled by the sequential movement of one axis at a time. To mill the facets the test piece is positioned by the movement of the C-axis. In each milling step the Z-surface is machined first by moving the tool in X-direction, followed by a movement in Y-direction for milling the X-facets and a movement in Y-direction for milling the Y-facets. The thermal test piece is fixed on the machine tool table by three screws supported with precision washers.

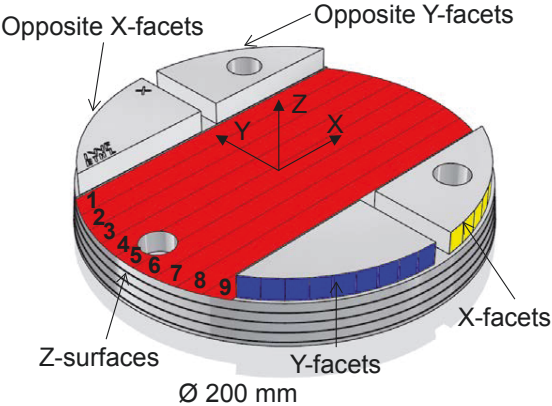


Fig. 1. Thermal test piece with highlighted functional surfaces according to [11]

The used test cycle includes a 4 hour warm up phase and a 4 hour cool down phase, one set of deviations each hour is milled. The thermal load is induced into the machine structure by the rotary axis of the machine tool. In each hour of the warm up cycle the table rotates at maximum speed. During the cool down phase the machine is in NC-hold.

## 2.2 Machine tools under investigation

Thermal errors of two different 5-axis machine tools are evaluated by machining a thermal test piece. The different kinematic setups of the vertical machining centres with two rotary axes located on the workpiece side are schematically illustrated in Figure 2 a) and b).

The machine tool shown in Figure 2 a) can be described in accordance with ISO 10791-2 [13] as: V [w C2' A' X' b Y Z (C1) t]

Further on this type is called machine tool A/C. This machine tool is located in an air conditioned lab. The machine tool has only one coolant circuit for the A/C-axis unit and the main spindle in this sequence. The coolant temperature is controlled to follow the ambient air temperature. The maximum speed of the C2-axis of machine tool A/C is limited to 60 rpm.

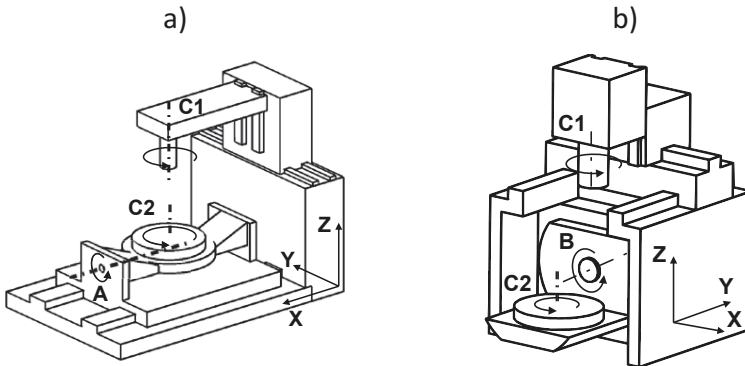


Fig. 2. Schematic of 5-axis machine tool (a) A/C, adapted from [11] (b) B/C, adapted from [14]

The kinematic chain of the second vertical machining centre can be described in accordance with ISO 10791-2 [13] as: V [w C2' B' b [Y1 Y2] X [Z1 Z2] (C1) t]

For simplicity this type is called machine tool B/C. The linear axes of this machine tool are arranged in a box in box design. The rotary axes, B and axis C2, are driven with direct drives. The machine tool B/C has two closed cooling circuits, one is used for the rotary and swivelling axis and one for the main spindle and the linear axes. The C2 axis of this machine tool can be used in turning mode with a maximum rotational speed of 1'200 rpm. The coolant flow is controlled to the machine bed temperature. In contrary to machine tool A/C this machine tool is located in a standard non air conditioned shop floor.

### 2.3 Measuring devices

Three types of measurements are used to evaluate the machined test pieces, respectively the machine tool errors. On-machine (OM) measurements, coordinate measuring machine (CMM) measurements as well as R-Test measurements. The on-machine (OM) measurements are performed with a touch trigger probe. A repeatability of  $\pm 1 \mu\text{m}$  is guaranteed at a probing velocity of

480 mm/min by the manufacturer. Measurements are performed with a probing velocity of 200 mm/min, a probe length of 50 mm and a probe tip diameter of 6 mm. In addition to the touch trigger probe the machine repeatability of  $\pm 2 \mu\text{m}$  has to be added which results in a total error of  $\pm 3 \mu\text{m}$  for this measurement. To verify the OM measurements a CMM is used to measure the functional faces of the test piece with maximum possible accuracy. The CMM used for the results in this paper is located in an air conditioned measuring room, controlled to  $20 \pm 0.5^\circ\text{C}$ . According to ISO 10360-2 [15], the used CMM is specified with a maximal permissible error (MPE) of  $1.2 \mu\text{m} + L/400$ .

To verify the thermal investigation by test piece the discrete R-Test is performed on both machine tools. With a precision sphere eccentrically mounted on the machine table, four linear probes mounted in a sensor nest and clamped into the spindle. The R-Test was set up as explained by Ibaraki and Knapp in [16]. The uncertainty of the R-Test can be estimated as  $\pm 2 \mu\text{m}$ , according to Gebhardt [17]. The evaluated errors are defined as shown in table 1.

Table 1. Overview of thermally induced errors [11]

<b>Thermally induced position and orientation errors of a vertical C-axis</b>	
$E_X [\mu\text{m}]$	Thermal error in X-axis direction
$E_Y [\mu\text{m}]$	Thermal error in Y-axis direction
$E_Z [\mu\text{m}]$	Thermal error in Z-axis direction
$E_B [\mu\text{m}/\text{m}]$	Thermal error in B-direction; squareness of C to X
$E_{ROT} [\mu\text{m}]$	Radius error of the table
<b>Unwanted thermally induced errors on test piece</b>	
$E_{TTP} [\mu\text{m}]$	thermal material expansion error of the test piece

The symmetric design of the thermal test piece, enables to evaluate the thermal errors in a non-air conditioned environment, assuming that the environmental temperature is sufficiently stable during the measurement.

### 3 Results

The evaluation of machine tool A/C is shown in Figure 4. Results of the OM measurements are in good agreement to the R-Test measurements and the CMM measurements of the thermal test piece. Solely in the cool down phase the curves slightly differ, influences of geometric errors of the C2-axis can account for these dissimilarities. The difference of the R-Test and test piece measurements in  $E_y$  can be explained by the position depended thermal errors of the rotary axis, as explained by Wiessner *et al.* [11]. For better comparison errors  $E_{ROT}$  and  $E_{TTP}$ , in Figure 4 d), the reconstructed temperature change is



depicted. This temperature can be calculated by material constants of machine table and test piece together with radial position of the measured data points, according to [11]. It is a fact that especially on large workpieces with large thermal material expansion coefficients the temperature change of the work-piece has a significant impact and cannot be neglected. The environmental temperature is measured during the procedures and shown in Figure 4 d). The temperature is stable around  $23^{\circ} \pm 1^{\circ}\text{C}$  and an influence of those temperature variations on the length measurements cannot be observed.

The OM measurements on machine tool B/C, seen in Figure 5, are as well in good agreement compared to the results of the CMM measurements of the thermal test piece. As a consequence of the thermally symmetric design of machine tool B/C the deviations in X-axis direction are negligible small. This can be seen in the measurements of  $E_X$  in Figure 5 a). The changes in the environmental temperature are higher as for machine tool A/C but as a result of the two efficient cooling circuits, these effects are not observably influencing the thermal errors. The general agreement between CMM and OM measurements is due to the fact that the design of the test piece minimized the influence of the geometrical errors from the machine tool.

In addition to the errors shown in Figure 4 and Figure 5,  $E_B$  was analysed for machine tool A/C, seen in Figure 3. As a result of the thermal test piece diameter of 200 mm the measurement uncertainty of  $E_B$  is rather big. Nevertheless a clear trend is visible and the results of the OM measurements are in agreement with the R-Test measurements.

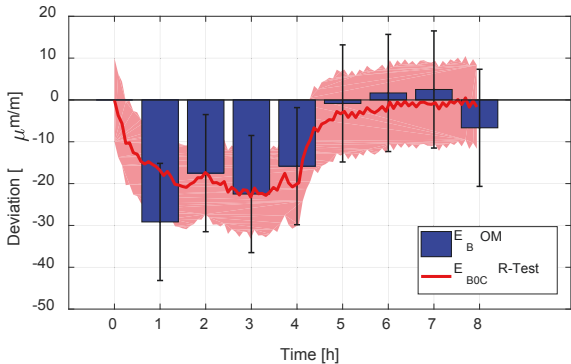


Fig. 3. Error  $E_B$  on machine tool A/C, the measurement uncertainty is illustrated by the light red surface and the error bars respectively

The evaluation of machine tool B/C revealed a thermally stable behaviour in B-direction, therefore measurements are not shown.

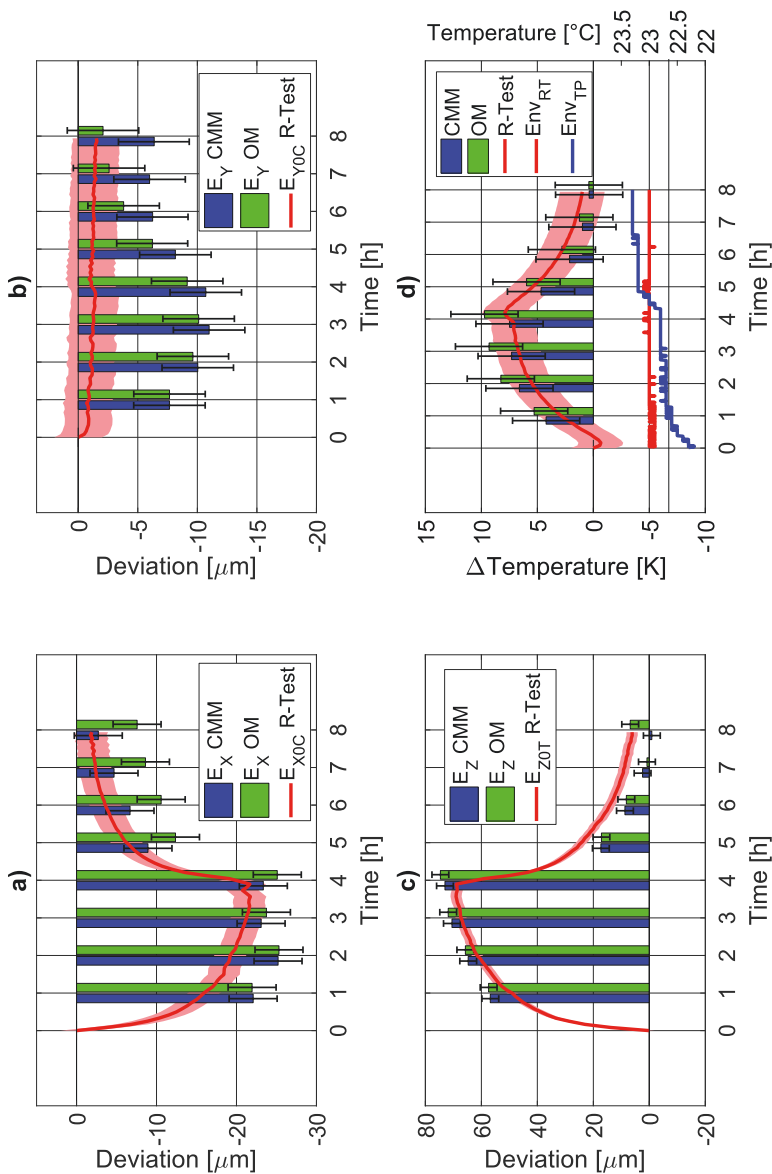


Fig. 4. Evaluation of machine tool A/C with test piece and R-Test: (a) Thermal error  $E_x$  (b) Thermal error  $E_y$  (c) Thermal error  $E_z$  (d) Temperature change of the test piece (OM and CMM) as well as the machine table (R-Test). The measurement uncertainty is illustrated by the light red surface and the error bars respectively. Additionally the environmental temperature is illustrated in (d). CMM and R-Test measurements are published in [11]

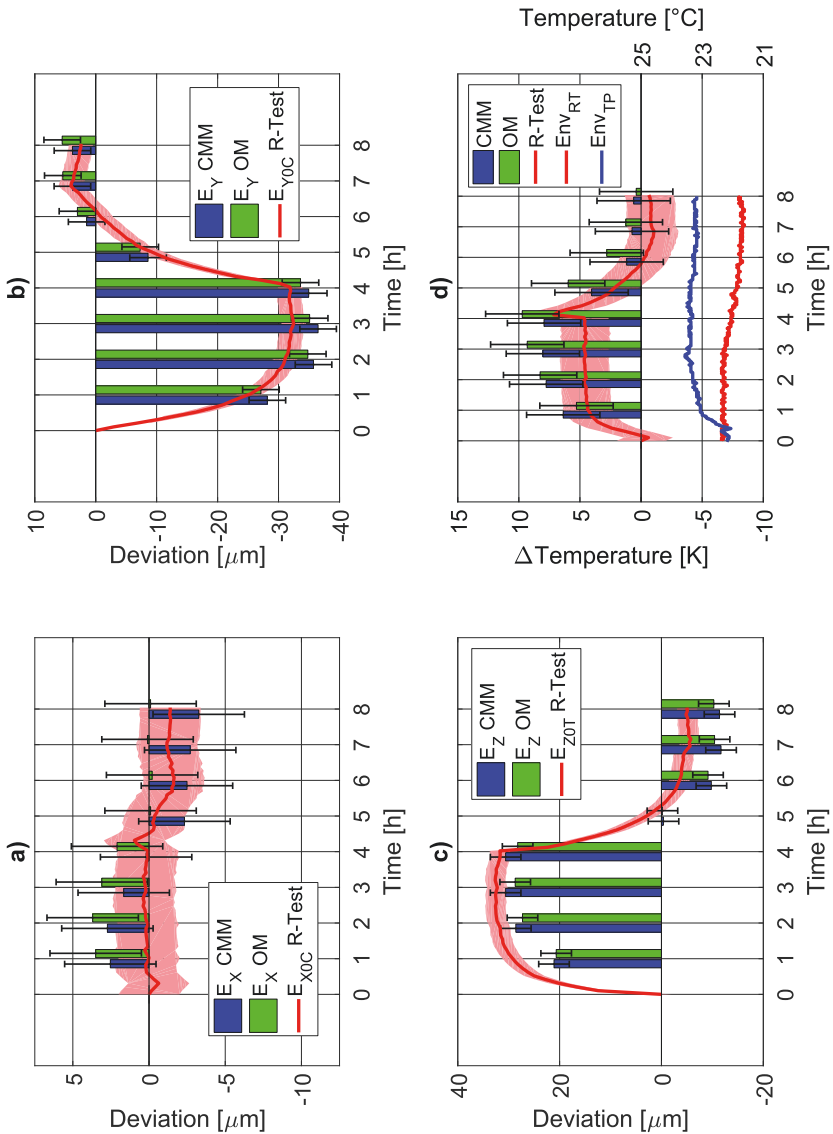


Fig. 5. Evaluation of machine tool B/C with test piece and R-Test: (a) Thermal error  $E_x$  (b) Thermal error  $E_y$  (c) Thermal error  $E_z$  (d) Temperature change of the test piece (OM and CMM) as well as the machine table (R-Test). The measurement uncertainty is illustrated by the light red surface and the error bars respectively. Additionally the environmental temperature is illustrated in (d). CMM and R-Test measurements are published in [11]

## 4 Conclusion and Discussion

The results of R-Test, CMM and OM measurements are generally in good agreement with sufficient low measurement uncertainties. Only exception is the discrepancy between R-Test and test piece measurement results of  $E_Y$  for machine A/C Shown in Figure 4 b). An environmental temperature influence on the measurements could not be observed. The machine tool was before starting the observation several hours in NC-hold. Also an influence of the environmental temperature during the OM measurements cannot be observed. Subsequent facts can be stated:

- The proposed test piece can be measured by on machine measurement
- With an automatically tool and work piece changer a thermal analysis and compensation of a machine tool can be done completely autonomous, using an adequate adapter
- If the thermal error is dominant, even errors in B- respectively A-direction can be evaluated
- The thermal test piece still lacks of  $E_C$ , the facets are too small for a feasible analysis
- Machining and analyses of the test piece takes roughly 8 hours and 30 minutes with the chosen test cycle
- A feasible thermal analysis of machine tools is shown with the proposed thermal test piece and measuring methods for industry are presented, that enable the next step towards new standards in this field for evaluation of machine tool capabilities

### Acknowledgements

*The authors would like to thank the Machine Tool Technologies Research Foundation (MTTRF), the Swiss Federal Office for Professional Education and Technology (CTI), Heidenhain (Schweiz) AG and the Swiss National Science Foundation (SNSF) for their support.*

## 5 References

- [1] Mayr, J., Jedrzejewski, J., Uhlmann, E., Alkan Donmez, M., Knapp, W., et al., 2012, Thermal issues in machine tools, CIRP Annals - Manufacturing Technology, 61/2:771–791.
- [2] ISO 10791-10:2007, Test conditions for machining centres—Part 10: Evaluation of thermal distortions, International Organization for Standardization ISO, Geneva, Switzerland.
- [3] ISO 13041-8:2004, Test conditions for numerically controlled turning machines and

turning centres, Part 8: Evaluation of thermal distortions, International Organization for Standardization ISO, Geneva, Switzerland.

- [4] ISO 230-1:2012, Test code for machine tools — Part 1: Geometric accuracy of machines operating under no-load or quasi-static conditions, International Organization for Standardization ISO, Geneva, Switzerland.
- [5] ISO 10791-7:2014, Test Conditions for Machining Centers - Part 7: Accuracy of Finished Test Pieces, International Organization for Standardization ISO, Geneva, Switzerland.
- [6] NCG, 2005, NCG-Prüfwerkstück für die 5-Achs-Simultan-Fräsbearbeitung, [NCG test piece for 5-axis-simultaneous milling], NC-Gesellschaft.
- [7] VDI/NCG 5211:2013, Testing guidelines and testing workpieces for high speed cutting (HSC) - Milling machines and machining centers for the 5-axis simultaneous milling.
- [8] Ibaraki, S., Ota, Y., 2013, Error calibration for five-axis machine tools by on-the-machine measurement using a touch-trigger probe, *International Journal of Automation Technology*, 8/1:20–27.
- [9] Höfer, H., Wiemer, H., 2017, Generation of motion sequences for thermal load of machine tools, *Production Engineering*, 11/1:75–83.
- [10] Wiessner, M., Gebhardt, M., Knapp, W., Wegener, K., 2014, Test piece for visualization of thermally induced deviations on five-axis machine tools, in *euspen Special Interest Group Meeting: Thermal Issues*.
- [11] Wiessner, M., Blaser, P., Böhl, S., Mayr, J., Knapp, W., et al., Thermal test piece for 5-axis machine tools, “under review,” *Precision Engineering*.
- [12] ISO 230-3:2007, Test code for machine tools — Part 3 : Determination of thermal effects, International Organization for Standardization ISO, Geneva, Switzerland.
- [13] ISO 10791-2:2001, Test conditions for machining centres -- Part 2: Geometric tests for machines with vertical spindle or universal heads with vertical primary rotary axis (vertical Z-axis), International Organization for Standardization ISO, Geneva, Switzerland.
- [14] Blaser, P., Pavliček, F., Mori, K., Mayr, J., Weikert, S., et al., 2017, Adaptive Learning Control for Thermal Error Compensation of 5-Axis Machine Tools, *Journal of Manufacturing Systems*.
- [15] ISO 10360-2:2009, Geometrical product specifications (GPS) — Acceptance and reverification tests for coordinate measuring machines (CMM) — Part 2: CMMs used for measuring linear dimensions, International Organization for Standardization ISO, Geneva, Switzerland.
- [16] Ibaraki, S., Knapp, W., 2012, Indirect measurement of volumetric accuracy for three-axis and five-axis machine tools: A review, *International Journal of Automation Technology*, 6/2:110–124.
- [17] Gebhardt, M., 2014, Thermal behaviour and compensation of rotary axes in 5-axis machine tools, *Diss ETH Zurich*.